Ultrasound responsive microbubbles for the targeted treatment of thrombotic diseases

Louise Fournier

▶ **To cite this version:**

Louise Fournier. Ultrasound responsive microbubbles for the targeted treatment of thrombotic diseases. Chemical Sciences. Université Paris Cité, 2023. English. NNT : 2023UNIP5040 . tel-04607283

HAL Id: tel-04607283
https://theses.hal.science/tel-04607283

Submitted on 10 Jun 2024

HAL is a multi-disciplinary open access archive for the deposit and dissemination of scientific research documents, whether they are published or not. The documents may come from teaching and research institutions in France or abroad, or from public or private research centers.

L'archive ouverte pluridisciplinaire **HAL**, est destinée au dépôt et à la diffusion de documents scientifiques de niveau recherche, publiés ou non, émanant des établissements d'enseignement et de recherche français ou étrangers, des laboratoires publics ou privés.

Université Paris Cité

Soumis en réponse à l'exigence du diplôme de :

DOCTEUR EN SCIENCE

Spécialité :
Interface Chimie-Biologie

ÉCOLE DOCTORALE MÉDICAMENT, TOXICOLOGIE, CHIMIE, IMAGERIES
(ED MTCI 563)

Ultrasound responsive microbubbles for the targeted treatment of thrombotic diseases

Par :
Louise FOURNIER

Supervisée par :
Dr. Cédric CHAUVIERRE
Laboratoire de Recherche Vasculaire Translationnelle, INSERM UMRS1148
Équipe 3 : Bio-ingénierie cardiovasculaire

Soutenue le 24 mars 2023 face au jury :

Dr. Lori BRIDAL, DR, Sorbonne Université	Rapporteur
Pr. Paolo DECUZZI, Senior Research Scientist, Istituto Italiano di Tecnologia, Genova	Rapporteur
Pr. Isabelle MARGAILL, PU, Université Paris Cité	Examinateur
Pr. Mikael MAZIGHI, PU-PH, Université Paris Cité	Examinateur
Pr. Chantal PICHON, PU, Université d'Orléans	Examinateur
Dr. Cédric CHAUVIERRE, DR, Université Paris Cité	Directeur de thèse

À **Leo**,
À **mes Parents** et ma **Famille**,
pour leur soutien infaillible qui a permis l'aboutissement de ce projet.

Acknowledgments

First, I wish to thank Dr. Lori Bridal and Pr. Paolo Decuzzi for agreeing to be reporter of this manuscript and assessing my work. I also acknowledge Pr. Isabelle Margaill, Pr. Mikael Mazighi and Pr. Chantal Pichon for their role as examinator and all of them for dedicating their time to my PhD defense.

My most sincere gratitude goes toward my PhD supervisor, Dr. Cédric Chauvierre, for always supporting me and pushing me to be a better scientist. I can easily admit that his time dedication for his student and sincere empathy are some of the reasons why I have decided to start this PhD, after 5 months of internship. I couldn't have asked for a better supervision, providing me enough independence to manage my time, pushing me to present in front of hundreds of scientists but above all always having my back. His scientific expertise and social sympathy are a famous added value of the team that irradiate to everyone he meets.

I would also thanks Dr. Didier Letourneur, head of the LVTS laboratory and of the Team 3 "Cardiovascular Bioengineering" for having me in his laboratory for over 4 years and always enjoying scientific discussion around the famous 3rd floor candies. I am most grateful for his valuable outlook of my work, in addition with the opportunities to present in various international conferences.

I was very lucky to work in collaboration with two laboratories, internationally famous for their expertise in neurovascular research and US imaging. First the BB@C team in Cyceron (Caen, France) directed by Pr. Denis Vivien, thank you for having me multiples times in Caen and sharing your expertise. I sincerely thank Pr. Cyrille Orset for his availability and his belief in the project. It was a real pleasure to collaborate with him and always have a pleasant working environment. I would also like to put forward Myriam Abioui-Mourgues, PhD student in the BB@C team, who performed all the *in vivo* experiment. Second author on my result publication, she performed an outstanding work, with motivation and rigor, it was a pleasure developing this method with her and learning from her expertise. In second, I thank the Laboratoire d'Imagerie Biomedicale (LIB) in Paris, the Physiologie and Pathologie de la Microcirculation team (PPM) and their director Dr. Olivier Couture. His involvement since the early days of the project had a key role in the maturation of my PhD project. I kindly thank him for sharing his expertise and providing interesting perspectives to my work. I express my gratitude to Dr. Georges Chabouh, Post-Doc of the LIB, for helping me breaking the frontier between physicists

and biologists and I thank him for is dedication to the project, his constant motivation to perform innovative research and kind encouragements.

I am truly grateful to all the members of our LVTS team for their support, mutual assistance and fun moments all along the three years of my PhD. I especially thank Rachid Aid for teaching me most of the characterization technics that she transmits to new team members with patience and dedication. It is my pleasure to warmly thank Dr. Teresa Simon Yarza and Dr. Graciela Pavon David for the nice talks and scientific discussions. I thank the former LVTS members, Dr. Camille Le Guilcher, Dr. Soraya Lanouar, Dr. Paola Aprile, and Dr. Alessandra Dellaquila for sharing their experience and insights of the research field and improving my work organization and critical analysis. I was very fortunate to be able to look up to strong and determined women of the scientific community. I also acknowledge the current young researchers' team with Dr. Chau Le Bao, Chloé Dujardin, Thibault de La Taille, Pierre Sarfati, Eliott Lopez and Dr Mathilde Maillard for their friendly advices and for bringing light-heartedness to the laboratory. I sincerely thank Dr. Véronique Ollivier and Stéphane Loyau for their encouragements and for sharing their knowledge in coagulation processes, Pr. Frédéric Chaubet and Murielle Maire for their kind assistance and expertise in polymer chemistry. I warmly acknowledge the futures doctors that accompanied me from my early intern position, Rodolphe Migneret, Ophélie Le Chapelin, Célina Madjene and Zakaria Mougin for sharing your doubts, success and failures. I am especially grateful that this project allowed me to meet my dear friend Zakaria Mougin, I am looking forward to following his brilliant carrier and I will miss our entertaining talks in the office.

I can't thank enough my parents for giving me the chance to perform this long academic journey, their unconditional love and their forever support. I warmly thank my friends and family for always calling when I needed it and being my best supporting team. Finally, I address my most affectionate gratitude to my boyfriend, Leo, for his love, his patience and for always giving the strength to move forward.

« On ne fait jamais attention à ce qui a été fait ; on ne voit que ce qui reste à faire. »

Marie Curie

Table of content

Acknowledgments ***2***

Table of content ***6***

Abbreviations ***8***

List of figures ***9***

List of tables ***10***

General introduction and project presentation ***12***

Chapter I: Introduction ***18***

Part 1: The global burden of thrombotic diseases **20**

Pathophysiology of arterial and venous thrombosis 21

Clinical treatment of acute thrombotic diseases 25

Encapsulation of fibrinolytics, the rise of nanomedicine 27

Part 2: Microbubbles **31**

Microbubbles characterization 31

Microbubbles for imaging 42

Microbubbles for therapy 49

New scales and technology 64

Chapter II: Experimental results ***78***

Part 1: Microbubbles synthesis optimization **80**

Cyanoacrylate polymerization 80

The targeting polysaccharide: Fucoidan 82

Polymer MBs hydrodynamic cavitation 82

Acoustic cavitation 83

Patent definition 88

Part 2: rtPA-loaded fucoidan MBs for the targeted treatment of stroke **93**

Introduction 94

Materials and methods 97

Results and discussion 106

Conclusion 118

Supplementary data 120

Part 3: What we explored but need to optimize **124**

Fucoidan and drug incorporation 124

In vivo targeting 127

Freeze drying 129

Sonothrombolysis 131

Chapter III: Discussion and Perspectives ***138***

General conclusion ***150***

Résumé substantiel en français ***154***

References ***160***

Abstract ***196***

Résumé ***198***

Annexes ***200***

Abbreviations

3T3: Fibroblasts	HAS: Human serum albumin	PFB: Perfluorobutane
AFM: Atomic Force Microscopy	HUVEC: Human umbilical vein endothelial cell	PFC: Perfluorocarbon
ARF: Acoustic Radiation Force	IP: Isoelectric point	PFD: Perfluorodecalin
BBB: Blood-brain barrier	IS: Ischemic Stroke	PFOB: Perfluoro-octyl-Bromide
BCA: Bicinchoninic Acid Assay	JAM-A: Junctional Adhesion Molecule A	PFOC: Perfluorocarbon-based Oxygen Carrier
BSA: Bovine serum albumin	KDR: Kinase Insert Domain	PIBCA: Poly-Isobutyl Cyanoacrylate
BT: Brachytherapy	LDH: Lactate Dehydrogenase	PLGA: Poly(lactic-co-glycolic acid)
CMDex: Carboxymethyl Dextran	LDL: Low-Density Lipoproteins	PRF: Pulse Repetition Frequency
CNS: Central Nervous System	LPS: Lipopolysaccharide	PSF: Point Spread Function
CO: Carbon Monoxide	mAb: Monoclonal antibodies	PSGL-1: P-selectin glycoprotein ligand-1
CORM: Carbon Monoxide Releasing Molecule	MB: Microbubble	PVP: Polyvinyl pyrrolidone
CT: Computed Tomography	MCA: Middle cerebral artery	RBC: Red blood cell
CVD: Cardiovascular diseases	MCP-1: Monocyte Chemoattractant Protein-1	RES: Reticuloendothelial System
DBCO: Dibenzocyclooctyne-amine	MI: Mechanical Index	RF: Resonance Frequency
DMEM: Dulbecco's Modified Eagle Medium	MI: Myocardial Infarction	ROI: Region Of Interest
DSPC: (1,2-distearoyl-sn-glycero-3-phosphocholine)	MMP: Matrix metallo-proteinases	ROS: Reactive Oxygen Species
DSPE-PEG2000: (1, 2-distearoyl-sn-glycero-3-phosphoethanolamine-N- [amino (polyethylene glycol)-2000])	MRI: Magnetic Resonance Imaging	rtPA: recombinant tissue Plasminogen Activator
DVT: Deep Vein Thrombosis	MT: Mechanical thrombectomy	SD: Standard Deviation
EDC / NHS: 1-Ethyl-3-(3-dimethylaminopropyl) carbodiimide / N-Hydroxy succinimide	MTT: 3-(4,5-dimethyl-2thiazolyl)-2,5-diphenyl-2H-tetrazolium bromide	SH: Subharmonic
EGR-1: Early Growth Response 1	MW: Molecular weight	SK: Streptokinase
EPR: Enhanced Permeability and Retention	NB: Nanobubble	sLex: Sialyl Lewis X peptide
ESEM: Environmental Scanning Electron Microscopy	NCL: Nucleolin	SPAAC: Strain Promoted Alkyne-Azide Cycloaddition
FDA: U.S. Food and Drug Administration	ND: Nanodroplet	STAT3: Signal Transducer and Activation of Transcription 3
FIB: Focused Ion Beam	NET: Neutrophil Extracellular Trap	STORM Stochastic Optical Reconstruction Microscopy
FSHR: Follicle Stimulating Hormone Receptor	NIR: Near Infrared	TCCS: Transcranial Color Doppler Ultrasound
FTIR: Fourier-Transform InfraRed spectroscopy	NO: Nitric Oxide	Thyc1: Thymocyte Antigen 1
FUS: Focused Ultrasound	NP: Nanoparticle	ULM: Ultrasound Localized Microscopy
fUSI: Functional Ultrasound Imaging	NPMB: Nanoparticles assembled as Microbubble	uPA: Urokinase
GA: Gadoteric Acid	PA: Plasminogen Activators	US: Ultrasound
GMP: Good Manufacturing Practice	PAI-1: Plasminogen Activator Inhibitor-1	VCAM1: Vascular Cell Adhesion Molecule 1
GV: Gas Vesicle	PALM: Photoactivated Localization Microscopy	VEGFR2: Vascular Endothelial Growth Factor Receptor 2
HA: Hyaluronic Acid	PBS: Phosphate Buffer Saline	VT: Venous Thrombosis
HDL: High-Density Lipoproteins	PCCA: Phase Change Contrast Agent	VWF: Von Willebrand Factor
HGN: Hallow Gold Nanoshell	PEG: Polyethylene Glycol	WB: Working Buffer
HIF-1: Hypoxia-Inducible Factor-1	PET: Positron Emission Tomography	WHB: Whole Human Blood
HIFU: High Intensity Focused Ultrasound	PFA: Paraformaldehyde	WHO: World Health Organization

List of figures

Figure 1: Schematic of thrombotic diseases. 21

Figure 2: Comparison of the arterial and venous thrombosis. 24

Figure 3: Methods for Microbubbles synthesis 33

Figure 4: Microbubbles behavior with their environment and under US insonation 46

Figure 5: Therapeutic strategies for tumors, thrombi, infection and Blood-Brain-Barrier 54

Figure 6: MBs and US insonation for sonothrombolysis and Blood Brain Barrier permeability. 62

Figure 7: MBs and US insonation for sonobactericide and tumor growth control. 63

Figure 8: New scales of US sensitive objects 70

Figure 9: Two major applications of Ultrafast Ultrasound imaging 73

Figure 10: Anionic copolymerization of cyanoacrylate and polysaccharides 81

Figure 11: Batch yield production depending on the energy of cavitation and the incorporated gas 85

Figure 12: Influence of the temperature on the production of polymer MBs with acoustic cavitation 87

Figure 13: Graphical abstract of functionalized MBs for the treatment of stroke. 96

Figure 14: Functionalized polymer MBs characterization. 107

Figure 15: Echogenicity characterization of MBs 109

Figure 16: Functionalization of MBs. 111

Figure 17: Biocompatibility study of Fuco MBs on different cell types 113

Figure 18: *In vivo* stroke model study on mice comparing rtPA-loaded Fuco MBs treatment to systemic injection of rtPA 115

Figure 19: Biodistribution of fluorescent MBs and MBs residues in mice. 117

Figure 20: Approximation of Fuco MBs maximum loading capacity of rtPA. 125

Figure 21: Comparison of EDC NHS covalent bounding to adsorption of rtPA 126

Figure 22: *In vivo* targeting of Fuco MBs compared to CMDex MBs on ferric chloride thrombotic model 128

Figure 23: Freeze drying experiment on Rhodamine B MBs 130

Figure 24: Sonothrombolysis precept for enhanced thrombolysis 131

Figure 25: *In vitro* validation of MBs inertial cavitation.. 133

Figure 26: *In vivo* sonothrombolysis 134

Figure 27: Illustration résumée du projet 159

Supplementary Figure 1: MBs size distribution and surface charge. 120

Supplementary Figure 2: Fucoidan quantification with methylene blue colorimetric assay sulfate specific. 120

Supplementary Figure 3: MBs shell thickness characterization. 121

Supplementary Figure 4: Fibrinolytic activity of rtPA-loaded MBs with fibrin gel degradation evaluation.. 121

Supplementary Figure 5: Microscopy images of fibroblasts and endothelial cells after MTT assay. 122

Supplementary Figure 6: Full MRI scan of mouse brain. 122

Supplementary Figure 7: FTIR spectra 123

List of tables

Table 1: Thrombolytic agents approved by the FDA. 25

Table 2: Different nanocarriers for thrombolytic therapy 27

Table 3: Non exhaustive list of targeting ultrasound responsive strategies for molecular imaging since 2015. 48

Table 4: Synergic therapies of MBs associated with US and drug for thrombosis and cancer. 59

Table 5: Advantages and limitations of recent contrast agent innovations, based on their imaging, capabilities, circulation properties and tissue penetration. 69

Table 6: Fixed parameters inspired by established hydrodynamic cavitation synthesis for polymer MBs 84

Table 7: Parameters differences between standard hydrodynamic cavitation and original acoustic cavitation. 87

General introduction and project presentation

Cardiovascular diseases are a global burden of contemporary humankind. Described as the first cause of mortality and disability, it is a medical priority with the global aging of the world population. Among the various pathologies related to the cardiovascular system, our group focused on thrombotic diseases. They are the consequence of the pathological formation of a blood clot due to deregulation in the hemostatic system and/or atherosclerotic disease. Indeed, blood equilibrium is a fine balance governed by chemical, biological and mechanical factors. In physiological conditions, blood clots are essential for maintaining the vessel's integrity and protect from foreign body contamination. Nevertheless, this biological barrier is highly reactive and small disturbances including genetic factors, sedentary life style, smoking habit or fat diet can lead to dramatic consequences. Thrombi are mainly composed of fibrin mesh entrapping erythrocytes, activated platelets and circulating inflammatory cells, and either form in the veins or in the arteries. In both cases the major risk is the occlusion of vessels caused by thrombus travelling to the lungs (pulmonary embolism), small vessels in the heart (myocardial infarction) and brain (stroke).

The gold standard thrombolysis therapy relies on the injection of recombinant Tissue Plasminogen Activator (rtPA) that will activate plasminogen into plasmin, the major fibrinolytic protease. Hence, plasmin will disassemble the cross-linked fibrin into Fibrin Degradation Products (FDP) and free the entrapped cells. Current systemic injection of thrombolytic treatment for ischemic stroke can only be operated under 4.5 hours post event because of the possibility of hemorrhagic transformation. In addition, thrombolytic injection can be accompanied by endovascular catheter removal thrombectomy with the added possibility of surgical complication like bleeding. Injected systemically, rtPA has a relatively short half-life (around 4 minutes) due to the presence of its natural inhibitor (PAI-1) and the liver detoxification. In consequence, the drug is injected at a high concentration (0.9 mg/kg body weight) implying dose related side effects such as neurotoxicity and hemorrhagic transformation of the event. **Overall, the major unmet medical need for the treatment of thrombotic diseases is a more efficient, more specific therapy reducing the life-threatening side effects**.

This problematic was the primary goal of this PhD work, to explore a new strategy for the encapsulation and the targeted delivery of a thrombolytic drug. Previous work from the laboratory validated the targeted delivery of rtPA with polymer or polysaccharide nanoparticles showing promising results. The group also explored new carriers such as microcapsules and microbubbles. The advantage of these micro sized objects is their versatility for US imaging and potential for mechanical disruption of clot with sonothrombolysis.

In that context, **this PhD work aimed to validate the efficient treatment of thrombotic diseases with rtPA loaded targeting Microbubbles (MBs).**

This PhD manuscript is divided in three chapters: I) Introduction, II) Experimental results and III) Discussion and Perspectives.

The introduction chapter is composed of two parts: the first one is adapted from the literature review published in 2020 in *Biomaterials* written in collaboration with Alina Zenych (former PhD student). It presents the context of thrombotic diseases, the major available treatments and unmet medical needs. The second part of the introduction is adapted from the recent literature review published online in January 2023 in *Biomaterials* that I wrote with Thibault de La Taille (PhD student). This part describes the use of microbubbles for human diagnosis and treatment, giving an overview of their physicochemical properties and highlighting the various applications for which they have been studied.

Thereafter, the second chapter presents the methods and results of the experimental work. The first part of this second chapter, focused on the first year of this PhD project that consisted in the optimization and the development of the acoustic cavitation protocol for MBs synthesis. Helped with the laboratory expertise for cyanoacrylate polymerization, a new method for MBs synthesis has been developed, using ultrasound as cavitation initiator instated of standard rotational helix. This original method reduced the synthesis time by three and a patent request to the European patent office was filed in February 2022 (PCT/FR2022/050309). The second part of this experimental chapter is adapted from the article submitted in January 2023 to *Biomaterials* (with Editor), demonstrating the main results for the efficient treatment of stroke in a preclinical study. The polymer MBs were functionalized with fucoidan, known for its nanomolar specificity for P-selectins and loaded with the fibrinolytic agent. The physicochemical and biocompatible properties were validated in order to perform the *in vivo* ischemic stroke model in mice. Briefly, the functionalized MBs demonstrated high brain injury reduction at lower thrombolytic dose compared to gold standard treatment, and promising perspective for thrombotic event follow-ups. Finally, this chapter is completed by an overview of the on-going experiments that were not ready for publishing but which bring stimulating insights for future objectives and publications.

The last Chapter is the overall discussion of this PhD project, highlighting the major results as well as the obstacles that we faced during these three and a half years. It deals with the achievements of these targeted MBs as thrombolytic agents but also their potential for molecular diagnosis and applications for other pathologies.

Chapter I: Introduction

Part 1: The global burden of thrombotic diseases

Adapted from:
A. Zenych, L. Fournier and C. Chauvierre, "Nanomedicine progress in thrombolytic therapy". *Biomaterials*, vol. 258, no.120297, August 2020. (Annex 1)

Cardiovascular diseases (CVD), the major global health threat, are associated with high morbidity and mortality that account for an estimated 17.9 million lives each year (31% of all deaths worldwide) [1], and this figure is expected to rise to >23.6 million annual deaths by 2030 [2]. CVD are a group of disorders of the heart (e.g., heart failure, rheumatic heart disease, abnormal heart rhythms, inflammatory heart diseases, cardiomyopathy) and blood vessels (coronary artery disease, cerebrovascular disease, aortic aneurysms, peripheral artery disease, etc.). CVD affect almost equally men as women, however, the disease develops about seven to ten years later in women as compared to men [3]. Furthermore, CVD are associated with substantial health-care costs, which are estimated at $329.7 billion annually in the United States [2] and nearly €200 billion in the European Union [4].

A large number of CVD may be prevented by addressing major risk factors through lifestyle interventions and pharmaceutical treatment where necessary [1]. Nevertheless, hypertension, the leading cardiovascular risk factor, is attributed to ~13% of global deaths (7.5 million deaths), followed by tobacco use 9%, diabetes 6%, physical inactivity 6%, obesity 5%, and high cholesterol level 4.5% [3].

Three major cardiovascular disorders – myocardial infarction (heart attack), ischemic stroke, and venous thromboembolism defined as deep vein thrombosis and/or pulmonary embolism – are severe complications of thrombosis, the formation of a blood clot in the vessels (*Fig. 1*).Within all deaths from CVD, 85% are caused by heart attacks and strokes, one-third of them in people under the age of 70 years [1]. To improve human survival and quality of life, early detections and effective treatments are principal.

Thrombolytic drugs are administered to dissolve a thrombus and restore the blood flow in acute thrombotic events, however, they are rapidly inactivated in the blood and trigger hemorrhagic complications, as we explain below. Paradoxically, while rapid reperfusion is the standard of care to minimize the infarct size, the restoration of blood flow itself may provoke irreversible tissue damage in a process called reperfusion injury [5]. Therefore, the pursuit of innovative solutions for the management of thrombotic diseases remains an open field of

research, where nanomedicine is emerging to be a promising strategy to improve both the efficacy and safety of thrombolytic therapy.

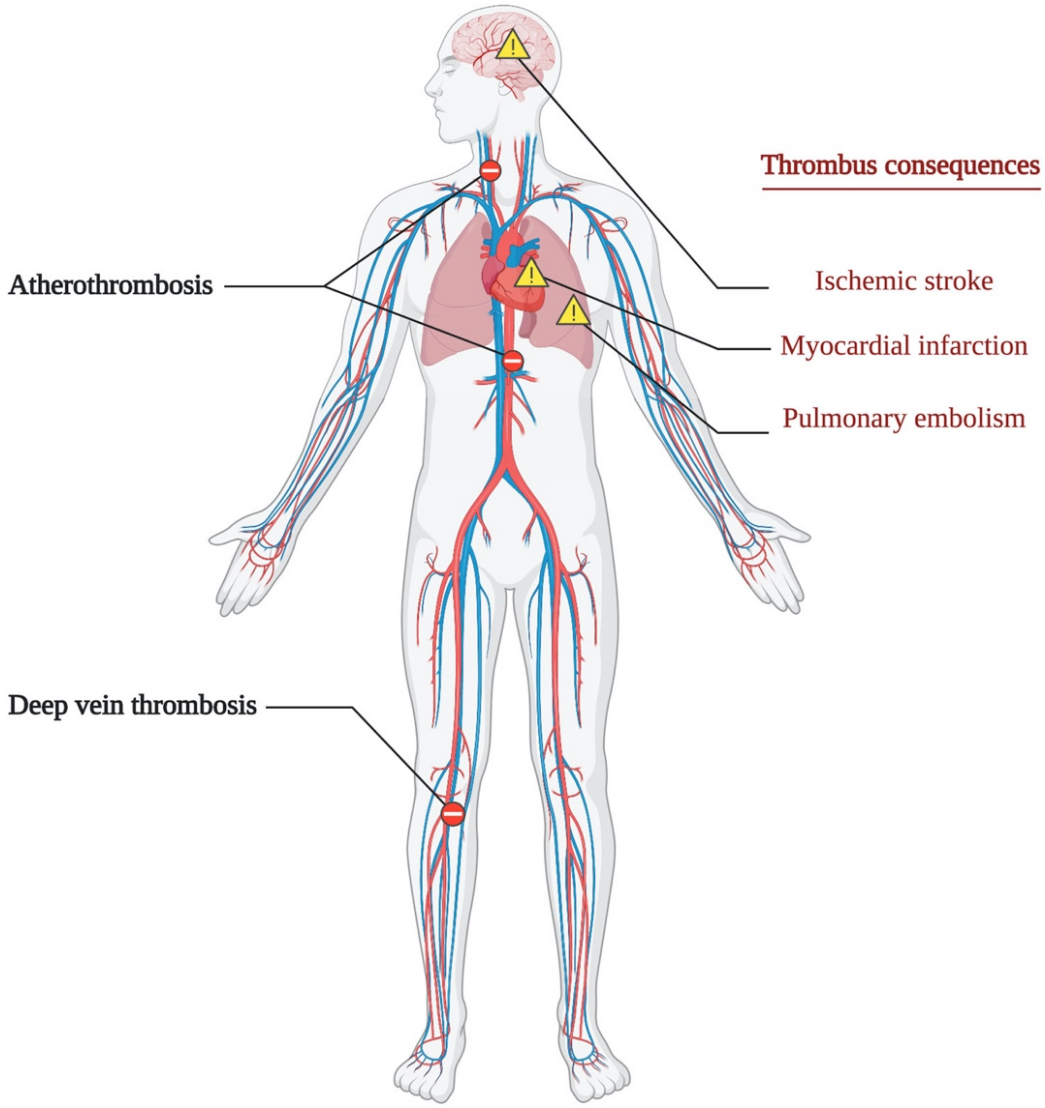

Figure 1: Schematic of thrombotic diseases. *Blot clot formation both in arteries (atherothrombosis) and veins (deep vein thrombosis) are influenced by congenital diseases and environmental factors. When the clot detaches from their initial location, it may obstruct blood vessels and induce life-threatening consequences such as stroke, pulmonary embolism, or myocardial infarction.*

Pathophysiology of arterial and venous thrombosis

- **Arterial thrombosis: Atherosclerosis**

Atherosclerosis is the key precursor of cardiovascular pathologies and it starts in adolescence. Atherosclerosis is a complex immune-inflammatory disorder whose progression involves multiple biological pathways that are influenced by genetic and environmental factors. Elevated plasma cholesterol level, hypertension, diabetes, tobacco smoking, male gender, and some inflammatory markers are among the proatherogenic risk factors of atherosclerosis, while

physical exercise, a healthy diet, and high High-Density Lipoproteins (HDL) counts have an atheroprotective role [6].

Atherosclerotic lesions are initiated when the endothelium is activated by atherogenic and pro-inflammatory stimuli, such as primarily Vascular Cell Adhesion Molecule-1 (VCAM-1), intercellular adhesion molecule-1, E-selectin, and P-selectin [7]. It has been demonstrated a direct hemodynamic role in atherogenesis, notably by endothelial cells as their numerous signaling pathways are dependent on the hemodynamic patterns [8], [9]. Low shear stress and turbulent flow at arterial curvature and branch points are major drivers of plaque development and instability. Plasma molecules and Low-Density Lipoproteins (LDL) penetrate dysfunctional endothelium into the subendothelial space where atherogenic lipoproteins are oxidized, mediated by myeloperoxidase, 15-lipoxygenase, and/or Nitric Oxide Synthase (NOS) [7]. Low-grade inflammation contributes to the disease progression due to the focal recruitment of circulating monocytes and T-lymphocytes [10]. Modulated by chemotactic cytokines, such as oxidized LDL and Monocyte Chemoattractant Protein-1 (MCP-1) [11], monocytes infiltrate arterial intima through transendothelial migration and differentiate into macrophages by internalizing the atherogenic lipoproteins via scavenger receptors. The incidence of the foam cells (lipid-laden macrophages) and their death by apoptosis and necrosis contribute to the formation of destabilizing atheromatous lipid-rich core within the plaque. Moreover, the foam cells express an array of inflammatory factors and produce proteolytic enzymes, such as Matrix MetalloProteinases (MMPs) [11], that are implicated in matrix degradation and plaque disruption [12]. To insulate the thrombogenic lipid-rich core of the atheroma from the bloodstream, the fibrous cap develops at the lesion site as a fibroproliferative response mediated by intimal smooth muscle cells. The recruitment of the smooth muscle cells and the production of the collagen-rich matrix are considered as beneficial since they protect the plaques against rupture and subsequent thrombosis. Conversely, the disintegration of foam cells and loss of smooth muscle cells may have detrimental consequences, leading to the formation of a destabilizing lipid-rich core and a fragile and rupture-prone fibrous cap. Atherosclerotic plaque calcification is an inflammation-driven process that manifests in all stages of the disease and should be defined as a two-phase process: microcalcification, the early stage of intimal calcium formation, and the end-stage of macrocalcification. While coronary Computed Tomography (CT)-detected macroscopic calcification in artery plaque acts as a biomarker of the overall disease progression, it is believed to stabilize the plaque and prevent acute events [13]. On the contrary, microcalcification, which can be identified by Positron Emission Tomography (PET)/CT imaging with ^{18}F-sodium fluoride, is associated with plaque vulnerability and an

increased risk of rupture since it aggravates plaque inflammation and augments mechanical stress in the fibrous cap [14].

Injury of the fibrous cap of atherosclerotic plaque is a primary trigger for arterial thrombosis, promoting hemorrhage and luminal pro-thrombotic response [15]. For initial flow obstruction, the blood coagulation cascade activates the platelets that are rapidly recruited to the site and aggregate, resulting in rapid thrombus growth [16] (*Fig. 2A*). Fibrin network then develops for the stabilization of platelet-rich thrombosis. Although most episodes of the ruptured fibrous cap occur silently without clinical symptoms, plague rupture with subsequent thrombosis often culminates in devastating clinical events such as myocardial infarction (MI) or ischemic stroke [15].

- **Venous Thrombosis**

Contrary to atherothrombosis, the pathogenesis of Venous Thrombosis (VT) is only partially understood. The main components of the venous thrombi are fibrin and erythrocytes, and less activated platelets [17] (*Fig. 2B*). VT is initiated at the venous valves where stasis may occur under low shear blood flow [18]. Valvular sinus stasis aggravates hypoxia, promoting activation of the endothelium and leukocytes via mainly Hypoxia-Inducible Factor-1 (HIF-1) and Early Growth Response 1 (EGR-1) pathways. Besides, hypoxia condition modulates hypercoagulability. HIF-1 and EGR-1 pathways up-regulate the expression of P-selectin on endothelium, prompting monocytes to release microvesicles bearing tissue factor, which initiates thrombin production and fibrin deposition around the intact endothelial wall [19]. Both inherited and environmental factors raise the likelihood of the occurrence of venous thrombotic diseases such as an imbalance of pro- vs. anti-coagulation proteins, as well as cancer, obesity, and major surgery [16].

For either arterial or venous thrombosis, blood clot formation can be the consequence of any of the Virchow's Triad factor that includes, endothelial disfunction, flow stasis or hypercoagulability [20]. Overall the major life threatening consequence is the obstruction of vessels either on the location of the clot formation or on distal vessels after detachment and travelling of this last.

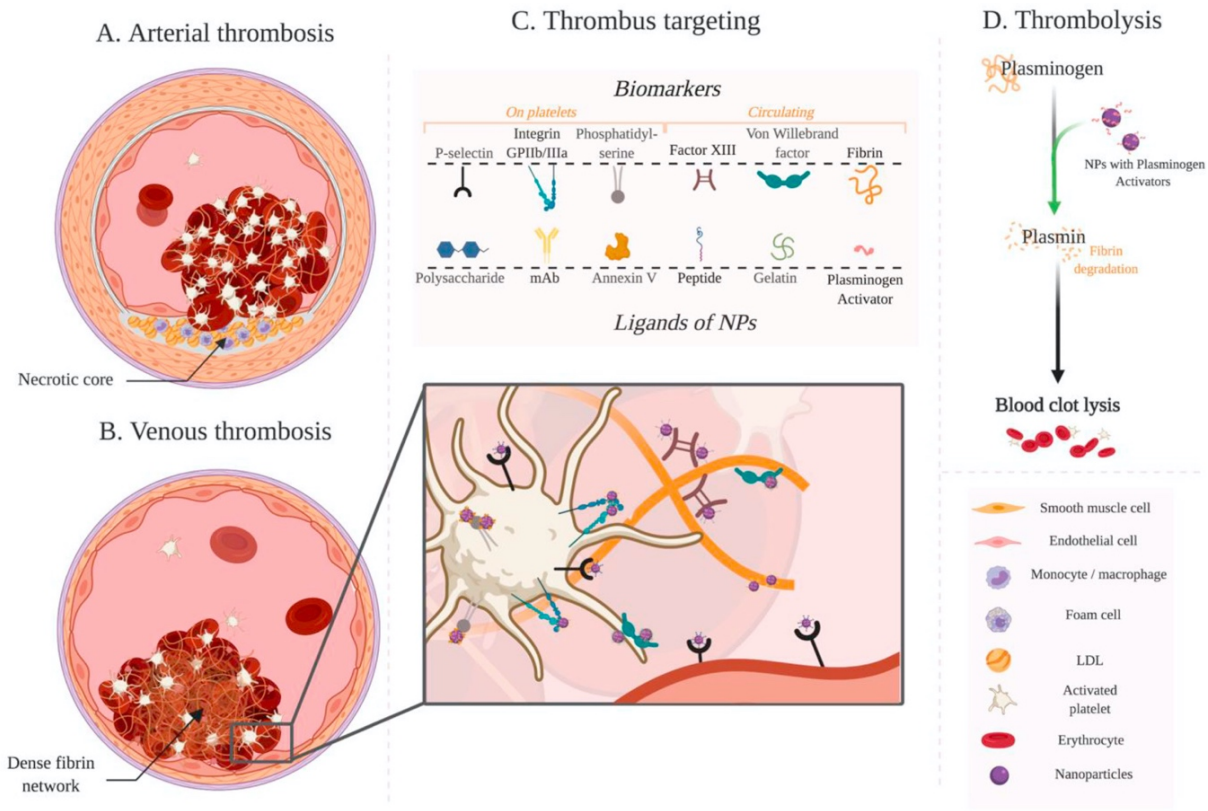

Figure 2: Comparison of the arterial and venous thrombosis. *Arterial clots (A) are composed of a high platelet ratio and are so-called "white thrombi". They are mostly the result of atherosclerosis. Multiple cellular pathways that initiate the activation of the endothelial cells are involved in thrombus formation. LDL penetrate the tissue, causing local inflammation and recruitment of circulating inflammatory cells. The disruption of the atherosclerotic plaque triggers the recruitment of smooth muscle cells to prevent wall rupture. Eventually, platelets aggregate on the impaired vessel wall with a consecutive formation of a fibrin network. On the other hand, venous clots (B), "red thrombi", contain erythrocytes and a denser fibrin network with fewer platelets. The thrombus formation is responsive to the following triggers: a vessel wall injury, a stasis of the blood flow, and hypercoagulability of the blood.* ***C.*** *Thrombus targeting with functionalized nano- / microparticles. Thrombi express a variety of cellular and molecular components – the surface of activated platelets (P-selectin, integrin GPIIb/IIIa, phosphatidylserine) or circulating proteins (Factor XIII, vWF, or fibrin) – that can be employed for specific targeting. NPs are designed with different ligands to these biomarkers: polysaccharide fucoidan, peptides, monoclonal antibodies, etc.* ***D.*** *Thrombolysis with PA-bearing and targeted to the thrombi NPs. The PA convert plasminogen into plasmin that breaks down the fibrin network and releases the components of the blood clot.* ***Abbreviations****: LDL, low-density lipoproteins; vWF, von Willebrand factor; mAb, monoclonal antibodies; NPs, nanoparticles; PA, plasminogen activators.*

Clinical treatment of acute thrombotic diseases

- **Fibrinolytic drugs**

For the treatment of acute arterial or venous thrombotic events, fibrinolytic drugs can be administered in order to proteolytically disrupt blood clots and restore blood flow. Fibrinolytic, or thrombolytic, agents are Plasminogen Activators (PA) that activate the proenzyme plasminogen to plasmin that then cleaves fibrin network into soluble degradation products. This activation of the fibrinolytic system destabilizes the structure of a thrombus [21]. Thrombolytic therapy is thereby used in patients with such pathologies as acute MI, acute ischemic stroke, peripheral arterial disease, deep vein thrombosis, and massive pulmonary embolism [22].

U.S. Food and Drug Administration (FDA)-approved "clot busters" drugs for use in thrombotic diseases are recombinant-based plasminogen activators (e.g., Alteplase – rtPA, Reteplase – rPA, and Tenecteplase – TNK), Streptokinase (SK), and Urokinase (uPA). The main differences between them relate to their antigenicity, half-life, lytic potential, fibrin specificity, and hemorrhagic risks [23]. First-generation thrombolytic drugs (Urokinase, Streptokinase) are non-fibrin specific when second and third-generation (Alteplase and its variants) overcome this issue. Generally, human protein-derived PA (Urokinase, Alteplase, Reteplase, Tenecteplase) are nonantigenic, contrary to those derived from a bacterial species (Streptokinase) [24]. The half-life of each PA determines their mode of administration (a bolus injection, short infusion, or continuous intravenous infusion). A comparison of different FDA-approved PA with their clinical indications is summarized in *Table 1*.

***Table 1**: **Thrombolytic agents approved by the FDA**. **Abbreviations**: DVT, Deep Vein Thrombosis; MI, Myocardial Infarction, PAO, Peripheral Arterial Occlusion; PE, Pulmonary Embolism; IS, Ischemic Stroke; IU, International Units.*

Agent	Abbreviation	Source	Safety [immunogenicity, fibrin specificity]	Half-life, min	Regimen	Total Dose	Metabolism	Indication
			First-generation					
Streptokinase	SK	β-hemolytic streptococcus	Immunogenic Non-fibrin specific	20	Infusion	1.5×10^6 IU	Renal	PE Acute MI PAO, DVT
Urokinase	uPA	Human urine & kidney cell culture	Non-fibrin specific	15	Infusion	2.25-6.25 x 10^6 IU	Renal	PE Acute MI PAO, DVT
			Second-generation					
Alteplase	rtPA	Recombinant DNA technology	Fibrin specific (++)	4-8	Infusion	MI: 50-100 mg IS: 0.9 mg/kg PE: 100 mg	Hepatic	Acute MI Acute IS PE
			Third-generation					
Reteplase	rPA	Recombinant DNA technology	Fibrin specific (+)	14-18	Double bolus	20 IU	Renal	Acute MI PAO
Tenecteplase	TNK		Fibrin specific (+++)	11-20	Bolus	30-50 mg	Renal	Acute MI

The leading drawbacks of fibrinolytic therapy include treatment failures such as ineffectiveness, re-thrombosis as a result of a persistent vascular lesion and plasma hypercoagulability, and a high risk of bleeding complications, with intracerebral hemorrhages occurring in 1 to 7% of treated patients [22]. Moreover, PA are physiologically inhibited by Plasminogen Activator Inhibitors (PAI) such as PAI-1 and PAI-2 while alpha 2-antiplasmin and alpha 2-macroglobulin inactivate plasmin, thereby reducing the treatment efficacy [25]. In view of these limitations, the constant development of novel molecules aims to address the problems associated with available thrombolytics.

- **Mechanical Thrombectomy**

The association of thrombolytic drugs with endovascular methods significantly improved interventional management of acute thrombotic events. The percutaneous coronary intervention has become more common for reperfusion, improving survival rates in patients with myocardial infarction [26], [27]. When available, this catheter-based procedure that is performed by an interventional cardiologist has to be offered promptly after / or in place of initial thrombolytic therapy. Since 2015, mechanical thrombectomy (MT) using a stent retriever is recommended as a complementary treatment to fibrinolytic therapy for ischemic stroke related to large vessel occlusions in the anterior circulation such as in the internal carotid artery and proximal middle cerebral artery [28], [29] after multiple positive randomized control trials [30], [31]. Yet, since MT needs to be performed by a qualified neurointerventionist at comprehensive stroke centers, access to them often remains difficult. In France, in particular, out of 135 nationwide neurovascular centers, only 40 are capable of performing thrombectomy to date [32]. Therefore, there is still a dire need for a safe and non-invasive solution.

With the advent of the field of nanotechnology, there has been considerable interest in integrating nanomedicine and thrombolytic therapy for the treatment of acute thrombotic events. Nanomedical approaches for targeted fibrinolysis could advance clinical outcomes by improving current pharmaceutical methods when interventional catheter-based strategies are not available or not recommended (as, for example, in ischemic stroke due to occlusions in smaller vessels or posterior circulation). By acting locally at the thrombus site, there is a promise that nanomedicine-delivered “clot-busting” agents deliver superior recanalization rates and attenuate life-threatening bleeding complications associated with their intravenous

administration. One may also expect the chance to replace intravenous infusion by bolus injection of the first- and second-generation PA due to the extended drug half-life. In the ideal treatment settings, the synergic combination of endovascular and nanotherapeutic methods would represent a more precise approach to manage thrombotic pathologies.

Encapsulation of fibrinolytics, the rise of nanomedicine

The main goals for PA encapsulation include the protection from inactivation by PAI-1, the improvement in the blood half-life, the enhanced thrombolytic effect at a lower dose, the reduction in systemic bleeding and the reduction of post-ischemic infarct zone. Recent studies have demonstrated that nanocarriers, such as liposomes, polymeric or inorganic NPs, bio-inspired nanocarriers, and microbubbles, provide benefits for thrombolytic therapy either alone or in combination with ultrasound or magnetic force (*Table 2*). Among the numerous thrombolytic-bearing carriers that are tested in preclinical models, sonothrombolysis with lipid-based microbubbles and intravenous rtPA is already being validated in clinical trials with thrombolysis improvement.

Table 2: Different nanocarriers for thrombolytic therapy

Nanocarriers	Advantages	Disadvantages	Therapeutic effects
Liposomes	• Biodegradable, biocompatible, non-toxic • Clinically approved	• Low PA encapsulation rate • Low stability • Phospholipids may undergo oxidation and hydrolysis	• Improved thrombolysis rate • Lower risks of hemorrhages
Polymeric	• Biocompatible and often biodegradable • Easy surface functionalization	• High PA encapsulation rate • Improved stability	• Superior thrombolytic efficacy • Accelerated thrombolysis • Protection BBB permeability damage • Increased survival *in vivo* • Improved neurological deficit • Reduction in cerebral ROS • Reduction in subarachnoid hemorrhage
Inorganic Fe_3O_4 NPs AuNPs	• Biocompatible • Superparamagnetic properties • Magnet-guided thrombolysis • Optical and photothermal properties • Multifunctional theranostic systems	• May enter BBB and generate ROS • Accumulation in the body • May induce immunogenic response or inflammation	• Faster vessel recanalization • Mechanical clot dissolution with an external magnet • Hyperthermia as adjuvant therapy • Increased blood flow rate • Reduction in infarct volume

Bio-inspired	• Prolonged *in vivo* circulation • Natural thrombus targeting	• Low reproducibility • Lack of standardization • Source availability • Immunogenicity • Scale-up	• Improved survival rate • Superior thrombolytic efficacy • Lower neurological deficit score • Smaller ischemic zone • Better neurological outcome • Diminished ROS level in the brain • Lower risk of hemorrhages
US-responsive	• Enhanced thrombolysis with US insonation • Biocompatibility • US imaging	• Low stability • Vessel occlusion	• US stable cavitation - higher penetration of drugs or MBs into the clot • US inertial cavitation: sonothrombolysis

PA are hydrophilic macromolecules (40-70 kDa) that require special design for drug complexation methods. While PA can be incorporated into the aqueous phase during carriers fabrication for lipid or polymeric ones, harsh synthesis conditions – high energy processes (ultrasound, ultraturrax), elevated temperatures, the use of organic solvents – are not suitable for fragile molecules such as proteins [33]. Otherwise, the fibrinolytic agent may be attached to the surface through covalent or non-covalent protocols. The covalent methods provide more stable conjugation (avoiding "burst effect"), however, they sometimes require chemical modification of the drug and might affect changes in the protein structure that might result in its partial denaturation and loss of enzymatic activity [34]. Physical adsorption is a mild drug encapsulation method that results in high loading efficacy for the nanocarriers with hydrophilic surfaces. As PA are predominantly positively charged at physiological pH with an isoelectric point (IP) >7 (except for SK, IP = 5.12), they can form a complexation with anionic surfaces due to electrostatic interactions. The existence of a positive charge on the polymer, as, for instance, chitosan, limits the encapsulation of cationic drugs because of repulsive interactions between a drug and polymer [33]. Comparing covalent vs. non-covalent methods, adsorptive bound PA liberates faster from the carriers and diffused more readily into the fibrin matrix of the clot than covalently bound PA [35] and does not impair the biological activity of the drug [36] that may be beneficial in targeted thrombolysis.

To sum up, depending on the type and composition of the drug carrier, different encapsulation techniques may be applied. Extensive *in vitro* tests demonstrating high loading efficiency, sustainable release, preservation of the amidolytic and fibrinolytic activates of the PA after conjugation must be verified. If we could hypothesize on a complete drug carrying tool it would have the following properties for a safe and efficient treatment of thrombotic diseases.

- **Biocompatible for fast clinical translation**

It is critical to face the challenges of nanomedicine, particularly in an attempt for clinical translation. To ensure clinical safety, the potential toxicity of NPs or MBs needs to be considered with a careful examination of their physical and chemical characteristics and accumulation in the non-target organs and tissues [37]. Indeed, some NPs may cause oxidative stress generation, immunological response, protein misfolding, immune response, and DNA damage [38]. Selecting biocompatible and fully biodegradable materials with FDA-approval, as well as a scalable production of the formulations according to Good Manufacturing Practice (GMP), is essential [39]. Incorporation of sophisticated designs (e.g., cell-derived biomimetic surfaces) should accord with a risk analysis of reproducibility, quality control, and toxicity that might complicate regulatory approvals [40].Indeed, there is an evident gap between scientific discovery and clinical practice in nanomedicine-guided thrombolytic therapy. An astonishing ~10-fold increase from 2010 to 2020 in the number of publications in the field with beneficial therapeutic effects demonstrates a solid argument towards an imminent clinical translation. At the development stage, the tendency is to design complex targeted biomimetic multifunctional nanocarriers, sometimes bearing several active molecules. By examining nanoparticle delivery systems that are currently approved or under clinical investigation [41], [42], we speculate that the first candidate for site-specific delivery of PA tested in humans will probably be built on long-established technologies or nanocarriers from FDA-approved polymers. More sophisticated systems with targeting moieties, stimuli-responsive control of drug release will follow.

- **Targeting for rapid recanalization**

The rapid recanalization of the vascular occlusion is of the utmost importance for the patients suffering from acute thrombotic diseases. The innovative nanomedical approaches have been intensively proposed for targeted thrombolytic therapy to address the challenges of systemic drug administration. The idea of the “magic bullet” imagined over a century ago by Pr. Paul Ehrlich now begins to materialize through the identification of specific biomarkers. In the case of thrombotic diseases, they are mainly identified on platelets (selectins, integrins or serines) or circulating (VWF, factor XIII, fibrin) (*Fig. 2*). Specific thrombus targeting can be achieved by modifying the surface of nanocarriers with targeting moieties (antibodies, aptamers, polysaccharides, peptides, and small molecules) and/or application of magnetic energy, enhancing the therapeutic effect due to accumulation of thrombolytic drug at the clot

surface [43]. Active drug targeting of the nanocarriers allows drug accumulation at the thrombus site and has the potential to enhance thrombolytic penetration into deeply localized thrombi. This is currently realized by directing carriers towards fibrin and platelets, though, identification of the new target molecules and development of the inexpensive and specific targeting moieties will be useful. Fucoidan, which is at present under clinical investigation as a diagnostic agent for the imaging of thrombosis [44], [45], may become an affordable and high-quality alternative to antibodies and peptides.

- **Added imaging value**

The design of theranostic systems with both thrombolytics and imaging agents (e.g., NIR fluorescent probes, gold, iron oxides, or US responsive perfluorocarbon) integrates diagnostic and therapeutic modalities. This strategy may not only provide visualization of drug delivery in real-time but also evaluate the effectiveness of treatment by MRI, CT, or US.

To conclude, the development of novel strategies with plasminogen activators for the treatment of thrombotic disease will continue to flourish as they represent a potent evolution to free drug administration. The encouraging results in preclinical research predict future clinical translation of some of the formulations and progress in the nanomedicine-based precise therapy of thrombotic pathologies. In the next part of this introduction chapter, we describe the characteristic and potential of the chosen carrier, microbubbles, for the treatment of thrombotic diseases.

Part 2: Microbubbles

Adapted from:
L. Fournier, T. de La Taille and C. Chauvierre "Microbubbles for human diagnosis and therapy". *Biomaterials*, vol 294, January 2023. (Annex 2)

Microbubbles (MBs) are defined as microscale objects composed of a shell and a gas core. They were firstly described in 1968 by Gramiak and Shah [46] as the reason of "ultrasonic contrast in the anatomic identification of the mitral valve" after image analysis. US imaging was poorly resolved and quick saline injection was used to produce "clouds of echoes" [46] contrasting with surrounding tissue. Gramiak and Shah hypothesized that this contrast enhancement was probably caused by "mini bubbles" entering the blood with the saline injection. These first observations led to the perspective for their clinical application. Indeed, a long journey has happened since Gramiak and Shah with a focus on criteria validation prior to the injection in living bodies. Some are common to many injectable biomaterials like biocompatibility and biodegradation but MBs also have their specific features. For instance, size has to be controlled under the 10 µm limit to prevent from the obstruction risk in the microvasculature [47] and more preferably in the range of erythrocytes diameter [48]. Those characteristics are defined with the careful choice of gas core, shell composition and surface modification. As presented below, MBs are highly versatile objects that will behave differently *in vivo* depending on their characteristics.

Microbubbles characterization

- **Synthesis methods for Microbubbles generation**

Various methods have been developed for the synthesis of microbubbles (*Fig. 3*) endowing them with different properties. Most of the studied MBs are echogenic liposomes and the main methods for their synthesis consist in the hydration of dried lipids film [49]. It relies on dissolving a mix of lipids into chloroform and using a rotational evaporation system to obtain a thin dried film. The addition of emulsifier (Polyethylene Glycols: PEG) allows the bubble formation and the dried film is hydrated with a buffer solution such as phosphate buffer saline [50]. At last, the solution is heated to its glass transition temperature to help with lipid resuspension [51] and homogenized with US, using a sonicating horn, for several minutes to produce the MBs suspension. Lipids dissolution in chloroform and rehydration in phosphate buffered solution constitutes the precursor lipid suspension for all lipid MBs synthesis, and the

process can be time-consuming as the chloroform evaporation step can last up to 12 hours [52]. Despite the wide practice of this technic, it presents some drawbacks as a complex control on the size distribution. In order to narrow the size dispersity, microfluidics have been a widely explored alternative to obtain reproducible and size tunable protocol. The general idea consists in constraining a liquid flow and/or a gaseous flow into microchannels to generate size monitored MBs. The main advantage is the reduction of reagent volumes meaning a decrease in the total cost of the experiment but also an increased yield of production. Two main systems are leading the field, the T-junction system and the flow focusing setup [53]. Both rely on the convergence of the gas phase and shell material phase with monitored flow rate and optimized channel width to entrap the gas into the shell. Nevertheless, the technology still relies on an advanced miniaturized system with development costs and a time of production slower than other process like sonication or homogenization [54]. A nice review written by Pulsipher *et al.* presents the various microfluidic technologies developed for MBs generation [53]. Carugo *et al.* figured out a smart way to overcome the poor production yield without compromising the narrow distribution of microfluidics systems [55]. Instead of direct production of micrometer size MBs, they produce large precursors bubbles with a regular T-junction gas-in-oil system but expose them to a low frequency US field to generates narrow size distribution MBs. This method enables the production of microfluidic-like MBs but with a production yield in the same order of magnitude than conventional batch sonication. Indeed, high yield production methods like hydrodynamic cavitation and sonication have a relatively faster production rate but require post synthesis treatment like filtration to narrow the size distribution. The hydrodynamic cavitation method uses the shear force of a homogenizer in an aqueous solution to induce polymer MBs formation that can be stabilized with the wanted shell component. It briefly consists in the addition of a monomer into an aqueous solution with the constant hydrodynamic stirring of an homogenizer like Ultraturrax for an hour [56]. As for sonication, it is the fastest method and is involved in the generation of the majority of protein shelled MBs [57]. As underlined by Stride *et al.*, sonication is in majority a preparatory step and extensive study about standardization of sonication protocols is not described yet [58]. It consists in the activation of an ultrasonic horn at the solution/air interface causing compression refraction of the liquid [50]. This generation of energy usually creates high local temperature rise and the overall temperature of the solution can be cooled down by placing the setup in ice. Nevertheless, it is known to have strong potential in the obtention of high yield synthesis at low cost and high speed. However, new shell compositions might be studied with this technique to overcome the issue of stability and fast blood clearance known for protein shelled MBs.

Alternative technics also exists like shaking, used for the synthesis of Definity® MBs by simply shaking a lipid solution in a sealed vial with a shaking device [58]. Moreover, electrohydrodynamic atomization is employed for the generation of lipid MBs by applying a constant electric field on monitored flow rate of a lipid solution in contact with air [59]. Overall, gold standard of MBs synthesis should include the high yield of hydrodynamic cavitation, the size regulation of microfluidic, the fast production time and cost effectiveness of sonication.

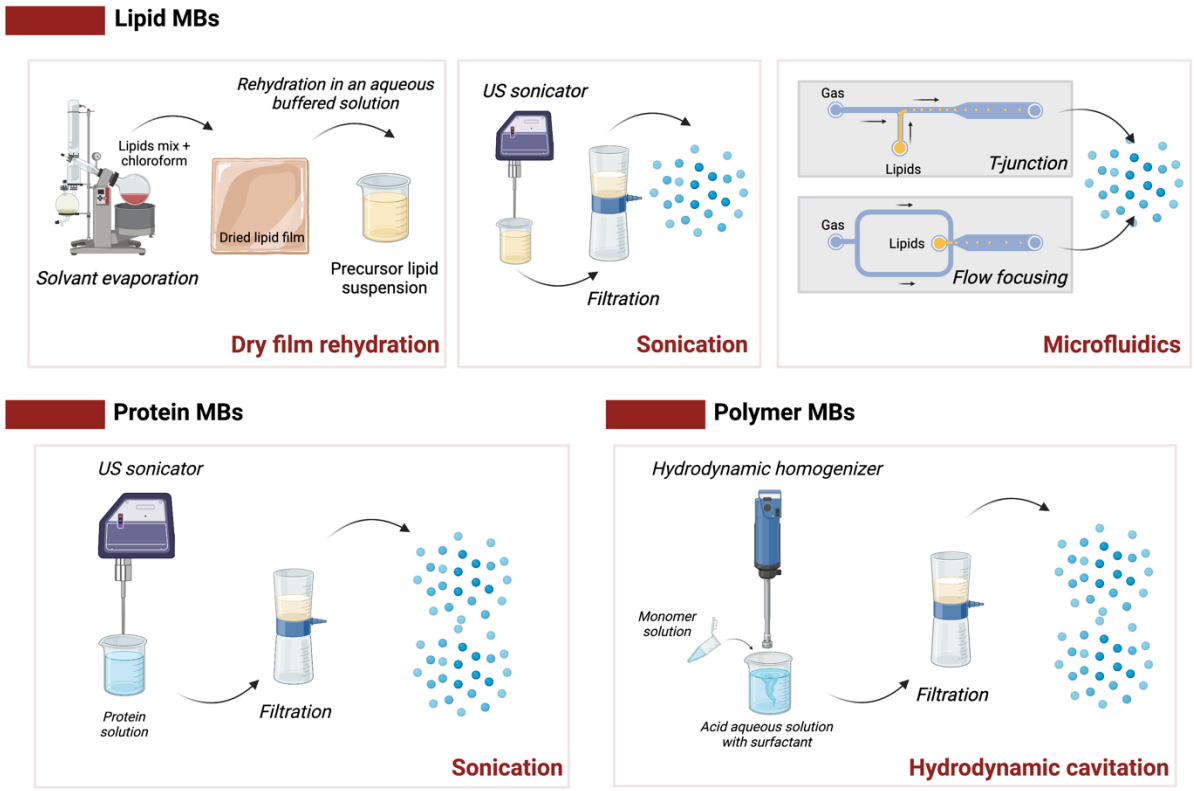

***Figure 3: Methods for Microbubbles synthesis**. Lipid MBs are mainly produced following two different methods: Sonication or Microfluidics. The first step consists in dry film rehydration. It requires the solvent evaporation of the lipid + chloroform mix using a rotary evaporator. The obtained film is rehydrated at glass transition temperature and the precursor lipid suspension is homogenized with the help of US sonication. This precursor suspension is either used for a sonication protocol or microfluidics. This method relies on the encounter of the gaseous phase and the lipids phase either with a T-junction or a flow-focusing system. Both allow the generation of highly monodisperse MBs population. Comparing the two methods, dry film rehydration requires day-scale preparation while microfluidics production is obtained in hours scale. Protein MBs are obtained following US insonation of a protein solution followed by filtration of the polydisperse population. Polymer MBs are generated with hydrodynamic cavitation. Monomer solution is incorporated to an acidic aqueous solution under shear stress perturbation. Again, the polydisperse suspension is filtered. Created with BioRender.com*

- **Microbubbles shell composition**

The shell integrity of MBs was originally established with albumin polymerization but the resulting MBs quickly showed limitations due to their fast clearance in the body. The most studied protein for MBs application was Human Serum Albumin (HSA) firstly mentioned by Reisner *et al.* in 1989 [60] and furtherly developed with the addition of additives like Dextrose

5% [61] or fructose 5% [62] through the 90's and 2000's. They had the advantage of providing a sufficient robustness to keep the gas trapped inside and their chemical characteristics implies the possibility to graft targeting or therapeutic agents. The major drawback was attributed to their vulnerability *in vivo*, because of the fast recognition by the patrolling scavenging cells leading to a rapid elimination in the bloodstream [63]. Nowadays, the vast majority of MBs are composed of lipids and a mixture of them arranged as a monolayer [64]. The mixture of phospholipids usually consists of various ratios of DSPC (1,2-distearoyl-sn-glycero-3-phosphocholine) and DSPE-PEG2000 (1, 2-distearoyl-sn-glycero-3-phosphoethanolamine-N-[amino (polyethylene glycol)-2000]). Phosphatidylcholines are a natural component of cell membranes, generally extracted from soybean or egg yolks, and are already used and FDA approved as excipient in various intravenous treatments [65]. The resulting shell is flexible and confers the ability of structural rearrangement. This can be an advantage for an easy reconstitution after freeze drying storage but lipid monolayer reorganization can disservice the overall stability due to weak interaction forces involved in the geometry (hydrophobicity and van Der Walls [50]). In consequence, it does not efficiently prevent the gas diffusion and the coalescence. Therefore, lipid shelled MBs strategy relies on the flexible property of lipids and small immunogenicity, as their lipophilic property protect them from reticuloendothelial system clearance [66].

When looking at MBs stability, interaction of MBs between themselves has to be studied. Indeed, during and after their synthesis they will be in close contact as the floatation phenomenon occurs, and unwanted events like the Ostwald ripening or coalescence are more likely to happen [67] (*Fig.4*). Ostwald ripening can be defined as the expansion of bigger MBs to the detriment of small and less stable MBs based on thermodynamic equilibrium [68]. This phenomenon can be managed by selecting a low solubility-to-biological-fluid gas and a low solubility-to-biological-fluid shell but also by increasing the stiffness of the shell to prevent exchanges between the surrounding fluid and MBs. In case of lipid shelled MBs, it is recommended to increase the molar volume of the oil phase to reduce their solubility [68]. When two bubbles merge to form a larger bubble, it is called coalescence. It can be prevented by reducing the interaction between MBs using surfactants [69] or by increasing of the synthesis temperature [70]. Hence, MBs shelf stability depends on various parameters like shell and gas composition, shell elasticity, surface tension and viscosity of the aqueous solution. Sridhar *et al.* [71] proposed a mathematical model to estimate MBs half-life in suspension and focused the attention on shell resistance and the viscosity of the storage solution. Storage stability of

MBs in suspension can be extended with stiffer shell material (like polymers) and with the addition of glycerol like ingredient to thicken the aqueous solution [72].

To overcome the shell fragility without compromising the functionalization of the MBs, polymerized cyanoacrylates were introduced as a substitute of lipid shells. Cyanoacrylates are traditionally used in medicine as surgical adhesive for wound closing [73]. They are chemically composed of an ethylene group, a cyano-group and a variable alkyl chain. Initially presented as a monomer solution, their anionic polymerization happens in contact with aqueous media like blood or body tissues conferring adhesive property to the polymer [74]. N-butyl cyanoacrylates are also used in clinics for arterial embolization to prevent from major bleeding in hard to reach regions such as pelvic area [75]. Cyanoacrylate ability to polymerize in water constitutes a new strategy for gas encapsulation in aqueous solution as presented before using hydrodynamic cavitation method. Because of its chemical structure, cyanoacrylate shell are stiffer and thicker (hundreds of nanometers compared to 3-5 nm range for lipid shells [76]) allowing multiple functionalization possibilities including drug loading [77] and targeting peptide grafting [78]. This versatility is accompanied by some drawbacks, the main one relies on the biocompatibility of cyanoacrylate degradation products *in vivo.* Even if the cyanoacrylate glue has been injected in humans [79], it is known that its hydrolysis releases cyanoacetate and formaldehyde which can lead to local ischemia [74].

- **Microbubbles surface modification**

MBs are now also designed as carriers and they not only need a safe and resistant shell, but also tunability for better biocompatibility, targeting or drug encapsulation. MBs' half-life in the bloodstream is sufficient to perform several rounds in the circulatory system and reach their target but they will get destabilized because of their inevitable gas exchange with the environment. Most lipid MBs are stabilized with PEGs working as a steric shield and avoiding a quick uptake from the reticuloendothelial system and protecting the gas core [80]. Nevertheless, this protection may also lead to generation of anti-polyethylene glycol antibodies with repeated injection [81]. Foreign body recognition can also be limited by fooling the immune system. This interesting approach presented by Yang *et al.* relies on the surface modification of liposomes by mixing them with platelet membrane [82]. This confers the MBs a safe passage through the blood recognition system because of the incorporation of transmembrane proteins of the platelet membranes. This approach is used here for asepsis

induced acute kidney injury diagnosis but is an interesting cloaking strategy also used in nanomedicine for cancer [83] or inflammation [84].

With the acknowledgement that every foreign organism will eventually be discharged, it is also a smart strategy to focus on the targeting of a biomarker rather than the long lasting of MBs *in vivo*. Many innovations are derived from the nanoparticles surface modification [85] with the objective to graft targeting agents for molecular imaging or promoting drug delivery. J. Shue-Min Yeh *et al*. present a very complete table summarizing the state of the art of surface modification for lipid shell MBs until 2015 [86]. Interestingly out of 94 published papers, 58,5 % are based on streptavidin biotin interaction [87], [88], 18% on maleimide thiol strategy and the rest are specific lipid-peptide linkage before MBs formulation. Those numbers are interesting because some controversies rely on the immunogenic response to streptavidin in humans due to its bacterial origin. Nevertheless, it remains the strongest non covalent interaction with an affinity constant K_D of 10^{-14} M, shadowing any antibody for antigen recognition. This is why teams are working on improving the immunogenic response [89] and recent work showed great promises about the injection of avidin in humans [90]. This functionalization can be obtained via *in situ* incorporation of streptavidin and with later association of the molecule of interest coupled with biotin, or with chemical incorporation post synthesis of avidin using EDC/NHS (1-Ethyl-3-(3-dimethylaminopropyl) carbodiimide / N-Hydroxy succinimide) coupling [91].

The maleimide thiol bioconjugation strategy relies on the reactivity between maleimides and thiols groups naturally present in biomolecules like cysteines, allowing grafting of fluorochrome, PEGs or proteins [92]. Maleimide groups are added to the structure of the shells and act as an intermediate for drug grafting to the MBs but the chemical reaction has to be monitored because of two competitive reactions. One reversible linkage allowing delivery of agent but easily eliminated in the bloodstream and one irreversible linkage. Therefore, depending on the application and to avoid competition of thiol present in albumin, a fine balance has to be found to improve the stability of this reaction which heavily depends on pH [93].

Covalent bonding of functionalizing agent can be performed via EDC/NHS peptide bond formation. By definition, it allows on the covalent bounding between a carboxymethyl group and a primary amine group [94]. However, standardized protocols are hard to obtain and its accessibility and ease of use does not exclude optimization [95]. A major drawback of this approach is the immobilization of the N-terminus or C-terminus regions of proteins that can be hosting their functional features. Thus, alternative strategies emerged to be more specific regarding the anchoring point. For example, Lui *et al.* put forward the click chemistry coupling

of various desired compounds onto their albumin MBs, conferring a high versatility to the system [96]. Briefly, the method depends on the strain promoted alkyne-azide cycloaddition (SPAAC) where the triple liaison of the Dibenzocyclooctyne-amine (DBCO) grafted onto the MBs has a high and speed reactivity with azide groups present on the desired ligand.

Functionalizing strategy can also simply rely on weak interaction with a positively charged [97] or negatively charged shell [43]. Indeed, comparing the incorporation of anionic DNA onto neutral or positively charged MBs, Panje *et al.* highlighted a significant difference in the incorporation of the plasmid when positively charged MBs could bind up to 0.03 pg of DNA per MB, while neutral MBs incorporated only a residual amount [98]. Addition of surfactant in the MBs composition was also demonstrated to improve lipophilic payload, here using natural lung surfactant protein validating the importance of charge on the surface and its environment [99].

Therefore, the balance has to be found for surface modification to obtain weak or strong linkage to functionalizing object, and it must not be forgotten that surface modification has to be strong enough to sustain its functionality in flow condition according to the *in vivo* environment hemodynamics. Moreover, it must not be forgotten that surface modification can influence MBs dynamics, first in term of stability because of Laplace pressure's influence on the MBs but also in terms of acoustic response [100].

- **Microbubbles gas core**

Another level of MBs tuning consist in choosing a gas of interest for its echogenic, stability or therapeutic properties. The gas can be entrapped into the solution by bubbling in the initial solution and is often saturated in the headspace after freeze drying to avoid the gas exchange after resuspension. The importance of gas for microbubble stability has recently been of main interest while first generation of MBs were mainly composed of air core [63]. A gas with higher solubility like nitrogen contained in air (20 mg/ml in water) would be more likely to diffuse than a fluorinated gas like perfluorobutane (1.5 mg/L in water). The balance has to found between the thickness of the shell and the incorporated gas property to avoid gas loss from the MBs. Indeed, intra-bubble pressure with the surrounding medium (like blood) drastically depends on the bubble radius and the shell resistance at gas-liquid interface, also known as Laplace pressure (*Fig. 4*):

$$P = P_{inside} - P_{outside} = 2\sigma/r$$

where σ is the surface tension between the phases and r the radius of the MB. Hence, Laplace pressure P is defined the pressure difference between the internal pressure (P_{inside}) and the external pressure ($P_{outside}$) of non-miscible phases. In addition, smaller MBs will disappear faster than bigger ones and even faster if the surrounding medium isn't saturated in gas [63], this time according to Henry' law (*Fig. 4*):

$$C = kP$$

where C is the concentration of a dissolved gas, k a constant and P the pressure of the gas above the suspension or in the MBs [101]. In order to maintain the gas trapped inside it is recommended to have a thicker shell and a stabilizing gas.

An additional strategy to overcome the rapid gas exchange of air between MBs and the surrounding medium resulted in the second generation of MBs where low solubility gas like sulfur hexafluoride (SF_6) or perfluorocarbons (PFCs) replaced the air core. Fluorinated gas and especially perfluorocarbons (PFCs) are now widely used to maintain a longer half-life of the MBs in the blood circulation because of their inert property. Indeed, PFCs are synthetic molecules descending from hydrocarbons where the hydrogen atoms have been substituted by fluorine atoms. They are known to be chemically inert and their intrinsic atomic structure give them the property to be hydrophobic and lipophobic at the same time [67]. Omata *et al*. studied the effect of the encapsulated gas on their MBs stability and compared lipid based MBs with either SF_6, C_3F_6 or C_4F_{10} [102]. They concluded that PFCs MBs (C_3F_6 and C_4F_{10}) were highly stable *in vitro* compared to the other MBs (including commercial ones) and their half-life *in vivo* was at least two times higher. Those results are strongly correlated to the Ostwald coefficient formula:

$$L = C_{liquid}/C_{gas}$$

where C_{liquid} and C_{gas} respectively correspond to the concentration of an entity in the liquid phase or the gaseous phase [103]. The higher this coefficient is, the more affinity the entity would have for the aqueous phase. On the opposite, a very inert entity would more likely be highly concentrated in the gaseous phase, leading to a small Ostwald coefficient [104]. For example, O_2 possesses an Ostwald coefficient of 27730 ($x10^6$), while perfluorobutane (C_4F_{10}) and decafluoropentane (C_5F_{12}) respectively have an Ostwald coefficient of 202 ($x10^6$) and 117 ($x10^6$) at 25°C. This translates to the fact that dioxygen will be more likely to dissolve in the surrounding aqueous phase than perfluorocarbons. Kabalnov *et al.* then demonstrated this theory in an experimental set up validating the correlation between the increase of MBs lifetime *in vivo* and the diminishing of the Ostwald coefficient of the entrapped gas [105]. They also mentioned that the administrated dose did not influence the time of circulation.

This second generation of MBs are now the clinical standards like mentioned below with Sonovue® (Sulfur Hexafluoride: SF_6), Definity® (Perflutren: C_3F_8) or Sonanzoid® (Perfluorobutane: C_4F_{10}). Nevertheless, entrapping other gas may have therapeutic properties, as this review will discuss below, and teams keep innovating on oxygen MBs formulation to increase their *in vivo* circulation time [51].

- **Microbubbles adapted characterizations**

Considering their gas core composition, MBs will inevitably rise to the top of the suspension (*Fig. 4*). This buoyancy phenomenon leads to a "cake" formation that constantly need to be resuspended to recover a homogeneous suspension. In consequence, most of the characterizations have to be thought differently compared to regular particle analysis where everything is affected by sedimentation. For most applications, alternative approaches exist to overcome this constrain like centrifugating into a syringe to be able to easily discard the infranatant. Eventually, characterization in fluidic condition is more relevant than static condition due to the buoyancy force dominating the sedimentation for MBs, which otherwise dominates in the study of other particles. To overcome the buoyancy issue some adapted characterizations are presented below like acoustic sorting for MBs triage, flow phantoms for US evaluation and atomic force microscopy for mechanical characterization.

As US contrast agents, MBs can be characterized by their resonance frequency (RF) which must match the US transducer frequency to get the best acoustic response. It is highly dependent on the mass of the bubble-liquid system (m) and the stiffness (s) of the shell [106], with the formula:

$$f_r = \frac{1}{2\pi}\sqrt{\frac{s}{m}}$$

Thus, it can be deduced that there is an inversely proportional relationship between the size of the MBs and their resonance frequency. Moreover, an increase in the shell elasticity will increase the magnitude of the backscattered signal [107]. Of course, the surrounding medium plays a role on the resistance and MBs in water won't have the same resonance frequency than MBs in blood. Considering their response to US, acoustic sorting has been a great way to narrow size distribution of the sample. In the theory, since MBs resonance frequency depends on MBs size, their displacement in a microfluidic system under US insonation also depends on their size [108]. Thus, acoustic sorting consists in flow focusing MBs in a microfluidic chip, at a concentration where MBs do not overlap, and inducing the emission of US perpendicularly to the flow. The output of the channel is divided in separated exits where MBs will be directed in

function of their response to US, the bigger bubbles being derived the most from their original trajectory. It can be used to separate the resonant MBs at a specific frequency to ensure the best response *in vivo*, and to better model the scattering and attenuation of MBs under US insonation [109].

For the evaluation of MBs to US response, flow phantoms are designed to mimic *in vivo* parameters. It can easily be established in the laboratory with an agar gel mold representing the surrounding tissues and a wall free vessel representing the vascular network [110]. Thus, a clinical transducer can easily be employed on top of the system to image the channel where a monitored MBs suspension is flowed. Echogenicity parameters can be observed through this *in vitro* method like the MBs disruption threshold as developed by O. Couture *et al.* [111]. Starting from home-made agar gels with channel, industrials developed long lasting phantoms with different channel size or morphology for vascular doppler flow (Cirsinc®).

Mechanical properties of individual MBs can be hard to determine firstly because of their size but also because of their flotation behavior. Atomic force microscopy (AFM) might be the right alternative to get an idea of MBs mechanical properties [112]. The measurement consists in the immobilization of microbubbles on AFM discs with a specific coating like poly-L-lysine or biotinylated self-assembled monolayer for streptavidin functionalized MBs. Consequently, a tipless cantilever is approached to a single MB and several loads are applied on the MB surface to evaluate the resistance to strain. It has been established with this method that Fe_3O_4 nanoparticles decorated polymer shell MBs had an elastic ratio of 4.6 ± 1.2 GPa [113], thin polymer shell Young's modulus was around 1.5 to 3 GPa [114] while lipid MBs' was lower, around 1.2 to 2 GPa [115]. This last study also validated that not only the shell composition but also the shell coating can increase this elastic ratio. Similar conclusion was obtained for the stiffness: the more decorated the stiffer.

- ***In vivo* behavior of Microbubbles**

After all, MBs are meant to be intravenously injected but there is a broad gap between *in vitro* flow phantoms and *in vivo* bodies. Hemodynamically speaking, MBs tend to behave like erythrocytes in the blood as their size is similar. It means that in a bloodstream environment where none of the Virchow's Triad event happens (Stasis, Endothelial injury, Hypercoagulability) [20], the MBs will tend to have a luminal position inside the vessel [116]. Unfortunately, this hemodynamic behavior does not protect them from *in vivo* clearance systems. According to Upadhyay *et al., in vivo* stability of lipids MBs are limited to a maximum

of 30 min [50]. Most likely, MBs clearance will occur through two pathways: the inevitable ripening and coalescence of the MBs due to excess of environmental or internal pressure, or the scavenging by macrophages and distribution to the reticuloendothelial systems (RES) organs like spleen, liver, bone marrow or lungs [67].

On one side, the gas saturation of the environment will influence the gas exchange between the MBs and the blood and consequently the stability of MBs. For instance, if an animal is under isoflurane anesthesia, the ratio of oxygen in the inhaled gas mixture must be watched or a disequilibrium will appear between dissolved gas in the blood and injected air filled MBs. A study on dogs [117] validated that the rapid clearance of albumin air filled MBs depends on the oxygen ratio of the air mixture inhaled by animals: the more oxygen, the more rapid clearance of air filled MBs in US imaging control. On the other side, the main organ involved in the clearance of MBs is the liver. Some MBs can be used to specifically target the liver, like Sonazoid® shell of which is composed of egg phosphatidylserine, a marker externalized by cells undergoing apoptosis and generating phagocytosis induction [118]. This mechanism was studied to evaluate the clearance through liver Kupffer cells *in vivo* microscopy. It was shown that Sonazoid® MBs were almost immediately internalized but survived almost 30 minutes as MBs inside the macrophage cells of the liver [119]. It validates the possibility of internalization of MBs by macrophages and their survival for several minutes inside the cells before being degraded, allowing potential gas delivery before the gas escape. Biodistribution and liver uptake was also studied with polymer MBs with the work of Warzecha *et al.* to better understand the impact on liver cell function and viability. First, fluorescence mediated tomography validated that 40% of the MBs uptake was performed by the liver and half of it was still observable after 2 hours [120]. At a tissue level, fluorescent MBs where mainly observed in the myeloid cells of the liver endowed with the capacity of phagocytosis. Using flow cytometry analysis, they demonstrated that MBs are almost instantly fragmented after macrophages or monocytes internalization without affecting their viability. However, the use of US on monocytes that had internalized MBs induced some cell death that they attributed to the fact that some MBs might still be intact after monocytes uptake. Finally, the study validated that even after liver injury with CCl_4, the injection of polymer MBs did not affect the injury extent nor compromise the recruitment of inflammatory cells.

Once degraded, MBs debris could also enter the endothelial cells especially if their shell is composed of a phospholipid layer. Indeed, those cells would inevitably be the first barrier to be in contact with MBs debris. A micro-vessel on a chip study performed by Park *et al.* highlighted this MBs-to-cells interaction, and especially after stable cavitation of the MBs induced by US

insonation [121]. Endothelial cells interaction was also demonstrated with doxorubicin loaded liposomes inducing an increase in the targeted endothelial cells toxicity due to the liposome endocytosis by endothelial cells. We could eventually extrapolate that *in vivo* internalization could be harder to demonstrate according to constant flow and very few studies really explored this pathway [122].

Finally, the major risk after validation of the biocompatibility of the shell and gas, is the occurrence of a micro embolism due to the residual shell aggregating in small vessels. Air embolism is less likely to be a threat as clinical death due to air injection happens with more than 100 mL of injected air [123]. In comparison, considering an injection of MBs of a mean diameter around 3 µm and neglecting the shell width, a standard injection of MBs in humans corresponds to a gas volume in the magnitude of the microliter.

Microbubbles for imaging

Currently available MBs for medical application are mostly lipid shell based and have not yet been put to use as targeting and drug encapsulating agents. Their exclusive function is defined as US contrast enhancers for vascular and cardiac cavity imaging. Nevertheless, the US insonation influence on MBs behavior can promote more than conventional US imaging ability as described below.

- **Commercial Microbubbles**

Twenty-five years ago, FDA approved the first MBs for contrast enhancement purpose: Albunex® from Molecular Biosystems®, composed of a human albumin shell and air core [117], which was then slowly replaced by new generations of Albumin MBs like Albuminex® and Optizon®. Sonovue® (BR1) from Bracco is probably the most widely used commercial MBs in research and was approved by the FDA since 2001 [124]. It is a phospholipid shell MB with a Sulfur Hexafluoride (SF_6) gas core, employed for cardiac, vascular and hepatic imaging. Definity® from Lantheus Medical Imaging is also frequently described and share the same shell composition as Sonovue®, but with an octafluoropropane (C_3F_8) gas core. In clinical application, it is also approved for cardiac, abdomen and pelvis imaging [125]. Lastly, General Electrics provides two types of clinically approved MBs, Sonazoid® and Optison® with respectively a lipid stabilized shell with perfluorobutane core and an albumin shell with perfluoropropane core. The first one was developed for abdominal imaging while the second one is exclusively used for cardiac application. According to their general guidelines, Sonovue®

must be used within the six hours after resuspension of the dried product and Definity® within 12 hours after shaking of the suspension. As for Sonazoid®, the use-in period after opening is two hours and Optison® is limited to 30 minutes. In consequence, those products are limited to single patient utilization. In terms of dose administration for instance, Sonovue® injections can be administered in bolus or infusion up to two times 2 mL for cardiac cavity study. According to the company, this represents around twice 200 million of MBs.

In addition, established companies in the ultrasound imaging field also developed microbubbles for preclinical research like Visual Sonics and their Vevo MicroMarker® which can be provided as a target ready carrier thanks to its streptavidin coating [126], allowing research teams to graft any biotinylated agent. Other companies like Bracco based their strategy on VEGFR2 (Vascular Endothelial Growth Factor Receptor 2) targeting for the imaging of endothelial cells involved in angiogenesis, a key factor in some tumor's growth. With a first introduction of BR55 MBs [127] in the literature in 2010, they completed the first-in-humans injection for the molecular imaging of prostate cancer in 24 patients in 2013 [128]. Using KDR (Kinase Insert Domain) as another targeting agent, BR55 MBs were also injected in humans for the diagnosis of breast and ovarian lesion [129] enhancing US contrast in 93% of the malignant breast lesion and 85% of the ovarian malignant lesion.

- **US insonation's influence on Microbubbles**

To better understand why microbubbles have been such an interesting alternative in the contrast agent domains for imaging, we have to better understand the physics behind it. Ultrasound imaging relies on the ability of sound waves to reflect on materials depending on their composition and structure [130]. The rationale of the methods consists on the analysis of the acoustic impedance on different tissues, which depends on to the sound waves speed of propagation and tissue density. What is mainly noticeable are the boundaries between soft tissues with different material properties like bone, fat, water and collagen [131]. Harmless, non-invasive and accessible method, it is mostly known for pregnancy follow-up but can bring quick and reliable answers to many more anatomic observation (ligament observation, breast check-up, circulatory system...). Indeed US imaging can address anatomical examination with B-mode imaging (2D) or functional evaluation with Doppler setting for blood flow monitoring [132]. Ultrasound imaging in clinics is usually performed in a range from 1 to 50 MHz, knowing that the higher the frequency the shorter the tissue penetration will be [130]. High frequencies (over 15 MHz) enable differentiation of objects less than 100 microns apart in depth [133] but

are limited to superficial skin and superficial structures. Breast and thyroid can be observed in the range of 10 MHz, deeper organs like general abdomen and gynecological structures are observed around 3.5 MHz and below. Nevertheless, high frequencies are quite frequently used in animal study because it does not require deep tissue penetration and confers a better special resolution than low frequency US. There are some limitations of this imaging modality and especially the difficulty to image small structures like narrow vasculature or delimitations of the heart cavities. According to Yong *et al*., even in transesophageal echography, up to 15% of cardiac function evaluation fails due to poor contrast delimitation of the heart cavity [134]. Furthermore, US imaging highly depends on the distance to the observed object. In consequence, there has been an interest in the development in contrast enhancing agent capable of a high response to US signal.

Compared to surrounding tissue, MBs' response to US stimuli induces an increased contrast. The effect of US waves on MBs is the induction of their oscillation in a non-linear way [135]. The general oscillation of the MBs is not in phase because their response to acoustic stimuli depends on their distance to the source. This non-linear property makes them dependent on the amplitude of the signal which can be controlled by the voltage. This response is known as subharmonic (SH) emission generated by MBs themselves (rational fraction of the fundamental) after insonation which distinguishes them from surrounding tissue, unable to produce SH [135]. Those harmonics have a lower frequency and are consequently less attenuated by organs. Sojahrood *et al.* investigated the conditions for the best signal of SH by insonating MBs and demonstrated that, for a non-destructive regime, the optimum response signal was obtained when the emitted frequency was between 1.5 and 1.8 times the resonance frequency of the MBs [135] (see part MBs adapted characterization). However, this range decreases with the MBs concentration elevation due to MBs/MBs interaction. Also, polydispersity of the suspension can play a role as larger MBs can influence the behavior of smaller MBs. Haghi *et al*. studied the consequence of MBs clustering on the generation of resonance frequency and highlighted that proximity between MBs induced the increase of their resonance frequency [136].

In terms of MBs behavior under US insonation, two categories can be distinguished: stable cavitation and inertial cavitation which differ by the outcome of the mechanical process (*Fig. 4*). Stable cavitation of MBs happens at low intensity of US signal allowing stable oscillations of the MBs with an alternance between compression and dilatation episodes without inducing MBs rupture [137]. This behavior is the one observed during US imaging thanks to the emitted subharmonics and ultra-harmonics at low acoustic pressure [138]. Among non-

destructive cavitations, microstreaming has been described as the biological effect on surrounding fluids [58]. In other words, the stable oscillation of MBs in living systems creates local fluid motion [139] and temperature rising [140] that can locally destabilize its environment. This behavior is described as one of the enhancing effect helping thrombus penetration [141], drug delivery but also local generation of sonoporation, a method for increasing cell membrane permeability by sonic disruption [142]. Along with the same phenomenon, Acoustic Radiation Force (ARF) emission by US insonation of MBs *in vivo* can be observed. ARF is believed to help drug delivery of loaded agents [143] because of primary ARF that will displace MBs away from the US source and because of secondary ARF (or Bjerkness force) that will improve MBs attraction among themselves by the accordance of their oscillation phase [144]. In addition, the subsequent expansion of MBs influenced by US insonation is described as rectified diffusion [145]. On the other hand, inertial cavitation results in the implosion of the MBs and is caused by the increase of US signal acoustic pressure [146]. Indeed, the rise in the radial expansion/compression amplitudes of MBs will eventually lead to MBs destabilization and shell rupture. It can be observed acoustically by the diminution of ultra-harmonic emission and the rise of broadband emission which translates macroscopically by rapid growth and collapse of MBs [147]. It is a strategic property for drug delivery of targeting MBs but it can also impact its environment as a mechanical disrupting agent [146] with shock waves emission that can disrupt endothelial cell integrity [121]. In association with inertial cavitation, microjetting has been described as the result of asymmetric MBs collapse promoting acceleration of surrounding medium and/or fragment of ruptured MBs. Those microjets were revealed to trigger membrane damage around 1 µm of diameter [148]. Eventually, this kind of disruption would be more likely to happens in case of anisotropic and heterogeneous shell composition [137].

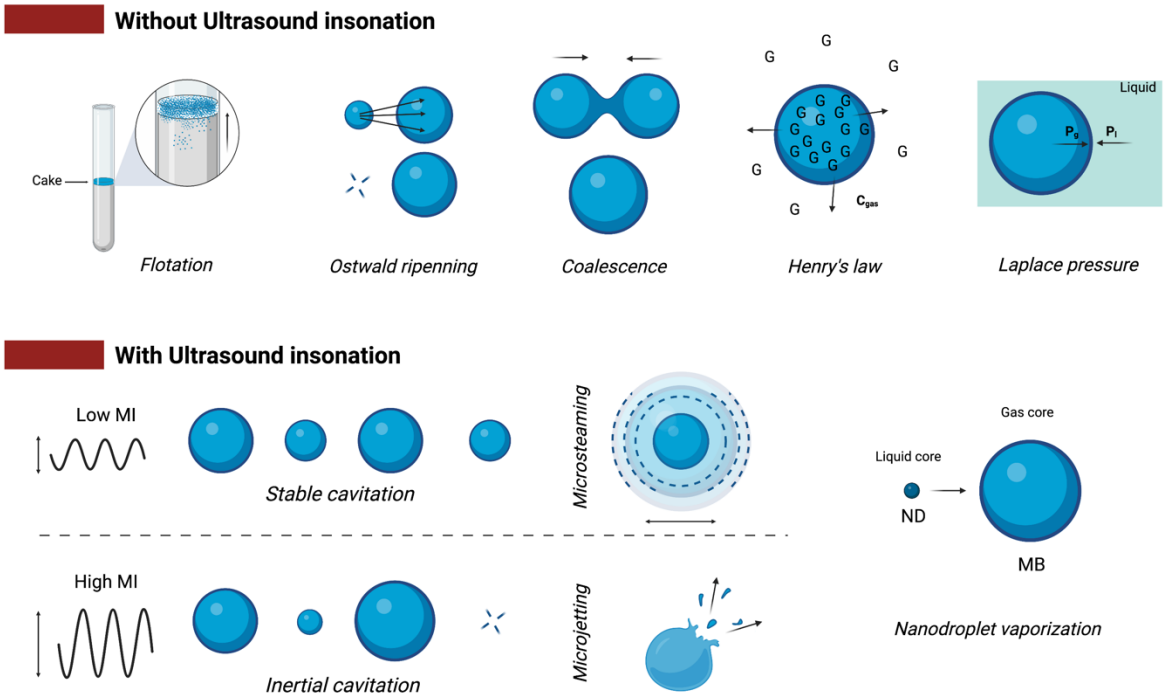

Figure 4: Microbubbles behavior with their environment and under US insonation. *Microbubbles in static condition will rise to the top of the suspension to form a cake. Depending on the shell properties and surface tension of the MBs/liquid interphase, MBs can undergo Ostwald ripening or coalescence. They are also affected by the gas concentration of their environment according to Henry's Law and to pressure of the surrounding medium according to Laplace's Law. Under US insonation, MBs are distinguished by the US regime. Low intensity US (low Mechanical Index) will induce stable oscillations of the MBs leading to microstreaming. High intensity US (high Mechanical Index) will induce unstable oscillations of the MBs leading to MBs inertial cavitation and microjetting. Also, the liquid core of nanodroplets can undergo vaporization under specific acoustic parameters. ND = Nanodroplets, MB = microbubble, MI = Mechanical Index. Created with BioRender.com*

- **Microbubbles molecular imaging**

Molecular imaging represents a new era of early and precise diagnosis that is in development for several imaging technics from X-ray technology to MRI, including US imaging [131]. Characterized as the merging point between molecular biology and *in vivo* imaging, the goal of molecular imaging is to visualize and quantify biological processes from early stages, end points and sequels. In contrast to other imaging methods, molecular imaging tends to break free from structural imaging to reach a molecular range precision. To that purpose, contrast enhancers must be functionalized with the targeting property toward specific biomarkers.

Early studies used fluorescence microscopy to overcome the lack of precision of US imaging with the objective to better understand MBs behavior in the microcirculation. Mark Keller *et al.* were among the first to investigate intravascular distribution of albumin MBs

compared to red blood cells in golden hamsters [149]. They highlighted how MBs displayed a similar velocity and frequency of distribution across the lumen compared to red blood cells, providing MBs an interesting property as intravascular tracers for contrast echocardiography.

As presented in the table below (*Table 3*), biomarkers of the endothelium can be applied for a wide range of conditions like cancer, vascular injury or inflammation. They all have in common the importance of vascular network, and transmembrane protein like VEGFR2 are targeted because

of their involvement in neo-vascularization. However, one target can fit different strategies with lipids or polymer MBs and various targeting agent like peptides, antibodies or polysaccharides. The establishment of specific biomarkers like B7-H3 for breast cancer [150], [151], thymocyte antigen 1 (Thy1) particular for carcinoma lesion only in pancreatic diseases [152] or the specific targeting of transmembrane Nucleolin (NCL) as angiogenesis marker [153] gives rise to a huge versatility to MBs as molecular imaging contrast agents. Vascular pathologies like thrombosis, atherosclerosis or endothelium inflammation are more likely to be targeted adhesion proteins like VCAM1 (Vascular Cell Adhesion Molecule 1) [154], [155], JAM-A (Junctional Adhesion Molecule A) [154], [156] or P-selectin [56], [157].

Recent progresses were attributed to the combined targeting strategies with the association of several targeting agents like VEGFR1 and FSHR (Follicle Stimulating Hormone Receptor) which has recently been demonstrated as overexpressed in renal carcinoma [158]. In case of atherosclerosis early diagnostic, the combination of VCAM-1 and ICAM1 antibodies as well as a synthetic sialyl Lewis X peptide (sLe^X) grafted onto MBs surface to mimic leucocyte behavior allowed a strong recognition from the atherosclerotic endothelium [159].

This table (*Table 3*) displays a non-exhaustive list of MBs used for molecular imaging since 2015 with however only two of them that were injected in humans thanks to the clinical trials of the BR55 MBs as contrast agent [128], [129]. Otherwise, the most accessible animal model remains the mouse or the rat even though big animal like pig [160], [161] or dog [157] are more relevant for human imaging translation. Extravascular targets were also introduced by Köse *et al.* as potential biomarkers especially in cancer leaky vasculature but would be more suitable for nanoscale bubbles [162]. However, some limitations remain about US molecular imaging technology detection limit of static MBs by conventional US transducers, discussed below in the new scales chapter.

Table 3: Non exhaustive list of targeting ultrasound responsive strategies for molecular imaging since 2015*. GPIIb/IIIa = Glycoprotein IIb/IIIa; VCAM-1= Vascular Cell Adhesion Protein 1; vWF = von Willebrand Factor; JAM-A = Junctional Adhesion Molecule A; VEGFR2 = Vascular Endothelial Growth Factor Receptor 2.*

Application	*MBs composition*	*Targeting agent*	*Biomarker*	*Clinical advancement*	*Year*	*Ref.*
Cancer						
Prostate	Lipids	Peptide	VEGFR2	Clinical trials	2017	[128]
Breast and	Lipids	Peptide	KDR	Clinical trials	2017	[129]
ovarian	Lipids	Peptide/ Antibody	B7-H3	Mouse model	2020	[151]
	Lipids	Type III fibronectin	VEGFR2	Mouse model	2016	[163]
	Lipids	Antibody	B7-H3	Mouse model	2015	[150]
Pancreas	Lipids	scAntibody	Thy-1	Mouse model	2018	[152]
Colon	Lipids	Antibody	VEGFR1/ FSHR	Mouse model	2020	[158]
Kidney	Lipids	Peptide	VEGFR2	Mouse model	2016	[164]
Angiogenesis	Lipid	Peptide	Nucleolin	Mouse model	2017	[153]
	Polymer	Peptide	E-selectin	Mouse model	2016	[165]
	Lipids	Peptide	Neuropilin-1	Mouse model	2015	[166]
Vascular						
Thrombosis	Polymer	Fucoidan	P-selectin	Mouse model	2019	[56]
	Lipids	scAntibody	GPIIb/IIIa	Mouse model	2016	[167]
	Lipids	Peptide	Thrombin	*In vitro* model	2017	[168]
Vessel injury	Polymer	Antibody	VCAM-1	Mouse model	2015	[169]
	Polymer	RGD peptide	αvβ3-integrin	Pig model	2016	[160]
Atherosclerosis	Lipids	Nanobodies	VCAM-1	Mouse model	2019	[155]
	Lipids	Peptide	VCAM-1/vWF/ P-selectin/LOX1	Mouse model	2018	[170]
	Polymer	Antibody	JAM-A	Mouse model	2018	[154]
	Lipids	Antibody/sLe^X	VCAM-1/ICAM-1/ Selectins	Mouse model	2018	[159]
	Lipids	Antibody	JAM-A	Rabbit Model	2016	[156]
Inflammation						
Liver injury	Polymer	RGD peptide	Myeloid integrins	Mouse model	2018	[120]
Endothelium	Lipids	Peptide	P-selectin	Dog model	2020	[157]
	Lipids	Peptide/ Antibody	P-selectin/VCAM-1/ vWF-A1/GPIbα	Mouse model	2018	[171]
Abdominal aorta	Lipids	Antibody	P-selectin/VCAM-1	Mouse model	2017	[172]
Liver fibrosis	Lipids	Antibody	VEGFR2	Rat model	2021	[173]
Bowel	Lipids	Peptide	P and E-selectins	Pig model	2015	[161]

Microbubbles for therapy

Microbubbles as therapeutic tools are the combination of three elements: the therapeutic effect of the gas, the therapeutic effect of the US and the functionalized MBs system as a drug carrier and/or a targeting object. Gas therapy and US therapy have been studied before the democratization of encapsulated MBs and new therapeutic approaches now tend to combine these strategies for a synergic effect.

- **Gas therapy**

Gas delivery for therapy is extremely dose dependent as low doses will show no effect and high doses can be lethal. Also, if not encapsulated their diffusible property remain a major challenge. Gas entrapped in the MBs has not only the advantage of being echogenic but can also be part of the therapeutic activity of the carrier [174] (*Fig. 5*).

- Dioxygen

In pathologies like cancer, gas balance is a major component of their development. For example, surrounding microenvironment of tumors is known to be more acidic and more hypoxic [175] conferring them a chemo/radiotherapy resistance [176]. Oxygen based treatment are in development to overcome tumors growth with the encapsulation of oxygen into MBs. Fix *et al*. pointed out that intra-tumoral injection of lipid based oxygen MBs in the tumor site significantly improved radiotherapy treatment [177]. They highlighted that the bigger the tumor the more likely it had developed hypoxic environment, and thus more likely it would respond to the oxygen treatment. Unfortunately, most tumors are not accessible for intra-tumoral injection and gas therapy might be delivered via intravenous route. Improvement of radiosensitivity was observed with the intravenous injection of surfactant shelled oxygen MBs on a breast cancer rat model [178]. By increasing tumor oxygenation by 20 mmHg with oxygen MBs, radiosensitivity was almost tripled. This anti-hypoxic treatment leads also to a significant delay in the tumor growth of approximately 30 days compared to radiotherapy only, highlighting great promises for the use of oxygen delivery therapy as a complement of cancer treatment [179]. In order to improve oxygen MBs stability, Peng *et al.* associated SF_6 to the gas core which showed a 3 times improvement of the circulation half-life *in vivo* [180] (*Fig. 6*). The study presents lipids O_2SF_6 MBs injected in a nasopharyngeal carcinoma mouse model. Using local US triggered destruction of the MBs, tumor volume significantly dropped from 614 $\pm$157 mm^3 with regular treatment to 229 $\pm$ 31 mm^3. Oxygen therapy is also a promising strategy for wound healing with the embedding of MBs into hydrogels [181].

- Nitric oxide

Apart from oxygen therapy, nitric oxide (NO) delivery is a studied strategy because of its function in the regulation of angiogenesis. Thanks to its chemical structure with a very unstable peripherical electron, it is largely used by the cells for signaling and is known for its important role in the promotion of angiogenesis and expending blood vessels [182]. In other words, instead of asphyxiating the tumor, improving its vasculature may overcome the radiotherapy resistance caused by the hypoxic state: it is called tumor vasculature normalization [183]. This hypothesis was studied with the injection of NO micelles combined with radiotherapy [184]. As a result, tumor weight was divided by two compared to the radiotherapy only and survival rate of the mice was also significantly improved. NO is also implicated in the resolution of deep vein thrombosis, by playing a role with the platelets an inflammatory cells aggregation, as well as stimulation the endothelium. Wang *et al.* injected rats with NO MBs after deep vein thrombosis induction surgery and the resolution of the clot was studied by weighting the clots 8 days later [185]. Interestingly, weight over length ratio of extracted thrombi at day 8 showed a decrease of 40% compared to control group. Compared to anticoagulant therapy this strategy does not involve the risk of collateral bleeding as they measured major indexes of coagulation function. They hypothesized that the antithrombotic effect mainly affected the vessel wall by limiting the leukocyte extravasation (decrease of the expression of VCAM-1 on thrombosis site) and thus maintaining endothelium integrity.

- Carbon monoxide

Other gases are potential therapies for cancer such as carbon monoxide (CO) which increases mitochondrial respiration leading to excess production of Reactive Oxygen Species (ROS) and the onset of cell apoptosis [186]. CO also plays a dual role on the nervous central system. Similarly to NO, it is considered as a gasotransmitter in cell signaling and intracellular production of CO can provide neuroprotective effect by upregulating cyclic guanosine phosphate production [187]. Inhalation treatment already proved an infarct volume reduction up to 62.2% in brain ischemia on mice [188]. On the other side, excessive concentration of CO can lead to hypoxia damaging brain cells. Indeed, a strict control of the administered dose creates an unmet medical need for targeted encapsulation of CO as neuroprotective treatment. Looking at another cell signaling pathway, low doses of CO were demonstrated to have an important protective function in inflammatory diseases [189]. Briefly, macrophages stimulated with a lipopolysaccharide (LPS) inflammatory protocol shown a significant accumulation of anti-inflammatory cytokine IL-10 in contact with low concentration of CO. Same results were observed *in vivo,* allowing interesting perspectives for the role of CO on the regulation of an

inflammatory response. This treatment strategy would be all the more interesting as macrophages have the ability to perform phagocytosis on circulating elements of the blood, here MBs. In the recent years, the development of carbon monoxide releasing molecule (CORM) has been studied to control its generation. Pathak *et al.* adapted this strategy to develop light triggered carbon monoxide generating MBs [190]. By loading CORM onto poly(butyl-cyanoacrylate) (PBCA) based MBs, they evidenced the enhancement of M2-like anti-inflammatory phenotype upon light triggering CO production on human blood samples. This proof of concept was also studied for the protection over oxidative stress induced in cardiac issue injury. Again, CO triggered delivery allowed a significant reduction of the apoptotic ratio on cardiomyocytes. Altogether, these results indicate the high potential for low dose CO delivery in the resolution of cardiovascular diseases.

- Perfluorocarbons

Perfluorocarbons (PFC) do not have direct therapeutic effect; however, they are used as intermediate transporter for oxygen. As mentioned before, O_2 plays an important role in the physiology and consequently in pathologies. PFC in their liquid state like Perfluoro-octyl-bromide (PFOB), or perfluorobutane (PFB) can be employed as O_2, NO and CO carriers [191]. Their very inert property enables the uptake of dioxygen. If we compare the capacity of dissolution of oxygen in water or in a PFC, the molar ratio of dissolved O_2 is 1 mol of O_2 in 200 mol of water compared to 1 mol of O_2 in 0.2 mol of Perfluorodecalin (PFD) [67]. Perfluorocarbons-based oxygen carriers (PFOCs) have nicely been reported in the review from Jäger *et al.*, presenting how PFOCs are an innovative tool from cancer therapy to blood substitute [67]. As presented before, the fluorine atomic structure tends to attract electrons from surrounding atoms giving a stiff structure to the molecules that are not affined to dissolve in aqueous media meaning that PFCs are good candidates as solvent for other gas and especially oxygen, carbon dioxide and nitric oxide [191].

• Ultrasound therapy

US treatments are already widely used without the need of MBs injection. The main advantage of US therapy is the non-invasive characteristic of the method. It is now possible to avoid surgical intervention over kidney stone disease by the use of shock wave lithotripsy [192]. The current use of high peak pressure (up to 100 MPa) and very low rate (2 Hz) safely helps with the resolution of kidney stones [193]. Recent clinical trials of a more efficient burst wave lithotripsy (<12 MPa, <200 Hz) helped to reposition 95% of kidney stones in human [194].

US are also used for ablation therapy without the requirement of surgical intervention. This method called histotripsy uses focused US to destroy tissue, thanks to the induced cavitation, without thermal or ionizing related event [195].It was first observed as a collateral damaging consequence of lithotripsy, which was finally studied by itself as a new form of non-invasive therapy. Typically used US parameters are performed up to 6 MHz with a high negative pressure up to 15 MPa with low duty cycle to avoid heat generation. Phase I clinical trials were conducted on benign prostatic hyperplasia, liver cancer and calcified aortic stenosis [195]. Limitations of US therapy are still attributed to organs containing gas or acoustically unreachable organs because of bone blockage. If recent clinical trials have not confirmed the evidence of US enhanced sonothrombolysis in limb ischemia yet [196], clinical studies are still ongoing to replace invasive mechanical thrombectomy and overcome collateral damages of high dose thrombolytic therapy. This issue can be resolved by using US as an accelerator of thrombolysis, in supplement of drug delivery. Li *et al*. meta-analysis highlighted that, out of 5 clinical trials, thrombolytic injection associated with US insonation for acute ischemic stroke showed a significant recanalization rate over thrombolytic injection alone [197]. The studied trials had US parameters from 1.8 MHz to 4 MHz for over 1 h of US monitoring.

For a more local treatment, US emitting catheter can be introduced in the popliteal vein along with plasminogen activator delivery catheter. This method was presented by Kartal *et al.* and showed 60% of partial reopening in deep vein thrombosis events [198]. Even though the significance was not established compared to local delivery only, they concluded that ultrasound-accelerated-catheter-assisted-thrombolytic therapy had the advantage of preventing from bleeding complications by maintaining a local treatment.

Overall, US exposure can be adapted via different forms, from non-invasive to local US emitting catheter. In opposition to wide range US imaging, focused US can accurately target a zone by focusing high pressure amplitude. Nevertheless, this high accuracy method usually requires the association of MRI imaging to define the area to treat [195], [199]. Lastly, US imaging and treatment of brain related events is still a major challenge because of the skull thickness. Hence, the most accessible part is through the temporal bone enable the visualization and potential treatment with transcranial Doppler approach [200].

- **Microbubbles as therapeutic tools**

The application of MBs for therapy must be preceded by the study of the interaction between vessel wall and MBs interaction. Indeed, confined behavior of MBs differs from unbounded ones and it seems reasonably clear that the bioeffect of MBs disruption has to be studied to determine therapeutic boundaries. Known limitations consist in the damage of surrounding tissue attributed to vessel distention or wall impairment due to microjetting (*Fig. 4*). Mathematical models were established by Hosseinkhah *et al.* to evaluate the wall shear stress and circumferential stress and have been validated with experimental data [201]. *In silico* results assessed that wall shear stress within microvessels could reach 18.3 kPa during MBs expansion and 74 kPa during MB collapse. As constrained MBs behave differently, an *ex vivo* model from perfused rat caecum led to the conclusion that the angle of US insonation on vessels had no impact on the interaction between MBs and the endothelium. It also showed that constrained bubbles in the capillary network had an increased oscillatory lifetime compared to big vessels and that bigger MBs (>4 μm) tend to interact better with the endothelium than very small MBs [202]. Those observed interactions under US insonation consisted in an asymmetrical collapse onto the vessel wall and repeated expansion beyond the vessel limits and the study suggested that the efficacy of ultrasound mediated MBs therapy strongly depends on the MBs concentration and size distribution. On the other hand, *in vitro* vessel phantoms lithotripsy set up with albumin MBs demonstrated that the induced expansion of very large bubble could cause rupture of the vessel wall and therefore pointing out the importance of size distribution regulation [203]. Those general examples are important to understand the mechanical behavior of MBs. Indeed, despite the wide use of MBs for therapy for cancer, inflammation or thrombotic diseases, some therapeutic strategies are actually very similar. As many innovative therapies, the balance has to be found between the different parameters to get the best advantage over risks ratio. The first parameter that can be monitored is the mechanical index (MI) of the US wave. It is a unitless ratio representing the pic of negative pressure (MPa) over the square root of the frequency (MHz) of the signal [204].

$$MI = \frac{P}{\sqrt{f}}$$

This ratio strongly depends on the US device used and the distance to the object, and it can be measured with an hydrophone calibration [205]. Below 0.1, MI will generate only linear oscillation of the MBs; between 0.1 and 1, these oscillations become non-linear allowing the imaging of the MBs. From 1, inertial cavitation leading to disruption of the MBs can be observed [50]. Eventually, these numbers can be adapted to each application but the scientific

community and the FDA agreed on the limit of MI to 1.9 in humans to avoid any damaging bioeffect [206] (except for ophthalmological evaluation where the MI is limited to 0.23 [207]).

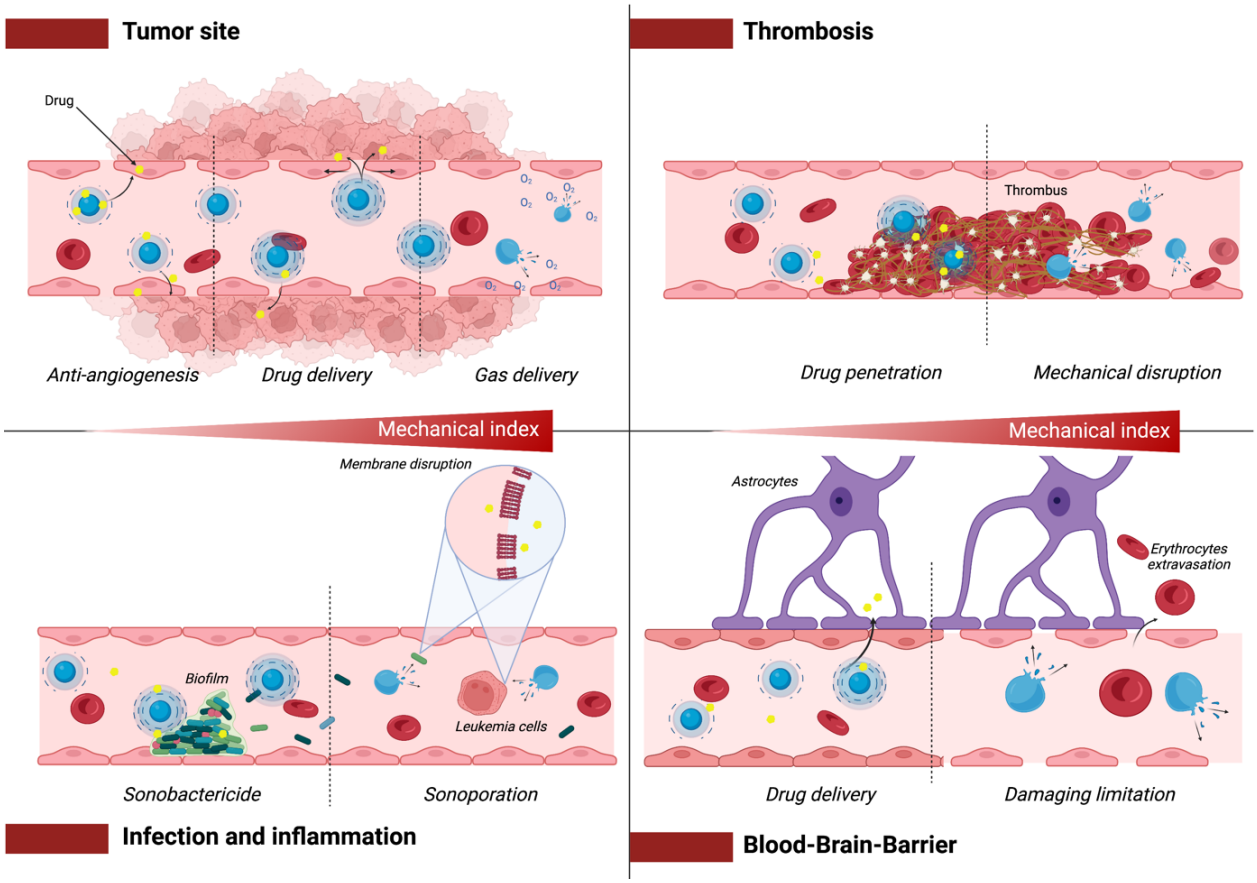

Figure 5: Therapeutic strategies for tumors, thrombi, infection and Blood-Brain-Barrier. *Depending on the mechanical impact of the US signal, MBs therapy can be adapted for different pathologies. Microbubble microstreaming can improve drug delivery to the epithelium and the thrombus. It also destabilizes membrane permeation by fragilizing biofilms and BBB epithelium tight-junctions. The increasing of US mechanical index induces a stronger mechanical impact on the surrounding tissue. Indeed, MBs implosion helps mechanically disrupt thrombi by loosening up the fibrin mesh. This disruption has to be carefully monitored because it promotes cell membrane sonoporation for a therapeutic approach but also vascular permeation causing cerebral hemorrhages. Created with BioRender.com*

- Thrombosis

As mentioned before, MBs can be triggered to explode by increasing the amplitude of the US signal (*Fig. 5*). This bursting associated with thrombi therapy is called sonothrombolysis. Basically, sonothrombolysis consists in the use of ultrasound waves and MBs to mechanically disrupt the clot [85]. It can be influenced by the duration of insonation, the composition and the concentration of MBs or the time between pathological incident and treatment. Positive outcomes are evaluated with the recanalization rate [167] or the study of the related ischemic lesion, like presented by Dixon *et al.* on an ischemic stroke model [54] (*Fig. 5*). A very complete review from Nederhoed *et al.* describes the different therapeutic use of MBs and US on peripheral arterial thrombosis based on 26 preclinical studies and 9 clinical

ones [208]. They compared the localization of the thrombosis (middle cerebral artery, abdominal aorta, internal carotid artery…), the age of the clot and the number of subjects for preclinical and clinical studies. Recanalization rate was one of the primary outcomes, meaning the ability of the blood flow to be restored after the treatment. There were two ways of quantifying the reperfusion rate: angiography or transcranial Doppler.

Among the *in vivo* preclinical studies (*Table 4*) using a thrombolytic drug as a control, here are the interesting conclusions: the US settings used for sonothrombolysis were very heterogeneous varying frequency of the transducer from 1 MHz [209] to 6 MHz [210], the MI from 0.2 [211] to 2 [212] and different pulse length [213]. Preferentially, the strategy was to infuse the MBs over several minutes [211], [212], [214], [215] while continuously insonating the clot with different MI. On the other hand, some studies injected the MBs in bolus but always with long treatment insonation [216]–[218], which is in contradiction with the fact that MBs are relatively quickly cleared out from the blood. The total exposition of clot to the US remains unclear and very heterogeneous to most of the studies. There is a clear need for *in vivo* study to accurately describe the frequency of the probe, the mechanical index, the duty cycle and the total duration of insonation, in order to better establish comparisons. Moreover, lack of control groups using MBs and thrombolytic agent with US insonation has been highlighted as well as lack of comparison with different shell compositions. According to Nederhoed *et al*, all the studies included for the *in vivo* sonothrombolysis using contrast enhancer agent and a thrombolytic agent presented a minimum recanalization rate of 56% up to 100% while US alone never allow a reperfusion superior to 63% [208]. The lower recanalization rate was attributed to Tomkins *et al*. because of the platelet rich composition of the clot that responds less efficiently to thrombolytic therapy [215].

Moving on to clinical studies for sonothrombolysis, most of them were performed on ischemic stroke patient with duration therapy from 1 to 2 hours with 2 MHz US insonation but with low or non-indicated MI. The biggest clinical study of sonothrombolysis for ischemic stroke patient was performed at the University Hospital of Vall d'Hebron in Barcelona, including 296 patient with acute stroke [219]. After thrombolytic drug bolus, patients received 3 doses of 2.5 g of air-filled galactose-based MBs along with 2 hours of transcranial Doppler monitoring. Conclusion of the study was that MBs administration associated with US insonation helped early recanalization without increasing the risk of intracranial hemorrhage. One limitation however remains, since these results were obtained with an operator dependent technique which is the transcranial doppler imaging. The therapeutic window was not meant to be improved in this study but presents potential leads for reduction of thrombolytic drug dose

that still can cause collateral hemorrhages. Short pulse duration (< 5 µs) is explored in randomized clinical trial to reduce US exposition [220]. In this study, myocardial infarction patients were randomly treated with high MI and Definity® MBs injection before and after undergoing percutaneous coronary intervention. In combination with regular treatment, MBs treatment help doubling the recanalization rate. One key data was the improvement of the systolic function that remained higher with MBs treatment even after 6 months. Consequently, only 5% of the patients required the implantation of a removable defibrillator while 18 % of percutaneous coronary only treated patient required one.

The clinical translation of therapeutic MBs still faces obstacles in order to find the right conditions for an efficient sonothrombolysis and standardize the protocols. Furthermore, the actual clinical studies are based on already approved MBs as contrast enhancers, but have not included payload-carrying or targeted MBs yet. Also, as Porter *et al.* mentioned, one major drawback to overcome with the use of MBs for therapy is the microvascular obstruction after recanalization of myocardial infarction [221]. Despite many strategies evaluated for its resolution, research has failed finding a solution and recanalization of microvasculature still remains an unmet medical need [222].

- Cancer

In certain cases, tumor growth is associated with neo-vascularization allowing nutrient transport to the tumor. As presented before with gas therapy for tumors, the hypoxic environment reduces the action potential of radiotherapy. Injection of chemotherapy is still promoting various side effects because of the apoptosis of rapidly dividing cells that include cancer cells but also immune cells or hair follicles. The three mains strategies for US meditated MBs for cancer therapy rely on the oxygenation to overcome the hypoxic state [177], the anti-tumor drug delivery and the anti-angiogenesis strategy [139] (*Fig. 5, Table 4*).

In terms of drug delivery, biological barriers are a limiting factor, even for nanoparticles (NPs), because of the lack of homogeneity in the tumor vasculature. US assisted delivery with MBs could help drug penetration with the generated microstreaming. This advantage was evaluated by Snipstad *et al.* in 2017 with polymeric NPs assembled as a MB (NPMBs) [223]. The goal is to take the advantage of MBs behavior under US insonation to disturb the surrounding tissue and deliver the drug loaded NPs. Tumor uptake of drug loaded NPs after US insonation is evaluated with fluorescence confocal microscopy. In the 3rd week following the tumor cells inoculation, animals are treated with Cabazitaxel (mitosis blocker) loaded NPMBs with or without US insonation. The conclusions of this study highlight the influence of US (MI

over 0.25) on the uptake efficiency of drug loaded MBs. Attributed to the enhancement of the vasculature permeability, Cabazitaxel loaded NPs were incorporated 2.3 more times in the tumor and complete remission was observed after 50 days. Limits are defined by the heterogenicity of vasculature between every tumor and tissue damage over 1 MI. Overall it suggested that the higher the tumor is vascularized, the more efficient the treatment will be. Also, Enhanced Permeability and Retention (EPR) effect is not sufficient enough for the effective delivery of drug loaded NPs. The subsequent question was, is the drug encapsulation required for cellular uptake? Answering this question could accelerate clinical translation by co-administration of drug and MBs with US insonation. The question was addressed on the same protocol, with either drug loaded NPMBs or free drug co-administered with NPMBs to evaluate the true potential of US induced sonopermeation [224]. Interestingly, no difference in the survival of the two groups was observed with 50% of survival after 72 days, and free drug uptake was equally effective to encapsulated one. Here again, this indicates the mechanical incidence of US insonated MBs on their environment.

In order to overcome the collateral damages of US insonation, focused US is developed to restrict the size of the insonated area. Using focused low intensity US, drug resistance reversing effect can be studied as the results of enhanced drug incorporation [225]. In this *in vitro* study, focused US and MBs destruction with free Paclitaxel inhibit the proliferation and increase the apoptosis of drug resistant ovarian tumor cells. The inhibition of autophagy developed by those drug resistant cells was defeated by the influence of MBs reaction to focused US. More than overcoming a drug resistance pathway, it gives new direction for *in vivo* treatments. The same strategy was validated *in vivo* with a murine squamous cell carcinoma model [226]. This time, MBs were loaded with a transcription factor for the inhibition of STAT3 (Signal Transducer and Activation of Transcription 3) acting for tumor progression. Gene therapy was proven efficient with a reduction of 51 % of the tumor size with encapsulated transcription delivery using focused US. The actual size limit for drug enhanced uptake was evaluated by comparing Evans Blue and FITC dextran as drug model for the respective size of 3.7 nm and 30.6 nm [227]. While neovascular established cut off stands in a range from 380 to 780 nm [227], tumor distribution of free drug is not exactly related [228]. Indeed, US associated decrease of internal pressure of new vessels helps deeper penetration of bigger sized drugs. Even small drugs need environmental stimulation to cross the barriers because of *in vivo* extracellular matrix barrier and circulating protein adsorption that can compromise the uptake.

Antiangiogenic strategy is developed to help depleting tumors from their blood supply. Gene therapy was proven efficient with targeting MBs compared to untargeted MBs with a

specific targeting to endoglin (specific marker to newly formed blood vessels higher than VEGFR2) [229]. *In vivo* studies performed on triple negative breast carcinoma xenografts established that low MI focused treatment (0.2) of Sonovue® was sufficient to improve the antiangiogenic effect of the free Apatinib (a tyrosine kinase inhibitor) without observing the drug related systemic effects [230], [231]. Regardless, this strategy show some limitations with the emergence of studies promoting the maturation of tumor blood vessels phenotype to reduce their hypoxic state and radiotherapy resistance [183], [232]. Recent work from Yi-Ju Ho *et al.* demonstrated the potential of this tumor vasculature normalization with oxygen MBs [233]. The oxygen release inducing vessels maturation increase the anti-drug treatment penetration by 3-4 folds.

These new cancer strategies are of a worldwide interest. Looking up to clinical trials (up to October 2022), 8 trials are currently recruiting patients in 5 different countries (USA, Canada, Norway, France and Germany). The use of non-targeted commercial MBs in those trials are meant to improve treatment for various cancers type like breast (NCT04431674, NCT03477019, NCT05445050), liver (NCT03199274, NCT02764801), colorectal (NCT03458975, NCT03477019), and pancreas (NCT04146441).

Table 4: Synergic therapies of MBs associated with US and drug for thrombosis and cancer. *Non exhaustive list of recent pre-clinical studies evaluating the improvement of drug therapy with MBs. (tPA: tissue Plasminogen Activator; TCCS: Transcranial Color Doppler Ultrasound; MI: Mechanical Index; Ab: Antibody)*

Application	*Targe-ting agent*	*Drug*	*Loaded on MBs*	*Co-injected*	*US*	*Outcome*	*Ref.*
Stroke	No	tPA	No	Infusion (NA)	1 MHz, 0.9 MI, 20 min	TCCS + MBs required tPA co-injection for an efficient thrombolysis	[209]
Stroke	No	tPA	No	Infusion (10 mg/kg)	3 MHz, 1.7 MI, 40 min	Resistance of platelet rich clot resolution to any condition	[215]
Stroke	No	Urokinase	No	Infusion (20,000 U/kg)	2 MHz, no MI	Synergy in the recanalization rate using co-injection of drug and MBs	[217]
Coronary thrombosis	Yes (IIb/IIIa)	Pro-Urokinase, Heparin, Aspirin	No	Infusion (50,000 U/kg)	1.5 MHz, MI 1.9, on/off 30 min	Synergy of clot targeting and high MI sequence	[211]
Coronary thrombosis	No	tPA	No	Infusion (1 or 0.5 mg/kg)	1 MHz, 2.0 MI, 30 min	Synergy of high MI with MBs and low drug dose	[212]
Coronary and microvascular thrombosis	No	tPA	No	Infusion (1 or 0.5 mg/kg)	- 1.6 MHz, 1.0 MI, 30 min - 1.6 MHz, 2.0 MI, 30 min	Longer duration pulse over higher MI is more efficient	[213]
Abdominal aorta thrombosis	No	tPA	Yes (rehydration with tPA solution, 200 µg/ rabbit)	Control	- 6 MHz, MI 0.4, 2 min - 6 MHz, MI 0.2, 30 min	No difference in the US conditions, efficient thrombolysis but no significant difference between co-injection and tPA-loaded MBs	[210]
Limb arterial thrombosis	No	Urokinase	No	Intra-arterial Infusion (50,000 U/kg)	1.6 MHz, 1.2 MI, 60 min	Synergy of US with MBs and low drug dose for faster resolution	[214]
Limb arterial thrombosis	Yes (RGD)	tPA	Yes (rehydration with tPA solution, 0.06 mg/kg)	Control	12 MHz, 0.5 MI, 30 min	Reduced dose of tPA loaded on MBs with US showed similar recanalization rate compared to free rtPA regular dose with MBs and US	[218]
Breast cancer	No	Cabazitaxel	Yes, loaded during synthesis (10 mg/kg)	Control	1.1 MHz, 0.5 MI, 2 min	US + encapsulated drug onto MBs resulted in the complete remission in all treated animals	[223]
Anti-angiogenic for breast cancer	Yes (CD105 Ab)	Gene therapy (endostatin)	Yes, loaded during synthesis	No	1 MHz, No MI, 30 sec	Tumor volume reduction after targeted gene therapy compared to untargeted MBs	[229]
Anti-angiogenic for breast cancer	No	Endostar (endostatin)	Yes (avidin-biotin) (10 mg/kg)	Control	1 MHz 0.5, MI, 30 sec	Efficient anti-angiogenesis effect of drug loaded MBs + US compared to group without US insonation.	[230]
Ovarian Cancer	No	Paclitaxel	No	Infusion (10 mg/kg)	1 MHz, 0.4 MI, 3 min	Reversal of drug resistance with the co-injection of MBs associated with US	[225]
Prostate cancer	No	Cabazitaxel	Yes, loaded during synthesis	Control	1 MHz, 0.5 MI,15 min	Efficient reduction of tumor growth with US and either free drug + MBs or drug loaded MBs	[224]
Prostate cancer	No	Oxygen + Doxorubicin	No	Control (7 mg/kg)	2 MHz, 1.4 MI, 30 min	Tumor oxygenation with oxygen MBs assisted with US improved the intratumoral accumulation of anti-cancer drug	[233]
Tumor model	No	Doxorubicin	No	Infusion (6 mg/kg)	1 MHz, 1.0 MI, 10 min	Improved delivery of drug on tumor site with MBs associated with US	[228]
Skin cancer	No	STAT3 decoy	Yes, loaded during synthesis (10 µg)	Control	1.3 MHz, 1.6 MI, 25 min	Tumor growth inhibition after the specific delivery of the encapsulated STAT3 decoy associated with US	[226]

- Blood brain barrier

Major controversy on US associated to MBs treatment is the Blood Brain Barrier (BBB) trespassing. Acting as a highly controlled barrier which limits the penetration of most compound, BBB prevents brain from blood contamination for its own neuroprotection. Consequently, systemic injection of treatments for Central Nervous System (CNS) pathologies are challenging as only 2% of molecules below 600 Da can cross [234]. As presented before, MBs expansions generated by US insonation can overcome microvasculature elastic limit and cause microvasculature leakage even in very specific tight junction of the cerebral endothelium. Parallelly, human skull (> 6 mm) represents a major obstacle for the use of clinical US transducer because of the large absorption of the emitted waves giving a transmission coefficient only estimated of about 14% [234]. Overall, CNS access is limited both to circulating drugs and US exposure. This limitation is prevented in preclinical studies with the thin thickness of the mouse skull (0.5 to 1 mm) [235].

On one hand, the improvement of BBB permeability is a major milestone for drug delivery in the brain tissue (*Fig. 5*). Firstly, boundaries have to be established to obtain a positive advantage over risk ratio for brain treatments. Histology for red blood cells extravasation, Evans Blue permeability test or dynamic contrast enhanced MRI are morphologic evaluation of BBB permeability. McMahon *et al.* evaluated it through the study of proinflammatory mediators 4h following US insonation of 3 types of injected MBs [236] (*Fig. 6*). They exhibited that the MBs size distribution plays a role in the inflammation response. Polydisperse lipids MBs like Definity® or BG8774 (Bracco®) were less likely induce the production of inflammatory mediators compared to monodisperse populations (MSB4, Bracco®). Nevertheless, the elevation of inflammatory response without tissue damage can be an advantage for application linked to the neuroinflammatory system. The study concludes on the relevance of acoustic feedback controls to limit wideband generation and thus diminishing the destructive inertial cavitation [199]. This temporarily opening can be improved with the chemical functionalization into targeting MBs without increasing the required US amplitude [237]. Focused US is currently the best solution for non-invasive and targeting application for CNS treatment with microbubbles widely described in Chen *et al.* review [238]. Those findings are high potential therapies for degenerative diseases like Alzheimer's [239] or Parkinson's [240]. Once again therapeutic targets are unreachable with BBB impermeability. Parkinson's treatment with MRI guided focused US to the putamen has reached phase I clinical trial in Canada concluding on the safety and feasibility of US assisted drug delivery [240]. A decrease

of 12% of Parkinson's disease rating scale motor score evaluation was observed in treated patient who were off medication.

On the other hand, MBs induced leakage of the BBB vasculature may have significant adverse effect (*Fig. 5*) like hemorrhages [241], sterile inflammation [242] or neurotoxicity [234]. The objective remains to limit inertial cavitation, with previously presented monitoring of the acoustic feedback, in order to keep the permeabilization temporary and localized.

- Other pathologies

Other strategies are emerging by taking all the advantages of US mediated MBs treatment. One major complication observed in clinics are nosocomial infections. Particularly life threatening, biofilms cause majors problems in health care system. Bacteria adhering to tissue or surfaces will develop a protective matrix and behavior limiting the action of antibiotics. *In vitro* proof of concept of sonobactericide potential MBs was presented for the infective endocarditis [243]. Briefly, induced *staphylococcus aureus* biofilms on human blood clots were treated under flow conditions. The major factor identified as contributing to the sonobactericide phenomenon (*Fig. 5*) was the acoustic streaming produced by insonated MBs. In Lattwein *et al.* study performed in 2018, US alone did not show any improvement in the infected clot resolution compared to regular treatment (antibiotics + thrombolytic). However, the use of commercial bubbles with US insonation at low frequency parameters (120 kHz, 0.44 MPa) achieve almost 100% of infected clot resolution. This strategy can be applied to several sources of infection like chronic bacterial prostatitis, pneumonia or urinary tract infection [139]. Lattwein *et al.* study was recently updated by comparing five US parameters from 100 kPa to 400 kPa with different duty cycles [244]. This time, the study of sonoporation by measuring the intake of propidium iodide, which is unable to permeate cell membrane and bacteria dispersion, were mostly observed in the high-pressure US rather than high duty cycles ones. This means that the mechanical index has more influence than the continuity of the emitted US on untargeted MBs for biofilms resolution. Also, this study really demonstrated the key role of US and MBs because no significance in the sonobactericide study was shown with the addition of antibiotics (*Fig. 7*).

Sonoporation induction can also be a strategy for DNA transfection improvement *in vivo* [98]. Ability of MBs to facilitate intracellular delivery by sonoporation has to be further investigated for an innovative gene therapy strategy. Indeed, as mentioned by Duan *et al.*, there is a lack of information about the membrane repair after MBs + US induced sonoporation [245]. They studied the impact on leukemia cells and found that US insonation in presence of

untargeted MBs induced the upregulation of cytoprotective gene (heat shock protein) (*Fig. 5*). In consequence, if a cytoprotective behavior was observed in the first hours, many of them failed to maintain an ordered proliferative cycle and underwent necrosis or apoptosis. Thus, the addition of targeting MBs should improve the selectivity toward leukemia cells before an eventual emergence of new antitumoral treatment. Additionally, endocytosis enhancement was demonstrated by the alteration of clathrin-mediated endocytosis pathway after US microbubble treatment giving more argument for intracellular drug delivery [246].

It can be recapitulated from these different applications that US triggered MBs disruption therapy is not meant to replace drug therapy. Most probably MBs must be used in complement to improve drug efficacy and/or drug delivery. Overall, the use of MBs for therapeutic application is mainly driven by the aim to reduce drug-dose related side effect and improve the treatment outcome (*Table 4*). The availability of clinically approved microbubbles helped better understand the effect of US with MBs and co-injection of drugs. The latest works now tend to study the synergy of drug loaded targeting MBs and the use of mechanical disruption with US.

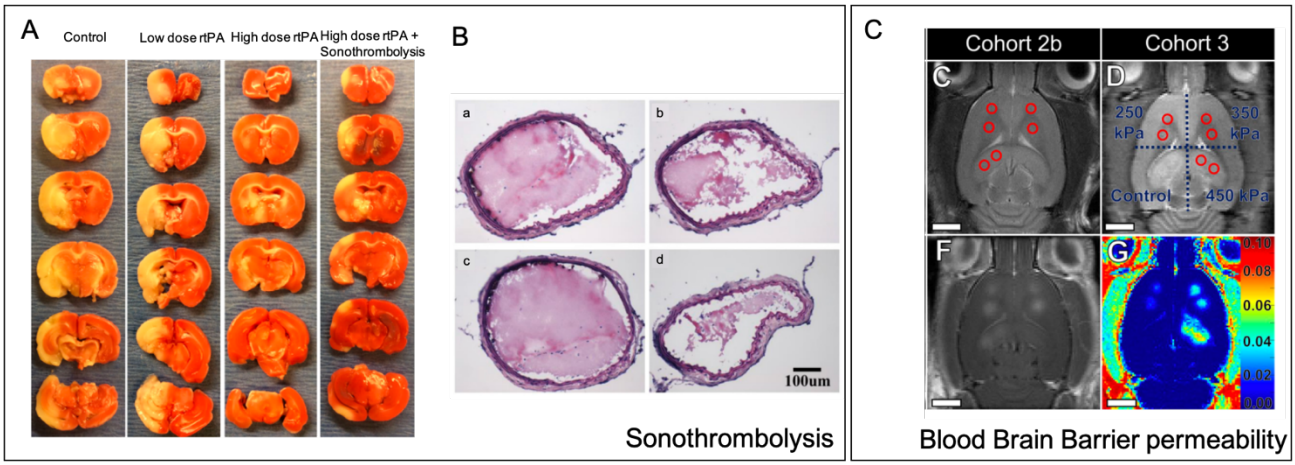

Figure 6: MBs and US insonation for sonothrombolysis and Blood Brain Barrier permeability. ***A)*** *and* ***B)*** *In vivo sonothrombolysis using MBs and US.* ***A)*** *TTC staining of stroke induced cross sectioned brain. Infarct is identified by yellowish areas. Groups are presented as below: control with saline injection; low dose of rtPA (0.09 mg/kg); high dose of rtPA (0.9 mg/kg); low dose of rtPA (0.09 mg/kg) + MBs + US.* ***B)*** *Representative images of hematoxylin and eosin-stained thrombi from mice carotid arteries after different treatments and US imaging. a) Platelet targeted MBs + low dose of rtPA (75 U/g); b) rtPA loaded platelet targeted MBs; c) Platelet targeted MBs + saline; d) Platelet targeted MBs + high dose of rtPA (500U/g).* ***C)*** *MRI images of Targeting Focused US (FUS) on rats. First row red circles represent the MRI guided FUS targets before insonation. Second row corresponds to images after FUS.* ***C-F)*** *Gadolinium contrast enhancement in T1 MRI highlighting BBB permeation on FUS targets.* ***C-G)*** *Dynamic contrast-enhanced-MRI after MBs FUS exposure depending on several US amplitude. TTC = Triphenyltetrazolium Chloride. Adapted with permission from A)* [54]*; B)* [167]*; C)* [236].

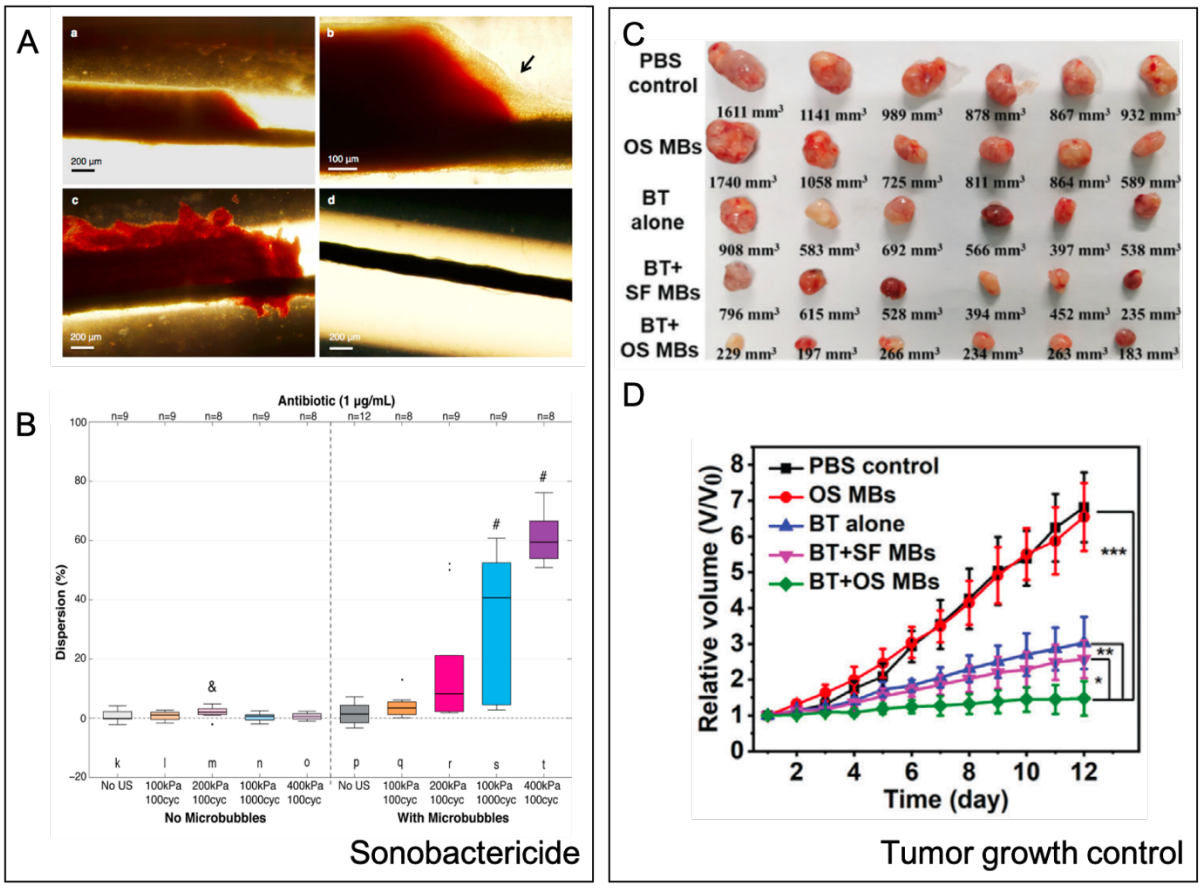

Figure 7: MBs and US insonation for sonobactericide and tumor growth control. ***A)*** *and* ***B)*** *In vitro sonobactericide.* ***A)*** *Bright-field light microscopy images of infected clots following treatments. Groups are presented as follow: a) plasma control; b) control magnification; c) antibiotic + rtPA; d) antibiotic + rtPA + US + MBs.* ***B)*** *Dispersion of bacteria within biofilms with several insonation intensity and duty cycle. Comparing antibiotic treatment with or without MBs (* $p < 0.05$. or ** $p < 0.01$). **C)** and **D)** In vivo tumor growth evaluation with US and MBs mediated radiotherapy treatment. Groups were defined as follow: administration of PBS (PBS control); administration of Oxygen/SF_6 MBs followed by US activation (OS MBs); Brachytherapy (radiotherapy with 125I seeds) alone (BT alone); Brachytherapy with SF6 MBs followed by US activation (BT + SF MBs); Brachytherapy with Oxygen/SF_6 MBs followed by US activation (BT + OS MBs).* ***C)*** *Representative images of ex vivo tumor volumes with different treatments.* ***D)*** *Tumor relative volume growth curve of different groups for 12 days (n=6, *p = 0.001, **p = 0.001, and ***p = 0.0004). cyc = cycles; PBS = Phosphate Buffer Saline. Adapted with permission from A)* [243]*; B)* [244]*; C-D)* [180].

New scales and technology

MBs also suffer from several limitations, including their size which limits extravasation of the vascular compartments, as well as a usually short circulation time (in the magnitude of a few minutes [247]). On the other hand, new approaches based on nanotechnologies offer significant advantages such as surface properties, access to the surrounding tissues and longer circulation time thanks to an array of new materials and expertise in various formulations of both organic and inorganic objects [248].

As such, nanobubbles (NBs) were developed as an alternative to ultrasound-active compounds like MBs to achieve extended circulation time, extravasation to surrounding tissue (especially tumor tissue) and potential molecular targeting capacities[249]. New technological developments have also allowed the emergence of more complex acoustically active objects, while also illustrating some limitations and risks of the current nanoscale ultrasound-active approach. Lastly, US imaging in clinical application shows limitation for a more precise imaging leading to the development of innovative ultrafast imaging.

- **Nanobubbles**

Among the wide use of MBs for clinical imaging application, the existence of NBs themselves was debated for a long time [250], even after being evidenced as existing in commercially available MBs suspensions [251]. For the most part, their stability was not compatible with standard bubble models and as described above, the ultrasound backscatter significantly decreases with the micro/nanobubble size [249], nullifying NB's participation to ultrasound signal. The main takeaway from the literature before 2010 was therefore that NBs, if existing, were present at traces level and would not contribute in any way to a relevant ultrasound contrast enhancement [252]. However, Oeffinger and Wheatley published their work in 2014 with comprehensive description of ultrasound contrast agents with diameters ranging from 400 to 750 nm and formulated from a previously described model of 1.5 micron microbubbles [252], [253]. Hereafter, the field started taking off with the emergence of multiple approaches, notably in the field of cancer imaging and therapy.

Typically, NBs consist of similar components as traditional MBs while having a diameter in the range of 100-500 nm [254]. A gaseous core, mostly filled with PFC gas (or mixtures of them) is encapsulated in a shell which, as for the MBs, is often composed of self-assembling lipids. A broad range of phospholipids, either in single or cocktail formulation, have been used over the years while being coupled to various methods of synthesis [255]. Mostly two

approaches exist: either isolation from a bulk heterogeneous microbubble suspension [256] (based on centrifugation [257] or filtration [258]), or *ab initio* synthesis with similar techniques as microbubbles with careful optimization of composition and synthesis parameters, such as sonication, mechanical stirring or thin-layer evaporation [254], as well as recently microfluidics [259]. Other interesting NBs have been formulated with different shell formulations, including surfactants [260] or polymers (e.g., organic polymers such as PLGA nanobubbles from Yang *et al.* [261] or polysaccharide crosslinking as shown by Bhandari *et al.* [262]). Others have described various synthetic methods for NBs generation [248], [262]–[264], and since they mostly resemble techniques for MBs synthesis recapitulated above, we will focus in the following discussion on their applications.

First, the advantage of NBs over MBs is their much smaller size, which allows for extravasation in leaky vasculature (*Fig. 8*). This has been especially investigated in cancer theranostics, with much attention on the Enhanced Permeation and Retention (EPR) effect, associated to leaky endothelium in certain tumors with fenestrations of a few hundreds of nanometers [254]. As such, NBs have an ideal size for specific imaging of tumors with the generally recognized safe and easy-to-implement ultrasound imaging. Several authors described the use of NBs as means of tumor imaging; among them, Zhang *et al.* showed in 2019 that a carefully controlled preparation method based on differential centrifugation could yield acoustically active NBs with diameters of 475.2 ± 5.7 nm with significant passive targeting of solid tumors *in vivo* when compared to microbubbles [257], as well as similar ultrasound contrast *in vitro* as MBs across a range of 10^5 to 10^9 bubbles/mL. Similar works demonstrated this by various imaging methods [263], [265]; however, precise localization of the acoustically active components inside or outside the vasculature was not evident, and mostly macro-imaging methods or efficacy of a fluorophore or drug delivery were often used as endpoint. Therefore, the results from Pellow *et al.*, were particularly interesting as they demonstrated that acoustically active nanobubbles effectively extravasated, and not only fragments and payloads which could have otherwise been detected: they managed this by careful kinetic assessments including destructive cavitation of extravasated NBs [266]. Furthermore, they described an extravasation enhancement with ultrasound stimulation of their NBs, by showing a contrast enhancement of 1.5x the baseline in tumors and 5x when subjected to ultrasound stimulation. Other groups have coupled passive and active targeting of tumors, with for instance by Kumar *et al.*, 2022, who covalently conjugated anti-PD-L1 nanobodies to NBs for molecular imaging of PD-L1 expression in tumors, with promises related to diagnosis and prognosis of multiple cancer types [259].

Moreover, the use of NBs is not limited to cancer imaging, as therapeutics can be delivered with the combined benefits of NBs. The cavitation properties of MBs and NBs can be utilized to improve delivery of gene therapies [265]. In comparison to MBs, NBs benefit from their smaller size for extravasation and tissue penetration [267] and publications from various groups demonstrated the potential of NBs for tissue gene therapy. For example, since 2020 Kida *et al*. described the optimization of NBs size to improve genetic material delivery [267] and feasibility of *in vivo* gene transfection in mice with a hand-held ultrasound scanner [268]. Such a controlled release is also relevant for drug delivery as shown by Tan *et al*., among others, who used nanobubbles loaded with an immune checkpoint inhibitor and a sonosensitizer for antitumoral activity in a xenograft mouse model [269]. Interestingly, growing knowledge on the influence of shell properties and NBs size might allow in the future a better controlled acoustic response of NBs, which might allow multiplexing of NBs in the future for differential imaging or therapy [258].

- **Beyond nanobubbles**

Over the years, more complex approaches have emerged to benefit from micro/nanobubbles related acoustic properties while ensuring a better control over the objects, including switchable properties, multimodal imaging or increased stability and robustness [270]. This partly stems from limitations of the NBs.

Indeed, multiple studies showed that in fundamental-mode (or in B-mode) ultrasound imaging, nanobubbles contribute to a negligible extent to the acoustic signal [251], [252], [271], which is coherent with the backscatter theory in ultrasound imaging [272]. A recent study by Myers *et al.* in 2020, while limited in its scope, raised doubts about the risk of MB contamination in a NB preparation, where only a small proportion of 2.5 microns MB would be responsible for most of the US acoustic signal when mixed with 700 nm NBs [273]. Even though this work was limited to a single formulation, and focused on fundamental imaging at a classical setting, it pinpoints the extreme care that needs to be taken in formulating such NBs. It is however interesting to note that NBs were repeatedly shown to have strong nonlinear effects which can be detected [249], [250], [266]. This recapitulates another limitation of NBs: comparison to MBs is rather complex since imaging modalities differ. While some publications directly compare NBs and MBs with standard ultrasound imaging [253], [263], [274], rigorous comparison based on volume or molar concentrations equivalence is often lacking. Furthermore, imaging modalities differ especially since several publications using the

nonlinearity of Nanodroplets (NDs) response to ultrasound for contrast enhancement, in contrast to MBs. On the other hand, an interesting work by Batchelor *et al*. in 2020 with NBs nested inside liposomes revealed that in their formulations, both NBs of perfluorobutane (PFB) and PFB droplets were actually present, with the PFB droplets being responsible for the cavitation that allowed payload delivery in their liposomes [275]: this pinpointed another rich area of PFC-based acoustically active objects.

Such nanodroplets (NDs) or Phase-Change Contrast Agents (PCCA) have been investigated extensively since 2010 [276], [277]. These emulsions of PFC gas in nanoscale droplets can undergo a phase-transition under stimuli to form nano/microbubbles that are acoustically active [278], [279]. Interestingly, this shift, which is linked to a vaporization temperature usually close to 37°C in the pressure conditions of such nanodroplets, can be triggered by both externally applied ultrasounds [264] or photoacoustically by near-infrared illumination [280]. This allows for both the advantages of nanoparticles/nanobubbles of easy extravasation, tissue penetration and targeting abilities, while benefiting from the high backscatter of microbubble *in-situ* formation for clear acoustic imaging (*Fig. 8*). As shown by Moyer *et al*. in 2015, these NDs when compared *in vivo* to MBs showed an improved HIFU (High Intensity Focused Ultrasound) effect, which is used for thermal ablation of tumors among others and can be enhanced by ultrasound contrast agents [281]. Moyer's article demonstrated that NDs allowed for more localized, more efficient and overall safer use of HIFU for in-depth tissue thermal ablation. Notably in a rat model, they showed efficacy of NDs from 4 to 10 mm deep in the liver while MBs caused surface and skin burns, due to prefocal heating. Multiple groups have similarly investigated the use of NDs both in imaging and therapy for solid tumors [282] and showed benefits of using NDs to selectively image cancer biomarkers [283].

Recently, super-resolution-based approaches have emerged in photoacoustic imaging with the works from the group of O. Couture starting with the publication of Errico *et al.*, who used MBs to break the diffraction limit in ultrasound imaging [284]; similar work was pursued with both microdroplets [285] for sub-diffraction drug delivery control through ultrasound, and later NDs [286] in a photoacoustic setting to reach unequaled spatial resolution in tissue (less than 10 microns spatial resolution). Such NDs therefore show promises in advancing ultrasound contrast agents further into the tissue and therapeutic potency [270].

Other innovative technologies have emerged: *in-situ* generation of nano/microbubbles without PFC gas, with for instance plasmonic nanobubble generation [287] with Hollow Gold Nanoshells (HGN) [288]. In these objects, HGN or simple gold nanoparticles are able under laser excitation to locally heat the surrounding water and create transient vapor bubbles (*Fig.*

8). Interestingly, using Nanoshell structure allowed excitation with Near Infrared (NIR) light, therefore enabling this technology to be used *in vivo* thanks to the NIR imaging window [288], [289]. As demonstrated by Shin *et al*. in 2020, a fine tuning of liposomes-loaded HGN based on size , from 10 to 40 nm, or wall thickness and aspect ratio, can be used in a precise delivery of Ca^{2+} and ATP by liposomal rupture, almost in a multiplex manner [290]. Other objects have been investigated to produce similar effects, by directly trapping gas nanobubbles on nanostructures. These include the polymeric nanocups designed by Kwan *et al.,* which can carry air nanobubbles, and use them under cavitation to enhance delivery of an antibody into tumors [291]. Another innovative approach relies on local chemical generation of bubbles: one such research was led by Shi *et al*. who loaded catalase on 50 nm mesoporous silica nanoparticles to generate locally O2 bubbles that enhanced the HIFU effect in tumors [292] (*Fig. 8*): under sufficiently low power so that no tumor damage could be observed with a saline injection, a 135 ± 30 mm^3 ablation could be observed with this catalytic nanoreactor. A key benefit of these objects relies in the extensive knowledge of such nanoparticles which allows fine control over synthesis, stability, functionalization, and characterization [293].

Notably, another source of nanoscale contrast agents takes a radically different approach, without requiring artificial synthesis of such compounds: Gas Vesicles (GVs) can be extracted from certain microorganisms, and under proper purification, can act as proper nanobubbles. Such GVs have been described for more than 100 years and can be found in various bacteria and archaea and play roles in buoyancy for these organisms when freely floating in water, but also in regulation of cytoplasm volume and surface-to-volume ratio [294]. They are composed exclusively of proteins self-assembling into cylinders or spindle ranging from 0.1–2 μm long vesicles, which are permeable to gas only. However, their use as nanotechnology had not yet been exploited. Pioneering work was led by Shapiro *et al.* who described the GVs produced in *Anabaena flos-aquae (Ana)* and *Halobacterium NRC-1 (Halo)*, their isolation and characterization as nanoscale nanobubbles both *in vitro* and *in vivo* [295]. Further engineering improved these GVs as contrast agents, with for instance work by Wang *et al.* which functionalized GVs with PEG and Hyaluronic Acid (HA) to increase their circulation time and escape immune clearance [296]. Shapiro's group also performed the exciting isolation of a minimal gene cluster which can be expressed in mammalian cells as reporter genes, with promising cell lineage tracking capabilities with the desired simplicity of ultrasound imaging [297]. Another proof-of-concept of the efficiency of GVs as NBs can be found in their use for ultrasound-mediated delivery of genetic material by bubble destruction, as described by Gao *et al*, who managed the gene editing of tumor cells both *in vitro* and *in vivo* with these GVs [298]

(*Fig. 8*). Relying on such bio-sourced nanobubbles allows for a strict monomodal size distribution and control over these objects, which answers to one of the major difficulties of nanobubble synthesis as described above.

Thus, the rich recent research surrounding nanoscale ultrasound contrast agents with the leading nanobubbles illustrate the potential yielded by the junction of microbubble-based ultrasound properties and nanotechnology: targeted, controlled objects with access to extravasation in various tissues for both imaging and therapy while also relying on a broad range of functional technologies brought forth by the vast nanoparticle field [248], [293]. The currently understood advantages and limitations of these new approaches are listed in the *Table 5*.

***Table 5** : Advantages and limitations of recent contrast agent innovations, based on their imaging, capabilities, circulation properties and tissue penetration*

	Nanobubbles	Nanodroplets	*In situ* bubble generation: plasmonic effect or enzyme-based	Gas vesicles
Advantages	• Extravasation, tissue penetration • Stability • Nonlinear imaging • EPR effects (tumor passive targeting)	• Extravasation, tissue penetration • Stability • Nonlinear imaging • EPR effects (tumor passive targeting) • MB switching for improved imaging	• Extravasation, tissue penetration • Inorganic (stable, controlled chemistry) • Fine tunability of NP physico-chemical properties • Spatial control, tissue-specific activation	• Extravasation, tissue penetration • Fine size control • Eukaryotic gene reporting • Cell tracking *in vivo* by US imaging
Limits	• Size control can be limited • MB contamination can affect US signal • Modality of imaging is not yet standardized: o Classical mode settings (resonance frequency, intensity) o Nonlinear modes (multiple methods for exploiting nonlinearity, which must be compared)	• Delicate choice of PFC: liquid/gas transition must be fitted to body temperature • Physical activation *in situ* is yet to be mastered (US, light-induced heating) • High pressure/longer pulses are typically required in US activation than usually administered	• No imaging prior activation • Activation control, due to multiple possibilities, is yet to be standardized: o HGN are limited by light penetration and O_2 availability o Enzyme-based NPs require sufficient substrate, ATP and tissue variability can be an issue	• Typically, high concentration is required for similar imaging power as MBs • Differences in imaging with NBs of similar size cannot yet be explained • Nanoengineering capabilities are still recent and requires further refining • *In vivo* cell imaging through gene expression is yet limited to destructive imaging, with possible negative cellular effects

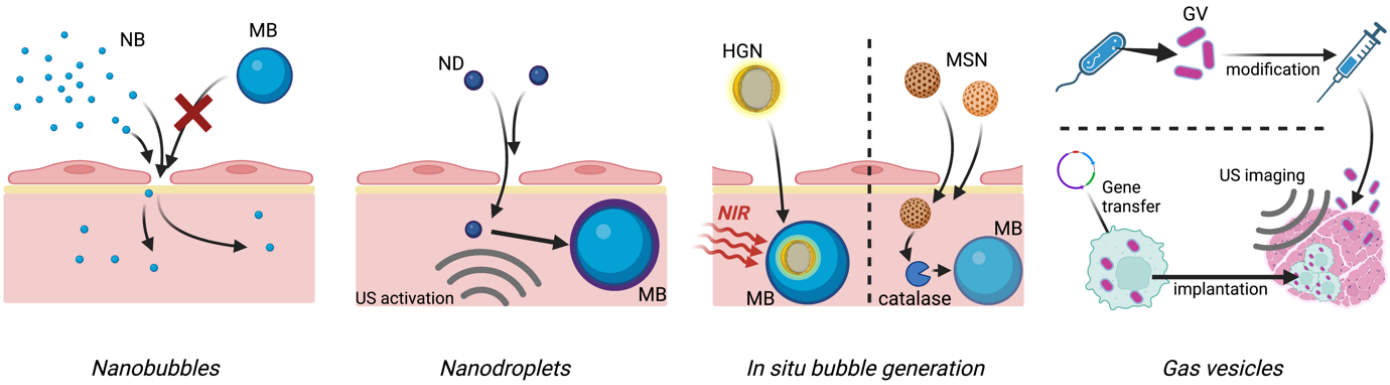

Figure 8: New scales of US sensitive objects. *The rationale behind the different innovations on the nanoscale to MB technologies are represented here. From left to right: NBs are typically smaller than 0.5 µm to allow extravasation, while NDs can be converted from nanosized droplets to MBs to combine NBs and MBs properties. HGNs use plasmonic resonance to locally create vapor MBs, and MSNs can be loaded with enzyme responsible for in situ O_2 bubble generation. Finally, gas vesicles can be extracted from bacteria and act as NBs. Otherwise, gas vesicles can be encoded on a genetic cassette, transfected in eukaryotic cells, for the live cell labelling during implantation. NB = nanobubble, MB = microbubble, ND = nanodroplet, HGN = hollow gold nanoparticle, MSN = mesoporous silica nanoparticle, loaded with the catalase enzyme, GV = gas vesicles. Created with BioRender.com*

- **Ultrafast imaging**

On the other hand, advances in the ultrasound imaging method have also benefited from specific MBs use. An especially notable one is the emergence of Ultrafast Ultrasound Imaging. Predicted and developed since the 70s [299]–[301], it was however first used in practical conditions after the 2000s (following work in 1984 by Shattuck *et al*. with only four simultaneous lines) [302], [303] with the development of new processing units (GPU) that allowed for a software-based parallelization which is especially demanding, in the range of several Gigabytes/s for data transfer to the processing unit, or of 1 to 2 Gigaflops/s (operations performed by the processing unit) computing power [304]. As explained above, the conventional imaging with an ultrasound probe is based on serialized lines reconstruction by focused beams, and therefore the frame rate is limited by the time to emit, receive, and process the beam on one hand, multiplied by the number of lines necessary for the image [305]; meaning that the building time of an image is directly correlated to the size of the zone being observed with for example at a given depth, an image needing twice more lines will take twice more time to acquire, which either limits the frame rate or the width of the images [304], [305]. This can be improved by built-in multiline computation probes, but the serialized design remains the main limitation to the frame rate, typically in the range of 30-100 Hz [304]. On the other hand, in ultrafast imaging the whole process is parallelized, as typically only one (or few) emission is used to simultaneously image the whole region of interest by relying on plane or divergent ultrasound waves [306], [307]. All the lines are acquired at once and thus the image frame rate

is only limited by the wave time-of-flight, as long as the processing power necessary for data treatment is sufficient. In such ultrafast architectures the image frame rate can reach tens of thousands of Hz [304]. This high frame rate can be put to use for multiple benefits, such as 3D imaging, high temporal resolution or two major innovations enabled by this technique: Shear Wave Elastography, where quantitative viscoelastic measurements of tissue can be acquired in real time without invasive procedures [308] (*Fig. 9*), or Ultrafast Doppler imaging with simultaneous qualitative and quantitative measurements at high speeds [309]. Notably, functional Ultrasound Imaging (fUSI) was developed, which relies on ultrasound plane waves to attain ultrafast ultrasound Doppler for cerebral blood volume measurement: this approach allows a high spatiotemporal resolution (200 μm, 1 ms) and has already been shown to be beneficial in measuring brain activity [310], and study neurovascular coupling. However, these improvements alone cannot increase the spatial resolution of US imaging beyond the diffraction limit.

Furthermore, when coupled with ultrasound contrast agents such as MBs, ultrafast ultrasound imaging has found an extremely powerful application. Not only can, the benefits of imaging MBs at ultrafast scale, improve the real-time imaging of vasculature or tissue, but it has also been used in a super resolution approach to break the diffraction limit and improve the resolution of ultrasound imaging down to a few microns, in an approach called Ultrasound Localization Microscopy (ULM)) [311], [312]. The rationale, inspired by optical super-resolution techniques such as Photo-Activated Localization Microscopy (PALM) and Stochastic Optical Reconstruction Microscopy (STORM*),* relies in imaging separable punctual sources (here, echoes from a single MB) and deconvoluting the Point Spread Function (PSF) to localize the source beyond the diffraction limit. The repetition of this process over thousands of sources allows the reconstruction of a resolution-enhanced image. In the context of ultrasound imaging, the high frame rate (over thousands of Hz) of ultrafast ultrasound imaging allows this method to be applied in ultrasound imaging of MBs or similar contrast agents [284]. Since the signal of MBs decorrelates much quicker than the surrounding tissue both spatially and temporally, they can be separated from the background and isolated individually [312] with either linear or nonlinear US imaging. This was demonstrated in 2015 by Christensen-Jeffries *et al.* [313] and by Errico *et al.* [284]. The latter described *in vivo* ULM and showed that the spatial resolution was improved more than ten times compared to conventional ultrasound imaging, allowing the distinction of 20 microns wide blood vessels, 20 microns apart and up to 8 mm deep in the brain of rats. This is illustrated with comparison of ULM to classic Doppler vasculature imaging in the Figure 7. Moreover, since this approach relies on individual MB

spotting, their tracking can be used to measure blood flow velocity inside the imaged vessels, with notable benefits when compared to conventional Doppler. The resolution is significantly enhanced (from hundreds of µm to around 15 µm), and Doppler velocity mapping is limited to the component orthogonal to the imaging direction [284]. In the recent years, several published works have demonstrated the potential of ULM technique, with among others, Hingot *et al*. (2021), who presented a normalized method to evaluate spatial resolution in ULM [314], Chavignon *et al.* (2022), who investigated the perfusion differences in ischemic or hemorrhagic strokes in rat models [315], or Andersen *et al.* (2022), who verified that ULM could correctly assess physiological velocity changes in the vasculature by chemically altering blood velocity in rat kidneys [316]. Most recently, new promising diagnostic applications were described with for instance ULM use in Alzheimer mouse models [317]. This array of publications illustrated the normalization of its use and helped the recognition of this powerful tool for non-invasive quantitative exploration of tissues. Interestingly, among multiple approaches to robustly implement this method, Chen *et al.* (2022) reported a Deep Learning-based method for MB localization, with apparent imaging benefits when compared to conventional localization [318], while Heiles *et al.* openly made available methods and metrics for benchmarking ULM algorithms in 2022 [319]. Notably, several groups have focused on bridging the gap to the clinical world, with for instance Yan *et al*., who translated this method to rhesus monkeys and thus opened the way to clinical trials [320], and Demené *et al.*, who first used ULM in human brain without the need for transcranial aperture and with significant improvement in spatial resolution with at least one order of magnitude enhancement at up to 120 mm depth when compared to a typical clinical contrast CT imaging [321], or Huang *et al.* who recently published a feasibility study in various human organs [322]. The diagnostic potential was also investigated in tumor bearing mice, then in human patients, by the group of Opacic in 2018 and opened new tumor assessment [323].

As mentioned earlier, this new imaging method can also be coupled to newly developed ultrasound contrast agents in order to further improve resolution and enhance the therapeutic efficacy. Indeed, several groups attempted to break through the diffraction limit with the use of optical super-resolution inspired techniques. For instance, Zhang *et al.*, described Cyanine 7.5-coated NDs for photoacoustic imaging, and similarly to PALM, STORM or ULM, single objects are localized and PSF-deconvoluted; but here, the laser illumination is tuned so that only a small fraction of NDs are converted to MBs which can be imaged by ultrasound, and therefore the tuning of the laser allowed for a fine control of detectable events [286]. Even though tissue penetration can be reduced with NIR light compared to ultrasound imaging (tens

of mm versus tens of centimeters [263,264]), the precise activation of these contrast agents and focal precision of NIR laser can prove useful in certain applications.

Thus, ultrafast ultrasound imaging has opened new opportunities in ultrasound imaging by reaching unprecedented imaging frame rates, which have among others been exploited with MBs to reach super-resolution imaging capabilities in ultrasound imaging. It can therefore be expected that innovations in the contrast enhancement agents might be repercussed in combination with ultrafast ultrasound imaging to reach new potential. For instance, further spatial resolution enhancement in super-resolution ultrasound imaging might benefit from the use of NBs or NDs [236,265]. Functional imaging allowed by targeted MBs or even NBs to extravasate deeper in tissues might open new insights with improved either temporal or spatial resolution through ultrafast or ULM ultrasound imaging, with encouraging results from already existing (though at a less fine spatial resolution) fUSI in terms of clinical applications. Overall, innovations in the contrast agents' field (MBs, NBs, NDs, echogenic NPs, etc…) can converge with advanced imaging methods (Doppler, 3D, ultrafast, ULM, etc…) to improve our exploration of physiology, diagnostics, and therapeutics.

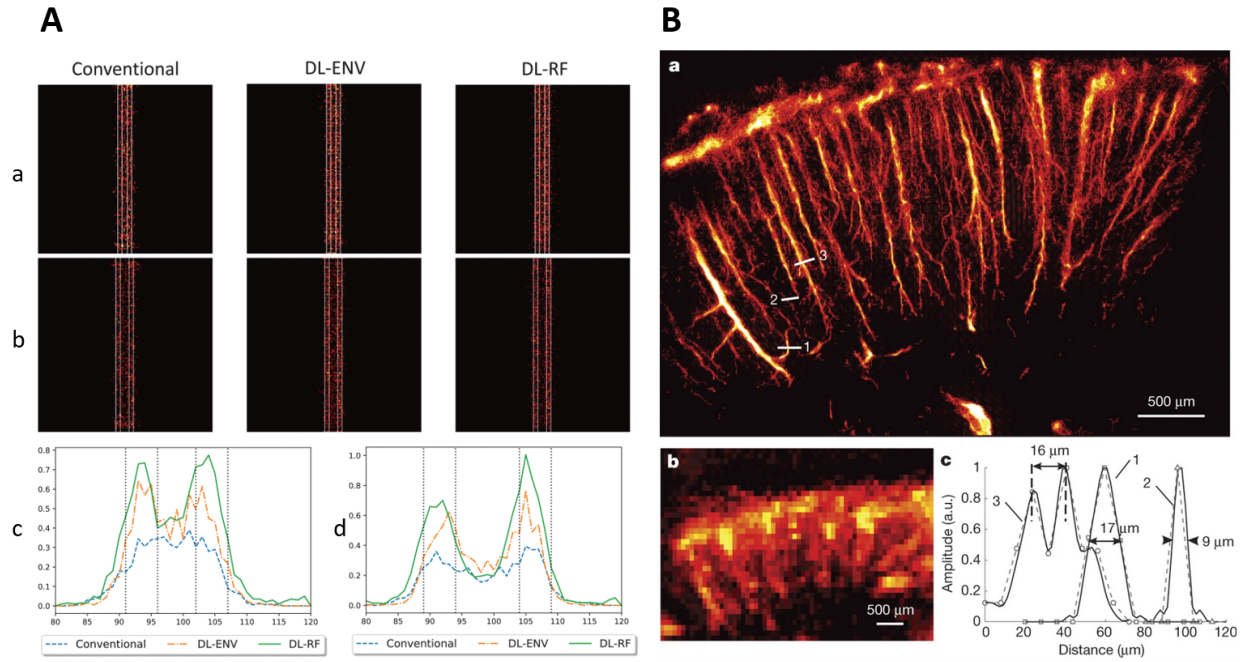

Figure 9: Two major applications of Ultrafast Ultrasound imaging: A) *Illustration of how different analysis method for MB localization can affect the spatial resolution of ULM. Two deep learning algorithms (DL-ENV and DL-RF) are compared to a conventional localization technique, with (a) and (b), simulated vessels separated by 3.0 µm or 4.9 µm. Transverse reconstruction with the different methods are respectively shown in (c) and (d).* ***B)*** *Comparison of an Ultrasound Localized Microscopy (ULM) images (a) reconstructed through microbubbles localization (pixel size of 10x8 µm), with the same area imaged in conventional power Doppler in (b). Based on the (a) image, a linear intensity projection along the displayed line (from 1 to 3) shows a spatial resolution below 16 µm. Adapted from A)[318]; B) [284]*

This work aimed to better understand the MBs strategies for human treatment and diagnosis. New approaches were described to overcome the unmet medical need for a non-invasive and targeted efficient treatment but also diagnosis tools. Indeed, therapeutic treatments relying on systemic drug injections are still bringing toxicity, collateral damages and uncontrolled pharmacokinetics, such as half-life in circulation or tissue penetration. The use of MBs in clinical application is currently reserved for US imaging thanks to their echogenic properties. Through this review we pointed out the importance of understanding MBs intrinsic characteristics (composition, behavior, stability) to better apprehend their translation to *in vivo* diagnosis and treatment. Secondly, the review focused on the use of commercial MBs for US imaging and the recent prolific development of targeted MBs for molecular imaging that brings a new dimension for early and precise diagnosis. We confronted the applications for cancer, cardiovascular diseases or inflammation to better understand MBs behavior. Depending on their application, MBs can be insonated with US at varying settings to take advantage of different oscillation response. It showed that the frontier between stable cavitation and inertial cavitation *in vivo* is still delicate to establish. According to most pre-clinical studies, it can be concluded that low mechanical index insonation of microbubbles would help mechanically destabilize the surrounding environment. This includes enhancement of drug delivery, biofilms impairment and BBB opening thanks to microstreaming. In addition, the rise of mechanical index would induce irreversible MBs destruction which can further cause fibrin clot disassembling, cells membrane sonoporation and sometimes vascular leakage with erythrocytes extravasation. Overall, the complete drug-loaded targeting US responsive tools are not yet ready for clinical translation, but the use of clinical MBs co-injected with therapeutic agent and enhanced with US signal showed promising results for the drug doses reduction. In addition, the exact boundaries to avoid damaging features are not established yet except for the FDA fixed 1.9 MI and are highly dependent on MBs intrinsic properties. It has to be understood that MBs mechanical response to US insonation have not been determined completely and a collective effort has to be made to better describe the US transducer parameters (frequency, amplitude, duty cycle) and the set-up characteristics (insonation duration, distance to object, etc.). Due to the broad interest in the MBs potential, there has been multiple advancements and innovations both in designing the right MBs for the right applications, and in adapting the MB rationale to new US contrast agents in order to overcome their limitations. This was described in the last part, including among others the use of nanoscale bubbles and droplets, as well *as in situ* generation of echogenic signals with nanoparticle approaches and new MBs' combined use with recent technologies to breach the physical limits of the US imaging.

In perspective work, it appeared that the emergence of combined technologies could add another dimension to MBs' behavior, including for example photodynamic therapy [326], [327], photoacoustic imaging [280], [328] or magnetic MBs [329]. Also, the development of US responsive piezoelectric nanomaterial are an interesting new strategy to open the MBs world to cell therapy [330]. As these new therapeutic approaches require the injection of foreign body material, the priority now stands on safety. Clinical trials are widely enrolling patients to established the best parameters for US combination with MBs. These strategies are obviously not meant to replace drug treatments yet but they have the potential to improve their outcome. Since MBs, their applications, and consequent innovations are thriving in multiple fields (oncology, cardiovascular diseases, inflammation), the convergence of expertise and standardization of certain practices are paramount to ensure a quick development and future translation to the clinic.

Chapter II: Experimental results

Part 1: Microbubbles synthesis optimization

As presented in the introduction part, MBs are widely studied for therapeutic application [331]. With the commercialization of MBs as contrast enhancers for US imaging (Sonazoid®, Optison®, Sonovue® or Definity®), therapeutic strategies involving the effect of oscillating MBs were easily explored. The functionalization of MBs is mainly addressed on their targeting and drug loading property, to obtain pathology specific agents. However, as commercial MBs, the most prevalent type of MBs is phospholipid shells MBs. While it demonstrated many advantages in terms of biocompatibility, bioresorbability and mechanical properties, it also brings some drawbacks [50]. Lipid shell MBs are often stabilized with polyethylene glycols (PEG) which were recently controverted for their immunogenic tendency [81]. In addition, the synthesis process of lipid shelled MBs is derived from a dry film rehydration process due to the non-miscibility of lipids into aqueous solutions. To overcome this problematic, the lipid mix is dissolved into chloroform and left for evaporation for several hours. Not only does this method uses toxic chemicals but it is also time consuming for the dried lipid film generation. Another drawback of lipid shelled MBs is their functionalization capacity. Indeed, the monolayer arrangement of lipids give small space for shell modification besides from avidin streptavidin. If some "ready to load" MBs are already available (MicroMarker®, BR55®), it either requires the modification of the functionalizing agent (e.g., biotinylating) or has a limited range of tunability. In this section, we present the shell components and the synthesis parameters that gave rise to the obtention of polymer MBs via acoustic cavitation.

Cyanoacrylate polymerization

The study of MBs versatility led us to consider polymer shell MBs. Widely used in industry, cyanoacrylates application has now also extended in medical application as surgical glues or vessel obstructing material to prevent from hemorrhagic complication [75]. In contact with moist surface, cyanoacrylate monomer almost instantly polymerized from where they get fast adhesion properties [332] (drying range in few minutes). The standard polymerization of cyanoacrylate relies on anionic polymerization of monomer in contact with water, that can be regulated with lowering the pH [333], [334]. The anionic polymerization relies on the activation of the methyl group of cyanoacrylate monomers by hydroxide anions, contained in the aqueous solution. Once activated, the monomer polymerization escalates quickly. The copolymerization with polysaccharides has also been described thoroughly by Bertholon *et al.* (*Fig. 10*)

highlighting the "brush-like" assembly of the obtained copolymer [333]. In those conditions, the monomers polymerization can also be initiated by any hydroxyl group from the polysaccharides (here dextran), leading to multiple elongation of cyanoacrylate on a single polysaccharide chain.

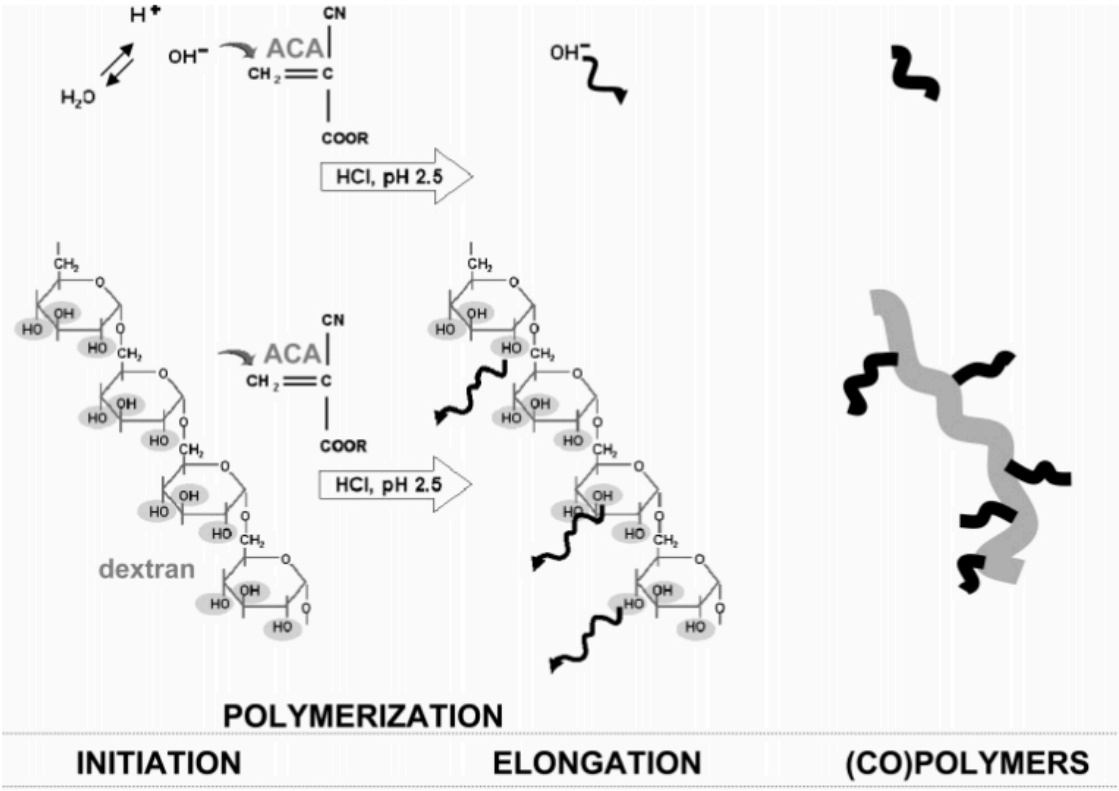

Figure 10: Anionic copolymerization of cyanoacrylate and polysaccharides. *Top: cyanoacrylate activation at pH 2.5 with hydroxyl groups contained in water. Bottom: cyanoacrylate activation from hydroxyl groups contained in Dextran. In the first case, it results in an homopolymer of cyanoacrylates; in the second case, it results in a copolymer of cyanoacrylates and polysaccharide. Adapted from* [333]

It has been described that the side chain length of cyanoacrylate monomers (R in *Fig.10*), confers different properties to the polymer. The increase of the side chain length decreases the adhesive properties of the glue but increases its elastic property [335]. Also, the hydrolysis degradation products of the side chains are known to be less toxic with an increased carbon chain molecular weight [336]. In consequence, the first FDA approved cyanoacrylates as surgical glues were mainly composed of octyl side chains (Dermabond®, INDERMIL® Flexifuze™), but we also observed the emergence of smaller side chain cyanoacrylate as tissue adhesive with LIQUIBAND® (10% octyl- and 90 % butyl-cyanoacrylates) [337]. The group expertise in Iso-Butyl Cyanoacrylates (IBCA), and the previous work on their polymerization for nanomedicine application [56], [338], allowed the availability of the monomer for the obtention of Poly-Isobutyl-Cyanoacrylate (PIBCA) MBs.

The targeting polysaccharide: Fucoidan

In our project, we replaced the dextran (*Fig. 10)*, used for PIBCA copolymerization with fucoidan, a sulfated polysaccharide derived from brown algae. Fucoidans have a fucose backbone and sulfated substitutions to some hydroxyl groups, making it fully biocompatible and now produced with GMP-grade for molecular diagnosis [44]. Additionally, fucoidans have been found to have a wide range of medical application including promoting hemostasis, reducing inflammation and fighting tumors [339]. The application we are interested in uses fucoidan similarities for P-selectin glycoprotein ligand-1 (PSGL-1) [340]. This glycoprotein is expressed on the surface of white blood cells and plays a role in inflammation by binding to the biomarkers of activated platelets and activated endothelial cells, P-selectins. PSGL-1 recognition domain for P-selectins is based on a trifucosylated and sialic acid domain. Thus, fucoidan has strong similarities for P-selectins natural ligand, to the point where fucoidan exhibited a nanomolar affinity for this thrombosis biomarker, compared to other sulfated polysaccharide such as heparin and dextran sulfate [341]. Our laboratory have been studying fucoidan anticoagulant properties since two decades [342], [343] and now focus on fucoidan targeting properties for thrombotic diseases with various project like NPs [338], [344], microcapsules [345], MBs [56] and radiotracers with technetium-99m radiolabeled fucoidan with for thrombosis molecular imaging in phase I and IIa clinical trials [45].

Polymer MBs hydrodynamic cavitation

The regular hydrodynamic cavitation method for polymer MBs synthesis was first described in 2008 by Palmowski *et al.* [346]. Briefly, it consists in the anionic polymerization by the addition of cyanoacrylate monomer onto pH 2.5 aqueous solution with surfactant (Triton X-100). In the meantime, the solution is "vigorously agitated" with a hydrodynamic homogenization for one hour. The obtained foam is then rinsed with the storage solution of 0.02% Triton X-100 suspension and filtered. High-speed agitation induces shear stress and sudden pressure changes which, with the presence of surfactant, induced the formation of bubbles. The addition of the hydrophobic monomer of cyanoacrylate into the aqueous solution initiates polymerization at the water-air interface, to which the cyanoacrylate is drawn. It results in polymerization at this interface, entrapping the previously formed gas bubbles.

This protocol has been the gold standard for cyanoacrylate MBs synthesis ever since its invention. Recently, our team published the functionalization of PIBCA MBs, with the incorporation of fucoidan into the aqueous solution [56]. Triton X-100 has been replaced by

Tween 20 to avoid any related cytotoxicity and the speed of homogenization has been set to 20,000 rpm. This protocol was defined as reproducible, non-toxic with a high yield for the production of targeted MBs. Nevertheless, we aimed to develop an original synthesis, so we considered the idea of introducing a new type of cavitation energy that would allow for more adjustments and customization. Therefore, the acoustic cavitation approach seemed like an interesting alternative as it is equally accessible and more parameter can be explored (duration, continuity of the signal or amplitude of the signal). In addition, the recent inclusion of perfluorocarbon in medical research demonstrated interesting advantages for the MBs stability because of it inert property and low diffusion in biological medium [67], [191].

Acoustic cavitation

Acoustic cavitation is defined as the formation of gas bubbles induced with an ultrasound signal. Briefly, the Sonifier converts domestic power into high-frequency electrical energy (20 kHz). This energy is transmitted to the horn converter which will vibrate in a longitudinal direction which is transmitted to the tip of the horn. Thus, when immerged in solution, the mechanical vibrations will induce bubbles formation. Our strategy was to define the parameters allowing the formation of polymer MBs with the replacement of high-speed stirring by US insonation. We can find in the literature the use of sonicating horn for MBs synthesis but it is primarily used for protein MBs or as a secondary step for lipid MBs. Polymer MBs synthesis is highly dependent of a lot of physicochemical parameters including, the volume of the aqueous phase the concentration of surfactant, the quantity of organic phase or the pH but also depends on the overall delivered energy of cavitation. *Table 6* displays the parameters that we kept from previous optimization of the hydrodynamic protocol so we could define the critical parameters for acoustic cavitation.

Table 6: Fixed parameters inspired by established hydrodynamic cavitation synthesis for polymer MBs

	Fixed parameters from hydrodynamic cavitation
Aqueous phase	50 mL H_2O + polysaccharides
Surfactant	Tween 20 1% (w/w)
Organic phase	IBCA 700 µL
pH	2.5
Rinsing/ Storage	0.02% Tween 20
Centrifugation	20 min, 500 rpm, 3X
Filtration	5 µm sieve mesh

○ Continuity, amplitude and duration of the signal

As it has not been documented in the literature yet, developing the acoustic cavitation protocol has been tedious. We knew that the shear force generated by the US was exothermic and more powerful than the circular motion generated by a helix. Also, most of the US based MBs synthesis protocol presented in the introduction are in the minute range and non-continuous. Thus, the first tests focused on the use of the US in a discontinuous manner in order to limit this temperature rise. To evaluate the success of a protocol, we observed the produced foam and the resistance to washing centrifugation steps. If no MB cake was observed on top of the storage solution after centrifugation, the batch was considered as not productive.

On/Off settings available on the Branson Sonifier were set as follows: 1s/1s; 2s/1s or 5s/2s. None of those settings allowed a satisfying synthesis of stable MBs, so we quickly switched to continuous insonation mode and placed the aqueous suspension on ice to reduce the temperature elevation. The next step focused on defining the right amplitude over duration balance. Even though cyanoacrylate polymerization is slowed down by the acidic pH (2.5) of the aqueous solution, our goal was to reduce the time of synthesis to get a significant advantage over hydrodynamic cavitation.

Little knowledge about cyanoacrylate polymerization in contact with the energy delivered by the ultrasonic horn implied multiple trials and failures to finally obtain stable MBs. In order to get closer to the energy provided by hydrodynamic cavitation, we estimated the Energy Density (ED) with the following equation:

$$ED = \frac{P\ (W)\ *\ t\ (s)}{S\ (cm^2)}$$

ED is defined as the ratio of the involved power *P* in Watts with the time *t* in seconds, over the area *S* in cm^2. The surface of US radiation was defined previously to remain the same as the hydrodynamic protocol so the tunable parameters were mostly the amplitude of the signal and the insonation time. The amplitude of the signal corresponds to the amplitude of displacement of the tip of the US horn and it varies depending of the viscosity of the solution and the radiation surface. In consequence, the emitted power (in Watt) is not the most relevant parameter here to discuss, considering the fact that it is setup dependent.

After multiple trials, increasing of synthesis duration with constant amplitudes, the final protocol was defined with the following parameters: 30 % amplitude and 20 min of constant US insonation. As presented in *Fig. 11A*, the total yield of MBs production was maintained compared to hydrodynamic cavitation with a reduction of the synthesis time by 3.

○ Incorporated gas

The choice for the incorporated gas was initially driven by the acoustic properties of perfluorocarbons presented in the Introduction Chapter but also for their capacity of induced phase shift for NBs production [277]. While we remained with objective of producing MBs, we quickly realized that the continuous bubbling of PFB played an extensive role in the batch production and batch stability. As we can observe in Fig. *11B*, the number of MBs synthetized with the perfluorocarbon (C_4F_{10}) was almost a hundred times more important compared to dinitrogen (N_2) or sulfur hexafluoride (SF_6).

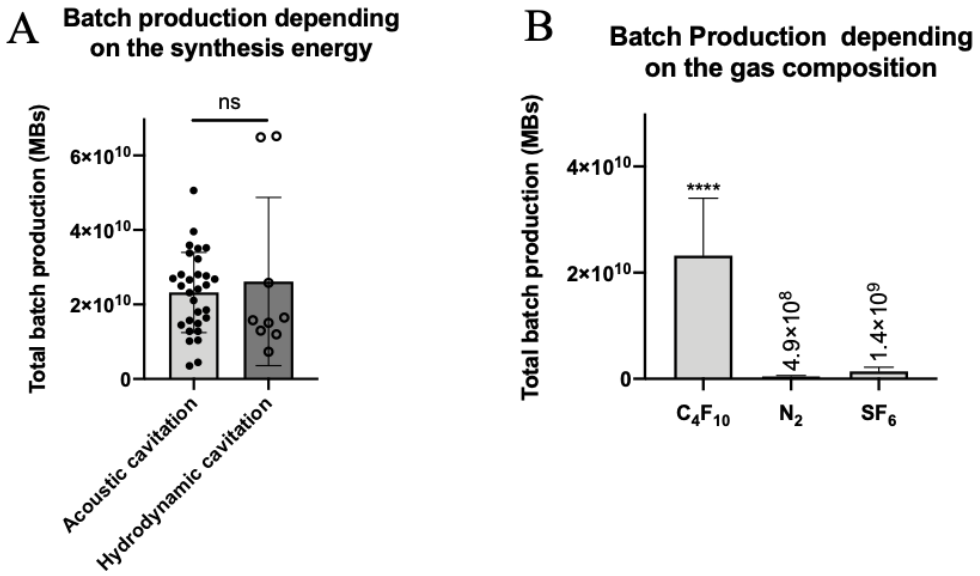

Figure 11: Batch yield production depending on the energy of cavitation and the incorporated gas. *The MBs quantities are obtained with the extrapolation of image analysis count.*

The main reason that could explain this significant difference, resides in the inert thermodynamic property of perfluorocarbons. There are described as very hydrophobic and their interfacial tension with water is reduced to 60 mN/m compared to air/water surface tension at 72.8 mN/m [347]. This stands for the fact that perfluorocarbons are less likely to get dissolved in water and thus are the perfect interface for highly hydrophobic cyanoacrylates.

○ Temperature of the synthesis

Lastly, the temperature of synthesis was studied to evaluate its influence on the MBs physicochemical properties. US insonation into aqueous solution intrinsically generates an elevation of the temperature as we can observe with US bath or US cell lysis process. In consequence, the aqueous solution was placed in ice from the beginning. What we did not expect was that this initial temperature could have an impact on the targeting properties. We compared two synthesis protocol where the initial solution was at 5°C (placed in the freezer for 15 min before synthesis) and a protocol where the initial solution was at room temperature (RT). First, we observed that the temperature of the synthesis had a non-significant influence on the batch production (*Fig. 12A*) but the targeting properties were impacted. The *in vitro* targeting assay presented in the next Chapter demonstrated that an initial cooling of the aqueous solution improved the targeting capacity of the Fuco MBs (*Fig. 12B*). Indeed, MBs synthetized with initial RT aqueous solution (Hot Fuco MBs) had a targeting ratio on platelet aggregate of 38.2 ± 15.4 % of their surface while MBs with an initial cold aqueous solution (Cold Fuco MBs) had a targeting ratio of 47.2 ± 17.2 % (P value = 0.0032). The underlying phenomenon explaining this shift has not been widely understood yet. Nevertheless, we believe that the reduced temperature may slow down the polymerization process and may be at the origin of a different arrangement of the fucoidan, presenting more domains for the targeting of activated platelets.

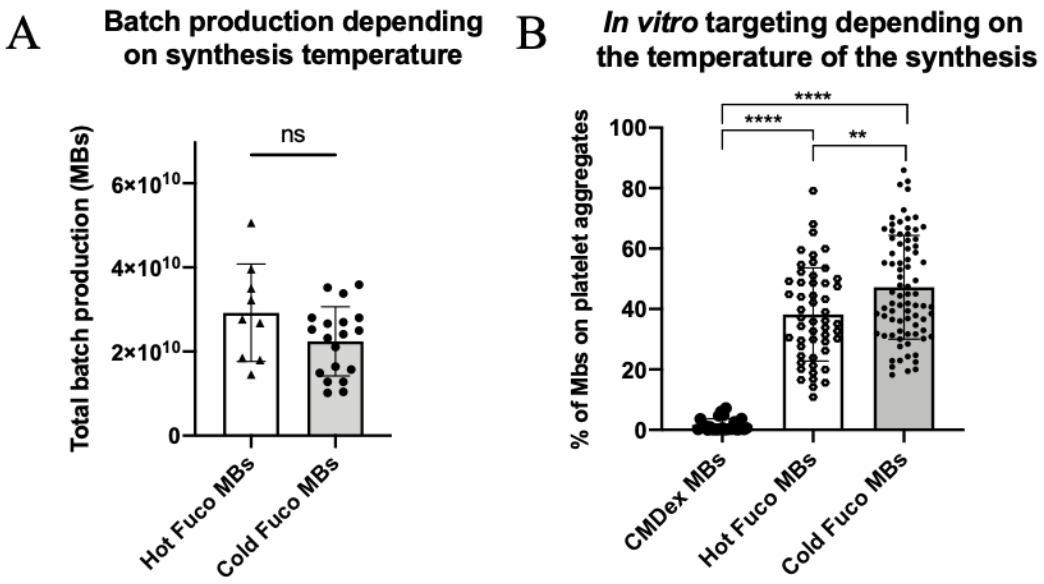

Figure 12: Influence of the temperature on the production of polymer MBs with acoustic cavitation. *Cold Fuco MBs refers to5°C initial aqueous solution and Hot Fuco MBs refers to RT initial solution.*

The main changes comparing the gold standard hydrodynamic cavitation and our original acoustic cavitation synthesis are presented in the following table (*Table 7*). In summary, the source of energy was replaced by US insonation, the duration of the synthesis was reduced by 3, the gas was replaced by a perfluorocarbon with better acoustic properties and the temperature was reduced for a better targeting efficiency. The originality of this method was pointed out by the editing of a Patent, supported with the help of INSERM Transfert, presented in the next section.

Table 7: Parameters differences between standard hydrodynamic cavitation and original acoustic cavitation. *rpm: rotation per minute, PFB: Perfluorobutane*

	Acoustic cavitation	**Hydrodynamic cavitation**
Device	Sonifier BRANSON SFX550	Homogenizer Ultra-Turrax IKA
Cavitation duration	20 min	60 min
Intensity	30%	20,000 rpm
Gaz incorporation	PFB: 10 min of saturation before and injection during all acoustic cavitation	Air
Temperature	In ice + cooling of the solution at -20°C for 15min	RT

Patent definition

This section provides an overview of the 37 claims of the patent filed in February 2022 (PCT/FR2022/050309): "**Method for manufacturing bubbles having a polymeric shell using sound waves for generating the bubbles".**

Inventors: Louise FOURNIER and Cédric CHAUVIERRE

Assignee: INSERM Tranfert (Annex 3)

With the help of INSERM Transfert and the Patent office Plasseraud, we defined the following claims to protect the originality of our protocol.

1. Method for manufacturing bubbles having a polymeric shell comprising the following steps:
   a) providing a first volume of an aqueous solution comprising a gas dissolved therein, a surfactant dissolved therein, and having a pH below 6, preferably comprised between 1.5 and 5, more preferably comprised between 2 and 4;
   b) in the aqueous solution, generating bubbles comprising the gas by applying sound waves to the aqueous solution;
   c) while generating the bubbles, adding a second volume of a cyanoacrylate monomer to the aqueous solution, thereby forming a suspension of the bubbles having a polymeric shell in the aqueous solution, wherein said polymeric shell is formed by polymerization of the cyanoacrylate monomer at the interface between the aqueous solution and the bubbles;
   d) recovering the bubbles having a polymeric shell;

   characterized in that the sound waves in step b) are applied during a period of at least 6 minutes, preferably between 8 and 30 minutes, more preferably between 15 and 30 minutes after the beginning of the addition of the cyanoacrylate monomer.

2. The method according to claim 1, wherein the gas dissolved in the solution has a molar mass of at least 100 g/mol, preferably of at least 200 g/mol.

3. The method according to claim 1 or 2, wherein the gas dissolved in the solution has a density at 20°C and 1013 mbar of at least 7 kg/m^3, preferably at least 9 kg/m^3.

4. The method according to any one of claims 1 to 3, wherein the gas dissolved in the solution is selected from the group consisting of alkanes, fluoroalkanes, and mixtures thereof, preferably wherein the gas dissolved in the solution is a perfluoroalkane or a mixture of perfluoroalkanes, preferably wherein the gas dissolved in the solution is perfluorobutane.

5. The method according to any one of claims 1 to 4, wherein the amount of the gas dissolved in the aqueous solution is maintained over 0.5 mg/L throughout steps b) and c), preferably wherein the aqueous solution is saturated with said gas throughout steps b) and c).

6. The method according to any one of claims 1 to 5, wherein the gas dissolved in the aqueous solution is bubbled through the aqueous solution during steps b) and c), preferably wherein the gas dissolved in the aqueous solution is bubbled through the aqueous solution throughout steps b) and c).

7. The method according to any one of claims 1 to 6, wherein the surfactant is a nonionic surfactant, for example a polysorbate, a poloxamer, an octylphenol, a nonylphenol, an ethoxylated fatty alcohol, a macrogol-glycerol ester, or a mixture thereof.

8. The method according to any one of claims 1 to 7, wherein the surfactant has a hydrophilic-lipophilic balance comprised between 8 and 18, preferably comprised between 10 and 18, more preferably comprised between 12 and 18.

9. The method according to any one of claims 1 to 8, wherein the amount of surfactant in the first volume of the aqueous solution of step a) is of at least 10 times the critical micelle concentration (CMC) of said surfactant, preferably of at least 50 times the CMC of said surfactant.

10. The method according to any one of claims 1 to 9, wherein a source of the sound waves is plunged in the aqueous solution

11. The method according to any one of claims 1 to 10, wherein the sound waves are not applied in pulsed mode, preferably wherein the time interval between two periods of application of the sound waves is lower than 10 seconds, more preferably the sound waves are applied continuously in one time.

12. The method according to any one of claims 1 to 11, wherein the source of the sound waves vibrates at an amplitude comprised between 50 µm and 500 µm, preferably between 100 µm and 500 µm, more preferably between 200 µm and 400 µm.

13. The method according to any one of claims 1 to 12, wherein the frequency of the sound waves is comprised between 10 kHz and 100 kHz, preferably between 15 kHz and 50 kHz.

14. The method according to any one of claims 10 to 13, wherein an emitting surface of the source of the sound waves plunged in the aqueous solution is of at least 1 mm^2 per 10 mL of the aqueous solution.

15. The method according to any one of claims 1 to 14, wherein the second volume of the cyanoacrylate monomer corresponds to at least 0.01 vol.%, preferably between 0.5 vol.% and 5 vol.%, of the first volume of the aqueous solution.

16. The method according to any one of claims 1 to 15, wherein the cyanoacrylate monomer is an alkyl cyanoacrylate monomer, preferably wherein said alkyl group comprises from 2 or 8 carbon atoms, more preferably wherein said alkyl group is a n-butyl or isobutyl group.

17. The method according to any one of claims 1 to 16, wherein the first volume of aqueous solution of step a) further comprises a saccharide or a derivative thereof, for example an oligosaccharide, a polysaccharide, or a derivative thereof, so as to produce the bubbles having a polymeric shell wherein the saccharide or derivative thereof is copolymerized with the cyanoacrylate monomer, preferably said saccharide or derivative thereof is present in the first volume of aqueous solution of step a) in an amount of 0.1 to 4% by weight relative to the weight of the first volume of aqueous solution.

18. The method according to claim 17, wherein the saccharide or derivative thereof is selected from the group consisting of fucoidans, dextrans, mannans, derivatives of fucoidans, derivatives of dextrans, derivatives of mannans, and mixtures thereof.

19. The method according to any one of claims 1 to 18, wherein the first volume of aqueous solution of step a) and/or the second volume of the cyanoacrylate monomer added in step c) further comprise a fluorescent probe so as to yield polymer-coated bubbles comprising the fluorescent probe, preferably said fluorescent probe is present in an amount of 0.1 to 40 ppm by weight relative to the weight of the first volume of aqueous solution.

20. The method according to any one of claims 1 to 19, wherein a fluorescent probe is incorporated in the bubbles having a polymeric shell, after steps b) and c) or at any later stage in the method, by adding said fluorescent probe to a suspension of the bubbles having a polymeric shell.

21. The method according to any one of claims 1 to 20, wherein steps b) and c) are performed while maintaining the temperature of the aqueous solution below 60°C, preferably below 35°C.

22. The method according to claim 21, wherein the first volume of aqueous solution just before step b) preferably has a temperature below 10°C.

23. The method according to any one of claims 1 to 22, wherein the first volume of the aqueous solution is obtained by the following steps:

a1. acidifying a volume a0 of an aqueous solution with a strong inorganic acid, such as HCl, H2SO4, or HNO3, to obtain the first volume of the aqueous solution having a pH below 5;

a2. dissolving the gas in the first volume of the aqueous solution to obtain the first volume of the aqueous solution comprising the gas dissolved therein and having a pH below 5;

a3. optionally, cooling the first volume of the aqueous solution comprising the gas dissolved therein and having a pH below 5, so as to reach a temperature below 10°C;

a4. while preventing of the aqueous solution from becoming depleted in the hydrophobic gas, preferably by bubbling the hydrophobic gas through the aqueous solution, and, optionally, while maintaining the aqueous solution at a temperature below 10°C, adding the surfactant to obtain the first volume of the aqueous solution comprising the gas dissolved therein, the surfactant dissolved therein, and having a pH below 5;

24. The method according to claim 23, wherein the saccharide is comprised in the aqueous solution before step a3, preferably wherein the saccharide is added to the aqueous solution before step a2, either before or after the acidification of step a1.

25. The method according to any one of claims 1 to 24, wherein step b) starts less than 30 s after the surfactant has been added.

26. The method according to any one of claims 1 to 25, wherein step d) comprises a step d1) of centrifugating the aqueous solution obtained after steps b) and c) and separating the floating bubbles having a polymeric shell from the rest of the aqueous solution obtained after steps b) and c), preferably said centrifugation is performed at a relative centrifugal force (RCF) comprised between 0.01 and 1, more preferably between 0.05 and 0.2.

27. The method according to claim 26, wherein step d) comprises, after step d1), a step d2) of washing the separated bubbles having a polymeric shell on a sieve to obtain a suspension of the bubbles having a polymeric shell with a size smaller than the sieve opening, preferably the sieve opening is lower than 10 µm, more preferably lower than 5 µm.

28. The method according to claim 27, wherein the washing of step d2) is performed using a washing solution comprising water and less than 0.1%, preferably less than 0.05% by mass of a surfactant.

29. The method according to any one of claims 26 to 28, wherein step d) comprises, after step d1) and, where applicable, before step d2), a step d1bis) of resuspending the separated bubbles having a polymeric shell in the washing solution and reseparating the bubbles having a polymeric shell through centrifugation, preferably the centrifugation of step d1bis) is

performed at a relative centrifugal force (RCF) comprised between 0.01 and 1, even more preferably between 0.05 and 0.2.

30. The method according to claim 29, wherein step d1bis) is performed at least two times.

31. The method according to any one of claims 26 to 30, wherein step d) comprises, after the last one of steps d1), d1bis) and d2), where applicable, a step d3) of suspending the bubbles having a polymeric shell in a storage solution, preferably the storage solution is identical to the washing solution.

32. The method according to any one of claims 26 to 31, wherein step d) comprises, after the last one of steps d1), d1bis), d2) and d3), where applicable, a step d4) of storing the suspension of the bubbles having a polymeric shell at a temperature of less than 10°C.

33. The method according to any one of claims 1 to 32, wherein the obtained bubbles having a polymeric shell have a smallest dimension of less than 10 µm, preferably less than 7 µm, even more preferably less than 5µm.

34. The method according to any one of claims 1 to 33, wherein the obtained bubbles having a polymeric shell have a median diameter by volume below 4 µm, preferably comprised between 1 and 4 µm, as measured by laser light scattering using the Mie model assuming that the solvent is water with a refraction index of 1.330 and that the bubbles are spherical polystyrene latex particles with a refraction index of 1.590 and an extinction coefficient of 0.010.

35. Bubbles obtainable by the process according to any one of claims 1 to 34.

36. Bubbles according to claim 35, said bubbles being spherical.

37. Bubbles according to claim 35 or 36 for use in a method of treatment and/or diagnosis.

38. Bubbles according to claim 37 for use as a contrast agent in a method of diagnosis.

39. Bubbles according to claim 37 for use in sonothrombolysis.

Overall, this protocol optimization distinguished from the literature over the following points: we validated the original synthesis of co-polymer MBs with acoustic cavitation without compromising their intrinsic properties. We also demonstrated that US insonation is not only a side step in the MBs production but can be a versatile approach with a lot of tunable parameters. The following part will present the therapeutic application of these polymer MBs.

Part 2: rtPA-loaded fucoidan MBs for the targeted treatment of stroke

Adapted from:
L. Fournier *et al*. "rtPA-loaded fucoidan MBs for the targeted treatment of stroke" Submitted in January 2023 to *Biomaterials*, with Editor (Annex 4)

Abstract:

Systemic injection of thrombolytic drugs is the gold standard treatment for non-invasive blood clot resolution. The most serious risks associated with the intravenous injection of tissue plasminogen activator-like proteins are the bleeding complication and the dose related neurotoxicity. Indeed, the drug has to be injected in high concentration since it has a short half-life, due to the presence of its natural blood inhibitor (PAI-1) and fast hepatic clearance (0.9 mg/kg in humans, 10 mg/kg in mouse models). Overall, there is a serious need for a dose reduced targeted treatment to overcome those issues. We present in this article a new acoustic cavitation-based method for polymer MBs synthesis, three times faster than current method. The generated MBs were ultrasound responsive, stable and biocompatible. Their functionalization enabled the efficient and targeted treatment of stroke, without side effects. First, the stabilizing shell of those MBs is composed of Poly-Isobutyl Cyanoacrylate (PIBCA), copolymerized with fucoidan. Widely studied for its targeting properties, fucoidan exhibit a nanomolar affinity for activated endothelium and activated platelets (P-selectins). Second, the thrombolytic agent (rtPA) was loaded onto microbubbles (MBs) with a simple adsorption protocol. Hence, the present study validated the *in vivo* efficiency of rtPA-loaded Fuco MBs to be over 50% more efficient than regular free rtPA injection for stroke resolution. In addition, the relative injected rtPA grafted onto targeting MBs was $1/10^{th}$ of the standard effective dose (1 mg/kg in mouse). As a result, no hemorrhagic event, BBB leakage nor unexpected tissue distribution were observed. The echogenic targeting MBs produced in this work now bring promising perspective for the development of US molecular imaging of thrombotic diseases and the US assisted clot resolution: sonothrombolysis.

Introduction

The global burden of cardiovascular diseases (CVD) places them as the leading cause of mortality around the world. Among those, thrombotic diseases including ischemic heart disease and stroke are the most prevalent and described as the main cause of disability [348]. Every year, 15 million of new cases of stroke are reported according to the World Health Organization (WHO). The prevalence of stroke increases with age with the highest rates typically occurring in people over the age of 75. Stroke is also more common in women, and is more prevalent in certain regions of the world, such as Southeast Asia and sub-Saharan Africa, compared to other region [349]. Overall, the prevalence of stroke is expected to continue to increase in the coming years due to the aging of global population and the increasing of risk factors such as high blood pressure, diabetes, and obesity. In medical terms, ischemic stroke is defined as the obstruction of vasculature in the brain caused by a thrombus. Those blood clots are highly heterogenous and composed of a variety of cell types [350] including erythrocytes, immune cells and platelets, with the addition of Von Willebrand Factor (VWF) and Neutrophil Extracellular Traps (NETs), tied together by a strong fibrin mesh [351]. Physiologically needed to repair impaired vessel walls, their pathological formation and their circulation in the bloodstream can lead to flow obstruction and distal tissue ischemia if the vessel recanalization is not quickly supported. Patients undergoing stroke event are treated with the gold standard systemic injection of a thrombolytic drug [352] in order to disassemble the fibrin mesh. There are several different types of "clot busters" used depending on their application (myocardial infarction, pulmonary embolism, stroke…) but there are mainly plasminogen activator like (Alteplase: rtPA, Reteplase: rPA, Tenecteplase: TNK) [85]. Indeed, this serine protease is naturally present in the body [353] allowing the cleavage of plasminogen into plasmin, responsible for fibrin degradation in homeostatic regulation. This thrombolytic injection can also be associated to mechanical thrombectomy [354] with the limitation of it being an invasive procedure. In addition, the systemic injection of the thrombolytic drug brings several drawbacks like hemorrhagic transformation [355] and neurotoxicity [356] with a recanalization rate below 50% [357]. To overcome those issues, the strategy to encapsulate rtPA has been explored with different carriers from nanoparticles [85] to microbubbles [132] with the common objective to reduce drug doses and improve the treatment efficiency. Besides drug encapsulation, nanomedicine is also focusing on targeted drug delivery on identified biomarkers. In thrombotic diseases, they are mainly described on activated platelets [7] with P-selectins, GPIIb/IIIa

integrins and phosphatidylserines or with circulating molecules like Factor XIII, VWF and fibrin [85]. We focused here on the highly specific interaction between P-selectins expressed on activated platelets or activated endothelium [358] and a sulfated polysaccharide: the fucoidan [15,16]. Their nanomolar affinity [341] makes the fucoidan a very promising targeting agent for thrombotic diseases and already showed its performance *in vivo* [344],[56]. The present strategy relies on polymer microbubbles (MBs) for their carrier ability but also their imaging property and treatment enhancement perspectives. Indeed, microbubbles are widely used as clinical contrast agent (Definity®, Sonovue®…) for US imaging due to their intrinsic echogenic properties [137] and have also been of main interest for the development of sonothrombolysis [360]. We present in this work, the innovative synthesis of polymer microbubbles via acoustic cavitation, never described in the literature yet and recently patented (PCT/FR2022/050309). Indeed, the use of US for MBs generation was only used for protein shelled MBs [63] or as a side step for lipid shell MBs [50]. This new method improved the yield of polymer MBs synthesis and reduce the synthesis time by 3 compared to standard polymer MBs synthesis with hydrodynamic cavitation.

Functionalized with fucoidan as a targeting agent and rtPA-loaded, these fully competent MBs were studied for the targeted treatment of thrombotic diseases (*Fig. 13*). We characterized those new MBs in terms of stability, biocompatibility, echogenicity, targeting property and thrombolytic activity. Then, in order to validate the efficacy of the treatment, we performed a mouse stroke model and compared gold standard treatment to drug-loaded targeted MBs by measuring the ischemic lesion reduction after 24 hours with MRI imaging. Overall, this paper gives interesting perspectives for the use of drug-loaded targeted polymer MBs for the treatment of thrombotic diseases.

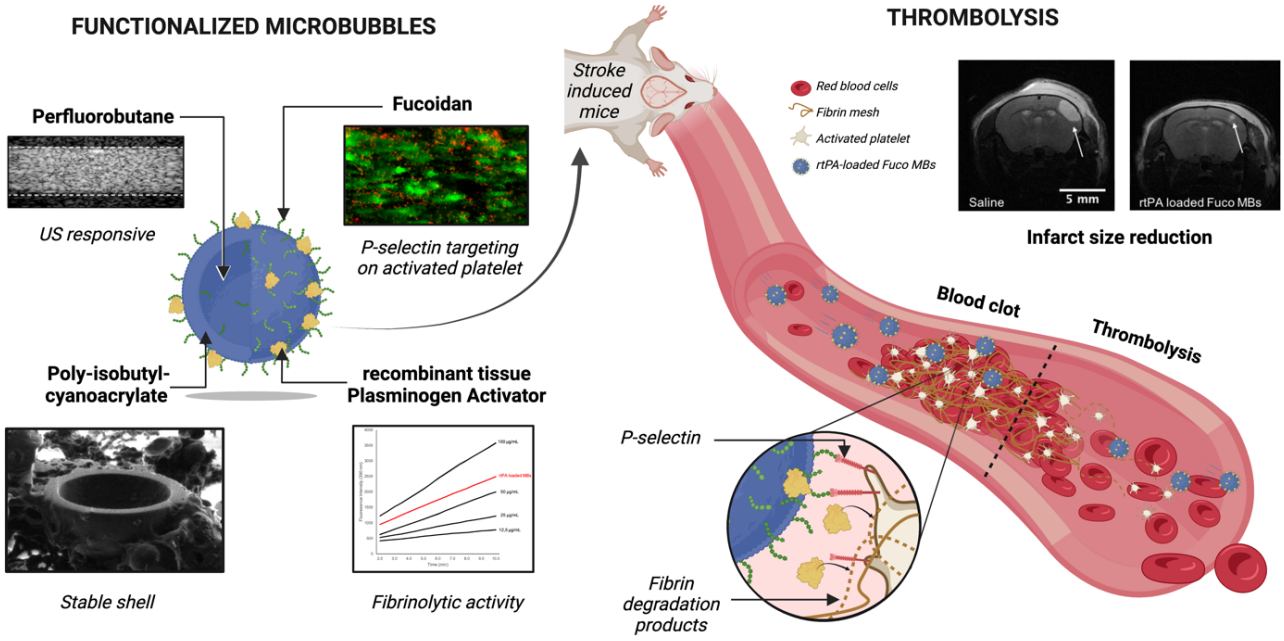

Figure 13: Graphical abstract of functionalized MBs for the treatment of stroke. *MBs are composed of a stable poly-isobutyl cyanoacrylate (PIBCA) shell with a perfluorobutane (PFB) gas core enabling US imaging. Their functionalization was validated for P-selectin targeting with fucoidan and for thrombolytic activity with recombinant tissue Plasminogen Activator (rtPA) loading. After in vitro validation, rtPA-loaded targeting MBs were injected in a mouse stroke model to improve thrombolysis recanalization compared to systemic injection of the drug. Fucoidan targeting onto activated platelet P-selectins allowed a specific delivery of rtPA to induce local fibrin degradation. The targeted delivery improved the treatment outcome by reducing the infarcted area after 24h as observed with MRI imaging.*

Materials and methods

Materials: Isobutyl cyanoacrylate (IBCA) monomers were purchased from Afinitica Technologies (Barcelona, Spain). Carboxymethyl dextran 40 (CMDex) was provided from TdB Labs (Uppsala Sweden). Sulfated polysaccharide fucoidan (Mn = 18 kDa Mw = 104 kDa) was obtained from Algues & Mer (Ouessant, France). Surfactant Tween 20 was purchased from Sigma Aldrich as well as the Rhodamine B fluorochrome. Perfluorobutane (PFB) was obtained from F2 Chemicals (Preston, UK).

- **Polymer MBs synthesis**

Poly-isobutyl cyanoacrylate (PIBCA) microbubbles were obtained from the anionic polymerization of IBCA monomer at the water gas interface. Briefly, 50 mL of an aqueous solution was prepared with HCl 1M to reach a pH of 2.5. This solution was saturated with perfluorobutane for 10 min and put into a freezer for 15 min to cool it down. Meanwhile, 700 µl of IBCA solution was loaded into a 1 mL syringe and placed onto a syringe pump (AL-300, World Precision Instrument, Florida, USA). The aqueous solution was then placed on ice, under the microtip of the Sonifier (SFX 550, BRANSON Ultrasonic Corp, Danbury, USA) so the tip is centered and half of a centimeter plunged into the aqueous solution. The organic solution and the PFB tank were connected into the aqueous solution with polyethylene catheters (Bioseb Lab Instrument, Salon de Provence, France). Just before the insonation, 500 µL of Tween 20 detergent was added drop by drop into the aqueous phase. The Sonifier was turned on for 20 min at 30% of amplitude and the IBCA was injected at a controlled speed of 0.45 mL/min. For the MBs containing polysaccharide, 1 g (2% w/w) was dissolved at the first step of synthesis into the aqueous solution giving fucoidan MBs (Fuco MBs) or carboxymethyl dextran MBs (CMDex MBs) used here as a non-targeting polysaccharide control. Similarly, for the fluorescent MBs, 500 µg of Rhodamine B was added in the first step of the aqueous phase preparation.

The obtained foam was centrifuged 3 times at 0.1 g in 50 mL falcon tubes for 20 min, and a solution of 0.02% Tween 20 was used to resuspend the floating MBs. MBs are then filtered through a 5 µm sieve using a sieve shaker. The obtained suspension was stored at 5 °C in a 0.02% Tween 20 solution. For all experiment requiring fluorescence microscopy visualization, MBs were labelled with Rhodamine B.

- **MBs concentration, size and zeta potential measurements**

MBs concentration is expressed in MBs/mL and measured with image analysis. Briefly, a diluted suspension of MBs was injected into a Malassez cell and imaged with an optical microscope (10x objective, Axio Observer, Zeiss). Counting was performed with ImageJ thresholding of MBs signal allowing an evaluation of the mean concentration with count extrapolation. MBs' size was measured with a Mastersizer 3000 (Malvern Instruments, UK), in water and flow speed of 1500 rpm. For each sample the 10^{th}, 50^{th} and 90^{th} percentile of size in volume (Dv10; Dv50; Dv90) were collected. The measurements were reproduced over the weeks to validate the shelf stability. Zeta potential was measured with electrophoretic light scattering method (Nano ZS, Malvern Instrument, UK). Briefly, MBs were diluted to 1/10 in a KCl 1 mM solution and added to the chamber allowing surface charge measurement, each sample was measured three times and averaged.

- **FTIR analysis**

Fourier-transform infrared spectroscopy (FTIR) spectrums were measured using a Thermo Nicolet AVATAR 370 FTIR spectrometer (Thermo Electron Corporation, Waltham, MA). The lyophilized samples were blended with KBr (1% mass) and compressed to obtain a pellet. Transmission spectra were acquired between 4000 cm^{-1} and 400 cm^{-1}.

- **Confocal Imaging and Scanning Electron Microscopy**

Confocal imaging was performed with Zeiss LSM 780 microscope in phase contrast or filtered for Rhodamine B MBs observation. Environmental Scanning Electron Microscopy (ESEM, Philips XL30, ESEM-FEG, Amsterdam, Netherland) images were performed with the following parameters: HV 10 kV, WD 13.7 mm, pressure $2.50e^{-4}$ Pa and magnification from 2500 to 10000 x. To evaluate the internal structure of the MBs, Focused Ion Beam (FIB) assisted Scanning Electron Microscopy (SEM, Aquilos™ Cryo-FIB, Thermofisher Scientific) was used to cut through the MBs. Samples were deposited onto the SEM grid and dried with paper. The FIB parameters were defined with: HV 30 kV, current 0.10 nA and pressure $1.66e^{-4}$ Pa.

- **Fucoidan quantification with methylene blue dosage**

Fucoidan sulfated groups can be recognized by methylene blue colorimetric assay like previously described [361]. On a grade 1 chromatography paper (Whatman®, GE Healthcare),

squares of 1 cm^2 were drawn to delimit the samples. Standard solutions of fucoidan MMW (Algues & Mer, France) were prepared with a serial dilution from 0.5 to 0.3125 mg/mL and the negative control was prepared with a suspension of CMDex MBs. MBs suspension were hydrolyzed with an alkaline solution of NaOH (0.1 M) until no further accumulation at the surface. MBs suspension at a concentration of 1 x 10^{10} MBs/mL and standard samples were successively deposited 5 times 2 µL with an intermediate drying step at 50°C for 10min. Once dry, the paper was treated with a solution of Methanol/Acetone (6:4) for 3 minutes, then treated with the Methylene blue solution of Methanol/Acetone/Water (6:4:15) containing 0.1% (w/w) methylene blue and 50 mM HCl (1M) for 10 min. The paper was then washed with several bath of washing solution (Acetic acid/Methanol/Acetone/Water, 5:6:4:75) until the bath remains translucid. To help with the paper manipulation, it was left to dry under the hood. The drawn squared were then cut and placed in 1.5 mL Eppendorf tubes. 500 µL of 2% SDS methanol solution was incubated with the cut papers at 50°C for 15 min. Then, 200 µL of the tainted solution was then extracted to a 96 well plate and the absorbance was read at 663 nm. Fucoidan final concentration was determined with the linear regression of the standard solution curve.

- **US phantom model and US burst model**

In vitro echogenic MBs properties were studied through a home-made setup. The US phantom employed was a tissue mimicking Doppler flow phantom (ATS Laboratories, CIRS) with a wall-less channel of 8 mm in diameter at 20 mm depth. US imaging were conducted using a medical probe, GE-L3-12-D (General Electrics; 256 elements, 0.2 mm pitch size) connected to a research ultrasound scanner, Vantage 256 (Verasonics, Kirkland, USA) and driven at 5 MHz center frequency. Amplitude modulation sequence used here (checkerboard) was programmed with Matlab (The MathWorks, Inc., Natick, MA). The *in vitro* acquisition consisted of 3 blocks of 200 images each, using a compounded framerate of 150 Hz and five angles (-4°; -2°; 0; 2°; 4°) pulse repetition frequency (PRF) of 3 kHz. Prior to the experiments, the emitted pressures of the probe were measured and calibrated using a 0.2 mm needle hydrophone (Precision Acoustic, UK). Flow rate was modulated using butterfly valves to stop the flow. The probe was positioned on top of wall-less phantom and various amplitude of signal (from 8 V to 17 V corresponding to Mechanical Index from 0.23 to 0.60) were evaluated to establish the burst threshold of the MBs, with a constant duty cycle of 67%. In that manner, MBs suspension flow was stopped to evaluate the signal before and after US insonation. The signal intensity was measured by image analysis with background noise subtraction.

- **rtPA incorporation onto MBs**

Adsorption method was performed by rising the pH of the MBs suspension to 10 with NaOH 1M. 2 mL of suspension containing 10^{10} MBs at pH 10 was gently mixed with 500 µg of rtPA (Actilyse®, Boehringer) for 2 hours at 5°C. The mix was then placed in a 5 mL syringe with a closing cap and centrifuged for 20 min at 0.1 g. The undernatent was discharged and the mix was rinsed with the storage solution of 0.02 % Tween 20, 3 times. The stability of the incorporated drug was measured with the enzyme activity evaluation over 4 days with a washing step between each day.

- **Amidolytic activity of incorporated rtPA with PefaFluor® assay**

The amidolytic activity of rtPA-loaded MBs was measured by recording the fluorescent signal of the degradation product of PefaFluor® in contact with the serine protease. Briefly, 2.5 µL of the rtPA-loaded MBs were put in contact with 97.5 µL of working buffer (0.1 M HEPES, 0.05 % BSA, 0.9 % NaCl) in a 96 well plate. 10 µL of PefaFluor® (Interchim, France) solution (1M) was added with a multi pipette and measurement of the fluorescence was performed with monochromatic spectrophotometer (TECAN, Infinite M200 PRO) at λ_{em} = 390, λ_{ex} = 440 during 70 min. A standard range was obtained by serial dilution of rtPA (Actilyse®, Boehringer) from 400 µg/mL to 6.25 µg/mL and negative control was obtained with Tween 0.02% solution. The kinetic of the fluorescent substrate generation is proportional to the concentration of the enzyme. The leading coefficients of the linear part of the standard curves were then used to established the linear regression of the concentration.

- **Fibrinolytic activity**

rtPA ability to lyse fibrin was evaluated *in vitro*, comparing free rtPA to rtPA-loaded MBs on a fibrin gel model. The gel was prepared by mixing a fibrinogen solution and a thrombin solution. A TRIS buffer (TRIS 0.1 M, NaCl 0.9%, pH 7.6) was prepared to mix the different component of the solutions. In two separated water baths, 5 mL of the fibrinogen solution (5 mg/mL, from Human plasma, Sigma Aldrich) was heated to 37°C while 5 mL of 3% low melting agarose (Thermo Scientific) was heated to 65°C. Once agarose has reached its melting temperature, the solution was cooled down to 37°C and 2.5 U of thrombin (from Human plasma, Sigma Aldrich) was added. The two solutions were mixed and quickly poured into a 9 cm petri dish plate and left for gelation 30 min at 5°C. Holes were defined with a 3 mm punch

and 5 µL of samples diluted to 1/15 were dropped where the gel was extracted. The set-up was placed at 37°C overnight and fibrin degradation rings were measured with Fiji software.

- ***In vitro* targeting flow experiment on human platelet aggregates**

The specific binding of Fuco MBs on P-selectins expressed on activated platelet was evaluated with a microfluidic model [345]. Using the Vena8 Fluoro+ biochip (Cellix Ltd, Ireland). Microchannels were coated overnight with a 200 µg/mL solution of collagen type I at 4°C (equine tendon collagen, Collagen Reagens HORM®, Takeda). Whole human blood (WHB) was collected from healthy volunteers in 75 mM PPACK tubes, and platelets were stained with a DIOC6 solution of 50 µg/mL right before injection into the channel. DIOC6 specifically stains mitochondria membranes in living cells [362], excluding erythrocytes staining. For each channel, the following sequence was performed: channel washing with saline solution (NaCl 0.9 %) for 3 min at arterial flow rate (60 µL/min), WHB with DIOC6 injection at arterial flow rate up to 5 min until platelet aggregates start to appear without obstructing the channel; WHB washing with saline solution (NaCl 0.9 %) for 5 min; Rhodamine B stained Fuco MBs injection at venous flow rate (4 µL/min) for 5 min; Washing of Rhodamine B Fuco MBs with saline solution (NaCl 0.9 %) at venous flow rate (4 µL/min) until no more free MBs were circulating. A microscopy image (Axio Observer, Zeiss) was taken between each step to control the platelet aggregates and the targeting properties of the MBs. A negative control was obtained with the injection of CMDex MBs. Quantification was established by measuring the amount of MBs colocalized on platelet aggregates after the final rinsing and normalized to the size of the aggregates using Fiji thresholding analysis.

- **Cytotoxicity assays**

The evaluation of cytotoxicity was performed with a LDH (Lactate Dehydrogenase) mortality assay and MTT [3-(4,5-dimethyl-2thiazolyl)-2,5-diphenyl-2H-tetrazolium bromide] viability assay. Both HUVECs (Human Umbilical Vein Endothelial Cells, CRL-1730, ATCC) and BALB/3T3 (mouse embryo fibroblast, clone A31, CCL-163, ATCC) were cultured until confluency, at 37°C in a 5% CO_2 incubator, with Dulbecco's Modified Eagle Medium (DMEM) with 10% (v/v) fetal bovine medium, 4mmol of L-glutamine, 1% (v/v) of penicillin and 1% (v/v) of streptomycin. For LDH mortality assay (Cytotoxicity detection kit PLUS, Roche), HUVECs and BALB/3T3 were culture in 96 wells plates. Briefly, after incubation with various concentrations of MBs diluted in cell culture medium (10^8, 10^7, 10^6, 10^5 and 10^4 MBs/mL),

supernatants were recovered either after 2, 4 or 6 hours. The recovered culture medias were incubated with LDH reaction mix according to the supplier guidelines for 15 min at room temperature. After addition of the stop solution, the absorbance of the samples was read at 492 and 690 nm (control wavelength). The cell cytotoxicity was then determined by subtracting the control wavelength to the absorbance at 492 nm and normalized to dead cells absorbance: Cell mortality = [(Abs of the sample - Abs of culture medium) / (Abs of 100% of dead cells- Abs of culture medium) x 100].

For the MTT assay, cells were seeded in 24 well plates. This assay was performed with cell culture insert (Falcon®, 1 µm of mesh diameter) to avoid the sedimentation of MBs residues onto the cells, allowing the focus on the degradation product toxicity rather than cell asphyxia in static conditions. Indeed, due to the experimental conditions, 37°C for 6 hours, we expected MBs burst and consequently MBs residues sedimentation rather than intact MBs floating property. Cell culture medium was discharged and replaced by 300 µL of new medium, inserts were placed in each well and 300 µL of MBs diluted in cell culture medium were added inside the inserts for a final MBs concentration of 10^8, 10^7, 10^6, 10^5 and 10^4 MBs/mL. After 6 hours of incubation, cells insert and medium were replaced by 300 µL of MTT solution (0.05% in PBS 1X) and incubated for 3 hours at 37°C in dark environment. The medium was removed by gentle plate reversal on dry paper and the 300 µL of isopropanol was added to each well. After 1 hour at room temperature, absorbance was measured at 490 nm in a TECAN (Infinite M200 PRO) plate reader. The cell viability was measured as: Cell viability = [(Abs of sample - Abs of dead cells control) / (Abs of living cells control - Abs of dead cells control) x 100].

- **Hemolysis evaluation**

Whole human blood from healthy volunteers was centrifuged 5 min at 500 g to isolate Red Blood Cells (RBC) in 25 µM PPACK tube to avoid coagulation. Hematocrit and plasma level were labelled on the tube, plasma phase was aspirated and replaced by 0.9 % saline solution twice. Then 0.9% NaCl was replaced by PBS 1X. The final RBC suspension was diluted to 1/50 in PBS 1X. In a V-bottom 96 well plate, 10 µL of MBs suspension was added at different concentration (from 0.125 x 10^8 to 10^8 MBs/mL). 190 µL of previously prepared RBC suspension was added to the wells and incubated at 37°C for one hour on an orbital shaker. Plates were centrifuged to the same conditions to recover the RBC pellet. Supernatant was then transferred into a clean flat bottomed 96 wells plate and absorbance was measured at 450 nm with a monochromator (TECAN, Infinite M200 PRO). Positive control was obtained with

Triton 10X allowing a complete lysis of the RBCs and negative control was performed with PBS 1X. Percentage of hemolysis was obtained with the following formula: Hemolysis = [(Abs of sample - Abs of negative control) / (Abs of positive control - Abs of negative control)].

- ***In vivo* stroke model**

Animal studies were performed on 6 to 8 weeks old (30 to 40 g) Swiss wild type male (Janvier Labs, Le Genest-Saint-Isle, France). All experiment were adapted according to French (Decree 87/848) and European (2010/63/EU) ethical guidelines. The local committee of Normandy (CENOMEXA) approved the fulfilling of the experiments with the reference number APAFIS#35158. Mice were anesthetized with 5% of isoflurane inhalation and maintained to 2% during the entire procedure. As analgesic, they subcutaneously received buprenorphine (0.1 mg/kg) and ear local anesthesia with lidocaine spay. Mice heads were stabilized in a stereotaxic platform and a catheter was placed in the tail vein for the treatment injection. After a local craniotomy on top of the middle cerebral artery (MCA), the dura mater was excised to expose the MCA bifurcation. Precise pneumatical injection of 1 µL of murine thrombin (1 IU, Stago BNL) was carried out by elongated glass capillaries in the MCA to induce fibrin rich thrombus formation [363]. The treatment procedures were performed intravenously, 30 min after thrombin injection with either, free rtPA (Actilyse®, Boehringer) at 1 mg/kg in infusion (300 µL, 10% bolus + 90% infusion for 40 min, $N \geq 16$); rtPA-loaded Fuco MBs at 1 mg/kg equivalence in bolus (300µL, 3 x 10^9 MBs, $N \geq 16$); or saline in infusion (300µL, 10% bolus + 90% infusion for 40 min, $N \geq 16$).

- **Speckle imaging**

Monitoring of the *in vivo* brain perfusion was obtained with Laser Speckle Contrast Imager (MOOR FLPI-2, Moor Instruments), allowing the visualization of blood figurative elements. Speckle images were taken before and after the stroke induction as well as before and after the treatment to control the occlusion. The quantification of the flow mean was generated by comparing stroke Region of Interest (ROI) to the same region on the contralateral hemisphere, before and after treatment. Mice with pre-stroke contrast difference in both hemisphere and mice with complete reperfusion right after treatment were excluded from the study. For the first scenario, it was not possible to define if the clot was ever obtained. For the second scenario, it was not possible to attest if the clot was not formed correctly or completely dissolved by the treatment.

- **Magnetic Resonance Imaging and BBB permeability**

24 hours after treatment, mice brains were imaged with MRI to measure the size of the infarcted areas. Briefly, mice were anesthetized with 5% of isoflurane inhalation and maintained to 2% during the acquisitions. All acquisitions were obtained with a Pharmascan 7 T (Bruker Biospin, France), T2 sequence (echo time 39.9 ms, repetition time 3,500 ms, 2 averages) were used for ischemic lesion visualization and T2 Star sequence (echo time 8.7 ms, repetition time 500 ms, 2 averages) were used for hemorrhagic lesion visualization. Lesion volumes were quantified with image analysis of the hyper signal cut off area on all the brain slices (0.5 mm thickness) with the formula: Ischemic lesion volume = $(\sum ischemic\ areas)\ x\ 0.5$.

For the evaluation of Blood Brain Barrier (BBB) permeability, Gadoteric Acid (GA, Clariscan Gé, GE Healthcare) was injected intravenously in the tail vein (200 µL at 0.75 mmol/kg). After 15 minutes, three dimensional T1 Flash acquisition (echo time 4.4 ms, repetition time 15 ms, 3 averages) was recorded and white hyper signal volume was quantified as BBB leakage of GA compared to acquisition before injection, using Fiji software using the same formula than ischemic lesion volume.

- ***Ex vivo* fluorescence biodistribution on complete or sectioned organs**

Organs from previously described procedures were harvested 24 hours after treatment. Biodistribution of the Fuco MBs was imaged by near-infrared fluorescence imaging (IVIS® Lumina III, Perkin Elmer, USA). The imaging of complete organs (N=3) was performed on brain, liver, lungs, bladder, spleen, intestines and kidney right after euthanasia without PFA fixation. The quantification of fluorescence intensities (λ_{Ex} = 550 nm, λ_{Em} = 620 nm) in regions of interest (ROIs) were analyzed using Living Image® software. For histology analysis, mice received buprenorphine (0.1 mg/kg) and were deeply anesthetized with 5% of isoflurane inhalation before procedure. After a thoracotomy, a cannula was inserted into the left ventricle, and the right atrium was incised to rinse the circulatory system. Transcardiac perfusion was then performed with 50 mL of heparinized saline (0.5 mL/L) followed by 30 mL of 4% paraformaldehyde (PFA) at a constant speed of 14 mL/min. Organs were post-fixed in 4% PFA overnight at 4°C then plunged in cryoprotective solution (20% sucrose in PBS 1X) overnight before to be stored at -80°C. Organs were subsequently sliced with a cryostat at a 10 µm thickness. Slices were stained with DAPI mounting medium (ABCAM) for nucleus recognition

and with rat anti-mouse CD68 primary antibody (Biolegend) followed by a FITC secondary antibody (Biolegend) to highlight tissue macrophages.

- **Statistical analysis**

Quantitative data underwent the statistical analysis of GraphPad PRISM 8 with a 95% confidence level. All presented data are means of at least triplicates expressed with their standard deviation (SD). Normality test were performed using Kolmogorov-Smirnov test and if needed outliers were identified and excluded with ROUT method (1% of aggressivity of the Gaussian distribution). Depending on the design of the experiment and after normality validation, data were evaluated with unpaired t-test (two groups) or ANOVA (more than two groups) in association with multiple comparison in between groups (Tukey's test). P-values were represented as followed, and deemed significant below the 0.05 threshold: * $p < 0.05$; ** $p < 0.01$; *** $p < 0.001$, **** $p < 0.0001$.

Results and discussion

- **Polymer MBs synthesis and characterization**

MBs synthesis was inspired by the well-described hydrodynamic cavitation method like recently published by Bo Li. *et al* [56]. In this work, the cavitation energy was replaced by ultrasonic insonation into the polysaccharide solution. This recently patented acoustic cavitation method enabled the production of polymer MBs within 20 minutes (*Fig. 14A*) (PCT/FR2022/050309). The set-up was placed on ice to regulate the synthesis temperature rise and perfluorobutane (PFB) was constantly injected into the polysaccharide solution. The entrapped gas helped for the stability of the anionic copolymerization between cyanoacrylate monomer and polysaccharide chains. Fucoidan (Fuco) was used here as the targeting agent and so carboxymethyl dextran (CMDex) was used as the control polysaccharide for untargeted MBs. Comparing Fuco MBs and CMDex MBs (*Fig. 14B*), it was demonstrated that the amount of MBs produced was independent from the polysaccharide composition with a yield around 2.5×10^{10} MBs per batch. The mean size after sieve filtration was measured at 3.13 (± 0.81) µm for Fuco MBs and 3.07 (± 1.49) µm for CMDex MBs, showing no significant difference depending on the shell compositions, in accordance with the close size range of both polysaccharides (*Fig. S1A*). The evaluation of the surface charge was shown negative with a zeta potential close to -45 mV for Fuco MBs and close to -30 mV for CMDex MBs, also in accordance with the negatively charged groups in fucoidan and carboxymethyl dextran (*Fig. S1B*). The size stability was monitored over a month by measuring the size of the MBs. A size augmentation would be attributed to shell destabilization leading to MBs aggregation detected by the apparatus as bigger MBs. In *Fig. 14C,* the shelf stability was measured right after synthesis, after 3 and 4 weeks (independently of their incorporated polysaccharide). MBs were either placed at -5°C or 20°C to establish the best storage conditions for MBs suspension. It has been demonstrated that 5°C was the best storage temperature as the mean MBs was stable at 3.27 (± 0.71) µm for 4 weeks. Room temperature storage showed an increased mean size to 4.09 (± 0.22) µm after 4 weeks, which is still in the range for possible animal injection. The whole size distribution presenting the Dv10, Dv50, Dv90 are plotted on the *Fig. S1C*, highlighting the size stability after 4 weeks. In complement to this size distribution study, we validated that the incorporation of rtPA presented below did not affect the mean size of the MBs *(Fig. S1D*).

The characterization of fucoidan content was obtained with the quantification of sulfated groups as presented in the Supplementary data (*Fig. S2A-B-C*). This colorimetric method based on Methylene Blue staining pointed out the presence of the sulfated polysaccharide in the range of 1x 10^{-14} g/MB using CMDex MBs as negative control. Environmental Scanning Electron Microscopy (ESEM) images presented in *Fig. 14D* validated the rounded shape of MBs as well as the short polydispersity after filtration. To ensure the hollow structure of the MBs observed in confocal imaging (*Fig. S3A*), Focused Ion Beam (FIB) technology was used to cut through individual MBs (*Fig. 14E*). The shell homogeneity was then demonstrated and an estimation of the shell thickness was measured in the range of 500 nm, subsequently emphasized with confocal fluorescence imaging (*Fig. S3B-C-D*).

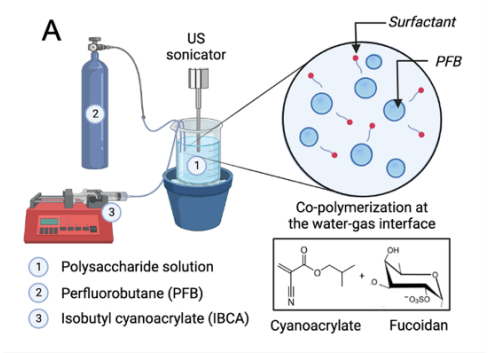

B

	Yield (MBs / Batch)	Mean size (µm)	Zeta potential (mV)	Fuco content (g / MBs)
Fuco MBs	2.46 (± 0.97) x 10^{10}	3.13 (± 0.81)	-44.9 (± 1.9)	1.0 (± 0.1) x 10^{-14}
CMDex MBs	2.64 (± 1.43) x 10^{10}	3.07 (± 1.49)	-30.6 (± 0.8)	-

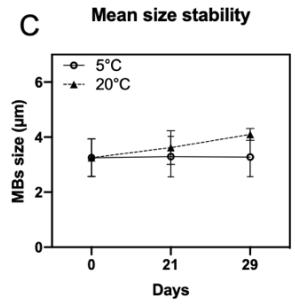

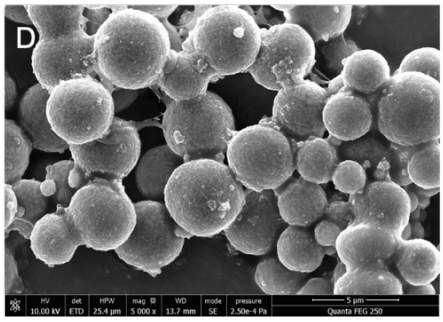

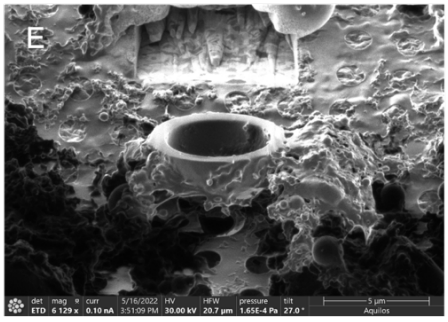

Figure 14: Functionalized polymer MBs characterization. *A) Innovative synthesis method. Monomer of isobutyl cyanoacrylate (IBCA) was injected with a needle pusher into the acidic aqueous polysaccharide solution while constant bubbling of perfluorobutane was ongoing. US sonicator was immerged inside the aqueous solution and generates continuous signal for 20 min at 30% of amplitude. The system is placed on ice to avoid temperature rising. Due to high hydrophobicity, IBCA will tend to polymerized at the water-gas interface, copolymerizing with polysaccharides dissolved into the solution and entrapping PFB. B) Summary of principal physicochemical characterization depending on the incorporated polysaccharide. Yield was measured with MBs counting on Malassez cell, mean size was measured with laser diffraction granulometry, zeta potential was obtained with electrophoretic light scattering and fucoidan content was dosed with methylene blue colorimetric assay. C) Mean size of MBs suspension over a month measured with laser diffraction granulometry, comparing 5°C and 20°C for shelf storage. D) Environmental Scanning Electron Microscopy (ESEM) image of MBs pointing out their homogenous rounded shape Scale bar is 5 µm. E) Focus Ion Beam (FIB) cut through a single polymer MBs pointing out the hollow structure and the thick shell around 500 nm thick. Scale bar is 5 µm.*

- **Echogenicity of MBs**

One intrinsic property of MBs is their ability to respond to an ultrasound signal [28,29]. Indeed, microbubbles are now widely used in clinic as US contrast agents for US imaging. Their ability to resonate under US creates bright signal compared to surrounding tissues in cardiac echography for example. The proposed agent can be an answer for the problem of specificity in diagnostic or treatment thanks to its precise targeting. To ensure the echogenic properties of those newly synthetized MBs, a home-made *in vitro* model was established to determine the burst threshold of MBs in function of the intensity of the signal (*Fig. 15A*). Intensities varied from 8 V, 9 V 10 V, 11 V, 12 V, 13 V, 14 V and 17 V corresponding respectively to the following mechanical index 0.230 (± 0.002), 0.270 (± 0.003), 0.310 (± 0.004), 0.350 (± 0.002), 0.390 (± 0.003), 0.430 (± 0.003), 0.470 (± 0.002) and 0.600 (± 0.001). The imaging sequences were measured with a 2 V signal before and after 2 sequences of the burst periods (*Fig. 15B*). The signal was normalized to water and to MBs insonated with 2 V all along. The intensity rise at the beginning of each burst sequence corresponds to a "blinking" phenomenon of MBs before ongoing inertial cavitation. The last part of the graph displays the loss of signal due to some MBs implosion. The difference between the initial intensity signal and the final intensity one in plotted on *Fig. 15C* as the disruptive ratio. This ratio determines the amount of disrupted MBs and clearly states that over 10 V (MechanicaI Index = 0.31) more than 50 % of MBs underwent inertial cavitation. This is illustrated with *Fig. 15D*, displaying the US images of the channels before and after 8 V or 17 V US insonation.

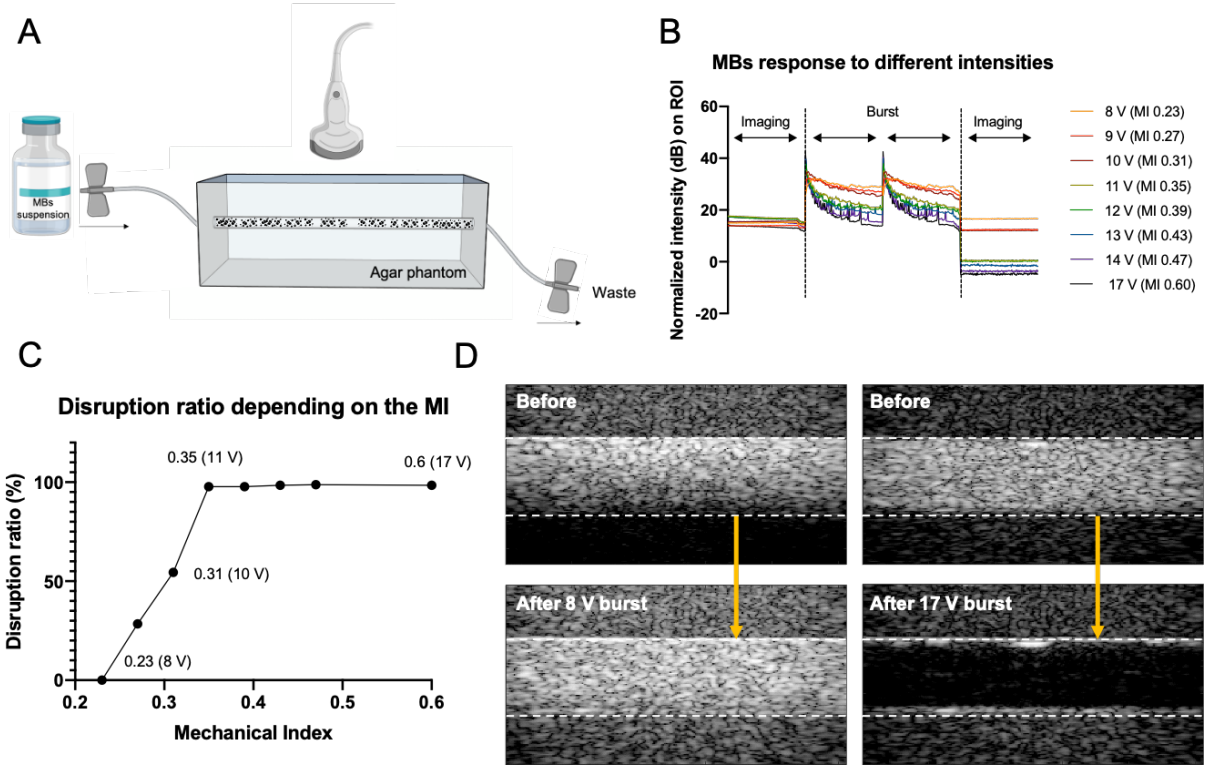

Figure 15: Echogenicity characterization of MBs. *A) Flow phantom setup mimicking blood vessel circulation. The flow can be monitored with a butterfly closure system and the US transducer is placed on top of the phantom. B) Echogenic response of MBs at 5 MHz frequency and different intensities in volt (from 8 to 17). The curve is composed of 4 sequences: 1 imaging at 2 V, 2 burst sequences depending on the different intensities and 1 more imaging sequence at 2 V to compare before and after bursting signal. C) Disruptive ratio calculated from the normalized intensitiy difference before and after burst sequence. Mechanical Index 0.230 (± 0.002), 0.270 (± 0.003), 0.310 (± 0.004), 0.350 (± 0.002), 0.390 (± 0.003), 0.430 (± 0.003), 0.470 (± 0.002) and 0.600 (± 0.001)) correspond to the voltage signal of 8V to 17 V. D) US images from phantom setup before and after 8 V burst and before and after 17 V burst. The channel is highlighted with a dotted line and MBs signal is visible in white contrast.*

- **Drug loading and targeting of MBs**

MBs were functionalized with rtPA (Actilyse®), the recombinant tissue Plasminogen Activator used for human treatment. The incorporation was obtained with an adsorption protocol (*Fig. 16A*) where the pH rising of the MBs suspension allowed the incorporation of the protein within 2 hours. To evaluate the amount of incorporated rtPA, the protein activity was measured, ensuring that its incorporation did not affect its enzymatic activity. Primarily noticed result was the high number of incorporated proteins onto Fuco MBs compared to CMDex MBs (*Fig. 16B*). This specific incorporation is believed to be related to the interaction with activated sulfated groups of fucoidan [92]. Indeed, Fucoidan MBs were able to incorporate 226 (± 32) µg of rtPA for 10^{10} MBs compared to 19 (± 16) µg of rtPA for 10^{10} MBs onto CMDex MBs. Then, rtPA incorporation stability was evaluated over 4 days with centrifugation washing between each day (*Fig. 16C*), pointing out a stable incorporation threshold of 108 (± 5) µg of rtPA for 10^{10} MBs from day 1 to day 4. This stable incorporated score was observed after the 4th centrifugation washing step on day 1 and stable after the next washing steps. With the aim of producing reproducible results, the stable quantity of incorporated rtPA onto Fuco MBs was set to 100 µg/10^{10} MBs. The fibrinolytic activity of incorporated rtPA was validated with a fibrin agar assay (*Fig. S4A*) by measuring the degradation area of the gel after 2, 5 and 24 hours at 37°C. This semi quantitative method demonstrated that the fibrinolytic activity was maintained when rtPA was encapsulated compared to free rtPA (*Fig. S4B*).

The targeting property of Fuco MBs were evaluated in fluidic condition mimicking *in vivo* blood circulation (*Fig. 16D-F*). Platelet aggregates formation on collagen coating is highly dependent to flow rate (60 µL/min) [365] and was monitored with fluorescent microscopy to avoid channel cloaking. Fuco MBs targeting was measured with Fiji image analysis after rinsing the channel with saline solution and normalized to the platelet aggregate size. Previous work validated the specificity of fucoidan for P-selectins over E and L-selectins [344], here the focus was on expressed P-selectins by activated human platelets. The targeting (*Fig. 16F*) was highly significant (P Value < 0.0001) comparing CMDex MBs (*Fig. 16D)* to Fuco MBs (*Fig. 16E*). Also, the drug-loaded MBs were still enable to target activated platelet with a significant difference to control MBs (P Value < 0.0001). This targeting assay validated that *ex vivo* platelet targeting was highly efficient and that rtPA incorporation did not prohibit MBs targeting despite rtPA interaction with the targeting agent.

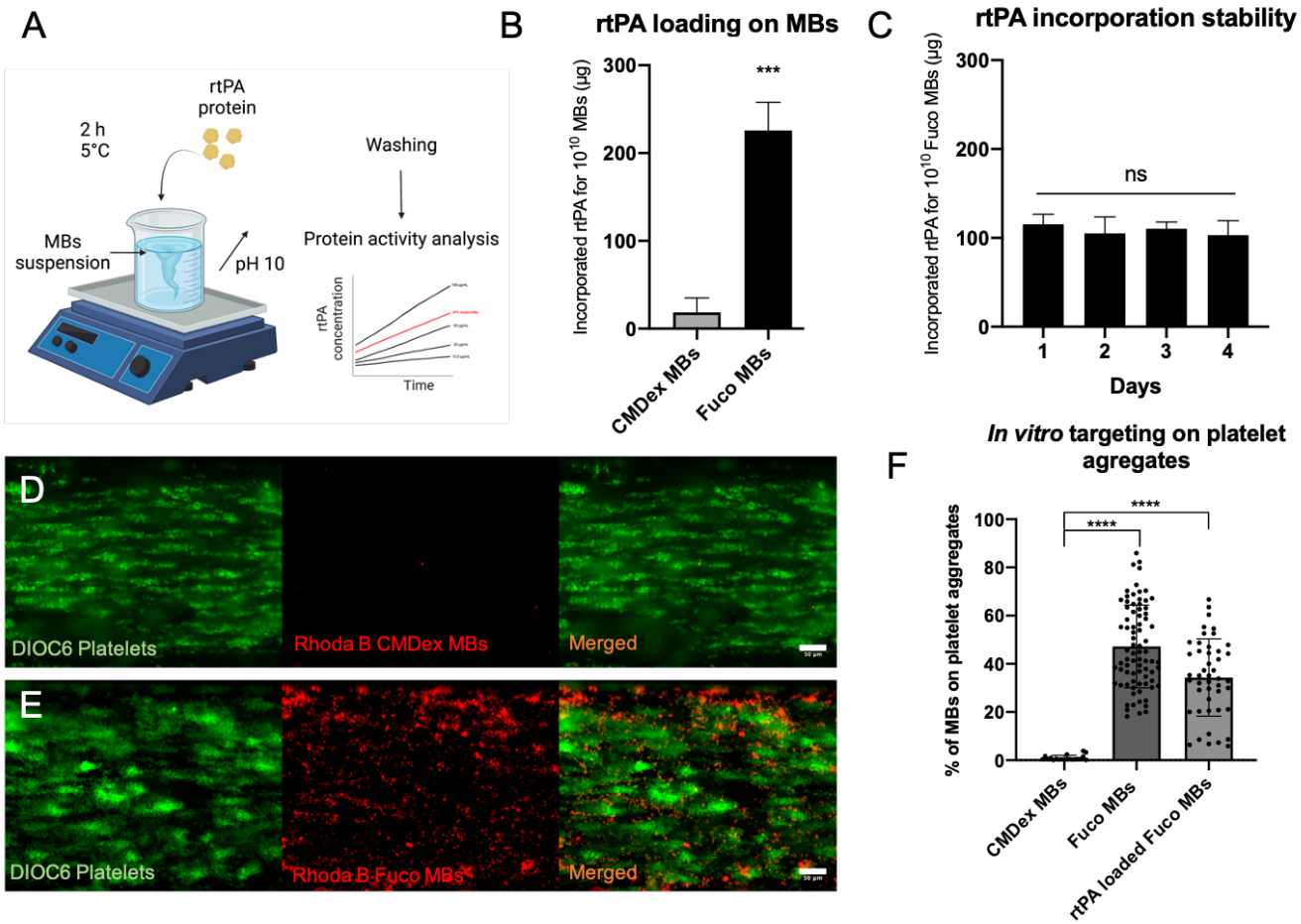

Figure 16: Functionalization of MBs. *A-B-C) Drug loading and validation of the rtPA activity after incorporation. A) Drug loading adsorption protocol. Briefly, 500 µg of rtPA in solution was added to a MBs suspension from which the pH has been risen to 10 with NaOH. The mix was left for 2 hours under gentle agitation and then rinsed 3 times by centrifugation and discharge of the undernantent. The protein activity is then monitored on drug-loaded MBs with a kinetic substrate degradation assay (PefaFluor®). B) Protein incorporation determined from protein activity assay of rtPA onto either Fuco MBs or CMDex MBs after 3 centrifugztion wasing step. C) Stability of rtPA incorporation onto Fuco MBs over 4 days with washing centrifugation step in between days. D-E-F) In vitro flow targeting. D-E) Microscopy images of Vena8 Fluoro+ microchannels. Platelets from whole human blood were labelled with DIOC6 and MBs were synthesized with Rhodamine B, the last image is a merge of both DIOC6 and Rhodamine B channels. Images are taken under venous flow indicating that stopped MBs are attached to platelet aggregates. D) is the control group of CMDex MBs and E) is the result of Fuco MBs. Scale bar is 50 µm. F) Quantification of MBs targeting on platelet aggregates normalized to the size of the aggregates. The evaluation of rtPA-loaded Fuco MBs targeting confirmed that the drug loading did not compromise the effective targeting on P-selectins.*

- **Biocompatibility of MBs**

Before *in vivo* injection, cytotoxicity towards red blood cells (RBC), endothelial cells (HUVEC) and fibroblast (3T3) were assessed (*Fig. 17*). Lactate Dehydrogenase (LDH) is a cytoplasmic enzyme, thus its presence in the culture medium is a marker of cell membrane rupture. This mortality assay was performed on two cell types likely to encounters MBs *in vivo*. Mortality tests on endothelial cells were on average of 4.73 (± 2.07) % all conditions reunited (*Fig. 17A*) while fibroblasts showed a mortality of 7.9 (± 3.5) % independently of the condition *(Fig. 17B*). Overall, no mortality was measured (above 30% threshold), neither for HUVECs and 3T3 nor 2 hours, 4 hours or 6 hours times points and likewise for increasing MBs concentrations. The second cytocompatibility evaluation was performed on RBC by the measurement of hemoglobin release in the supernatant also marker of cell lysis (*Fig. 17C*). Normalized to Triton 10X lysis, MBs incubation with RBC for one hour did not induce cell lysis even at 10^8 MBs/mL (<4%). Lastly, viability assay was performed for 6 hours with MTT assay. To prevent from cell asphyxia because of MBs debris sedimentation (caused by the assay temperature and time conditions), the MBs suspension was added on top of a 1 µm cell culture insert. The MTT assay evaluates the cell metabolic activity by the reduction of MTT to formazan with mitochondrial reductases. After 6 hours of incubation, none of the conditions showed a diminution in the cell's metabolic activity for HUVECs or 3T3 (*Fig. 17D*) with a mean survival rate above 100% compared to MBs control cells cultured without MBs. The 0.02% tween working buffer (WB) did not influence the cell viability neither. Images of formazan crystals were also taken with optical microscopy comparing the highest concentration (10^8 MBs/mL) to cells that were not in contact with MBs (*Fig. S5*). Those pictures highlighted the healthy phenotypes of cells and the correct metabolization of MTT. Therefore, no cytotoxicity was demonstrated on three different cell types in contact high concentrations of MBs, using three different assays.

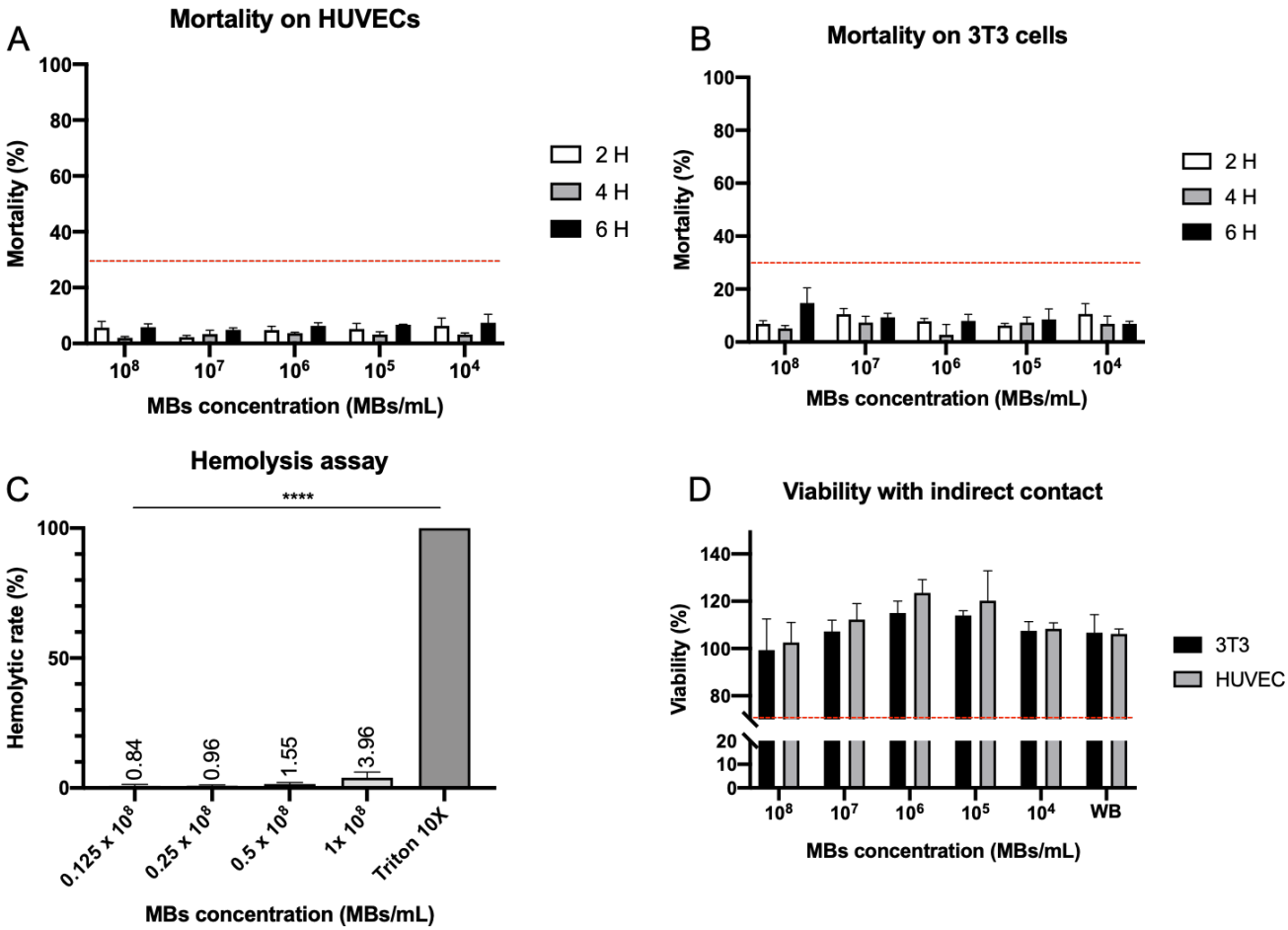

Figure 17: Biocompatibility study of Fuco MBs on different cell types. *A-B) LDH quantification assay on endothelial cells (A) and fibroblasts (B) for increasing concentration of MBs and different time points. LDH is a cytoplasmic enzyme only present in the culture medium if cells undergo apoptosis. Here, none of the concentrations or time of contact induced a mortality above the red dotted line of 30% indicating the biocompatibility of Fuco MBs. C) Hemolysis assay of Fuco MBs on human red blood cells. The time of contact here was one hour and showed less that 4% of hemolysis at the highest MBs concentration (10^8 MBs/ml) compared to Triton 10X. D) MTT assay with indirect contact of Fuco MBs on endothelial cells and fibroblasts for 6 hours. The same Fuco MBs concentration was used as the mortality assay and 0.02% tween working buffer (WB) was also put to the test. Again, no condition induced a viability below 70 % (red dotted line). The MBs suspension was added on top of a cell culture insert with 1 µm mesh to avoid the asphyxia of cells due to MBs debris sedimentation after long contact time in culture medium.*

- ***In vivo* stroke model**

The *in vivo* stroke model was performed as presented in *Fig. 18A*. After a local craniotomy over the MCA, thrombin injection generated fibrin rich clot formation. Speckle imaging was performed before and after each step to validate the reduction of blood flow in the region of the stroke. The clot was left to stabilize for 40 min and treatment were carried out with intravenous tail vein injection. The final checkup was obtained at 24 hours with MRI imaging analysis of the ischemic region. In pre-clinical application, the treatment for an efficient thrombolysis using rtPA injection in mice models is usually performed with 10 mg/kg ratio while we set the threshold here to 1mg/kg of rtPA for both free rtPA and rtPA-loaded MBs [363]. In consequence, there is no significant difference in the ischemic lesion volume between the saline group (N = 16, 10.35 ± 4.84 mm^3) and the free rtPA group (N = 17, 8.08 ± 6.12 mm^3). Nevertheless, the rtPA-loaded Fuco MBs treatment significantly reduced the infarcted area by more than 50 % (N = 16, 3.75 ± 3.67 mm^3) compared to free rtPA treatment (*Fig. 18B*). In addition, we compared the size prevalence in each group (*Fig. 18C*) by defining 4 groups: no lesion, small lesion (<5 mm^3), medium lesions (from 5 to 10 mm^3) and large lesions (>10 mm^3). Large lesions were only observed once in rtPA-loaded Fuco MBs treatment with a majority of small lesion (N = 8). On the contrary, saline group presented a majority of large lesion (N = 9) and free rtPA group presented a similar amount of small and large lesion (N = 6). The MRI images displayed on *Fig. 18D* were taken 24 hours after the treatment, and the white region pointed by an arrow represents the ischemic region on the same coronal plane for the three groups (more images on *Fig. S6A*). Since MBs treatment involves micron size bubbles, we also monitored the Blood Brain Barrier (BBB) permeability (*Fig. 18E-F*). By injecting Gadoteric Acid (GA) intravenously, the leakage of BBB permeability can be observed with T1 MRI acquisition as white spots around the infarcted areas. Nevertheless, this test showed no evidence of BBB impairment comparing saline, free rtPA and rtPA-loaded Fuco MBs groups (*Fig. 18E*). Some spots were identified with saline treatment compared to MRI images taken before GA injection (*Fig. 18F*), but isolated events could also be the consequence of the surgery itself (more images on *Fig. S6B*). Overall, the targeted treatment with rtPA-loaded Fuco MBs was significantly more efficient than gold standard treatment and neither collateral hemorrhage or BBB leakage was observed.

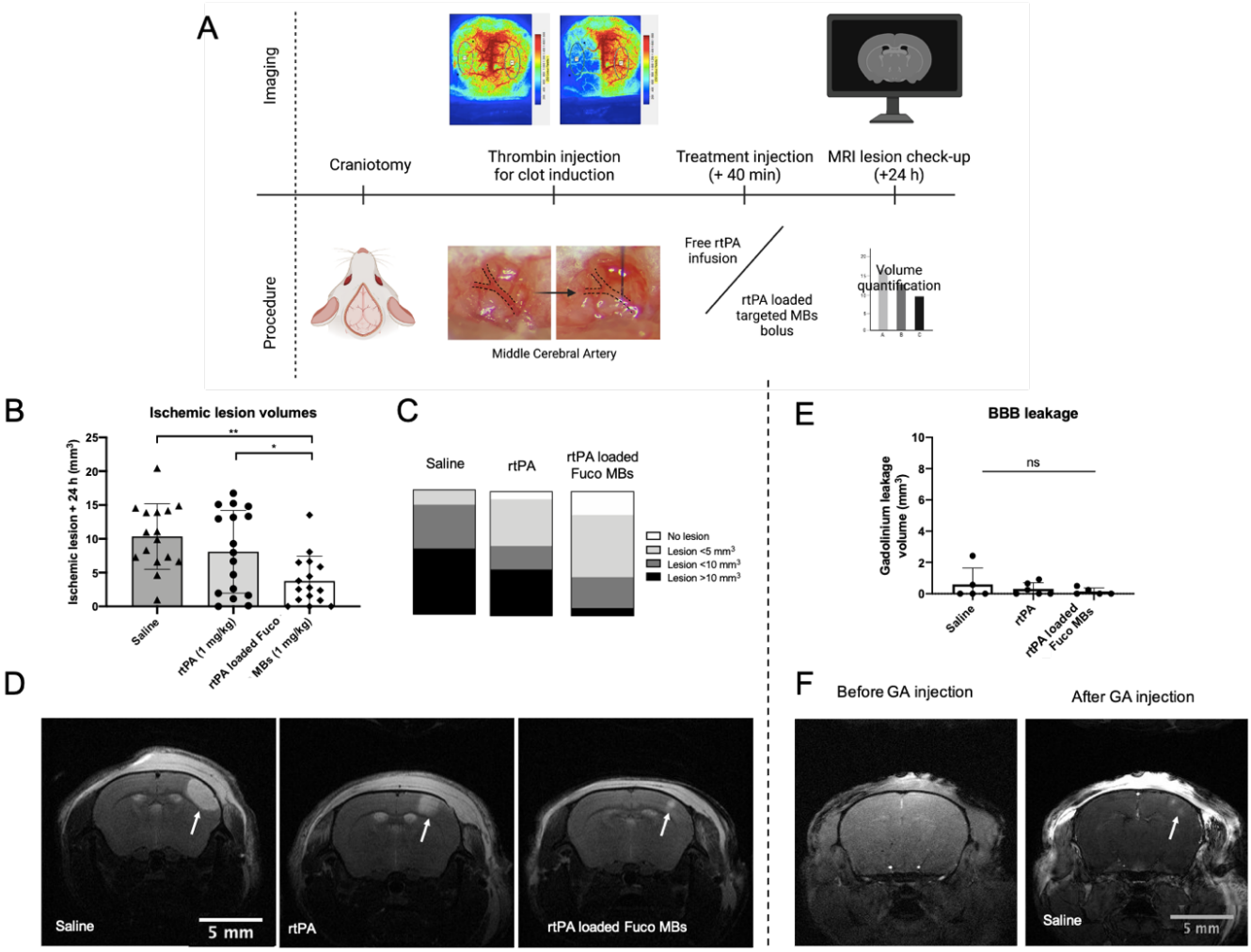

Figure 18: In vivo stroke model study on mice comparing rtPA-loaded Fuco MBs treatment to systemic injection of rtPA. *A) Graphical abstract of the experimental setup. Briefly, mice were anesthetized and placed onto a stereotaxic platform. A craniotomy allowed the direct access to the Middle Cerebral Artery (MCA) to inject thrombin. After a few minutes the clot partial occlusion was validated with Speckle imaging looking at the two hemispheres perfusion. After 40 min, either saline infusion, free rtPA infusion or rtPA-loaded Fuco MBs bolus were used as stroke treatment. The MRI images of the mouse brain were taken 24h after the treatement to evaluate the infarcted area volume. B) Lesions volumes quantification from MRI images. Volumes were measured with the Fiji software by compiling areas of all brain slices for saline, free rtPA and rtPA-loaded Fuco MBs treatment. C) Lesion distribution according to their severity from: no lesion, small lesion (<5 mm³), medium lesion (>5; <10 mm³) to large lesion (>10 mm³) depending on the treatment. D) MRI images of the same slice number of the three treatment conditions. The white arrows point out the infarcted area and the scale bar is 5 mm. E-F) Blood Brain Barrier (BBB) permeability evaluation. Gadoteric Acid (GA) was injected intravenously before MRI T1 flash imaging. E) Quantification of GA leakage volume in the brain 24 hours after stroke treatment (ns: not significant). F) MRI T1 flash acquisition of mouse brain before and after GA injection for saline treatment condition. The white arrow is pointing out the contrast generated by BBB leakage of GA, the scale bar is 5 mm.*

- ***Ex vivo* fluorescence biodistribution on sectioned or complete organs**

The biodistribution of rtPA-loaded Fuco MBs has been studied with organ fluorescence macroscopy (*Fig. 19A-B*). *Ex vivo* organ macroscopy was performed 24 hours after treatment on brain, liver, lungs, bladder, spleen, intestine and kidney compared to saline groups. As MBs were labelled with Rhodamine B, the fluorescence residues of MBs can be observed with an excitation wavelength of 550 nm (*Fig. 19A*). Normalized to the size of the organ, fluorescence count (*Fig. 19B*) gives a qualitative evaluation of MBs biodistribution in the body. As expected, the majority of fluorescence was observed in the liver, fulfilling its function of blood detoxification. Also, some MBs residues were observed in the lungs most likely related to the gas exchange ongoing after MBs degradation. No fluorescence was observed in the bladder, spleen, intestines or kidney. Interestingly, the specific fluorescence in the stroke area was observed after 24 hours. It enhanced the validation of Fuco MBs targeting capacity *in vivo* but also brings new insights for the P-selectins expression on activated endothelium, after clot resolution and thus interesting perspectives for molecular imaging. In regards to those results, the histology study was performed on liver explanted 2 hours after Fuco MBs injection, to assess their uptake by resident macrophages. In *Fig. 19C*, cell nuclei were colored with DAPI and macrophages were labeled in green with an antibody against CD68 biomarker. Rhodamine B Fuco MBs residues were observed to be colocalized with macrophages biomarker CD68 indicating a potential internalization by the scavenger cells.

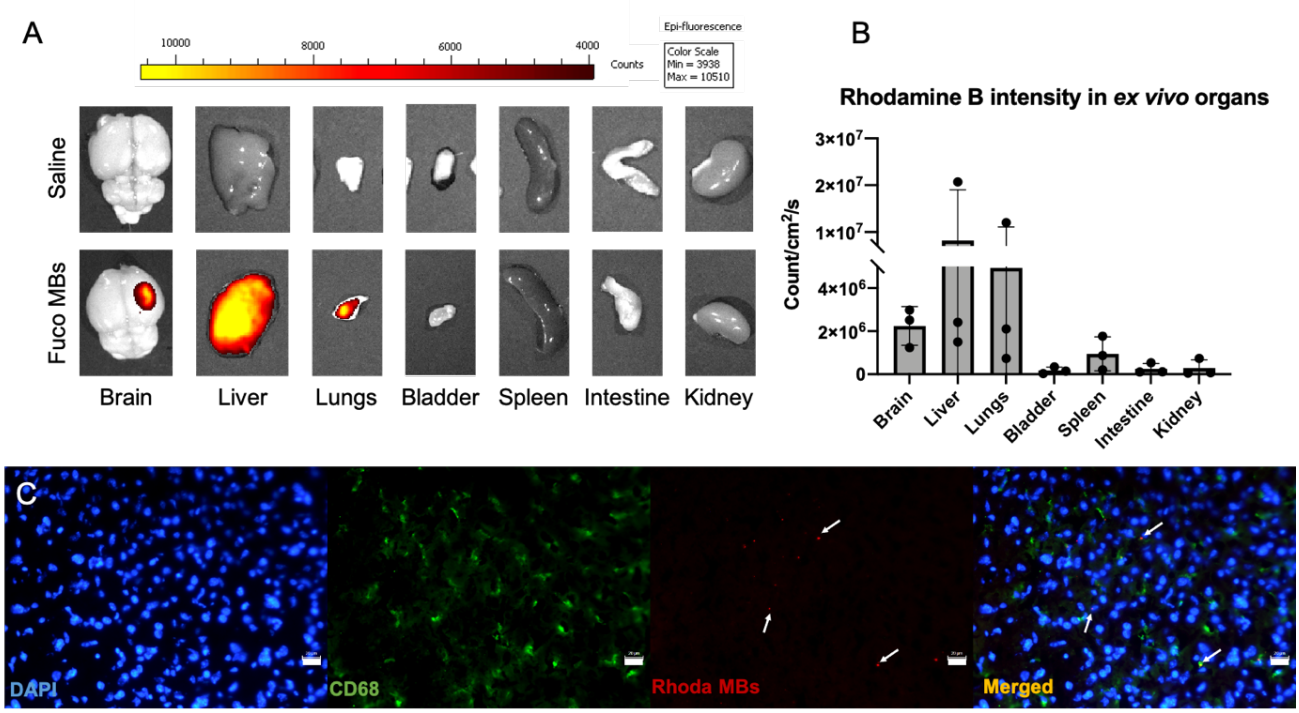

Figure 19: Biodistribution of fluorescent MBs and MBs residues in mice. *A-B) Ex vivo fluorescence macroscopy quantification of MBs outcome in brain, liver, lungs, bladder, spleen, intestine and kidney. A) Fluorescence macroscopy images of various organs after stroke treatment (saline: top row, rtPA-loaded Fuco MBs: bottom row). Organs were retrieved 24 hours after treatment and imaged without tissue fixation. The epi fluorescence scale was set between 3938 and 10510 counts. Specific targeting of MBs to the stroke area was still visible after 24 hours and liver and lungs were fulfilling their blood cleaning property as the rest of the fluorescence was observed in those two organs. B) Quantification of the fluorescence in each organ in counts/cm²/s. The quantification gave similar conclusion to the fluorescence images, with a high fluorescent signal of MBs residues in the liver and the lungs (N=3). C) Histology coloration of liver tissue 2 hours after injection of rhodamine B Fuco MBs in mice. From left to right, DAPI coloration of cell nuclei, CD68 immunostaining of macrophages, Rhodamine B Fuco MBs, Merged image. The white arrows point out the MBs fluorescent residues in red and scale bar is 20 µm. MBs residues were found in liver tissue after 2 hours and some of them seemed to be internalized in liver macrophages.*

Conclusion

In the present study, we developed ultrasound responsive microbubbles for the targeted treatment of stroke. Acoustic cavitation synthesis was optimized for the production of targeting polymer MBs, firstly described here in the literature. This innovative protocol reduced the production time by three compared to gold standard hydrodynamic cavitation. The physicochemical properties and biocompatibility assessments were intensively evaluated to conclude on their contrast enhancement with US signal, effective targeting of P-selectins, and fibrinolytic potential. The *in vivo* evaluation on mice stroke model demonstrated the efficiency of rtPA-loaded Fuco MBs over clinical systemic injection of the drug. Indeed, we observed a volume reduction of the brain injury by more than 50% with a $1/10^{th}$ lower dose of rtPA than recommended in mice. No BBB permeability or hemorrhagic complication was observed and expected biodistribution was found in detoxification organs including lungs and liver, indicating a high potentiality for a safe and scalable treatment. Our finding now rises new possibilities for the application of drug-loaded targeting MBs, without life-threatening side effects and efficient thrombolysis at lower dose.

The main perspectives of this work now rely on the US responsive property of MBs. The ischemic memory observed after 24 hours on the stroke region with residual fluorescence on activated endothelium, allowed us to think about the potential of Fuco MBs for molecular imaging [162]. We demonstrated the contrast enhancement capacity of MBs for US signal and targeted imaging with US is an active research field. Indeed, US technology is a non-invasive, safe for pregnant patients and less expensive method compared to other imaging modalities. With the recent advances in stroke US imaging in rats [315], P-selectin targeted MBs present new possibilities for the early diagnosis and clot resolution follow-up of stroke events. Also, chemical thrombolysis alone only achieve good outcomes for 40% of patients [352] and clot migration can cause a variety of serious problems including distal vessels obstruction. The need for non-invasive clot damaging treatment led the scientific community to study microbubble-assisted US clot bursting: the sonothrombolysis. Especially since tissue plasminogen treatment is less efficient on distal occlusions [357], sonothrombolysis could mechanically disrupt the clot [354] in addition to fibrinolysis. Despite the fact that it is an area of active research [221], these therapies are not yet widely available or fully understood. Few boundaries are nevertheless already established, including Mechanical Index threshold of 1.9 and the need of biocompatible MBs. Our technology is then a great candidate for the development of targeted sonothrombolysis for stroke resolution.

Supplementary data

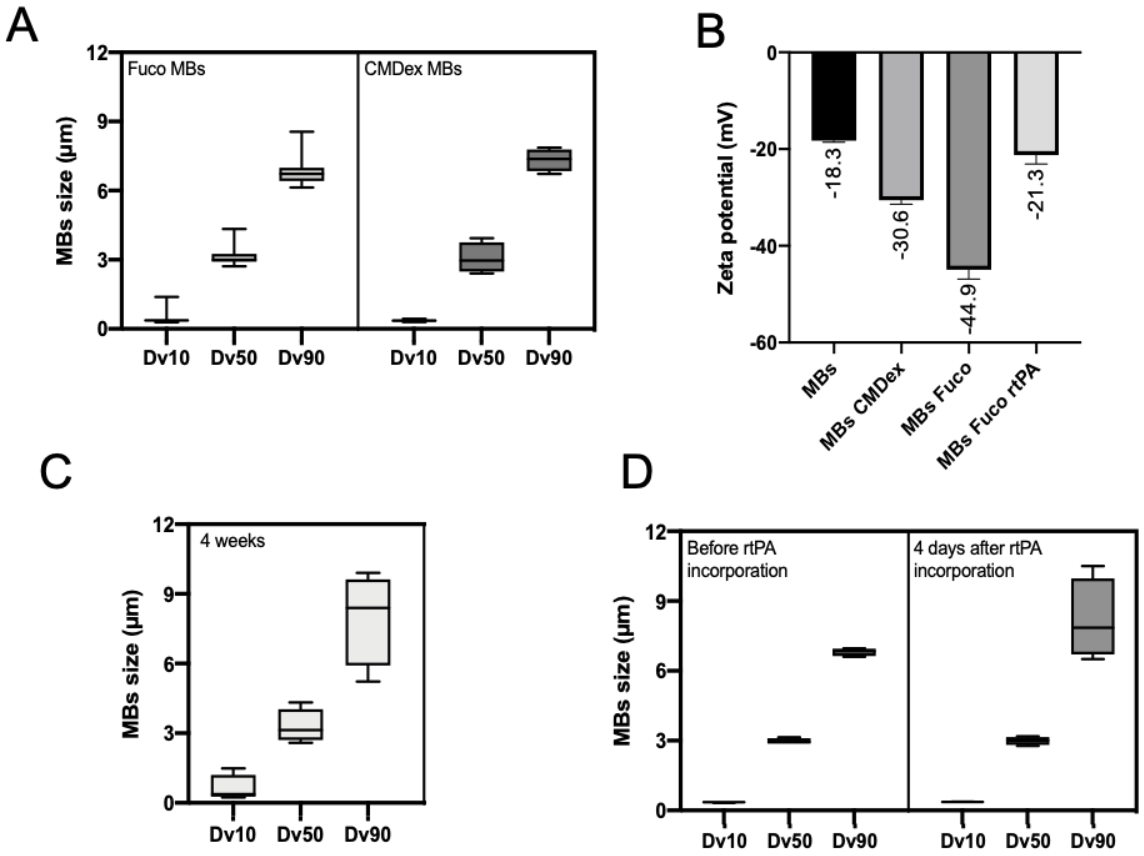

Supplementary Figure 1: MBs size distribution and surface charge. *A-C-D) Size measurement of MBs with laser diffraction granulometry. Here, the Dv10; Dv50 and Dv90 are related to the size distribution. For each graph, it corresponds to the size of MBs measured below this percentage. A) MBs size distribution depending on the incorporated polysaccharide, fucoidan or control carboxymethyl dextran. B) Zeta potential measurement with Electrophoretic Light Scattering (ELS). Fuco MBs were demonstrated to be highly negative compared to bare MBs. Carboxymethyl dextran was used as a control polysaccharide not only for its similar size, but for its negative charges close to fucoidan. Also, the incorporation of rtPA onto Fuco MBs decreased the negativity of MBs surface charge. C) MBs size distribution in suspension after 4 weeks at 5°C in 0.02% Tween working buffer. D) MBs size distribution 4 days after rtPA incorporation. The main difference was observed in the big MBs, but still in the range for injection in vivo.*

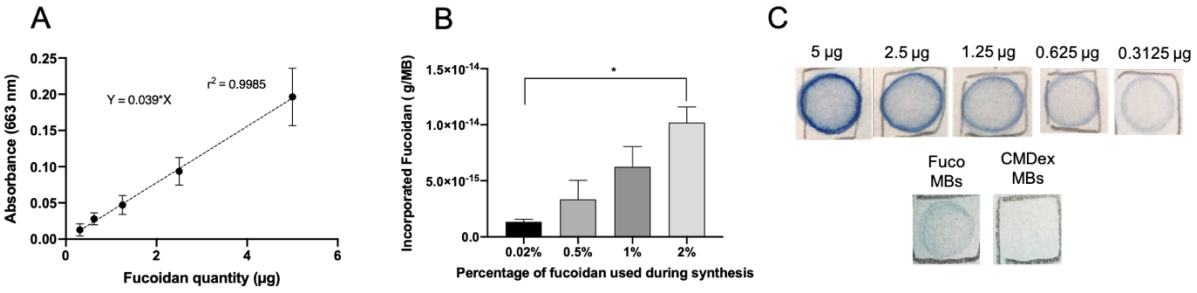

Supplementary Figure 2: Fucoidan quantification with methylene blue colorimetric assay sulfate specific. *A) Standard range absorbance of methylene blue in function of fucoidan quantity. B) Linear correlation between the quantity of Fucoidan used for synthesis and the quantity of incorporated Fucoidan. C) Images of methylene blue colorimetric assay. On top, from the most to the least concentrated fucoidan sample. On the bottom, Fucoidan MBs sample compared to Carboxymethyl Dextran MBs.*

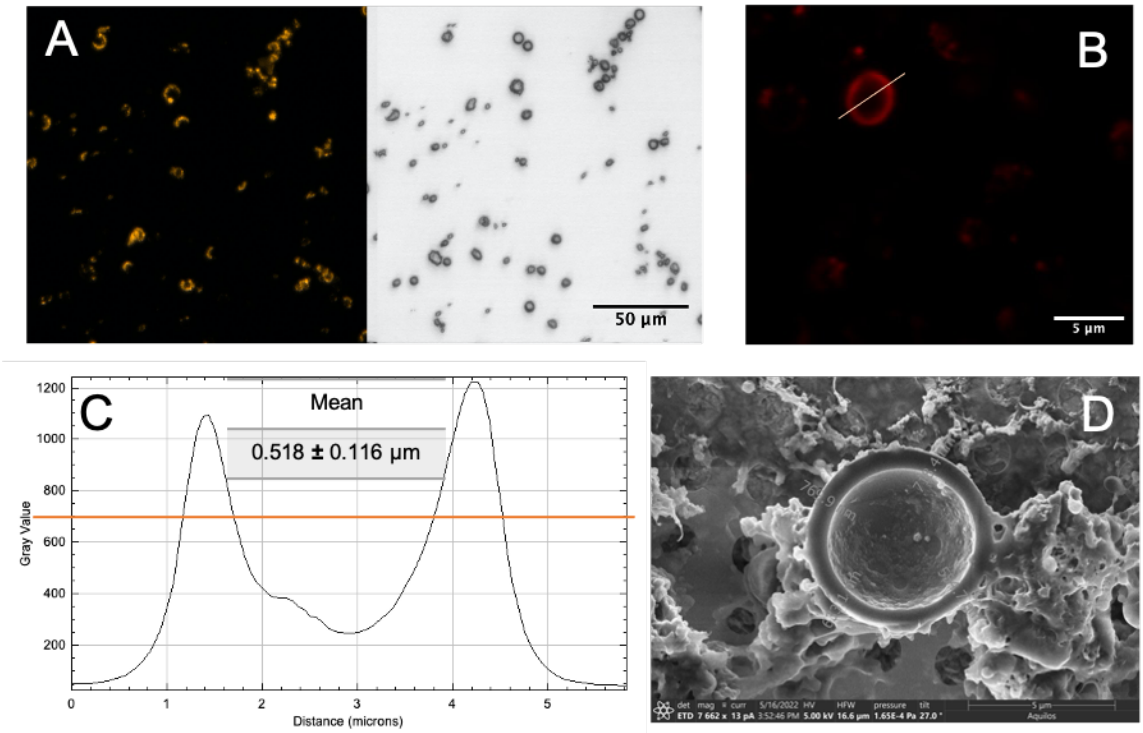

Supplementary Figure 3: MBs shell thickness characterization. *A) Confocal images of Rhodamine B MBs. The fluorescent image on the left showed the incorporation of Rhodamine B into MBs shell. The Brightfield image on the right highlighted the hollow structure of the MBs. The scale bar is 50 µm. B-C-D) MBs shell thickness evaluation. B) Confocal fluorescent image of MBs shell and the drawn tangent line. Scale bar is 5 µm. C) Measurement of fluorescent signal with Fiji by plotting the grey value graph of a tangent line to the MBs. The orange line on the graph determines the measured shell thickness reported on the x-axis. It is placed at the mean height of the grey value intensity. D) Scanning Electron Microscopy image of a MBs from the top after being sectioned by a focused ion beam. The shell thickness measured here validated the range of MBs shell thickness. Scale bar is 5 µm.*

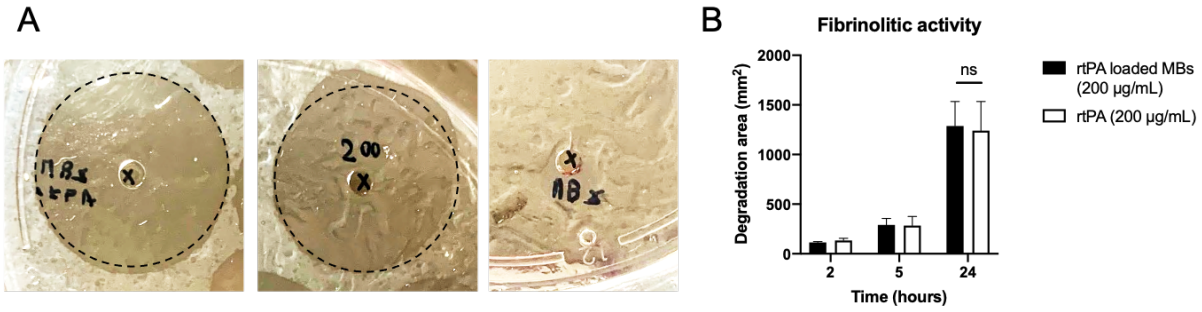

Supplementary Figure 4: Fibrinolytic activity of rtPA-loaded MBs with fibrin gel degradation evaluation. *A) Images of fibrin gel degradation circles at same time points. From left to right rtPA-loaded Fuco MBs, free rtPA, Fuco MBs. The well for sample deposition in the center was 5 mm diameter. B) Fibrinolytic activity of rtPA-loaded MBs compared to free rtPA quantification of the degraded area over 24 hours. The degradation kinetic was demonstrated to be similar to free rtPA.*

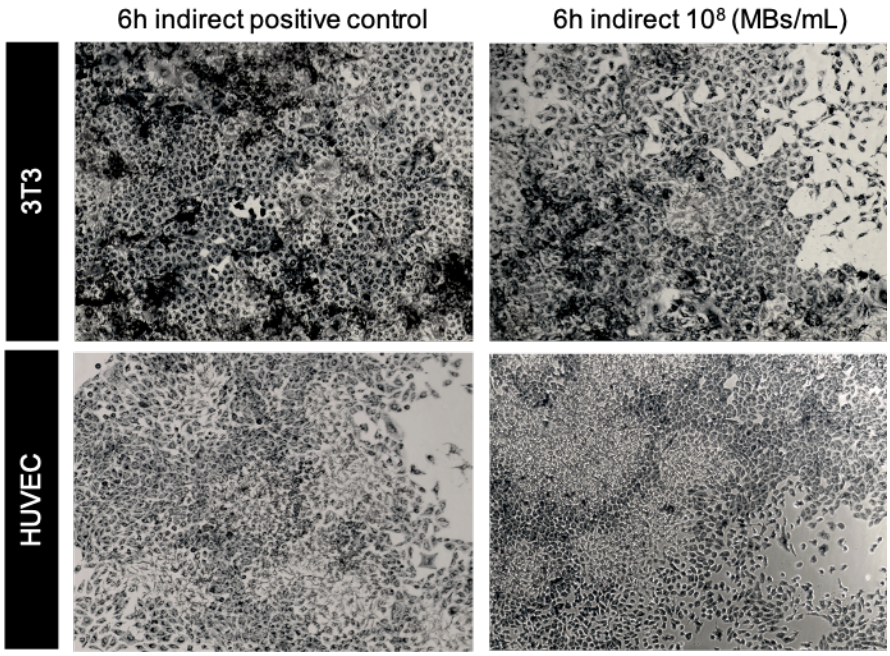

Supplementary Figure 5: Microscopy images of fibroblasts and endothelial cells after MTT assay*. The Fuco MBs were incubated for 6 hours with 3T3 and HUVECs. On the left, images of the cells after incubation with Fuco MBs, on the right, images of cells without MBs incubation. The MTT assay consists in the evaluation of the metabolic activity of cells by the reduction of MTT to formazan. Here we can observe the formazan crystals in the cell around the nucleus in the highly concentrated MBs condition and in the control group that validate the harmless behavior of MBs in static conditions.*

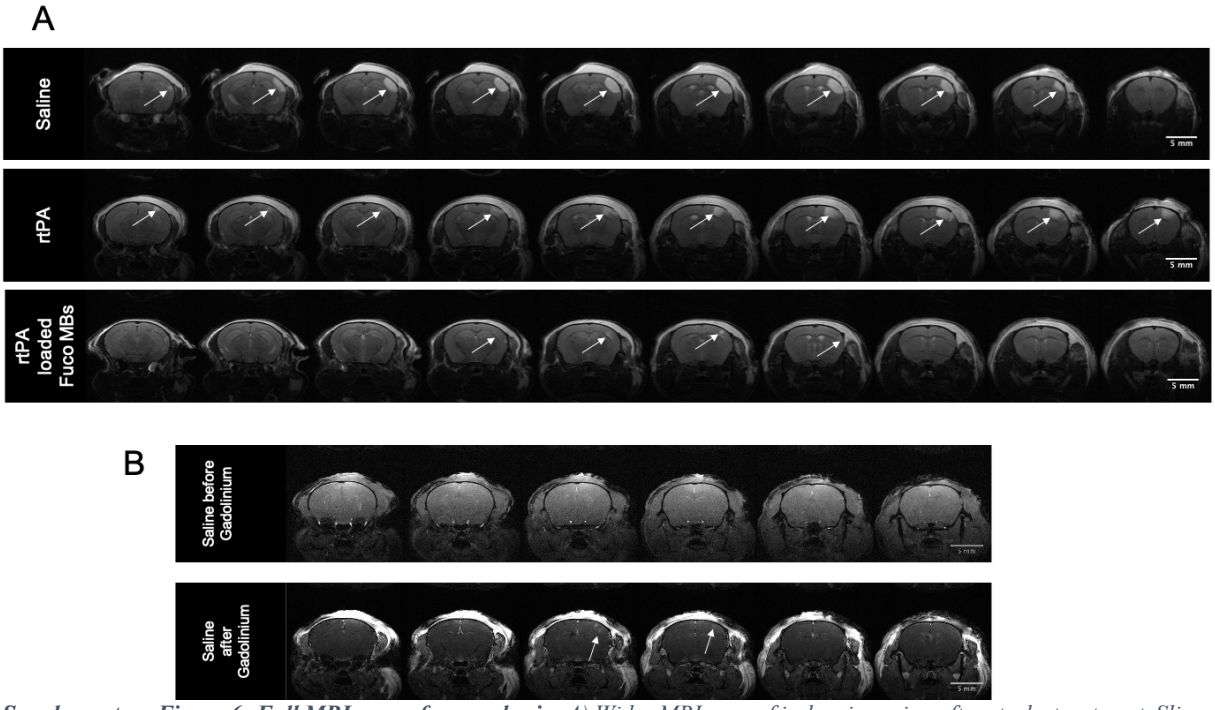

Supplementary Figure 6: Full MRI scan of mouse brain. *A) Wider MRI scan of ischemic region after stroke treatment. Slices are ordered from dorsal to frontal and white arrows are pointing at ischemic regions. We observed that the ischemic lesion volume was bigger and present in more plans with saline and free rtPA treatment rather than rtPA-loaded Fuco MBs. Scale bar is 5mm. B) Wider MRI scan of BBB leakage evaluation of stroke mice treated with saline. On top T1 acquisition before injection of Gadoteric Acid (GA), on the bottom after injection ones. White arrows are pointing out what we can observe as a leakage like BBB. Nevertheless, for none of the conditions, a major leakage was observed. Scale bar is 5 mm B.*

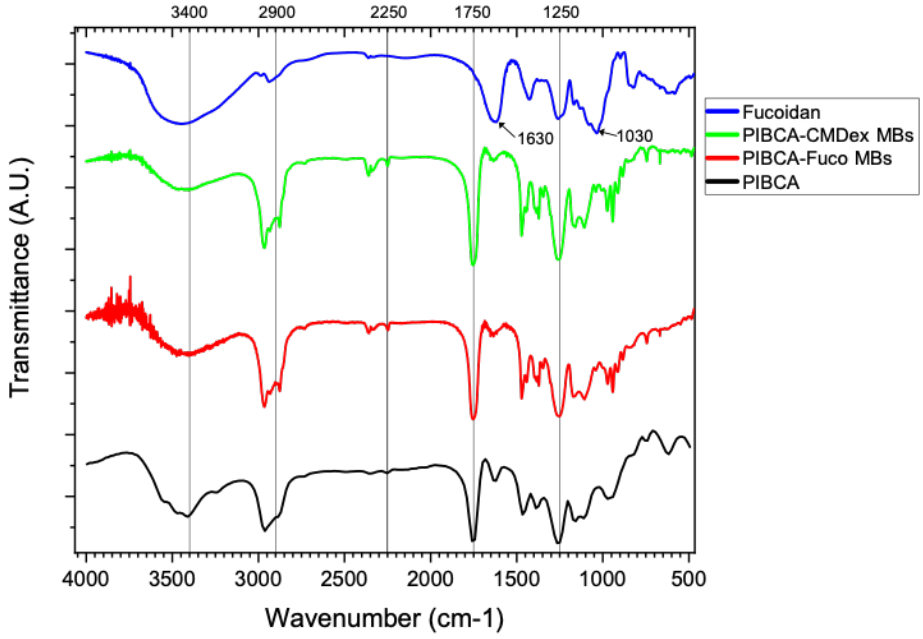

Supplementary Figure 7: FTIR spectra *were obtained for different MBs formulations used in this article. The reference formulation is represented with the PIBCA spectrum (black). Fuco MBs are shown in red and CMDex MBs in green. Comparison to fucoidan alone (blue) implies that no fucoidan can be detected by FTIR in MBs formulation, most likely due to its low mass ratio in the MBs. Based on the literature, cyanoacrylate-representative peaks are illustrated (2,900 cm^{-1}, 2,250 cm^{-1}, 1,750 cm^{-1}).*

Part 3: What we explored but need to optimize

This part aimed to present unpublished data that showed promising results but still require optimization or repetition. From drug loading capacity to *in vivo* sonothrombolysis, we described each protocol briefly and highlighted the major conclusions.

Fucoidan and drug incorporation

We presented in the previous section, the close interaction between fucoidan and the incorporated rtPA, where the presence of the sulfated polysaccharide was essential to the successful incorporation of the thrombolytic drug (*Fig. 16A*). This interaction is related to the presence of negatively charged sulfated groups into Fucoidan structure that interacts with the rtPA protein and the presence of non-sulfated polysaccharide did not allow such incorporation (*Fig. 16B*). The successful loading was validated with a kinetic amidolytic assay and a fibrin degradation assay, and also proven stable after multiple centrifugation steps (*Fig. 16C*). Nevertheless, the loading capacity on Fuco MBs under those conditions was limited around 100 µg of rtPA for 10^{10} MBs in regard with the enzymatic assay.

The significant issue with this loading limit is that high concentration of MBs must be injected to achieve the 1 mg/kg dose used in the *in vivo* study. In clinical setting, MBs are typically injected at a final concentration in the range of 10^5 to 10^6 MBs/mL in humans [366], whereas in our preclinical study, a final concentration of 10^8 MBs/mL was required to reach the desired rtPA level. Obviously, we have established that the high concentration of MBs used in the study did not cause harm to the animals and there were no deaths related to it. Nevertheless, reducing the amount of required MBs would aid in its clinical translation. To achieve this goal, we explored options to enhance rtPA encapsulation onto MBs and have identified potential avenues for future research.

- **Maximum loading capacity**

The maximum loading capacity was determined using the approximation shown in *Fig. 20*. The radius of rtPA dimer was estimated to be 40 Ångstrom, using crystallography analysis [367]. When simplified to a sphere, its surface projection was approximated to $50*10^{-6}$ µm^2. For Fuco MBs, considering a mean radius of 1.5 µm, the estimated plane surface was 28.30 µm^2. The final calculation estimates that the maximum rtPA loading onto Fuco MBs is around 600 µg per 10^{10} MBs. This approximation was based on a simplified model and did not take

into account the curvature of the MBs, the steric hindrance or electrostatic interactions of the incorporated proteins. However, it was understood that our loading capacity was already in the range of high encapsulation rate, with potential room for improvement.

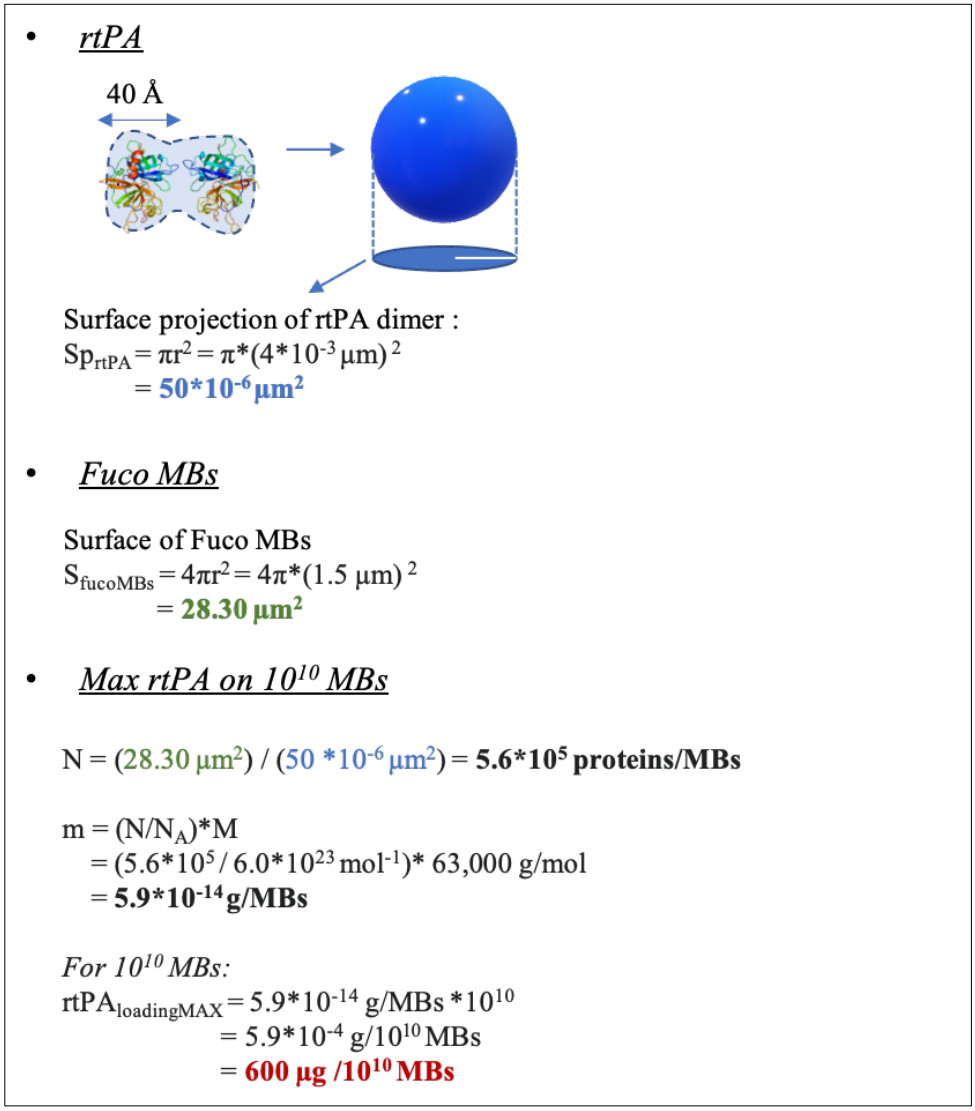

Figure 20: Approximation of Fuco MBs maximum loading capacity of rtPA.

- **Covalent bonding strategy**

In order to improve the incorporation of rtPA onto MBs we attempted to perform covalent bonding using EDC/NHS protocol. This process involves activating a carboxymethyl group by increasing the pH, then using EDC/NHS as a stabilizer for the formation of a stable and covalent amide bond with an amine group. Our approach involved the saponification of the ester isobutyl side chain of the PIBCA shell with 1M NaOH for 15 min [368]. After that, EDC/NHS (2:5

ratio) was added to the pH 10 MBs suspension, followed by free rtPA solution (500 µg). The mix was left for 2 hours under gentle agitation before the centrifugation rinsing process.
The graphs in *Fig. 21* compare the results of rtPA incorporation using the EDC/NHS method to the adsorption protocol, with the amidolytic assay described previously. The first observation is that EDC/NHS did not result in better incorporation of rtPA on polysaccharide-free MBs nor CMDex MBs when compared to adsorption protocol (*Fig. 21A*). Additionally, it was believed that covalent bonding would enhance the long-term stability of the incorporation, however *Fig. 21B* showed the opposite. Those results helped in the decision of the most suitable rtPA incorporation strategy where easy and chemical free adsorption was sufficient. Also, EDC/NHS protocols are hard to standardize and it may appear that it could be improved with different incubation time and pH variation. Nevertheless, a stable covalent bonding is sometimes a constrains for the drug delivery.

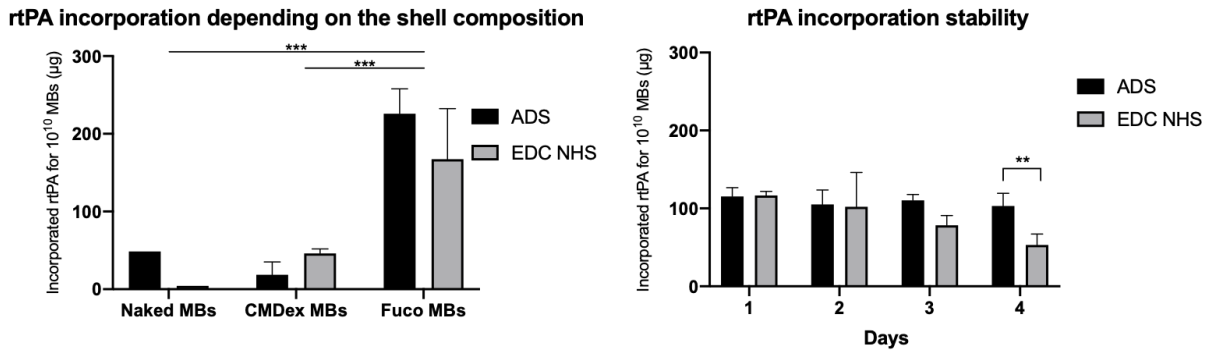

Figure 21: Comparison of EDC NHS covalent bounding to adsorption of rtPA. *Left: rtPA incorporation on various MBs shell compositions with amidolytic assay. Naked MBs corresponds to PIBCA MBs with no polysaccharide in the shell. Right: stability of rtPA incorporation over 4 days with centrifugation steps every day, performed with the same amidolytic assay.*

As a result, our strategy moving forward to increase rtPA incorporation is by enhancing fucoidan incorporation. We believe that this electrostatic interaction may enable more rtPA loading. The current protocol utilized 2% of fucoidan (w/v) in the starting aqueous solution, but this ratio could be increased as we have demonstrated the linear incorporation of fucoidan in *Fig. S2*.

In vivo targeting

The targeting properties of Fuco MBs were evaluated *in vitro* with the microfluidic platelet aggregation assay presented in Part 2 of this Chapter. Nevertheless, the optimization of this protocol took a few months to be validated. Indeed, microfluidic systems are highly dependent on the coating efficiency and also the quality of the equipment. It may happen that the system gets clogged if the blood is infused for too long. On the opposite, platelet aggregation may never occur if the coating is not correctly done or if the withdrawn blood has limited platelet count or aggregation factors. Overall, we explored in parallel the *in vivo* targeting of Fuco MBs on the ferric chloride clot model [369]. This model is widely studied for deep vein thrombosis and briefly consist in the following protocol [338], [370].

Mice were anesthetized with a mixture of ketamine and xylazine through intraperitoneal injection and placed in lateral position. An incision was performed in the abdomen and the mesenterial vein was exposed with the attached bowel (*Fig. 22A*). The focus was set on the mesenteric vein with an intravital microscope and retro-orbital injection of DIOC6 solution allowed the labelling of circulating platelets. Then, a 1 mm large rectangle of chromatography paper, soaked into a 10% w/v ferric chloride solution ($Fe^{3+}Cl^{-}$), was placed for 1 min on the targeted vein. The chemical aggression of the vessel triggered the formation cascade of a thrombus on the injured endothelium. The surgical window was washed with saline to remove any ferric chloride excess. The thrombus formation was then monitored with real-time fluorescence microscopy and Rhodamine B MBs were injected after its stabilization. Live microscopy also recorded the MBs circulation in the vessel, and image analysis was performed to determine the percentage of MBs fluorescence on the obtained thrombus (*Fig. 22B*). For each condition, we had an animal number of 4, which gives an interesting insight but not enough data to conclude on the statistical significance. Indeed, fluorescence microscopy and fluorescence quantification (*Fig. 22C*) tend to the conclusion that Fuco MBs are more specific to the thrombus than non-targeting CMDex MBs but yet, the P-value was not significant ($P = 0.14$). If the targeting capacity was more than validated *in vitro* with whole human blood microfluidic system, this result can be explained by various reasons. The first one relies on the small number of animals (N=4) and the variability in between them. In the objective of the 3Rs (Replace, Reduce, Refine), the animals were selected from our laboratory breeding availabilities. In consequence, male and female as well as different ages (10 to 21 weeks) C57BL/6 were chosen for this study. The ferric chloride deposition time was very dependent of mice sizes and sex, for instance females showed a significantly higher required time for

thrombus formation compared to males. Thus, over a few numbers of animals, we observed a high standard deviation even though the fluorescence was normalized to the clot size. Another reason for the similarities between groups can be explained by the steric entrapment of the MBs independently from the targeting properties of the MBs. We indeed observed that the clot obstruction would inevitably trap circulating MBs but also the clot will continue to form without any therapeutic intervention entrapping any MBs in the complex.

Ferric chloride model for targeting validation remains an interesting approach because it generates platelet rich clot, where P-selectins are the most expressed. We concluded that the preliminary results have a tendency to validate *in vivo* targeting but a larger number of animals with less phenotype differences would be needed to truly compare the results. Finally, secondary validation of the efficient targeting was still obtained *in vivo* with the experiment performed in mice stroke model (*Fig. 18)* showing the residual fluorescence observed on the thrombotic event site after 24 hours.

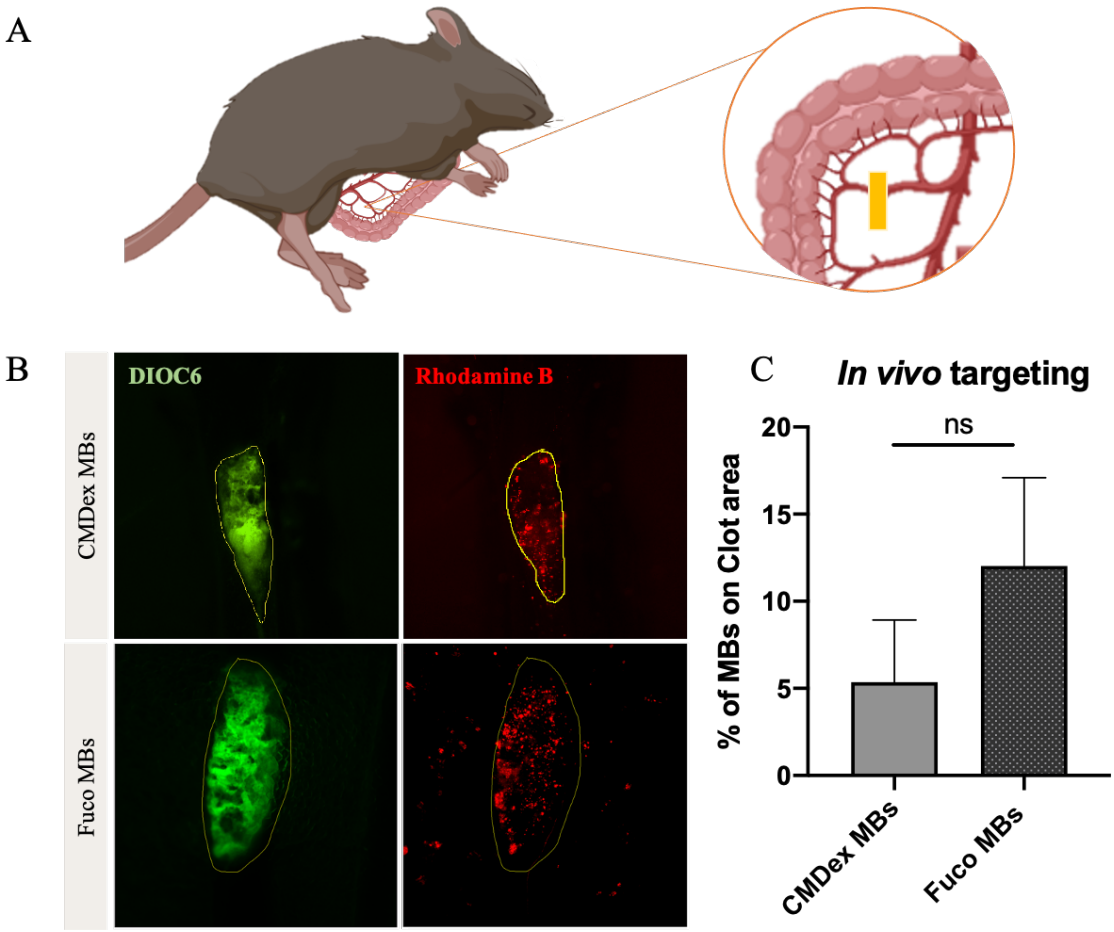

Figure 22: In vivo targeting of Fuco MBs compared to CMDex MBs on ferric chloride thrombotic model*. A) Graphical abstract of ferric chloride thrombosis model. The mesenteric vein is exposed and a small chromatography paper soaked in the ferric chloride solution (orange rectangle) is deposited for 30 seconds to 2 minutes. B) In vivo fluorescent microscopy of the induced clot. In green we observed the platelet aggregation, in red the rhodamine labeled MBs and MBs residues .C) Fluorescence quantification of Rhodamine B signal normalized to the clot area (yellow line in B).*

Freeze drying

The development of new agents for therapeutic application is a long process before reaching commercialization, including safety control, complete physicochemical characterization and clinical trials. Nevertheless, it is important to think about scalability of production and long-term storage. If we look at commercial MBs, they are exclusively distributed as a dry powder to be rehydrated before injection. This process of lyophilization (freeze drying) is a standard process for storage time prolongation in industry. Briefly, it consists in the water removal process by water sublimation, under vacuum conditions. It has the added advantage of reducing the storage weight and space, with the possibility of easy sterilization (UV, gamma rays…). In the case of lipid shell MBs, the adaptability of the material from "dry" to "wet" is well described as their initial synthesis is obtained from a dry lipid film. However, cyanoacrylate MBs are the result of an irreversible polymerization leading to the characteristic stiff shell. Our idea to extend the shelf storage was guided from the recent publication from Ojha *et al*. (2019) about lyophilization parameters of PBCA-based polymeric MBs [371]. This work pointed out the importance as sucrose and Polyvinylpyrrolidone (PVP) for the cryoprotection of the samples. In this study the cryoprotectant (5% w/v) were added to the storage solution of PBCA MBs before the freeze-drying protocol. They produced MBs with the standard hydrodynamic cavitation and used 0.02% Triton-X-100 as a storage solution. The main differences from our work were: the entrapped gas (here is air while we worked with PFB), the cyanoacrylate structure (here n-butyl-cyanoacrylate compared to our iso-butyl-cyanoacrylate) and the freeze-drying protocol (here the freezing step is in liquid nitrogen while our freeze dryer has a temperature slope monitoring).

The first trials performed in the lab, using 5% sucrose or glucose (based on lab stock availabilities), did not allow a successful resuspension of the MBs. Based on information collected during scientific conferences, a second attempt was performed using 12.5 % w/v cryoprotectant (sucrose or glucose). The freeze-drying protocol was based on existing settings used in the laboratory for hydrogel lyophilization (3 hours 15 min of freezing at -40°C, then vacuum to 1.995 mBar and gradual temperature rise to 10°C in 14 hours). The obtained powder was resuspended in 0.02% tween 20 storage solution with vortex and gentle mixing overnight, then MBs size were measured for comparison to prior freeze drying. *Fig. 23* displays the rhodamine labeled MBs before and after the lyophilization protocol. After resuspension some MBs aggregates were floating to the surface, also observed in fluorescence microscopy. The

size measurement emphasized this observation with an augmentation in the MBs mean size to 16 µm (*Fig. 23*).

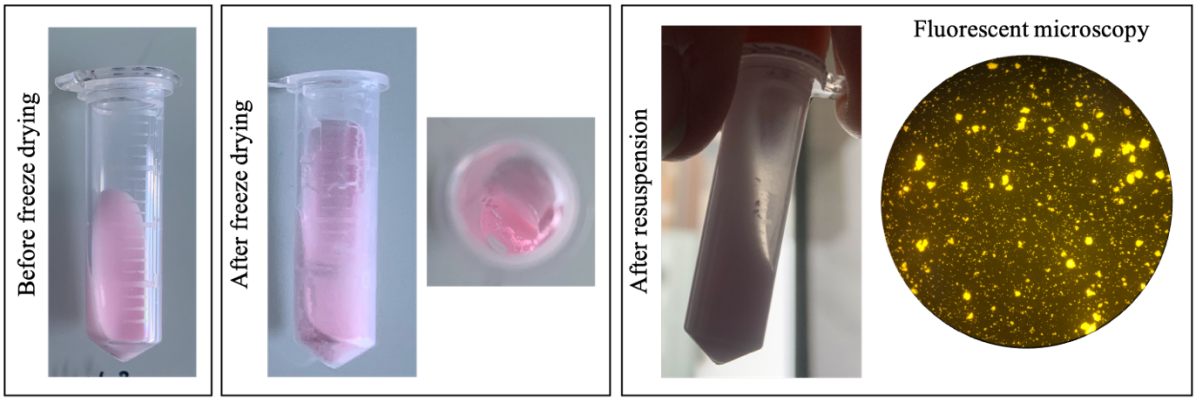

MBs size measurements

	Dv (10)	Dv (50)	Dv (90)
Before freeze-drying	1.48 µm	4.32 µm	9.90 µm
After freeze-drying	2.47 µm	16.00 µm	42.70 µm

Figure 23: Freeze drying experiment on Rhodamine B MBs. *Images of MBs suspension before and after freeze-drying. Size measurement of MBs were performed with laser diffraction granulometry. Here, the Dv(10); Dv(50) and Dv(90) are related to the size distribution. For each graph, it corresponds to the size of MBs measured below this percentage.*

We believe that the protocol can be optimized in order to recover the mean size of the initial suspension (around 4 µm here) without compromising the overall concentration. The quantity of cryoprotectant may be an important parameter as we are working with a perfluorocarbon with a high boiling temperature (-2° C). In consequence, the freeze-drying protocol can induce a change in the gas phase compromising the structure of the polymeric shell. The overall results were promising for long term storage of polymer MBs, but the lack of time postponed this optimization that will be performed in the future projects.

Sonothrombolysis

The process of mechanical disruption with the combination of US and MBs oscillation is described as sonothrombolysis (*Fig. 24*). It relies on MBs acoustic parameters presented in the introduction chapter, MBs behavior indeed is highly dependent on the acoustic pressure of the US signal. Response to US is not only useful for imaging but stable cavitation can induce microstreaming that may improve drug delivery and inertial cavitation could induce MBs burst and destabilize the clot (*Fig. 24*). With the availabilities of commercial MBs for US imaging, several clinical trials were already conducted for stroke [219] or myocardial infarction [220] with promising results but the lack of standard protocols. Indeed, acoustic parameters for reproducible results depend on the frequency, the mechanical index, the insonation duration and the distance to the clot. With this project we aimed to improve the sonothrombolysis effect with the targeting property and with the incorporation of the thrombolytics inside the MBs.

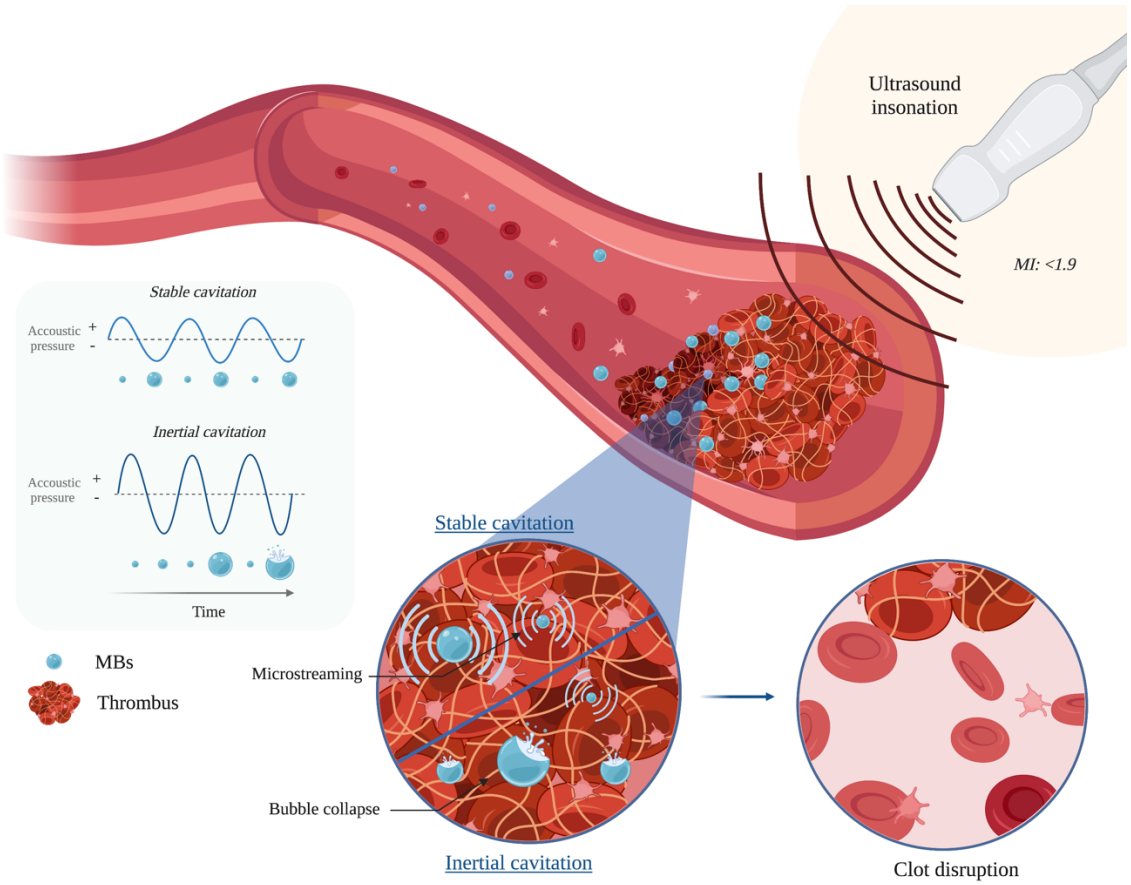

Figure 24: Sonothrombolysis precept for enhanced thrombolysis*. Sonothrombolysis is performed by the ultrasound insonation of MBs on the thrombus site. Microbubble radial oscillation properties are sensitive to acoustic pressure. The bubbles can undergo stable cavitation inducing microstreaming of the surrounding environment or inertial cavitation leading to the collapse of the bubble. While MBs alone are proven to destabilize a clot with US insonation, sonothrombolysis efficacy is enhanced with the thrombus specific targeting and loaded thrombolytic agent on the MBs. Abbreviations: MI, mechanical index; MBs, microbubbles. Created with Biorender.com and adapted from Zenych et al. 2020 [85].*

In collaboration with the team of Olivier Couture from the Laboratoire d'Imagerie Biomédicale (LIB) and the help of the Post-Doc Georges Chabouh, we established a transportable US setup for *in vivo* sonothrombolysis. The general objective was the *in vitro* validation of the MBs destruction with a home-made setup that we could be easily translated to the *in vivo* experiment for targeted MBs enhanced sonothrombolysis. Considering the fact that the *in vivo* experiments were performed with the team of Denis Vivien in the Cyceron facility (Caen), we had to think about an easy to use and easy to transport setup to avoid the operator dependent bias. Instead of a computer driven signal, we thought it would be more practical to define fixed parameters with the single need to use an on/off switch. Therefore, the transportable setup was composed of a monoelement transducer with a 0.75 MHz frequency, connected to an electrical generator fixed to 20 V (estimated MI around 0.8). Indeed, what we knew from the literature was the necessity of high mechanical index signal to ensure MBs burst but the insonation duration was not explicitly standardized. In terms of duration two parameters must be addressed, the overall insonation time and the duty cycle of the signal. The overall insonation time was set here to 1 minute, considering the blood velocity *in vivo* and the capacity of a 20 V signal to induce MBs implosion. The duty cycle on the other hand is related to the continuity of the signal, the higher the duty cycle, the more continuous the signal will be.

- ***In vitro* model**

In that manner we developed the following setup (*Fig. 25A*) for the *in vitro* validation of MBs burst parameters. It was composed of a home-made 10 % agar phantom model with a 2 mm wide channel and a lateral opening allowing the addition of the monoelement transducer perpendicularly to the channel axis. Briefly, the L3-12-D (General Electrics; 256 elements, 0.2 mm pitch size) transducer was positioned on top of the system to image the channel and the independent 0.75 MHz monoelement transducer (SNX, 131124, Sonaxis) was positioned on the front side, perpendicular to the channel (*Fig. 25A*) to induce MBs burst. The top transducer was only used to image MBs signal before and after the burst induction by the monoelement one. It allowed the evaluation of different burst parameters *in vitro* with a constant amplitude (20V, 0.8 MI) and burst cycle (50 cycles). The following parameters were studied: burst period (0.05 ms, 0.1 ms, 1 ms) corresponding to the duty cycle (100%, 50%, 5%) of the burst event, the smaller the burst period the more continuous the signal will be. The protocol was performed as followed: MBs flow was stopped and the imaging sequence was 2 blocks of 200 images each, using a compounded framerate of 150 Hz, Pulse Repetition Frequency (PRF) of 3 kHz

and 2V amplitude. The electric generator was turned on with the previously described parameters for 1 minute. Finally, the same imaging sequence recorded the US signal of remaining MBs and the channel was washed with flowing MBs for the experiment repetition.

Thus, the burst response was evaluated in stopped flow condition, comparing before and after images acquisition of the L3-12-D transducer with image analysis and background noise subtraction. The results are displayed in *Fig. 25C-D*, with the MBs US intensity before and after burst sequence and with the calculated disruption ratio of the MBs depending on the continuity of the signal. The evaluation of MBs intensity to US imaging signal clearly assessed that above 50 % of duty cycle with 20 V amplitude for 1 minute, no more MBs were observed in the channel compared to no burst (0%) and highly discontinuous signal (5%). This result was confirmed by the disruptive ratio calculation in *Fig. 25C*. Those data highlight the importance of the continuity of the signal to induce burst potential of MBs even with high amplitude signal which information is often lacking in preclinical sonothrombolysis model. With the validation of the burst parameters, we were able to translate this model to preclinical sonothrombolysis in a mice stroke model.

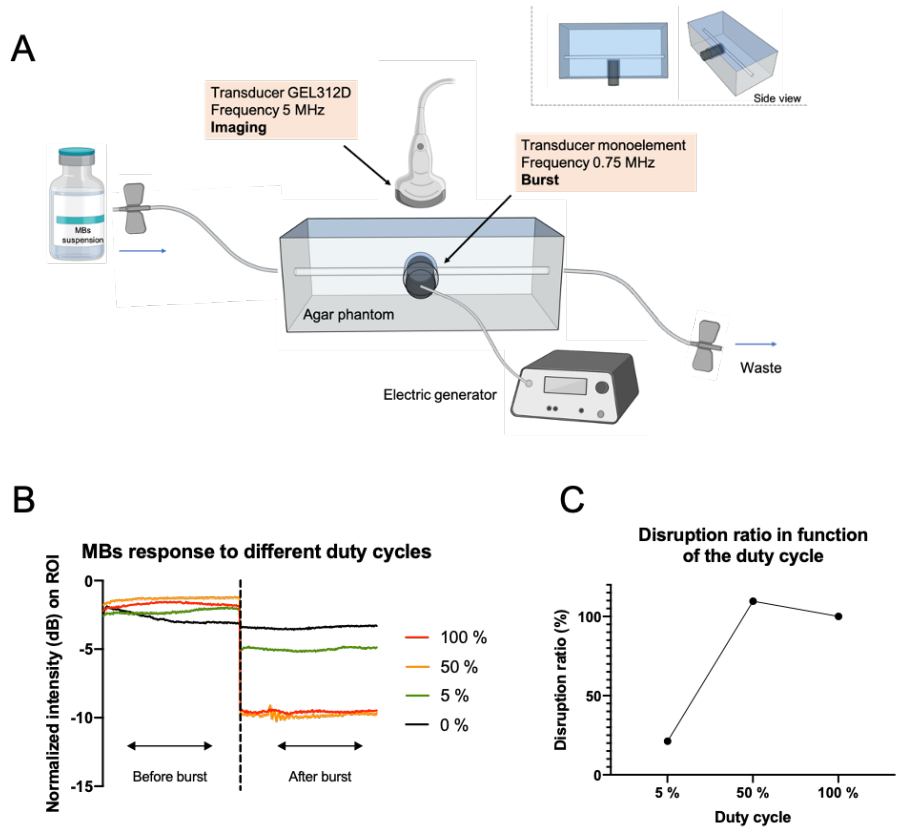

Figure 25: In vitro validation of MBs inertial cavitation. *A) Home-made setup of the agar phantom with a lateral position designed for the monoelement transducer. L3-12-D transducer was used for imaging purpose only. B) MBs signal intensity to different duty cycles before and after burst signal. C) Calculated disruption ratio in function of the continuity of the signal, calculated from the normalized intensities.*

- ***In vivo* translation**

In vivo sonothrombolysis was performed in parallel to the *in vivo* experiments presented in the previous part. In addition to the treated animal with rtPA-loaded Fuco MBs and free rtPA, two other conditions were also performed: free rtPA + US (N = 17) and rtPA-loaded Fuco MBs + US (N = 16). In those conditions, 5 minutes following to the previously presented treatment protocol, US insonation was performed for 1 min (0.75 MHz, continuous with 100% duty cycle, MI 0.8), with the transportable US setup validated *in vitro* positioned on the mice skull and directed to the stroke region on top of echogenic gel to ensure signal continuity (*Fig. 26A*).

The addition of US insonation to free rtPA or rtPA-loaded Fuco MBs did not improve the size reduction of the ischemic region after 24 hours, as presented in *Fig. 26B*. Indeed, saline group ischemic volume was measured at 10.35 ± 4.84 mm^3, showing no statistical significance to the free rtPA group (8.11 ± 5.82 mm^3) nor rtPA-loaded Fuco MBs group (8.40 ± 6.38 mm^3). In consequence it seems that this US insonation protocol was not adapted for an efficient sonothrombolysis in this stroke model. However, we observed that BBB barrier was not compromised as no leakage was observed in gadoteric acid MRI evaluation (*Fig. 26C*).

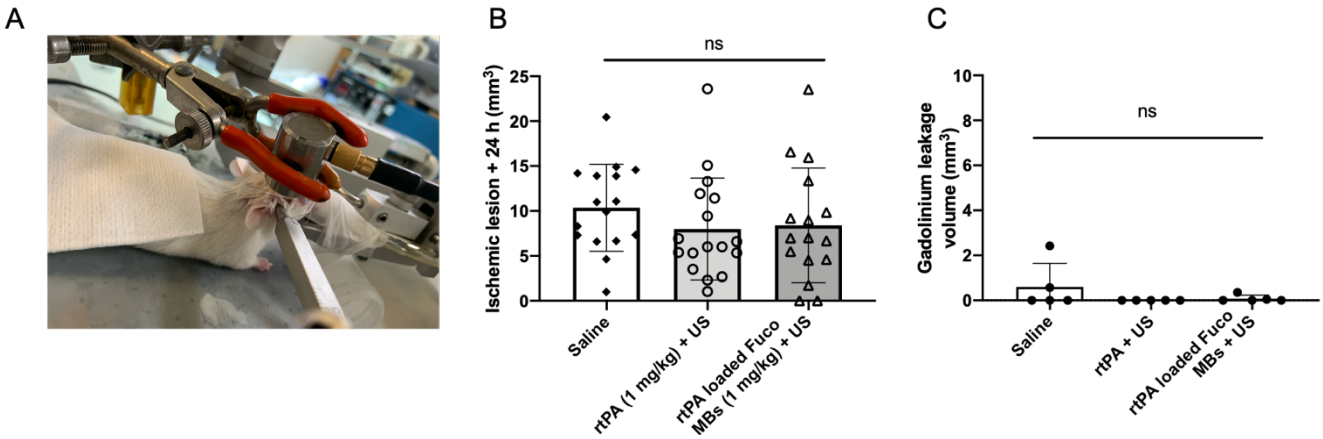

Figure 26: In vivo sonothrombolysis. *A) Monoelement transducer position on the mouse head during US insonation. B) Ischemic lesion volumes of free rtPA + US and rtPA-loaded Fuco MBs + US compared to saline injection of rtPA. C) BBB leakage evaluation with Gadoteric Acid injection comparing the previous group.*

What we can conclude from this preliminary study of *in vivo* sonothrombolysis with drug loaded targeted MBs, is that *in vitro* to *in vivo* translation is not a linear path and require adjustments. The large number of animals allowed to conclude that this insonation strategy was not more efficient than rtPA-loaded Fuco MBs without US, in terms of ischemic lesion reduction at 24 hours but still safe for the animals. It may suggest that the induced cavitation was too "powerful" thus limiting MBs to reach the clot or not specific enough compared to other techniques like MRI assisted focused US [238]. In consequence it may be interesting to

work on the microstreaming effect instead of MBs implosion to destabilize the clot and improve the drug delivery. This could be obtained by reducing the duty cycle and/or the intensity of the US signal and it may be interesting also to have prolonged US signal with slow MBs infusion. In conclusion, the results of this work will help us improve further treatment protocol, with the added skill of better understanding the MBs behavior under US insonation adapted to *in vivo* experiment.

Chapter III: Discussion and Perspectives

In the United States, we estimate the occurrence of acute ischemic stroke every 40 sec, and the thrombotic diseases in their whole are one of the main cause of mortality worldwide [372]. Despite the availability of thrombolytic drugs, there are still a number of unmet medical needs for more effective and safer treatments. After reviewing the pathophysiology of thrombotic diseases, the importance of environmental factor and the lack of early diagnosis, we got interested in the available treatments for fibrinolytic therapy. From 1995, Alteplase (rtPA) has been the gold standard for intravenous thrombolysis allowing the disassembling of the fibrin network entrapping the clots [372]. Despite the introduction of genetically modified thrombolytics like Tenecteplase or Reteplase, with an improved half-life and a high specificity for fibrin, the systemic injection of drug will always require high concentration of drugs to reach an efficient activity on the thrombotic site. High concentration then translates to potentiality for side effects like neurotoxicity or hemorrhagic transformation and consequently longer hospitalization time. The need for drug encapsulation and dose reduction matches with the duty to provide accessible, easy to administer and non-invasive treatments. This is where nanomedicine comes into play in the history of innovative therapies. We presented in the introduction, a glimpse of NPs strategies for thrombolytic therapy including lipid, polymer, inorganic and bioinspired NPs with their pros and cons. We defined the ideal characteristics for the development of an innovative nanomedicine strategy and MBs seemed to check most of the boxes. Indeed, their micro scale prevents from crossing biological barriers like BBB or endothelium, assuring their local action to the vascular system. Compared to small NPs, MBs do not present size dependent toxicity like hemolysis and ROS production [373] nor affect the function of erythrocytes oxygen delivery ability [374]. The major drawback related to their size would be attributed to the possibility of small vessel occlusion because of their red blood cells size range. Nevertheless, their half-life in the bloodstream usually never exceeds 10 minutes, limiting the tissue damages. MBs were also selected for their acoustic properties and the perspective of their use in molecular imaging. Indeed, MBs such as Sonovue® or Optison®, are commonly used for ultrasound imaging in clinic as their non-linear compression dilatation properties under US insonation enables an efficient contrast compared to biological tissues. However, their lipid and albumin shell bring limitations for the functionalization of MBs and as a result our focus was on the design of tunable polymer MBs.

The synthesis process was inspired from the work of the former PhD student Bo LI, who developed targeted MBs composed of cyanoacrylate and fucoidan copolymers via hydrodynamic cavitation. The goal of my PhD project was to pursue the development of those polymer MBs, by encapsulating the thrombolytic drug and validate their *in vivo* efficacy for the

treatment of thrombotic diseases. The project started with the study of existing synthesis protocols for lipid and polymer MBs. We were confronted with the fact that lipids MBs had a multitude synthesis protocol (shaking, sonication, microfluidic) while polymer MBs synthesis had been barely explored. In order to reduce synthesis time and provide more customizable parameters we developed an original synthesis method for polymer MBs. By replacing the air by a perfluorocarbon and using acoustic cavitation instead of hydrodynamic energy, we managed to reduce the time of synthesis by 3 and patented the methodology in 2022. The overall advantage of this technique is the addition of more tunable parameters that could extend the application window of those polymer MBs. For example, with pressure/temperature management and insonation optimization it may be possible to develop Nanobubbles that showed promising perspectives for cancer treatment and diagnostic based on the EPR effect or for drug delivery across the BBB. The remaining drawback of this method is attributed to the required filtration procedure for the obtention of tuned size MBs. Nevertheless, we believe that the synthesis parameters, may still be optimized to reduce the post production step, providing a more scalable method. Hence, once we secured a safe, reproducible and time saving method, MBs were characterized and tested for *in vivo* application.

Thus, we presented in this PhD manuscript, the development of drug-loaded targeting polymer MBs for the improvement of stroke treatment. Their stability over time was validated over 4 weeks in suspension (*Fig. S1C*) and their biodistribution aligns with the liver primary function to detoxify the blood. In addition, the shell composition did not affect the shelf stability (*Fig. S1D*) allowing data compilation and the preliminary trials on freeze drying MBs (*Fig. 23*) demonstrated the potential of the newly synthetized MBs for long term storage. Cyanoacrylates are strong adhesives commonly used in surgical procedures for wound closure but are also injected in humans to seal blood vessels [79]. Fucoidans on the other hand are extracted from brown algae [44] and were injected in humans with NANO-ATHERO project (NCT03422055) [16,30]. Thereby, this easy to make and scalable acoustic cavitation protocol draws new perspectives for the development of biocompatible microbubbles. The shell composition was validated by Fourier Transform Infrared (FTIR) as presented on *Fig. S7,* displaying the characteristic pics of ester bound around 1,750 and 2,250 cm^{-1} for cyanoacrylates. However, the polysaccharide incorporation with either fucoidan or carboxymethyl dextran was challenging to identify given the small amount of it. This quantification was better performed with sulfate dosage (*Fig. S2A-B*) and fucoidan targeting properties (*Fig. 16D-E*). In addition, the use of whole human blood rather than P-selectin coating for the evaluation of targeting properties is a much more accurate model for *in vivo* translation. The micron size of MBs helped

for imaging characterization with ESEM (*Fig. 14D*), confocal (*Fig. S3A*) and FIB (*Fig. 14E; Fig. S3D*) imaging. In that manner, we were able to estimate the shell thickness by two methods (FIB and confocal fluorescence) to 518 ± 116 nm (*Fig. S3B-C-D*). The wide standard deviation is also the consequence of the FIB sample preparation that affected the MBs integrity limiting the sample number (N=4). After validation of MBs physicochemical properties, rtPA incorporation was obtained with a simple adsorption protocol using no additive chemical, no critical temperature and no need for the use of covalent bonding like EDC/NHS (*Fig. 21*). We validated the rtPA activity through two enzymatic assays, the fibrinolytic activity on agar gel (*Fig. S4A-B*) and the amidolytic activity on fluorescent substrate (*Fig 4 A-B*). Regular protein quantification with copper reduction (BCA assay) was not possible due to the reactivity of MBs without any incorporated drug. The incorporation was also validated by the shift in the surface charge (zeta potential) of rtPA-loaded Fuco MBs compared to Fuco MBs (*Fig. S1A*). Lastly, the activity of the incorporated protein was stable over 4 days (*Fig. 16C*) with no shift in the mean size of the MBs (*Fig. S1E*). Therefore, to ensure the effectiveness and the quality of the treatment, rtPA-loaded MBs were not use after 4 days for *in vivo* injection.

MBs are of main interest because of their acoustic property in US imaging also validated here with a homemade US setup. Establishing echogenic evaluation is not standardized yet and it mainly relies on contrast enhancement validation. Moreover, the system is highly setup dependent (distance, probe, medium) and required probe calibration. The test was computer driven with different voltage but, in order to translate to Mechanical Index, a hydrophone calibration was performed to measure the negative pressure of the signal. Nevertheless, it gives good insights for *in vivo* translation. We wanted to determine the threshold of MBs stability for US imaging but also the disruptive ratio of MBs for later sonothrombolysis experimentation. Indeed, many teams [20;21;22] have been exploring the impact of bursting MBs with US for the mechanical impairment of blood clots. No standards have been determined yet, except for bio-damaging boundaries of high Mechanical Index (MI, 1.9) [206]. A better understanding of MBs response to US signal *in vivo* is a key element to perform safe and monitored sonothrombolysis.

Before *in vivo* injection, we validated the *in vitro* biocompatibility of cyanoacrylates degradation products [74] with hemolytic tests (*Fig. 17C*), viability (*Fig. 17D*) and mortality assays (*Fig. 17A-B*) on endothelial cells and fibroblasts. The safety of MBs was demonstrated for each cell type independently from the MBs concentration (up to 1 x 10^8 MBs/ml) or the duration of the experiment (from 2 hours to 6 hours). The assays durations were selected according to the fact that MBs are not designed to be circulating after a few hours in the

bloodstream. Overall, in accordance with the International Standard (ISO 10993-5) the 70% viability and 30% for mortality threshold were not exceeded. Thus, the safety of polymer MBs allowed the translation to the animal stroke model.

Thrombin injection triggers the formation of fibrin rich clot compared to ferric chloride model [377] that induces platelet rich thrombi. In consequence, thrombin-induced clots are more likely to respond to rtPA treatment. In this study rtPA was injected to $1/10^{th}$ of the treatment usually used in mice [378]. This choice was driven by the ultimate goal to limit rtPA dose related side effects. This constraint did not prevent an efficient clot resolution thanks to the specific targeting of rtPA-loaded Fuco MBs. Indeed, 1 mg/kg injection of rtPA loaded onto targeting MBs, reduced by more than 50% the size of the ischemic lesion for 16 animals (out of 16). The drug loading helped protect the protein and the specific clot targeting lead to the treatment improvement. This result is even more promising as free rtPA treatment at the same concentration was not significantly more efficient than treatment with saline only. In consequence, we can hypothesize about the synergic action of rtPA loaded onto Fucoidan MBs for a successful thrombolysis. The specific targeting of fucoidan may also be enhanced with the known affinity of rtPA for fibrin [372] and consequently improve the precise drug delivery. Finally, this efficient targeted drug delivery treatment gets in the range of human recommended dose of 0.9 mg/kg (according to the National Institute of Neurological disorders and Stroke), suggesting that lower dosage of encapsulated rtPA could have beneficial outcomes and reduce dose related side effects in humans too.

No animal was harmed with the injection of rtPA-loaded MBs and we aimed to reduce the number of animals. Hence, control conditions like Fuco MBs, rtPA-loaded CMDex MBs and free rtPA at 10 mg/kg for stroke treatment were not explored. Firstly, Fuco MBs would have been interesting to validate targeting properties *in vivo* compared to rtPA-loaded Fuco MBs. Nevertheless, we demonstrated *in vitro* that the rtPA incorporation did not impair the targeting properties of Fuco MBs (*Fig. 16F*). Secondly, rtPA loaded CMDex MBs treatment evaluation could highlight the importance of targeting for the clot resolution. However, efficient rtPA loading on CMDex MBs was not possible as presented in *Fig. 16B*. Lastly, free rtPA treatment validation of 10 mg/kg efficient thrombolysis on thrombin clot mouse model was largely studied [363], suggesting the real advantage of our dose reduced treatment.

We also studied the outcome and clearance process of MBs after stroke treatment. The circulation time of polymer MBs in the body depends on a number of factors, including size of the MBs, type of polymer, and the density of the gas core [58]. In addition, the circulation time can be influenced by opsonization, the presence of plasma proteins that can bind to the surface

of MBs and alter their fate through the body. The half-life measurement is part of the supplementary studies that would complete this work and US imaging is the most relevant way to determine MBs integrity by observing their non-linear signal or on/off contrast with higher mechanical index [379]. Unfortunately, the lack of availability of an US device for small animal evaluation postponed this evaluation. Overall, circulation time is widely dependent of the MBs composition but is usually ranging from minutes to tens of minutes, long enough for conventional diagnosis or therapeutic methods.

The biodistribution study was performed 2 hours after injection in the liver tissue with immunolabelling of resident macrophages to evaluate the early blood detoxification in the liver (*Fig. 19C*). More organs including brains, livers and lungs were actually collected from of all the groups after 24 hours and stored for further histology evaluation. The lack of time by the end of this project did not permit a full histology study, but the harvest of infarcted areas in the brain and study of liver residual fluorescence would bring necessary insight for further animal studies. In addition, the biodistribution on *ex vivo* organs revealed the final whereabout of MBs in the body with the expected contrast in liver and lungs (*Fig. 19A*). The residual fluorescence of rtPA-loaded Fuco MBs was also observed in the stroke region after 24 hours (*Fig. 19A*) validating the specific targeting of fucoidan on P-selectin but also pointed out the long-term expression of this biomarker after the treatment by activated endothelial cells. This confers an interesting horizon for further molecular imaging of thrombotic diseases. Especially since the residual fluorescence is not due to BBB permeability as demonstrated with Gadoteric Acid (GA) injection (*Fig. 18E-F; Fig. S6B*). P-selectin is a known endothelial-related inflammation biomarker [380] and an increase in its concentration within 72 hours could predict the incidence of post stroke infection [381]. Nevertheless, some controversies still remain in the significance of P-selectin expression in stroke versus non stroke patients [382] and molecular imaging could be an alternative way to resolve the debate. In that manner the study of thrombo-inflammation with Fuco MBs may be investigated over different time points with either fluorescent microscopy or US imaging.

We also wondered about the further clinical translation of those US responsive agents regarding the high MBs concentration injected in order to reach the 0.9 mg/kg of rtPA. In fact, the final concentration of rtPA used for stroke treatment was restricted due to the potential harm of high concentration of MBs *in vivo*. For clinical US imaging, the final concentration of MBs depends of the US contrast agent [379], but is usually up to 10^6 MBs/ml of blood. If we compare to the final concentration of our animal model, the final concentration was elevated to 10^8 MBs/ml of blood. As presented before, no animal presented any distress during the injection,

no crossing of the BBB was observed and no unspecific residual fluorescence was recorded. Right now, it is hard to evaluate on the possible translation to human with the actual amount of required MBs. Besides the fact that commercial MBs are exclusively lipid or protein made, the potential harmful degradation products of cyanoacrylates, cyanoacetate and formaldehyde could be measured, even though formaldehyde half-life was of 1.5 min in monkey plasma [383]. In order to overcome this issue, we expect that the final MBs concentration can be reduced. First, we know that rtPA encapsulation can still be improved by enhancing its interaction with fucoidan. Also, regarding the first *in vivo* test, lower dose of rtPA may be enough for an efficient treatment and injections in double bolus or infusion are conceivable options to inject smaller quantities at the time. Lastly, the synergy between MB drug delivery and US insonation has not been validated yet and could also help reducing the required amount of injected MBs. Indeed, sonothrombolysis trials were performed on mice, along with the injection of rtPA-loaded MBs. The inertial cavitation of MBs did not improve the resolution of the thrombolytic treatment but neither induce harmful complications. We can discuss how the US regime should be modified to ensure that MBs behavior does not prevent them from reaching their biological target. So, the next strategy may be to reduce the mechanical index and increase the US exposure to use microstreaming behavior of MBs instead of their implosion. This could enhance drug delivery and improve the deeper penetration of MBs inside the clot through mechanical disturbance of the environment (*Fig. 5*). However, the translation of this kind of treatment is still on the edge of development as bones are US absorbent and the mouse skull is less that a millimeter thick while human skull can reach up to 6 mm.

The targeted treatment of thrombotic diseases was a success in the performed evaluation of stroke resolution and some modifications would be interesting to explore to keep reducing the adverse effects of acute ischemic stroke. The time window for rtPA treatment is still limited by the hemorrhagic transformation risk after 4.5 hours, because of the action of metalloproteinase, limiting the treatment accessibility to only 10% of patients [384]. Indeed, a few hours after the ischemic event, metalloproteinase precursors are expressed in the brain and become active with rt-PA cleavage, leading to destruction of the endothelium extracellular matrix. Recent studies already demonstrated the prevention of hemorrhagic transformation with metalloprotease inhibitors and their incorporation into MBs may expand the therapeutic window [385]. Combined strategies with optimized plasminogen activators and deoxyribonuclease would also have an interest for the dissolution of NETs, recently described on thrombi [386]. In addition, oxygen delivery could be performed as a therapeutic gas could reduce the hypoxic state of the surrounding tissue. Overall, a more complex design of MBs

could embrace the synergic effect of gas, chemical and mechanical actors for the efficient treatment of thrombotic diseases.

The future investigations related to this project include the development of the US molecular imaging and the enlargement of their application spectrum. Currently, ultrasound imaging is physically limited in resolution by the diffraction of approximately half of the wavelength of the transmitted beam. By combining clinical microbubbles with ultrasound, a breakthrough resolution was possible with the technique called Ultrasound Localization Microscopy [284], [312]. ULM maps the *in vivo* microcirculation down to few microns deep in organs. However, the microvasculature is a complex 3D network, hence 2D ULM suffers from out-of-plane motion; thus 3D ULM was recently introduced [312], [314] for whole organ imaging and was sensitive to stroke [315]. So far, the smallest ever imaged vessel with ULM is about 30 microns (arterioles, venules) where microbubbles speed is higher than 20 µm/s. Various functional blood vessels in the human body such as the capillary beds in the brain, glomeruli in the kidney or the islets of Langerhans in the pancreas are known to have very slow flows (about 1-10 µm/s). With the current ULM techniques, the spatiotemporal filtering that is used to separate flowing MBs and tissue is limited on such low velocities, hindering the capability of ULM to reveal such microenvironments. The fast improvement of US imaging with ULM and the detection of single static MBs are the future key perspective for an efficient US molecular imaging with targeting MBs [315]. Thus, the validation of these new imaging modalities with different ultrasound pulse schemes such as non-linear techniques to correct for the loss in actual filters are the next step of the ANR FightClot project with the collaboration of the LIB.

Another interesting perspective will be explored with the application of targeted MBs with chronic inflammatory diseases. Their prevalence is estimated at about 5% of the world population [387] and these diseases are associated with the occurrence of inflammatory outbreaks, which are the main source of clinical complaints and organ dysfunction. Despite the many therapeutic strategies currently used, the control of inflammatory outbreaks remains difficult. Circulating monocytes are key players in these inflammatory pathologies and the broad spectrum of immunological functions performed by these cells is based on an adaptable metabolism. Reprogramming monocytes is then a new strategy for the modulation of the inflammatory response. In collaboration with Dr. Arnaud Millet from Institut pour l'Avancée des Biosciences (IAB, Grenoble, France), we proposed to achieve a fine control of inflammatory hypoxic monocytes by inhibiting their pro-inflammatory glycolytic metabolism through oxygen delivery. To achieve this goal, the REPRO-BULLES project (StratEx-

IdExUP2019-secondaire) is developing an innovative strategy to transport and deliver oxygen specifically to circulating monocytes using functionalized oxygen MBs. The advantage of MBs over nanocarriers is their high gas encapsulation capacity and their size prevent from extravasation allowing a strict encounter of blood circulating monocytes. We performed preliminary tests with mannose instead of fucoidan as a targeting agent for the CD33 receptor of monocyte and with dioxygen encapsulation instead of PFB. The phagocytosis capacity of those circulating cells allowed a reorientation of the inflammatory profile of the monocytes through the oxygen control of the Dihydropyrimidine Dehydrogenase metabolic pathway. The validation of the anti-inflammatory reprogramming with oxygen delivery was validated *in vitro* and we are now working on the full characterization for the *in vivo* translation.

A thesis is only a step in the scientific advancement towards potential clinical translation. The long-term prospects of this project would be, of course, the valorization of targeting MBs for the treatment of thrombotic diseases in a clinical study project. We are aware that this perspective requires the validation of many stages on which we will finalize this discussion, with the idea that a future student will resume the project and/or its valorization through the creation of a start-up. First, regulatory toxicology must be performed on all elements of the MBs, individually and on their combination. Cyanoacrylate is probably the main actor that may require additional modifications to strengthen the biocompatibility of the model. It is indeed described that longer lateral chains are less likely to be toxic for injection in humans. The modification of the main component of the shell thus also implies the validation and complete characterization of the physicochemical and acoustic properties of these polymer MBs. Regulatory toxicology is also accompanied by the development of long-term stabilization for the industrialization of the therapeutic tool. Based on existing ultrasonic contrast agents, the best way to preserve MBs is to freeze-dry them. The first tests highlighted the ability of MBs to be resuspended in aqueous solution but still require optimization and complete characterization. Also, lyophilization was only tested on MBs that did not include a therapeutic agent. We know that rtPA in solution is obtained from the solubilization of a lyophilizate and it seems that the freeze-drying of the rtPA+ MBs complex is possible without altering its enzymatic properties.

Finally, the question of the dose of MBs needed for an effective treatment should be addressed. Currently, the highest recommended dose for MBs injection is only defined for US imaging application at a dose of $5*10^8$MBs. Concerning the use of MBs for a clinical therapeutic point of view, the dose still needs to be established. If we translate our preclinical results to humans, i.e., a ten times reduction of rtPA dose for an efficient thrombolysis, the MBs

dose to be injected will still be higher than the current requirements of MBs for US imaging. From a theoretical point of view, the development of ultrasonic imaging is necessary for the visualization of targeting and therefore static MBs for the development of US molecular imaging. Also, it will be necessary to highlight the interest of these barely studied polymer MBs compared to gold standard ultrasound imaging enhancers such as Sonovue®. Thus, the versatility of these therapeutic tools and the constant theoretical development of imaging techniques are the key to the multiplication of the applications for these US responsive drug delivering MBs.

General conclusion

The aging of the population, the degradation of life styles and population sedentariness will be the major contributors for the increase of cardiovascular diseases prevalence in the future years. Despite the availability of efficient treatment, there is an unmet medical need to extend the therapeutic window and reduce the life-threatening side effects to be able to treat all the patients. The objective of this PhD project was to develop an innovative strategy for the efficient treatment of thrombotic diseases. We successfully managed to establish an original synthesis for targeted polymer MBs, patented in 2022 for its inventiveness. Those MBs were successfully targeting activated platelets and activated endothelium with fucoidan on their shell composition and rtPA incorporation was stable over several days ensuring an efficient loading. The *in vivo* model of ischemic stroke was efficiently treated with rtPA-loaded Fuco MBs, and the ischemic lesion was reduced by more than 50% compared to gold standard systemic injection. The biodistribution studies validated the specificity of Fuco MBs for the biomarker (P-selectin) and no harmful side effects were observed. In conclusion we validated the objective of providing an efficient targeted treatment for thrombotic diseases with a reduction of the therapeutic dose and no side effects. Along with their encapsulation capacity, MBs are also used as contrast enhancers for US imaging and their behavior towards US can have therapeutic applications. While we explored and validated the echogenicity of MBs in a flow phantom model, the *in vivo* translation for sonothrombolysis was not efficient in terms of stroke resolution yet. In consequence the US studies *in vivo* for sonothrombolysis and for molecular imaging are the main further perspectives of this project, that will keep running until 2024. Also, some more characterizations, including histology study, long term storage optimization and drug encapsulation improvement will be essential for a final objective of clinical translation.

The fulfillment of those objectives will be accompanied by the development of a new application during my Post-Doc (April 2023-March 2024). I am very pleased to be able to work on this topic for another year, with the solid knowledge and expertise that this project already brought me. In collaboration with Dr. Arnaud Millet from the Institut pour l'Avancée des Biosciences in Grenoble, we are going to study the therapeutic use of MBs as oxygen carriers for the reprogramming of monocytes in chronic inflammatory diseases. I was always eager to explore strategies for other application and this opportunity was a perfect transition for my future projects. I have been attracted to entrepreneurship for several years now, and the development of project during my thesis make me want to experience this kind of challenge in a start-up or smaller company scale. Far from running my own business, I am eager to get as many professional experiences from newly developed companies.

In conclusion to my personal feeling toward this PhD, I would like to address that despite the constraints of the pandemic, I probably experienced the most thriving years of my life. This PhD allowed me to work with amazing teams and understand that research is mostly a big collaborative work. My academic formation as a biomedical engineer never allowed me to specialize in a restricted field but it allowed me to build bridges between biologists and physicists that sometimes do not speak the same language. I learned so much from watching and observing my collaborators and I am truly grateful from those experiences. I had the chance to participate to 6 international conferences including 3 oral presentations (Annexes 7, 9, 11) and 3 posters (Annexes 6, 12). As a young scientist, I was very intimidated presenting my work in front of an audience of hundreds of people but I somehow managed to take the best from it. I am proud to say that I won two prizes for best oral presentations (Annexes 8 and 10) and 1 prize for the best poster presentation. (Annex 13). I have to admit that I was surprised about the benevolence of the scientific community and the inclusion of PhD students. For a long-time I have been afraid to fulfill my academic journey with a doctorate, being aware of the financial difficulties of academic research and the competition for grant obtention. Nevertheless, I decided to trust my PhD supervisor in this adventure and it was definitely the best professional experience of my short carrier. Academic research is not only money-driven but brings a lot of freedom in the way of thinking and the way of working. I would say that the hardest task is to determine the moment to end an optimization or the moment to end a project. I would not lie about scientific redaction being my favorite part, but I learned from that I was endowed with a great resilience. These 3 years helped me overcome the fear of failure and forced me to acknowledge that I am not only lucky to have come that far, but that work and dedication are the keys to success. As a reference to Marie Curie's quote, I used to always look at what was missing instead of focusing on what we had accomplished and I maybe finally learned to be more indulgent with my work and with myself.

Résumé substantiel en français

Contexte

Les maladies cardiovasculaires sont le fardeau mondial de l'humanité contemporaine. Décrit comme la première cause de mortalité et d'invalidité, c'est devenu une priorité médicale avec le vieillissement constant de la population mondiale. Parmi les différentes pathologies liées au système cardiovasculaire, notre groupe s'est concentré sur les maladies thrombotiques. Elles sont la conséquence de la formation pathologique d'un caillot sanguin dû à une dérégulation dans le système hémostatique et/ou à une maladie athérosclérotique. En effet, l'équilibre sanguin est fin et régi par des facteurs chimiques, biologiques et mécaniques. Dans des conditions physiologiques, les caillots de sang (thrombus) sont essentiels pour maintenir l'intégrité des vaisseaux et protéger contre la contamination des corps étrangers. Néanmoins, cette barrière biologique est très réactive et de petites perturbations, y compris des facteurs génétiques, le style de vie sédentaire, le tabagisme ou une alimentation grasse peuvent entraîner des conséquences dramatiques. Les thrombus sont principalement composés de mailles de fibrine piégeant les érythrocytes, les plaquettes activées et les cellules inflammatoires circulantes, et se forment dans les veines ou dans les artères. Dans les deux cas, le risque majeur est l'occlusion des vaisseaux causée par le déplacement du thrombus vers les poumons (embolie pulmonaire), les petits vaisseaux du cœur (infarctus du myocarde) et le cerveau (accident vasculaire cérébral).

Limites du traitement actuel

La thrombolyse standard repose sur l'injection d'activateur tissulaire du plasminogène recombinant (rtPA) qui activera le plasminogène en plasmine, la principale protéase fibrinolytique. Par conséquent, la plasmine désassemble la fibrine réticulée en produits de dégradation de la fibrine (FDP) et libère les cellules piégées. Cependant, l'injection systémique actuelle de traitement thrombolytique pour un AVC ischémique ne peut être opérée que 4,5 heures après l'événement. En effet, des précurseurs de métalloprotéases sont exprimés dans la région ischémique plusieurs heures après la survenue de l'accident et leur activation par le rtPA conduit à un désassemblage de la matrice extracellulaire, fragilisant ainsi l'intégrité des vaisseaux et entrainant une hémorragie. Par ailleurs, au-delà de cette limite de temps, une thrombectomie (retrait par cathéter endovasculaire) peut envisagée mais avec la possibilité de complication chirurgicale. Injecté de façon systémique, le rtPA a une demi-vie relativement

courte (environ 4 minutes) en raison de la présence de son inhibiteur naturel (PAI-1) et de sa détoxification par le foie. En conséquence, le médicament est injecté dans une concentration (0,9 mg/kg de poids corporel) impliquant des effets secondaires liés à la dose tels que la neurotoxicité et la transformation hémorragique de l'événement. Dans l'ensemble, le principal besoin médical non satisfait pour le traitement des maladies thrombotiques est une thérapie spécifique efficace réduisant les effets secondaires potentiellement mortels.

Stratégie proposée

De cette problématique résulte le principal objectif de ce travail de Doctorat, d'explorer une nouvelle stratégie pour l'encapsulation et la délivrance ciblée du médicament thrombolytique. Des travaux antérieurs du laboratoire ont validé la délivrance ciblée de rtPA avec des nanoparticules de polymère ou de polysaccharide montrant des résultats prometteurs. Mais le groupe a également exploré de nouveaux vecteurs comme les microcapsules et les microbulles. L'avantage de ces micro-objets est leur polyvalence pour l'imagerie ultrasonore et le potentiel de perturbation mécanique du caillot avec la sonothrombolyse. Dans ce contexte, ce travail de Doctorat vise au développement de microbulles (MBs) stables et biocompatibles permettant l'encapsulation du rtPA et le ciblage efficace des caillots sanguins afin de réduire la dose thérapeutique nécessaire à la résolution des accidents thrombotiques.

Pourquoi des microbulles ?

Les MBs sont déjà employées pour l'imagerie Ultrasonore (US) clinique en tant que rehausseurs de contraste (Sonazoid®, Optison®, Sonovue® ou Definity®), permettant ainsi l'étude de leurs effets oscillants pour des fins diagnostics/thérapeutiques. Cependant, il n'existe pas encore de MBs ciblantes et capables de transporter des actifs en clinique. La question de la fonctionnalisation des MBs est principalement abordée sur leur propriété de ciblage et de chargement de médicaments, pour traiter des agents pathologiques spécifiques. Toutefois, comme les MBs commerciales, le type de MBs le plus répandu est celui des coques phospholipidiques. Bien qu'elles aient démontré de nombreux avantages en termes de biocompatibilité, de biorésorbabilité et de propriétés mécaniques, elles présentent également certains inconvénients. Les MBs à coquille lipidique sont souvent stabilisées avec des glycols de polyéthylène (PEG) qui ont été récemment mis en cause pour leur tendance immunogène. En outre, le processus de synthèse des MBs enrobées de lipides est dérivé d'un processus de réhydratation par film sec dû à la non-miscibilité des lipides en solution aqueuse. Pour

surmonter cette problématique, le mélange lipidique est dissous dans du chloroforme et laissé pour évaporation pendant plusieurs heures. Non seulement cette méthode révèle l'utilisation de produits chimiques toxiques, mais elle est aussi chronophage. Une autre limite des MBs lipidiques est leur capacité de fonctionnalisation. En effet, l'arrangement monocouche des lipides donne peu d'espace pour la modification de la coquille à part en utilisant le complexe streptavidine/avidine. Si certaines MBs « prêtes à être chargées » sont déjà disponibles (MicroMarker®, BR55®), il faut parfois modifier l'agent de fonctionnalisation (par biotinylation) où la possibilité de modification est limitée. Afin de pallier ces inconvénients, nous avons mis en place une méthode de synthèse originale par cavitation acoustique pour la production de MBs polymères biocompatibles et à forte capacité de fonctionnalisation.

Synthèse innovante et microbulles fonctionnalisées

Cette synthèse par cavitation acoustique a récemment été brevetée par notre équipe pour son caractère innovant en comparaison à la méthode classique de cavitation hydrodynamique, en réduisant notamment le temps de synthèse par trois. Ces MBs sont formées à partir de la copolymérisation entre un monomère : le cyanoacrylate d'isobutyle, et un polysaccharide sulfaté : le fucoïdane, autour d'un gaz biocompatible connu pour ses propriétés acoustiques : le perfluorobutane (*Fig. 27*). Les propriétés de ciblage du fucoïdane résident dans son analogie anatomique comparée au ligand naturel (PSGL-1) de la P-sélectine, protéine transmembranaire exprimée lors de l'activation des plaquettes ou de l'endothélium. Il est actuellement en phase d'étude clinique comme agent diagnostic pour l'imagerie de la thrombose, et peut devenir une alternative abordable et de haute qualité comparé aux anticorps et peptides. Après l'obtention de ces MBs stables et leur caractérisation complète, de la mesure de taille (3µm de moyenne), à la stabilité en suspension (1 mois), nous avons validé leur fonctionnalisation *in vitro*. L'incorporation de l'agent thérapeutique (rtPA) s'est faite après synthèse par simple adsorption et interaction électrostatique entre les groupes sulfates du fucoïdane et les charges positives de la protéine. Nous avons validé l'activité du rtPA chargé par deux essais enzymatiques, l'activité fibrinolytique sur gel d'agar et l'activité amidolytique sur substrat fluorescent. Enfin, l'activité de la protéine chargée a été stable pendant 4 jours sans changement de la taille moyenne des MBs. La propriété de ciblage MBs fonctionnalisées a été évaluée en microfluidique imitant les conditions de la circulation sanguine *in vivo*. Le ciblage a été très significatif en comparant les MBs non ciblantes (CMDEX MBs) à celles avec le fucoïdane (Fuco MBs). De plus, les MBs ciblantes chargées de médicaments ont encore été en mesure de cibler les plaquettes activées avec une différence significative par rapport au contrôle. Après validation de la biocompatibilité

sur des érythrocytes, fibroblastes et cellules endothéliales, nous avons poursuivi le projet avec la validation thérapeutique des MBs fonctionnalisées *in vivo*.

Traitement de l'AVC chez la souris

En accord avec les décrets en vigueur sur l'expérimentation animale, nous avons mis en place un modèle d'AVC chez la souris afin de tester l'efficacité de notre traitement ciblant. Après une craniotomie locale au niveau de l'artère cérébrale moyenne, l'injection de thrombine a généré la formation de caillots riches en fibrine. Le caillot se stabilise durant 40 minutes, puis le traitement est effectué par injection intraveineuse via la veine de la queue. L'examen final a été obtenu à 24 heures par l'analyse des images IRM de la lésion cérébrale ischémique générée par l'absence d'apport en oxygène autour du caillot obstructif. Nous avons ainsi comparé l'injection systémique du rtPA au rtPA chargé dans des MBs ciblantes aux mêmes doses. Dans cette étude, nous avons injecté le rtPA à une concentration au 1/10e du traitement habituellement utilisé chez les souris. Ce choix a été motivé par le but ultime de limiter les effets secondaires liés à la dose de rtPA injecté. Cette forte contrainte n'a pas empêché une résolution de caillot efficace grâce au ciblage spécifique des MBs fonctionnalisées. En effet, 1 mg/kg d'injection de rtPA chargé sur des MBs ciblantes, à réduit de plus de 50% la taille de la lésion ischémique en moyenne sur 16 animaux. Le chargement du médicament a aidé à protéger la protéine et le ciblage spécifique du caillot mène à l'amélioration du traitement. Ce résultat est d'autant plus prometteur que le traitement avec le rtPA libre à la même concentration n'a pas été significativement plus efficace que le contrôle négatif avec une solution saline. De plus, nous avons surveillé la perméabilité de la barrière hématoencéphalique, étant donné que les bulles sont à la taille du micron, en injectant de l'acide gadotérique (AG) par voie intraveineuse. La fuite de la barrière hématoencéphalique peut être observée avec l'acquisition IRM T1 sous forme de taches blanches autour des zones victimes d'infarctus. Néanmoins, ce test n'a montré aucun signe d'altération de la barrière hématoencéphalique en comparant tous les groupes. Dans l'ensemble, le traitement ciblé avec des MBs fonctionnalisées a été beaucoup plus efficace que le traitement de référence et aucune hémorragie collatérale ou fuite hématoencéphalique n'a été observée.

Les résidus de fluorescence des MBs peuvent être observés par un marquage à la rhodamine. Normalisé à la taille de l'organe, le comptage par fluorescence donne une évaluation qualitative de la biodistribution des MBs dans le corps. Comme prévu, la majorité de la fluorescence a été observée dans le foie, remplissant sa fonction de détoxification sanguine. De plus, certains résidus de MBs ont été observés dans les poumons très

probablement liés à l'échange gazeux en cours après la dégradation des MBs. Aucune fluorescence n'a été observée dans la vessie, la rate, les intestins ou les reins. Fait intéressant, la fluorescence spécifique dans la zone de l'AVC a été observée après 24 heures. Cela appuie la validation de la capacité de ciblage des MBs fonctionnalisées *in vivo* et apporte également de nouvelles perspectives sur l'expression des P-sélectines par l'endothélium activé après résolution du caillot, et donc des perspectives intéressantes pour le développement de l'imagerie moléculaire des pathologies vasculaires ischémiques.

Conclusion et perspectives

En conclusion, nous avons validé l'objectif de fournir un traitement ciblé et efficace pour les maladies thrombotiques avec une réduction de la dose thérapeutique et sans effets secondaires. En plus de leur capacité d'encapsulation, les MBs sont également utilisées comme rehausseurs de contraste pour l'imagerie US et leur comportement envers les ultrasons peut avoir des applications thérapeutiques. Bien que nous ayons exploré et validé l'échogénicité des MBs dans un modèle de flux, la translation *in vivo* pour la sonothrombolyse n'est pas encore efficace en termes de résolution de l'AVC. En conséquence, des études complémentaires vont être menées jusqu'à fin 2024 avec les US *in vivo* pour la sonothrombolyse et l'imagerie moléculaire. Enfin, l'amélioration de l'encapsulation des médicaments, la toxicologie réglementaire et l'optimisation du stockage à long terme seront des études essentielles à mettre en œuvre pour atteindre l'objectif final de la translation clinique.

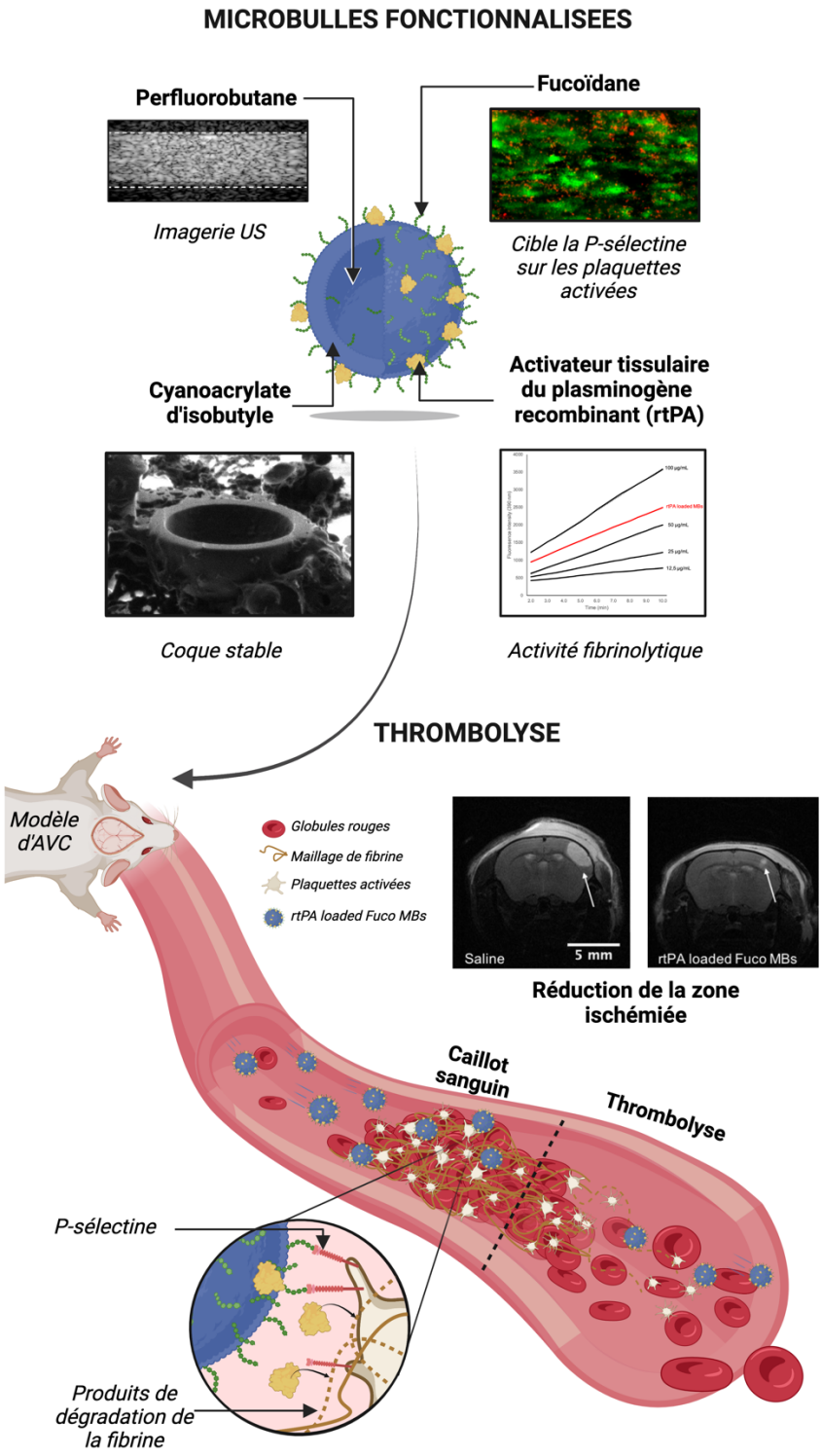

Figure 27 : Illustration résumée du projet. *Les MBs sont composées d'une enveloppe stable de poly(cyanoacrylate d'isobutyle) (PIBCA) avec un noyau gazeux de perfluorobutane (PFB) permettant l'imagerie ultrasonore. Leur fonctionnalisation a été validée pour le ciblage des P-sélectines avec le fucoïdane et pour l'activité thrombolytique avec chargement d'activateur tissulaire du plasminogène recombinant (rtPA). Après la validation in vitro, les MBs ciblantes chargées de rtPA ont été injectées dans un modèle d'AVC chez la souris pour améliorer la thrombolyse par rapport à l'injection systémique du médicament seul. Le ciblage par le fucoïdane sur les P-sélectines des plaquettes activées a permis une délivrance spécifique du rtPA permettant la dégradation locale de la fibrine. L'administration ciblée a ainsi amélioré l'issue du traitement en réduisant la zone de l'infarctus après 24h comme observé avec l'imagerie IRM.*

References

[1] World Health Organisation (WHO), "[Internet] World Health Organization. Media Centre: Cardiovascular disease," 2020. .

[2] E. J. Benjamin *et al.*, "Heart Disease and Stroke Statistics—2019 Update: A Report From the American Heart Association," *Circulation*, 2019, doi: 10.1161/CIR.0000000000000659.

[3] H. Thomas *et al.*, "Global Atlas of Cardiovascular Disease 2000-2016: The Path to Prevention and Control," *Glob. Heart*, vol. 13, no. 3, pp. 143–163, 2018, doi: 10.1016/j.gheart.2018.09.511.

[4] J. Leal, R. Luengo-Fernández, A. Gray, S. Petersen, and M. Rayner, "Economic burden of cardiovascular diseases in the enlarged European Union," *Eur. Heart J.*, vol. 27, no. 13, pp. 1610–1619, 2006, doi: 10.1093/eurheartj/ehi733.

[5] D. N. Granger and P. R. Kvietys, "Reperfusion injury and reactive oxygen species: The evolution of a concept," *Redox Biol.*, vol. 6, pp. 524–551, 2015, doi: 10.1016/j.redox.2015.08.020.

[6] C. K. Glass and J. L. Witztum, "Atherosclerosis: The Road Ahead," *Cell*, vol. 104, no. February, pp. 503–516, 2001, doi: 10.5005/jp/books/12883_4.

[7] E. Falk, "Pathogenesis of Atherosclerosis," *J. Am. Coll. Cardiol.*, vol. 47, no. 8 SUPPL., pp. 0–5, 2006, doi: 10.1016/j.jacc.2005.09.068.

[8] Y. S. Chatzizisis, A. U. Coskun, M. Jonas, E. R. Edelman, C. L. Feldman, and P. H. Stone, "Role of Endothelial Shear Stress in the Natural History of Coronary Atherosclerosis and Vascular Remodeling. Molecular, Cellular, and Vascular Behavior," *J. Am. Coll. Cardiol.*, vol. 49, no. 25, pp. 2379–2393, 2007, doi: 10.1016/j.jacc.2007.02.059.

[9] G. G. Caro, "Discovery of the role of wall shear in atherosclerosis," *Arterioscler. Thromb. Vasc. Biol.*, vol. 29, no. 2, pp. 158–161, 2009, doi: 10.1161/ATVBAHA.108.166736.

[10] J. Jongstra-Bilen, M. Haidari, S. N. Zhu, M. Chen, D. Guha, and M. I. Cybulsky, "Low-grade chronic inflammation in regions of the normal mouse arterial intima predisposed to atherosclerosis," *J. Exp. Med.*, vol. 203, no. 9, pp. 2073–2083, 2006, doi: 10.1084/jem.20060245.

[11] P. Libby, "Inflammation in atherosclerosis," *Nature*, vol. 420, no. December, pp. 868–

874, 2002, doi: 10.1038/nature01323.

[12] Z. S. Galis, G. K. Sukhova, R. Kranzhöfer, S. Clark, and P. Libby, "Macrophage foam cells from experimental atheroma constitutively produce matrix-degrading proteinases," *Proc. Natl. Acad. Sci. U. S. A.*, vol. 92, no. 2, pp. 402–406, 1995, doi: 10.1073/pnas.92.2.402.

[13] M. R. Dweck *et al.*, "Noninvasive Molecular Imaging of Disease Activity in Atherosclerosis," *Circ. Res.*, vol. 119, no. 2, pp. 330–340, 2016, doi: 10.1161/CIRCRESAHA.116.307971.

[14] A. Shioi and Y. Ikari, "Plaque calcification during atherosclerosis progression and regression," *J. Atheroscler. Thromb.*, vol. 25, no. 4, pp. 294–303, 2018, doi: 10.5551/jat.RV17020.

[15] G. Lippi, M. Franchini, and G. Targher, "Arterial thrombus formation in cardiovascular disease," *Nat. Rev. Cardiol.*, vol. 8, no. 9, pp. 502–512, 2011, doi: 10.1038/nrcardio.2011.91.

[16] N. Mackman, "Triggers, targets and treatments for thrombosis," *Nature*, vol. 451, no. 7181. Nature Publishing Group, pp. 914–918, Feb-2008, doi: 10.1038/nature06797.

[17] I. Martinelli, P. Bucciarelli, and P. M. Mannucci, "Thrombotic risk factors: Basic pathophysiology," *Crit. Care Med.*, vol. 38, no. SUPPL. 2, 2010, doi: 10.1097/CCM.0b013e3181c9cbd9.

[18] C. T. Esmon, "Basic mechanisms and pathogenesis of venous thrombosis," *Blood Rev.*, vol. 23, no. 5, pp. 225–229, 2009, doi: 10.1016/j.blre.2009.07.002.

[19] J. A. López and J. Chen, "Pathophysiology of venous thrombosis," *Thromb. Res.*, vol. 123, no. SUPPL. 4, pp. 30–34, 2009, doi: 10.1016/S0049-3848(09)70140-9.

[20] D. D. Monie and E. P. DeLoughery, "Pathogenesis of thrombosis: Cellular and pharmacogenetic contributions," *Cardiovasc. Diagn. Ther.*, vol. 7, no. Suppl 3, pp. S291–S298, 2017, doi: 10.21037/cdt.2017.09.11.

[21] A. Bivard, L. Lin, and M. W. Parsonsb, "Review of Stroke Thrombolytics," *J. Stroke*, vol. 15, no. 2, p. 90, 2013, doi: 10.5853/jos.2013.15.2.90.

[22] C. Kluft, J. J. Sidelmann, and J. B. Gram, "Assessing Safety of Thrombolytic Therapy," *Semin. Thromb. Hemost.*, vol. 43, no. 3, pp. 300–310, 2017, doi: 10.1055/s-0036-1584130.

[23] R. S. Marshall, "Progress in intravenous thrombolytic therapy for acute stroke," *JAMA Neurology*, vol. 72, no. 8. American Medical Association, pp. 928–934, Aug-2015, doi: 10.1001/jamaneurol.2015.0835.

[24] V. J. Marder, “Thrombolytic Therapy,” in *Consultative Hemostasis and Thrombosis*, Elsevier, 2013, pp. 526–537.

[25] J. Schaller and S. S. Gerber, “The plasmin-antiplasmin system: structural and functional aspects,” *Cell. Mol. Life Sci.*, vol. 68, pp. 785–801, 2011, doi: 10.1007/s00018-010-0566-5.

[26] G. N. Levine *et al.*, “2015 ACC/AHA/SCAI Focused Update on Primary Percutaneous Coronary Intervention for Patients with ST-Elevation Myocardial Infarction An Update of the 2011 ACCF/AHA/SCAI Guideline for Percutaneous Coronary Intervention and the 2013 ACCF/AHA Guideline for th,” *J. Am. Coll. Cardiol.*, vol. 67, no. 10, pp. 1235–1250, 2016, doi: 10.1016/j.jacc.2015.10.005.

[27] B. Ibanez *et al.*, “2017 ESC Guidelines for the management of acute myocardial infarction in patients presenting with ST-segment elevation,” *Eur. Heart J.*, vol. 39, no. 2, pp. 119–177, 2018, doi: 10.1093/eurheartj/ehx393.

[28] G. Turc *et al.*, “European Stroke Organisation (ESO) – European Society for Minimally Invasive Neurological Therapy (ESMINT) Guidelines on Mechanical Thrombectomy in Acute Ischaemic StrokeEndorsed by Stroke Alliance for Europe (SAFE),” *Eur. Stroke J.*, vol. 4, no. 1, pp. 6–12, 2019, doi: 10.1177/2396987319832140.

[29] W. J. Powers *et al.*, “Guidelines for the Early Management of Patients With Acute Ischemic Stroke: 2019 Update to the 2018 Guidelines for the Early Management of Acute Ischemic Stroke: A Guideline for Healthcare Professionals From the American Heart Association/American Stroke ,” *Stroke*, vol. 50, no. 12, pp. e344–e418, 2019, doi: 10.1161/STR.0000000000000211.

[30] L. Derex and T. H. Cho, “Mechanical thrombectomy in acute ischemic stroke,” *Rev. Neurol. (Paris).*, vol. 173, no. 3, pp. 106–113, 2017, doi: 10.1016/j.neurol.2016.06.008.

[31] S. A. Munich, K. Vakharia, and E. I. Levy, “Overview of Mechanical Thrombectomy Techniques,” *Clin. Neurosurg.*, vol. 85, no. 1, pp. S60–S67, 2019, doi: 10.1093/neuros/nyz071.

[32] G. Forestier *et al.*, “Mechanical thrombectomy practices in France: exhaustive survey of centers and individual operators,” *J. Neuroradiol.*, pp. 1–14, 2020, doi: 10.1016/j.neurad.2020.05.001.

[33] S. Vrignaud, J. P. Benoit, and P. Saulnier, “Strategies for the nanoencapsulation of hydrophilic molecules in polymer-based nanoparticles,” *Biomaterials*, vol. 32, no. 33, pp. 8593–8604, 2011, doi: 10.1016/j.biomaterials.2011.07.057.

[34] M. Di Marco *et al.*, “Overview of the main methods used to combine proteins with

nanosystems : absorption, bioconjugation, and encapsulation," *Int. J. Nanomedicine*, vol. 5, pp. 37–49, 2010.

[35] R. P. Friedrich *et al.*, "Tissue Plasminogen Activator Binding to Superparamagnetic Iron Oxide Nanoparticle-Covalent Versus Adsorptive Approach," *Nanoscale Res. Lett.*, vol. 11, no. 1, pp. 1–11, 2016, doi: 10.1186/s11671-016-1521-7.

[36] L. Arnfast, C. G. Madsen, L. Jorgensen, and S. Baldursdottir, "Design and processing of nanogels as delivery systems for peptides and proteins," *Ther. Deliv.*, vol. 5, no. 6, pp. 691–708, 2014, doi: 10.4155/tde.14.38.

[37] J. Matuszak *et al.*, "Comparative analysis of nanosystems' effects on human endothelial and monocytic cell functions," *Nanotoxicology*, vol. 12, no. 9, pp. 957–974, 2018, doi: 10.1080/17435390.2018.1502375.

[38] T. Wu and M. Tang, "Review of the effects of manufactured nanoparticles on mammalian target organs," *J. Appl. Toxicol.*, vol. 38, no. 1, pp. 25–40, 2018, doi: 10.1002/jat.3499.

[39] I. Cicha *et al.*, "From design to the clinic: Practical guidelines for translating cardiovascular nanomedicine," *Cardiovasc. Res.*, vol. 114, no. 13, pp. 1714–1727, 2018, doi: 10.1093/cvr/cvy219.

[40] E. Blanco, H. Shen, and M. Ferrari, "Principles of nanoparticle design for overcoming biological barriers to drug delivery," *Nat. Biotechnol.*, vol. 33, no. 9, pp. 941–951, 2015, doi: 10.1038/nbt.3330.

[41] A. C. Anselmo and S. Mitragotri, "Nanoparticles in the clinic," *Bioeng. Transl. Med.*, vol. 1, no. 1, pp. 10–29, 2016, doi: 10.1002/btm2.10003.

[42] A. C. Anselmo and S. Mitragotri, "Nanoparticles in the clinic: An update," *Bioeng. Transl. Med.*, vol. 4, no. 3, pp. 1–16, 2019, doi: 10.1002/btm2.10143.

[43] V. Karagkiozaki, S. Logothetidis, and A. M. Pappa, "Nanomedicine for atherosclerosis: Molecular imaging and treatment," *J. Biomed. Nanotechnol.*, vol. 11, no. 2, pp. 191–210, 2015, doi: 10.1166/jbn.2015.1943.

[44] C. Chauvierre *et al.*, "Pharmaceutical development and safety evaluation of a GMP-grade fucoidan for molecular diagnosis of cardiovascular diseases," *Mar. Drugs*, vol. 17, no. 12, 2019, doi: 10.3390/md17120699.

[45] K. H. Zheng *et al.*, "99Mtc-Fucoidan As Diagnostic Agent For P-Selectin Imaging: First-In-Human Evaluation (Phase I)," *Atherosclerosis*, vol. 287, no. 2019, p. e143, 2019, doi: 10.1016/j.atherosclerosis.2019.06.425.

[46] R. Gramiak and M. P. Shah, "Echocardiography of the Aortic." .

[47] J. Steinman, M. M. Koletar, B. Stefanovic, and J. G. Sled, "3D morphological analysis of the mouse cerebral vasculature: Comparison of in vivo and ex vivo methods," *PLoS One*, vol. 12, no. 10, pp. 1–17, 2017, doi: 10.1371/journal.pone.0186676.

[48] M. Diez-Silva, M. Dao, J. Han, C. T. Lim, and S. Suresh, "Shape and biomechanics characteristics of human red blood cells in health and disease," *MRS Bull.*, vol. 35, no. 5, pp. 382–388, 2010, doi: 10.1557/mrs2010.571.

[49] C. I. Ezekiel, A. M. Bapolisi, R. B. Walker, and R. W. M. Krause, "Ultrasound-triggered release of 5-fluorouracil from soy lecithin echogenic liposomes," *Pharmaceutics*, vol. 13, no. 6, pp. 1–14, 2021, doi: 10.3390/pharmaceutics13060821.

[50] A. Upadhyay and S. V. Dalvi, "Microbubble Formulations: Synthesis, Stability, Modeling and Biomedical Applications," *Ultrasound Med. Biol.*, vol. 45, no. 2, pp. 301–343, 2019, doi: 10.1016/j.ultrasmedbio.2018.09.022.

[51] T. D. Reusser, K. H. Song, D. Ramirez, R. K. P. Benninger, V. Papadopoulou, and M. A. Borden, "Phospholipid oxygen microbubbles for image-guided therapy," *Nanotheranostics*, vol. 4, no. 2, pp. 83–90, 2020, doi: 10.7150/ntno.43808.

[52] D. Liu *et al.*, "Sinapultide-loaded lipid microbubbles and the stabilization effect of sinapultide on the shells of lipid microbubbles," *J. Mater. Chem. B*, vol. 6, no. 9, pp. 1335–1341, 2018, doi: 10.1039/c7tb02799k.

[53] K. W. Pulsipher, D. A. Hammer, D. Lee, and C. M. Sehgal, "Engineering Theranostic Microbubbles Using Microfluidics for Ultrasound Imaging and Therapy: A Review," *Ultrasound Med. Biol.*, vol. 44, no. 12, pp. 2441–2460, 2018, doi: 10.1016/j.ultrasmedbio.2018.07.026.

[54] A. J. Dixon, J. Li, J. M. R. Rickel, A. L. Klibanov, Z. Zuo, and J. A. Hossack, "Efficacy of Sonothrombolysis Using Microbubbles Produced by a Catheter-Based Microfluidic Device in a Rat Model of Ischemic Stroke," *Ann. Biomed. Eng.*, 2019, doi: 10.1007/s10439-019-02209-0.

[55] D. Carugo, R. J. Browning, I. Iranmanesh, W. Messaoudi, P. Rademeyer, and E. Stride, "Scaleable production of microbubbles using an ultrasound-modulated microfluidic device," *J. Acoust. Soc. Am.*, vol. 150, no. 2, pp. 1577–1589, 2021, doi: 10.1121/10.0005911.

[56] B. Li *et al.*, "Functionalized polymer microbubbles as new molecular ultrasound contrast agent to target P-selectin in thrombus," *Biomaterials*, vol. 194, no. 2019, pp. 139–150, 2019, doi: 10.1016/j.biomaterials.2018.12.023.

[57] A. H. Liao, H. C. Ho, Y. C. Lin, H. K. Chen, and C. H. Wang, "Effects of microbubble

size on ultrasound-induced transdermal delivery of high-molecular-weight drugs," *PLoS One*, vol. 10, no. 9, pp. 1–14, 2015, doi: 10.1371/journal.pone.0138500.

[58] E. Stride *et al.*, "Microbubble Agents: New Directions," *Ultrasound Med. Biol.*, vol. 00, no. 00, 2020, doi: 10.1016/j.ultrasmedbio.2020.01.027.

[59] U. Farook, E. Stride, and M. J. Edirisinghe, "Preparation of suspensions of phospholipid-coated microbubbles by coaxial electrohydrodynamic atomization," *J. R. Soc. Interface*, vol. 6, no. 32, pp. 271–277, 2009, doi: 10.1098/rsif.2008.0225.

[60] S. A. Reisner *et al.*, "Myocardial perfusion imaging by contrast echocardiography with use of intracoronary sonicated albumin in humans," *J. Am. Coll. Cardiol.*, vol. 14, no. 3, pp. 660–665, 1989, doi: 10.1016/0735-1097(89)90107-1.

[61] S. L. Lin *et al.*, "Left ventricular opacification after peripheral venous injection of a modified albumin solution," *Int. J. Card. Imaging*, vol. 8, no. 1, pp. 53–61, 1992, doi: 10.1007/BF01137566.

[62] S. Chen, Z. Wang, Y. T. Zhou, and P. A. Grayburn, "Optimization of the size distribution and myocardial contrast effect of perfluorocarbon-filled albumin microbubbles by lyophilization under continuous negative pressure," *J. Am. Soc. Echocardiogr.*, vol. 13, no. 8, pp. 748–753, 2000, doi: 10.1067/mje.2000.104644.

[63] A. L. Klibanov, "Ultrasound Contrast: Gas Microbubbles in the Vasculature," *Invest. Radiol.*, vol. 56, no. 1, pp. 50–61, 2021, doi: 10.1097/RLI.0000000000000733.

[64] K. Ferrara, R. Pollard, and M. Borden, "Ultrasound microbubble contrast agents: Fundamentals and application to gene and drug delivery," *Annu. Rev. Biomed. Eng.*, vol. 9, pp. 415–447, 2007, doi: 10.1146/annurev.bioeng.8.061505.095852.

[65] P. van Hoogevest and A. Wendel, "The use of natural and synthetic phospholipids as pharmaceutical excipients," *Eur. J. Lipid Sci. Technol.*, vol. 116, no. 9, pp. 1088–1107, 2014, doi: 10.1002/ejlt.201400219.

[66] S. Al-Jawadi and S. S. Thakur, "Ultrasound-responsive lipid microbubbles for drug delivery: A review of preparation techniques to optimise formulation size, stability and drug loading," *Int. J. Pharm.*, vol. 585, p. 119559, 2020, doi: 10.1016/j.ijpharm.2020.119559.

[67] J. Jägers, A. Wrobeln, and K. B. Ferenz, "Perfluorocarbon-based oxygen carriers: from physics to physiology," *Pflugers Arch. Eur. J. Physiol.*, vol. 473, no. 2, pp. 139–150, 2021, doi: 10.1007/s00424-020-02482-2.

[68] T. J. Wooster, M. Golding, and P. Sanguansri, "Impact of oil type on nanoemulsion formation and ostwald ripening stability," *Langmuir*, vol. 24, no. 22, pp. 12758–12765,

2008, doi: 10.1021/la801685v.

[69] Y. Iida *et al.*, "Bubble population phenomena in sonochemical reactor: II. Estimation of bubble size distribution and its number density by simple coalescence model calculation," *Ultrason. Sonochem.*, vol. 17, no. 2, pp. 480–486, 2010, doi: 10.1016/j.ultsonch.2009.08.017.

[70] T. Segers, A. Lassus, P. Bussat, E. Gaud, and P. Frinking, "Improved coalescence stability of monodisperse phospholipid-coated microbubbles formed by flow-focusing at elevated temperatures," *Lab Chip*, vol. 19, no. 1, pp. 158–167, 2019, doi: 10.1039/c8lc00886h.

[71] S. Sridhar, A. Patel, and S. V. Dalvi, "Estimation of Storage Stability of Aqueous Microbubble Suspensions," *Colloids Surfaces A Physicochem. Eng. Asp.*, vol. 489, pp. 182–190, Jan. 2016, doi: 10.1016/J.COLSURFA.2015.10.044.

[72] R. H. Abou-Saleh *et al.*, "Molecular Effects of Glycerol on Lipid Monolayers at the Gas-Liquid Interface: Impact on Microbubble Physical and Mechanical Properties," *Langmuir*, vol. 35, no. 31, pp. 10097–10105, 2019, doi: 10.1021/acs.langmuir.8b04130.

[73] A. J. Singer, J. V. Quinn, and J. E. Hollander, "The cyanoacrylate topical skin adhesives," *Am. J. Emerg. Med.*, vol. 26, no. 4, pp. 490–496, 2008, doi: 10.1016/j.ajem.2007.05.015.

[74] D. García Cerdá, A. M. Ballester, A. Aliena-Valero, A. Carabén-Redaño, and J. M. Lloris, "Use of cyanoacrylate adhesives in general surgery," *Surg. Today*, vol. 45, no. 8, pp. 939–956, 2015, doi: 10.1007/s00595-014-1056-4.

[75] H. S. Cho, Y. Kim, J. Lee, K. S. Yi, and C. H. Choi, "Use of N-butyl cyanoacrylate in the successful transcatheter arterial embolization of an arteriovenous fistula caused by blunt pelvic fracture: A case report and review of literature," *Medicine (Baltimore).*, vol. 100, no. 1, p. e24215, 2021, doi: 10.1097/MD.0000000000024215.

[76] S. R. Sirsi and M. A. Borden, "Microbubble compositions, properties and biomedical applications," *Bubble Sci. Eng. Technol.*, vol. 1, no. 1–2, pp. 3–17, 2009, doi: 10.1179/175889709X446507.

[77] M. Liu *et al.*, "Drug Loading in Poly (butyl cyanoacrylate) -based Polymeric Microbubbles," 2020, doi: 10.1021/acs.molpharmaceut.0c00242.

[78] P. Koczera, L. Appold, Y. Shi, M. Liu, and A. Dasgupta, "PBCA-based Polymeric Microbubbles for Molecular Imaging and Drug Delivery," pp. 128–135, 2017, doi: 10.1016/j.jconrel.2017.03.006.PBCA-based.

[79] O. Chevallier *et al.*, "Efficacy, safety and outcomes of transcatheter arterial embolization

with N-butyl cyanoacrylate glue for non-variceal gastrointestinal bleeding: A systematic review and meta-analysis," *Diagn. Interv. Imaging*, vol. 102, no. 7–8, pp. 479–487, 2021, doi: 10.1016/j.diii.2021.03.004.

[80] N. J. Butcher, G. M. Mortimer, and R. F. Minchin, "Drug delivery: Unravelling the stealth effect," *Nat. Nanotechnol.*, vol. 11, no. 4, pp. 310–311, 2016, doi: 10.1038/nnano.2016.6.

[81] S. M. Fix, G. A. Nyankima, M. D. McSweeney, J. K. Tsuruta, S. K. Lai, and P. A. Dayton, "Accelerated clearance of ultrasound contrast agents containing polyethylene glycol is associated with the generation of anti- polyethylene glycol antibodies," *Ultrasound Med. Biol.*, vol. 176, no. 1, pp. 139–148, 2016, doi: 10.1016/j.ultrasmedbio.2018.02.006.Accelerated.

[82] J. Yang *et al.*, "Microbubble Functionalization with Platelet Membrane Enables Targeting and Early Detection of Sepsis-Induced Acute Kidney Injury," *Adv. Healthc. Mater.*, vol. 10, no. 23, pp. 1–14, 2021, doi: 10.1002/adhm.202101628.

[83] H. Wang *et al.*, "Platelet-membrane-biomimetic nanoparticles for targeted antitumor drug delivery," *J. Nanobiotechnology*, vol. 17, no. 1, pp. 1–16, 2019, doi: 10.1186/s12951-019-0494-y.

[84] Z. Fang, J. Fang, C. Gao, R. Gao, P. Lin, and W. Yu, "Recent trends in platelet membrane-cloaked nanoparticles for application of inflammatory diseases," *Drug Deliv.*, vol. 29, no. 1, pp. 2805–2814, 2022, doi: 10.1080/10717544.2022.2117434.

[85] A. Zenych, L. Fournier, and C. Chauvierre, "Nanomedicine progress in thrombolytic therapy," *Biomaterials*, vol. 258, no. January, 2020, doi: 10.1016/j.biomaterials.2020.120297.

[86] J. S. M. Yeh *et al.*, "A targeting microbubble for ultrasound molecular imaging," *PLoS One*, vol. 10, no. 7, pp. 1–23, 2015, doi: 10.1371/journal.pone.0129681.

[87] J. M. Warram, A. G. Sorace, R. Saini, H. R. Umphrey, K. R. Zinn, and K. Hoyt, "A triple-targeted ultrasound contrast agent provides improved localization to tumor vasculature," *J. Ultrasound Med.*, vol. 30, no. 7, pp. 921–931, 2011, doi: 10.7863/jum.2011.30.7.921.

[88] B. Wu *et al.*, "Preparation of novel targeting nanobubbles conjugated with small interfering RNA for concurrent molecular imaging and gene therapy in vivo.," *FASEB J.*, p. fj201900716RR, 2019, doi: 10.1096/fj.201900716RR.

[89] K. Yumura *et al.*, "Mutations for decreasing the immunogenicity and maintaining the function of core streptavidin," *Protein Sci.*, vol. 22, no. 2, pp. 213–221, 2013, doi:

10.1002/pro.2203.

[90] F. Petronzelli *et al.*, "Therapeutic use of avidin is not hampered by antiavidin antibodies in humans," *Cancer Biother. Radiopharm.*, vol. 25, no. 5, pp. 563–570, 2010, doi: 10.1089/cbr.2010.0797.

[91] S. Fokong *et al.*, "Image-guided, targeted and triggered drug delivery to tumors using polymer-based microbubbles," *J. Control. Release*, vol. 163, no. 1, pp. 75–81, 2012, doi: 10.1016/j.jconrel.2012.05.007.

[92] K. Renault, J. W. Fredy, P. Y. Renard, and C. Sabot, "Covalent Modification of Biomolecules through Maleimide-Based Labeling Strategies," *Bioconjug. Chem.*, vol. 29, no. 8, pp. 2497–2513, 2018, doi: 10.1021/acs.bioconjchem.8b00252.

[93] M. Lahnsteiner, A. Kastner, J. Mayr, A. Roller, B. K. Keppler, and C. R. Kowol, "Improving the Stability of Maleimide–Thiol Conjugation for Drug Targeting," *Chem. - A Eur. J.*, vol. 26, no. 68, pp. 15867–15870, 2020, doi: 10.1002/chem.202003951.

[94] N. J. de Mol and M. J. E. Fischer, "Amine Coupling Through EDC/NHS: A Practical Approach," *Life Sci.*, p. 255, 2010, doi: 10.1007/978-1-60761-670-2.

[95] Y. Zhang, J. L. Xu, Z. H. Yuan, W. Qi, Y. Y. Liu, and M. C. He, "Artificial intelligence techniques to optimize the EDC/NHS-mediated immobilization of cellulase on Eudragit L-100," *Int. J. Mol. Sci.*, vol. 13, no. 7, pp. 7952–7962, 2012, doi: 10.3390/ijms13077952.

[96] X. Liu *et al.*, "Fast functionalization of ultrasound microbubbles using strain promoted click chemistry," *Biomater. Sci.*, vol. 6, no. 3, pp. 623–632, 2018, doi: 10.1039/c8bm00004b.

[97] S. Manta *et al.*, "Characterization of Positively Charged Lipid Shell Microbubbles with Tunable Resistive Pulse Sensing (TRPS) Method: A Technical Note," *Ultrasound Med. Biol.*, vol. 42, no. 2, pp. 624–630, 2016, doi: 10.1016/j.ultrasmedbio.2015.10.010.

[98] C. M. Panje *et al.*, "Ultrasound-mediated gene delivery with cationic versus neutral microbubbles: Effect of DNA and microbubble dose on In Vivo transfection efficiency," *Theranostics*, vol. 2, no. 11, pp. 1078–1091, 2012, doi: 10.7150/thno.4240.

[99] S. R. Sirsi, C. Fung, S. Garg, M. Y. Tianning, P. A. Mountford, and M. A. Borden, "Lung surfactant microbubbles increase lipophilic drug payload for ultrasound-targeted delivery," *Theranostics*, vol. 3, no. 6, pp. 409–419, 2013, doi: 10.7150/thno.5616.

[100] E. Stride, "The influence of surface adsorption on microbubble dynamics," *Philos. Trans. R. Soc. A Math. Phys. Eng. Sci.*, vol. 366, no. 1873, pp. 2103–2115, 2008, doi: 10.1098/rsta.2008.0001.

[101] A. Agarwal, W. J. Ng, and Y. Liu, "Principle and applications of microbubble and nanobubble technology for water treatment," *Chemosphere*, vol. 84, no. 9, pp. 1175–1180, 2011, doi: 10.1016/j.chemosphere.2011.05.054.

[102] D. Omata *et al.*, "Effects of encapsulated gas on stability of lipid-based microbubbles and ultrasound-triggered drug delivery," *J. Control. Release*, vol. 311–312, no. August, pp. 65–73, 2019, doi: 10.1016/j.jconrel.2019.08.023.

[103] R. Battino, "The Ostwald coefficient of gas solubility," *Fluid Phase Equilib.*, vol. 15, no. 3, pp. 231–240, 1984, doi: 10.1016/0378-3812(84)87009-0.

[104] A. Kabalnov, D. Klein, T. Pelura, E. Schutt, and J. Weers, "Dissolution of multicomponent microbubbles in the bloodstream: 1. Theory," *Ultrasound Med. Biol.*, vol. 24, no. 5, pp. 739–749, 1998, doi: 10.1016/S0301-5629(98)00034-9.

[105] A. Kabalnov *et al.*, "Dissolution of multicomponent microbubbles in the bloodstream: 2. Experiment," *Ultrasound Med. Biol.*, vol. 24, no. 5, pp. 751–760, 1998, doi: 10.1016/S0301-5629(98)00033-7.

[106] N. De Jong, A. Bouakaz, and P. Frinking, "Basic acoustic properties of microbubbles," *Echocardiography*, vol. 19, no. 3, pp. 229–240, 2002, doi: 10.1046/j.1540-8175.2002.00229.x.

[107] D. B. Khismatullin, "Resonance frequency of microbubbles: Effect of viscosity," *J. Acoust. Soc. Am.*, vol. 116, no. 3, pp. 1463–1473, 2004, doi: 10.1121/1.1778835.

[108] T. Segers and M. Versluis, "Acoustic bubble sorting for ultrasound contrast agent enrichment," *Lab Chip*, vol. 14, no. 10, pp. 1705–1714, 2014, doi: 10.1039/c3lc51296g.

[109] T. Segers, N. de Jong, and M. Versluis, "Uniform scattering and attenuation of acoustically sorted ultrasound contrast agents: Modeling and experiments," *J. Acoust. Soc. Am.*, vol. 140, no. 4, pp. 2506–2517, 2016, doi: 10.1121/1.4964270.

[110] D. I. Nikitichev, A. Barburas, K. McPherson, J. M. Mari, S. J. West, and A. E. Desjardins, "Construction of 3-dimensional printed ultrasound phantoms with wall-less vessels," *J. Ultrasound Med.*, vol. 35, no. 6, pp. 1333–1339, 2016, doi: 10.7863/ultra.15.06012.

[111] O. Couture, S. Bannouf, G. Montaldo, J. F. Aubry, M. Fink, and M. Tanter, "Ultrafast Imaging of Ultrasound Contrast Agents," *Ultrasound Med. Biol.*, vol. 35, no. 11, pp. 1908–1916, 2009, doi: 10.1016/j.ultrasmedbio.2009.05.020.

[112] R. H. Abou-Saleh, M. Swain, S. D. Evans, and N. H. Thomson, "Poly(ethylene glycol) lipid-shelled microbubbles: Abundance, stability, and mechanical properties," *Langmuir*, vol. 30, no. 19, pp. 5557–5563, 2014, doi: 10.1021/la404804u.

[113] X. Chu *et al.*, "Mechanical Properties of Sub-Microbubbles with a Nanoparticle-Decorated Polymer Shell," *Langmuir*, vol. 35, no. 52, pp. 17090–17095, 2019, doi: 10.1021/acs.langmuir.9b02930.

[114] E. Glynos, V. Sboros, and V. Koutsos, "Polymeric thin shells: Measurement of elastic properties at the nanometer scale using atomic force microscopy," *Mater. Sci. Eng. B Solid-State Mater. Adv. Technol.*, vol. 165, no. 3, pp. 231–234, 2009, doi: 10.1016/j.mseb.2009.06.016.

[115] R. H. Abou-Saleh, S. A. Peyman, K. Critchley, S. D. Evans, and N. H. Thomson, "Nanomechanics of lipid encapsulated microbubbles with functional coatings," *Langmuir*, vol. 29, no. 12, pp. 4096–4103, 2013, doi: 10.1021/la304093t.

[116] W. Wiedemair, Z. Tukovic, H. Jasak, D. Poulikakos, and V. Kurtcuoglu, "The breakup of intravascular microbubbles and its impact on the endothelium," *Biomech. Model. Mechanobiol.*, vol. 16, no. 2, pp. 611–624, 2017, doi: 10.1007/s10237-016-0840-z.

[117] J. H. Wible, J. K. Wojdyla, G. L. Bales, W. N. McMullen, E. A. Geiser, and D. D. Buss, "Inhaled gases affect the ultrasound contrast produced by Albunex in anesthetized dogs.," *J. Am. Soc. Echocardiogr.*, vol. 9, no. 4, pp. 442–451, 1996, doi: 10.1016/S0894-7317(96)90115-7.

[118] R. B. Birge *et al.*, "Phosphatidylserine is a global immunosuppressive signal in efferocytosis, infectious disease, and cancer," *Cell Death Differ.*, vol. 23, no. 6, pp. 962–978, 2016, doi: 10.1038/cdd.2016.11.

[119] R. Watanabe, M. Matsumura, T. Munemasa, M. Fujimaki, and M. Suematsu, "Mechanism of hepatic parenchyma-specific contrast of microbubble-based contrast agent for ultrasonography: Microscopic studies in rat liver," *Invest. Radiol.*, vol. 42, no. 9, pp. 643–651, 2007, doi: 10.1097/RLI.0b013e31805f2682.

[120] K. T. Warzecha *et al.*, "Targeting and Modulation of Liver Myeloid Immune Cells by Hard-Shell Microbubbles," *Adv. Biosyst.*, vol. 2, no. 5, pp. 1–11, 2018, doi: 10.1002/adbi.201800002.

[121] Y. C. Park *et al.*, "Microvessels-on-a-chip to assess targeted ultrasound-assisted drug delivery," *ACS Appl. Mater. Interfaces*, vol. 8, no. 46, pp. 31541–31549, 2016, doi: 10.1021/acsami.6b09071.

[122] A. Presset *et al.*, "Endothelial Cells, First Target of Drug Delivery Using Microbubble-Assisted Ultrasound," *Ultrasound Med. Biol.*, vol. 46, no. 7, pp. 1565–1583, 2020, doi: 10.1016/j.ultrasmedbio.2020.03.013.

[123] N. Malik *et al.*, "Air embolism: Diagnosis and management," *Future Cardiol.*, vol. 13,

no. 4, pp. 365–378, 2017, doi: 10.2217/fca-2017-0015.

[124] K. Seitz and D. Strobel, "A Milestone: Approval of CEUS for Diagnostic Liver Imaging in Adults and Children in the USA," *Ultraschall der Medizin*, vol. 37, no. 3, pp. 229–232, 2016, doi: 10.1055/s-0042-107411.

[125] J. D. Berry and P. S. Sidhu, "Microbubble ultrasound contrast agents," in *Clinical Doppler Ultrasound*, 2006, pp. 337–355.

[126] J. M. Hyvelin *et al.*, "Use of ultrasound contrast agent microbubbles in preclinical research : Recommendations for small animal imaging," *Invest. Radiol.*, vol. 48, no. 8, pp. 570–583, 2013, doi: 10.1097/RLI.0b013e318289f854.

[127] S. Pochon *et al.*, "BR55: A lipopeptide-based VEGFR2-targeted ultrasound contrast agent for molecular imaging of angiogenesis," *Invest. Radiol.*, vol. 45, no. 2, pp. 89–95, 2010, doi: 10.1097/RLI.0b013e3181c5927c.

[128] M. Smeenge *et al.*, "First-in-human ultrasound molecular imaging with a VEGFR2-specific ultrasound molecular contrast agent (BR55) in prostate cancer a safety and feasibility pilot study," *Invest. Radiol.*, vol. 52, no. 7, pp. 419–427, 2017, doi: 10.1097/RLI.0000000000000362.

[129] J. K. Willmann *et al.*, "Ultrasound molecular imaging with BR55 in patients with breast & ovarian lesions: First-in-human results," *J. Clin. Oncol.*, vol. 35, no. 19, pp. 2133–2140, 2017, doi: 10.1200/JCO.2016.70.8594.

[130] S. Wang, J. A. Hossack, and A. L. Klibanov, "Targeting of microbubbles: contrast agents for ultrasound molecular imaging," *J. Drug Target.*, vol. 26, no. 5–6, pp. 420–434, 2018, doi: 10.1080/1061186X.2017.1419362.

[131] O. Schober, F. Kiessling, J. Debus, Debus, and J. Debus, *Molecular Imaging in Oncology*, vol. 216. 2020.

[132] A. Rix, A. Curaj, E. Liehn, and F. Kiessling, "Ultrasound Microbubbles for Diagnosis and Treatment of Cardiovascular Diseases," *Semin. Thromb. Hemost.*, 2019, doi: 10.1055/s-0039-1688492.

[133] V. S. Lucas, R. S. Burk, S. Creehan, and M. J. Grap, "Utility of High-Frequency Ultrasound: Moving Beyond the Surface to Detect Changes in Skin Integrity," *Plast Surg Nurs.*, vol. 23, no. 1, pp. 1–7, 2014, doi: 10.1097/PSN.0000000000000031.Utility.

[134] Y. Yong *et al.*, "Diagnostic accuracy and cost-effectiveness of contrast echocardiography on evaluation of cardiac function in technically very difficult patients in the intensive care unit," *Am. J. Cardiol.*, vol. 89, no. 6, pp. 711–718, 2002, doi: 10.1016/S0002-9149(01)02344-X.

[135] A. J. Sojahrood *et al.*, *Nonlinear dynamics of acoustic bubbles excited by their pressure-dependent subharmonic resonance frequency: influence of the pressure amplitude, frequency, encapsulation and multiple bubble interactions on oversaturation and enhancement of the subharmonic*, vol. 103, no. 1. 2021.

[136] H. Haghi and M. C. Kolios, "The role of primary and secondary delays in the effective resonance frequency of acoustically interacting microbubbles," *Ultrason. Sonochem.*, vol. 86, no. April, p. 106033, 2022, doi: 10.1016/j.ultsonch.2022.106033.

[137] G. Chabouh, B. Dollet, C. Quilliet, and G. Coupier, "Spherical oscillations of encapsulated microbubbles: Effect of shell compressibility and anisotropy," *J. Acoust. Soc. Am.*, vol. 149, no. 2, pp. 1240–1257, 2021, doi: 10.1121/10.0003500.

[138] P. Martinez, N. Bottenus, and M. Borden, "Cavitation Characterization of Size-Isolated Microbubbles in a Vessel Phantom Using Focused Ultrasound," *Pharmaceutics*, vol. 14, no. 9, 2022, doi: 10.3390/pharmaceutics14091925.

[139] K. Kooiman *et al.*, "Ultrasound-Responsive Cavitation Nuclei for Therapy and Drug Delivery," *Ultrasound Med. Biol.*, vol. 00, no. 00, 2020, doi: 10.1016/j.ultrasmedbio.2020.01.002.

[140] R. G. Holt and R. A. Roy, "Measurements of bubble-enhanced heating from focused, MHz-frequency ultrasound in a tissue-mimicking material," *Ultrasound Med. Biol.*, vol. 27, no. 10, pp. 1399–1412, 2001, doi: 10.1016/S0301-5629(01)00438-0.

[141] S. Wang *et al.*, "Accelerating thrombolysis using a precision and clot-penetrating drug delivery strategy by nanoparticle-shelled microbubbles," *Sci. Adv.*, vol. 6, no. 31, 2020, doi: 10.1126/sciadv.aaz8204.

[142] H. Yu and S. Chen, "A model to calculate microstreaming-shear stress generated by oscillating microbubbles on the cell membrane in sonoporation," *Biomed. Mater. Eng.*, vol. 24, no. 1, pp. 861–868, 2014, doi: 10.3233/BME-130878.

[143] Y. H. Chuang, P. W. Cheng, and P. C. Li, "Combining radiation force with cavitation for enhanced sonothrombolysis," *IEEE Trans. Ultrason. Ferroelectr. Freq. Control*, vol. 60, no. 1, pp. 97–104, 2013, doi: 10.1109/TUFFC.2013.2541.

[144] P. A. Dayton, K. E. Morgan, A. L. Klibanov, G. Brandenburger, K. R. Nightingale, and K. W. Ferrara, "A preliminary evaluation of the effects of primary and secondary radiation forces on acoustic contrast agents," *IEEE Trans. Ultrason. Ferroelectr. Freq. Control*, vol. 44, no. 6, pp. 1264–1277, 1997, doi: 10.1109/58.656630.

[145] A. R. Naji Meidani and M. Hasan, "Mathematical and physical modelling of bubble growth due to ultrasound," *Appl. Math. Model.*, vol. 28, no. 4, pp. 333–351, 2004, doi:

10.1016/j.apm.2003.10.001.

[146] A. Goyal *et al.*, "Inertial Cavitation Ultrasound with Microbubbles Improves Reperfusion Efficacy When Combined with Tissue Plasminogen Activator in an In Vitro Model of Microvascular Obstruction," *Ultrasound Med. Biol.*, vol. 43, no. 7, pp. 1391–1400, 2017, doi: 10.1016/j.ultrasmedbio.2017.02.013.

[147] Y. Lin *et al.*, "Effect of acoustic parameters on the cavitation behavior of SonoVue microbubbles induced by pulsed ultrasound," *Ultrason. Sonochem.*, vol. 35, pp. 176–184, 2017, doi: 10.1016/j.ultsonch.2016.09.016.

[148] N. Kudo, K. Okada, and K. Yamamoto, "Sonoporation by single-shot pulsed ultrasound with microbubbles adjacent to cells," *Biophys. J.*, vol. 96, no. 12, pp. 4866–4876, 2009, doi: 10.1016/j.bpj.2009.02.072.

[149] M. W. Keller, S. S. Segal, S. Kaul, and B. Duling, "The behavior of sonicated albumin microbubbles within the microcirculation: A basis for their use during myocardial contrast echocardiography," *Circ. Res.*, vol. 65, no. 2, pp. 458–467, 1989, doi: 10.1161/01.RES.65.2.458.

[150] S. V. Bachawal, K. C. Jensen, K. E. Wilson, L. Tian, A. M. Lutz, and J. K. Willmann, "Breast Cancer Detection by B7-H3 Targeted Ultrasound Molecular Imaging," *Cancer Res.*, vol. 95, no. 6, pp. 1336–1356, 2015, doi: 10.1158/0008-5472.CAN-14-3361.Breast.

[151] R. Bam *et al.*, "Efficacy of affibody-based ultrasound molecular imaging of vascular B7-H3 for breast cancer detection," *Clin Cancer Res.*, vol. 26, no. 9, pp. 2140–2150, 2020, doi: 10.1158/1078-0432.CCR-19-1655.Efficacy.

[152] L. Abou-Elkacem *et al.*, "Thy1-targeted microbubbles for ultrasound molecular imaging of pancreatic ductal adenocarcinoma," *Clin. Cancer Res.*, vol. 24, no. 7, pp. 1574–1585, 2018, doi: 10.1158/1078-0432.CCR-17-2057.

[153] H. Zhang *et al.*, "In vitro characterization and in vivo ultrasound molecular imaging of nucleolin-targeted microbubbles," *Biomaterials*, vol. 118, pp. 63–73, 2017, doi: 10.1016/j.biomaterials.2016.11.026.

[154] A. Curaj *et al.*, "Molecular Ultrasound Imaging of Junctional Adhesion Molecule A Depicts Acute Alterations in Blood Flow and Early Endothelial Dysregulation," *Arterioscler. Thromb. Vasc. Biol.*, vol. 38, no. 1, pp. 40–48, 2018, doi: 10.1161/ATVBAHA.117.309503.

[155] M. Punjabi *et al.*, "Ultrasound Molecular Imaging of Atherosclerosis with Nanobodies: Translatable Microbubble Targeting Murine and Human VCAM (Vascular Cell

Adhesion Molecule) 1," *Arterioscler. Thromb. Vasc. Biol.*, vol. 39, no. 12, pp. 2520–2530, 2019, doi: 10.1161/ATVBAHA.119.313088.

[156] Y. J. Zhang *et al.*, *Ultrasound-guided imaging of junctional adhesion molecule-A-targeted microbubbles identifies vulnerable plaque in rabbits*, vol. 94. Elsevier Ltd, 2016.

[157] A. Luong *et al.*, "Development of a Translatable Ultrasound Molecular Imaging Agent for Inflammation," *Ultrasound Med. Biol.*, vol. 46, no. 3, pp. 690–702, 2020, doi: 10.1016/j.ultrasmedbio.2019.11.009.

[158] A. Ingels *et al.*, "Ultrasound Molecular Imaging of Renal Cell Carcinoma: VEGFR targeted therapy monitored with VEGFR1 and FSHR targeted microbubbles," *Sci. Rep.*, vol. 10, no. 1, pp. 1–8, 2020, doi: 10.1038/s41598-020-64433-2.

[159] F. Yan *et al.*, "Ultrasound molecular imaging of atherosclerosis for early diagnosis and therapeutic evaluation through leucocyte-like multiple targeted microbubbles," *Theranostics*, vol. 8, no. 7, pp. 1879–1891, 2018, doi: 10.7150/thno.22070.

[160] A. Rix *et al.*, "Molecular ultrasound imaging of αvβ3-integrin expression in carotid arteries of pigs after vessel injury," *Invest. Radiol.*, vol. 51, no. 12, pp. 767–775, 2016, doi: 10.1097/RLI.0000000000000282.

[161] H. Wang *et al.*, "US molecular imaging of acute ileitis: Anti-inflammatory treatment response monitored with targeted microbubbles in a preclinical model," *Radiology*, vol. 289, no. 1, pp. 90–100, 2018, doi: 10.1148/radiol.2018172600.

[162] G. Köse, M. Darguzyte, and F. Kiessling, "Molecular ultrasound imaging," *Nanomaterials*, vol. 10, no. 10, pp. 1–28, 2020, doi: 10.3390/nano10101935.

[163] L. Abou-Elkacem *et al.*, "Ultrasound molecular imaging of the breast cancer neovasculature using engineered fibronectin scaffold ligands: A novel class of targeted contrast ultrasound agent," *Theranostics*, vol. 6, no. 11, pp. 1740–1752, 2016, doi: 10.7150/thno.15169.

[164] J. Zhou *et al.*, "Vegfr2-targeted three-dimensional ultrasound imaging can predict responses to antiangiogenic therapy in preclinical models of colon cancer," *Cancer Res.*, vol. 76, no. 14, pp. 4081–4089, 2016, doi: 10.1158/0008-5472.CAN-15-3271.

[165] I. Spivak *et al.*, "Low-Dose Molecular Ultrasound Imaging with E-Selectin-Targeted PBCA Microbubbles," *Mol. Imaging Biol.*, vol. 18, no. 2, pp. 180–190, 2016, doi: 10.1007/s11307-015-0894-9.

[166] H. Zhang *et al.*, "Ultrasound Molecular Imaging of Tumor Angiogenesis with a Neuropilin-1-Targeted Microbubble," *Biomaterials*, vol. 176, no. 12, pp. 139–148, 2015,

doi: 10.1016/j.biomaterials.2015.03.043.Ultrasound.

[167] X. Wang *et al.*, "Thrombus-targeted theranostic microbubbles: A new technology towards concurrent rapid ultrasound diagnosis and bleeding-free fibrinolytic treatment of thrombosis," *Theranostics*, vol. 6, no. 5, pp. 726–738, 2016, doi: 10.7150/thno.14514.

[168] J. Lux *et al.*, "Thrombin-Activatable Microbubbles as Potential Ultrasound Contrast Agents for the Detection of Acute Thrombosis," *ACS Appl. Mater. Interfaces*, vol. 9, no. 43, pp. 37587–37596, 2017, doi: 10.1021/acsami.7b10592.

[169] A. Curaj *et al.*, "Noninvasive Molecular Ultrasound Monitoring of Vessel Healing after Intravascular Surgical Procedures in a Preclinical Setup," *Arterioscler. Thromb. Vasc. Biol.*, vol. 35, no. 6, pp. 1366–1373, 2015, doi: 10.1161/ATVBAHA.114.304857.

[170] F. Moccetti *et al.*, "Ultrasound Molecular Imaging of Atherosclerosis Using Small-Peptide Targeting Ligands Against Endothelial Markers of Inflammation and Oxidative Stress," *Ultrasound Med. Biol.*, vol. 44, no. 6, pp. 1155–1163, 2018, doi: 10.1016/j.ultrasmedbio.2018.01.001.

[171] F. Moccetti *et al.*, "Myocardial Infarction Produces Sustained Pro-Inflammatory Endothelial Activation in Remote Arteries," *J Am Coll Cardiol.*, vol. 176, no. 1, pp. 139–148, 2018, doi: 10.1016/j.jacc.2018.06.044.Myocardial.

[172] S. Wang, S. Unnikrishnan, E. B. Herbst, A. L. Klibanov, F. W. Mauldin, and J. A. Hossack, "Ultrasound Molecular Imaging of Inflammation in Mouse Abdominal Aorta," *Invest Radiol.*, vol. 176, no. 1, pp. 139–148, 2017, doi: 10.1097/RLI.0000000000000373.Ultrasound.

[173] C. Qiu *et al.*, "VEGFR2-targeted ultrasound molecular imaging of angiogenesis to evaluate liver allograft fibrosis," *Biomater. Sci.*, vol. 9, no. 17, pp. 5802–5811, 2021, doi: 10.1039/d1bm00100k.

[174] X. M. Lingling *et al.*, "Targeted Delivery of Therapeutic Gas by Microbubbles," *Adv. Ultrasound Diagnosis Ther.*, vol. 5, no. 3, p. 173, 2021, doi: 10.37015/audt.2021.200059.

[175] P. Vaupel, M. Höckel, and A. Mayer, "Detection and characterization of tumor hypoxia using pO2 histography," *Antioxidants Redox Signal.*, vol. 9, no. 8, pp. 1221–1235, 2007, doi: 10.1089/ars.2007.1628.

[176] H. E. Barker, J. T. E. Paget, A. A. Khan, and K. J. Harrington, "Barker HE_tumour microenvironment after IRR_cancer reviews 2015.pdf," *Nat. Publ. Gr.*, vol. 15, no. 7, pp. 409–425, 2016, doi: 10.1038/nrc3958.The.

[177] S. M. Fix *et al.*, "Oxygen microbubbles improve radiotherapy tumor control in a rat

fibrosarcoma model – A preliminary study," *PLoS One*, vol. 13, no. 4, pp. 1–18, 2018, doi: 10.1371/journal.pone.0195667.

[178] J. R. Eisenbrey *et al.*, "Sensitization of Hypoxic Tumors to Radiation Therapy Using Ultrasound-Sensitive Oxygen Microbubbles," *Int. J. Radiat. Oncol. Biol. Phys.*, vol. 101, no. 1, pp. 88–96, 2018, doi: 10.1016/j.ijrobp.2018.01.042.

[179] C. McEwan *et al.*, "Oxygen carrying microbubbles for enhanced sonodynamic therapy of hypoxic tumours," *J. Control. Release*, vol. 203, pp. 51–56, 2015, doi: 10.1016/j.jconrel.2015.02.004.

[180] S. Peng *et al.*, "A Robust Oxygen Microbubble Radiosensitizer for Iodine-125 Brachytherapy," *Adv. Sci.*, vol. 8, no. 7, pp. 1–10, 2021, doi: 10.1002/advs.202002567.

[181] J. Esmaeili, F. S. Rezaei, F. M. Beram, and A. Barati, "Integration of microbubbles with biomaterials in tissue engineering for pharmaceutical purposes," *Heliyon*, vol. 6, no. 6, p. e04189, 2020, doi: 10.1016/j.heliyon.2020.e04189.

[182] J. P. Cooke and D. W. Losordo, "Nitric oxide and angiogenesis," *Circulation*, vol. 105, no. 18, pp. 2133–2135, 2002, doi: 10.1161/01.CIR.0000014928.45119.73.

[183] R. Zheng, F. Li, F. Li, and A. Gong, "Targeting tumor vascularization: promising strategies for vascular normalization," *J. Cancer Res. Clin. Oncol.*, vol. 147, no. 9, pp. 2489–2505, 2021, doi: 10.1007/s00432-021-03701-8.

[184] S. L. Huang *et al.*, "Improving ultrasound reflectivity and stability of echogenic liposomal dispersions for use as targeted ultrasound contrast agents," *J. Pharm. Sci.*, vol. 90, no. 12, pp. 1917–1926, 2001, doi: 10.1002/jps.1142.

[185] C. Wang *et al.*, "Intravenous release of NO from lipidic microbubbles accelerates deep vein thrombosis resolution in a rat model," *Thromb. Res.*, vol. 131, no. 1, pp. e31–e38, 2013, doi: 10.1016/j.thromres.2012.11.002.

[186] L. Chen, S. F. Zhou, L. Su, and J. Song, "Gas-Mediated Cancer Bioimaging and Therapy," *ACS Nano*, vol. 13, no. 10, pp. 10887–10917, 2019, doi: 10.1021/acsnano.9b04954.

[187] B. Li, J. Xiong, H. X. Liu, D. Li, and G. Chen, "Devil or angel: two roles of carbon monoxide in stroke," *Med. Gas Res.*, vol. 12, no. 4, pp. 125–130, 2022, doi: 10.4103/2045-9912.337993.

[188] E. Zeynalov and S. Doré, "Low Doses of Carbon Monoxide Protect Against Experimental Focal Brain Ischemia," *Neurotox Res.*, vol. 15, no. 2, pp. 133–137, 2009, doi: 10.1007/s12640-009-9014-4.

[189] A. M. K. Choi *et al.*, "Carbon monoxide has anti-inflammatory effects involving the

mitogen-activated protein kinase pathway," *Nat. Med.*, vol. 6, no. 4, pp. 422–428, 2000.

[190] V. Pathak *et al.*, "Theranostic Trigger-Responsive Carbon Monoxide-Generating Microbubbles," *Small*, vol. 18, no. 18, 2022, doi: 10.1002/smll.202200924.

[191] P. CABRALES, B. Y. S. VÁZQUEZ, A. C. NEGRETE, and M. INTAGLIETTA, " Perfluorocarbons as gas transporters for O 2 , NO, CO and volatile anesthetics ," *Transfus. Altern. Transfus. Med.*, vol. 9, no. 4, pp. 294–303, 2007, doi: 10.1111/j.1778-428x.2007.00085.x.

[192] T. T. Chen, P. C. Samson, M. D. Sorensen, and M. R. Bailey, "Burst wave lithotripsy and acoustic manipulation of stones," *Curr. Opin. Urol.*, vol. 30, no. 2, pp. 149–156, 2020, doi: 10.1097/MOU.0000000000000727.

[193] Y. Xing *et al.*, "Comparison of Broad vs Narrow Focal Width Lithotripter Fields," *J. Endourol.*, vol. 31, no. 5, pp. 502–509, 2017, doi: 10.1089/end.2016.0560.

[194] J. C. Dai *et al.*, "Quantitative Assessment of Effectiveness of Ultrasonic Propulsion of Kidney Stones," *J. Endourol.*, vol. 33, no. 10, pp. 850–857, 2019, doi: 10.1089/end.2019.0340.

[195] Z. Xu, T. L. Hall, E. Vlaisavljevich, and F. T. Lee, "Histotripsy: the first noninvasive, non-ionizing, non-thermal ablation technique based on ultrasound," *Int. J. Hyperth.*, vol. 38, no. 1, pp. 561–575, 2021, doi: 10.1080/02656736.2021.1905189.

[196] S. T. Araujo, D. H. Moreno, and D. G. Cacione, "Percutaneous thrombectomy or ultrasound-accelerated thrombolysis for initial management of acute limb ischaemia," *Cochrane Database Syst. Rev.*, vol. 2022, no. 1, 2022, doi: 10.1002/14651858.CD013486.pub2.

[197] X. Li *et al.*, "Efficacy and safety of sonothrombolysis in patients with acute ischemic stroke: A systematic review and meta-analysis," *J. Neurol. Sci.*, vol. 416, no. May, p. 116998, 2020, doi: 10.1016/j.jns.2020.116998.

[198] H. Kartal, D. Erer, G. L. Oktar, M. H. Zor, K. Akkan, and M. Arslan, "Ultrasound-accelerated catheter-assisted thrombolytic therapy applicatıons in deep vein thrombosis," *Niger. J. Clin. Pract.*, vol. 22, no. 3, pp. 399–405, 2019, doi: 10.4103/njcp.njcp_27_18.

[199] N. McDannold *et al.*, "Acoustic feedback enables safe and reliable carboplatin delivery across the blood-brain barrier with a clinical focused ultrasound system and improves survival in a rat glioma model," *Theranostics*, vol. 9, no. 21, pp. 6284–6299, 2019, doi: 10.7150/thno.35892.

[200] K. B. Bader, G. Bouchoux, and C. K. Holland, *Sonothrombolysis*, vol. 880. 2016.

[201] N. Hosseinkhah, H. Chen, T. J. Matula, P. N. Burns, and K. Hynynen, "Mechanisms of microbubble–vessel interactions and induced stresses: A numerical study," *J. Acoust. Soc. Am.*, vol. 134, no. 3, pp. 1875–1885, 2013, doi: 10.1121/1.4817843.

[202] C. F. Caskey, S. M. Stieger, S. Qin, P. A. Dayton, and K. W. Ferrara, "Direct observations of ultrasound microbubble contrast agent interaction with the microvessel wall," *J. Acoust. Soc. Am.*, vol. 122, no. 2, pp. 1191–1200, 2007, doi: 10.1121/1.2747204.

[203] P. Zhong, Y. Zhou, and S. Zhu, "Dynamics of bubble oscillation in constrained media and mechanisms of vessel rupture in SWL," *Ultrasound Med. Biol.*, vol. 27, no. 1, pp. 119–134, 2001, doi: 10.1016/S0301-5629(00)00322-7.

[204] T. Şen, O. Tüfekçioğlu, and Y. Koza, "Mechanical index," *Anadolu Kardiyol. Derg.*, vol. 15, no. 4, pp. 334–336, 2015, doi: 10.5152/akd.2015.6061.

[205] V. Wilkens and C. Koch, "Improvement of hydrophone measurements on diagnostic ultrasound machines using broadband complex-valued calibration data," *J. Phys. Conf. Ser.*, vol. 1, pp. 50–55, 2004, doi: 10.1088/1742-6596/1/1/012.

[206] Y. Deng, M. L. Palmeri, N. C. Rouze, G. E. Trahey, C. M. Haysteas, and K. R. Nightingale, "QUANTIFYING IMAGE QUALITY IMPROVEMENT USING ELEVATED ACOUSTIC OUTPUT IN B-MODE HARMONIC IMAGING," *Ultrasound Med Biol.*, vol. 43, no. 10, pp. 2416–2425, 2017, doi: 10.1016/j.ultrasmedbio.2017.06.024.QUANTIFYING.

[207] M. Modrzejewska, "Guidelines for ultrasound examination in ophthalmology. Part iii: Color doppler ultrasonography," *J. Ultrason.*, vol. 19, no. 77, pp. 128–136, 2019, doi: 10.15557/JoU.2019.0019.

[208] J. H. Nederhoed *et al.*, "Therapeutic Use of Microbubbles and Ultrasound in Acute Peripheral Arterial Thrombosis: A Systematic Review," *Ultrasound Med. Biol.*, vol. 47, no. 10, pp. 2821–2838, 2021, doi: 10.1016/j.ultrasmedbio.2021.06.001.

[209] X. Ren *et al.*, "Thrombolytic therapy with rt-PA and transcranial color Doppler ultrasound (TCCS) combined with microbubbles for embolic thrombus," *Thromb. Res.*, vol. 136, no. 5, pp. 1027–1032, 2015, doi: 10.1016/j.thromres.2015.08.027.

[210] S. T. Laing *et al.*, "Thrombolytic efficacy of tissue plasminogen activator-loaded echogenic liposomes in a rabbit thrombus model," *Thromb. Res.*, vol. 130, no. 4, pp. 629–635, Oct. 2012, doi: 10.1016/j.thromres.2011.11.010.

[211] F. Xie, J. Lof, T. Matsunaga, R. Zutshi, and T. R. Porter, "Diagnostic ultrasound combined with glycoprotein IIb/IIIa-targeted microbubbles improves microvascular

recovery after acute coronary thrombotic occlusions," *Circulation*, vol. 119, no. 10, pp. 1378–1385, 2009, doi: 10.1161/CIRCULATIONAHA.108.825067.

[212] J. Wu, F. Xie, J. Lof, S. Sayyed, and T. R. Porter, "Utilization of modified diagnostic ultrasound and microbubbles to reduce myocardial infarct size," *Heart*, vol. 101, no. 18, pp. 1468–1474, 2015, doi: 10.1136/heartjnl-2015-307625.

[213] F. Xie *et al.*, "Diagnostic Ultrasound Induced Inertial Cavitation to Non-Invasively Restore Coronary and Microvascular Flow in Acute Myocardial Infarction," *PLoS One*, vol. 8, no. 7, pp. 1–7, 2013, doi: 10.1371/journal.pone.0069780.

[214] H. P. Ebben *et al.*, "Therapeutic application of contrast-enhanced ultrasound and low-dose urokinase for thrombolysis in a porcine model of acute peripheral arterial occlusion," *J. Vasc. Surg.*, vol. 62, no. 2, pp. 477–485, 2015, doi: 10.1016/j.jvs.2014.02.057.

[215] A. J. Tomkins *et al.*, "Platelet rich clots are resistant to lysis by thrombolytic therapy in a rat model of embolic stroke," *Exp. Transl. Stroke Med.*, vol. 7, no. 1, pp. 1–9, 2015, doi: 10.1186/s13231-014-0014-y.

[216] S. T. Laing *et al.*, "Ultrasound-enhanced thrombolytic effect of tissue plasminogen activator-loaded echogenic liposomes in an in vivo rabbit aorta thrombus model-brief report," *Arterioscler. Thromb. Vasc. Biol.*, vol. 31, no. 6, pp. 1357–1359, 2011, doi: 10.1161/ATVBAHA.111.225938.

[217] W. S. Liu, Z. Z. Huang, X. W. Wang, and J. Zhou, "Effects of microbubbles on transcranial Doppler ultrasound-assisted intracranial urokinase thrombolysis," *Thromb. Res.*, vol. 130, no. 3, pp. 547–551, 2012, doi: 10.1016/j.thromres.2012.06.020.

[218] X. Hua *et al.*, "In vivo thrombolysis with targeted microbubbles loading tissue plasminogen activator in a rabbit femoral artery thrombus model," *J. Thromb. Thrombolysis*, vol. 38, no. 1, pp. 57–64, 2014, doi: 10.1007/s11239-014-1071-8.

[219] L. Dinia *et al.*, "Reperfusion after stroke sonothrombolysis with microbubbles may predict intracranial bleeding," *Neurology*, vol. 73, no. 10, pp. 775–780, 2009, doi: 10.1212/WNL.0b013e3181b6bb45.

[220] W. Mathias *et al.*, "Sonothrombolysis in ST-Segment Elevation Myocardial Infarction Treated With Primary Percutaneous Coronary Intervention," *J. Am. Coll. Cardiol.*, vol. 73, no. 22, pp. 2832–2842, 2019, doi: 10.1016/j.jacc.2019.03.006.

[221] T. Porter, P. Zeng, and F. Xie, "Advances in Ultrasound Therapeutics," *Curr. Cardiol. Rep.*, vol. 23, no. 10, pp. 4–11, 2021, doi: 10.1007/s11886-021-01563-7.

[222] S. H. Rezkalla, K. C. Dharmashankar, I. B. Abdalrahman, and R. A. Kloner, "No-reflow

phenomenon following percutaneous coronary intervention for acute myocardial infarction: Incidence, outcome, and effect of pharmacologic therapy," *J. Interv. Cardiol.*, vol. 23, no. 5, pp. 429–436, 2010, doi: 10.1111/j.1540-8183.2010.00561.x.

[223] S. Snipstad *et al.*, "Ultrasound Improves the Delivery and Therapeutic Effect of Nanoparticle-Stabilized Microbubbles in Breast Cancer Xenografts," *Ultrasound Med. Biol.*, vol. 43, no. 11, pp. 2651–2669, 2017, doi: 10.1016/j.ultrasmedbio.2017.06.029.

[224] S. Snipstad *et al.*, "Sonopermeation Enhances Uptake and Therapeutic Effect of Free and Encapsulated Cabazitaxel," *Ultrasound Med. Biol.*, vol. 47, no. 5, pp. 1319–1333, 2021, doi: 10.1016/j.ultrasmedbio.2020.12.026.

[225] G. Fan *et al.*, "Low-Intensity Focused Ultrasound Targeted Microbubble Destruction Enhanced Paclitaxel Sensitivity by Decreasing Autophagy in Paclitaxel-Resistant Ovarian Cancer," *Front. Oncol.*, vol. 12, no. April, pp. 1–12, 2022, doi: 10.3389/fonc.2022.823956.

[226] J. A. Kopechek *et al.*, "Ultrasound targeted microbubble destruction-mediated delivery of a transcription factor decoy inhibits STAT3 signaling and tumor growth," *Theranostics*, vol. 5, no. 12, pp. 1378–1387, 2015, doi: 10.7150/thno.12822.

[227] Y. Wei *et al.*, "Penetration of different molecule sizes upon ultrasound combined with microbubbles in a superficial tumour model," *J. Drug Target.*, vol. 27, no. 10, pp. 1068–1075, 2019, doi: 10.1080/1061186X.2019.1588279.

[228] N. Xiao, J. Liu, L. Liao, J. Sun, W. Jin, and X. Shu, "Ultrasound Combined With Microbubbles Increase the Delivery of Doxorubicin by Reducing the Interstitial Fluid Pressure," *Ultrasound Q.*, vol. 35, no. 2, pp. 103–109, 2019, doi: 10.1097/RUQ.0000000000000381.

[229] Y. Zhou *et al.*, "Targeted antiangiogenesis gene therapy using targeted cationic microbubbles conjugated with CD105 antibody compared with untargeted cationic and neutral microbubbles," *Theranostics*, vol. 5, no. 4, pp. 399–417, 2015, doi: 10.7150/thno.10351.

[230] Y. Jing *et al.*, "Ultrasound-targeted microbubble destruction improved the antiangiogenic effect of Endostar in triple-negative breast carcinoma xenografts," *J. Cancer Res. Clin. Oncol.*, vol. 145, no. 5, pp. 1191–1200, 2019, doi: 10.1007/s00432-019-02866-7.

[231] D. Hong, J. Yang, J. Guo, Y. Zhang, and Z. Chen, "Ultrasound-Targeted Microbubble Destruction Enhances Inhibitory Effect of Apatinib on Angiogenesis in Triple Negative Breast Carcinoma Xenografts," *Anal. Cell. Pathol.*, vol. 2021, 2021, doi:

10.1155/2021/8837950.

[232] C. Viallard and B. Larrivée, "Tumor angiogenesis and vascular normalization: alternative therapeutic targets," *Angiogenesis*, vol. 20, no. 4, pp. 409–426, 2017, doi: 10.1007/s10456-017-9562-9.

[233] Y. J. Ho *et al.*, "Normalization of tumor vasculature by oxygen microbubbles with ultrasound," *Theranostics*, vol. 9, no. 24, pp. 7370–7383, 2019, doi: 10.7150/thno.37750.

[234] J. Deprez, G. Lajoinie, Y. Engelen, S. C. De Smedt, and I. Lentacker, "Opening doors with ultrasound and microbubbles: Beating biological barriers to promote drug delivery," *Adv. Drug Deliv. Rev.*, vol. 172, pp. 9–36, 2021, doi: 10.1016/j.addr.2021.02.015.

[235] M. A. O'Reilly, A. Muller, and K. Hynynen, "Ultrasound Insertion Loss of Rat Parietal Bone Appears to Be Proportional to Animal Mass at Submegahertz Frequencies," *Ultrasound Med. Biol.*, vol. 37, no. 11, pp. 1930–1937, 2011, doi: 10.1016/j.ultrasmedbio.2011.08.001.

[236] D. McMahon, A. Lassus, E. Gaud, V. Jeannot, and K. Hynynen, "Microbubble formulation influences inflammatory response to focused ultrasound exposure in the brain," *Sci. Rep.*, vol. 10, no. 1, pp. 1–15, 2020, doi: 10.1038/s41598-020-78657-9.

[237] O. Vince *et al.*, "Microbubbles Containing Lysolipid Enhance Ultrasound-Mediated Blood–Brain Barrier Breakdown In Vivo," *Adv. Healthc. Mater.*, vol. 10, no. 3, pp. 1–11, 2021, doi: 10.1002/adhm.202001343.

[238] K. T. Chen, K. C. Wei, and H. L. Liu, "Focused ultrasound combined with microbubbles in central nervous system applications," *Pharmaceutics*, vol. 13, no. 7, pp. 1–22, 2021, doi: 10.3390/pharmaceutics13071084.

[239] Y. Shen *et al.*, "Ultrasound with microbubbles improves memory, ameliorates pathology and modulates hippocampal proteomic changes in a triple transgenic mouse model of alzheimer's disease," *Theranostics*, vol. 10, no. 25, pp. 11794–11819, 2020, doi: 10.7150/thno.44152.

[240] Y. Huang, R. M. Jones, L. M. Oliveira, B. Davidson, A. Bethune, and P. Maralani, "Putaminal Recombinant Glucocerebrosidase Delivery with Magnetic Resonance – Guided Focused Ultrasound in Parkinson ' s Disease : A Phase I Study," pp. 1–7, 2022, doi: 10.1002/mds.29190.

[241] K. F. Timbie, B. P. Mead, and R. J. Price, "Drug and Gene Delivery Across the Blood-Brain Barrier with Focused Ultrasound," *J Control Release*, vol. 176, no. 1, pp. 139–148, 2015, doi: 10.1016/j.jconrel.2015.08.059.Drug.

[242] Z. I. Kovacsa *et al.*, "Disrupting the blood-brain barrier by focused ultrasound induces

sterile inflammation," *Proc. Natl. Acad. Sci. U. S. A.*, vol. 114, no. 1, pp. E75–E84, 2017, doi: 10.1073/pnas.1614777114.

[243] K. R. Lattwein *et al.*, "An in vitro proof-of-principle study of sonobactericide," *Sci. Rep.*, vol. 8, no. 1, pp. 1–12, Dec. 2018, doi: 10.1038/s41598-018-21648-8.

[244] K. R. Lattwein *et al.*, "Dispersing and Sonoporating Biofilm-Associated Bacteria with Sonobactericide," *Pharmaceutics*, vol. 14, no. 6, 2022, doi: 10.3390/pharmaceutics14061164.

[245] X. Duan, Q. Zhou, J. M. F. Wan, and A. C. H. Yu, "Sonoporation generates downstream cellular impact after membrane resealing," *Sci. Rep.*, vol. 11, no. 1, pp. 1–12, 2021, doi: 10.1038/s41598-021-84341-3.

[246] F. Fekri, R. C. Delos Santos, R. Karshafian, and C. N. Antonescu, "Ultrasound microbubble treatment enhances clathrin-mediated endocytosis and fluid-phase uptake through distinct mechanisms," *PLoS One*, vol. 11, no. 6, pp. 1–22, 2016, doi: 10.1371/journal.pone.0156754.

[247] K. E. Landmark, P. W. Johansen, J. A. Johnson, B. Johansen, S. Uran, and T. Skotland, "Pharmacokinetics of perfluorobutane following intravenous bolus injection and continuous infusion of sonazoid in healthy volunteers and in patients with reduced pulmonary diffusing capacity," *Ultrasound Med. Biol.*, vol. 34, no. 3, pp. 494–501, Mar. 2008, doi: 10.1016/j.ultrasmedbio.2007.09.019.

[248] M. J. Mitchell, M. M. Billingsley, R. M. Haley, M. E. Wechsler, N. A. Peppas, and R. Langer, "Engineering precision nanoparticles for drug delivery," *Nat. Rev. Drug Discov.*, vol. 20, no. 2, pp. 101–124, Feb. 2021, doi: 10.1038/s41573-020-0090-8.

[249] A. A. Exner and M. C. Kolios, "Bursting microbubbles: How nanobubble contrast agents can enable the future of medical ultrasound molecular imaging and image-guided therapy," *Curr. Opin. Colloid Interface Sci.*, vol. 54, p. 101463, 2021, doi: 10.1016/j.cocis.2021.101463.

[250] M. Alheshibri, J. Qian, M. Jehannin, and V. S. J. Craig, "A History of Nanobubbles," *Langmuir*, vol. 32, no. 43, pp. 11086–11100, Nov. 2016, doi: 10.1021/acs.langmuir.6b02489.

[251] C. T. Chin and P. N. Burns, "Predicting the acoustic response of a microbubble population for contrast imaging in medical ultrasound," *Ultrasound Med. Biol.*, vol. 26, no. 8, pp. 1293–1300, Oct. 2000, doi: 10.1016/S0301-5629(00)00299-4.

[252] P. C. Sontum, J. Østensen, K. Dyrstad, and L. Hoff, "Acoustic Properties of NC100100 and Their Relation With the Microbubble Size Distribution," *Invest. Radiol.*, vol. 34, no.

4, p. 268, Apr. 1999.

[253] B. E. Oeffinger and M. A. Wheatley, "Development and characterization of a nano-scale contrast agent," *Ultrasonics*, vol. 42, no. 1, pp. 343–347, Apr. 2004, doi: 10.1016/j.ultras.2003.11.011.

[254] C. Su *et al.*, "Current advances in ultrasound-combined nanobubbles for cancer-targeted therapy: a review of the current status and future perspectives," *RSC Adv.*, vol. 11, no. 21, pp. 12915–12928, May 2021, doi: 10.1039/D0RA08727K.

[255] N. Güvener *et al.*, "Recent advances in ultrasound-based diagnosis and therapy with micro- and nanometer-sized formulations," *Methods*, vol. 130, pp. 4–13, Nov. 2017, doi: 10.1016/j.ymeth.2017.05.018.

[256] E. C. Abenojar *et al.*, "Effect of Bubble Concentration on the in Vitro and in Vivo Performance of Highly Stable Lipid Shell-Stabilized Micro- And Nanoscale Ultrasound Contrast Agents," *Langmuir*, vol. 35, no. 31, pp. 10192–10202, 2019, doi: 10.1021/acs.langmuir.9b00462.

[257] J. Zhang *et al.*, "The Optimized Fabrication of a Novel Nanobubble for Tumor Imaging," *Front. Pharmacol.*, vol. 10, p. 610, May 2019, doi: 10.3389/fphar.2019.00610.

[258] A. Jafari Sojahrood *et al.*, "Toward Precisely Controllable Acoustic Response of Shell-Stabilized Nanobubbles: High Yield and Narrow Dispersity," *ACS Nano*, vol. 15, no. 3, pp. 4901–4915, Aug. 2021, doi: 10.1021/acsnano.0c09701.

[259] U. S. Kumar, A. Natarajan, T. F. Massoud, and R. Paulmurugan, "FN3 linked nanobubbles as a targeted contrast agent for US imaging of cancer-associated human PD-L1," *J. Control. Release*, vol. 346, pp. 317–327, Jun. 2022, doi: 10.1016/j.jconrel.2022.04.030.

[260] Z. Xing *et al.*, "The fabrication of novel nanobubble ultrasound contrast agent for potential tumor imaging," *Nanotechnology*, vol. 21, no. 14, p. 145607, Apr. 2010, doi: 10.1088/0957-4484/21/14/145607.

[261] H. Yang *et al.*, "Multifunctional PLGA Nanobubbles as Theranostic Agents: Combining Doxorubicin and P-gp siRNA Co-Delivery Into Human Breast Cancer Cells and Ultrasound Cellular Imaging," *J. Biomed. Nanotechnol.*, vol. 11, no. 12, pp. 2124–2136, 2015, doi: 10.1166/jbn.2015.2168.

[262] P. Bhandari, X. Wang, and J. Irudayaraj, "Oxygen Nanobubble Tracking by Light Scattering in Single Cells and Tissues," *ACS Nano*, vol. 11, no. 3, pp. 2682–2688, Mar. 2017, doi: 10.1021/acsnano.6b07478.

[263] M. A. Wheatley, F. Forsberg, N. Dube, M. Patel, and B. E. Oeffinger, "Surfactant-

stabilized contrast agent on the nanoscale for diagnostic ultrasound imaging," *Ultrasound Med. Biol.*, vol. 32, no. 1, pp. 83–93, Jan. 2006, doi: 10.1016/j.ultrasmedbio.2005.08.009.

[264] P. S. Sheeran *et al.*, "Methods of generating submicrometer phase-shift perfluorocarbon droplets for applications in medical ultrasonography," *IEEE Trans. Ultrason. Ferroelectr. Freq. Control*, vol. 64, no. 1, pp. 252–263, 2017, doi: 10.1109/TUFFC.2016.2619685.

[265] Y. Endo-Takahashi and Y. Negishi, "Microbubbles and nanobubbles with ultrasound for systemic gene delivery," *Pharmaceutics*, vol. 12, no. 10, pp. 1–14, 2020, doi: 10.3390/pharmaceutics12100964.

[266] C. Pellow, E. C. Abenojar, A. A. Exner, G. Zheng, and D. E. Goertz, "Concurrent visual and acoustic tracking of passive and active delivery of nanobubbles to tumors," *Theranostics*, vol. 10, no. 25, pp. 11690–11706, 2020, doi: 10.7150/thno.51316.

[267] H. Kida *et al.*, "Nanobubble Mediated Gene Delivery in Conjunction With a Hand-Held Ultrasound Scanner," *Front. Pharmacol.*, vol. 11, p. 363, Apr. 2020, doi: 10.3389/fphar.2020.00363.

[268] H. Kida, L. B. Feril, Y. Irie, H. Endo, K. Itaka, and K. Tachibana, "Influence of Nanobubble Size Distribution on Ultrasound-Mediated Plasmid DNA and Messenger RNA Gene Delivery," *Front. Pharmacol.*, vol. 13, 2022.

[269] Y. Tan *et al.*, "Nanobubbles Containing sPD-1 and Ce6 Mediate Combination Immunotherapy and Suppress Hepatocellular Carcinoma in Mice," *Int. J. Nanomedicine*, vol. 16, pp. 3241–3254, 2021, doi: 10.2147/IJN.S305857.

[270] A. Yildirim, N. Blum, and A. Goodwin, "Colloids, nanoparticles, and materials for imaging, delivery, ablation, and theranostics by focused ultrasound (FUS)," *Theranostics*, vol. 9, pp. 2572–2594, Apr. 2019, doi: 10.7150/thno.32424.

[271] J. M. Gorce, M. Arditi, and M. Schneider, "Influence of bubble size distribution on the echogenicity of ultrasound contrast agents: a study of SonoVue," *Invest. Radiol.*, vol. 35, no. 11, pp. 661–671, 2000, doi: 10.1097/00004424-200011000-00003.

[272] L. Hoff, *Acoustic Characterization of Contrast Agents for Medical Ultrasound Imaging*. Dordrecht: Springer Netherlands, 2001.

[273] J. Z. Myers, J. A. Navarro-Becerra, and M. A. Borden, "Nanobubbles are Non-Echogenic for Fundamental-Mode Contrast-Enhanced Ultrasound Imaging," *Bioconjug. Chem.*, Apr. 2022, doi: 10.1021/acs.bioconjchem.2c00155.

[274] W. Bin Cai *et al.*, "The Optimized Fabrication of Nanobubbles as Ultrasound Contrast

Agents for Tumor Imaging," *Sci. Rep.*, vol. 5, no. 1, p. 13725, Sep. 2015, doi: 10.1038/srep13725.

[275] D. V. B. Batchelor, R. H. Abou-Saleh, P. L. Coletta, J. R. McLaughlan, S. A. Peyman, and S. D. Evans, "Nested Nanobubbles for Ultrasound-Triggered Drug Release," *ACS Appl. Mater. Interfaces*, vol. 12, no. 26, pp. 29085–29093, Jul. 2020, doi: 10.1021/acsami.0c07022.

[276] P. S. Sheeran and P. A. Dayton, "Phase-Change Contrast Agents for Imaging and Therapy," *Curr. Pharm. Des.*, vol. 18, no. 15, pp. 2152–2165, 2012.

[277] N. Rapoport, "Phase-shift, stimuli-responsive perfluorocarbon nanodroplets for drug delivery to cancer," *WIREs Nanomedicine and Nanobiotechnology*, vol. 4, no. 5, pp. 492–510, 2012, doi: 10.1002/wnan.1176.

[278] N. Rapoport *et al.*, "Ultrasound-mediated tumor imaging and nanotherapy using drug loaded, block copolymer stabilized perfluorocarbon nanoemulsions," *J. Control. Release Off. J. Control. Release Soc.*, vol. 153, no. 1, pp. 4–15, Jul. 2011, doi: 10.1016/j.jconrel.2011.01.022.

[279] K.-H. NAM and N. Y. RAPOPORT, "Stable nanoemulsions for ultrasound-mediated drug delivery and imaging," no. US8709451B2. Apr-2014.

[280] M. Kuriakose and M. A. Borden, "Microbubbles and Nanodrops for photoacoustic tomography," *Curr. Opin. Colloid Interface Sci.*, vol. 55, p. 101464, 2021, doi: 10.1016/j.cocis.2021.101464.

[281] L. C. Moyer, K. F. Timbie, P. S. Sheeran, R. J. Price, G. W. Miller, and P. A. Dayton, "High-intensity focused ultrasound ablation enhancement in vivo via phase-shift nanodroplets compared to microbubbles," *J. Ther. Ultrasound*, vol. 3, p. 7, 2015, doi: 10.1186/s40349-015-0029-4.

[282] D. Qin *et al.*, "A Highly Efficient One-for-All Nanodroplet for Ultrasound Imaging-Guided and Cavitation-Enhanced Photothermal Therapy," *Int. J. Nanomedicine*, vol. 16, pp. 3105–3119, 2021, doi: 10.2147/IJN.S301734.

[283] A. Ishijima *et al.*, "Selective intracellular delivery of perfluorocarbon nanodroplets for cytotoxicity threshold reduction on ultrasound-induced vaporization," *Cancer Rep.*, vol. 2, no. 4, p. e1165, 2019, doi: 10.1002/cnr2.1165.

[284] C. Errico *et al.*, "Ultrafast ultrasound localization microscopy for deep super-resolution vascular imaging," *Nature*, vol. 527, no. 7579, pp. 499–502, Nov. 2015, doi: 10.1038/nature16066.

[285] V. Hingot *et al.*, "Subwavelength far-field ultrasound drug-delivery," *Appl. Phys. Lett.*,

vol. 109, p. 194102, Nov. 2016, doi: 10.1063/1.4967009.

[286] G. Zhang *et al.*, "Photoacoustic Super-Resolution Imaging using Laser Activation of Low-Boiling-Point Dye-Coated Nanodroplets in vitro and in vivo," in *IEEE International Ultrasonics Symposium, IUS*, 2019, vol. 2019-Octob, pp. 944–947, doi: 10.1109/ULTSYM.2019.8926179.

[287] S.-Y. Yu, C.-H. Tu, J.-W. Liaw, and M.-K. Kuo, "Laser-Induced Plasmonic Nanobubbles and Microbubbles in Gold Nanorod Colloidal Solution," *Nanomaterials*, vol. 12, no. 7, p. 1154, Jan. 2022, doi: 10.3390/nano12071154.

[288] A. Veeren, M. O. Ogunyankin, J. E. Shin, and J. A. Zasadzinski, "Liposome-Tethered Gold Nanoparticles Triggered by Pulsed NIR Light for Rapid Liposome Contents Release and Endosome Escape," *Pharmaceutics*, vol. 14, no. 4, p. 701, Apr. 2022, doi: 10.3390/pharmaceutics14040701.

[289] M. O. Ogunyankin, J. E. Shin, D. O. Lapotko, V. E. Ferry, and J. A. Zasadzinski, "Optimizing the NIR Fluence Threshold for Nanobubble Generation by Controlled Synthesis of 10 - 40 nm Hollow Gold Nanoshells," *Adv. Funct. Mater.*, vol. 28, no. 10, p. 1705272, Mar. 2018, doi: 10.1002/adfm.201705272.

[290] J. E. Shin, M. O. Ogunyankin, and J. A. Zasadzinski, "Near Infrared-Triggered Liposome Cages for Rapid, Localized Small Molecule Delivery," *Sci. Rep.*, vol. 10, p. 1706, Feb. 2020, doi: 10.1038/s41598-020-58764-3.

[291] J. J. Kwan *et al.*, "Ultrasound-Propelled Nanocups for Drug Delivery," *Small*, vol. 11, no. 39, pp. 5305–5314, Oct. 2015, doi: 10.1002/smll.201501322.

[292] T. Liu *et al.*, "Endogenous Catalytic Generation of O2 Bubbles for In Situ Ultrasound-Guided High Intensity Focused Ultrasound Ablation," *ACS Nano*, vol. 11, no. 9, pp. 9093–9102, Sep. 2017, doi: 10.1021/acsnano.7b03772.

[293] X. Cui, X. Han, L. Yu, B. Zhang, and Y. Chen, "Intrinsic chemistry and design principle of ultrasound-responsive nanomedicine," *Nano Today*, vol. 28, no. xxxx, p. 100773, 2019, doi: 10.1016/j.nantod.2019.100773.

[294] F. Pfeifer, "Distribution, formation and regulation of gas vesicles," *Nat. Rev. Microbiol.*, vol. 10, no. 10, pp. 705–715, Oct. 2012, doi: 10.1038/nrmicro2834.

[295] M. G. Shapiro *et al.*, "Biogenic gas nanostructures as ultrasonic molecular reporters," *Nat. Nanotechnol.*, vol. 9, no. 4, pp. 311–316, Apr. 2014, doi: 10.1038/nnano.2014.32.

[296] G. Wang *et al.*, "Surface-modified GVs as nanosized contrast agents for molecular ultrasound imaging of tumor," *Biomaterials*, vol. 236, p. 119803, Apr. 2020, doi: 10.1016/j.biomaterials.2020.119803.

[297] A. Farhadi, G. H. Ho, D. P. Sawyer, R. W. Bourdeau, and M. G. Shapiro, "Ultrasound Imaging of Gene Expression in Mammalian Cells," *Science*, vol. 365, no. 6460, pp. 1469–1475, Sep. 2019, doi: 10.1126/science.aax4804.

[298] R. Gao *et al.*, "Biosynthetic Nanobubble-Mediated CRISPR/Cas9 Gene Editing of Cdh2 Inhibits Breast Cancer Metastasis," *Pharmaceutics*, vol. 14, no. 7, p. 1382, Jul. 2022, doi: 10.3390/pharmaceutics14071382.

[299] B. Delannoy *et al.*, "Acoustical image reconstruction in parallel-processing analog electronic systems," *JAP*, vol. 50, no. 5, pp. 3153–3159, 1979, doi: 10.1063/1.326397.

[300] R. Torguet, C. Bruneel, E. Bridoux, J. M. Rouvaen, and B. Nongaillard, "Ultrafast Echotomographic System Using Optical Processing of Ultrasonic Signals," *Acoust. Hologr.*, pp. 79–85, 1977, doi: 10.1007/978-1-4757-0653-6_6.

[301] D. Shattuck, M. D. Weinshenker, S. W. Smith, and O. T. von Ramm, "Explososcan: a parallel processing technique for high speed ultrasound imaging with linear phased arrays," *J. Acoust. Soc. Am.*, vol. 75, no. 4, pp. 1273–1282, 1984, doi: 10.1121/1.390734.

[302] L. Sandrin, S. Catheline, M. Tanter, X. Hennequin, and M. Fink, "Time-resolved pulsed elastography with ultrafast ultrasonic imaging," *Ultrason. Imaging*, vol. 21, no. 4, pp. 259–272, 1999, doi: 10.1177/016173469902100402.

[303] M. Tanter, J. Bercoff, L. Sandrin, and M. Fink, "Ultrafast compound imaging for 2-D motion vector estimation: Application to transient elastography," *IEEE Trans. Ultrason. Ferroelectr. Freq. Control*, vol. 49, no. 10, pp. 1363–1374, Oct. 2002, doi: 10.1109/TUFFC.2002.1041078.

[304] J. Bercoff, "Ultrafast Ultrasound Imaging," *Ultrasound Imaging - Med. Appl.*, Aug. 2011, doi: 10.5772/19729.

[305] A. Ng and J. Swanevelder, "Resolution in ultrasound imaging," *Contin. Educ. Anaesth. Crit. Care Pain*, vol. 11, no. 5, pp. 186–192, Oct. 2011, doi: 10.1093/BJACEACCP/MKR030.

[306] H. Hasegawa and C. L. de Korte, "Ultrafast Ultrasound Imaging," *Ultrafast Ultrasound Imaging*, Sep. 2018, doi: 10.3390/BOOKS978-3-03897-128-3.

[307] G. Montaldo, M. Tanter, J. Bercoff, N. Benech, and M. Fink, "Coherent plane-wave compounding for very high frame rate ultrasonography and transient elastography," *IEEE Trans. Ultrason. Ferroelectr. Freq. Control*, vol. 56, no. 3, pp. 489–506, Mar. 2009, doi: 10.1109/TUFFC.2009.1067.

[308] A. Ozturk, J. R. Grajo, M. Dhyani, B. W. Anthony, and A. E. Samir, "Principles of ultrasound elastography," *Abdom. Radiol. 2018 434*, vol. 43, no. 4, pp. 773–785, Feb.

2018, doi: 10.1007/S00261-018-1475-6.

[309] J. Bercoff *et al.*, "Ultrafast compound Doppler imaging: providing full blood flow characterization," *IEEE Trans. Ultrason. Ferroelectr. Freq. Control*, vol. 58, no. 1, pp. 134–147, Jan. 2011, doi: 10.1109/TUFFC.2011.1780.

[310] C. Demene *et al.*, "Functional ultrasound imaging of brain activity in human newborns," *Sci. Transl. Med.*, vol. 9, no. 411, Oct. 2017, doi: 10.1126/SCITRANSLMED.AAH6756/SUPPL_FILE/AAH6756_VIDEO_S2.MP4.

[311] O. COUTURE, M. TANTER, and M. FINK, "PROCEDE ET DISPOSITIF D'IMAGERIE ULTRASONORE," *Eur. Pat. Off.*, no. PCT/FR2011/052810, Jun. 2012.

[312] O. Couture, V. Hingot, B. Heiles, P. Muleki-Seya, and M. Tanter, "Ultrasound localization microscopy and super-resolution: A state of the art," *IEEE Trans. Ultrason. Ferroelectr. Freq. Control*, vol. 65, no. 8, pp. 1304–1320, Aug. 2018, doi: 10.1109/TUFFC.2018.2850811.

[313] K. Christensen-Jeffries, R. J. Browning, M. X. Tang, C. Dunsby, and R. J. Eckersley, "In vivo acoustic super-resolution and super-resolved velocity mapping using microbubbles," *IEEE Trans. Med. Imaging*, vol. 34, no. 2, pp. 433–440, Feb. 2015, doi: 10.1109/TMI.2014.2359650.

[314] V. Hingot, A. Chavignon, B. Heiles, and O. Couture, "Measuring Image Resolution in Ultrasound Localization Microscopy," *IEEE Trans. Med. Imaging*, vol. 40, no. 12, pp. 3812–3819, Dec. 2021, doi: 10.1109/TMI.2021.3097150.

[315] A. Chavignon, V. Hingot, C. Orset, D. Vivien, and O. Couture, "3D transcranial ultrasound localization microscopy for discrimination between ischemic and hemorrhagic stroke in early phase," *Sci. Reports 2022 121*, vol. 12, no. 1, pp. 1–11, Aug. 2022, doi: 10.1038/S41598-022-18025-X.

[316] S. B. Andersen *et al.*, "Super-Resolution Ultrasound Imaging Can Quantify Alterations in Microbubble Velocities in the Renal Vasculature of Rats," *Diagnostics (Basel, Switzerland)*, vol. 12, no. 5, May 2022, doi: 10.3390/DIAGNOSTICS12051111.

[317] M. R. Lowerison *et al.*, "Super-resolution ultrasound imaging of cerebrovascular impairment in a mouse model of Alzheimer's disease," *bioRxiv*, p. 2022.10.05.511008, Oct. 2022, doi: 10.1101/2022.10.05.511008.

[318] X. Chen, M. R. Lowerison, Z. Dong, A. Han, and P. Song, "Deep Learning-Based Microbubble Localization for Ultrasound Localization Microscopy," *IEEE Trans. Ultrason. Ferroelectr. Freq. Control*, vol. 69, no. 4, pp. 1312–1325, Apr. 2022, doi: 10.1109/TUFFC.2022.3152225.

[319] B. Heiles, A. Chavignon, V. Hingot, P. Lopez, E. Teston, and O. Couture, "Performance benchmarking of microbubble-localization algorithms for ultrasound localization microscopy," *Nat. Biomed. Eng.*, 2022, doi: 10.1038/S41551-021-00824-8.

[320] L. Yan *et al.*, "Study on the Application of Super-Resolution Ultrasound for Cerebral Vessel Imaging in Rhesus Monkeys," *Front. Neurol.*, vol. 12, Nov. 2021, doi: 10.3389/FNEUR.2021.720320/PDF.

[321] C. Demené *et al.*, "Transcranial ultrafast ultrasound localization microscopy of brain vasculature in patients," *Nat. Biomed. Eng.*, vol. 5, no. 3, pp. 219–228, Mar. 2021, doi: 10.1038/S41551-021-00697-X.

[322] C. Huang *et al.*, "Super-resolution ultrasound localization microscopy based on a high frame-rate clinical ultrasound scanner: An in-human feasibility study," *Phys. Med. Biol.*, vol. 66, no. 8, Apr. 2021, doi: 10.1088/1361-6560/ABEF45.

[323] T. Opacic *et al.*, "Motion model ultrasound localization microscopy for preclinical and clinical multiparametric tumor characterization," *Nat. Commun. 2018 91*, vol. 9, no. 1, pp. 1–13, Apr. 2018, doi: 10.1038/S41467-018-03973-8.

[324] A. Sun *et al.*, "Evaluation of visible NIR-I and NIR-II light penetration for photoacoustic imaging in rat organs," *Opt. Express, Vol. 28, Issue 6, pp. 9002-9013*, vol. 28, no. 6, pp. 9002–9013, Mar. 2020, doi: 10.1364/OE.389714.

[325] H. Yoon, K. A. Hallam, C. Yoon, and S. Y. Emelianov, "Super-Resolution Imaging With Ultrafast Ultrasound Imaging of Optically Triggered Perfluorohexane Nanodroplets," *IEEE Trans. Ultrason. Ferroelectr. Freq. Control*, vol. 65, no. 12, pp. 2277–2285, Dec. 2018, doi: 10.1109/TUFFC.2018.2829740.

[326] Y. Jang *et al.*, "Development of an ultrasound triggered nanomedicine-microbubble complex for chemo-photodynamic-gene therapy," *Nanomedicine Nanotechnology, Biol. Med.*, vol. 27, p. 102194, 2020, doi: 10.1016/j.nano.2020.102194.

[327] H. Li *et al.*, "Instant Ultrasound-Evoked Precise Nanobubble Explosion and Deep Photodynamic Therapy for Tumors Guided by Molecular Imaging," *ACS Appl. Mater. Interfaces*, vol. 13, no. 18, pp. 21097–21107, 2021, doi: 10.1021/acsami.1c05517.

[328] R. Chen *et al.*, "Photoacoustic molecular imaging-escorted adipose photodynamic–browning synergy for fighting obesity with virus-like complexes," *Nat. Nanotechnol.*, vol. 16, no. 4, pp. 455–465, 2021, doi: 10.1038/s41565-020-00844-6.

[329] M. de Saint Victor, L. C. Barnsley, D. Carugo, J. Owen, C. C. Coussios, and E. Stride, "Sonothrombolysis with Magnetically Targeted Microbubbles," *Ultrasound Med. Biol.*, vol. 45, no. 5, pp. 1151–1163, 2019, doi: 10.1016/j.ultrasmedbio.2018.12.014.

[330] A. Marino, G. G. Genchi, E. Sinibaldi, and G. Ciofani, "Piezoelectric Effects of Materials on Bio-Interfaces," *ACS Appl. Mater. Interfaces*, vol. 9, no. 21, pp. 17663–17680, 2017, doi: 10.1021/acsami.7b04323.

[331] L. Fournier and T. D. La Taille, "Microbubbles for human diagnosis and therapy," *Biomaterials*, vol. 294, no. January, 2023, doi: 10.1016/j.biomaterials.2023.122025.

[332] H. G. M. Edwards and J. S. Day, "Fourier transform Raman spectroscopic studies of the curing of cyanoacrylate glue," *J. Raman Spectrosc.*, vol. 35, no. 7, pp. 555–560, 2004, doi: 10.1002/jrs.1184.

[333] I. Bertholon, S. Lesieur, D. Labarre, M. Besnard, and C. Vauthier, "Characterization of dextran-poly(isobutylcyanoacrylate) copolymers obtained by redox radical and anionic emulsion polymerization," *Macromolecules*, vol. 39, no. 10, pp. 3559–3567, 2006, doi: 10.1021/ma060338z.

[334] C. Duffy, P. B. Zetterlund, and F. Aldabbagh, "Radical polymerization of alkyl 2-cyanoacrylates," *Molecules*, vol. 23, no. 2, 2018, doi: 10.3390/molecules23020465.

[335] O. Altabal and C. Wischke, "Analyzing the Mechanical Properties of Free-Standing PACA Thin Films Using Microindentation Technique," *Polymers (Basel).*, vol. 14, no. 22, p. 4863, 2022, doi: 10.3390/polym14224863.

[336] B. Mizrahi *et al.*, "Elasticity and safety of alkoxyethyl cyanoacrylate tissue adhesives," *Acta Biomater.*, vol. 7, no. 8, pp. 3150–3157, 2011, doi: 10.1016/j.actbio.2011.04.022.

[337] S. Gao *et al.*, "Polybutylcyanoacrylate nanocarriers as promising targeted drug delivery systems," *J. Drug Target.*, vol. 23, no. 6, pp. 481–496, 2015, doi: 10.3109/1061186X.2015.1020426.

[338] M. Juenet *et al.*, "Thrombolytic therapy based on fucoidan-functionalized polymer nanoparticles targeting P-selectin," *Biomaterials*, vol. 156, pp. 204–216, 2018, doi: 10.1016/j.biomaterials.2017.11.047.

[339] E. Deniaud-Bouët, K. Hardouin, P. Potin, B. Kloareg, and C. Hervé, "A review about brown algal cell walls and fucose-containing sulfated polysaccharides: Cell wall context, biomedical properties and key research challenges," *Carbohydr. Polym.*, vol. 175, pp. 395–408, 2017, doi: 10.1016/j.carbpol.2017.07.082.

[340] K. Ley, "The role of selectins in inflammation and disease," *Trends Mol. Med.*, vol. 9, no. 6, pp. 263–268, 2003, doi: 10.1016/S1471-4914(03)00071-6.

[341] L. Bachelet *et al.*, "Affinity of low molecular weight fucoidan for P-selectin triggers its binding to activated human platelets," *Biochim. Biophys. Acta - Gen. Subj.*, vol. 1790, no. 2, pp. 141–146, 2009, doi: 10.1016/j.bbagen.2008.10.008.

[342] J. L. Giraux, S. Matou, A. Bros, J. Tapon-Bretaudiere, D. Letourneur, and A. M. Fischer, "Modulation of human endothelial cell proliferation and migration by fucoidan and heparin," *Eur. J. Cell Biol.*, vol. 77, no. 4, pp. 352–359, 1998, doi: 10.1016/S0171-9335(98)80094-0.

[343] C. E. Luyt *et al.*, "Low-molecular-weight fucoidan promotes therapeutic revascularization in a rat model of critical hindlimb ischemia," *J. Pharmacol. Exp. Ther.*, vol. 305, no. 1, pp. 24–30, 2003, doi: 10.1124/jpet.102.046144.

[344] A. Zenych *et al.*, "Fucoidan-functionalized polysaccharide submicroparticles loaded with alteplase for efficient targeted thrombolytic therapy," *Biomaterials*, vol. 277, no. August, 2021, doi: 10.1016/j.biomaterials.2021.121102.

[345] B. Li *et al.*, "Development of Polymer Microcapsules Functionalized with Fucoidan to Target P-Selectin Overexpressed in Cardiovascular Diseases," *Adv. Healthc. Mater.*, vol. 6, no. 4, 2017, doi: 10.1002/adhm.201601200.

[346] M. Palmowski *et al.*, "Pharmacodynamics of streptavidin-coated cyanoacrylate microbubbles designed for molecular ultrasound imaging," *Invest. Radiol.*, vol. 43, no. 3, pp. 162–169, 2008, doi: 10.1097/RLI.0b013e31815a251b.

[347] J. G. Riess, "Understanding the fundamentals of perfluorocarbons and perfluorocarbon emulsions relevant to in vivo oxygen delivery," *Artif. Cells. Blood Substit. Immobil. Biotechnol.*, vol. 33, no. 1, pp. 47–63, 2005, doi: 10.1081/BIO-200046659.

[348] G. A. Roth *et al.*, "GBD-NHLBI-JACC Global Burden of Cardiovascular Diseases Writing Group. Global burden of cardiovascular diseases and risk factors, 1990-2019: update from the GBD 2019 study," *J Am Coll Cardiol*, vol. 76, no. 25, pp. 2982–3021, 2020.

[349] C. W. Tsao *et al.*, *Heart Disease and Stroke Statistics-2022 Update: A Report from the American Heart Association*, vol. 145, no. 8. 2022.

[350] G. Alkarithi, C. Duval, Y. Shi, F. L. Macrae, and R. A. S. Ariëns, "Thrombus Structural Composition in Cardiovascular Disease," *Arterioscler. Thromb. Vasc. Biol.*, vol. 41, no. 9, pp. 2370–2383, 2021, doi: 10.1161/ATVBAHA.120.315754.

[351] P. Jolugbo and R. A. S. Ariëns, "Thrombus Composition and Efficacy of Thrombolysis and Thrombectomy in Acute Ischemic Stroke," *Stroke*, no. March, pp. 1131–1142, 2021, doi: 10.1161/STROKEAHA.120.032810.

[352] S. Prabhakaran, I. Ruff, and R. A. Bernstein, "Acute stroke intervention: A systematic review," *JAMA - J. Am. Med. Assoc.*, vol. 313, no. 14, pp. 1451–1462, 2015, doi: 10.1001/jama.2015.3058.

[353] D. Vivien, “Can the benefits of rtPA treatment for stroke be improved?,” *Rev. Neurol. (Paris).*, vol. 173, no. 9, pp. 566–571, 2017, doi: 10.1016/j.neurol.2017.07.003.

[354] A. Chang, E. Beheshtian, E. J. Llinas, O. R. Idowu, and E. B. Marsh, “Intravenous Tissue Plasminogen Activator in Combination With Mechanical Thrombectomy: Clot Migration, Intracranial Bleeding, and the Impact of ‘Drip and Ship’ on Effectiveness and Outcomes,” *Front. Neurol.*, vol. 11, no. December, pp. 1–10, 2020, doi: 10.3389/fneur.2020.585929.

[355] C. Liu *et al.*, “Hemorrhagic Transformation After Tissue Plasminogen Activator Treatment in Acute Ischemic Stroke,” *Cell. Mol. Neurobiol.*, vol. 42, no. 3, pp. 621–646, 2022, doi: 10.1007/s10571-020-00985-1.

[356] G. W. J. Harston, B. A. Sutherland, J. Kennedy, and A. M. Buchan, “The contribution of L-arginine to the neurotoxicity of recombinant tissue plasminogen activator following cerebral ischemia: A review of rtPA neurotoxicity,” *J. Cereb. Blood Flow Metab.*, vol. 30, no. 11, pp. 1804–1816, 2010, doi: 10.1038/jcbfm.2010.149.

[357] M. Gomis and A. DÃvalos, “Recanalization and Reperfusion Therapies of Acute Ischemic Stroke: What have We Learned, What are the Major Research Questions, and Where are We Headed?,” *Front. Neurol.*, vol. 5, no. November, pp. 1–12, 2014, doi: 10.3389/fneur.2014.00226.

[358] L. A. Perkins, C. J. Anderson, and E. M. Novelli, “Targeting P-selectin adhesion molecule in molecular imaging: P-selectin expression as a valuable imaging biomarker of inflammation in cardiovascular disease,” *J. Nucl. Med.*, vol. 60, no. 12, pp. 1691–1697, 2019, doi: 10.2967/jnumed.118.225169.

[359] F. Rouzet *et al.*, “Radiolabeled fucoidan as a P-selectin targeting agent for in vivo imaging of platelet-rich thrombus and endothelial activation,” *J. Nucl. Med.*, vol. 52, no. 9, pp. 1433–1440, 2011, doi: 10.2967/jnumed.110.085852.

[360] L. Auboire *et al.*, “Microbubbles combined with ultrasound therapy in ischemic stroke: A systematic review of in-vivo preclinical studies,” *PLoS One*, vol. 13, no. 2, pp. 1–19, 2018, doi: 10.1371/journal.pone.0191788.

[361] J. M. Lee, Z. U. Shin, G. T. Mavlonov, I. Y. Abdurakhmonov, and T. H. Yi, “Solid-phase colorimetric method for the quantification of fucoidan,” *Appl. Biochem. Biotechnol.*, vol. 168, no. 5, pp. 1019–1024, 2012, doi: 10.1007/s12010-012-9837-y.

[362] A. J. Koning, P. Y. Lum, J. M. Williams, and R. Wright, “DiOC6 staining reveals organelle structure and dynamics in living yeast cells,” *Cell Motil. Cytoskeleton*, vol. 25, no. 2, pp. 111–128, 1993, doi: 10.1002/cm.970250202.

[363] C. Orset *et al.*, "Mouse model of in situ thromboembolic stroke and reperfusion," *Stroke*, vol. 38, no. 10, pp. 2771–2778, 2007, doi: 10.1161/STROKEAHA.107.487520.

[364] O. Couture, M. Fink, and M. Tanter, "Ultrasound contrast plane wave imaging," *IEEE Trans. Ultrason. Ferroelectr. Freq. Control*, vol. 59, no. 12, pp. 2676–2683, 2012, doi: 10.1109/TUFFC.2012.2508.

[365] L. D. C. Casa and D. N. Ku, "Thrombus Formation at High Shear Rates," *Annu. Rev. Biomed. Eng.*, vol. 19, pp. 415–433, 2017, doi: 10.1146/annurev-bioeng-071516-044539.

[366] A. Sridharan, J. R. Eisenbrey, F. Forsberg, N. Lorenz, L. Steffgen, and A. Ntoulia, "Ultrasound contrast agents: microbubbles made simple for the pediatric radiologist," *Pediatr. Radiol.*, vol. 51, no. 12, pp. 2117–2127, 2021, doi: 10.1007/s00247-021-05080-1.

[367] Y. Itagaki, "Purification and Characterization of Tissue Plasminogen Activator secreted by Human Embryonic Lung Diploid Fibroblasts," vol. 55, no. 5, pp. 1225–1232, 1991.

[368] S. Fokong, M. Siepmann, Z. Liu, G. Schmitz, F. Kiessling, and J. Gätjens, "Advanced Characterization and Refinement of Poly N-Butyl Cyanoacrylate Microbubbles for Ultrasound Imaging," *Ultrasound Med. Biol.*, vol. 37, no. 10, pp. 1622–1634, 2011, doi: 10.1016/j.ultrasmedbio.2011.07.001.

[369] T. Bonnard and C. E. Hagemeyer, "Ferric chloride-induced thrombosis mouse model on carotid artery and mesentery vessel," *J. Vis. Exp.*, vol. 2015, no. 100, pp. 1–6, 2015, doi: 10.3791/52838.

[370] Y. Zhu, L. Guan, and Y. Mu, "Combined low-frequency ultrasound and urokinase-containing microbubbles in treatment of femoral artery thrombosis in a rabbit model," *PLoS One*, vol. 11, no. 12, pp. 1–13, 2016, doi: 10.1371/journal.pone.0168909.

[371] T. Ojha *et al.*, "Shelf-life evaluation and lyophilization of PBCA-based polymeric microbubbles," *Pharmaceutics*, vol. 11, no. 9, 2019, doi: 10.3390/pharmaceutics11090433.

[372] A. Zhu, P. Rajendram, E. Tseng, S. B. Coutts, and A. Y. X. Yu, "Alteplase or tenecteplase for thrombolysis in ischemic stroke: An illustrated review," *Res. Pract. Thromb. Haemost.*, vol. 6, no. 6, pp. 1–13, 2022, doi: 10.1002/rth2.12795.

[373] L. Shang, K. Nienhaus, and G. U. Nienhaus, "Engineered nanoparticles interacting with cells: Size matters," *J. Nanobiotechnology*, vol. 12, no. 1, pp. 1–11, 2014, doi: 10.1186/1477-3155-12-5.

[374] Z. He, J. Liu, and L. Du, "The unexpected effect of PEGylated gold nanoparticles on the

primary function of erythrocytes," *Nanoscale*, vol. 6, no. 15, pp. 9017–9024, 2014, doi: 10.1039/c4nr01857e.

[375] A. V. Alexandrov *et al.*, "Safety and efficacy of sonothrombolysis for acute ischaemic stroke: a multicentre, double-blind, phase 3, randomised controlled trial," *Lancet Neurol.*, vol. 18, no. 4, pp. 338–347, 2019, doi: 10.1016/S1474-4422(19)30026-2.

[376] T. R. Porter and W. Mathias, "Cardiovascular Sonothrombolysis," *Curr. Cardiol. Rep.*, vol. 21, no. 8, 2019, doi: 10.1007/s11886-019-1167-z.

[377] X. Lin *et al.*, "Establishment of a Modified and Standardized Ferric Chloride-Induced Rat Carotid Artery Thrombosis Model," *ACS Omega*, vol. 7, no. 10, pp. 8919–8927, 2022, doi: 10.1021/acsomega.1c07316.

[378] C. Orset *et al.*, "Efficacy of Alteplase® in a mouse model of acute ischemic stroke : a Retrospective Pooled Analysis," *Stroke*, vol. 47, no. 5, pp. 1312–1318, 2016, doi: 10.1161/STROKEAHA.116.012238.Efficacy.

[379] J. M. Correas, L. Bridal, A. Lesavre, A. Méjean, M. Claudon, and O. Hélénon, "Ultrasound contrast agents: Properties, principles of action, tolerance, and artifacts," *Eur. Radiol.*, vol. 11, no. 8, pp. 1316–1328, 2001, doi: 10.1007/s003300100940.

[380] D. D. Zhang *et al.*, "Inflammatory biomarkers and cerebral small vessel disease: a community-based cohort study," *Stroke Vasc. Neurol.*, vol. 7, no. 4, pp. 302–309, 2022, doi: 10.1136/svn-2021-001102.

[381] G. Pusch *et al.*, "Early Dynamics of P-selectin and Interleukin 6 Predicts Outcomes in Ischemic Stroke," *J. Stroke Cerebrovasc. Dis.*, vol. 24, no. 8, pp. 1938–1947, 2015, doi: 10.1016/j.jstrokecerebrovasdis.2015.05.005.

[382] S. Wiseman, F. Marlborough, F. Doubal, D. J. Webb, and J. Wardlaw, "Blood markers of coagulation, fibrinolysis, endothelial dysfunction and inflammation in lacunar stroke versus non-lacunar stroke and non-stroke: Systematic review and meta-analysis," *Cerebrovasc. Dis.*, vol. 37, no. 1, pp. 64–75, 2014, doi: 10.1159/000356789.

[383] U.S. DEPARTMENT OF HEALTH AND HUMAN SERVICES, "Toxicological Profile for Formaldehyde," *ATSDR's Toxicol. Profiles*, no. July, 2002, doi: 10.1201/9781420061888_ch87.

[384] J. N. Fink, M. H. Selim, and S. Kumar, "Why are stroke patients excluded from tPA therapy? An analysis of patient eligibility," *Neurology*, pp. 1–6, 2001.

[385] C. Orset, K. Arkelius, A. Anfray, K. Warfvinge, D. Vivien, and S. Ansar, "Combination treatment with U0126 and rt-PA prevents adverse effects of the delayed rt-PA treatment after acute ischemic stroke," *Sci. Rep.*, vol. 11, no. 1, pp. 1–10, 2021, doi:

10.1038/s41598-021-91469-9.

[386] C. Ducroux *et al.*, “Thrombus neutrophil extracellular traps content impair tPA-induced thrombolysis in acute ischemic stroke,” *Stroke*, vol. 49, no. 3, pp. 754–757, 2018, doi: 10.1161/STROKEAHA.117.019896.

[387] S. S. Seyedian, F. Nokhostin, and M. D. Malamir, “A review of the diagnosis, prevention, and treatment methods of inflammatory bowel disease,” *J. Med. Life*, vol. 12, no. 2, pp. 113–122, 2019, doi: 10.25122/jml-2018-0075.

Abstract

Ultrasound responsive microbubbles for the targeted treatment of thrombotic diseases

Keywords: Microbubbles, Original synthesis, Thrombotic diseases, Ultrasound, Targeted fibrinolysis, Fucoidan, Sonothrombolysis

Thrombotic diseases such as stroke, atherosclerosis or myocardial infarction are among the cardiovascular diseases, the leading causes of death in the World. These pathologies are the result of genetic but also environmental factors that will keep having an impact with the aging of the world population. Current treatments are effective in disassembling the fibrin mesh surrounding blood clots with plasminogen Tissue Activator (tPA), but are limited by a short therapeutic window (less than 4.5 hours) and their systemic injection leads to collateral damages (neurotoxicity, collateral hemorrhages). The aim of this research was to develop an original approach for the delivery of tPA at the site of the thrombotic accident to overcome the various life-threatening side effects of gold standard treatment.

Thus, we have developed functionalized microbubbles (MBs) allowing the targeted transport of tPA for an effective treatment of thrombotic diseases. Indeed, MBs are already widely used as contrast agents for ultrasound imaging and have a therapeutic potential for mechanical disruption of the clot with sonothrombolysis. Thereafter a deep study of MBs applications, we develop an original synthesis method for biocompatible polymer shell MBs with acoustic cavitation. The functionalization relied on the shell incorporation of fucoidan because of its nanomolar affinity for P-selectins, specific biomarker of thrombotic events. Following the validation of the efficient tPA loading, their complete characterization allowed the achievement of a proof-of-concept on a stroke mice model. These functionalized MBs have demonstrated the effectiveness of targeted therapeutic delivery, at a reduced drug dose, without generating deleterious side effects. So, this work opens ambitious prospects for the development of MBs for the targeted treatment and molecular diagnosis of thrombotic diseases.

Résumé

Microbulles échogènes pour le traitement ciblé des maladies thrombotiques

Mots-clés : Microbulles, Synthèse originale, Maladies thrombotiques, Ultrasons, Fibrinolyse ciblée, Fucoïdane, Sonothrombolyse

Les maladies thrombotiques telles que les Accidents Vasculaires Cérébraux (AVC), l'athérosclérose ou les infarctus du myocarde font partie des maladies cardiovasculaires, première cause de mortalité dans le monde. Ces pathologies sont la conséquence de facteurs génétiques mais aussi environnementaux qui ne cesseront d'avoir un impact avec le vieillissement de la population mondiale. Les traitements actuels sont efficaces pour désassembler le maillage de fibrine entourant les caillots sanguins grâce à l'Activateur tissulaire de Plasminogène (tPA), mais sont limités par le temps de prise en charge (moins de 4,5 heures) et leur injection systémique conduit à des dommages collatéraux (neurotoxicité, hémorragies collatérales). L'objectif de ces travaux de recherche est de développer une approche originale permettant la délivrance du tPA sur le lieu de l'accident thrombotique, afin de surmonter les divers effets secondaires potentiellement mortels des traitements cliniques actuels.

Ainsi, nous avons développé des microbulles (MBs) fonctionnalisées permettant le transport ciblé du tPA pour un traitement efficace des maladies thrombotiques. Les MBs sont déjà largement utilisées en tant qu'agent de contraste pour l'imagerie ultrasonore et possèdent un potentiel thérapeutique pour la destruction mécanique du caillot par sonothrombolyse. Ainsi, après l'étude approfondie des multiples applications des MBs, nous avons développé une méthode de synthèse originale pour la synthèse de MBs biocompatibles à coque polymère par cavitation acoustique. Leur propriété ciblante repose sur l'incorporation du fucoïdane dans la coque, ce dernier ayant une affinité nanomolaire pour les P-sélectines, biomarqueur spécifique des accidents thrombotiques. Suite à la validation de l'incorporation du tPA, leur caractérisation complète a permis l'accomplissement d'une preuve de concept sur un modèle d'AVC chez la souris. Ces MBs fonctionnalisées ont démontré l'efficacité de la délivrance thérapeutique ciblée sans générer d'effets secondaires délétères, à dose thérapeutique réduite. Ce travail ouvre ainsi des perspectives ambitieuses pour le développement des MBs pour le traitement ciblé et le diagnostic moléculaire des maladies thrombotiques.

Annexes

List of scientific publications as author or co-author:

- **ANNEX 1**: A. Zenych *et al.*, "*Biomaterials Fucoidan-functionalized polysaccharide submicroparticles loaded with alteplase for efficient targeted thrombolytic therapy*". *Biomaterials*, vol. 277, no. August, 2021. doi: 10.1016/j.biomaterials.2021.121102.
- **ANNEX 2**: L. Fournier *et al.*, "*Microbubbles for human diagnosis and therapy*". *Biomaterials*, vol. 294, no. January, 2023. doi: 10.1016/j.biomaterials.2023.122025.
- **ANNEX 3**: Patent: "*Method for manufacturing bubbles having a polymeric shell using sound waves for generating the bubbles*". PCT/FR2022/050309. Inventors: Louise Fournier and Cédric Chauvierre. Assignee: INSERM Tranfert.
- **ANNEX 4**: L. Fournier *et al*., "rtPA-loaded fucoidan MBs for the targeted treatment of stroke". *Biomaterials*, with Editor (January 2023).
- **ANNEX 5**: A. Zenych *et al.*, "*Fucoidan-functionalized polysaccharide submicro-particles loaded with alteplase for efficient targeted thrombolytic therapy*". *Biomaterials*, vol. 277, no. August, 2021. doi: 10.1016/j.biomaterials.2021.121102.

List of international presentation and associated prices:

ESB 2021: 31st Annual Conference of the European Society for Biomaterials (5th-9th September 2021, fully virtual).

- **ANNEX 6**: Poster presentation: *Ultrasound responsive polymer microbubbles for an efficient targeted treatment of thrombotic diseases*.

Biomarkers of the Future 2021: from bedside to practice (23rd-24th November 2021, Paris, France).

- **ANNEX 7**: Oral presentation: *Ultrasound responsive polymer microbubbles for an efficient targeted treatment of thrombotic diseases.*
- **ANNEX 8:** ***4th prize for best oral presentation*.**

SFNano 2021: 7th Annual meeting of the French Society of Nanomedicine (6th-8th December 2021, Angers, France).

- **ANNEX 9:** Oral presentation: *Ultrasound responsive polymer microbubbles for an efficient targeted treatment of thrombotic diseases.*
- **ANNEX 10:** ***1st prize for best oral presentation*.**

ESB 2022: 32nd Annual Conference of the European Society for Biomaterials (4th-8th September 2022, Bordeaux, France).

- **ANNEX 11**: Oral presentation: *Ultrasound responsive polymer microbubbles for a targeted treatment of thrombotic disease.*

SFNano 2022: 8th Annual meeting of the French Society of Nanomedicine (5th-7th December 2022, Strasbourg, France).

- **ANNEX 12:** Poster presentation: *US responsive polymer microbubbles for the targeted treatment of stroke.*

Early Career Research Congress 2022: 1st Annual meeting of the Institut des Sciences Cardiovasculaires (9th December 2022, Paris, France).

- **ANNEX 12**: Poster presentation: *US responsive polymer microbubbles for the targeted treatment of stroke.*
- **ANNEX 13:** ***1st prize for best poster presentation*.**

ANNEX 1

Biomaterials 258 (2020) 120297

Contents lists available at ScienceDirect

Biomaterials

journal homepage: www.elsevier.com/locate/biomaterials

Review

Nanomedicine progress in thrombolytic therapy

Alina Zenych, Louise Fournier, Cédric Chauvierre *

Université de Paris, Université Sorbonne Paris Nord, UMRS1148, INSERM, F-75018, Paris, France

ARTICLE INFO

Keywords:
Thrombolytics
Targeted thrombolysis
Thrombolytic therapy
Nanomedicine
Nanoparticles
Microbubbles

ABSTRACT

Thrombotic occlusions of blood vessels are responsible for life-threatening cardiovascular disorders such as myocardial infarction, ischemic stroke, and venous thromboembolism. Current thrombolytic therapy, the injection of Plasminogen Activators (PA), is yet limited by a narrow therapeutic window, rapid drug elimination, and risks of hemorrhagic complications. Nanomedicine-based vectorization of PA protects the drug from the enzymatic degradation, improves the therapeutic outcomes, and diminishes adverse effects in preclinical models. Herein, we review the pathophysiology of arterial and venous thrombosis and summarize clinically approved PA for the treatment of acute thrombotic diseases. We examine current challenges and perspectives in the recent key research on various (lipid, polymeric, inorganic, biological) targeted nanocarriers intended for the site-specific delivery of PA. Microbubbles and ultrasound-assisted sonothrombolysis that demonstrate thrombolysis enhancement in clinical trials are further discussed. Moreover, this review features strategies for the rational design of nanocarriers for targeted thrombolysis and effective PA encapsulation in view of interactions between nanomaterials and biological systems. Overall, nanomedicine represents a valued approach for the precise treatment of acute thrombotic pathologies.

1. Introduction

Cardiovascular diseases (CVD), the major global health threat, are associated with high morbidity and mortality that account for an estimated 17.9 million lives each year (31% of all deaths worldwide) [1], and this figure is expected to rise to >23.6 million annual deaths by 2030 [2]. CVD are a group of disorders of the heart (e.g., heart failure, rheumatic heart disease, abnormal heart rhythms, inflammatory heart diseases, cardiomyopathy) and blood vessels (coronary artery disease, cerebrovascular disease, aortic aneurysms, peripheral artery disease, etc.). CVD affect almost equally men as women, however, the disease develops about seven to ten years later in women as compared to men [3]. Furthermore, CVD are associated with substantial health-care costs, which are estimated at $329.7 billion annually in the United States [2] and nearly €200 billion in the European Union [4].

A large number of CVD may be prevented by addressing major risk factors through lifestyle interventions and pharmaceutical treatment where necessary [1]. Nevertheless, hypertension, the leading cardiovascular risk factor, is attributed to ~13% of global deaths (7.5 million deaths), followed by tobacco use 9%, diabetes 6%, physical inactivity 6%, obesity 5%, and high cholesterol level 4.5% [3].

Three major cardiovascular disorders – myocardial infarction (heart attack), ischemic stroke, and venous thromboembolism defined as deep vein thrombosis and/or pulmonary embolism – are severe complications of thrombosis, the formation of a blood clot in the vessels (Fig. 1). Within all deaths from CVD, 85% are caused by heart attacks and strokes, one-third of them in people under the age of 70 years [1]. To improve human survival and quality of life, early detections and effective treatments are principal.

Thrombolytic drugs are administered to dissolve a thrombus and restore the blood flow in acute thrombotic events, however, they are rapidly inactivated in the blood and trigger hemorrhagic complications, as we explain below. Paradoxically, while rapid reperfusion is the standard of care to minimize the infarct size, the restoration of blood flow itself may provoke irreversible tissue damage in a process called reperfusion injury [5]. Therefore, the pursuit of innovative solutions for the management of thrombotic diseases remains an open field of research, where nanomedicine is emerging to be a promising strategy to improve both the efficacy and safety of thrombolytic therapy.

This review delves into the preclinical research on nano- or microparticles of various composition for delivering fibrinolytic agents, reported during the last 10 years. Ultrasound (US)-responsive microbubbles with thrombolytics are highlighted as a potential theranostic system for both US visualization of the pathologic thrombi and

* Corresponding author.
E-mail address: cedric.chauvierre@inserm.fr (C. Chauvierre).

https://doi.org/10.1016/j.biomaterials.2020.120297
Received 22 January 2020; Received in revised form 10 July 2020; Accepted 1 August 2020
Available online 6 August 2020
0142-9612/© 2020 Elsevier Ltd. All rights reserved.

their destruction by a combination of mechanical stress with increased penetration and drug potency.

The database searched included MEDLINE/PubMed and Science Direct for research articles published in English from 2010 to present, using the combinations of the keywords “nanomedicine”, “nanoparticles”, “microbubbles”, “liposomes”, “streptokinase”, “urokinase”, “tissue plasminogen activator”, “nanothrombolysis”, “thrombolytic therapy”, “drug delivery systems”, “thrombolysis”, “targeted thrombolysis”, etc.

1.1. Pathophysiology of arterial and venous thrombosis

Atherosclerosis is the key precursor of cardiovascular pathologies and it starts in adolescence. Atherosclerosis is a complex immune-inflammatory disorder whose progression involves multiple biological pathways that are influenced by genetic and environmental factors. Elevated plasma cholesterol level, hypertension, diabetes, tobacco smoking, male gender, and some inflammatory markers are among the proatherogenic risk factors of atherosclerosis, while physical exercise, a healthy diet, and high High-Density Lipoproteins (HDL) counts have an atheroprotective role [6].

Atherosclerotic lesions are initiated when the endothelium is activated by atherogenic and pro-inflammatory stimuli, such as primarily Vascular Cell Adhesion Molecule-1 (VCAM-1), intercellular adhesion molecule-1, E-selectin, and P-selectin [7]. It has been demonstrated a direct hemodynamic role in atherogenesis, notably by endothelial cells as their numerous signaling pathways are dependent on the hemodynamic patterns [8,9]. Low shear stress and turbulent flow at arterial curvature and branch points are major drivers of plaque development and instability. Plasma molecules and Low-Density Lipoproteins (LDL) penetrate dysfunctional endothelium into the subendothelial space where atherogenic lipoproteins are oxidized, mediated by myeloperoxidase, 15-lipoxygenase, and/or Nitric Oxide Synthase (NOS) [7]. Low-grade inflammation contributes to the disease progression due to the focal recruitment of circulating monocytes and T-lymphocytes [10]. Modulated by chemotactic cytokines, such as oxidized LDL and Monocyte Chemoattractant Protein-1 (MCP-1) [11], monocytes infiltrate arterial intima through transendothelial migration and differentiate into macrophages by internalizing the atherogenic lipoproteins via scavenger receptors. The incidence of the foam cells (lipid-laden macrophages) and their death by apoptosis and necrosis contribute to the formation of destabilizing atheromatous lipid-rich core within the plaque. Moreover, the foam cells express an array of inflammatory factors and produce proteolytic enzymes, such as Matrix MetalloProteinases (MMPs) [11], that are implicated in matrix degradation and plaque disruption [12]. To insulate the thrombogenic lipid-rich core of the atheroma from the bloodstream, the fibrous cap develops at the lesion site as a fibroproliferative response mediated by intimal smooth muscle cells. The recruitment of the smooth muscle cells and the production of the collagen-rich matrix are considered as beneficial since they protect

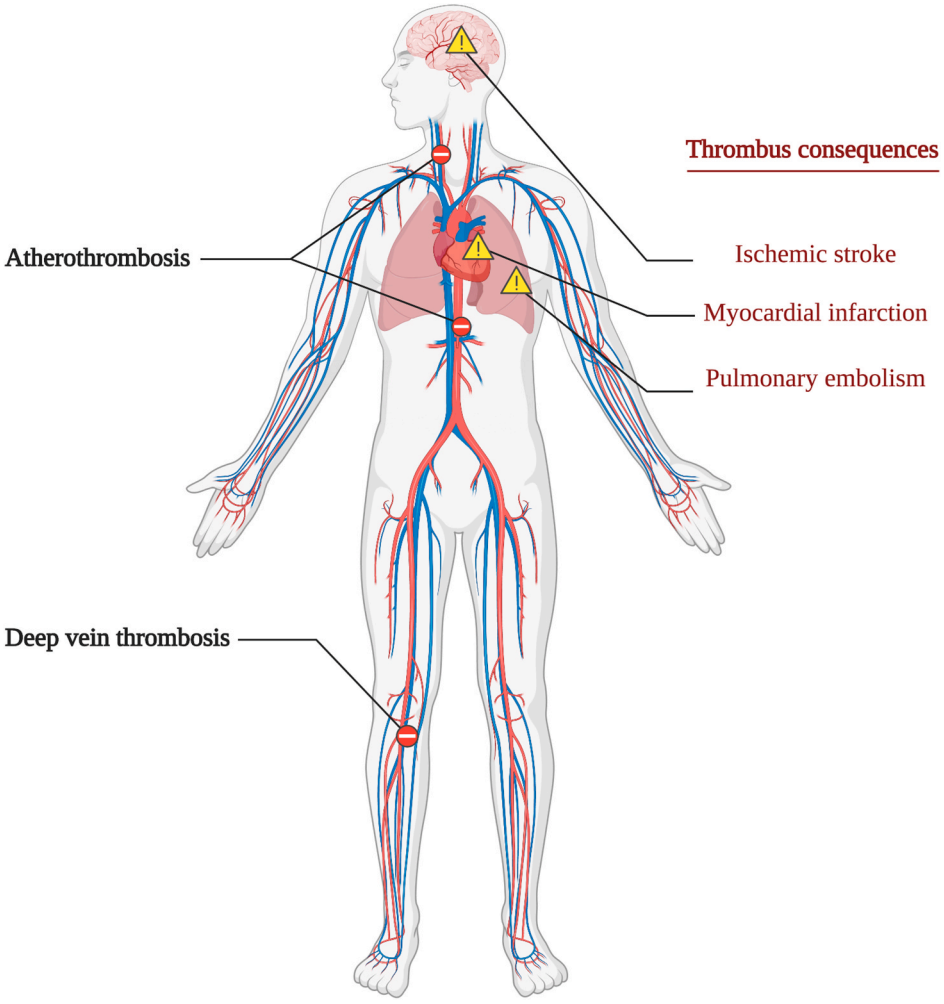

Fig. 1. Schematic of thrombotic diseases. Blot clot formation both in arteries (atherothrombosis) and veins (deep vein thrombosis) are influenced by congenital diseases and environmental factors. When the clot obstructs blood vessels in the brain, lungs, or heart, it may induce life-threatening consequences such as ischemic stroke, pulmonary embolism, or myocardial infarction.

the plaques against rupture and subsequent thrombosis. Conversely, the disintegration of foam cells and loss of smooth muscle cells may have detrimental consequences, leading to the formation of a destabilizing lipid-rich core and a fragile and rupture-prone fibrous cap. Atherosclerotic plaque calcification is an inflammation-driven process that manifests in all stages of the disease and should be defined as a two-phase process: microcalcification, the early stage of intimal calcium formation, and the end-stage of macrocalcification. While coronary Computed Tomography (CT)-detected macroscopic calcification in artery plaque acts as a biomarker of the overall disease progression, it is believed to stabilize the plaque and prevent acute events [13]. On the contrary, microcalcification, which can be identified by Positron Emission Tomography (PET)/CT imaging with ^{18}F-sodium fluoride, is associated with plaque vulnerability and an increased risk of rupture, since it aggravates plaque inflammation and augments mechanical stress in the fibrous cap [14].

Injury of the fibrous cap of atherosclerotic plaque is a primary trigger for arterial thrombosis, promoting hemorrhage and luminal prothrombotic response [15]. For initial flow obstruction, the blood coagulation cascade activates the platelets that are rapidly recruited to the site and aggregate, resulting in rapid thrombus growth [16] (Fig. 2A). Fibrin network then develops for the stabilization of platelet-rich thrombosis. Although most episodes of the ruptured fibrous cap occur silently without clinical symptoms, plague rupture with subsequent thrombosis often culminates in devastating clinical events such as myocardial infarction (MI) or ischemic stroke [15].

Contrary to atherothrombosis, the pathogenesis of Venous Thrombosis (VT) is only partially understood. The main components of the venous thrombi are fibrin and erythrocytes, and less activated platelets [17] (Fig. 2B). VT is initiated at the venous valves where stasis may occur under low shear blood flow [18]. Valvular sinus stasis aggravates hypoxia, promoting activation of the endothelium and leukocytes via mainly Hypoxia-Inducible Factor-1 (HIF-1) and Early Growth Response 1 (EGR-1) pathways. Besides, hypoxia condition modulates hypercoagulability. HIF-1 and EGR-1 pathways up-regulate the expression of P-selectin on endothelium, prompting monocytes to release microvesicles bearing tissue factor, which initiates thrombin production and fibrin deposition around the intact endothelial wall [19]. Both inherited and environmental factors raise the likelihood of the occurrence of venous thrombotic diseases, such as an imbalance of pro-vs. anti--coagulation proteins, as well as cancer, obesity, and major surgery [16].

1.2. Clinical treatment of acute thrombotic diseases

For the treatment of acute arterial or venous thrombotic events, fibrinolytic drugs can be administered in order to proteolytically disrupt blood clots and restore blood flow. Fibrinolytic, or thrombolytic, agents are Plasminogen Activators (PA) that activate the proenzyme

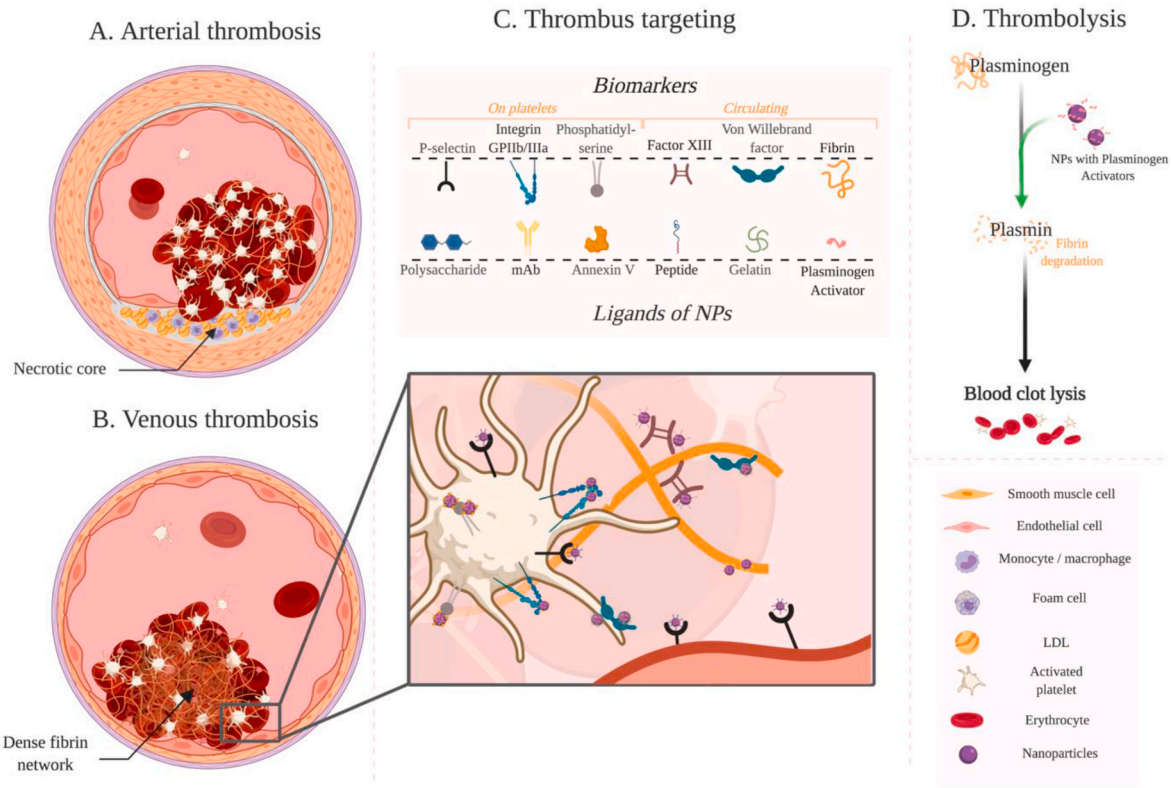

Fig. 2. Comparison of the arterial (A) and venous (B) thrombosis. Arterial clots (A) are composed of a high platelet ratio and are so-called "white thrombi". They are mostly the result of atherosclerosis. Multiple cellular pathways that initiate the activation of the endothelial cells are involved in thrombus formation. LDL penetrate the tissue, causing local inflammation and recruitment of circulating inflammatory cells. The disruption of the atherosclerotic plaque triggers the recruitment of smooth muscle cells to prevent wall rupture. Eventually, platelets aggregate on the impaired vessel wall with a consecutive formation of a fibrin network. On the other hand, venous clots (B), "red thrombi", contain erythrocytes and a denser fibrin network with fewer platelets. The thrombus formation is responsive to the following triggers: a vessel wall injury, a stasis of the blood flow, and hypercoagulability of the blood. C. Thrombus targeting with functionalized nano-/microparticles. Thrombi express a variety of cellular and molecular components – the surface of activated platelets (P-selectin, integrin GPIIb/IIIa, phosphatidylserine) or circulating proteins (Factor XIII, vWF, or fibrin) – that can be employed for specific targeting. NPs are designed with different ligands to these biomarkers: polysaccharide fucoidan, peptides, monoclonal antibodies, etc. D. Thrombolysis with PA-bearing and targeted to the thrombi NPs. The PA convert plasminogen into plasmin that breaks down the fibrin network and releases the components of the blood clot. Abbreviations: *LDL*, low-density lipoproteins; *vWF*, von Willebrand factor; *mAb*, monoclonal antibodies; *NPs*, nanoparticles; *PA*, plasminogen activators. (For interpretation of the references to color in this figure legend, the reader is referred to the Web version of this article.)

plasminogen to plasmin that then cleaves fibrin network into soluble degradation products. This activation of the fibrinolytic system destabilizes the structure of a thrombus [20]. Thrombolytic therapy is thereby used in patients with such pathologies as acute MI, acute ischemic stroke, peripheral arterial disease, deep vein thrombosis, and massive pulmonary embolism [21].

U.S. Food and Drug Administration (FDA)-approved "clot busters" drugs for use in thrombotic diseases are recombinant-based PA (e.g., alteplase – rtPA, reteplase – rPA, and tenecteplase – TNK), streptokinase (SK), and urokinase (uPA). The main differences between them relate to their antigenicity, half-life, lytic potential, fibrin specificity, and hemorrhagic risks [22]. First-generation thrombolytic drugs (urokinase, streptokinase) are non-fibrin specific when second and third-generation (alteplase and its variants) overcome this issue. Generally, human protein-derived PA (urokinase, alteplase, reteplase, tenecteplase) are nonantigenic, contrary to those derived from a bacterial species (streptokinase) [23]. The half-life of each PA determines their mode of administration (a bolus injection, short infusion, or continuous intravenous infusion). A comparison of different FDA-approved PA with their clinical indications is summarized in Table 1.

The leading drawbacks of fibrinolytic therapy include treatment failures such as ineffectiveness, re-thrombosis as a result of a persistent vascular lesion and plasma hypercoagulability, and a high risk of bleeding complications, with intracerebral hemorrhages occurring in 1–7% of treated patients [21]. Moreover, PA are physiologically inhibited by Plasminogen Activator Inhibitors (PAI) such as PAI-1 and PAI-2 while alpha 2-antiplasmin and alpha 2-macroglobulin inactivate plasmin, thereby reducing the treatment efficacy [24]. In view of these limitations, the constant development of novel molecules aims to address the problems associated with available thrombolytics. The novel candidates that are mutants of available PA or might be produced from the microbial, plant, and animal origin are discussed in the review [25].

The association of thrombolytic drugs with endovascular methods significantly improved interventional management of acute thrombotic events. The percutaneous coronary intervention has become more common for reperfusion, improving survival rates in patients with MI [26,27]. When available, this catheter-based procedure that is performed by an interventional cardiologist has to be offered promptly after/or in place of initial thrombolytic therapy. Since 2015, mechanical thrombectomy (MT) using a stent retriever is recommended as a complementary treatment to fibrinolytic therapy for ischemic stroke related to large vessel occlusions in the anterior circulation such as in the internal carotid artery and proximal middle cerebral artery [28,29] after multiple positive randomized control trials [30,31]. Yet, since MT needs to be performed by a qualified neurointerventionist at comprehensive stroke centers, access to them often remains difficult. In France, in particular, out of 135 nationwide neurovascular centers, only 40 are capable of performing thrombectomy to date [32]. Therefore, there is still a dire need for a safe and non-invasive solution.

With the advent of the field of nanotechnology, there has been considerable interest in integrating nanomedicine and thrombolytic therapy for the treatment of acute thrombotic events. Nanomedical approaches for targeted fibrinolysis could advance clinical outcomes by improving current pharmaceutical methods when interventional catheter-based strategies are not available or not recommended (as, for example, in ischemic stroke due to occlusions in smaller vessels or posterior circulation). By acting locally at the thrombus site, there is a promise that nanomedicine-delivered "clot-busting" agents deliver superior recanalization rates and attenuate life-threatening bleeding complications associated with their intravenous administration. One may also expect the chance to replace intravenous infusion by bolus injection of the first- and second-generation PA due to the extended drug half-life. In the ideal treatment settings, the synergic combination of endovascular and nanotherapeutic methods would represent a more precise approach to manage thrombotic pathologies.

2. Nanomedicine for targeted drug delivery

Nanomedicine, a medical application of nanotechnology, combines a powerful set of nano-engineered devices for diagnostic and/or therapeutic applications. Nanoparticle (NP)-based drug delivery can increase drug circulation time, improve therapeutic efficacy, and reduce unwanted off-target effects by delivering an active molecule to the injury site [33]. The liposomal formulation of doxorubicin – Doxil® – was the first clinically approved nanomedicine therapy by the FDA in 1995 for the Kaposi's sarcoma and other cancers that reduced cardiotoxicity compared with a conventional formulation [34]. Other NP formulations are approved for the treatment of distinct pathologies, such as cancers, fungal infections, iron-deficient anemia, macular degeneration, as well as vaccines for hepatitis A and influenza [35,36].

Different nano- or microcarriers (e.g., liposomes, polymeric, magnetic nano- & microparticles, quantum dots, nanotubes, dendrimers) are similarly researched in the therapeutic area of CVD [37]. Nanotechnology plays a role for wide-ranging cardiovascular applications, such as hypertension [38], atherosclerosis [39], prevention of restenosis following interventional cardiology [40], ablation for atrial fibrillation [41], cardiac tissue engineering [42], but also in the management of aneurysms [43] as well as CVD prevention [44].

Table 1
Thrombolytic agents approved by the FDA.

Agent	Abbreviation	Source	Safety [immunogenicity, fibrin specificity]	Half-life, min	Regimen	Total Dose	Metabolism	Indication
First-generation								
Streptokinase	SK	β-hemolytic streptococcus	Immunogenic Non-fibrin specific	20	Infusion	1.5×10^6 IU	Renal	PE Acute MI PAO, DVT
Urokinase	uPA	Human urine & kidney cell culture	Non-fibrin specific	15	Infusion	$2.25–6.25 \times 10^6$ IU	Renal	PE Acute MI PAO, DVT
Second-generation								
Alteplase	rtPA	Recombinant DNA technology	Fibrin specific (++)	4–8	Infusion	MI: 50–100 mg IS: 0.9 mg/kg PE: 100 mg	Hepatic	Acute MI Acute IS PE
Third-generation								
Reteplase	rPA	Recombinant DNA technology	Fibrin specific (+)	14–18	Double bolus	20 IU	Renal	Acute MI PAO
Tenecteplase	TNK		Fibrin specific (+++)	11–20	Bolus	30–50 mg	Renal	Acute MI

Abbreviations: *DVT*, Deep Vein Thrombosis; *MI*, Myocardial Infarction, *PAO*, Peripheral Arterial Occlusion; *PE*, Pulmonary Embolism; *IS*, Ischemic Stroke; *IU*, International Units.

2.1. Evolution and milestones in the progress of nanomedicine for fibrinolytic therapy

The field of nanomedicine in fibrinolytic therapy is evolving vibrantly, as evidenced by the expanding list of preclinical concepts of nanomaterial complexation with PA. An ideal vehicle for thrombolytic drug delivery should be biocompatible, non-toxic, non-immunogenic, biodegradable, and should avoid rapid clearance by the immune system [45]. The benefits of utilization of the nanoparticles (NPs) are attributed to their high surface-volume ratio, multifunctionality, high bioavailability, and possible control of therapeutic agent release. Control drug release facilitates the release of the payload from the NPs at the thrombus site upon internal or external stimuli such as temperature [46,47], pH [48], US [49], or magnetic field [46], etc. Specific thrombus targeting can be achieved by modifying the surface of nanocarriers with targeting moieties (antibodies, aptamers, polysaccharides, peptides, and small molecules) and/or application of magnetic energy, enhancing the therapeutic effect due to accumulation of thrombolytic drug at the clot surface [50] (Fig. 2C and D). Furthermore, encapsulation of the fibrinolytic drug onto the NPs can protect it from inactivation by PAI-1 in the bloodstream [51] and prolong its blood circulation time [48,52,53], thus achieving safe and effective thrombolysis at a lower dose [54,55]. Nanocarrier protection may further limit drug leakage during circulation, reducing the risk of hemorrhagic complications [56,57] such as cerebral hemorrhages that often accompany the injection of free plasminogen activators.

The timeline shown in Fig. 3 depicts evolution and milestones in the conceptual advances of nanomedicine-facilitated thrombolysis.

The story begins in the late '80s when dextran-coated iron oxide microparticles loaded with SK were utilized for magnetically driven thrombolysis of the carotid arteries in dogs [58]. Around the same time, SK-bearing liposomes entered the field by accelerating reperfusion in acute MI [59]. The first reported microbubbles for sonothrombolysis in 1996 were initially composed of denatured albumin shells, however, this formulation is no longer used due to stability/immunogenicity issues [60]. Polymeric platforms in thrombolytic therapy started to emerge a decade later in order to improve a stability profile of the liposomes in biological fluids. In 2004, first-reported polymer microparticles were designed from Polyethylene Glycol (PEG) and loaded with SK to tackle coronary thrombosis in a canine model [61]. The early success of the rtPA-conjugated erythrocytes in thromboprophylaxis in 2003 led to the further investigation and development of diverse bio-inspired nano solutions [62]. These initial studies evidenced an undoubtable potential of nanomedicine to boost thrombolytic therapy in animal models, however, they often lacked a complete analysis in terms of particle physico-chemistry and safety, drug loading efficiency/release, targeting and thrombolytic efficacy in appropriate *in vitro* and subsequently *in vivo* models, which is currently recognized and adopted [63]. The evolution of nanomedicine-based fibrinolysis continued with the development of surface-coated, mostly nanosized particles that exhibit considerably longer circulation half-life *in vivo* and superior safety profiles than uncoated microparticles. Notable examples from late 00′ are the PA-bearing polymer NPs that were coated with chitosan and cRGD peptide, a prototype of the utilization of a popular targeting ligand of GPIIb/IIIa [64], as well as magnetic NPs coated with dextran [65] and polyacrylic acid [66] for magnetically guided thrombolysis.

The last decade, which we review in this paper, was fruitful for progress in nanomedicine-assisted thrombolysis. During these years, researchers commonly used active targeting strategies. Apart from magnetic targeting of iron oxide NPs, the utilization of monoclonal antibodies (mAb) and peptides that recognize biomarkers associated with thrombotic pathologies have allowed the development of more selective nanosystems that advanced into the multivalent design in 2017 [57]. In 2018, polymeric NPs were functionalized with fucoidan, affordable high-quality P-selectin ligand for site-specific fibrinolytic activity [67] as an alternative to costly mAb and peptides. From 2012, theranostic hybrid approaches emerge: inorganic nanocarriers that serve for thrombolysis and optical imaging [68] or MRI [69]. Echogenic liposomes are widely studied with the *in vitro* clot model for sonothrombolysis due to tunable designs like targeting and/or rtPA loading [70]. Recently, targeting nanobubbles were published that complemented PA with sonothrombolysis, as they penetrate deeper into the clots comparing to microbubbles [71]. The nanoformulations with controlled release start appearing more frequently: via hemodynamic phenomena – increased shear stress in the stenotic arteries [72] and

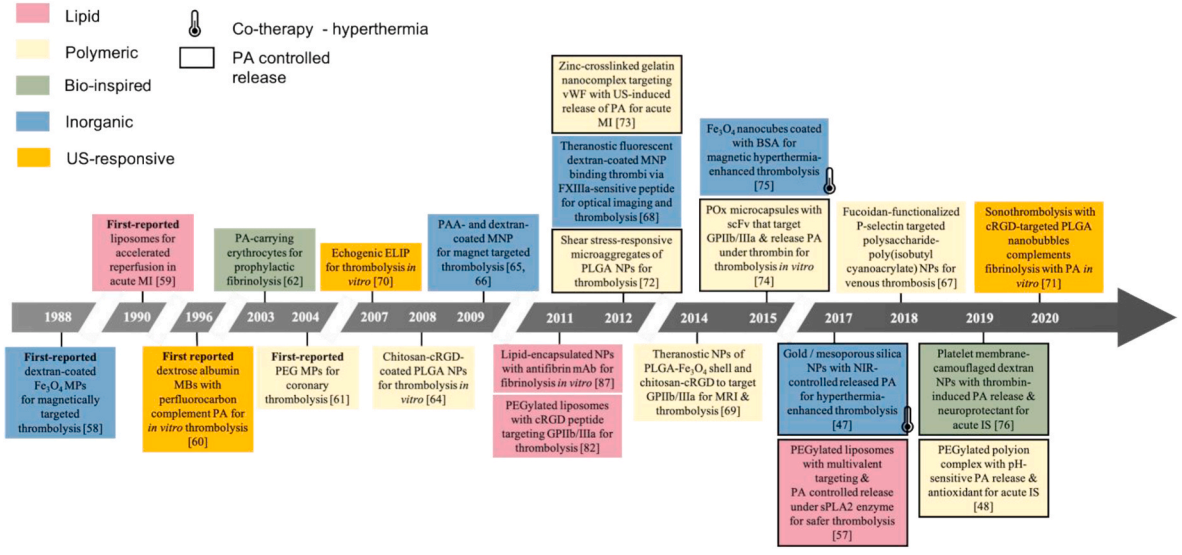

Fig. 3. The timeline of evolution and milestones in the progress of nanomedicine for fibrinolytic therapy: history and current trends. This figure mostly comprises the PA-loaded platforms tested with *in vivo* experiments; however, we also included several remarkable *in vitro* concepts. Abbreviations: *PA*, plasminogen activator; *MI*, myocardial infarction; *IS*, ischemic stroke; *PEG*, polyethylene glycol; *PLGA*, poly(lactic-co-glycolic acid); *PAA*, poly (acrylic acid); *BSA*, bovine serum albumin; *POx*, poly(2-oxazoline); *vWF*, von Willebrand Factor; *FXIIIa*, activated factor XIII; *$sPLA_2$*, secreted phospholipase A2 enzyme; *MNP*, magnetic nanoparticles; *MPs*, microparticles; *NPs*, nanoparticles; *MBs*, microbubbles; *ELIP*, echogenic liposomes; *mAb*, monoclonal antibodies; *scFv*, single-chain antibody; *MRI*, magnetic resonance imaging; *US*, ultrasound; *NIR*, near-infrared.

US-induced [73] in 2012, upon enzyme exposure since 2015 [74], elevated temperature since 2017 [47], and low pH in 2019 [48]. To enhance thrombolysis, adjuvant therapy in the form of local hyperthermia by a magnetic field [75] or near-infrared (NIR) light [47] was used in the late 10's.

Nowadays, the trend is to create complex multifunctional but, at the same time, biocompatible and biodegradable nanocarriers. Application of novel biomaterials, hybrid NPs with biomimetic surfaces, incorporating active targeting molecules, and the ability to modulate the release spatially and temporally is being widely researched. The researchers also commenced investigating the solution to complement nanomedicine-based fibrinolysis by counteracting the pathological processes related to ischemia with an antioxidant [48] and neuroprotection [76] approach for ischemic stroke in 2019.

In the next chapters, we are going to describe in detail the complexation of PA with different types of nanocarriers, which are summarized in Fig. 4, and their corresponding therapeutic effects in preclinical studies.

3. Lipid drug delivery

3.1. Liposomal drug delivery

Liposomes, first described in the mid-'60s, are defined as spherical vehicles made of an aqueous core surrounded by phospholipid bilayers. Since then, because of their excellent biocompatibility, low toxicity, and easy preparation methods, liposomes are considered as one of the most promising tools for drug delivery in medical fields of principally small molecules (e.g., chemotherapeutics) with some being clinically approved [77], but also proteins, DNA, RNA, and imaging probes [78].

Liposomes are generally fabricated by thin-film hydration, which consists of dissolving lipid components in an organic solvent, drying down by rotary evaporation, and rehydrating in water, as well as by freeze-drying, reverse-phase evaporation, or injection of ethanol with phospholipids into an aqueous phase. Membrane extrusion, sonication, and/or freeze-thawing are further employed to modulate the particle size [79]. In terms of the size and number of bilayers, different types of liposomes can be produced, such as small unilamellar vesicles (single phospholipid bilayer sphere), large unilamellar vesicles, and multilamellar vesicles (an onion structure of bilayers) [78]. The amphiphilic properties of liposomes allow them to internalize both hydrophilic and hydrophobic compounds.

Liposomal encapsulation of plasminogen activators for thrombus-specific drug delivery is frequently exploited to improve the drug half-life and reduce hemorrhagic side effects. Given that the conventional liposomes aggregate *in vivo* and undergo rapid systemic clearance via Mononuclear Phagocyte System (MPS) after contact with plasma proteins, decoration with FDA-approved PEG has been adopted to provide steric stabilization and reduce liposomal opsonization, and, therefore, to improve the pharmacokinetics of PA in blood [79].

The liposomal surface modification strategies by site-directed target ligands, such as antibodies, peptides, or stimuli-responsive drug release (thermo- or pH-sensitive liposomes) have been tested in the preclinical development. Most targeting approaches are directed towards Glyco-Protein IIb/IIIa (GPIIb/IIIa). GPIIb/IIIa is an integrin complex on the platelet membrane that mediates platelet adhesion and aggregation during hemostasis. Normally present in its inactive state on resting platelets, it undergoes conformational changes to allow the platelets to bind to fibrin upon platelet stimulation by physiologic ligands such as thrombin or collagen [80]. Thrombolytics are generally incorporated into the inner aqueous core of the liposomes during the synthesis process, however, they can also be adsorbed onto the surface or covalently grafted to the PEGylated liposomes [81].

In the study of Vaidya et al., long circulatory PEGylated liposomes were coupled with a cyclic Arg-Gly-Asp (cRGD) [CNPRGDY(OEt)RC] and targeted GPIIb/IIIa receptor both *in vitro* and *in vivo* [82]. Despite a low level of streptokinase release (12.20 ± 0.94%) over the course of 35 h, the study reported the improved thrombolysis rate of cRGD-targeting liposomal SK compared with free SK after 1 h in rats (34% vs. 22%). When rtPA was loaded onto both non-PEGylated and PEGylated GPIIb/IIIa-targeting liposomes, a favorable rtPA release profile from PEGylated ones was demonstrated in the work [52], with a substantial

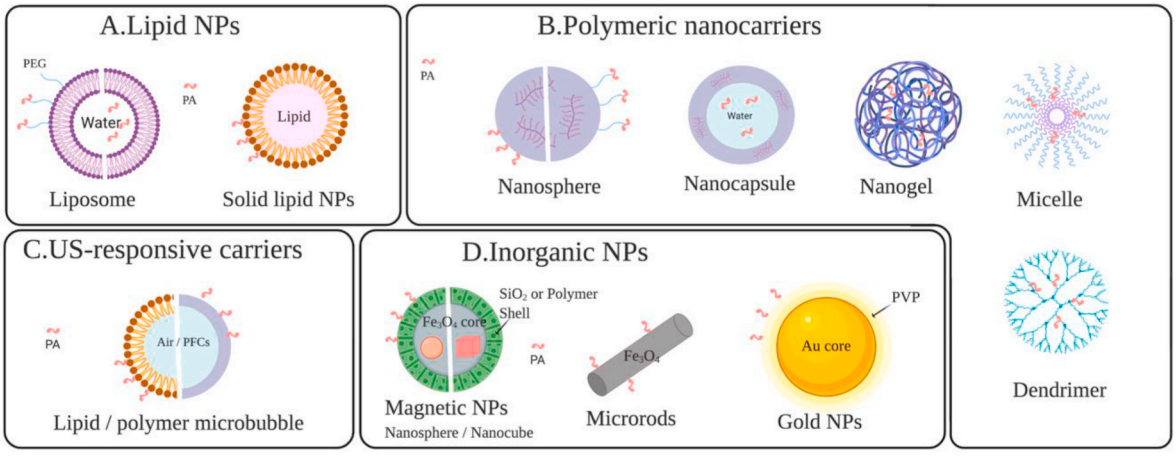

Fig. 4. Nanomedicine-based platforms with Plasminogen Activators. A. Lipid nanocarriers. In liposomes, PA may be embodied into the aqueous core or adsorbed/covalently conjugated onto the PEGylated phospholipid shell. In solid lipid NPs, PA is covalently grafted to their surface. B. Polymer-based nanoplatforms. PA are typically entrapped inside amphiphilic micelles and self-assembled gelatin or chitosan nanogels due to electrostatic interactions, incorporated into the aqueous core of nanocapsules, or covalently attached to the surface of the nanospheres and dendrimers via EDC/NHS chemistry. Surface decoration with PEGylation or polysaccharides is common for better stealth effects, particularly significant for the NPs from hydrophobic synthetic polymers. C. Ultrasound-responsive carriers. Microbubbles are microspheres filled with gas (e.g., C_4F_{10}, N_2, C_4F_8) or air, mostly coated with phospholipids or polymers that bind PA onto the outer layer via covalent interactions. Upon exposure to low-frequency ultrasound, microbubbles can burst to realize sonothrombolysis. D. Inorganic nanoparticles. In magnetic NPs, inner core – in the shape of nanospheres or nanocubes – is mostly iron oxide (Fe_3O_4), and the surface is decorated with organic (e.g., dextran, chitosan, polyacrylic acid) or inorganic (SiO_2) shell. PA is conjugated to the surface via EDC/NHS or simple adsorption. Uncoated iron oxide microrods may load PA via glutaraldehyde. Gold NPs immobilized PA via bio-affinity ligation. Abbreviations: *PEG*, Polyethylene glycol; *PA*, plasminogen activator; *NPs*, nanoparticles; *US*, ultrasound; *PVP*, polyvinyl pyrrolidone; *PFCs*, perfluorocarbons. (For interpretation of the references to color in this figure legend, the reader is referred to the Web version of this article.)

amount of drug released within 30 min after administration followed by a slow continuous release over 24 h. This strategy intends to achieve reperfusion and prevent re-thrombosis. The half-life of rtPA in plasma was prolonged from 7 min for native rtPA to 103 and 141 min for non-PEGylated and PEGylated liposomes. Besides, rtPA-loaded liposomes were 35% more potent than native rtPA for vessel recanalization but produced a 4.3-fold less depletion of circulating fibrinogen, potentially reducing hemorrhagic risks, in $FeCl_3$-rat venous thrombosis model.

Huang et al. exploited the targeted delivery and controlled release of rtPA incorporated into PEGylated liposomes coated with cRGD peptide [83]. Membrane fusion attributed to interactions between cRGD peptides on liposomes and GPIIb/IIIa integrins on activated platelets caused liposomal membrane destabilization and rtPA release. Due to this, over 90% of the entrapped rtPA was released within 1 h in targeted liposomes compared to <10% after 6 h in untargeted ones, and this release profile could be adjusted by altering the concentration of activated platelets. Zhang et al. [56] combined the active thrombus targeting with cRGD and gradual release of the drug from the liposomes without burst effect over 5 h. They improved the *in vivo* thrombolytic efficacy by ~4-fold over free uPA, at the same time shortening bleeding time of the tail bleeding assay of hemostasis, thereby potentially reducing the side effects of uPA.

In the elegant study [57], Pawlowski et al. took inspiration from platelet-derived microparticles that are plasma membrane vehicles shed from platelets that are undergoing activation, stress, or apoptosis (Fig. 5A) [84]. They designed a liposomal system with a multivalent targeting strategy towards both GPIIb/IIIa and P-selectin on activated platelets using the peptides CGSSSG*RGD*SPA and CDA*EWVDV*S, respectively (Fig. 5B and C). As the constructs could be degraded under secreted phospholipase A2 ($sPLA_2$) enzyme, secreted from leukocytes and active platelets in the thrombus, it could so release encapsulated SK (Fig. 5D and E). While thrombolytic efficacy of the targeted liposomes was comparable to free SK in $FeCl_3$-induced carotid artery thrombosis model, hemostatic capability for liposome-encapsulated SK was improved as measured by mouse tail bleeding time.

Hsu et al. [85] synthesized a hybrid NP-system, PEGylated thermosensitive magnetic liposomes (TMLs), encapsulating Fe_3O_4 NPs within liposomes, via solvent evaporation/sonication and freeze-thaw method.

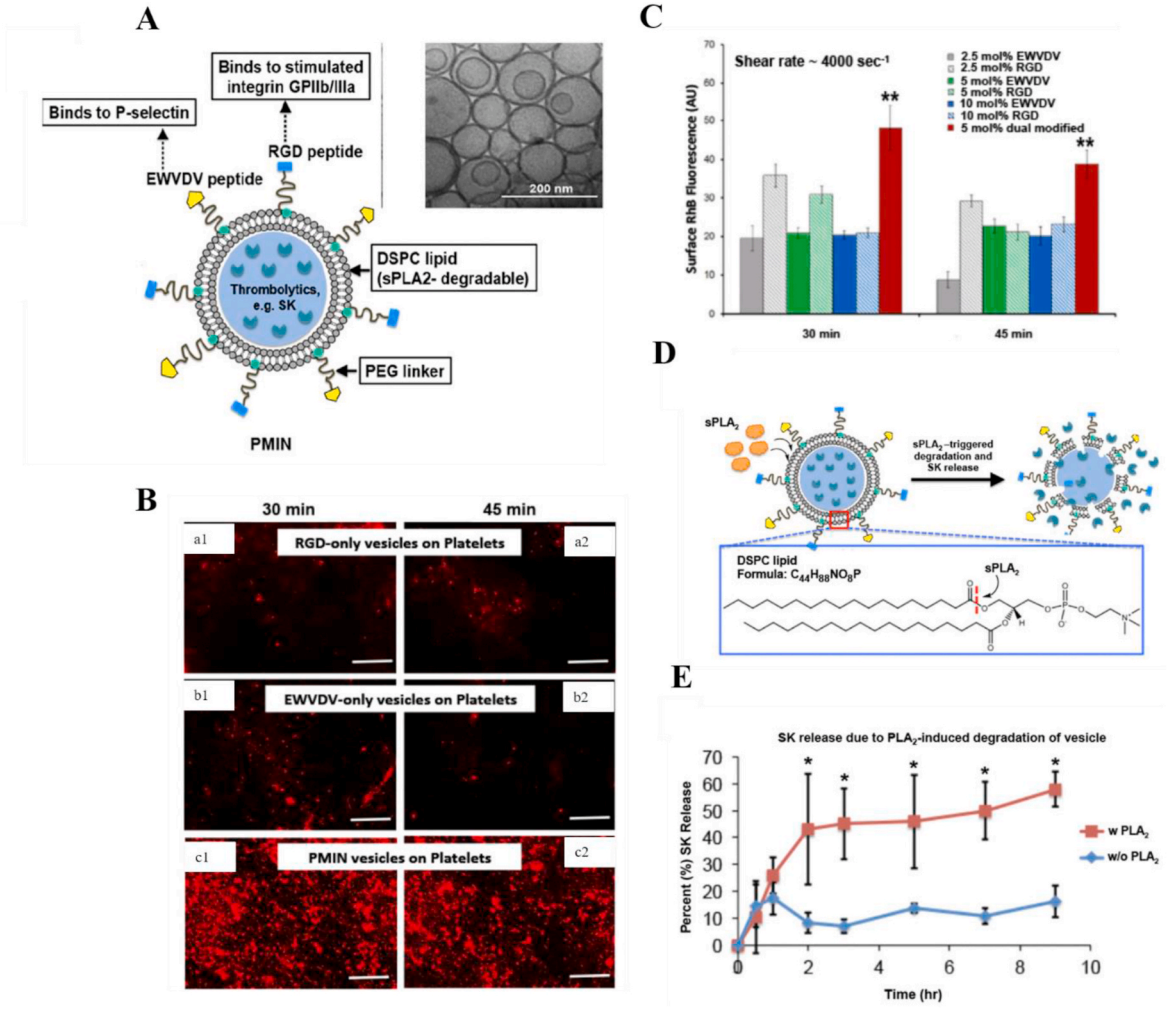

Fig. 5. A. Schematic representation of platelet-derived microparticles-inspired nanovesicle (PMIN) with dual-targeting strategy and controlled release of the thrombolytic upon sPLA2 enzyme exposure, with a representative cryo-TEM image of PMINs. B. Representative fluorescent images of particle binding show that RGD-decorated vesicles (a1, a2) and EWVDV-decorated vesicles (b1, b2) have a reasonable extent of binding and retention on the platelet-rich thrombus surface. However, the level of binding and retention levels are enhanced for dual modified PMINs (c1, c2). C. Quantitative analysis of fluorescence intensity shows that PMINs have significantly higher binding and retention capabilities compared to singly modified vesicles even when the mol% composition of single peptide modification is to twice (10 mol%) that of dual peptide modification (5 mol%) at high shear rate flow conditions. D. Schematic mechanism of sPLA2-induced membrane degradation due to cleavage of sn-2 acyl group of the phosphatidylcholine lipids. E. Release kinetics assessment of SK from PMINs shows that upon sPLA2 exposure, the percent (%) release of SK from PMINs is enhanced (~4 fold) compared to passive release without sPLA2 exposure. Adapted with permission from Ref. [57]. Copyright 2017 Elsevier Ltd.

Thrombolytic activity *in vitro* of rtPA-loaded TMLs at 43 °C was augmented as compared to at 37 °C due to enhanced drug release and higher enzyme activity at higher temperature. In addition to magnetic targeting, TMLs demonstrated a first-ever reported dual control mechanism of the drug release in serum: temperature- and magnet-sensitive, increasing at 43 °C and retarding with external magnetic force at 0.5 T in the follow-up work [46]. This technique could allow the liposomes to be magnetically guided toward the thrombus, preventing premature drug release. With appropriate biocompatibility of the nanocarriers, TML@rtPA restored arterial blood flow, iliac blood flow, and hind-limb perfusion, whereas the same dose of rtPA exerted no benefit in rat embolic model at 0.2 rtPA mg/kg under magnetic force at 43 °C.

3.2. Solid lipid nanoparticles

Solid Lipid Nanoparticles (SLNs) is an alternative drug delivery system. Contrary to conventional liposomes, which contain a lipid bilayer with an aqueous core, SLNs consist of lipid monolayer enclosing a solid lipid core stabilized by a surfactant, reaching a higher drug entrapment rate for a hydrophobic drug. Different preparation methods of SLNs include hot or cold homogenization, solvent emulsification/diffusion, or microemulsion [86]. Marsh et al. [87] prepared perfluorooctylbromide lipid-encapsulated NPs that can be assimilated to SLNs with a size 250 nm by emulsification/sonication method. Anti-fibrin mAb on the surface of the SLNs specifically targeted fibrin network in a canine model of the electrode-induced arterial thrombosis. Sulfhydryl functionalized uPA was covalently coupled to these SLNs and retained its fibrinolytic activity *in vitro*.

Overall, cRGD peptide-decorated PEGylated liposomes became a standard engineering approach in thrombolytic research owing to their cyto- and hemocompatibility [56] with a high potential for clinical translation, which might, in contrast, take longer for complex hybrid systems.

4. Polymeric drug delivery

Depending on the preparation method, polymeric NPs can have nanosphere or nanocapsule structures. Both naturally occurring hydrophilic polymers and synthetic biocompatible polymers are used in the NP fabrication and offer simple surface modification and functionalization [88]. Natural polymers such as polysaccharides (hyaluronan, alginate, and chitosan) and proteins (gelatin and albumin) are common [89]. Synthetic polymers come either in prepolymerized forms, such as polyesters like polycaprolactone (PCL), polylactic acid (PLA), or polymerized from the monomers, e.g., poly (methyl methacrylate), poly (alkyl cyanoacrylate) (PACA), poly (acrylic acid) (PAA), poly(lactic--*co*-glycolic acid) (PLGA), poly(2-oxazoline) (POx), and poly(amidoamine) (PAMAM). Synthetic polymers benefit from high purity and reproducibility over natural polymers; the latter, however, represent a significant interest due to their safety, abundance in nature, and low cost. Polymeric nanoparticles are conventionally fabricated by two methods: the dispersion of preformed polymers or the polymerization of monomers [90]. The plasminogen activators are typically dissolved and entrapped, or covalently attached to the surface of the NPs prepared from some of the above-mentioned polymers.

Chitosan (Cs), as well as its chemical derivatives, has been widely used because of its biocompatibility and biodegradability, low toxicity, and low immunogenicity in thrombolytic drug delivery. Chitosan is a cationic hydrophilic polysaccharide, derived from chitins, able to form polyelectrolyte complexes with negatively charged molecules [91].

Self-assembled chitosan NPs were produced via the ionic crosslinking with sodium tripolyphosphate, possessing a size 236 nm, and further loaded with uPA with encapsulation efficiency ~95% [92]. Both intravenous injection and catheter-driven drug delivery were tested in a thrombin-induced rabbit venous thrombosis, pointing out superior thrombolytic efficacy for the latter comparing with free uPA. Another group [93] elaborated a chitosan-based NPs/SK drug complexation via non-covalent interactions. Synthesis conditions such as pH and Cs concentration were optimized using a computational model. The team of Shamsi et al. reported the synthesis of uniform and spherical SK-entrapped chitosan NPs with a diameter 67 ± 13 nm and a narrow polydispersity by microfluidics [94]. A steady and sustained SK release was achieved during 48 h *in vitro* in addition to higher SK amidolytic activity in plasma in rats, comparing with free SK. Given that quaternized derivative of chitosan - N,N,N-Trimethyl Chitosan (TMC) has superior solubility and increased charge density, Liao et al. covalently grafted TMC with cRGD to target GPIIb/IIIa receptors [95]. The resulted cRGD-LK-NPs were formed with lumbrokinase (LK) via ionic gelation using sodium tripolyphosphate and could effectively accelerate thrombolysis in clot-occluded tubes and $FeCl_3$ rat carotid artery model at 90, 000 U/kg of LK.

Jin et al. prepared PEG crosslinked glycol chitosan hollow nanogels by an ultrasonic spray technique and loaded uPA with 80% loading efficiency. Such NP design improved uPA half-life in rats from 18 min to 40 min without causing biotoxicity. The application of diagnostic US at 2 MHz accelerated uPA release from the nanogels (90% of uPA released within 1 h vs. 80% within 6 h without the US) [53]. While the hollow cavity of the nanogels did not contain gas, they were responsive to the US due to the vibration of the polymer shell. The ultrasonic stimulation enhanced the thrombolysis *in vitro* for both free uPA and the uPA-loaded nanogels [53]. Notably, the nanogels allowed the delivery of uPA with no signs of a stroke or blood-brain barrier permeability damage after 24 h *in vivo* [96].

Gelatin, a protein obtained from the collagen hydrolysis, is an attractive natural macromolecule for a thrombolytic nanocarrier owing to its biocompatibility and biodegradability, and wide availability at low cost [97]. Gelatin-based NPs require crosslinking with glutaraldehyde or another bifunctional cross-linker during preparation, and their surface can be tuned with site-specific ligands, cationized with amine derivatives, or PEGylated.

Polyelectrolyte complex of cationized gelatin and anionic PEGylated gelatin with rtPA mutant (monteplase) fabricated a 200 nm thrombolytic delivery system [98]. While fibrinolytic activity *in vitro* was suppressed to 45% due to nanocomplexation, it was fully recovered under US stimulation (1 MHz, intensity 0.75 W/cm^2), demonstrating an ultrasound-responsive rtPA release. US control drug release can be explained by the production of the stable cavitation state and shear stress on the surrounding tissues [49]. In a rabbit thrombosis model, a combination of the US with rtPA-NPs allowed full vessel recanalization for all treated animals after 30 min, which was superior to free rtPA (10% recanalization after 60 min) and free rtPA + US (90% recanalization after 30 min).

Uesugi et al. further developed a zinc-crosslinked gelatin complex with monteplase [73], which restored its rtPA fibrinolytic activity upon US exposure *in vitro* [73] and *in vivo* to the level of free rtPA [54]. Monteplase-loaded NPs increased thrombus affinity 3-fold as a result of interactions of the gelatin with von Willebrand Factor (vWF), a blood glycoprotein that is a crucial component of platelet-rich thrombi. In a swine model of acute myocardial infarction, treatment with rtPA alone dissolved only 30% of occluded coronary thrombi at a dose of 55,000 IU/kg and no thrombi at 27,500 IU/kg within 60 min, while NPs carrying 55,000 IU/kg rtPA achieved recanalization of 90% thrombi within 30 min comparing to 60% of cases in 60 min at a dose of 27,500 IU/kg, under continuous-wave US field (1 MHz, 1 W/cm^2) [54].

Poly(d,l-lactic-co-glycolic acid) (PLGA), a synthetic biodegradable polymer that is relatively hydrophobic, has the FDA and the European Medicine Agency (EMA) approval for drug delivery systems. The PLGA micro- or nanoparticles are mostly synthesized by a double emulsion solvent evaporation system with poly(vinyl alcohol) (PVA) as an emulsion stabilizer [99].

In order to establish slow and controlled thrombolysis and prevent abdominal aortic aneurysm rupture, Sivaraman et al. produced PLGA

NPs with 10 μg rtPA using didodecyldimethylammonium bromide (DMAB) or PVA as a surfactant [100]. DMAB-stabilized NPs demonstrated gradual clot lysis and higher binding to the fibrin clots. Nano-delivery system overall improved the proliferation of the aneurysmal smooth muscle cells (EaRASMC) exposed to the clot lysis byproducts, attenuated the elastic matrix degradation and proteolytic enzyme activities within EaRASMC cultures.

Surface PEGylation of PLGA NPs plays a favorable role in biocompatibility and improves pharmacokinetics by preventing opsonization. Colasuonno et al. formulated discoidal porous nanoconstructs (DPNs) with a mixture of PLGA and PEG and loaded rtPA with efficiency ~100% via EDC/NHS reaction [101]. Despite the absence of active targeting, a high thrombolytic potential of these NPs might be attributed to their erythrocyte-mimicking shape and deformability, leading to efficient circulation profiles and accumulation of rtPA-DPNs at the clot site. A hybrid theranostic system was developed by Zhou et al., when rtPA was encapsulated into a shell of PLGA and Fe_3O_4, and a chitosan-cRGD peptide was grafted on the surface to target GPIIb/IIIa [69]. Such design addressed a dual function: the early detection of a thrombus and the dynamic monitoring of thrombolytic efficiency using a Magnetic Resonance Imaging (MRI) scanner. The obtained NPs showed a sustainable release profile: a slow-release during the first 15 min and a fast release until 60 min. MRI contrast enhancement was illustrated in the murine thrombus model; effective thrombolysis was performed in the *in vitro* blood clot.

Inspired by pathophysiological mechanisms [72], the microaggregates of multiple PLGA NPs dissociated into rtPA-bearing NPs when exposed to abnormally high hemodynamic shear stress (≥100 dyne/cm^2) in the vascular occlusions. The obtained Shear-Activated NanoTherapeutics with rtPA (rtPA-SA-NTs) performed effective thrombolysis in multiple preclinical models, as they delayed the time to full vessel occlusion in a $FeCl_3$ mouse arterial thrombus model, reversed the debilitating hemodynamic changes of acute pulmonary embolism *ex vivo* at a concentration 100-times lower of native rtPA, and increased survival in an otherwise fatal mouse pulmonary embolism model *in vivo*.

Poly(alkyl cyanoacrylate) (PACA) is an alternative to PLGA

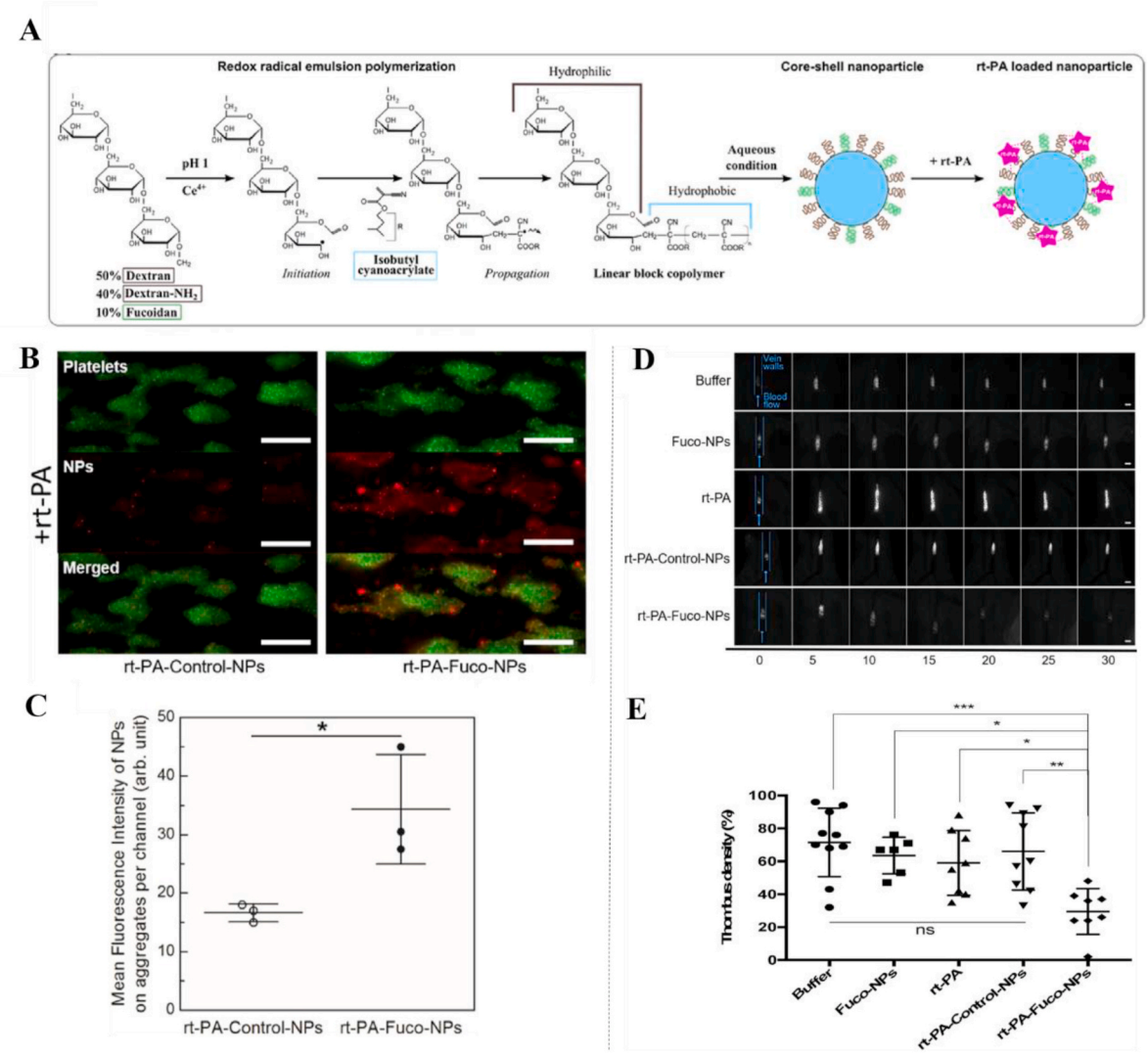

Fig. 6. A. Formulation of fucoidan-functionalized NPs with rtPA. Cerium (IV) ions oxidize polysaccharide chains. The free radical initiates the radical emulsion polymerization of isobutyl cyanoacrylate monomers and create amphiphilic linear blocks copolymers that assemble into core-shell NPs in water. rt-PA interacts with the NPs by electrostatic interactions. B. The fluorescence image shows that rtPA-loaded NPs (in red) with fucoidan adhere notably more onto activated platelet aggregates (in green) than the particles without fucoidan under flow conditions (scale bar = 50 μm). C. Corresponding quantitative analysis of rt-PA-loaded NPs on platelet aggregates. D. Evaluation of thrombolysis efficiency in a mouse model of venous thrombosis at the rtPA dose of 2.5 mg/kg. Fluorescence images of thrombus evolution after treatment injection as determined by platelet accumulation at different times (scale bar = 200 μm). E. Corresponding quantitative analysis of the thrombus density at 30 min after injection. Adapted with permission from Ref. [67]. Copyright 2017 Elsevier Ltd. (For interpretation of the references to color in this figure legend, the reader is referred to the Web version of this article.)

biodegradable polymer that was initially developed and approved as a surgical glue [102]. Juenet et al. prepared hydrophilic polysaccharide-decorated poly(isobutyl cyanoacrylate) core-shell NPs with a mean size of 130 nm by redox radical emulsion polymerization and loaded rtPA by adsorption [67] (Fig. 6A). Functionalization of the NPs with an algae-derived abundant and cost-effective sulfated polysaccharide fucoidan (Fuco) [103] allowed binding P-selectin on activated platelets under arterial or venous shear stress conditions (Fig. 6B and C). Fucoidan, as a targeting ligand for P-Selectin overexpression in cardiovascular pathologies, was prior validated on microscale particles, including polysaccharide microparticles with iron oxide for MRI imaging [104] and polymer microcapsules [105]. Thrombolytic efficacy was 2-fold enhanced for rtPA-loaded Fuco-NPs comparing with rtPA-Control-NPs and free rtPA in $FeCl_3$ murine model of venous thrombosis at the rtPA dose of 2.5 mg/kg [67], which is 4 times lower than the appropriate therapeutic dose in mice [106] (Fig. 6D and E).

Polycaprolactone (PCL). PCL is a non-toxic biodegradable hydrophobic polyester that is approved by the FDA for several medical applications, including for targeted drug delivery. Its slow degradation profile under physiological conditions (from months to years) makes it attractive for long-term drug delivery devices or implants [107].

Deng et al. synthesized the PEG-PCL NPs by single emulsion and solvent evaporation method and conjugated with rtPA via EDC/NHS [108]. rtPA preserved its amidolytic activity *in vitro* and remained active *in vivo* up to 3 h. Despite some reduction in lytic activity in the *in vitro* blood clot test, rtPA-loaded NPs reduced the infarct volume in the brain by ~70% comparing with free rtPA at 1 mg/kg.

Pan et al. produced cationic micelles with a mean size of ~190 nm [109]. Polymeric micelles are a frequently employed class of NPs with a distinct core-shell structure that are self-assembled from amphiphilic components in an aqueous solvent. They were prepared with a mixture of polymers: polycaprolactone-block-poly(2-(dimethylamino) ethylmethacrylate) (PCL-PDMAEMA) – to form NP core, methoxy-PEG-PCL – to enhance the colloidal stability and biocompatibility, and PCL-PEG conjugated with RGDfk peptide – to target GPIIb/IIIa. The micelles adsorbed anionic LM via electrostatic interactions [109]. They could target thrombus and exhibited thrombolytic potential *in vivo* with almost 2-fold reduced bleeding time vs. free LM, thus, mitigating hemorrhagic risks. Two years earlier, the same team published a work similarly dealing with LM-adsorbed micelles from triblock polymer – polycaprolactone-block-poly(2-(dimethylamino) ethyl methacrylate)-block-poly(2-hydroxyethyl methacrylate) (PCL-PDMAEMA-PHEMA) [110]. In a less common targeting strategy, Annexin V, a human phospholipid-binding protein that binds phosphatidylserine on the surface of activated platelets in a calcium-dependent manner and is proposed to play a role in the inhibition of blood coagulation [111], was conjugated to the micelles to target thrombi in a murine $FeCl_3$-induced model and perform the *in vivo* thrombolytic activity.

Poly(2-oxazoline) (POx). This hydrophilic biocompatible but non-biodegradable synthetic polymer features a stealth effect similar to PEG [107]. Gunawan et al. synthesized smart multifunctional polymer microcapsules based on a brushlike POx with alkyne functional groups (B-PEtOx$_{Alk}$) polymer via layer-by-layer assembly on removable mesoporous silica templates [74]. uPA was encapsulated onto these microcapsules via electrostatic interactions (6.4×10^{-15} g uPA per capsule) and could be released upon exposure to thrombin owing to the thrombin-sensitive cross-linker peptide (ELTPRGWRLE). The NP surface-functionalization with a single-chain antibody (scFv) enabled a high affinity toward the GPIIb/IIIa on activated platelets in microfluidic flow channels.

Poly(acrylic acid) (PAA) is an anionic polyelectrolyte, which is a synthetic polymer of acrylic acid. PAA is not biodegradable, although it displays excellent biocompatibility and low toxicity [107].

Mei et al. successfully combined the thrombolytic and antioxidant strategy, incorporating 4-amino-2,2,6,6-tetramethylpiperidine-1-oxyl (4-amino-TEMPO) antioxidant into polyion complex NPs as to eliminate Reactive Oxygen Species (ROS) after ischemia-reperfusion injury [48] (Fig. 7A). Self-assembled NPs were composed of anionic PAA, cationic poly(ethylene glycol)-b-poly[4-(2,2,6,6-tetra-methylpiperidine-1-oxyl) aminomethylstyrene] (PEG-b-PMNT) diblock amphiphilic copolymers, and rtPA. The NPs were colloidally stable due to the hydrophobic nature of the core-forming polycationic PMNT segment. Nanocomplexation extended the *in vivo* half-life of rtPA from 8.2 min to 71.2 min. The complex dissociation in the acidic pH, typical for the ischemia, released the drug. At rtPA dose 1 mg/kg, antioxidant-containing NPs improved neurological deficit, reduced cerebral infarct volume, decreased cerebral superoxide ROS and lipid peroxidation levels as well as subarachnoid hemorrhage, contrary to free rtPA and antioxidant-free nanocomplex (Fig. 7B–G).

Poly(amidoamine) (PAMAM) is a class of dendrimers – nano-sized, radially symmetric artificial macromolecules with highly branched three-dimensional polymeric structure. Due to the multiple functional surface groups, they are commonly exploited for conjugation with pharmaceutical compounds. Mukhametova et al. developed PAMAM dendrimers, containing ethylenediamine core with amidoamine internal structure and a primary amine terminal surface [112]. They were covalently grafted with SK by EDC/sulfo-NHS chemistry and preserved up to 85% of thrombolytic activity *in vitro* compared with free SK [112]. Nonetheless, the clinical use of the dendrimers is limited because of high toxicity, unknown biocompatibility, biodistribution, biodegradation, and pharmacokinetic profile, and high cost of production [113].

To sum up, multiple excellent papers reported superior thrombolytic potential and favorable therapeutic outcomes with PA-loaded polymeric nanocarriers. These NPs are expected to prevail in thrombolysis research, considering their benefits: simple surface modification & functionalization, "smart" nanoparticulate design with controlled drug release, FDA-approval of some polymers that are both biodegradable and biocompatible.

5. Inorganic nanoparticles

5.1. Magnetic nanoparticles

Magnetic nanoparticles (MNP) are of great interest in thrombolytic drug delivery due to their large surface area, small particle size (1–100 nm), strong superparamagnetic properties that permit their detection by MRI, excellent biocompatibility with low toxicity. Initially, MNP were introduced to the MRI field to overcome the low sensitivity of the standard imaging method. The assumption was to avoid the proton relaxation effect of MRI imaging with direct visualization of NPs containing iron oxide nanocrystals [114]. The system was functionalized with a fibrin-binding peptide that indicated promising results for MRI visualization of *in vitro* blood clots. MNP are usually composed of a metal core of magnetite Fe_3O_4 or maghemite γ-Fe_2O_3 and a functionalized shell. Co-precipitation and thermal decomposition are among the most widely studied synthesis methods for magnetic NPs. Aside from the typically used iron oxide, other magnetic elements such as Ni, Co, and their oxides can also be applied for NP manufacture. Cheng et al. [115] fabricated magnetic Ni nanorods via the oblique angle deposition method (physical vapor deposition technique). Hydrodynamic flows, induced by rotating nanorods suspension with rtPA by a pair of permanent magnets, enhanced rtPA mass transport and accelerated thrombolysis. Nevertheless, due to nickel toxicity, this technology cannot be translated into clinical settings.

Fibrinolytic drug-loaded MNPs can be concentrated at the thrombus under the external high-gradient magnetic field for targeted thrombolysis. Hu et al. [55] employed enzymatical (rtPA reaction) and mechanical clot lysis with rtPA-loaded rotating Fe_3O_4–C microrods (MRs) under an external magnetic field. These MRs were assembled from smaller particles with nanometric pores and possessed an average length L = 1.3 μm and a diameter D = 0.5 μm rtPA-MRs under magnetic field recanalized occluded cerebral artery faster and at a lower dose

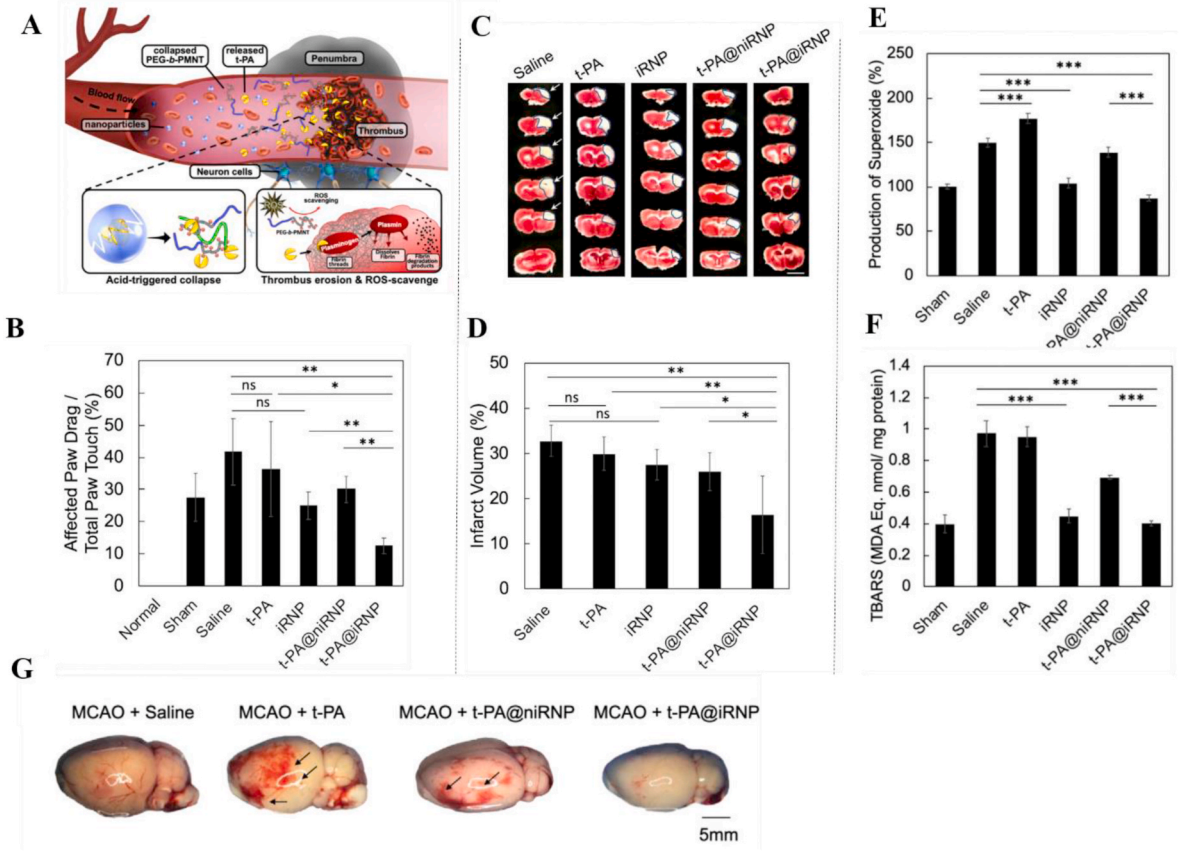

Fig. 7. A. Graphical illustration of the mode of action of t-PA-installed polyion complex possessing ROS-scavenging moieties (t-PA@iRNP) in the thrombus: t-PA@iRNP collapse within the acidic ischemic penumbra region, release t-PA, perform thrombosis and antioxidant activity. (B–G) The therapeutic effect of t-PA@iRNP *in vivo* after middle cerebral artery occlusion (MCAO). B. Analysis of paw-dragging behavior in the cylinder test reveals a reduction in the neurological deficit score for the t-PA@iRNP group. C. Representative images of TTC stained cerebral coronal of the mouse brain, white sections indicate the brain infarct zones (scale bar = 0.5 cm). D. Corresponding quantification of cerebral infarct volume (%). E. Treatment with t-PA@iRNP decreased cerebral superoxide levels, measured by dihydroethidium, at 24 h after injection. F. Treatment with iRNP and t-PA@iRNP reduced thiobarbituric acid-reactive substances (TBARS) level – index of lipid peroxidation in the brain – due to the antioxidant effect. G. Treatment with t-PA@iRNP suppressed t-PA induced cerebral subarachnoid hemorrhage (shown with arrows) with representative images at 24 h after treatment. Adapted with permission from Ref. [48]. Copyright 2019 Elsevier Ltd.

compared to free rtPA group (25 min at 0.13 mg/kg vs. 85 min at 10 mg/kg) and diminished the post-stroke infarct volume *in vivo*. Despite the absence of liver and kidney toxicity of the MRs, they aggregated *in vitro* and required sonication to remain homogeneously dispersed in the suspension.

The drawbacks of uncoated magnetite NPs is that they are prone to oxidation and rapidly aggregate due to strong magnetic dipole-dipole attraction between particles, leading to a loss of magnetization. After the synthesis, a surface coating by SiO_2 or biopolymers is required to improve NP environmental stability, stealth effects, and prolong the blood circulation time. It may additionally provide a variety of high-capacity surface functional groups for bioconjugation of the molecules of interest.

Kempe et al. produced octahedral silica-coated Fe_3O_4 NPs for ferromagnetic implant-assisted magnetic drug targeting of in-stent thrombosis [116]. Silica coating enlarged the hydrodynamic size of the NPs from 10 to 30 nm–~300 nm due to the tight aggregation of naked NPs. rtPA was immobilized onto NP surface via EDC/sulfo-NHS chemistry (71 μg rtPA/1 mg magnetite NPs). In a preliminary experiment on the porcine brachial artery, rtPA-NPs were effective for magnetically guided lysis of in-stent thrombosis at a low rtPA dose of 0.38 mg. In another study [117], silica-coated magnetic nanoparticle (SiO_2-MNP), prepared by the sol-gel method, covalently grafted rtPA with a glutaraldehyde (0.5 mg/mL rtPA/5 mg SiO_2-MNP). After nano-conjugation, the rtPA storage stability increased 9.5-fold in the PBS and 2.8-fold in whole blood. Time of thrombolysis of SiO_2-MNP-rtPA improved by 65% vs. free rtPA in the *ex vivo* intravascular model under magnetic guidance.

The high porosity of the silica coating promotes the encapsulation of the pharmaceutical drugs inside the pores. Wang et al. reported that silica-coated magnetic NPs, prepared by the surfactant templating, with an expanded 6 nm pore size permitted 30-fold more efficient uPA adsorption with sustainable drug release [118]. *In vitro* thrombolytic efficiency was 2-fold superior vs. free uPA and ~1.5-fold faster vs. uPA-loaded supermagnetic non-mesoporous silica NPs under 0.2 T magnet. Yet, silica clinical application needs to be carefully regulated because of the hemolytic effect it might induce as it acts as a hydrogen donor in interactions with cell membrane phospholipids and generates ROS [119,120]. Additionally, silica is shown to provoke an immune response by releasing pro-inflammatory cytokines [121].

Common in cancer therapy *in vivo*, hyperthermia was used as adjuvant therapy for thrombolysis by Voros et al. [75]. Multiple clustered iron oxide nanocubes (NCs), synthesized by a high-temperature thermal decomposition, were surface-coated with a mixture of rtPA and Bovine Serum Albumin (BSA) and produced a local overheating under alternating magnetic fields (295 kHz). rtPA release from NCs doubled at 42 °C from the one at 37 °C within 24 h.

The presence of functional amino and hydroxyl groups makes chitosan and its derivatives a suitable candidate for the magnetic NP surface coating. Chen et al. [122] prepared iron oxide MNP by the chemical co-precipitation and coated with chitosan as a dispersing agent. They immobilized rtPA by glutaraldehyde-mediated amide bond formation

with loading efficiency 95% (0.5 mg rtPA/5 mg chitosan-MNP), maintaining its enzymatic and thrombolytic activities *in vitro*. *In vivo* rat arterial embolic model further evidenced tissue perfusion after treatment of 6,000 G magnetically guided Cs-MNP-rtPA at a dosage of 0.2 mg/kg but not of saline. Alternatively [123], chitosan coating of Fe_3O_4 MNPs was achieved by crosslinking with sodium tripolyphosphate via ionic gelation in the presence of rtPA. On top of targeted magnetic delivery, rtPA-encapsulated NPs unveiled a triggered release: in serum at 37 °C, but not in PBS, which was on/off magnet-sensitive and could be retarded in the presence of a magnetic field. According to the *in vivo* study on the rat embolic model, rtPA-NPs restored blood flow at rtPA dose of 2 mg/kg under magnetic guidance in contrast to NP administration alone.

Dextran, complex branched glucose, is largely used in the coating of MNP. Magneto-fluorescent crosslinked dextran-coated iron oxide (CLIO) NPs targeted arterial and venous thrombi *in vivo* via an activated factor XIII (FXIIIa)-sensitive peptide (GNQEQVSPLTLLKC-NH2) [68]. These theranostic NPs generated optical imaging with NIR VivoTag 680 fluorophore and were covalently functionalized with rtPA via PEG. Thrombolytic efficiency was comparable to the one of free rtPA in the humanized mouse model of pulmonary embolism.

Cytocompatibility of dextran-coated superparamagnetic iron oxide NPs (SPIONs) on human umbilical vein endothelial cells (HUVECs) (~85% cell viability) without changes in mitochondrial membrane potential, a DNA degradation or cell cycle alteration was stated by Heid et al. [124]. When comparing an adsorptive or covalent (EDC/NHS) method to load an arginine-purified rtPA, >80% loading efficiency was achieved for both approaches. Yet, SPIONs with covalently bound rtPA were more efficient to be targeted by a 0.4 T magnet into fibrin clot and to perform a local *in vitro* thrombolysis.

Owing to its natural, biodegradable, and non-toxic character, agarose, a linear polysaccharide extracted from red seaweed, is applied in diverse biotechnological applications. Agarose gel-coated Fe_3O_4 NPs were covalently grafted with uPA via EDC/sulfo-NHS [125]. Urokinase-loaded NPs increased the thrombolytic rate by 50% in the *in vitro* blood clot assay vs. free uPA, as well as in microfluidics test under a static magnetic field of 624 A/m.

Prilepskii et al. [126] crosslinked MNPs with heparin, FDA-approved polysaccharide with anticoagulant activity, and adsorbed uPA with encapsulation of 99% (Fig. 8A). The size of the resulting nanocomposite was around 100 nm (Fig. 8B). Without the inhibitory effect of the heparin on uPA, the thrombolysis rate amplified in the presence of a permanent magnet *in vitro* (12 min vs. 7 min for 60% clot reduction) (Fig. 8C). In the $FeCl_3$ rat carotid artery and rabbit femoral artery models, the MNPs@uPA group speeded reperfusion time and increased blood flow rate ~4 times compared to that of native uPA (Fig. 8D and E).

The synthetic polymer coating is similarly explored for the preparation of magnetic field-responsive and biocompatible NPs. Huang et al. [127] stabilized MNPs with PAA by providing electrostatic and steric repulsion and loaded rtPA via EDC/NHS due to PAA abundant carboxyl groups. The clot lysis efficiency of MNP-rtPA was improved under the rotating magnetic field compared to free rtPA *in vitro*. Besides, MNP-rtPA diminished the brain infarct area in the distal cerebral occlusion *in vivo* model vs. free rtPA (8.65 ± 3.63 mm^3 vs. 4.40 ± 2.46 mm^3).

Another publication compared covalent vs. non-covalent methods of rtPA loading to polyacrylic acid-co-maleic acid (PAM)-coated SPIONs [128]. Better loading efficiency was reported with a covalent method vs. adsorption ($98.6 \pm 0.8\%$ vs. $47.7 \pm 5.4\%$). Amidolytic and fibrinolytic activities on the PAM-SPIONs with covalent loading were superior and better preserved after 40 days of storage. Hence, the covalent binding of the rtPA was advantageous for the application with SPIONs.

Hung-Wei Yang et al. [129] synthesized the magnetic nanocarriers (MNCs) with a water-soluble poly [aniline-co-N-(1-one-butyric acid) aniline] (SPAnH) shell that could load a high amount of rtPA via

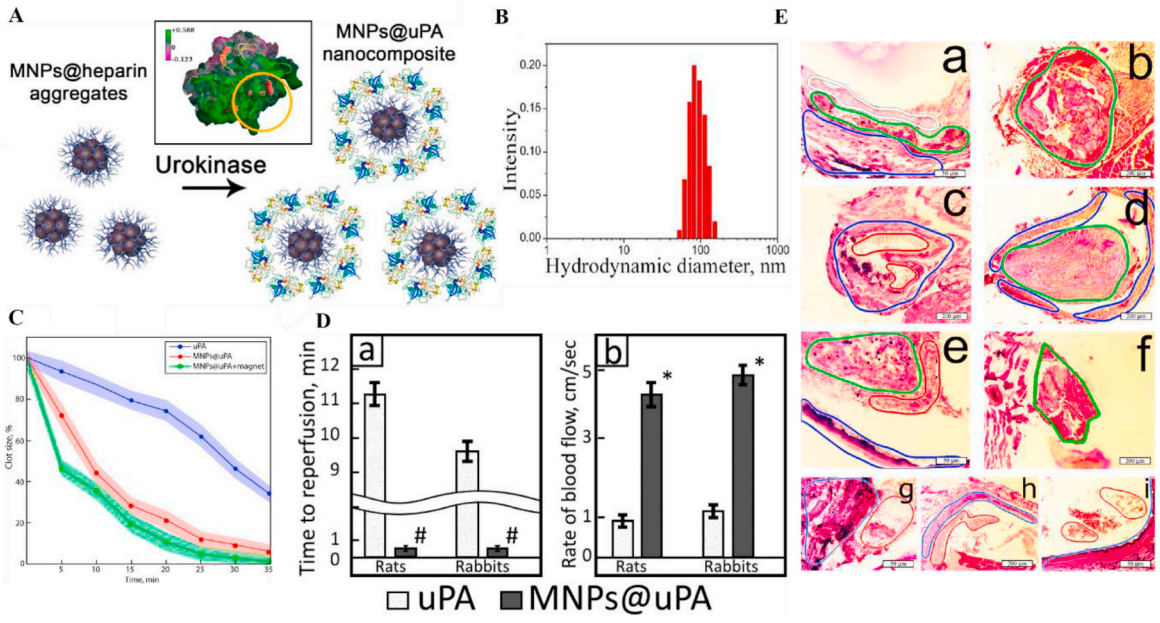

Fig. 8. A. Schematic of the adsorption of uPA to the heparin-coated MNPs to obtain MNPs@uPA. Inset: 3D structure of urokinase with colored electrostatic potentials. Kringle domains responsible for interaction with heparin are in orange. B. The hydrodynamic diameter of MNPs@uPA composite. C. *In vitro* clot lysis rate upon exposure to uPA and MNPs@uPA with or without a magnetic field. The difference in the thrombolysis for MNPs@uPA with and without magnet within the initial 25 min is statistically significant ($p < 0.05$). D. Restoration of blood flow *in vivo* of uPA and MNPs@uPA. (a) Time to vessel reperfusion. (b) Rate of blood flow 24 h post-injection. E. Sections of the rat carotid artery and (g–i) rabbit femoral artery 24 h post-clot formation. Colors: blue, vessel walls; red, erythrocyte aggregates; green, red clot; white, white clot. (a, b, g) Saline. The clot tightly adhered to the vessel wall observed in (a) (marked in green). The vessel fully occluded by the clot (encircled in green) presented in (b). (c, d, h) uPA. Note a clear vessel lumen space between the clot (green) and the vessel wall (blue) in (d). (e, f, i) MNPs@uPA. Note a bigger free space in the vessel lumen and reduced size of the clot in (f) and (i). (a, c, e, g–i): H&E staining. (b, d, f): Picro-Mallory staining. Adapted with permission from Ref. [126]. Copyright 2018 American Chemical Society. (For interpretation of the references to color in this figure legend, the reader is referred to the Web version of this article.)

1-ethyl-3-(3-dimethylaminopropyl)carbodiimide/N-hydroxysuccinimide (EDC/NHS) chemistry (276 μg rtPA per 1 mg MNC). Magnet-guided MNC-rtPA demonstrated significantly improved thrombolysis in rat iliac embolism model at 0.2 mg/kg rtPA dose.

5.2. Gold nanoparticles

Gold nanoparticles (AuNPs) benefit from diverse optical and photothermal properties. They are synthesized by the reduction of gold salts to gold metals in the presence of stabilizing agents to prevent the aggregation during NP formation, and their tunable size modulates their toxicity and biodistribution. Gold NPs can be applied in photothermal therapy in cancer [130] as well as in drug delivery. Moreover, AuNPs are characterized by their high X-ray absorption coefficient enhancing CT signal. The quantitative imaging method *in vivo* was established to monitor the thrombolysis with rtPA using fibrin-targeted glycol chitosan-coated gold NPs [131]. Direct discrimination of thrombi from the underlying tissue was obtained with gold NPs conjugated with a thrombin activatable fluorescent peptide that discharged a near-infrared signal (NIRF) when cleaved [132]. This dual NIRF/micro-CT imaging protocol was tested *in vivo* and suggested a high spatial resolution for a rapid and direct thrombi diagnosis. Indeed, gold NPs represent an interesting perspective to overcome the pitfalls of standard imaging protocols and might allow a better triaging of patients according to their thrombotic conditions.

Gold nanoparticles are similarly capable of delivering large biomolecules, like plasminogen activators. Tang et al. conjugated rtPA with AuNPs with a diameter of 37.8 nm via bio-affinity ligation that is based on the interactions between rtPA and 3-lysine ligand on the AuNPs surface through polyvinyl pyrrolidone (PVP) spacer [51]. Notably, obtained conjugate indicated protection from inhibition by PAI-1 *in vitro* by pre-incubation with the enzyme and prolonged circulation time *in vivo* (6.5 min vs. 20.5 min). Another intelligent nanoplatform for hyperthermia-induced thrombolysis was documented by Wang et al. [47]. Gold@mesoporous silica core-shell nanospheres immobilized uPA in the pores by a solid 1-tetradecanol (tet) (Fig. 9A). Owing to hyperthermia caused by Au absorption of NIR under NIR laser irradiation, tet transformation to liquid phase stimulated a temperature-sensitive controlled release of uPA, whereas only 10.5% of the drug was released at 37 °C vs. 89.5% at 39 °C (Fig. 9B and C). In the carrageenan-induced murine tail thrombus model, NIR-irradiated uPA-NPs group enhanced thrombolytic effect ~2-fold vs. free uPA (Fig. 9D).

In conclusion, several remarkable concepts of inorganic PA-bearing NPs for targeted thrombolysis were published in the last 10 years that have the potential to become theranostics. Despite most of MNP rely on magnet-assisted accumulation on the thrombus, this targeting approach seems to be tricky to accomplish in healthcare settings. An interesting application of inorganic NPs is hyperthermic exposure as adjuvant therapy to fibrinolytic therapy. Nevertheless, it must be remembered

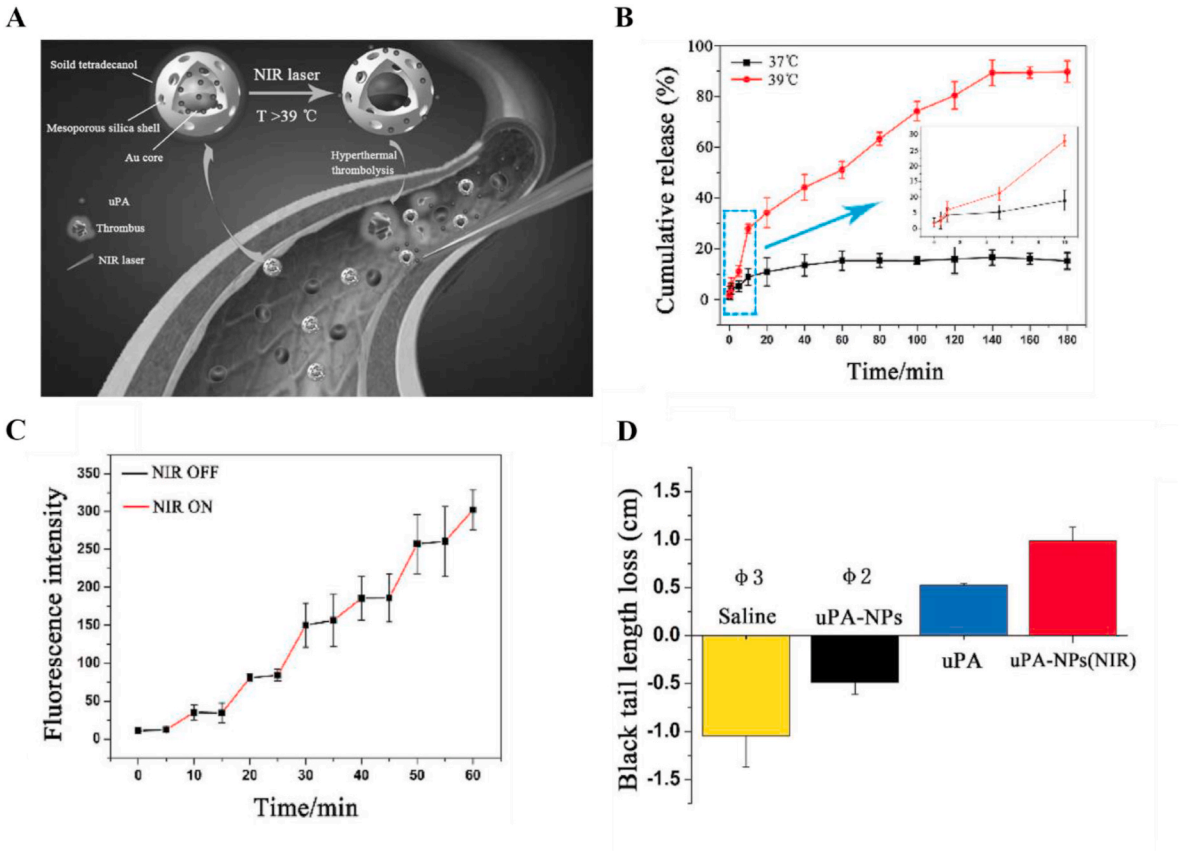

Fig. 9. A. Schematic illustration of the hyperthermia-induced enhanced thrombolysis with uPA-immobilized gold@mesoporous silica nanospheres. B. *In vitro* release profiles of fluorescent uPA from uPA-NPs at 37 °C and 39 °C, respectively. The enlarged release profile in 10 min is shown at the inset graph. C. NIR laser triggers pulsed uPA release profile *in vitro* of fluorescent uPA-NPs. D. *In vivo* thrombolysis in murine tail thrombus model via injecting carrageenan. The statistical black tail length loss (thrombolytic effect) of mice after treatment for 9 days, where ϕ represents the amputated tail, and the number represents the number of mice with the amputated tail. Adapted with permission from Ref. [47]. Copyright 2017 WILEY-VCH Verlag GmbH & Co. KGaA, Weinheim. (For interpretation of the references to color in this figure legend, the reader is referred to the Web version of this article.)

that NPs from inorganic materials are difficult to degrade *in vivo* and they persist for long periods (more details on safety and metabolism in Section 8.1).

6. Bio-inspired nanocarriers

Nature inspires the development of nanotechnological solutions in drug-delivery systems. Bio-inspiration and biomimicry technologies can not only simulate biological materials by their chemical structure but also by their biological functions [133].

Camouflage. An elegant strategy to reduce thrombolytic drug elimination and increase its plasma half-life is to camouflage it as endogenous proteins. This approach was demonstrated by Absar et al. [134] when the targeted/triggered release of rtPA was mediated by the presence of thrombin in the thrombus. rtPA was camouflaged by conjugating with human serum albumin (HSA) via a thrombin-cleavable peptide (tcP) and decorated with a homing-peptide targeting GPIIb/IIIa. This construct permitted to temporarily suppress the enzymatic and fibrinolytic activities of camouflaged rtPA, however, to spontaneously restore it upon incubation with thrombin by the cleavage of the peptide linker.

Red blood cell (RBC)-derived nanocarriers. Erythrocytes are recognized for their extended blood circulation as they manage to avoid clearance by the macrophages up to 3 months. A number of factors are believed to contribute to that, including their discoidal shape, deformability, and the expression of self-recognition biomarkers, such as CD47 and CD200 [133,135]. RBC seem to be a particularly promising carrier of thrombolytic drugs that exert their pharmacological activity within blood vessels.

Vankayala et al. [136] designed theranostic nanoconstructs for near-infrared (NIR) fluorescence imaging and thrombolytic activity. Specifically, after hypotonic treatment of RBCs, obtained erythrocyte ghosts were coupled with indocyanine green, FDA-approved NIR imaging agent, and conjugated with rtPA via amine-aldehyde chemistry. Their thrombolytic efficacy was comparable to the free rtPA *in vitro*. Erythrocytes have already reached clinical trials as nanocarriers for drug delivery (Clinicaltrials.gov Identifiers: NCT01255358, NCT01171807, NCT00484965) but not in thrombolytic therapy yet [133].

Platelet-like nanocarriers. Platelet membrane-camouflaged PLGA-core NPs, conjugated with rtPA, were recently proposed as a biomimetic technique by Xu et al. [76]. These so-called "nanoplatelets" behave like platelets in the blood circulation (Fig. 10A and B) and bind to the thrombus *in vitro* and *ex vivo*. rtPA-NPs treatment was beneficial in multiple *in vivo* models: improved the mouse survival time from 4-7 days to 14.5 days and ~4.5-fold reduced the thrombus area vs. free rtPA in the pulmonary embolism model (Fig. 10C and D); stimulated complete thrombus removal contrary to free rtPA in the $FeCl_3$-induced mesenteric arterial model. Notably, post-thrombolytic brain damage was weaker for the rtPA-NPs group as defined by a lower neurological deficit score and smaller ischemic area in the ischemic stroke mouse model, as depicted on Fig. 10E–G.

There has been a growing interest in exploring neuroprotective strategies following acute ischemic stroke to reduce brain injury [137]. Another version of the "nanoplatelets" was proposed as a combinational approach for the treatment of acute ischemic stroke based on thrombolysis and neuroprotection [138]. The NPs with a size of ~150 nm contained the core of acetal modified dextran & neuroprotective agent and were covered with a platelet membrane conjugated with thrombin-cleavable Tat-peptide (Tat-LTPRGWRLGGC) that coupled rtPA (Fig. 11A). In this nanodesign, rtPA could be released upon thrombin presence while exposing Tat-peptide on the NPs and

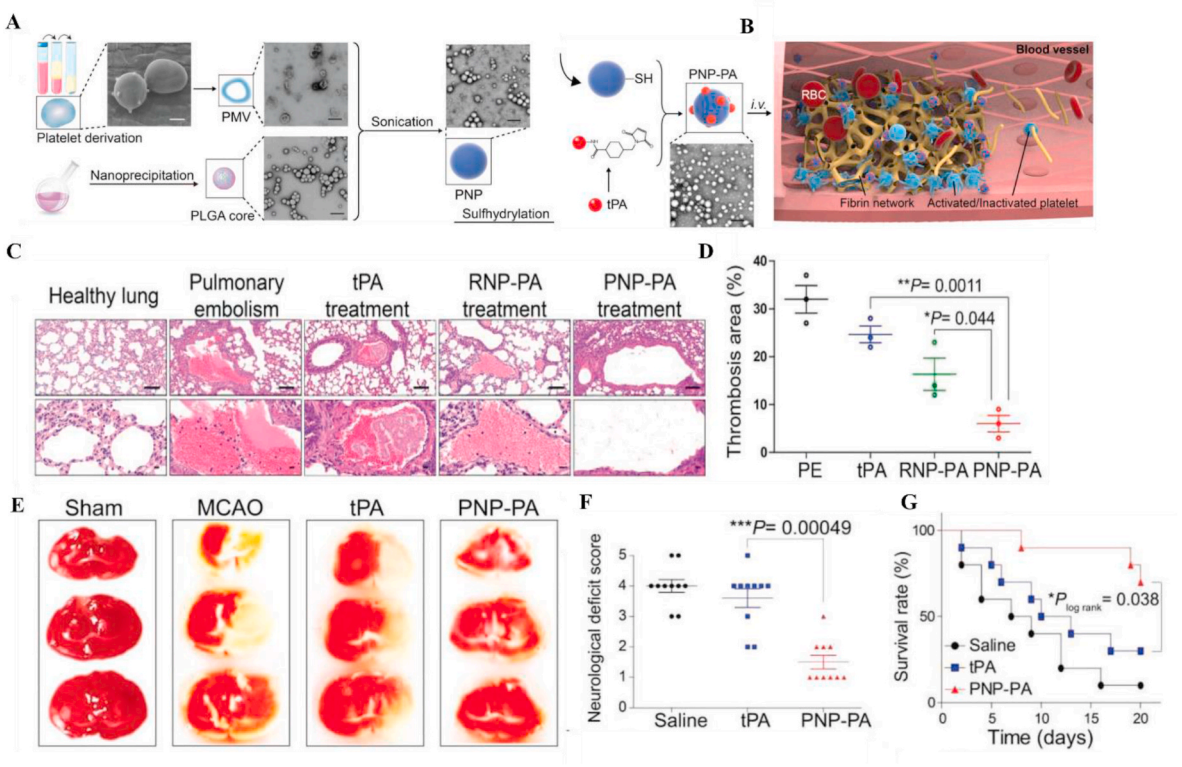

Fig. 10. A. Schematic illustration of the synthesis of PNP-PA NPs. Briefly, the membrane of platelets (scale bar = 1 μm), acquired from the whole blood of mice, were used to coat the PLGA cores (scale bar = 400 nm). t-PA was subsequently conjugated via –SH groups onto the surface of the platelet membrane to form PNP-PA. B. The proposed mechanism of action *in vivo*: mimicking platelets, PNP-PA are specifically targeted to the thrombus and dissolve the fibrin clot. C. Therapeutic potential of PNP-PA in a pulmonary embolism mouse model. Lung sections with H&E staining administered the indicated treatments (scale bar = 50 μm). D. Quantitative analysis of the thrombus area in panel C. E-G. Therapeutic effects of PNP-PA in the ischemic stroke mouse model. E. Representative TTC staining images of MCAO mouse brains treated with the indicated formulations. F. Neurological deficit scores in the treatment groups of MCAO mice. G. The survival rate of MCAO mice treated with the mentioned formulations. Adapted with permission from Ref. [76]. Copyright 2019 WILEY-VCH Verlag GmbH & Co. KGaA, Weinheim.

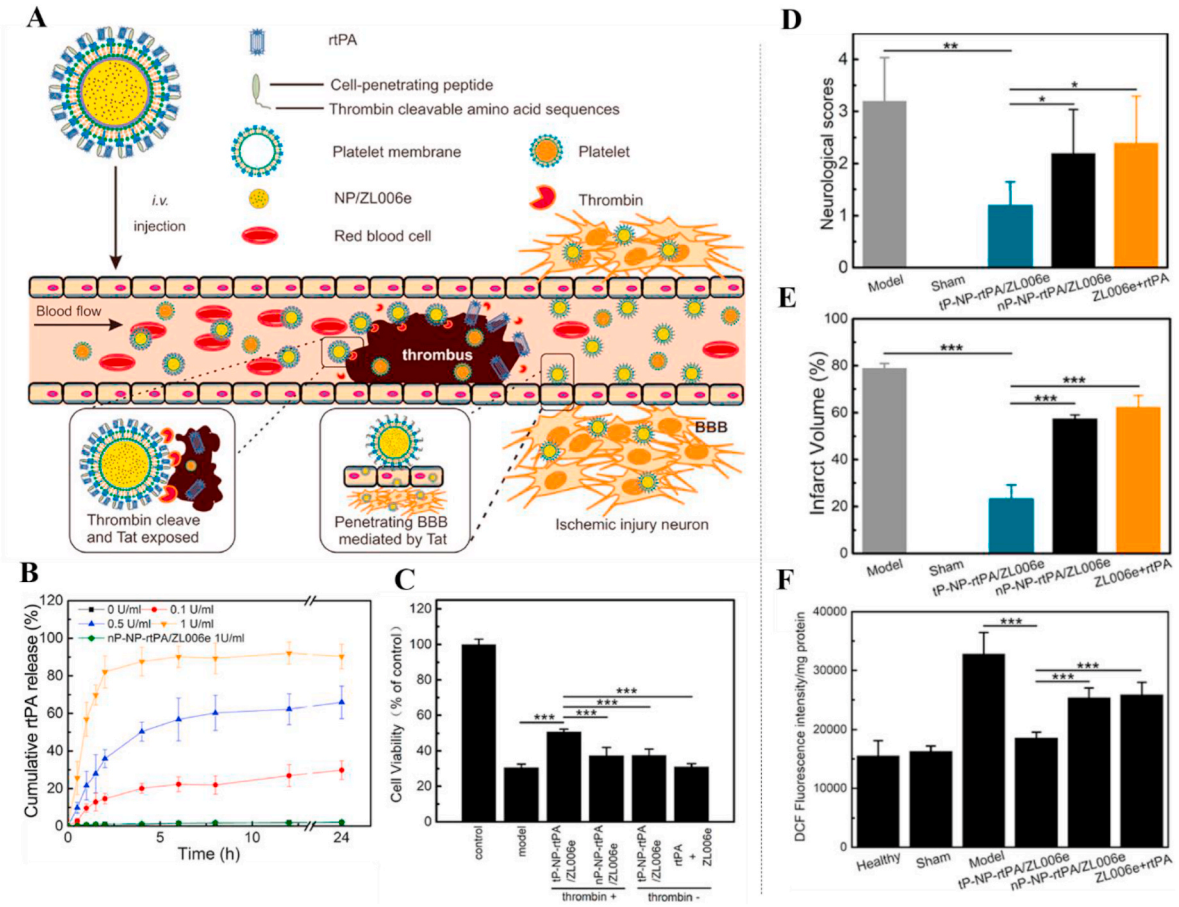

Fig. 11. A. Schematic design of tP-NP-rtPA/ZL006e and its components and mode of action. After intravenous injection, tP-NP-rtPA/ZL006e are targeted to the thrombus for thrombin-triggered release of rtPA and thrombolysis. Nanocarrier transport into the brain via Tat-mediated transcytosis for neuroprotective activity. B. Cumulative release of rtPA from tP-NP-rtPA/ZL006e with different thrombin concentrations. nP-NP-rtPA/ZL006e are the control particles in 1 U/mL thrombin. C. *In vitro* neuroprotective effect of tP-NP-rtPA/ZL006e and nP-NP-rtPA/ZL006e with or without thrombin and free ZL006e + rtPA via the coculture model of the BCEC monolayer and glutamate-stimulated PC-12 cells. D. Neurological scores of the MCAO rats after the treatment. E. Quantification of brain infarct volume/ischemic brain hemisphere at 24 h post-treatment MCAO rats. F. ROS level in the ischemic region. Adapted with permission from Ref. [138]. Copyright 2019 American Chemical Society.

penetrating BBB for neuroprotectant delivery in the brain (Fig. 11B and C). In the *in vivo* model of middle cerebral artery (MCA) occlusion, a treatment with this nanocomplex decreased infarct size by 63%, ameliorated neurological deficit, and diminished ROS level of the ischemic region by 52% compared to the free drug combination (Fig. 11D–F).

Leukocyte-derived microvesicles. Cell microvesicles that originate from the plasma membrane of most cell types, including blood cells, are essential effectors in the intercellular communication and may transport bioactive molecules [139]. Silva et al. reported an unconventional method when microvesicles (D = 673 ± 168 nm), secreted from macrophages upon serum depletion cellular stress, were capable of enclosing both iron oxide NPs and rtPA [140]. The work exemplified a biogenic strategy of theranostic application of hybrid microvesicles for MRI imaging and spatially-controlled rtPA delivery via magnetic field gradient targeting.

Bacterial spores. In another bio-inspired approach, the spores of bacterium *Bacillus amyloliquefaciens* with peptidoglycans on their surface were prior inactivated with a high-pressure steam sterilizer and used as nanocarriers with uPA and RGDS peptide [141]. The solid monodisperse oval spheres ([0.67 ± 0.20 μm] × [1.27 ± 0.20 μm]) were non-biotoxic following histological evaluation of the heart, kidneys, and liver. With a higher thrombolysis rate *in vitro*, *in vivo* tail bleeding times of the uPA-NPs group were shorter than that of free uPA (601 s vs. 1145 s), suggesting a lower risk of hemorrhages.

Viral nanoparticles. Based on bacteriophages and plant viruses, viral nanoparticles (VNPs) are biocompatible, biodegradable, and nonpathogenic nanocarriers in humans. Because of the remarkable proliferation of viruses, they could be easily manufactured up to an industrial scale. In the NPs based on the tobacco mosaic virus, the nucleic acids are tightly enclosed in a stiff hollow tubular capsid comprising coat proteins [142]. To develop a nanocarrier with optimal flow properties for thrombolytic therapy, Pitek et al. conjugated rtPA to tobacco mosaic virus mutant soft elongated nanorods containing lysine side chain (TMV-Lys) via PEG linkers, obtaining the NPs with dimensions of 300 × 18 nm [143]. TMV-rtPA could passively accumulate at the thrombus at a higher rate than TMV-PEG *in vivo*. Both rtPA and TMV-rtPA resumed the circulation in the mouse thrombosis model, but TMV-rtPA reduced bleeding time ~2-fold vs. free rtPA. Despite an absence of pathogenicity, the potential immunogenicity of nanodelivery systems based on pathogens such as bacteria and viruses should be not be neglected.

To conclude, biomimetic delivery systems have the countless potential for the advancement of drug delivery technologies. The reproduction of the biological complexity on nanocarriers' surface imitates biological features, like biocompatibility, targeting to the thrombus tissue, efficient circulation profiles, etc. To be suitable for clinical translation, both toxicological (e.g., safety, immunogenicity) and pharmaceutical (e.g., reproducibility, scale-up, standardization of chemical composition) concerns have to be examined [144].

7. Ultrasound-responsive carriers & sonothrombolysis

Microbubbles (MBs) are defined as spheroid objects stabilized by a coating material [145], such as lipids, polymers [146], or denatured proteins, and filled with a gas or a combination of gases (air or perfluorocarbons). Their average size should not exceed red blood cell size (6–8 μm) to avoid embolization [147].

The application of these novel therapeutic agents originated from US imaging, since local US insonation induces acoustic steaming of the surrounding tissues [148] that may help drugs to penetrate deeper into the clot by local mechanical stress induction. Sawaguchi et al. illustrated this hypothesis with an *in vitro* blood clot lysis experiment and demonstrated that the US itself can accelerate thrombolysis [149]. Using 500 kHz US insonation, the authors pointed out that the thrombolysis acceleration ratio was about 2.5 times greater with rtPA combined with the US than rtPA treatment alone. Thrombolytic therapy combined with the US could reduce the dose of rtPA by 60% owing to the synergistic effect.

In the cardiovascular field, microbubbles are mostly designed as contrast agents for ultrasound molecular imaging due to their ability of radiation oscillation, upraising the contrast of tissues. Every bubble is subjected to stable cavitation in low range frequencies and can undergo inertial cavitation (burst) under higher frequencies [150]. Cavitation is the process of induced bubble growth and collapse and can be achieved by different mechanisms [151], including ultrasonic waves [152]. Association of ultrasound insonation and microbubble stimulation is called sonothrombolysis (Fig. 12) and is promising to enhance thrombolysis.

The focus on MBs for thrombolytic therapy was initially published by Tachibana et al. [153] and Porter et al. in 1996 [60] with an *in vitro* model of enhanced thrombolysis using dextrose albumin MBs and a low-frequency transducer. Nowadays, most of the lab-made microbubbles are phospholipid-based and obtained from a sonication-lyophilization-rehydration process [154–157], microfluidics [158], or coaxial electrohydrodynamic atomization process [159], and called echogenic liposomes (ELIP) [160]. Laing et al. took benefit from the rehydration step to incorporate rtPA and obtain thrombolytic-loaded ELIP. With natural rtPA affinity to fibrin [156], the authors highlighted the significant contribution of a high mechanical index (0.4) on the recanalization rate of the obstructed artery in the rabbit model. Mechanical Index (MI) is a unitless ratio between the peak of negative pressure and the square root of the frequency in MHz. It is applied to predict the bioeffect of ultrasound; when MI is > 0.3, microbubbles are easily destructed [161] but may have harmful bioeffects above 1.9 value [162]. One of the limitations of this study was the lack of stable cavitation of these air-filled MBs. To remediate this issue, other gas fillers were explored, like Shekhar's [155] octafluoropropane targeting ELIP that allowed more robust stable cavitation, significantly enhancing thrombolysis *in vitro*.

Literature accordingly claims that US insonation of microbubbles on the thrombus site triggers sonothrombolysis due to the cavitation process [157]. The average lytic rate obtained with rtPA loaded ELIP and the US was recorded to be over 2-fold higher than free rtPA with an *in vitro* flow model [155]. Zhu et al. [163] published similar results with their uPA loaded targeted microbubbles from Targerson Inc. and the US.

Microbubble targeting agents are similar to other functionalized NPs: mostly RGDS peptide targeting GPIIb/IIIa on activated platelets [163–166], heat denaturated collagen that binds vWF [167], or scFv targeting GPIIb/IIIa grafted on Nonlinear Ultrasound Contrast Agent by Visual Sonics® via biotin/streptavidin coupling [168]. Hua et al. [164] published the *in vivo* study presenting the theranostic potential of their rtPA-loaded MBs with RGD peptide and 2 MHz ultrasound. A high recanalization rate was obtained with a 15 times lower dose of rtPA.

The magnetic field was also observed as a targeting strategy [169] by using ferrofluid in the composition of the MBs. As expected, significant enhancement of the cavitation energy was observed when a magnet was placed on the thrombi location, limiting the prolonged exposure of ultrasonic waves. Potentially, this magnetic element in the MBs may allow MRI imaging [167].

A complete overview of small animal sonothrombolysis stroke models has been published by Auboire et al. [170] in 2018. The overall perspective for further treatment model is suggested to be on the range of sub-Mhz frequencies and intensities that favor stable cavitation of the MBs. It described sonothrombolysis as a potential treatment for small vessel impairment or larger arteries occlusion.

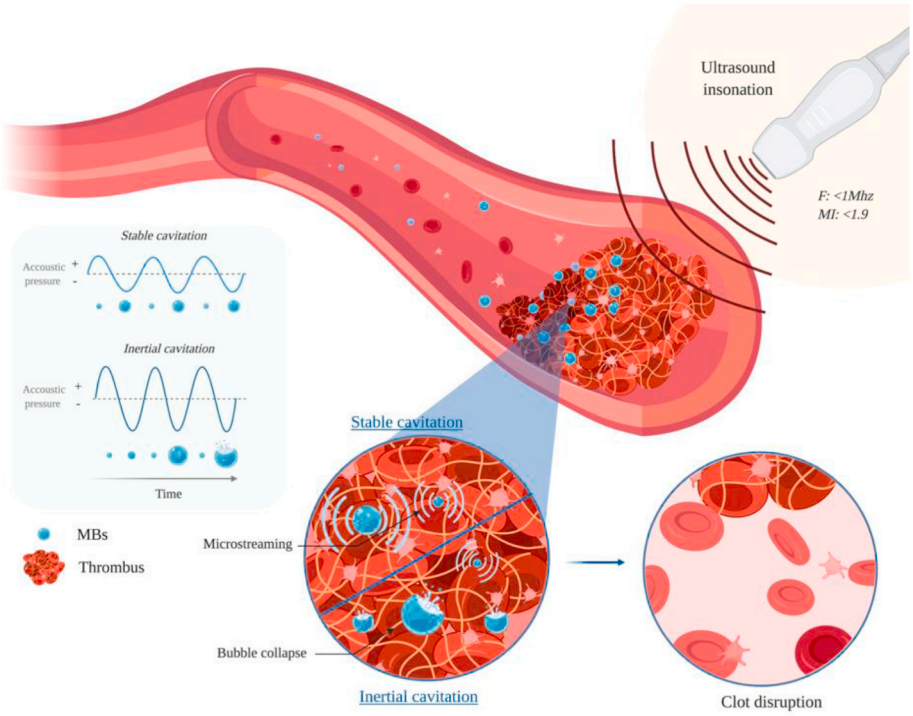

Fig. 12. Sonothrombolysis precept for enhanced thrombolysis. Sonothrombolysis is performed by the ultrasound insonation of MBs on the thrombus site. Microbubble radial oscillation properties are sensitive to acoustic pressure. The bubbles can undergo stable cavitation inducing microstreaming of the surrounding environment or inertial cavitation leading to the collapse of the bubble. While MBs alone are proven to destabilize a clot with US insonation, sonothrombolysis efficacy is enhanced with the thrombus specific targeting and loaded thrombolytic agent on the MBs. Abbreviations: *F*, frequency; *MI*, mechanical index; *MBs*, microbubbles.

Preclinical trial on big animals was performed on a porcine model at the VU University Medical center in the Netherlands [166] with RGDS targeted SonoVue® microbubbles loaded with uPA. Pigs received the premedication to prevent the potential allergic reactions to the lipid shells of the MBs. MBs were injected intraluminally to simulate a clinical setting, and 1.1 MI was applied. Three out of 5 pigs of the uPA targeted MBs group showed an increase in the arterial flow and recanalization rate, whereas only 1 out of 4 in the uPA group showed a slight improvement. A major limitation of this study was a lack of information about the exact concentration of the encapsulated drug.

Because of their echogenic properties, some microbubbles are already clinically used as a diagnostic tool [171], such as DEFINITY® (Lantheus Medical Imaging) or SonoVue® (Bracco Diagnostics), in order to enhance ventricular opacification and US imaging of tumor angiogenesis. Those approved microbubbles are composed of a phospholipid shell but not yet loaded with therapeutic agents. Yet, preclinical studies on acute cerebral ischemia on rats demonstrated that focused weak energy US associated with SonoVue® injection was as efficient as fibrinolysis with rtPA [172]. Recanalization in an occluded vein model was efficient with microbubble cavitation only under US insonation directly on the vein within 10 min [173], which may be advantageous to limit hemorrhage risks induced by PA.

Sonothrombolysis treatment has already stepped up to clinical trials with the following ones: MUST (Microbubbles and Ultrasound in Stroke Trial, Clinicaltrials.gov Identifiers: NCT00132691) performed at the University of Toulouse in France and CLOTBUST Hands-Free (Combined Lysis of Thrombus in Brain Ischemia With Transcranial Ultrasound and Systemic T-PA-Hands-Free, ClinicalTrials.gov Identifier: NCT01240356) at The University of Texas Health Science Center, Houston. While MUST trial was aborted after incidences of intracerebral hemorrhages [171], CLOTBUST Hands-Free showed great recanalization rates in combination with systemic rtPA on ischemic stroke patients [174]. Finally, an ongoing clinical trial is evaluating the efficacy of SonoVue® MBs associated with rtPA and US insonation compared to classic rtPA injection on acute ischemic stroke patients in the 4.5 h window treatment. This study takes place in Barcelona, Spain on 24 participants and results have not been reported yet (ClinicalTrials.gov Identifier: NCT01678495).

Recent work focused on nanobubbles (NBs) coupled with cRGD peptide [71], instead of their microscale peers, to facilitate deeper blood clot penetration. Jiang et al. used the high-frequency US to burst these NBs to decrease the risk of clinical bleeding due to the enhancement of permeability of low frequencies. Comparing SonoVue® MBs to the NBs, both in combination with uPA and submitted to the US, it was observed a difference in the clot degradation: a peripheral relaxation in the MBs group vs. a fissure like a collapse in the NBs one. The nanometric scale of these particles seemed to deconstruct the clot from the inside.

Ultrasound is mainly applied in diagnostics in the clinic because it is safe, easy and quick to utilize at an affordable cost. The therapeutic potential of US-responsive carriers and sonothrombolysis is promising in fibrinolytic therapy. The main goal is to improve the efficiency of thrombolytic therapy on highly retracted thrombi where the medications struggle to penetrate [175], but where the mechanical properties of the MBs and NBs could be a significant gain.

8. Nanoparticle optimal design for thrombolytic therapy

8.1. Pharmacokinetics, biodistribution, and safety

After the intravenous administration, nanocarriers for fibrinolytic therapy are subjected to biological barriers and might pose particular safety concerns that would limit a desirable therapeutic outcome. What would be an optimal nanoparticle design to incorporate in order to load plasminogen activator and perform a safe and efficient local thrombolysis?

Primarily, favorable *in vivo* biodistribution and pharmacokinetics of the injectable inorganic, lipid, and polymeric micelle/nanoparticle must be ensured. Particle *in vivo* fate is varied and dictated by the interaction between multiple parameters: nanoparticle size, surface characteristics, stability, etc. For site-specific accumulation of the thrombolytic agent, NPs need to have sufficient circulation time *in vivo*. Ultra-small NPs with diameters <5.5 nm are rapidly filtered out by renal clearance upon intravenous administration [176]. The elimination of the larger engineered NPs by the MPS represents a substantial obstacle. Plasma proteins, including serum albumin, apolipoproteins, complement components, and immunoglobulins, bind onto the surface of circulating NPs and form the protein corona in a process called particle opsonization [177]. Subsequently, phagocytic cells of MPS – mainly resident macrophages in the spleen, lymph nodes, and liver – sequesters the NPs. There is an evident direct correlation between particle size and serum protein absorption, also meaning faster elimination [178]. Typically, rigid spherical NPs with a size of 100–200 nm are long-circulating, being large enough to avoid uptake in the liver but small enough to avoid filtration in the spleen [135]. Particles in the micrometer range (2–5 μm) accumulate within capillaries of the lungs, as well as in spleen and liver [33]. The shape of the particles has a dramatic effect on their *in vivo* destiny, as demonstrated in the filamentous polymer micelles that persisted in the circulation for up to one week after the intravenous injection – 10 times longer than the spherical ones [179]. In addition, softer, prone to deformability, NPs have prolonged circulation profiles than solid ones with reduced splenic filtration, as investigated in the nanogels with different levels of crosslinking [180]. Irrespective of the size and shape, softer nanoconstructs evaded up to 5 times more efficiently macrophage internalization as compared to rigid nanoconstructs [181].

The biodistribution of nanomaterials is influenced by their surface characteristics. NPs with a neutral and negative surface charge, in contrast to cationic formulations, experience reduced protein adsorption that results in more extended circulation half-lives [33]. Other concerns of the cationic NPs are the stimulation of inflammatory responses of human neutrophils and increased ROS production that was demonstrated on the cationic liposomes [182] and solid lipid NPs [183]. Cytotoxicity was induced by both cationic polymeric and lipid NPs [184]. In addition, positively charged NPs have a high rate of cellular uptake, as revealed that polymeric microparticles with a primary amine at the surface underwent more phagocytosis as compared to the ones having sulfate, hydroxyl, or carboxyl groups [178]. This makes cationic NPs a suitable vehicle for gene delivery; however, it would probably be preferred to design anionic nanoformulation for thrombolysis.

To avert the opsonization of the naked circulating NPs, their surface can be functionalized with PEG to create a hydrating layer that hinders the formation of a protein corona [33]. In addition to prevalent PEG, that is non-biodegradable and may cause complement activation, alternative hydrophilic polymers, such as polaxamer, polyvinyl alcohol, poly(amino acid)s, and polysaccharides [185] as well as "self" peptide CD47 [186] are researched. As a biomimetic surface, the coating of NPs with cell membranes extracted from autologous leukocytes and erythrocytes similarly extends their *in vivo* circulation [133].

Collectively, these findings demonstrate the importance of tunable particle size and surface composition & functionality for the development of long-circulating NPs for thrombolysis.

While the full analysis of the toxicology of NPs is beyond the scope of this paper, it is necessary to comment on certain safety issues of the nanomaterials used for a thrombolytic application.

NPs can perturbate vascular hemostasis and blood platelet function. Saikia et al. reported that silica NPs induced the overexpression of platelet endothelial cell adhesion molecule-1 on the endothelium that augmented the platelet-endothelial interaction [187]. Moreover, silica NPs triggered inflammation-coagulation response and thrombotic effects *in vivo* via JAK1/TF signaling pathway [188]. Amorphous silica NPs penetrated the platelet plasma membrane and stimulated an unfavorably low nitric oxide to peroxynitrite [NO]/[$ONOO^-$] ration that is crucial for cardiovascular homeostasis; they also induced platelet activation and aggregation via the MMP2 and ADP pathways [189].

Increasing concentrations of gold NPs led to a reduction in mouse body weight, red blood cell count, and hematocrit [190].

Multiple publications reported nanoparticle size-dependent toxicity. For instance, smaller gold, SiO_2, or polymer NPs were more hemolytic and provoked a higher level of ROS production than larger particles [191]. Cytotoxicity in four different cell lines was observed with the triphenylphosphine-stabilized gold NPs of 1–2 nm diameter, while 15-nm particles were non-toxic even at 100-fold higher concentration [192]. In a size-dependent manner, PEGylated AuNPs affected the normal function of human erythrocytes, such as deformability and oxygen-delivering ability [193]. Alterations of renal, hepatic, and splenic functions were dependent on the particle size and surface chemistry in ultrasmall SPION [194].

Distribution of the NPs in the non-target cells and organs is one of the challenges. The report of Lasagna-Reeves et al. suggested that gold NPs were able to cross the blood-brain barrier (BBB) and accumulated in the neural tissue [195]. Poly(alkyl cyanoacrylate) NPs could enter into the brain both in healthy animals and models of central nervous system diseases [196]. Siddiqi et al. concluded that AuNPs generated oxidative stress and an impairment of the antioxidant enzyme glutathione peroxidase in rat brain as well as significantly decreased the levels of dopamine and serotonin neurotransmitters [197]. Given that the BBB integrity is disrupted during ischemic stroke [198], and nano-formulation is assumed to limit the accumulation of nanoparticle-associated rtPA within the brain parenchyma to reduce the risk of cerebral hemorrhages and rtPA-mediated neurotoxicity [199], it would be vital to ensure that the nanotherapeutics are retained within the vascular compartment and do not cross the BBB.

The nanomaterials accumulate substantially in the liver upon intravenous injection. Bartneck et al. found that peptide-functionalized gold nanorods induced the prepolarization of hepatic macrophages, which aggravated a liver injury in a model of acute hepatitis [200]. High doses of silica nanorattle particles could induce liver damages, presumably due to decreased activity of superoxide dismutase [201]. Treatment with silica NPs revealed the hepatic microgranulation and splenic megakaryocyte accumulation by histological analysis [202]. Iron oxide NPs accumulated in liver phagocytes and elicited hepatic lipid peroxidation [203].

It is likely that organic biodegradable engineered NPs are of lesser concern to toxicity, as they will degrade by metabolic pathways. While the *in vitro* tests indicated that amphiphilic polymeric micelles induced an inflammatory response, no pathological changes were observed in the target organs *in vivo* [204]. Both PLGA and Cs NPs at concentrations relevant for drug-delivery application (<10 μg/mL) were platelet-compatible [205].

In contrast, inorganic non-biodegradable NPs, including multifunctional magnetic NPs, may persist for considerable periods, sometimes up to several years [206], and result in prolonged exposure with still-to-be-determined consequences. Apart from that, the growing presence of non-degradable nanotechnology products and the environmental risks need to be seriously assessed [207]. NPs composed of inorganic materials are difficult to break down by lysosomal enzymes. As an example, AuNPs accumulation in Kupffer cells in the liver and lysosome/endosome-like vesicles was present after six months post-injection in mice [208]. Moreover, Feng et al. found that dextran-coated and uncoated SPION administration affected several metabolism pathways, including energy, lipid, glucose, and amino acid metabolism in rodents [209]. PAA-coated iron oxide NPs triggered an inflammatory process *in vivo*, evidenced by abnormal differential blood count of neutrophils and large lymphocytes [203]. Fe_3O_4-MNPs significantly augmented ROS production *in vivo*. A sharp decline in RBC counts and hemoglobin concentration indicated an excessive degradation of erythrocytes, suggesting an associated anemia risk [210].

Generally, higher metabolic and functional injuries are prompted by uncoated NPs compared to coated ones with potential aggregation in the biological fluids. Surface modification with polymeric chains ameliorates the nanoparticle stability, masks the existing toxicity of the NPs, and extends their circulation half-life [121,211]. It is worth admitting that the NPs do not exhibit any toxicity until a certain threshold dose [121]. During the preclinical thrombolytic evaluation, it is also important to verify that the required dose of the NPs is based on estimates of potential future human exposure to avoid unrealistically high nanoparticle doses with no relevance to the clinics. Overall, this is critical to evaluate each newly engineered NPs as an individual case, since even slight changes in physicochemical properties to an existing and well-studied particle can result in a completely different toxicological profile.

8.2. Strategies for the nanoencapsulation of PA

PA are hydrophilic macromolecules (40–70 kDa) that require special nanoparticle design and drug complexation methods. While PA can be incorporated into the aqueous phase during nanoparticle fabrication for lipid or polymeric particles, harsh synthesis conditions – high energy processes (ultrasound, ultraturrax), elevated temperatures, the use of organic solvents – are not suitable for fragile molecules such as proteins [212]. Otherwise, the fibrinolytic agent may be attached to the surface through covalent or non-covalent protocols. The covalent methods provide more stable conjugation (avoiding “burst release”), however, they sometimes require chemical modification of the drug and might affect changes in the protein structure that might result in its partial denaturation and loss of enzymatic activity [213]. Physical adsorption is a mild drug encapsulation method that results in high loading efficacy for the nanocarriers with hydrophilic surfaces. As PA are predominantly positively charged at physiological pH with an isoelectric point (IP) > 7 (except for SK, IP $= 5.12$), they can form a complexation with anionic NPs due to electrostatic interactions. The existence of a positive charge on the polymer, as, for instance, chitosan, limits the encapsulation of cationic drugs because of repulsive interactions between a drug and polymer [212]. Comparing covalent vs. non-covalent methods, adsorptive bound PA liberates faster from the particles and diffused more readily into the fibrin matrix of the clot than covalently bound PA [128] and does not impair the biological activity of the drug [214] that may be beneficial in targeted thrombolysis. In addition, effective entrapment of hydrophilic drugs may occur in the crosslinked polymeric network of hydrogel nanoparticles that imbibe large quantities of water [215].

To sum up, depending on the type and composition of the nanocarrier, different encapsulation techniques may be applied. Extensive *in vitro* tests demonstrating high loading efficiency, sustainable release, preservation of the amidolytic and fibrinolytic activates of the PA after conjugation must be verified.

9. Discussion & conclusion

The rapid recanalization of the vascular occlusion is of the utmost importance for the patients suffering from acute thrombotic diseases. The innovative nanomedical approaches have been intensively proposed for targeted thrombolytic therapy to address the challenges of systemic drug administration.

The accomplishments of nanomedicine in thrombotic diseases include the protection of thrombolytics from inactivation by PAI-1, improvement in the blood half-life, enhanced thrombolytic effect at a lower dose, reduction in systemic bleeding, and post-ischemic infarct zone, etc. Recent studies have demonstrated that nanocarriers, such as liposomes, polymeric or inorganic NPs, bio-inspired nanocarriers, and microbubbles, provide benefits for thrombolytic therapy either alone or in combination with ultrasound or magnetic force (Table 2). Current nano-approaches in targeted thrombolysis are summarized schematically in Fig. 13. Among the numerous thrombolytic-bearing nanocarriers that are tested in preclinical models, sonothrombolysis with lipid-based microbubbles and intravenous rtPA is already being validated in clinical trials with thrombolysis improvement. However, lipid microbubbles

Table 2
Different nanocarriers for thrombolytic therapy.

Nanocarriers	Advantages	Disadvantages	Therapeutic effects
Liposomes	• Biodegradable, biocompatible, non-toxic • Clinically approved	• Low PA encapsulation rate • Low stability • Phospholipids may undergo oxidation and hydrolysis	• Improved thrombolysis rate • Lower risks of hemorrhages
Polymeric	• Biocompatible and often biodegradable • Easy surface functionalization	• High PA encapsulation rate • Improved stability	• Superior thrombolytic efficacy • Accelerated thrombolysis • Protection BBB permeability damage • Increased survival *in vivo* • Improved neurological deficit • Reduction in cerebral ROS • Reduction in subarachnoid hemorrhage
Inorganic Fe_3O_4 NPs AuNPs	• Biocompatible • Superparamagnetic properties • Magnet-guided thrombolysis • Optical and photothermal properties • Multifunctional theranostic systems	• May enter BBB and generate ROS • Accumulation in the body • May induce immunogenic response or inflammation	• Faster vessel recanalization • Mechanical clot dissolution with an external magnet • Hyperthermia as adjuvant therapy • Increased blood flow rate • Reduction in infarct volume
Bio-inspired	• Prolonged *in vivo* circulation • Natural thrombus targeting	• Low reproducibility • Lack of standardization • Source availability • Immunogenicity • Scale-up	• Improved survival rate • Superior thrombolytic efficacy • Lower neurological deficit score • Smaller ischemic zone • Better neurological outcome • Diminished ROS level in the brain • Lower risk of hemorrhages
US-responsive	• Enhanced thrombolysis with US insonation • Biocompatibility • US imaging	• Low stability • Merging into big MBs • Vessel occlusion	• US stable cavitation - higher penetration of drugs or MBs into the clot • US inertial cavitation: sonothrombolysis

Abbreviations: *PA*, plasminogen activator; *BBB*, blood-brain barrier; *NPs*, nanoparticles; *ROS*, reactive oxygen species; *US*, ultrasound; *MBs*, microbubbles.

may coalesce and form resonant bubbles with a size of over 20 μm [158], inducing the risk of pulmonary embolism [155]. Alternatively, polymeric microbubbles have enhanced stability *in vivo* over the soft shell ones [216], and the recent work [217] described echogenic polymeric fucoidan-functionalized microbubbles, able to target thrombosis via P-selectin interactions.

Active drug targeting of the nanocarriers allows drug accumulation at the thrombus site and has the potential to enhance thrombolytic penetration into deeply localized thrombi. This is currently realized by directing NPs mostly towards fibrin and platelets, though, identification of the new target molecules and development of the inexpensive and specific targeting moieties will be useful. Fucoidan, which is at present under clinical investigation as a diagnostic agent for the imaging of thrombosis [218,219], may become an affordable and high-quality alternative to antibodies and peptides. Another thrombus targeting strategy relies on the use of magnetic NPs under external magnetic force irradiation. Yet, despite an abundance of preclinical works dealing with magnetic field-assisted guiding, there is no clinically approved medical device to impose a high magnetic force on NPs in deep blood vessels. Therefore, it is probably preferable to design NPs capable of targeting thrombosis without external triggers.

A growing number of reports demonstrate a controlled release of the thrombolytics. On top of the ultrasound that can control the drug release from the echogenic liposomes, microbubbles, and some polymer (gelatin and chitosan) NPs, other strategies, such as enzyme exposure ($sPLA_2$ or thrombin), pH, temperature, shear stress, magnet, are employed (Fig. 13).

Apart from the necessity of the rapid restoration of blood flow after thrombotic occlusions, combating the ischemia-reperfusion injury such as inflammation and oxidative damage is vital for a good prognosis. Hence, complementing fibrinolytic therapy with nanodelivery of a potent antioxidant would be a sensible approach. For instance, poly (isobutyl cyanoacrylate)-polysaccharide NPs bearing microRNA-155–5p were proposed as a cardio-protective therapy for MI due to their antioxidant and cytoprotective properties [220]. Besides, rtPA might be accompanied by neuroprotection to prevent brain injury and neuronal damage during or after exposure to ischemia following acute ischemic stroke [221]. Discovery of next-generation thrombolytic drugs is further required to improve the safety and efficacy of nanomedicine-based thrombolysis. Goulay et al. engineered a non-neurotoxic rtPA variant with an equal fibrinolytic potential but without stimulating NMDA-dependent neurotoxicity [222].

The design of theranostic nanosystems with both thrombolytics and imaging agents (e.g., NIR fluorescent probes, gold, iron oxides, or perfluorocarbon) integrates diagnostic and therapeutic modalities. This strategy may not only provide visualization of drug delivery in real-time but also evaluate the effectiveness of treatment by MRI, CT, or US.

It is critical to face the challenges of nanomedicine, particularly in an attempt for clinical translation. To ensure clinical safety, the potential toxicity of NPs needs to be considered with a careful examination of their physical and chemical characteristics and accumulation in the non-target organs and tissues [223]. Indeed, some NPs may cause oxidative stress generation, immunological response, protein misfolding, immune response, and DNA damage [121]. Selecting biocompatible and fully biodegradable materials with FDA-approval, as well as a scalable production of the nanoformulations according to Good Manufacturing Practice (GMP), is essential [224]. Incorporation of sophisticated nanodesigns (e.g., cell-derived biomimetic surfaces) should accord with a risk analysis of reproducibility, quality control, and toxicity that might complicate regulatory approvals [33].

There is an evident gap between scientific discovery and clinical practice in nanomedicine-guided thrombolytic therapy. An astonishing ~10-fold increase from 2010 to 2020 in the number of publications in the field with beneficial therapeutic effects demonstrates a solid argument towards an imminent clinical translation. At the development stage, the tendency is to design complex targeted biomimetic multifunctional nanocarriers, sometimes bearing several active molecules. By examining nanoparticle delivery systems that are currently approved or under clinical investigation [35,36], we speculate that the first nanoparticulate candidate for site-specific delivery of PA tested in humans will probably be built on long-established technologies – primarily PEGylated liposomes, but also albumin-coated PA or nanocarriers from FDA-approved polymers. More sophisticated systems with targeting moieties, stimuli-responsive control of drug release will follow.

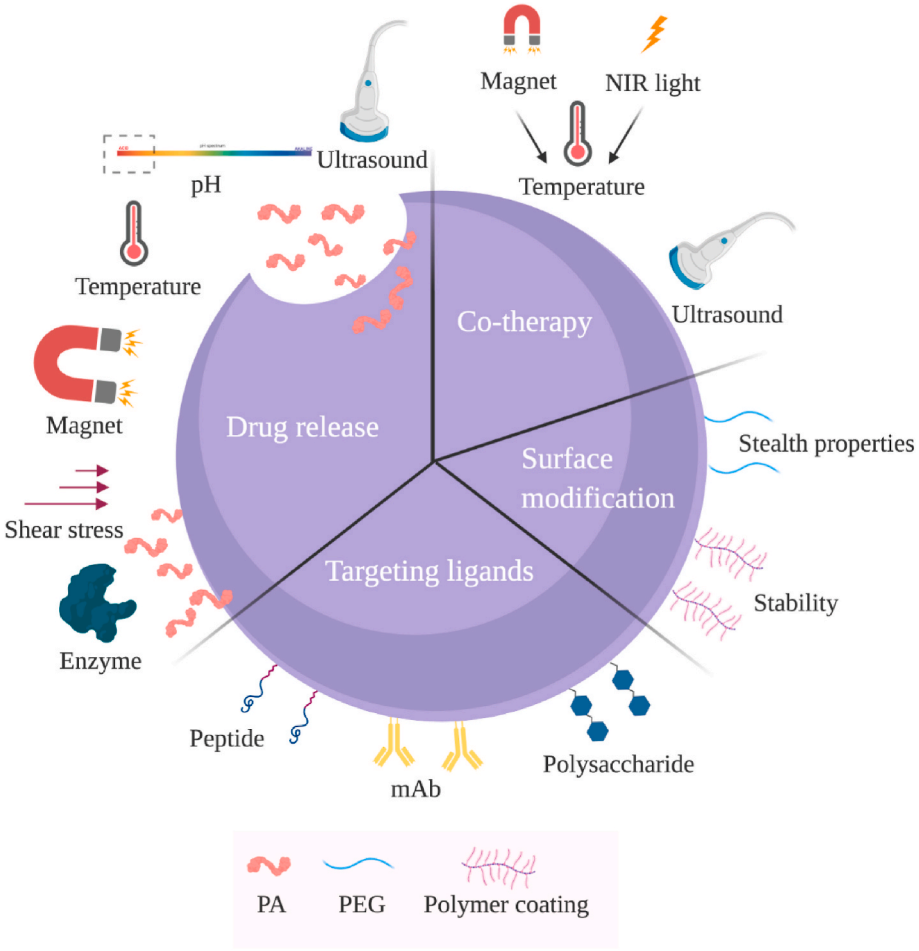

Fig. 13. Schematic illustration of the main strategies in the development of thrombolytic drug delivery nanocarriers. Surface modification with PEG or other hydrophilic polymeric chains is effectuated to ameliorate the nanoparticle stability, prevent the opsonization, and extend the nanoparticle blood circulation time. Nanoparticles may be decorated with targeting moieties against thrombus biomarkers with monoclonal antibodies, peptides, or sulfated polysaccharide fucoidan to attain site-specific thrombolysis. Several endogenous (enzymes in the thrombi, high shear stress in stenotic vessels, or low pH in the ischemic area) and exogenous (magnetic field, elevated temperature, ultrasound) principles are researched for the spatial & temporal control of PA release, prior incorporated either in the core of the nanoparticles or onto their surface. As an adjuvant therapy, ultrasound irradiation or elevated temperature by magnet and NIR light enhances nanomedicine-assisted thrombolytic efficacy. Abbreviations: *PA*, plasminogen activator; *mAb*, monoclonal antibody; *PEG*, Polyethylene glycol; *NIR*, near-infrared.

Meanwhile, public initiatives contribute to nanomedicine development. Recently, the European Union project NanoAthero (http://www.nanoathero.eu/) was completed. It intended to use nanomedicine for molecular imaging and targeted treatment of atherothrombosis with research activities ranging from nanosystems design to clinical validation and industrial production [225]. Several Phase I clinical trials demonstrated its feasibility for patients [219,226–228]. This consortium of 16 partners lasted 5.5 years (February 2013–July 2018) with the European Commission contribution of 10 million euros.

To conclude, the development of novel nanoparticulate strategies with plasminogen activators for the treatment of thrombotic disease will continue to flourish as they represent a potent evolution to free drug administration. The encouraging results in preclinical research predict future clinical translation of some of the formulations and progress in the nanomedicine-based precise therapy of thrombotic pathologies.

Author contributions

Alina Zenych: Conceptualization, Writing - original draft, Visualization; Louise Fournier: Writing - original draft (Section: 7 Ultrasound-Responsive Carriers & Sonothrombolysis), Visualization; Cédric Chauvierre: Writing - review & editing, Supervision, Funding acquisition.

Declaration of competing interest

The authors declare that they have no known competing financial interests or personal relationships that could have appeared to influence the work reported in this paper.

Acknowledgment

Authors thank INSERM, Université de Paris, and Université Sorbonne Paris Nord for the financial support. This work also received funding from the EU project FP7-NMP-2012-LARGE-6-309820 “NanoAthero”. Alina Zenych is grateful for the Ph.D. fellowship from the INSPIRE program of the European Union’s Horizon 2020 research and innovation program (Marie Sklodowska-Curie grant # 665850). The illustrations were designed with BioRender software (biorender.com).

References

[1] World Health Organisation (WHO), [Internet] World Health Organization, Media Centre: Cardiovascular disease, 2020. https://www.who.int/health-topics/cardiovascular-diseases/#tab=tab_1.

[2] E.J. Benjamin, P. Muntner, A. Alonso, M.S. Bittencourt, C.W. Callaway, A. P. Carson, A.M. Chamberlain, A.R. Chang, S. Cheng, S.R. Das, F.N. Delling, L. Djousse, M.S.V. Elkind, J.F. Ferguson, M. Fornage, L.C. Jordan, S.S. Khan, B. M. Kissela, K.L. Knutson, T.W. Kwan, D.T. Lackland, T.T. Lewis, J.H. Lichtman, C. T. Longenecker, M.S. Loop, P.L. Lutsey, S.S. Martin, K. Matsushita, A.E. Moran, M.E. Mussolino, M. O'Flaherty, A. Pandey, A.M. Perak, W.D. Rosamond, G. A. Roth, U.K.A. Sampson, G.M. Satou, E.B. Schroeder, S.H. Shah, N.L. Spartano, A. Stokes, D.L. Tirschwell, C.W. Tsao, M.P. Turakhia, L.B. VanWagner, J. T. Wilkins, S.S. Wong, S.S. Virani, Heart disease and stroke statistics—2019 update: a report from the American heart association, Circulation (2019), https://doi.org/10.1161/CIR.0000000000000659.

[3] H. Thomas, J. Diamond, A. Vieco, S. Chaudhuri, E. Shinnar, S. Cromer, P. Perel, G.A. Mensah, J. Narula, C.O. Johnson, G.A. Roth, A.E. Moran, Global atlas of cardiovascular disease 2000-2016: the path to prevention and control, Glob. Heart. 13 (2018) 143–163, https://doi.org/10.1016/j.gheart.2018.09.511.

[4] J. Leal, R. Luengo-Fernández, A. Gray, S. Petersen, M. Rayner, Economic burden of cardiovascular diseases in the enlarged European Union, Eur. Heart J. 27 (2006) 1610–1619, https://doi.org/10.1093/eurheartj/ehi733.

[5] D.N. Granger, P.R. Kvietys, Reperfusion injury and reactive oxygen species: the evolution of a concept, Redox Biol 6 (2015) 524–551, https://doi.org/10.1016/j.redox.2015.08.020.

[6] C.K. Glass, J.L. Witztum, Atherosclerosis: the road ahead, Cell 104 (2001) 503–516, https://doi.org/10.5005/jp/books/12883_4.

[7] E. Falk, Pathogenesis of atherosclerosis, J. Am. Coll. Cardiol. 47 (2006) C7–C12, https://doi.org/10.1016/j.jacc.2005.09.068.

[8] Y.S. Chatzizisis, A.U. Coskun, M. Jonas, E.R. Edelman, C.L. Feldman, P.H. Stone, Role of endothelial shear stress in the natural history of coronary atherosclerosis and vascular remodeling. Molecular, cellular, and vascular behavior, J. Am. Coll. Cardiol. 49 (2007) 2379–2393, https://doi.org/10.1016/j.jacc.2007.02.059.

[9] G.G. Caro, Discovery of the role of wall shear in atherosclerosis, Arterioscler. Thromb. Vasc. Biol. 29 (2009) 158–161, https://doi.org/10.1161/ATVBAHA.108.166736.

[10] J. Jongstra-Bilen, M. Haidari, S.N. Zhu, M. Chen, D. Guha, M.I. Cybulsky, Low-grade chronic inflammation in regions of the normal mouse arterial intima predisposed to atherosclerosis, J. Exp. Med. 203 (2006) 2073–2083, https://doi.org/10.1084/jem.20060245.

[11] P. Libby, Inflammation in atherosclerosis, Nature 420 (2002) 868–874, https://doi.org/10.1038/nature01323.

[12] Z.S. Galis, G.K. Sukhova, R. Kranzhöfer, S. Clark, P. Libby, Macrophage foam cells from experimental atheroma constitutively produce matrix-degrading proteinases, Proc. Natl. Acad. Sci. U.S.A. 92 (1995) 402–406, https://doi.org/10.1073/pnas.92.2.402.

[13] M.R. Dweck, E. Aikawa, D.E. Newby, J.M. Tarkin, J.H.F. Rudd, J. Narula, Z. A. Fayad, Noninvasive molecular imaging of disease activity in atherosclerosis, Circ. Res. 119 (2016) 330–340, https://doi.org/10.1161/CIRCRESAHA.116.307971.

[14] A. Shioi, Y. Ikari, Plaque calcification during atherosclerosis progression and regression, J. Atherosclerosis Thromb. 25 (2018) 294–303, https://doi.org/10.5551/jat.RV17020.

[15] G. Lippi, M. Franchini, G. Targher, Arterial thrombus formation in cardiovascular disease, Nat. Rev. Cardiol. 8 (2011) 502–512, https://doi.org/10.1038/nrcardio.2011.91.

[16] N. Mackman, Triggers, targets and treatments for thrombosis, Nature 451 (2008) 914–918, https://doi.org/10.1038/nature06797.

[17] I. Martinelli, P. Bucciarelli, P.M. Mannucci, Thrombotic risk factors: basic pathophysiology, Crit. Care Med. 38 (2010), https://doi.org/10.1097/CCM.0b013e3181c9cbd9.

[18] C.T. Esmon, Basic mechanisms and pathogenesis of venous thrombosis, Blood Rev. 23 (2009) 225–229, https://doi.org/10.1016/j.blre.2009.07.002.

[19] J.A. López, J. Chen, Pathophysiology of venous thrombosis, Thromb. Res. 123 (2009) 30–34, https://doi.org/10.1016/S0049-3848(09)70140-9.

[20] A. Bivard, L. Lin, M.W. Parsonsb, Review of stroke thrombolytics, J. Stroke. 15 (2013) 90, https://doi.org/10.5853/jos.2013.15.2.90.

[21] C. Kluft, J.J. Sidelmann, J.B. Gram, Assessing safety of thrombolytic therapy, Semin. Thromb. Hemost. 43 (2017) 300–310, https://doi.org/10.1055/s-0036-1584130.

[22] R.S. Marshall, Progress in intravenous thrombolytic therapy for acute stroke, JAMA Neurol 72 (2015) 928–934, https://doi.org/10.1001/jamaneurol.2015.0835.

[23] V.J. Marder, Thrombolytic therapy. Consult. Hemost. Thromb., Elsevier, 2013, pp. 526–537, https://doi.org/10.1016/B978-1-4557-2296-9.00028-2.

[24] J. Schaller, S.S. Gerber, The plasmin-antiplasmin system: structural and functional aspects, Cell, Mol. Life Sci. 68 (2011) 785–801, https://doi.org/10.1007/s00018-010-0566-5.

[25] A. Pal Khasa, Y. Pal Khasa, The evolution of recombinant thrombolytics: current status and future directions, Bioengineered 8 (2017) 331–358, https://doi.org/10.1080/21655979.2016.1229718.

[26] G.N. Levine, E.R. Bates, J.C. Blankenship, S.R. Bailey, J.A. Bittl, B. Cercek, C. E. Chambers, S.G. Ellis, R.A. Guyton, S.M. Hollenberg, U.N. Khot, R.A. Lange, L. Mauri, R. Mehran, I.D. Moussa, D. Mukherjee, H.H. Ting, P.T. O'Gara, F. G. Kushner, D.D. Ascheim, R.G. Brindis, D.E. Casey, M.K. Chung, J.A. De Lemos, D.B. Diercks, J.C. Fang, B.A. Franklin, C.B. Granger, H.M. Krumholz, J. A. Linderbaum, D.A. Morrow, L.K. Newby, J.P. Ornato, N. Ou, M.J. Radford, J. E. Tamis-Holland, C.L. Tommaso, C.M. Tracy, Y.J. Woo, D.X. Zhao, 2015 ACC/AHA/SCAI focused update on primary percutaneous coronary intervention for patients with ST-elevation myocardial infarction an update of the 2011 ACCF/AHA/SCAI guideline for percutaneous coronary intervention and the 2013 ACCF/AHA guideline for th, J. Am. Coll. Cardiol. 67 (2016) 1235–1250, https://doi.org/10.1016/j.jacc.2015.10.005.

[27] B. Ibanez, S. James, S. Agewall, M.J. Antunes, C. Bucciarelli-Ducci, H. Bueno, A.L. P. Caforio, F. Crea, J.A. Goudevenos, S. Halvorsen, G. Hindricks, A. Kastrati, M. J. Lenzen, E. Prescott, M. Roffi, M. Valgimigli, C. Varenhorst, P. Vranckx, P. Widimský, A. Baumbach, R. Bugiardini, I.M. Coman, V. Delgado, D. Fitzsimons, O. Gaemperli, A.H. Gershlick, S. Gielen, V.P. Harjola, H.A. Katus, J. Knuuti, P. Kolh, C. Leclercq, G.Y.H. Lip, J. Morais, A.N. Neskovic, F.J. Neumann, A. Niessner, M.F. Piepoli, D.J. Richter, E. Shlyakhto, I.A. Simpson, P.G. Steg, C. J. Terkelsen, K. Thygesen, S. Windecker, J.L. Zamorano, U. Zeymer, M. Chettibi, H.G. Hayrapetyan, B. Metzler, F. Ibrahimov, V. Sujayeva, C. Beauloye, L. Dizdarevic-Hudic, K. Karamfiloff, B. Skoric, L. Antoniades, P. Tousek, C. J. Terkelsen, S.M. Shaheen, T. Marandi, M. Niemelᵭa, S. Kedev, M. Gilard, A. Aladashvili, A. Elsaesser, I.G. Kanakakis, B. Merkely, T. Gudnason, Z. Iakobishvili, L. Bolognese, S. Berkinbayev, G. Bajraktari, M. Beishenkulov, I. Zake, H. Ben Lamin, O. Gustiene, B. Pereira, R.G. Xuereb, S. Ztot, V. Juliebø, J. Legutko, A.T. Timoteo, G. Tatu-Chitoiu, A. Yakovlev, L. Bertelli, M. Nedeljkovic, M. Studencan, M. Bunc, A.M.G. de Castro, P. Petursson, R. Jeger, M.S. Mourali, A. Yildirir, A. Parkhomenko, C.P. Gale, 2017 ESC Guidelines for the management of acute myocardial infarction in patients presenting with ST-segment elevation, Eur. Heart J. 39 (2018) 119–177, https://doi.org/10.1093/eurheartj/ehx393.

[28] G. Turc, P. Bhogal, U. Fischer, P. Khatri, K. Lobotesis, M. Mazighi, P. D. Schellinger, D. Toni, J. de Vries, P. White, J. Fiehler, European stroke organisation (ESO) – European society for minimally invasive neurological therapy (ESMINT) guidelines on mechanical thrombectomy in acute ischaemic StrokeEndorsed by stroke alliance for europe (SAFE), Eur. Stroke J. 4 (2019) 6–12, https://doi.org/10.1177/2396987319832140.

[29] W.J. Powers, A.A. Rabinstein, T. Ackerson, O.M. Adeoye, N.C. Bambakidis, K. Becker, J. Biller, M. Brown, B.M. Demaerschalk, B. Hoh, E.C. Jauch, C. S. Kidwell, T.M. Leslie-Mazwi, B. Ovbiagele, P.A. Scott, K.N. Sheth, A. M. Southerland, D.V. Summers, D.L. Tirschwell, Guidelines for the early management of patients with acute ischemic stroke: 2019 update to the 2018 guidelines for the early management of acute ischemic stroke: a guideline for healthcare professionals from the American heart association/American stroke, Stroke 50 (2019) e344–e418, https://doi.org/10.1161/STR.0000000000000211.

[30] L. Derex, T.H. Cho, Mechanical thrombectomy in acute ischemic stroke, Rev. Neurol. (Paris) 173 (2017) 106–113, https://doi.org/10.1016/j.neurol.2016.06.008.

[31] S.A. Munich, K. Vakharia, E.I. Levy, Overview of mechanical thrombectomy techniques, Clin. Neurosurg. 85 (2019) S60–S67, https://doi.org/10.1093/neuros/nyz071.

[32] G. Forestier, B. Kerleroux, K. Janot, F. Zhu, V. Dumas, J.-F. Hak, E. Shotar, W. BenHassen, R. Bourcier, S. Soize, J. Berge, O. Naggara, H. Desal, G. Boulouis, A. Rouchaud, Mechanical thrombectomy practices in France: exhaustive survey of centers and individual operators, J. Neuroradiol. (2020) 1–14, https://doi.org/10.1016/j.neurad.2020.05.001.

[33] E. Blanco, H. Shen, M. Ferrari, Principles of nanoparticle design for overcoming biological barriers to drug delivery, Nat. Biotechnol. 33 (2015) 941–951, https://doi.org/10.1038/nbt.3330.

[34] Y. Barenholz, Doxil® - the first FDA-approved nano-drug: lessons learned, J. Contr. Release 160 (2012) 117–134, https://doi.org/10.1016/j.jconrel.2012.03.020.

[35] A.C. Anselmo, S. Mitragotri, Nanoparticles in the clinic, Bioeng. Transl. Med. 1 (2016) 10–29, https://doi.org/10.1002/btm2.10003.

[36] A.C. Anselmo, S. Mitragotri, Nanoparticles in the clinic: an update, Bioeng. Transl. Med. 4 (2019) 1–16, https://doi.org/10.1002/btm2.10143.

[37] T. Matoba, J.-I. Koga, K. Nakano, K. Egashira, H. Tsutsui, Nanoparticle-mediated drug delivery system for atherosclerotic cardiovascular disease, J. Cardiol. 70 (2017) 206–211, https://doi.org/10.1016/j.jjcc.2017.03.005.

[38] T. Alam, S. Khan, B. Gaba, M.F. Haider, S. Baboota, J. Ali, Nanocarriers as treatment modalities for hypertension, Drug Deliv. 24 (2017) 358–369, https://doi.org/10.1080/10717544.2016.1255999.

[39] C.K.W. Chan, L. Zhang, C.K. Cheng, H. Yang, Y. Huang, X.Y. Tian, C.H.J. Choi, Recent advances in managing atherosclerosis via nanomedicine, Small 14 (2018) 1–16, https://doi.org/10.1002/smll.201702793.

[40] T. Cyrus, S.A. Wickline, G.M. Lanza, Nanotechnology in interventional cardiology, Wiley Interdiscip. Rev. Nanomedicine Nanobiotechnology. 4 (2012) 82–95, https://doi.org/10.1002/wnan.154.

[41] L. Yu, B.J. Scherlag, K. Dormer, K.T. Nguyen, C. Pope, K.M. Fung, S.S. Po, Autonomic denervation with magnetic nanoparticles, Circulation 122 (2010) 2653–2659, https://doi.org/10.1161/CIRCULATIONAHA.110.940288.

[42] T. Simon-Yarza, I. Bataille, D. Letourneur, Cardiovascular bio-engineering: current state of the art, J. Cardiovasc. Transl. Res. 10 (2017) 180–193, https://doi.org/10.1007/s12265-017-9740-6.

[43] D.R. Esfahani, V. Viswanathan, A. Alaraj, Nanoparticles and stem cells–has targeted therapy for aneurysms finally arrived? Neurol. Res. 37 (2015) 269–277, https://doi.org/10.1179/1743132814Y.0000000435.

[44] C. Psarros, R. Lee, M. Margaritis, C. Antoniades, Nanomedicine for the prevention, treatment and imaging of atherosclerosis, Nanomed. Nanotechnol. Biol. Med. 8 (2012) S59–S68, https://doi.org/10.1016/j.nano.2012.05.006.

[45] B. Singh, T. Garg, A.K. Goyal, G. Rath, Recent advancements in the cardiovascular drug carriers, Artif. Cells, Nanomedicine Biotechnol 44 (2016) 216–225, https://doi.org/10.3109/21691401.2014.937868.

[46] C.H. Liu, H.L. Hsu, J.P. Chen, T. Wu, Y.H. Ma, Thrombolysis induced by intravenous administration of plasminogen activator in magnetoliposomes: dual targeting by magnetic and thermal manipulation, Nanomed. Nanotechnol. Biol. Med. 20 (2019) 1–12, https://doi.org/10.1016/j.nano.2019.03.014.

[47] X. Wang, C. Wei, M. Liu, T. Yang, W. Zhou, Y. Liu, K. Hong, S. Wang, H. Xin, X. Ding, Near-infrared triggered release of uPA from nanospheres for localized hyperthermia-enhanced thrombolysis, Adv. Funct. Mater. 27 (2017) 1–8, https://doi.org/10.1002/adfm.201701824.

[48] T. Mei, A. Kim, L.B. Vong, A. Marushima, S. Puentes, Y. Matsumaru, A. Matsumura, Y. Nagasaki, Encapsulation of tissue plasminogen activator in pH-sensitive self-assembled antioxidant nanoparticles for ischemic stroke treatment-Synergistic effect of thrombolysis and antioxidant, Biomaterials 215 (2019) 1–12, https://doi.org/10.1016/j.biomaterials.2019.05.020.

[49] Q.L. Zhou, Z.Y. Chen, Y.X. Wang, F. Yang, Y. Lin, Y.Y. Liao, Ultrasound-mediated local drug and gene delivery using nanocarriers, BioMed Res. Int. 2014 (2014), https://doi.org/10.1155/2014/963891.

[50] V. Karagkiozaki, S. Logothetidis, A.M. Pappa, Nanomedicine for atherosclerosis: molecular imaging and treatment, J. Biomed. Nanotechnol. 11 (2015) 191–210, https://doi.org/10.1166/jbn.2015.1943.

[51] Z. Tang, D. Li, X. Wang, H. Gong, Y. Luan, Z. Liu, J.L. Brash, H. Chen, A t-PA/nanoparticle conjugate with fully retained enzymatic activity and prolonged circulation time, J. Mater. Chem. B. 3 (2015) 977–982, https://doi.org/10.1039/c4tb01625d.
[52] S. Absar, K. Nahar, Y.M. Kwon, F. Ahsan, Thrombus-targeted nanocarrier attenuates bleeding complications associated with conventional thrombolytic therapy, Pharm. Res. (N. Y.) 30 (2013) 1663–1676, https://doi.org/10.1007/s11095-013-1011-x.
[53] H. Jin, H. Tan, L. Zhao, W. Sun, L. Zhu, Y. Sun, H. Hao, H. Xing, L. Liu, X. Qu, Y. Huang, Z. Yang, Ultrasound-triggered thrombolysis using urokinase-loaded nanogels, Int. J. Pharm. 434 (2012) 384–390, https://doi.org/10.1016/j.ijpharm.2012.06.001.
[54] H. Kawata, Y. Uesugi, T. Soeda, Y. Takemoto, J.H. Sung, K. Umaki, K. Kato, K. Ogiwara, K. Nogami, K. Ishigami, M. Horii, S. Uemura, M. Shima, Y. Tabata, Y. Saito, A new drug delivery system for intravenous coronary thrombolysis with thrombus targeting and stealth activity recoverable by ultrasound, J. Am. Coll. Cardiol. 60 (2012) 2550–2557, https://doi.org/10.1016/j.jacc.2012.08.1008.
[55] J. Hu, S. Huang, L. Zhu, W. Huang, Y. Zhao, K. Jin, Q. Zhuge, Tissue plasminogen activator-porous magnetic microrods for targeted thrombolytic therapy after ischemic stroke, ACS Appl. Mater. Interfaces 10 (2018) 32988–32997, https://doi.org/10.1021/acsami.8b09423.
[56] N. Zhang, C. Li, D. Zhou, C. Ding, Y. Jin, Q. Tian, X. Meng, K. Pu, Y. Zhu, Cyclic RGD functionalized liposomes encapsulating urokinase for thrombolysis, Acta Biomater. 70 (2018) 227–236, https://doi.org/10.1016/j.actbio.2018.01.038.
[57] C.L. Pawlowski, W. Li, M. Sun, K. Ravichandran, D. Hickman, C. Kos, G. Kaur, A. Sen Gupta, Platelet microparticle-inspired clot-responsive nanomedicine for targeted fibrinolysis, Biomaterials 128 (2017) 94–108, https://doi.org/10.1016/j.biomaterials.2017.03.012.
[58] V. Torchilin, M. Papisov, N. Orekhova, A. Belyaev, A. Petrov, S. Ragimov, Magnetically driven thrombolytic preparation containing immobilized streptokinase-targeted transport and action, Haemostasis 18 (1988) 113-116, https://doi.org/10.1159/000215791.
[59] P.D. Nguyen, E.A. O'Rear, A.E. Johnson, E. Patterson, T.L. Whitsett, R. Bhakta, Accelerated thrombolysis and reperfusion in a canine model of myocardial infarction by liposomal encapsulation of streptokinase, Circ. Res. 66 (1990) 875–878, https://doi.org/10.1161/01.RES.66.3.875.
[60] T.R. Porter, R.F. LeVeen, R. Fox, A. Kricsfeld, F. Xie, Thrombolytic enhancement with perfluorocarbon-exposed sonicated dextrose albumin microbubbles, Am. Heart J. 132 (1996) 964–968, https://doi.org/10.1016/S0002-8703(96)90006-X.
[61] J.K. Leach, E. Patterson, E.A. O'Rear, Encapsulation of a plasminogen activator speeds reperfusion, lessens infarct and reduces blood loss in a canine model of coronary artery thrombosis, Thromb, Haemostasis 91 (2004) 1213–1218, https://doi.org/10.1160/th03-11-0704.
[62] J.-C. Murciano, S. Medinilla, D. Eslin, E. Atochina, D.B. Cines, V.R. Muzykantov, Prophylactic fibrinolysis through selective dissolution of nascent clots by tPA-carrying erythrocytes, Nat. Biotechnol. 21 (2003) 891–896, https://doi.org/10.1038/nbt846.
[63] M. Faria, M. Björnmalm, K.J. Thurecht, S.J. Kent, R.G. Parton, M. Kavallaris, A.P. R. Johnston, J.J. Gooding, S.R. Corrie, B.J. Boyd, P. Thordarson, A.K. Whittaker, M.M. Stevens, C.A. Prestidge, C.J.H. Porter, W.J. Parak, T.P. Davis, E.J. Crampin, F. Caruso, Minimum information reporting in bio–nano experimental literature, Nat. Nanotechnol. 13 (2018) 777–785, https://doi.org/10.1038/s41565-018-0246-4.
[64] T.W. Chung, S.S. Wang, W.J. Tsai, Accelerating thrombolysis with chitosan-coated plasminogen activators encapsulated in poly-(lactide-co-glycolide) (PLGA) nanoparticles, Biomaterials 29 (2008) 228–237, https://doi.org/10.1016/j.biomaterials.2007.09.027.
[65] F. Bi, J. Zhang, Y. Su, Y.C. Tang, J.N. Liu, Chemical conjugation of urokinase to magnetic nanoparticles for targeted thrombolysis, Biomaterials 30 (2009) 5125–5130, https://doi.org/10.1016/j.biomaterials.2009.06.006.
[66] Y.-H. Ma, S.-Y. Wu, T. Wu, Y.-J. Chang, M.-Y. Hua, J.-P. Chen, Magnetically targeted thrombolysis with recombinant tissue plasminogen activator bound to polyacrylic acid-coated nanoparticles, Biomaterials 30 (2009) 3343–3351, https://doi.org/10.1016/j.biomaterials.2009.02.034.
[67] M. Juenet, R. Aid-Launais, B. Li, A. Berger, J. Aerts, V. Ollivier, A. Nicoletti, D. Letourneur, C. Chauvierre, Thrombolytic therapy based on fucoidan-functionalized polymer nanoparticles targeting P-selectin, Biomaterials 156 (2018) 204–216, https://doi.org/10.1016/j.biomaterials.2017.11.047.
[68] J.R. McCarthy, I.Y. Sazonova, S.S. Erdem, T. Hara, B.D. Thompson, P. Patel, I. Botnaru, C.P. Lin, G.L. Reed, R. Weissleder, F.A. Jaffer, Multifunctional nanoagent for thrombus-targeted fibrinolytic therapy, Nanomedicine 7 (2012) 1017–1028, https://doi.org/10.2217/nnm.11.179.
[69] J. Zhou, D. Guo, Y. Zhang, W. Wu, H. Ran, Z. Wang, Construction and evaluation of Fe3O4-based PLGA nanoparticles carrying rtPA used in the detection of thrombosis and in targeted thrombolysis, ACS Appl. Mater. Interfaces 6 (2014) 5566–5576, https://doi.org/10.1021/am406008k.
[70] S.D. Tiukinhoy-Laing, S. Huang, M. Klegerman, C.K. Holland, D.D. McPherson, Ultrasound-facilitated thrombolysis using tissue-plasminogen activator-loaded echogenic liposomes, Thromb. Res. 119 (2007) 777–784, https://doi.org/10.1016/j.thromres.2006.06.009.
[71] L. Ma, Y. Wang, S. Zhang, X. Qian, N. Xue, Z. Jiang, O. Akakuru, J. Li, Y. Xu, A. Wu, Deep penetration of targeted nanobubbles enhanced cavitation effect on thrombolytic capacity, Bioconjugate Chem. 31 (2020) 369–374, https://doi.org/10.1021/acs.bioconjchem.9b00653.
[72] N. Korin, M. Kanapathipillai, B.D. Matthews, M. Crescente, A. Brill, T. Mammoto, K. Ghosh, S. Jurek, S.A. Bencherif, D. Bhatta, A.U. Coskun, C.L. Feldman, D. D. Wagner, D.E. Ingber, Shear-activated nanotherapeutics for drug targeting to obstructed blood vessels, Science 337 (2012) 738–742, https://doi.org/10.1126/science.1217815.
[73] Y. Uesugi, H. Kawata, Y. Saito, Y. Tabata, Ultrasound-responsive thrombus treatment with zinc-stabilized gelatin nano-complexes of tissue-type plasminogen activator, J. Drug Target. 20 (2012) 224–234, https://doi.org/10.3109/1061186X.2011.633259.
[74] S.T. Gunawan, K. Kempe, T. Bonnard, J. Cui, K. Alt, L.S. Law, X. Wang, E. Westein, G.K. Such, K. Peter, C.E. Hagemeyer, F. Caruso, Multifunctional thrombin-activatable polymer capsules for specific targeting to activated platelets, Adv. Mater. 27 (2015) 5153–5157, https://doi.org/10.1002/adma.201502243.
[75] E. Voros, M. Cho, M. Ramirez, A.L. Palange, E. De Rosa, J. Key, Z. Garami, A. B. Lumsden, P. Decuzzi, TPA immobilization on iron oxide nanocubes and localized magnetic hyperthermia accelerate blood clot lysis, Adv. Funct. Mater. 25 (2015) 1709–1718, https://doi.org/10.1002/adfm.201404354.
[76] J. Xu, Y. Zhang, J. Xu, G. Liu, C. Di, X. Zhao, X. Li, Y. Li, N. Pang, C. Yang, Y. Li, B. Li, Z. Lu, M. Wang, K. Dai, R. Yan, S. Li, G. Nie, Engineered nanoplatelets for targeted delivery of plasminogen activators to reverse thrombus in multiple mouse thrombosis models, Adv. Mater. 1905145 (2019) 1–14, https://doi.org/10.1002/adma.201905145.
[77] U. Bulbake, S. Doppalapudi, N. Kommineni, W. Khan, Liposomal formulations in clinical use: an updated review, Pharmaceutics 9 (2017) 1–33, https://doi.org/10.3390/pharmaceutics9020012.
[78] S. Mallick, J.S. Choi, Liposomes: versatile and biocompatible nanovesicles for efficient biomolecules delivery, J. Nanosci. Nanotechnol. 14 (2014) 755–765, https://doi.org/10.1166/jnn.2014.9080.
[79] K. Bowey, J.F. Tanguay, M. Tabrizian, Liposome technology for cardiovascular disease treatment and diagnosis, Expet Opin. Drug Deliv. 9 (2012) 249–265, https://doi.org/10.1517/17425247.2012.647908.
[80] J. Jamasbi, K. Ayabe, S. Goto, B. Nieswandt, K. Peter, W. Siess, Platelet receptors as therapeutic targets: past, present and future, Thromb. Haemostasis 117 (2017) 1249–1257, https://doi.org/10.1160/TH16-12-0911.
[81] S. Koudelka, R. Mikulik, J. Mašek, M. Raška, P. Turánek Knotigová, A.D. Miller, J. Turánek, Liposomal nanocarriers for plasminogen activators, J. Contr. Release 227 (2016) 45–57, https://doi.org/10.1016/j.jconrel.2016.02.019.
[82] B. Vaidya, G.P. Agrawal, S.P. Vyas, Platelets directed liposomes for the delivery of streptokinase: development and characterization, Eur. J. Pharmaceut. Sci. 44 (2011) 589–594, https://doi.org/10.1016/j.ejps.2011.10.004.
[83] Y. Huang, L. Yu, J. Ren, B. Gu, C. Longstaff, A.D. Hughes, S.A. Thom, X.Y. Xu, R. Chen, An activated-platelet-sensitive nanocarrier enables targeted delivery of tissue plasminogen activator for effective thrombolytic therapy, J. Contr. Release 300 (2019) 1–12, https://doi.org/10.1016/j.jconrel.2019.02.033.
[84] D. Varon, E. Shai, Platelets and their microparticles as key players in pathophysiological responses, J. Thromb. Haemostasis 13 (2015) S40–S46, https://doi.org/10.1111/jth.12976.
[85] H.-L. Hsu, J.-P. Chen, Preparation of thermosensitive magnetic liposome encapsulated recombinant tissue plasminogen activator for targeted thrombolysis, J. Magn. Magn Mater. 427 (2017) 188–194, https://doi.org/10.1016/j.jmmm.2016.10.122.
[86] P. Ghasemiyeh, S. Mohammadi-Samani, Solid lipid nanoparticles and nanostructured lipid carriers as novel drug delivery systems: applications, advantages and disadvantages, Res. Pharm. Sci. 13 (2018) 288–303, https://doi.org/10.4103/1735-5362.235156.
[87] J.N. Marsh, G. Hu, M.J. Scott, H. Zhang, M.J. Goette, J. Patrick, S.D. Caruthers, S. A. Wickline, D. Abendschein, M. Gregory, A fibrin-specific thrombolytic nanomedicine approach to acute ischemic stroke, Nanomedicine 6 (2011) 605–615, https://doi.org/10.2217/nnm.11.21.A.
[88] A. Bolhassani, S. Javanzad, T. Saleh, M. Hashemi, M.R. Aghasadeghi, Polymeric nanoparticles. Potent vectors for vaccine delivery targeting cancer and infectious diseases, Hum. Vaccines Immunother. 10 (2014) 321–332, https://doi.org/10.4161/hv.26796.
[89] Y. Zhang, T. Sun, C. Jiang, Biomacromolecules as carriers in drug delivery and tissue engineering, Acta Pharm. Sin. B. 8 (2018) 34–50, https://doi.org/10.1016/j.apsb.2017.11.005.
[90] K.S. Soppimath, T.M. Aminabhavi, A.R. Kulkarni, W.E. Rudzinski, Biodegradable polymeric nanoparticles as drug delivery devices, J. Contr. Release 70 (2001) 1–20, https://doi.org/10.1016/S0168-3659(00)00339-4.
[91] J. Zhang, W. Xia, P. Liu, Q. Cheng, T. Tahirou, W. Gu, B. Li, Chitosan modification and pharmaceutical/biomedical applications, Mar. Drugs 8 (2010) 1962–1987, https://doi.org/10.3390/md8071962.
[92] H.J. Jin, H. Zhang, M.L. Sun, B.G. Zhang, J.W. Zhang, Urokinase-coated chitosan nanoparticles for thrombolytic therapy: preparation and pharmacodynamics in vivo, J. Thromb. Thrombolysis 36 (2013) 458–468, https://doi.org/10.1007/s11239-013-0951-7.
[93] H. Baharifar, G. Tavoosidana, R. Karimi, S.A. Bidgoli, H. Ghanbari, M. A. Faramarzi, A. Amani, Optimization of self-assembled chitosan/streptokinase nanoparticles and evaluation of their cytotoxicity and thrombolytic activity, J. Nanosci. Nanotechnol. 15 (2015) 10127–10133, https://doi.org/10.1166/jnn.2015.11696.
[94] M. Shamsi, P. Zahedi, On-chip preparation of streptokinase entrapped in chitosan nanoparticles used in thrombolytic therapy potentially, J. Pharmacol. Sci. 106 (2017) 3623–3630, https://doi.org/10.1016/j.xphs.2017.08.001.
[95] J. Liao, X. Ren, B. Yang, H. Li, Y. Zhang, Z. Yin, Targeted thrombolysis by using c-RGD-modified N,N,N-Trimethyl Chitosan nanoparticles loaded with

lumbrokinase, Drug Dev. Ind. Pharm. 45 (2019) 88–95, https://doi.org/10.1080/03639045.2018.1522324.
[96] Y. Teng, H. Jin, D. Nan, M. Li, C. Fan, Y. Liu, P. Lv, W. Cui, Y. Sun, H. Hao, X. Qu, Z. Yang, Y. Huang, In vivo evaluation of urokinase-loaded hollow nanogels for sonothrombolysis on suture embolization-induced acute ischemic stroke rat model, Bioact. Mater. 3 (2018) 102–109, https://doi.org/10.1016/j.bioactmat.2017.08.001.
[97] R. Yasmin, M. Shah, S.A. Khan, R. Ali, Gelatin nanoparticles: a potential candidate for medical applications, Nanotechnol. Rev. 6 (2017) 191–207, https://doi.org/10.1515/ntrev-2016-0009.
[98] Y. Uesugi, H. Kawata, J.I. Jo, Y. Saito, Y. Tabata, An ultrasound-responsive nano delivery system of tissue-type plasminogen activator for thrombolytic therapy, J. Contr. Release 147 (2010) 269–277, https://doi.org/10.1016/j.jconrel.2010.07.127.
[99] C. Englert, J.C. Brendel, T.C. Majdanski, T. Yildirim, S. Schubert, M. Gottschaldt, N. Windhab, U.S. Schubert, Pharmapolymers in the 21st century: synthetic polymers in drug delivery applications, Prog. Polym. Sci. 87 (2018) 107–164, https://doi.org/10.1016/j.progpolymsci.2018.07.005.
[100] B. Sivaraman, A. Sylvester, A. Ramamurthi, Fibrinolytic PLGA nanoparticles for slow clot lysis within abdominal aortic aneurysms attenuate proteolytic loss of vascular elastic matrix, Mater. Sci. Eng. C-Materials Biol. Appl. 59 (2016) 145–156, https://doi.org/10.1016/j.msec.2015.09.056.
[101] M. Colasuonno, A.L. Palange, R. Aid, M. Ferreira, H. Mollica, R. Palomba, M. Emdin, M. Del Sette, C. Chauvierre, D. Letourneur, P. Decuzzi, Erythrocyte-inspired discoidal polymeric nanoconstructs carrying tissue plasminogen activator for the enhanced lysis of blood clots, ACS Nano 12 (2018) 12224–12237, https://doi.org/10.1021/acsnano.8b06021.
[102] C. Vauthier, C. Dubernet, E. Fattal, H. Pinto-Alphandary, P. Couvreur, Poly (alkylcyanoacrylates) as biodegradable materials for biomedical applications, Adv. Drug Deliv. Rev. 55 (2003) 519–548, https://doi.org/10.1016/S0169-409X(03)00041-3.
[103] L. Chollet, P. Saboural, C. Chauvierre, J.-N. Villemin, D. Letourneur, F. Chaubet, Fucoidans in Nanomedicine, Mar. Drugs. 14 (2016) 1–24, https://doi.org/10.3390/md14080145.
[104] T. Bonnard, J.-M. Serfaty, C. Journé, B. Ho Tin Noe, D. Arnaud, L. Louedec, M. Derkaoui, D. Letourneur, C. Chauvierre, C. Le Visage, Leukocyte mimetic polysaccharide microparticles tracked in vivo on activated endothelium and in abdominal aortic aneurysm, Acta Biomater. 10 (2014) 3535–3545, https://doi.org/10.1016/j.actbio.2014.04.015.
[105] B. Li, M. Juenet, R. Aid-Launais, M. Maire, V. Ollivier, D. Letourneur, C. Chauvierre, Development of polymer microcapsules functionalized with fucoidan to target P-selectin overexpressed in cardiovascular diseases, Adv. Healthc. Mater. 6 (2017) 1–11, https://doi.org/10.1002/adhm.201601200.
[106] H.R. Lijnen, B. Van Hoef, V. Beelen, D. Collen, Characterization of the murine plasma fibrinolytic system, Eur. J. Biochem. 224 (1994) 863–871, https://doi.org/10.1111/j.1432-1033.1994.00863.x.
[107] C. Englert, J.C. Brendel, T.C. Majdanski, T. Yildirim, S. Schubert, M. Gottschaldt, N. Windhab, U.S. Schubert, Pharmapolymers in the 21st century: synthetic polymers in drug delivery applications, Prog. Polym. Sci. 87 (2018) 107–164, https://doi.org/10.1016/j.progpolymsci.2018.07.005.
[108] J. Deng, H. Mei, W. Shi, Z.-Q. Pang, B. Zhang, T. Guo, H.-F. Wang, X.-G. Jiang, Y. Hu, Recombinant tissue plasminogen activator-conjugated nanoparticles effectively targets thrombolysis in a rat model of middle cerebral artery occlusion, Curr. Med. Sci. 38 (2018) 427–435, https://doi.org/10.1007/s11596-018-1896-z.
[109] Y. Pan, X. Wang, Z. Yin, Synthesis and evaluation of cationic polymeric micelles as carriers of lumbrokinase for targeted thrombolysis, Asian J. Pharm. Sci. 14 (2019) 144–153, https://doi.org/10.1016/j.ajps.2018.03.004.
[110] Y. Pan, X. Ren, S. Wang, X. Li, X. Luo, Z. Yin, Annexin V-conjugated mixed micelles as a potential drug delivery system for targeted thrombolysis, Biomacromolecules 18 (2017) 865–876, https://doi.org/10.1021/acs.biomac.6b01756.
[111] J.F. Tait, M.D. Cerqueira, T.A. Dewhurst, K. Fujikawa, J.L. Ritchie, J.R. Stratton, Evaluation of annexin V as a platelet-directed thrombus targeting agent, Thromb. Res. 75 (1994) 491–501, https://doi.org/10.1016/0049-3848(94)90224-0.
[112] L.I. Mukhametova, R.B. Aisina, E.M. Zakharyan, E.A. Karakhanov, K. B. Gershkovich, S.D. Varfolomeyev, Thrombolytic and fibrinogenolytic properties of bioconjugate streptokinase-polyamidoamine dendrimers in vitro, Thromb. Res. 154 (2017) 50–52, https://doi.org/10.1016/j.thromres.2017.04.008.
[113] M. Labieniec-Watala, C. Watala, PAMAM dendrimers: destined for success or doomed to fail? Plain and modified PAMAM dendrimers in the context of biomedical applications, J. Pharmacol. Sci. 104 (2015) 2–14, https://doi.org/10.1002/jps.24222.
[114] L.W.E. Starmans, D. Burdinski, N.P.M. Haex, R.P.M. Moonen, G.J. Strijkers, K. Nicolay, H. Grüll, Iron oxide nanoparticle-micelles (ION-micelles) for sensitive (molecular) magnetic particle imaging and magnetic resonance imaging, PloS One 8 (2013) 1–9, https://doi.org/10.1371/journal.pone.0057335.
[115] R. Cheng, W. Huang, L. Huang, B. Yang, L. Mao, K. Jin, Q. Zhuge, Y. Zhao, Acceleration of tissue plasminogen activator-mediated thrombolysis by magnetically powered nanomotors, ACS Nano 8 (2014) 7746–7754, https://doi.org/10.1021/nn5029955.
[116] H. Kempe, M. Kempe, The use of magnetite nanoparticles for implant-assisted magnetic drug targeting in thrombolytic therapy, Biomaterials 31 (2010) 9499–9510, https://doi.org/10.1016/j.biomaterials.2010.07.107.
[117] J.P. Chen, P.C. Yang, Y.H. Ma, S.J. Tu, Y.J. Lu, Targeted delivery of tissue plasminogen activator by binding to silica-coated magnetic nanoparticle, Int. J. Nanomed. 7 (2012) 5137–5149, https://doi.org/10.2147/IJN.S36197.
[118] M. Wang, J. Zhang, Z. Yuan, W. Yang, Q. Wu, H. Gu, Targeted thrombolysis by using of magnetic mesoporous silica nanoparticles, J. Biomed. Nanotechnol. 8 (2012) 624–632, https://doi.org/10.1166/jbn.2012.1416.
[119] B.L. Razzaboni, P. Bolsaitis, Evidence of an oxidative mechanism for the hemolytic activity of silica particles, Environ. Health Perspect. 87 (1990) 337–341, https://doi.org/10.1289/ehp.9087337.
[120] V. Murashov, M. Harper, E. Demchuk, Impact of silanol surface density on the toxicity of silica aerosols measured by erythrocyte haemolysis, J. Occup. Environ. Hyg. 3 (2006) 718–723, https://doi.org/10.1080/15459620601015950.
[121] T. Wu, M. Tang, Review of the effects of manufactured nanoparticles on mammalian target organs, J. Appl. Toxicol. 38 (2018) 25–40, https://doi.org/10.1002/jat.3499.
[122] J.P. Chen, P.C. Yang, Y.H. Ma, Y.J. Lu, Superparamagnetic iron oxide nanoparticles for delivery of tissue plasminogen activator, J. Nanosci. Nanotechnol. (2011) 11089–11094, https://doi.org/10.1166/jnn.2011.3953.
[123] J.P. Chen, C.H. Liu, H.L. Hsu, T. Wu, Y.J. Lu, Y.H. Ma, Magnetically controlled release of recombinant tissue plasminogen activator from chitosan nanocomposites for targeted thrombolysis, J. Mater. Chem. B. 4 (2016) 2578–2590, https://doi.org/10.1039/c5tb02579f.
[124] S. Heid, H. Unterweger, R. Tietze, R.P. Friedrich, B. Weigel, I. Cicha, D. Eberbeck, A.R. Boccaccini, C. Alexiou, S. Lyer, Synthesis and characterization of tissue plasminogen activator-functionalized superparamagnetic iron oxide nanoparticles for targeted fibrin clot dissolution, Int. J. Mol. Sci. 18 (2017), https://doi.org/10.3390/ijms18091837.
[125] M. Chang, Y.H. Lin, J.L. Gabayno, Q. Li, X. Liu, Thrombolysis based on magnetically-controlled surface-functionalized Fe3O4 nanoparticle, Bioengineered 8 (2017) 29–35, https://doi.org/10.1080/21655979.2016.1227145.
[126] A.Y. Prilepskii, A.F. Fakhardo, A.S. Drozdov, V.V. Vinogradov, I.P. Dudanov, A. A. Shtil, P.P. Bel'Tyukov, A.M. Shibeko, E.M. Koltsova, D.Y. Nechipurenko, V. V. Vinogradov, Urokinase-conjugated magnetite nanoparticles as a promising drug delivery system for targeted thrombolysis: synthesis and preclinical evaluation, ACS Appl. Mater. Interfaces 10 (2018) 36764–36775, https://doi.org/10.1021/acsami.8b14790.
[127] L. Huang, J. Wang, S. Huang, F. Siaw-Debrah, M. Nyanzu, Q. Zhuge, Polyacrylic acid-coated nanoparticles loaded with recombinant tissue plasminogen activator for the treatment of mice with ischemic stroke, Biochem. Biophys. Res. Commun. 516 (2019) 565–570, https://doi.org/10.1016/j.bbrc.2019.06.079.
[128] R.P. Friedrich, J. Zaloga, E. Schreiber, I.Y. Tóth, E. Tombácz, S. Lyer, C. Alexiou, Tissue plasminogen activator binding to superparamagnetic iron oxide nanoparticle-covalent versus adsorptive approach, Nanoscale Res. Lett. 11 (2016) 1, https://doi.org/10.1186/s11671-016-1521-7.
[129] H.W. Yang, M.Y. Hua, K.J. Lin, S.P. Wey, R.Y. Tsai, S.Y. Wu, Y.C. Lu, H.L. Liu, T. Wu, Y.H. Ma, Bioconjugation of recombinant tissue plasminogen activator to magnetic nanocarriers for targeted thrombolysis, Int. J. Nanomed. 7 (2012) 5159–5173, https://doi.org/10.2147/IJN.S32939.
[130] J.B. Vines, J.H. Yoon, N.E. Ryu, D.J. Lim, H. Park, Gold nanoparticles for photothermal cancer therapy, Front. Chem. 7 (2019) 1–16, https://doi.org/10.3389/fchem.2019.00167.
[131] D.E. Kim, J.Y. Kim, D. Schellingerhout, J.H. Ryu, S.K. Lee, S. Jeon, J.S. Lee, J. Kim, H.J. Jang, J.E. Park, E.J. Kim, I.C. Kwon, C.H. Ahn, M. Nahrendorf, K. Kim, Quantitative imaging of cerebral thromboemboli in vivo: the effects of tissue-type plasminogen activator, Stroke 48 (2017) 1376–1385, https://doi.org/10.1161/STROKEAHA.117.016511.
[132] S.P. Kwon, S. Jeon, S.H. Lee, H.Y. Yoon, J.H. Ryu, D. Choi, J.Y. Kim, J. Kim, J. H. Park, D.E. Kim, I.C. Kwon, K. Kim, C.H. Ahn, Thrombin-activatable fluorescent peptide incorporated gold nanoparticles for dual optical/computed tomography thrombus imaging, Biomaterials 150 (2018) 125–136, https://doi.org/10.1016/j.biomaterials.2017.10.017.
[133] A. Parodi, R. Molinaro, M. Sushnitha, M. Evangelopoulos, J.O. Martinez, N. Arrighetti, C. Corbo, E. Tasciotti, Bio-inspired engineering of cell- and virus-like nanoparticles for drug delivery, Biomaterials 147 (2017) 155–168, https://doi.org/10.1016/j.biomaterials.2017.09.020.
[134] S. Absar, Y.M. Kwon, F. Ahsan, Bio-responsive delivery of tissue plasminogen activator for localized thrombolysis, J. Contr. Release 177 (2014) 42–50, https://doi.org/10.1016/j.jconrel.2013.12.036.
[135] R.A. Petros, J.M. Desimone, Strategies in the design of nanoparticles for therapeutic applications, Nat. Rev. Drug Discov. 9 (2010) 615–627, https://doi.org/10.1038/nrd2591.
[136] R. Vankayala, S.R. Corber, J.T. Mac, M.P. Rao, M. Shafie, B. Anvari, Erythrocyte-derived nanoparticles as a theranostic agent for near-infrared fluorescence imaging and thrombolysis of blood clots, Macromol. Biosci. 18 (2018), https://doi.org/10.1002/mabi.201700379, 1700379–1700379.
[137] S. Nozohouri, A.E. Sifat, B. Vaidya, T.J. Abbruscato, Novel approaches for the delivery of therapeutics in ischemic stroke, Drug Discov. Today 25 (2020) 535–551, https://doi.org/10.1016/j.drudis.2020.01.007.
[138] J. Xu, X. Wang, H. Yin, X. Cao, Q. Hu, W. Lv, Q. Xu, Z. Gu, H. Xin, Sequentially site-specific delivery of thrombolytics and neuroprotectant for enhanced treatment of ischemic stroke, ACS Nano 13 (2019) 8577–8588, https://doi.org/10.1021/acsnano.9b01798.
[139] G. Camussi, M.C. Deregibus, S. Bruno, V. Cantaluppi, L. Biancone, Exosomes/microvesicles as a mechanism of cell-to-cell communication, Kidney Int. 78 (2010) 838–848, https://doi.org/10.1038/ki.2010.278.
[140] A.K.A. Silva, N. Luciani, F. Gazeau, K. Aubertin, S. Bonneau, C. Chauvierre, D. Letourneur, C. Wilhelm, Combining magnetic nanoparticles with cell derived

microvesicles for drug loading and targeting, Nanomed. Nanotechnol. Biol. Med. 11 (2015) 645–655, https://doi.org/10.1016/j.nano.2014.11.009.
[141] Y. Zhong, W.J. Gong, X.H. Gao, Y.N. Li, K. Liu, Y.G. Hu, J.S. Qi, Synthesis and evaluation of a novel nanoparticle carrying urokinase used in targeted thrombolysis, J. Biomed. Mater. Res. 108 (2019) 193–200, https://doi.org/10.1002/jbm.a.36803.
[142] K.J. Koudelka, A.S. Pitek, M. Manchester, N.F. Steinmetz, Virus-based nanoparticles as versatile nanomachines, Annu Rev Virol 2 (2015) 379–401, https://doi.org/10.1146/annurev-virology-100114-055141.
[143] A.S. Pitek, J. Park, Y. Wang, H. Gao, H. Hu, D.I. Simon, N.F. Steinmetz, Delivery of thrombolytic therapy using rod-shaped plant viral nanoparticles decreases the risk of hemorrhage, Nanoscale 10 (2018) 16547–16555, https://doi.org/10.1039/c8nr02861c.
[144] J.W. Yoo, D.J. Irvine, D.E. Discher, S. Mitragotri, Bio-inspired, bioengineered and biomimetic drug delivery carriers, Nat. Rev. Drug Discov. 10 (2011) 521–535, https://doi.org/10.1038/nrd3499.
[145] E.C. Unger, T. Porter, W. Culp, R. Labell, T. Matsunaga, R. Zutshi, Therapeutic applications of lipid-coated microbubbles, Adv. Drug Deliv. Rev. 56 (2004) 1291–1314, https://doi.org/10.1016/j.addr.2003.12.006.
[146] B. Li, R. Aid-Launais, M.N. Labour, A. Zenych, M. Juenet, C. Choqueux, V. Ollivier, O. Couture, D. Letourneur, C. Chauvierre, Functionalized polymer microbubbles as new molecular ultrasound contrast agent to target P-selectin in thrombus, Biomaterials 194 (2019) 139–150, https://doi.org/10.1016/j.biomaterials.2018.12.023.
[147] C.M. Moran, Ultrasonic contrast agents, Clin. Ultrasound. 1 (2011) 77–89, https://doi.org/10.1016/B978-0-7020-3131-1.00006-7.
[148] K.B. Bader, G. Bouchoux, C.K. Holland, Sonothrombolysis (2016), https://doi.org/10.1007/978-3-319-22536-4_19.
[149] Y. Sawaguchi, Z. Wang, Ultrasound acceleration of rt-PA thrombolysis depends on acoustic intensity, Biol. Pharm. Bull. 40 (2017) 97–103, https://doi.org/10.1248/bpb.b16-00702.
[150] A. Goyal, F.T.H. Yu, M.G. Tenwalde, X. Chen, A. Althouse, F.S. Villanueva, J. J. Pacella, Inertial cavitation ultrasound with microbubbles improves reperfusion efficacy when combined with tissue plasminogen activator in an in vitro model of microvascular obstruction, Ultrasound Med. Biol. 43 (2017) 1391–1400, https://doi.org/10.1016/j.ultrasmedbio.2017.02.013.
[151] T.R. Porter, The utilization of ultrasound and microbubbles for therapy in acute coronary syndromes, Cardiovasc, Res. 83 (2009) 636–642, https://doi.org/10.1093/cvr/cvp206.
[152] A. Agarwal, W.J. Ng, Y. Liu, Principle and applications of microbubble and nanobubble technology for water treatment, Chemosphere 84 (2011) 1175–1180, https://doi.org/10.1016/j.chemosphere.2011.05.054.
[153] K. Tachibana, S. Tachibana, Albumin microbubble echo-contrast material as an enhancer for ultrasound accelerated thrombolysis, Circulation 92 (1995) 1148–1150, https://doi.org/10.1161/01.CIR.92.5.1148.
[154] K.B. Bader, G. Bouchoux, T. Peng, M.E. Klegerman, D.D. McPherson, C. K. Holland, Thrombolytic efficacy and enzymatic activity of rt-PA-loaded echogenic liposomes, J. Thromb. Thrombolysis 40 (2015) 144–155, https://doi.org/10.1007/s11239-015-1204-8.
[155] H. Shekhar, K.B. Bader, S. Huang, T. Peng, S. Huang, D.D. McPherson, C. K. Holland, In vitro thrombolytic efficacy of echogenic liposomes loaded with tissue plasminogen activator and octafluoropropane gas, Phys. Med. Biol. 62 (2017) 517–538, https://doi.org/10.1088/1361-6560/62/2/517.
[156] S.T. Laing, M.R. Moody, H. Kim, B. Smulevitz, S.L. Huang, C.K. Holland, D. D. McPherson, M.E. Klegerman, Thrombolytic efficacy of tissue plasminogen activator-loaded echogenic liposomes in a rabbit thrombus model, Thromb. Res. 130 (2012) 629–635, https://doi.org/10.1016/j.thromres.2011.11.010.
[157] S.T. Laing, M. Moody, B. Smulevitz, H. Kim, P. Kee, S. Huang, C.K. Holland, D. D. McPherson, Ultrasound-enhanced thrombolytic effect of tissue plasminogen activator-loaded echogenic liposomes in an in vivo rabbit aorta thrombus model-brief report, Arterioscler. Thromb. Vasc. Biol. 31 (2011) 1357–1359, https://doi.org/10.1161/ATVBAHA.111.225938.
[158] M.A. Kandadai, P. Mukherjee, H. Shekhar, G.J. Shaw, I. Papautsky, C.K. Holland, Microfluidic manufacture of rt-PA -loaded echogenic liposomes, Biomed, Microdevices 18 (2016) 1–21, https://doi.org/10.1007/s10544-016-0072-0.
[159] W.C. Yan, Q.W. Chua, X.J. Ong, V.K. Sharma, Y.W. Tong, C.H. Wang, Fabrication of ultrasound-responsive microbubbles via coaxial electrohydrodynamic atomization for triggered release of tPA, J. Colloid Interface Sci. 501 (2017) 282–293, https://doi.org/10.1016/j.jcis.2017.04.073.
[160] D. Susan, Tiukinhoy-Laing, Ultrasound-facilitated thrombolysis using tissue-plasminogen activator-loaded echogenic liposomes, Bone 23 (2011) 1–7, https://doi.org/10.1161/CIRCULATIONAHA.110.956839.
[161] J.M. Correas, L. Bridal, A. Lesavre, A. Méjean, M. Claudon, O. Hélénon, Ultrasound contrast agents: properties, principles of action, tolerance, and artifacts, Eur. Radiol. 11 (2001) 1316–1328, https://doi.org/10.1007/s003300100940.
[162] T. Şen, O. Tüfekçioğlu, Y. Koza, Mechanical index, Anadolu Kardiyol. Derg. 15 (2015) 334–336, https://doi.org/10.5152/akd.2015.6061.
[163] Y. Zhu, L. Guan, Y. Mu, Combined low-frequency ultrasound and urokinase-containing microbubbles in treatment of femoral artery thrombosis in a rabbit model, PloS One 11 (2016) 1–13, https://doi.org/10.1371/journal.pone.0168909.
[164] X. Hua, L. Zhou, P. Liu, Y. He, K. Tan, Q. Chen, Y. Gao, Y. Gao, In vivo thrombolysis with targeted microbubbles loading tissue plasminogen activator in a rabbit femoral artery thrombus model, J. Thromb. Thrombolysis 38 (2014) 57–64, https://doi.org/10.1007/s11239-014-1071-8.
[165] X. Hua, P. Liu, Y.H. Gao, K. Bin Tan, L.N. Zhou, Z. Liu, X. Li, S.W. Zhou, Y.J. Gao, Construction of thrombus-targeted microbubbles carrying tissue plasminogen activator and their in vitro thrombolysis efficacy: a primary research, J. Thromb. Thrombolysis 30 (2010) 29–35, https://doi.org/10.1007/s11239-010-0450-z.
[166] J.H. Nederhoed, H.P. Ebben, J. Slikkerveer, A.W.J. Hoksbergen, O. Kamp, G. J. Tangelder, W. Wisselink, R.J.P. Musters, K.K. Yeung, Intravenous targeted microbubbles carrying urokinase versus urokinase alone in acute peripheral arterial thrombosis in a porcine model, Ann. Vasc. Surg. 44 (2017) 400–407, https://doi.org/10.1016/j.avsg.2017.05.011.
[167] C. Correa-Paz, M.F. Navarro Poupard, E. Polo, M. Rodríguez-Pérez, P. Taboada, R. Iglesias-Rey, P. Hervella, T. Sobrino, D. Vivien, J. Castillo, P. del Pino, F. Campos, B. Pelaz, In vivo ultrasound-activated delivery of recombinant tissue plasminogen activator from the cavity of sub-micrometric capsules, J. Contr. Release 308 (2019) 162–171, https://doi.org/10.1016/j.jconrel.2019.07.017.
[168] X. Wang, Y. Gkanatsas, J. Palasubramaniam, J.D. Hohmann, Y.C. Chen, B. Lim, C. E. Hagemeyer, K. Peter, Thrombus-targeted theranostic microbubbles: a new technology towards concurrent rapid ultrasound diagnosis and bleeding-free fibrinolytic treatment of thrombosis, Theranostics 6 (2016) 726–738, https://doi.org/10.7150/thno.14514.
[169] M. de Saint Victor, L.C. Barnsley, D. Carugo, J. Owen, C.C. Coussios, E. Stride, Sonothrombolysis with magnetically targeted microbubbles, Ultrasound Med. Biol. 45 (2019) 1151–1163, https://doi.org/10.1016/j.ultrasmedbio.2018.12.014.
[170] L. Auboire, C.A. Sennoga, J.M. Hyvelin, F. Ossant, J.M. Escoffre, F. Tranquart, A. Bouakaz, Microbubbles combined with ultrasound therapy in ischemic stroke: a systematic review of in-vivo preclinical studies, PloS One 13 (2018) 1–19, https://doi.org/10.1371/journal.pone.0191788.
[171] C.A. Sennoga, E. Kanbar, L. Auboire, P.A. Dujardin, D. Fouan, J.M. Escoffre, A. Bouakaz, Microbubble-mediated ultrasound drug-delivery and therapeutic monitoring, Expet Opin. Drug Deliv. 14 (2017) 1031–1043, https://doi.org/10.1080/17425247.2017.1266328.
[172] A. Moumouh, L. Barentin, F. Tranquart, S. Serrierre, I. Bonnaud, J.P. Tasu, Fibrinolytic effects of transparietal ultrasound associated with intravenous infusion of an ultrasound contrast agent: study of a rat model of acute cerebral stroke, Ultrasound Med. Biol. 36 (2010) 51–57, https://doi.org/10.1016/j.ultrasmedbio.2009.06.1103.
[173] R. Chen, D.G. Paeng, K.H. Lam, Q. Zhou, K.K. Shung, N. Matsuoka, M. S. Humayun, In vivo sonothrombolysis of ear marginal vein of rabbits monitored with high-frequency ultrasound needle transducer, J. Med. Biol. Eng. 33 (2013) 103–110, https://doi.org/10.5405/jmbe.1219.
[174] A.D. Barreto, A.V. Alexandrov, L. Shen, A. Sisson, A.W. Bursaw, P. Sahota, H. Peng, M. Ardjomand-Hessabi, R. Pandurengan, M.H. Rahbar, K. Barlinn, H. Indupuru, N.R. Gonzales, S.I. Savitz, J.C. Grotta, Clotbust-hands free: pilot safety study of a novel operator-independent ultrasound device in patients with acute ischemic stroke, Stroke 44 (2013) 3376–3381, https://doi.org/10.1161/STROKEAHA.113.002713.
[175] Jonathan T. Sutton, et al., Clot retraction affects the extent of ultrasound-enhanced thrombolysis in an ex vivo porcine thrombosis model Jonathan, Ultrasound Med. Biol. 23 (2013) 1–7, https://doi.org/10.1038/jid.2014.371.
[176] H. Soo Choi, W. Liu, P. Misra, E. Tanaka, J.P. Zimmer, B. Itty Ipe, M.G. Bawendi, J. V Frangioni, Renal clearance of quantum dots, Nat. Biotechnol. 25 (2007) 1165–1170, https://doi.org/10.1038/nbt1340.
[177] A.E. Nel, L. Mädler, D. Velegol, T. Xia, E.M.V. Hoek, P. Somasundaran, F. Klaessig, V. Castranova, M. Thompson, Understanding biophysicochemical interactions at the nano-bio interface, Nat. Mater. 8 (2009) 543–557, https://doi.org/10.1038/nmat2442.
[178] F. Alexis, E. Pridgen, L.K. Molnar, O.C. Farokhzad, Factors affecting the clearance and biodistribution of polymeric nanoparticles, Mol. Pharm. 5 (2008) 505–515, https://doi.org/10.1021/mp800051m.
[179] Y. Geng, P. Dalhaimer, S. Cai, R. Tsai, M. Tewari, T. Minko, D.E. Discher, Shape effects of filaments versus spherical particles in flow and drug delivery, Nat. Nanotechnol. 2 (2007) 249–255, https://doi.org/10.1038/nnano.2007.70.
[180] L. Zhang, Z. Cao, Y. Li, J.-R. Ella-Menye, T. Bai, S. Jiang, Softer zwitterionic nanogels for longer circulation and lower splenic accumulation, ACS Nano 6 (2012) 6681–6686, https://doi.org/10.1021/nn301159a.
[181] R. Palomba, A.L. Palange, I.F. Rizzuti, M. Ferreira, A. Cervadoro, M.G. Barbato, C. Canale, P. Decuzzi, Modulating phagocytic cell sequestration by tailoring nanoconstruct softness, ACS Nano 12 (2018) 1433–1444, https://doi.org/10.1021/acsnano.7b07797.
[182] N.Y. Lotosh, S.O. Aliaseva, I.K. Malashenkova, G.M. Sorokoumova, R.G. Vasilov, A.A. Selischeva, Cationic liposomes cause ROS generation and release of neutrophil extracellular traps, Biochem. Suppl. Ser. A Membr. Cell Biol. 13 (2019) 40–49, https://doi.org/10.1134/S1990747818040074.
[183] T.L. Hwang, I.A. Aljuffali, C.F. Hung, C.H. Chen, J.Y. Fang, The impact of cationic solid lipid nanoparticles on human neutrophil activation and formation of neutrophil extracellular traps (NETs), Chem. Biol. Interact. 235 (2015) 106–114, https://doi.org/10.1016/j.cbi.2015.04.011.
[184] T.L. Hwang, I.A. Aljuffali, C.F. Lin, Y.T. Chang, J.Y. Fang, Cationic additives in nanosystems activate cytotoxicity and inflammatory response of human neutrophils: lipid nanoparticles versus polymeric nanoparticles, Int. J. Nanomed. 10 (2015) 371–385, https://doi.org/10.2147/IJN.S73017.
[185] K. Knop, R. Hoogenboom, D. Fischer, U.S. Schubert, Poly(ethylene glycol) in drug delivery: pros and cons as well as potential alternatives, Angew. Chem. Int. Ed. 49 (2010) 6288–6308, https://doi.org/10.1002/anie.200902672.
[186] P.L. Rodriguez, T. Harada, D.A. Christian, D.A. Pantano, R.K. Tsai, D.E. Discher, Minimal "self" peptides that inhibit phagocytic clearance and enhance delivery of

nanoparticles, Science 339 (2013) 971–975, https://doi.org/10.1126/science.1229568.
[187] J. Saikia, R. Mohammadpour, M. Yazdimamaghani, H. Northrup, V. Hlady, H. Ghandehari, Silica nanoparticle-endothelial interaction: uptake and effect on platelet adhesion under flow conditions, ACS Appl. Bio Mater. 1 (2018) 1620–1627, https://doi.org/10.1021/acsabm.8b00466.
[188] J. Duan, S. Liang, Y. Yu, Y. Li, L. Wang, Z. Wu, Y. Chen, M.R. Miller, Z. Sun, Inflammation–coagulation response and thrombotic effects induced by silica nanoparticles in zebrafish embryos, Nanotoxicology 12 (2018) 470–484, https://doi.org/10.1080/17435390.2018.1461267.
[189] J. Jose Corbalan, C. Medina, A. Jacoby, T. Malinski, M.W. Radomski, Amorphous silica nanoparticles aggregate human platelets: potential implications for vascular homeostasis, Int. J. Nanomed. 7 (2012) 631–639, https://doi.org/10.2147/IJN.S28293.
[190] X.D. Zhang, H.Y. Wu, D. Wu, Y.Y. Wang, J.H. Chang, Z. Bin Zhai, A.M. Meng, P. X. Liu, L.A. Zhang, F.Y. Fan, Toxicologic effects of gold nanoparticles in vivo by different administration routes, Int. J. Nanomed. 5 (2010) 771–781, https://doi.org/10.2147/IJN.S8428.
[191] L. Shang, K. Nienhaus, G.U. Nienhaus, Engineered nanoparticles interacting with cells: size matters, J. Nanobiotechnol. 12 (2014) 1, https://doi.org/10.1186/1477-3155-12-5.
[192] Y. Pan, S. Neuss, A. Leifert, M. Fischler, F. Wen, U. Simon, G. Schmid, W. Brandau, W. Jahnen-Dechent, Size-dependent cytotoxicity of gold nanoparticles, Small 3 (2007) 1941–1949, https://doi.org/10.1002/smll.200700378.
[193] Z. He, J. Liu, L. Du, The unexpected effect of PEGylated gold nanoparticles on the primary function of erythrocytes, Nanoscale 6 (2014) 9017–9024, https://doi.org/10.1039/c4nr01857e.
[194] J. Feng, H. Liu, K.K. Bhakoo, L. Lu, Z. Chen, A metabonomic analysis of organ specific response to USPIO administration, Biomaterials 32 (2011) 6558–6569, https://doi.org/10.1016/j.biomaterials.2011.05.035.
[195] C. Lasagna-Reeves, D. Gonzalez-Romero, M.A. Barria, I. Olmedo, A. Clos, V. M. Sadagopa Ramanujam, A. Urayama, L. Vergara, M.J. Kogan, C. Soto, Bioaccumulation and toxicity of gold nanoparticles after repeated administration in mice, Biochem. Biophys. Res. Commun. 393 (2010) 649–655, https://doi.org/10.1016/j.bbrc.2010.02.046.
[196] K. Andrieux, P. Couvreur, Polyalkylcyanoacrylate nanoparticles for delivery of drugs across the blood-brain barrier 1, Wiley Interdiscip Rev Nanomed Nanobiotechnol, 2009, pp. 463–474, https://doi.org/10.1002/wnan.5.
[197] N.J. Siddiqi, M.A.K. Abdelhalim, A.K. El-Ansary, A.S. Alhomida, W.Y. Ong, Identification of potential biomarkers of gold nanoparticle toxicity in rat brains, J. Neuroinflammation 9 (2012) 1–7, https://doi.org/10.1186/1742-2094-9-123.
[198] R. Brouns, P.P. De Deyn, The complexity of neurobiological processes in acute ischemic stroke, Clin. Neurol. Neurosurg. 111 (2009) 483–495, https://doi.org/10.1016/j.clineuro.2009.04.001.
[199] D. Vivien, M. Gauberti, A. Montagne, G. Defer, E. Touzé, Impact of tissue plasminogen activator on the neurovascular unit: from clinical data to experimental evidence, J. Cerebr. Blood Flow Metabol. 31 (2011) 2119–2134, https://doi.org/10.1038/jcbfm.2011.127.
[200] M. Bartneck, T. Ritz, H.A. Keul, M. Wambach, J. Bornemann, U. Gbureck, J. Ehling, T. Lammers, F. Heymann, N. Gassler, T. Lüdde, C. Trautwein, J. Groll, F. Tacke, Peptide-functionalized gold nanorods increase liver injury in hepatitis, ACS Nano 6 (2012) 8767–8777, https://doi.org/10.1021/nn302502u.
[201] C.H. Fu, T.L. Liu, F.Q. Tang, D. Chen, L.L. Li, H.Y. Liu, X.M. Li, Acute toxicity and oxidative damage induced by silica nanorattle in vivo, Chin. Sci. Bull. 57 (2012) 2525–2532, https://doi.org/10.1007/s11434-012-5187-y.
[202] H. Nishimori, M. Kondoh, K. Isoda, S. ichi Tsunoda, Y. Tsutsumi, K. Yagi, Histological analysis of 70-nm silica particles-induced chronic toxicity in mice, Eur. J. Pharm. Biopharm. 72 (2009) 626–629, https://doi.org/10.1016/j.ejpb.2009.03.007.
[203] D. Couto, M. Freitas, V.M. Costa, R.C. Chisté, A. Almeida, M.A. Lopez-Quintela, J. Rivas, P. Freitas, P. Silva, F. Carvalho, E. Fernandes, Biodistribution of polyacrylic acid-coated iron oxide nanoparticles is associated with proinflammatory activation and liver toxicity, J. Appl. Toxicol. 36 (2016) 1321–1331, https://doi.org/10.1002/jat.3323.
[204] B. Zhao, X.Q. Wang, X.Y. Wang, H. Zhang, W.B. Dai, J. Wang, Z.L. Zhong, H. N. Wu, Q. Zhang, Nanotoxicity comparison of four amphiphilic polymeric micelles with similar hydrophilic or hydrophobic structure, Part, Fibre Toxicol 10 (2013) 1–16, https://doi.org/10.1186/1743-8977-10-47.
[205] X. Li, A. Radomski, O.I. Corrigan, L. Tajber, F. De Sousa Menezes, S. Endter, C. Medina, M.W. Radomski, Platelet compatibility of PLGA, chitosan and PLGA-chitosan nanoparticles, Nanomedicine 4 (2009) 735–746, https://doi.org/10.2217/nnm.09.65.
[206] Y. Zhao, D. Sultan, Y. Liu, Biodistribution, excretion, and toxicity of nanoparticles. Theranostic Bionanomaterials, Elsevier Inc., 2019, pp. 27–53, https://doi.org/10.1016/B978-0-12-815341-3.00002-X.
[207] K.D. Grieger, I. Linkov, S.F. Hansen, A. Baun, Environmental risk analysis for nanomaterials: review and evaluation of frameworks, Nanotoxicology 6 (2012) 196–212, https://doi.org/10.3109/17435390.2011.569095.
[208] E. Sadauskas, G. Danscher, M. Stoltenberg, U. Vogel, A. Larsen, H. Wallin, Protracted elimination of gold nanoparticles from mouse liver, Nanomed. Nanotechnol. Biol. Med. 5 (2009) 162–169, https://doi.org/10.1016/j.nano.2008.11.002.
[209] J. Feng, H. Liu, L. Zhang, K. Bhakoo, L. Lu, An insight into the metabolic responses of ultra-small superparamagnetic particles of iron oxide using metabonomic analysis of biofluids, Nanotechnology 21 (2010) 395101, https://doi.org/10.1088/0957-4484/21/39/395101.
[210] Q. Ran, Y. Xiang, Y. Liu, L. Xiang, F. Li, X. Deng, Y. Xiao, L. Chen, L. Chen, Z. Li, Eryptosis indices as a novel predictive parameter for biocompatibility of Fe3O4 magnetic nanoparticles on erythrocytes, Sci. Rep. 5 (2015) 16209, https://doi.org/10.1038/srep16209.
[211] K. de la Harpe, P. Kondiah, Y. Choonara, T. Marimuthu, L. du Toit, V. Pillay, The hemocompatibility of nanoparticles: a review of cell–nanoparticle interactions and hemostasis, Cells 8 (2019) 1209, https://doi.org/10.3390/cells8101209.
[212] S. Vrignaud, J.P. Benoit, P. Saulnier, Strategies for the nanoencapsulation of hydrophilic molecules in polymer-based nanoparticles, Biomaterials 32 (2011) 8593–8604, https://doi.org/10.1016/j.biomaterials.2011.07.057.
[213] M. Di Marco, K.A. Razak, A.A. Aziz, C. Devaux, E. Borghi, L. Levy, C. Sadun, Overview of the main methods used to combine proteins with nanosystems : absorption, bioconjugation, and encapsulation, Int. J. Nanomed. 5 (2010) 37–49.
[214] L. Arnfast, C.G. Madsen, L. Jorgensen, S. Baldursdottir, Design and processing of nanogels as delivery systems for peptides and proteins, Ther. Deliv. 5 (2014) 691–708, https://doi.org/10.4155/tde.14.38.
[215] S.R. Van Tomme, W.E. Hennink, Biodegradable dextran hydrogels for protein delivery applications, Expet Rev. Med. Dev. 4 (2007) 147–164, https://doi.org/10.1586/17434440.4.2.147.
[216] X. Xiong, F. Zhao, M. Shi, H. Yang, Y. Liu, Polymeric microbubbles for ultrasonic molecular imaging and targeted therapeutics, J. Biomater. Sci. Polym. Ed. 22 (2011) 417–428, https://doi.org/10.1163/092050610X540440.
[217] B. Li, R. Aid-Launais, M.-N. Labour, A. Zenych, M. Juenet, C. Choqueux, V. Ollivier, O. Couture, D. Letourneur, C. Chauvierre, Functionalized polymer microbubbles as new molecular ultrasound contrast agent to target P-selectin in thrombus, Biomaterials 194 (2019) 139–150, https://doi.org/10.1016/j.biomaterials.2018.12.023.
[218] C. Chauvierre, R. Aid-Launais, J. Aerts, M. Maire, L. Chollet, L. Rolland, R. Bonaf, S. Rossi, S. Bussi, C. Cabella, D. Laszlo, T. Fülöp, J. Szebeni, Y. Chahid, K. H. Zheng, E.S.G. Stroes, D. Le Guludec, F. Rouzet, D. Letourneur, Pharmaceutical development and safety evaluation of a GMP-grade fucoidan for molecular diagnosis of cardiovascular diseases, Mar. Drugs 17 (2019) 1–17, https://doi.org/10.3390/md17120699.
[219] K.H. Zheng, Y. Kaiser, E. Poel, H. Verberne, J. Aerts, F. Rouzet, E. Stroes, D. Letourneur, C. Chauvierre, 99Mtc-Fucoidan as diagnostic agent for P-selectin imaging: first-in-human evaluation (phase I), Atherosclerosis 287 (2019) e143, https://doi.org/10.1016/j.atherosclerosis.2019.06.425.
[220] J.C. Antunes, L. Benarroch, F.C. Moraes, M. Juenet, M.S. Gross, M. Aubart, C. Boileau, G. Caligiuri, A. Nicoletti, V. Ollivier, F. Chaubet, D. Letourneur, C. Chauvierre, Core-shell polymer-based nanoparticles deliver miR-155-5p to endothelial cells, Mol. Ther. Nucleic Acids 17 (2019) 210–222, https://doi.org/10.1016/j.omtn.2019.05.016.
[221] B. Ovbiagele, C.S. Kidwell, S. Starkman, J.L. Saver, Potential role of neuroprotective agents in the treatment of patients with acute ischemic stroke, Curr. Treat. Options Neurol. 5 (2003) 367–375, https://doi.org/10.1007/s11940-003-0027-7.
[222] R. Goulay, M. Naveau, T. Gaberel, D. Vivien, J. Parcq, Optimized tPA: a non-neurotoxic fibrinolytic agent for the drainage of intracerebral hemorrhages, J. Cerebr. Blood Flow Metabol. 38 (2018) 1180–1189, https://doi.org/10.1177/0271678X17719180.
[223] J. Matuszak, P. Dörfler, S. Lyer, H. Unterweger, M. Juenet, C. Chauvierre, A. Alaarg, D. Franke, G. Almer, I. Texier, J.M. Metselaar, R. Prassl, C. Alexiou, H. Mangge, D. Letourneur, I. Cicha, Comparative analysis of nanosystems' effects on human endothelial and monocytic cell functions, Nanotoxicology 12 (2018) 957–974, https://doi.org/10.1080/17435390.2018.1502375.
[224] I. Cicha, C. Chauvierre, I. Texier, C. Cabella, J.M. Metselaar, J. Szebeni, L. Dézsi, C. Alexiou, F. Rouzet, G. Storm, E. Stroes, D. Bruce, N. MacRitchie, P. Maffia, D. Letourneur, From design to the clinic: practical guidelines for translating cardiovascular nanomedicine, Cardiovasc. Res. 114 (2018) 1714–1727, https://doi.org/10.1093/cvr/cvy219.
[225] C. Chauvierre, D. Letourneur, The European project NanoAthero to fight cardiovascular diseases using nanotechnologies, Nanomedicine 10 (2015) 3391–3400, https://doi.org/10.2217/nnm.15.170.
[226] K.H. Zheng, J. Schoormans, L.C.A. Stiekema, C. Calcagno, I. Cicha, C. Alexiou, G. J. Strijkers, A.J. Nederveen, E.S.G. Stroes, B.F. Coolen, Plaque permeability assessed with DCE-MRI associates with USPIO uptake in patients with peripheral artery disease, JACC Cardiovasc. Imaging 12 (2019) 2081–2083, https://doi.org/10.1016/j.jcmg.2019.04.014.
[227] F.M. van der Valk, D.F. van Wijk, M.E. Lobatto, H.J. Verberne, G. Storm, M.C. M. Willems, D.A. Legemate, A.J. Nederveen, C. Calcagno, V. Mani, S. Ramachandran, M.P.M. Paridaans, M.J. Otten, G.M. Dallinga-Thie, Z.A. Fayad, M. Nieuwdorp, D.M. Schulte, J.M. Metselaar, W.J.M. Mulder, E.S. Stroes, Prednisolone-containing liposomes accumulate in human atherosclerotic macrophages upon intravenous administration, Nanomed. Nanotechnol. Biol. Med. 11 (2015) 1039–1046, https://doi.org/10.1016/j.nano.2015.02.021.
[228] K.H. Zheng, F.M. van der Valk, L.P. Smits, M. Sandberg, J.L. Dasseux, R. Baron, R. Barbaras, C. Keyserling, B.F. Coolen, A.J. Nederveen, H.J. Verberne, T.E. Nell, D.J. Vugts, R. Duivenvoorden, Z.A. Fayad, W.J.M. Mulder, G.A.M.S. van Dongen, E.S.G. Stroes, HDL mimetic CER-001 targets atherosclerotic plaques in patients, Atherosclerosis 251 (2016) 381–388, https://doi.org/10.1016/j.atherosclerosis.2016.05.038.

ANNEX 2

Biomaterials 294 (2023) 122025

Contents lists available at ScienceDirect

Biomaterials

journal homepage: www.elsevier.com/locate/biomaterials

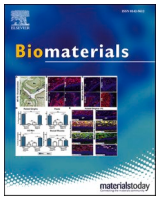

Microbubbles for human diagnosis and therapy

Louise Fournier, Thibault de La Taille, Cédric Chauvierre *

Université Paris Cité, Université Sorbonne Paris Nord, LVTS, UMRS 1148 INSERM, F- 75018, Paris, France

ARTICLE INFO

Keywords:
Microbubbles
Ultrasound
Molecular imaging
Targeted therapy
Sonothrombolysis
Sonoporation

ABSTRACT

Microbubbles (MBs) were observed for the first time *in vivo* as a curious consequence of quick saline injection during ultrasound (US) imaging of the aortic root, more than 50 years ago. From this serendipitous event, MBs are now widely used as contrast enhancers for US imaging. Their intrinsic properties described in this review, allow a multitude of designs, from shell to gas composition but also from grafting targeting agents to drug payload encapsulation. Indeed, the versatile MBs are deeply studied for their dual potential in imaging and therapy. As presented in this paper, new generations of MBs now opens perspectives for targeted molecular imaging along with the development of new US imaging systems. This review also presents an overview of the different therapeutic strategies with US and MBs for cancer, cardiovascular diseases, and inflammation. The overall aim is to overlap those fields in order to find similarities in the MBs application for treatment enhancement associated with US. To conclude, this review explores the new scales of MBs technologies with nanobubbles development, and along concurrent advances in the US imaging field. This review ends by discussing perspectives for the booming future uses of MBs.

1. Introduction

Conventional therapies are developed in the objective of including as many patients as possible. Therefore, researchers are looking for the best impact with the least adverse effects for their proposed therapies. At the same time, early and precise diagnosis is crucial as it allows early and accurate treatment. High dose injections, necessary for the accumulation of a sufficient drug amount on the pathological site, face major limitations attributed to the high clearance by the reticuloendothelial system (RES) but also potential collateral damages of non-pathological sites (depressed immune system in chemotherapy or collateral bleeding in stroke treatment). The lack of specificity can also be observed for diagnostic strategies where molecular scale observation could help early diagnosis and better understand the pathologies. Those drawbacks led researchers to work on the design and the development of carriers able to specifically targets pathological biomarkers and to encapsulate drugs for the improvement of conventional therapies. This approach was widely studied over the last 20 years at the nano scale with nanoparticles functionalization for various clinical applications [1]. In this review, the focus is on the micro scale with the evaluation of microbubbles (MBs) and their potential application for human therapy and diagnosis. Mostly associated to their response to Ultrasound (US)

Abbreviations: AFM, Atomic Force Microscopy; ARF, Acoustic Radiation Force; BBB, Blood Brain Barrier; BT, Brachytherapy; CNS, Central Nervous System; CO, Carbon Monoxide; CORM, Carbon Monoxide Releasing Molecule; DBCO, Dibenzocyclooctyne-amine; DSPC, (1,2-distearoyl-sn-glycero-3-phosphocholine); DSPE-PEG2000 (1, 2-distearoyl-sn-glycero-3-phosphoethanolamine-N- [amino (polyethylene glycol)-2000]); EDC / NHS, 1-Ethyl-3-(3-dimethylaminopropyl) carbodiimide; N-Hydroxy succinimide, EPR; Enhanced Permeability and Retention, FDA; Food and Drug Administration, FSHR; Follicle Stimulating Hormone Receptor, FUS; Focused Ultrasound, fUSI; Functional Ultrasound Imaging, HA; Hyaluronic Acid, HGN; Hallow Gold Nanoshell, HIFU; High Intensity Focused Ultrasound, GV; Gas Vesicle, HSA; Human Serum Albumin, JAM-A; Junctional Adhesion Molecule A, KDR; Kinase Insert Domain, LPS; Lipopolysaccharide, MB; Microbubble, MI; Mechanical Index, NB; Nanobubble, NCL; Nucleolin, ND; Nanodroplet, NIR; Near Infrared, NO; Nitric Oxide, NP; Nanoparticle, NPMB; Nanoparticles assembled as Microbubble, PALM; Photoactivated Localization Microscopy, PBS; Phosphate Buffer Saline, PCCA; Phase Change Contrast Agent, PEG; Polyethylene Glycol, PFC; Perfluorocarbon, PFD; Perfluorodecalin, PFOB; Perfluoro-octyl-Bromide, PFOC; Perfluorocarbon-based Oxygen Carrier, PSF; Point Spread Function, RES; Reticuloendothelial System, RF; Resonance Frequency, ROS; Reactive Oxygen Species, SH; Subharmonic, sLe^x: Sialyl Lewis X peptide; SPAAC, Strain Promoted Alkyne-Azide Cycloaddition; STAT3, Signal Transducer and Activation of Transcription 3; STORM, Stochastic Optical Reconstruction Microscopy; TCCS, Transcranial Color Doppler Ultrasound; Thyc1, Thymocyte Antigen 1; US, Ultrasound; ULM, Ultrasound Localized Microscopy; VCAM1, Vascular Cell Adhesion Molecule 1; VEGFR2, Vascular Endothelial Growth Factor Receptor 2.

* Corresponding author.
E-mail address: cedric.chauvierre@inserm.fr (C. Chauvierre).

https://doi.org/10.1016/j.biomaterials.2023.122025
Received 31 October 2022; Received in revised form 17 January 2023; Accepted 24 January 2023
Available online 25 January 2023
0142-9612/© 2023 Elsevier Ltd. All rights reserved.

waves, MBs are objects with the capacity to encapsulate various gas, drugs and functionalized with targeting agent. Here, we aimed at painting an overview of the latest published papers on MBs, trying to understand the links between seemingly disconnected fields, like oncology or cardiovascular system. This review aimed at describing the similarities and the differences of application of same echogenic agents in a field where standards have not been established yet. From MBs synthesis to composition characteristics, this work presents the various methods adapted to the microscopic field of imaging and drug delivery. Since MBs are intrinsically US responsive, they hold a considerable advantage over other clinical contrast agents used for diagnosis imaging like PET & SPECT scintigraphy, MRI or X-ray, and also over drug delivery nanoparticles. Here are discussed the advances in the use of MBs for imaging: from commercial MBs to molecular imaging. Among those, the therapeutic approach was studied with the potential of gas and US therapy as well as the synergic effect of the US + MBs system. Finally, this review explores the perspectives that the field offers with new generation of US contrast agent such as nanobubbles (NBs) or nanodrops (NDs) to conclude with the limitation of current US imaging and the latest development of this technique.

2. Microbubbles

MBs are defined as microscale objects composed of a shell and a gas core. They were firstly described in 1968 by Gramiak and Shah [2] as the reason of "ultrasonic contrast in the anatomic identification of the mitral valve" after image analysis. US imaging was poorly resolved and quick saline injection was used to produce "clouds of echoes" [2] contrasting with surrounding tissue. Gramiak and Shah hypothesized that this contrast enhancement was probably caused by "mini bubbles" entering the blood with the saline injection. These first observations led to the perspective for their clinical application. Indeed, a long journey happened since Gramiak and Shah with a focus on criteria validation prior to the injection in living bodies. Some are common to many injectable biomaterials like biocompatibility and biodegradation but MBs also have their specific features. For instance, size has to be controlled under the 10 μm limit to prevent from the obstruction risk in the microvasculature [3] and more preferably in the range of erythrocytes diameter [4]. Those characteristics are defined with the careful choice of gas core, shell composition and surface modification. As presented below, MBs are highly versatile objects that will behave differently *in vivo* depending on their characteristics.

2.1. Synthesis methods for microbubbles generation

Various methods have been developed for the synthesis of microbubbles (Fig. 1) endowing them with different properties. Most of the studied MBs are echogenic liposomes and the main methods for their synthesis consist in the hydration of dried lipids film [5]. It relies on dissolving a mix of lipids into chloroform and using a rotational evaporation system to obtain a thin dried film. The addition of emulsifier (Polyethylene Glycols: PEG) allows the bubble formation and the dried film is hydrated with a buffer solution such as phosphate buffer saline [6]. At last, the solution is heated to its glass transition temperature to help with lipid resuspension [7] and homogenized with US, using a sonicating horn, for several minutes to produce the MBs suspension.

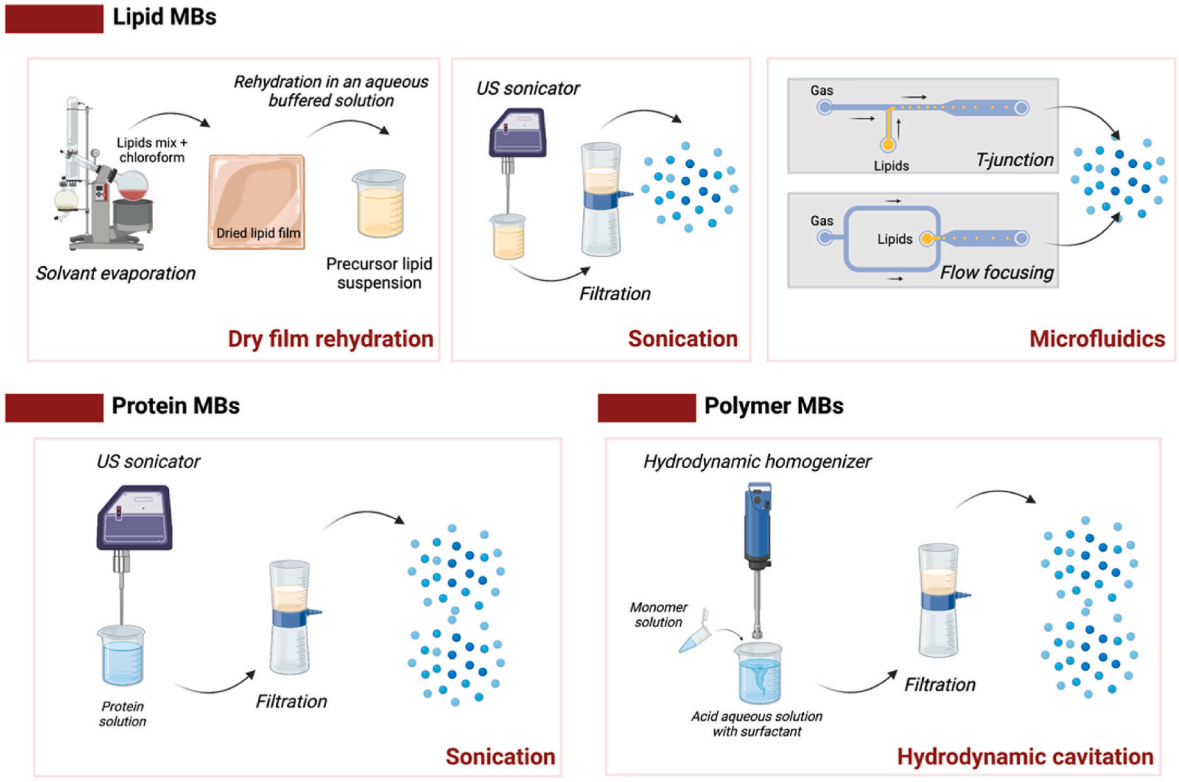

Fig. 1. Methods for Microbubbles synthesis. Lipid MBs are mainly produced following two different methods: Sonication or Microfluidics. The first step consists in dry film rehydration. It requires the solvent evaporation of the lipid + chloroform mix using a rotary evaporator. The obtained film is rehydrated at glass transition temperature and the precursor lipid suspension is homogenized with the help of US sonication. This precursor suspension is either used for a sonication protocol or microfluidics. This method relies on the encounter of the gaseous phase and the lipids phase either with a T-junction or a flow-focusing system. Both allow the generation of highly monodisperse MBs population. Comparing the two methods, dry film rehydration requires day-scale preparation while microfluidics production is obtained in hours scale. Protein MBs are obtained following US insonation of a protein solution followed by filtration of the polydisperse population. Polymer MBs are generated with hydrodynamic cavitation. Monomer solution is incorporated to an acidic aqueous solution under shear stress perturbation. Again, the polydisperse suspension is filtered. Created with BioRender.com.

Lipids dissolution in chloroform and rehydration in phosphate buffered solution constitutes the precursor lipid suspension for all lipid MBs synthesis, and the process can be time-consuming as the chloroform evaporation step can last up to 12 h [8]. Despite the wide practice of this technique, it presents some drawbacks as a complex control on the size distribution. In order to narrow the size dispersity, microfluidics have been a widely explored alternative to obtain reproducible and size tunable protocol. The general idea consists in constraining a liquid flow and/or a gaseous flow into microchannels to generate size monitored MBs. The main advantage is the reduction of reagent volumes meaning a decrease in the total cost of the experiment but also an increased yield of production. Two main systems are leading the field, the T-junction system and the flow focusing setup [9]. Both rely on the convergence of the gas phase and shell material phase with monitored flow rate and optimized channel width to entrap the gas into the shell. Nevertheless, the technology still relies on an advanced miniaturized system with development costs and a time of production slower than other process like sonication or homogenization [10]. A nice review written by Pulsipher et al. presents the various microfluidic technologies developed for MBs generation [9]. Carugo et al. figured out a smart way to overcome the poor production yield without compromising the narrow distribution of microfluidics systems [11]. Instead of direct production of micrometer size MBs, they produce large precursors bubbles with a regular T-junction gas-in-oil system but expose them to a low frequency US field to generates narrow size distribution MBs. This method enables the production of microfluidic-like MBs but with a production yield in the same order of magnitude than conventional batch sonication. Indeed, high yield production methods like hydrodynamic cavitation and sonication have a relatively faster production rate but require post synthesis treatment like filtration to narrow the size distribution. The hydrodynamic cavitation method uses the shear force of a homogenizer in an aqueous solution to induce polymer MBs formation that can be stabilized with the wanted shell component. It briefly consists in the addition of a monomer into an aqueous solution with the constant hydrodynamic stirring of an homogenizer like Ultraturrax for an hour [12]. As for sonication, it is the fastest method and is involved in the generation of the majority of protein shelled MBs [13]. As underlined by Stride et al., sonication is in majority a preparatory step and extensive study about standardization of sonication protocols is not described yet [14]. It consists in the activation of an ultrasonic horn at the solution/air interface causing compression refraction of the liquid [6]. This generation of energy usually creates high local temperature rise and the overall temperature of the solution can be cooled down by placing the setup in ice. Nevertheless, it is known to have strong potential in the obtention of high yield synthesis at low cost and high speed. However, new shell compositions might be studied with this technique to overcome the issue of stability and fast blood clearance known for protein shelled MBs.

Alternative techniques also exists like shaking, used for the synthesis of Definity® MBs by simply shaking a lipid solution in a sealed vial with a shaking device [14]. Moreover, electrohydrodynamic atomization is employed for the generation of lipid MBs by applying a constant electric field on monitored flow rate of a lipid solution in contact with air [15]. Overall, gold standard of MBs synthesis should include the high yield of hydrodynamic cavitation, the size regulation of microfluidic, the fast production time and cost effectiveness of sonication.

2.2. Microbubbles shell composition

The shell integrity of MBs was originally established with albumin polymerization but the resulting MBs quickly showed limitations due to their fast clearance in the body. The most studied protein for MBs application was Human Serum Albumin (HSA) firstly mentioned by Reisner et al. in 1989 [16] and furtherly developed with the addition of additives like Dextrose 5% [17] or fructose 5% [18] through the 90's and 2000's. They had the advantage of providing a sufficient robustness to keep the gas trapped inside and their chemical characteristics implies the possibility to graft targeting or therapeutic agents. The major drawback was attributed to their vulnerability *in vivo*, because of the fast recognition by the patrolling scavenging cells leading to a rapid elimination in the bloodstream [19]. Nowadays, the vast majority of MBs are composed of lipids and a mixture of them arranged as a monolayer [20]. The mixture of phospholipids usually consists of various ratios of DSPC (1,2-distearoyl-sn-glycero-3-phosphocholine) and DSPE-PEG2000 (1, 2-distearoyl-sn-glycero-3-phosphoethanolamine-N- [amino (polyethylene glycol)-2000]). Phosphatidylcholines are a natural component of cell membranes, generally extracted from soybean or egg yolks, and are already used and FDA approved as excipient in various intravenous treatments [21]. The resulting shell is flexible and confers the ability of structural rearrangement. This can be an advantage for an easy reconstitution after freeze drying storage but lipid monolayer reorganization can disservice the overall stability due to weak interaction forces involved in the geometry (hydrophobicity and van der Waals [6]). In consequence, it does not efficiently prevent the gas diffusion and the coalescence. Therefore, lipid shelled MBs strategy relies on the flexible property of lipids and small immunogenicity, as their lipophilic property protect them from reticuloendothelial system clearance [22].

When looking at MBs stability, interaction of MBs between themselves has to be studied. Indeed, during and after their synthesis they will be in close contact as the floatation phenomenon occurs, and unwanted events like the Ostwald ripening or coalescence are more likely to happen [23] (Fig. 2). Ostwald ripening can be defined as the expansion of bigger MBs to the detriment of small and less stable MBs based on thermodynamic equilibrium [24]. This phenomenon can be managed by selecting a low solubility-to-biological-fluid gas and a low solubility-to-biological-fluid shell but also by increasing the stiffness of the shell to prevent exchanges between the surrounding fluid and MBs. In case of lipid shelled MBs, it is recommended to increase the molar volume of the oil phase to reduce their solubility [24]. When two bubbles merge to form a larger bubble, it is called coalescence. It can be prevented by reducing the interaction between MBs using surfactants [25] or by increasing of the synthesis temperature [26]. Hence, MBs shelf stability depends on various parameters like shell and gas composition, shell elasticity, surface tension and viscosity of the aqueous solution. Sridhar et al. [27] proposed a mathematical model to estimate MBs half-life in suspension and focused the attention on shell resistance and the viscosity of the storage solution. Storage stability of MBs in suspension can be extended with stiffer shell material (like polymers) and with the addition of glycerol like ingredient to thicken the aqueous solution [28].

To overcome the shell fragility without compromising the functionalization of the MBs, polymerized cyanoacrylates were introduced as a substitute of lipid shells. Cyanoacrylates are traditionally used in medicine as surgical adhesive for wound closing [29]. They are chemically composed of an ethylene group, a cyano-group and a variable alkyl chain. Initially presented as a monomer solution, their anionic polymerization happens in contact with aqueous media like blood or body tissues conferring adhesive property to the polymer [30]. N-butyl cyanoacrylates are also used in clinics for arterial embolization to prevent from major bleeding in hard to reach regions such as pelvic area [31]. Cyanoacrylate ability to polymerize in water constitutes a new strategy for gas encapsulation in aqueous solution as presented before using hydrodynamic cavitation method. Because of its chemical structure, cyanoacrylate shell are stiffer and thicker (hundreds of nanometers compared to 3–5 nm range for lipid shells [32]) allowing multiple functionalization possibilities including drug loading [33] and targeting peptide grafting [34]. This versatility is accompanied by some drawbacks, the main one relies on the biocompatibility of cyanoacrylate degradation products *in vivo*. Even if the cyanoacrylate glue has been injected in humans [35], it is known that its hydrolysis releases cyanoacetate and formaldehyde which can lead to local ischemia [30].

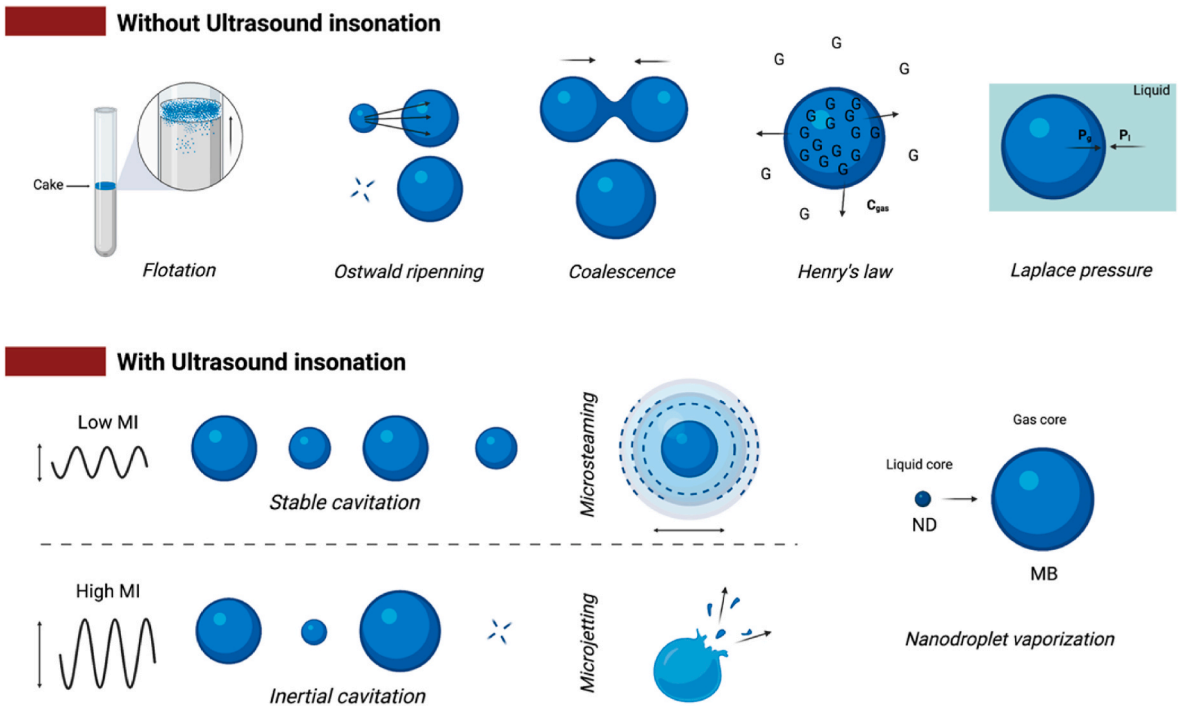

Fig. 2. Microbubbles behavior with their environment and under Us insonation. Microbubbles in static condition will rise to the top of the suspension to form a cake. Depending on the shell properties and surface tension of the MBs/liquid interphase, MBs can undergo Ostwald ripening or coalescence. They are also affected by the gas concentration of their environment according to Henry's Law and to pressure of the surrounding medium according to Laplace's Law. Under US insonation, MBs are distinguished by the US regime. Low intensity US (low Mechanical Index) will induce stable oscillations of the MBs leading to microstreaming. High intensity US (high Mechanical Index) will induce unstable oscillations of the MBs leading to MBs inertial cavitation and microjetting. Also, the liquid core of nanodroplets can undergo vaporization under specific acoustic parameters. ND = Nanodroplets, MB = microbubble, MI = Mechanical Index. Created with BioRender.com.

2.3. Microbubbles surface modification

MBs are now also designed as carriers and they not only need a safe and resistant shell, but also tunability for better biocompatibility, targeting or drug encapsulation. MBs' half-life in the bloodstream is sufficient to perform several rounds in the circulatory system and reach their target but they will get destabilized because of their inevitable gas exchange with the environment. Most lipid MBs are stabilized with PEGs working as a steric shield and avoiding a quick uptake from the reticuloendothelial system and protecting the gas core [36]. Nevertheless, this protection may also lead to generation of anti-polyethylene glycol antibodies with repeated injection [37]. Foreign body recognition can also be limited by fooling the immune system. This interesting approach presented by Yang et al. relies on the surface modification of liposomes by mixing them with platelet membrane [38]. This confers the MBs a safe passage through the blood recognition system because of the incorporation of transmembrane proteins of the platelet membranes. This approach is used here for asepsis induced acute kidney injury diagnosis but is an interesting cloaking strategy also used in nanomedicine for cancer [39] or inflammation [40].

With the acknowledgment that every foreign organism will eventually be discharged, it is also a smart strategy to focus on the targeting of a biomarker rather than the long lasting of MBs *in vivo*. Many innovations are derived from the nanoparticles surface modification [41] with the objective to graft targeting agents for molecular imaging or promoting drug delivery. J. Shue-Min Yeh et al. present a very complete table summarizing the state of the art of surface modification for lipid shell MBs until 2015 [42]. Interestingly out of 94 published papers, 58,5% are based on streptavidin biotin interaction [43,44], 18% on maleimide thiol strategy and the rest are specific lipid-peptide linkage before MBs formulation. Those numbers are interesting because some controversies rely on the immunogenic response to streptavidin in humans due to its bacterial origin. Nevertheless, it remains the strongest non covalent interaction with an affinity constant K_D of 10^{-14} M, shadowing any antibody for antigen recognition. This is why teams are working on improving the immunogenic response [45] and recent work showed great promises about the injection of avidin in humans [46]. This functionalization can be obtained via *in situ* incorporation of streptavidin and with later association of the molecule of interest coupled with biotin, or with chemical incorporation post synthesis of avidin using EDC/NHS (1-Ethyl-3-(3-dimethylaminopropyl) carbodiimide/N-Hydroxy succinimide) coupling [47].

The maleimide thiol bioconjugation strategy relies on the reactivity between maleimides and thiols groups naturally present in biomolecules like cysteines, allowing grafting of fluorochrome, PEGs or proteins [48]. Maleimide groups are added to the structure of the shells and act as an intermediate for drug grafting to the MBs but the chemical reaction has to be monitored because of two competitive reactions. One reversible linkage allowing delivery of agent but easily eliminated in the bloodstream and one irreversible linkage. Therefore, depending on the application and to avoid competition of thiol present in albumin, a fine balance has to be found to improve the stability of this reaction which heavily depends on pH [49].

Covalent bonding of functionalizing agent can be performed via EDC/NHS peptide bond formation. By definition, it allows on the covalent bounding between a carboxymethyl group and a primary amine group [50]. However, standardized protocols are hard to obtain and its accessibility and ease of use does not exclude optimization [51]. A major drawback of this approach is the immobilization of the N-terminus or C-terminus regions of proteins that can be hosting their functional features. Thus, alternative strategies emerged to be more specific regarding the anchoring point. For example, Lui et al. put forward the click chemistry coupling of various desired compounds onto their albumin MBs, conferring a high versatility to the system [52]. Briefly, the method

depends on the strain promoted alkyne-azide cycloaddition (SPAAC) where the triple liaison of the Dibenzocyclooctyne-amine (DBCO) grafted onto the MBs has a high and speed reactivity with azide groups present on the desired ligand.

Functionalizing strategy can also simply rely on weak interaction with a positively charged [53] or negatively charged shell [43]. Indeed, comparing the incorporation of anionic DNA onto neutral or positively charged MBs, Panje et al. highlighted a significant difference in the incorporation of the plasmid when positively charged MBs could bind up to 0.03 pg of DNA per MB, while neutral MBs incorporated only a residual amount [54]. Addition of surfactant in the MBs composition was also demonstrated to improve lipophilic payload, here using natural lung surfactant protein validating the importance of charge on the surface and its environment [55].

Therefore, the balance has to be found for surface modification to obtain weak or strong linkage to functionalizing object, and it must not be forgotten that surface modification has to be strong enough to sustain its functionality in flow condition according to the *in vivo* environment hemodynamics. Moreover, it must not be forgotten that surface modification can influence MBs dynamics, first in term of stability because of Laplace pressure's influence on the MBs but also in terms of acoustic response [56].

2.4. Microbubbles gas core

Another level of MBs tuning consist in choosing a gas of interest for its echogenic, stability or therapeutic properties. The gas can be entrapped into the solution by bubbling in the initial solution and is often saturated in the headspace after freeze drying to avoid the gas exchange after resuspension. The importance of gas for microbubble stability has recently been of main interest while first generation of MBs were mainly composed of air core [19]. A gas with higher solubility like nitrogen contained in air (20 mg/ml in water) would be more likely to diffuse than a fluorinated gas like perfluorobutane (1.5 mg/L in water). The balance has to found between the thickness of the shell and the incorporated gas property to avoid gas loss from the MBs. Indeed, intra-bubble pressure with the surrounding medium (like blood) drastically depends on the bubble radius and the shell resistance at gas-liquid interface, also known as Laplace pressure (Fig. 2):

$$P = P_{inside} - P_{outside} = 2\sigma/r$$

where σ is the surface tension between the phases and r the radius of the MB. Hence, Laplace pressure P is defined the pressure difference between the internal pressure (P_{inside}) and the external pressure ($P_{outside}$) of non-miscible phases. In addition, smaller MBs will disappear faster than bigger ones and even faster if the surrounding medium isn't saturated in gas [19], this time according to Henry' law (Fig. 2):

$$C = kP$$

where C is the concentration of a dissolved gas, k a constant and P the pressure of the gas above the suspension or in the MBs [57]. In order to maintain the gas trapped inside it is recommended to have a thicker shell and a stabilizing gas.

An additional strategy to overcome the rapid gas exchange of air between MBs and the surrounding medium resulted in the second generation of MBs where low solubility gas like sulfur hexafluoride (SF_6) or perfluorocarbons (PFCs) replaced the air core. Fluorinated gas and especially perfluorocarbons (PFCs) are now widely used to maintain a longer half-life of the MBs in the blood circulation because of their inert property. Indeed, PFCs are synthetic molecules descending from hydrocarbons where the hydrogen atoms have been substituted by fluorine atoms. They are known to be chemically inert and their intrinsic atomic structure give them the property to be hydrophobic and lipophobic at the same time [23]. Omata et al. studied the effect of the encapsulated gas on their MBs stability and compared lipid based MBs with either SF_6, C_3F_6 or C_4F_{10} [58]. They concluded that PFCs MBs (C_3F_6 and C_4F_{10}) were highly stable *in vitro* compared to the other MBs (including commercial ones) and their half-life *in vivo* was at least two times higher. Those results are strongly correlated to the Ostwald coefficient formula:

$$L = C_{liquid}/C_{gas}$$

where C_{liquid} and C_{gas} respectively correspond to the concentration of an entity in the liquid phase or the gaseous phase [59]. The higher this coefficient is, the more affinity the entity would have for the aqueous phase. On the opposite, a very inert entity would more likely be highly concentrated in the gaseous phase, leading to a small Ostwald coefficient [60]. For example, O_2 possesses an Ostwald coefficient of 27730 ($x10^6$), while perfluorobutane (C_4F_{10}) and decafluoropentane (C_5F_{12}) respectively have an Ostwald coefficient of 202 ($x10^6$) and 117 ($x10^6$) at 25 °C. This translates to the fact that dioxygen will be more likely to dissolve in the surrounding aqueous phase than perfluorocarbons. Kabalnov et al. then demonstrated this theory in an experimental set up validating the correlation between the increase of MBs lifetime *in vivo* and the diminishing of the Ostwald coefficient of the entrapped gas [61]. They also mentioned that the administrated dose did not influence the time of circulation.

This second generation of MBs are now the clinical standards like mentioned below with Sonovue® (Sulfur Hexafluoride: SF_6), Definity® (Perflutren: C_3F_8) or Sonanzoid® (Perfluorobutane: C_4F_{10}). Nevertheless, entrapping other gas may have therapeutic properties, as this review will discuss below, and teams keep innovating on oxygen MBs formulation to increase their *in vivo* circulation time [7].

2.5. Microbubbles adapted characterizations

Considering their gas core composition, MBs will inevitably rise to the top of the suspension (Fig. 2). This buoyancy phenomenon leads to a "cake" formation that constantly need to be resuspended to recover a homogeneous suspension. In consequence, most of the characterizations have to be thought differently compared to regular particle analysis where everything is affected by sedimentation. For most applications, alternative approaches exist to overcome this constrain like centrifugating into a syringe to be able to easily discard the infranatant. Eventually, characterization in fluidic condition is more relevant than static condition due to the buoyancy force dominating the sedimentation for MBs, which otherwise dominates in the study of other particles. To overcome the buoyancy issue some adapted characterizations are presented below like acoustic sorting for MBs triage, flow phantoms for US evaluation and atomic force microscopy for mechanical characterization.

As US contrast agents, MBs can be characterized by their resonance frequency (RF) which must match the US transducer frequency to get the best acoustic response. It is highly dependent on the mass of the bubble-liquid system (m) and the stiffness (s) of the shell [62], with the formula:

$$f_r = \frac{1}{2\pi}\sqrt{\frac{s}{m}}$$

Thus, it can be deduced that there is an inversely proportional relationship between the size of the MBs and their resonance frequency. Moreover, an increase in the shell elasticity will increase the magnitude of the backscattered signal [63]. Of course, the surrounding medium plays a role on the resistance and MBs in water won't have the same resonance frequency than MBs in blood. Considering their response to US, acoustic sorting has been a great way to narrow size distribution of the sample. In the theory, since MBs resonance frequency depends on MBs size, their displacement in a microfluidic system under US insonation also depends on their size [64]. Thus, acoustic sorting consists in flow focusing MBs in a microfluidic chip, at a concentration where MBs do not overlap, and inducing the emission of US perpendicularly to the flow. The output of the channel is divided in separated exits where MBs

will be directed in function of their response to US, the bigger bubbles being derived the most from their original trajectory. It can be used to separate the resonant MBs at a specific frequency to ensure the best response *in vivo*, and to better model the scattering and attenuation of MBs under US insonation [65].

For the evaluation of MBs to US response, flow phantoms are designed to mimic *in vivo* parameters. It can easily be established in the laboratory with an agar gel mold representing the surrounding tissues and a wall free vessel representing the vascular network [66]. Thus, a clinical transducer can easily be employed on top of the system to image the channel where a monitored MBs suspension is flowed. Echogenicity parameters can be observed through this *in vitro* method like the MBs disruption threshold as developed by O. Couture et al. [67]. Starting from home-made agar gels with channel, industrials developed long lasting phantoms with different channel size or morphology for vascular doppler flow (Cirsinc®).

Mechanical properties of individual MBs can be hard to determine firstly because of their size but also because of their flotation behavior. Atomic force microscopy (AFM) might be the right alternative to get an idea of MBs mechanical properties [68]. The measurement consists in the immobilization of microbubbles on AFM discs with a specific coating like poly-L-lysine or biotinylated self-assembled monolayer for streptavidin functionalized MBs. Consequently, a tipless cantilever is approached to a single MB and several loads are applied on the MB surface to evaluate the resistance to strain. It has been established with this method that Fe_3O_4 nanoparticles decorated polymer shell MBs had an elastic ratio of 4.6 ± 1.2 GPa [69], thin polymer shell Young's modulus was around 1.5–3 GPa [70] while lipid MBs' was lower, around 1.2–2 GPa [71]. This last study also validated that not only the shell composition but also the shell coating can increase this elastic ratio. Similar conclusion was obtained for the stiffness: the more decorated the stiffer.

2.6. *In vivo behavior of microbubbles*

After all, MBs are meant to be intravenously injected but there is a broad gap between *in vitro* flow phantoms and *in vivo* bodies. Hemodynamically speaking, MBs tend to behave like erythrocytes in the blood as their size is similar. It means that in a bloodstream environment where none of the Virchow's Triad event happens (Stasis, Endothelial injury, Hypercoagulability) [72], the MBs will tend to have a luminal position inside the vessel [73]. Unfortunately, this hemodynamic behavior does not protect them from *in vivo* clearance systems. According to Upadhyay et al., *in vivo* stability of lipids MBs are limited to a maximum of 30 min [6]. Most likely, MBs clearance will occur through two pathways: the inevitable ripening and coalescence of the MBs due to excess of environmental or internal pressure, or the scavenging by macrophages and distribution to the reticuloendothelial systems (RES) organs like spleen, liver, bone marrow or lungs [23].

On one side, the gas saturation of the environment will influence the gas exchange between the MBs and the blood and consequently the stability of MBs. For instance, if an animal is under isoflurane anesthesia, the ratio of oxygen in the inhaled gas mixture must be watched or a disequilibrium will appear between dissolved gas in the blood and injected air filled MBs. A study on dogs [74] validated that the rapid clearance of albumin air filled MBs depends on the oxygen ratio of the air mixture inhaled by animals: the more oxygen, the more rapid clearance of air filled MBs in US imaging control. On the other side, the main organ involved in the clearance of MBs is the liver. Some MBs can be used to specifically target the liver, like Sonazoid® shell of which is composed of egg phosphatidylserine, a marker externalized by cells undergoing apoptosis and generating phagocytosis induction [75]. This mechanism was studied to evaluate the clearance through liver Kupffer cells *in vivo* microscopy. It was shown that Sonazoid® MBs were almost immediately internalized but survived almost 30 min as MBs inside the macrophage cells of the liver [76]. It validates the possibility of internalization of MBs by macrophages and their survival for several minutes inside the cells before being degraded, allowing potential gas delivery before the gas escape. Biodistribution and liver uptake was also studied with polymer MBs with the work of Warzecha et al. to better understand the impact on liver cell function and viability. First, fluorescence mediated tomography validated that 40% of the MBs uptake was performed by the liver and half of it was still observable after 2 h [77]. At a tissue level, fluorescent MBs where mainly observed in the myeloid cells of the liver endowed with the capacity of phagocytosis. Using flow cytometry analysis, they demonstrated that MBs are almost instantly fragmented after macrophages or monocytes internalization without affecting their viability. However, the use of US on monocytes that had internalized MBs induced some cell death that they attributed to the fact that some MBs might still be intact after monocytes uptake. Finally, the study validated that even after liver injury with CCl_4, the injection of polymer MBs did not affect the injury extent nor compromise the recruitment of inflammatory cells.

Once degraded, MBs debris could also enter the endothelial cells especially if their shell is composed of a phospholipid layer. Indeed, those cells would inevitably be the first barrier to be in contact with MBs debris. A micro-vessel on a chip study performed by Park et al. highlighted this MBs-to-cells interaction, and especially after stable cavitation of the MBs induced by US insonation [78]. Endothelial cells interaction was also demonstrated with doxorubicin loaded liposomes inducing an increase in the targeted endothelial cells toxicity due to the liposome endocytosis by endothelial cells. We could eventually extrapolate that *in vivo* internalization could be harder to demonstrate according to constant flow and very few studies really explored this pathway [79].

Finally, the major risk after validation of the biocompatibility of the shell and gas, is the occurrence of a micro embolism due to the residual shell aggregating in small vessels. Air embolism is less likely to be a threat as clinical death due to air injection happens with more than 100 mL of injected air [80]. In comparison, considering an injection of MBs of a mean diameter around 3 μm and neglecting the shell width, a standard injection of MBs in humans corresponds to a gas volume in the magnitude of the microliter.

3. Microbubbles for imaging

Currently available MBs for medical application are mostly lipid shell based and have not yet been put to use as targeting and drug encapsulating agents. Their exclusive function is defined as US contrast enhancers for vascular and cardiac cavity imaging. Nevertheless, the US insonation influence on MBs behavior can promote more than conventional US imaging ability as described below.

3.1. *Commercial microbubbles*

Twenty-five years ago, FDA approved the first MBs for contrast enhancement purpose: Albunex® from Molecular Biosystems®, composed of a human albumin shell and air core [74], which was then slowly replaced by new generations of Albumin MBs like Albuminex® and Optizon®. Sonovue® (BR1) from Bracco is probably the most widely used commercial MBs in research and was approved by the FDA since 2001 [81]. It is a phospholipid shell MB with a Sulfur Hexafluoride (SF_6) gas core, employed for cardiac, vascular and hepatic imaging. Definity® from Lantheus Medical Imaging is also frequently described and share the same shell composition as Sonovue®, but with an octafluoropropane (C_3F_8) gas core. In clinical application, it is also approved for cardiac, abdomen and pelvis imaging [82]. Lastly, General Electrics provides two types of clinically approved MBs, Sonazoid® and Optison® with respectively a lipid stabilized shell with perfluorobutane core and an albumin shell with perfluoropropane core. The first one was developed for abdominal imaging while the second one is exclusively used for cardiac application. According to their general guidelines, Sonovue®

must be used within the 6 h after resuspension of the dried product and Definity® within 12 h after shaking of the suspension. As for Sonazoid®, the use-in period after opening is 2 h and Optison® is limited to 30 min. In consequence, those products are limited to single patient utilization. In terms of dose administration for instance, Sonovue® injections can be administered in bolus or infusion up to two times 2 mL for cardiac cavity study. According to the company, this represents around twice 200 million of MBs.

In addition, established companies in the ultrasound imaging field also developed microbubbles for preclinical research like Visual Sonics and their Vevo MicroMarker® which can be provided as a target ready carrier thanks to its streptavidin coating [83], allowing research teams to graft any biotinylated agent. Other companies like Bracco based their strategy on VEGFR2 (Vascular Endothelial Growth Factor Receptor 2) targeting for the imaging of endothelial cells involved in angiogenesis, a key factor in some tumor's growth. With a first introduction of BR55 MBs [84] in the literature in 2010, they completed the first-in-humans injection for the molecular imaging of prostate cancer in 24 patients in 2013 [85]. Using KDR (Kinase Insert Domain) as another targeting agent, BR55 MBs were also injected in humans for the diagnosis of breast and ovarian lesion [86] enhancing US contrast in 93% of the malignant breast lesion and 85% of the ovarian malignant lesion.

3.2. US insonation's influence on microbubbles

To better understand why microbubbles have been such an interesting alternative in the contrast agent domains for imaging, we have to better understand the physics behind it. Ultrasound imaging relies on the ability of sound waves to reflect on materials depending on their composition and structure [87]. The rationale of the methods consists on the analysis of the acoustic impedance on different tissues, which depends on to the sound waves speed of propagation and tissue density. What is mainly noticeable are the boundaries between soft tissues with different material properties like bone, fat, water and collagen [88]. Harmless, non-invasive and accessible method, it is mostly known for pregnancy follow-up but can bring quick and reliable answers to many more anatomic observation (ligament observation, breast check-up, circulatory system …). Indeed US imaging can address anatomical examination with B-mode imaging (2D) or functional evaluation with Doppler setting for blood flow monitoring [89]. Ultrasound imaging in clinics is usually performed in a range from 1 to 50 MHz, knowing that the higher the frequency the shorter the tissue penetration will be [87]. High frequencies (over 15 MHz) enable differentiation of objects less than 100 μm apart in depth [90] but are limited to superficial skin and superficial structures. Breast and thyroid can be observed in the range of 10 MHz, deeper organs like general abdomen and gynecological structures are observed around 3.5 MHz and below. Nevertheless, high frequencies are quite frequently used in animal study because it does not require deep tissue penetration and confers a better special resolution than low frequency US. There are some limitations of this imaging modality and especially the difficulty to image small structures like narrow vasculature or delimitations of the heart cavities. According to Yong et al., even in transesophageal echography, up to 15% of cardiac function evaluation fails due to poor contrast delimitation of the heart cavity [91]. Furthermore, US imaging highly depends on the distance to the observed object. In consequence, there has been an interest in the development in contrast enhancing agent capable of a high response to US signal.

Compared to surrounding tissue, MBs' response to US stimuli induces an increased contrast. The effect of US waves on MBs is the induction of their oscillation in a non-linear way [92]. The general oscillation of the MBs is not in phase because their response to acoustic stimuli depends on their distance to the source. This non-linear property makes them dependent on the amplitude of the signal which can be controlled by the voltage. This response is known as subharmonic (SH) emission generated by MBs themselves (rational fraction of the fundamental) after insonation which distinguishes them from surrounding tissue, unable to produce SH [92]. Those harmonics have a lower frequency and are consequently less attenuated by organs. Sojahrood et al. investigated the conditions for the best signal of SH by insonating MBs and demonstrated that, for a non-destructive regime, the optimum response signal was obtained when the emitted frequency was between 1.5 and 1.8 times the resonance frequency of the MBs [92] (see part MBs adapted characterization). However, this range decreases with the MBs concentration elevation due to MBs/MBs interaction. Also, polydispersity of the suspension can play a role as larger MBs can influence the behavior of smaller MBs. Haghi et al. studied the consequence of MBs clustering on the generation of resonance frequency and highlighted that proximity between MBs induced the increase of their resonance frequency [93].

In terms of MBs behavior under US insonation, two categories can be distinguished: stable cavitation and inertial cavitation which differ by the outcome of the mechanical process (Fig. 2). Stable cavitation of MBs happens at low intensity of US signal allowing stable oscillations of the MBs with an alternance between compression and dilatation episodes without inducing MBs rupture [94]. This behavior is the one observed during US imaging thanks to the emitted subharmonics and ultra-harmonics at low acoustic pressure [95]. Among non-destructive cavitations, microstreaming has been described as the biological effect on surrounding fluids [14]. In other words, the stable oscillation of MBs in living systems creates local fluid motion [96] and temperature rising [97] that can locally destabilize its environment. This behavior is described as one of the enhancing effect helping thrombus penetration [98], drug delivery but also local generation of sonoporation, a method for increasing cell membrane permeability by sonic disruption [99]. Along with the same phenomenon, Acoustic Radiation Force (ARF) emission by US insonation of MBs *in vivo* can be observed. ARF is believed to help drug delivery of loaded agents [100] because of primary ARF that will displace MBs away from the US source and because of secondary ARF (or Bjerkness force) that will improve MBs attraction among themselves by the accordance of their oscillation phase [101]. In addition, the subsequent expansion of MBs influenced by US insonation is described as rectified diffusion [102]. On the other hand, inertial cavitation results in the implosion of the MBs and is caused by the increase of US signal acoustic pressure [103]. Indeed, the rise in the radial expansion/compression amplitudes of MBs will eventually lead to MBs destabilization and shell rupture. It can be observed acoustically by the diminution of ultra-harmonic emission and the rise of broadband emission which translates macroscopically by rapid growth and collapse of MBs [104]. It is a strategic property for drug delivery of targeting MBs but it can also impact its environment as a mechanical disrupting agent [103] with shock waves emission that can disrupt endothelial cell integrity [78]. In association with inertial cavitation, microjetting has been described as the result of asymmetric MBs collapse promoting acceleration of surrounding medium and/or fragment of ruptured MBs. Those microjets were revealed to trigger membrane damage around 1 μm of diameter [105]. Eventually, this kind of disruption would be more likely to happens in case of anisotropic and heterogeneous shell composition [94].

3.3. Microbubbles molecular imaging

Molecular imaging represents a new era of early and precise diagnosis that is in development for several imaging techniques from X-ray technology to MRI, including US imaging [88]. Characterized as the merging point between molecular biology and *in vivo* imaging, the goal of molecular imaging is to visualize and quantify biological processes from early stages, end points and sequels. In contrast to other imaging methods, molecular imaging tends to break free from structural imaging to reach a molecular range precision. To that purpose, contrast enhancers must be functionalized with the targeting property toward specific biomarkers.

Early studies used fluorescence microscopy to overcome the lack of

precision of US imaging with the objective to better understand MBs behavior in the microcirculation. Mark Keller et al. were among the first to investigate intravascular distribution of albumin MBs compared to red blood cells in golden hamsters [106]. They highlighted how MBs displayed a similar velocity and frequency of distribution across the lumen compared to red blood cells, providing MBs an interesting property as intravascular tracers for contrast echocardiography.

As presented in the table below (Table 1), biomarkers of the endothelium can be applied for a wide range of conditions like cancer, vascular injury or inflammation. They all have in common the importance of vascular network, and transmembrane protein like VEGFR2 are targeted because of their involvement in neo-vascularization. However, one target can fit different strategies with lipids or polymer MBs and various targeting agent like peptides, antibodies or polysaccharides. The establishment of specific biomarkers like B7–H3 for breast cancer [107,108], thymocyte antigen 1 (Thy1) particular for carcinoma lesion only in pancreatic diseases [109] or the specific targeting of transmembrane Nucleolin (NCL) as angiogenesis marker [110] gives rise to a huge versatility to MBs as molecular imaging contrast agents. Vascular pathologies like thrombosis, atherosclerosis or endothelium inflammation are more likely to be targeted adhesion proteins like VCAM1 (Vascular Cell Adhesion Molecule 1) [111,112], JAM-A (Junctional Adhesion Molecule A) [111,113] or P-selectin [12,114].

Recent progresses were attributed to the combined targeting strategies with the association of several targeting agents like VEGFR1 and FSHR (Follicle Stimulating Hormone Receptor) which has recently been demonstrated as overexpressed in renal carcinoma [115]. In case of atherosclerosis early diagnostic, the combination of VCAM-1 and ICAM1 antibodies as well as a synthetic sialyl Lewis X peptide (sLe^X) grafted onto MBs surface to mimic leukocyte behavior allowed a strong recognition from the atherosclerotic endothelium [116].

This table displays a non-exhaustive list of MBs used for molecular imaging since 2015 with however only two of them that were injected in humans thanks to the clinical trials of the BR55 MBs as contrast agent [85,86]. Otherwise, the most accessible animal model remains the mouse or the rat even though big animal like pig [124,129] or dog [114] are more relevant for human imaging translation. Extravascular targets were also introduced by Köse et al. as potential biomarkers especially in cancer leaky vasculature but would be more suitable for nanoscale bubbles [130]. However, some limitations remain about US molecular imaging technology detection limit of static MBs by conventional US transducers, discussed below in the new scales chapter.

4. Microbubbles for therapy

Microbubbles as therapeutic tools are the combination of three elements: the therapeutic effect of the gas, the therapeutic effect of the US and the functionalized MBs system as a drug carrier and/or a targeting object. Gas therapy and US therapy have been studied before the democratization of encapsulated MBs and new therapeutic approaches now tend to combine these strategies for a synergic effect.

4.1. Gas therapy

Gas delivery for therapy is extremely dose dependent as low doses will show no effect and high doses can be lethal. Also, if not encapsulated their diffusible property remain a major challenge. Gas entrapped in the MBs has not only the advantage of being echogenic but can also be part of the therapeutic activity of the carrier [131] (Fig. 3).

4.1.1. Dioxygen

In pathologies like cancer, gas balance is a major component of their development. For example, surrounding microenvironment of tumors is known to be more acidic and more hypoxic [132] conferring them a chemo/radiotherapy resistance [133]. Oxygen based treatment are in development to overcome tumors growth with the encapsulation of oxygen into MBs. Fix et al. pointed out that intra-tumoral injection of lipid based oxygen MBs in the tumor site significantly improved radiotherapy treatment [134]. They highlighted that the bigger the tumor the more likely it had developed hypoxic environment, and thus more likely

Table 1
Non exhaustive list of targeting ultrasound responsive strategies for molecular imaging since 2015. GPIIb/IIIA = Glycoprotein IIb/IIIa; VCAM-1 = Vascular Cell Adhesion Protein 1; vWF = von Willebrand Factor; JAM-A = Junctional Adhesion Molecule A; VEGFR2 = Vascular Endothelial Growth Factor Receptor 2.

Application	MBs composition	Targeting agent	Biomarker	Clinical advancement	Year	Ref.
Cancer						
Prostate	Lipids	Peptide	VEGFR2	Clinical trials	2017	[85]
Breast and ovarian	Lipids	Peptide	KDR	Clinical trials	2017	[86]
	Lipids	Peptide/Antibody	B7–H3	Mouse model	2020	[108]
	Lipids	Type III fibronectin	VEGFR2	Mouse model	2016	[117]
	Lipids	Antibody	B7–H3	Mouse model	2015	[107]
Pancreas	Lipids	scAntibody	Thy-1	Mouse model	2018	[109]
Colon	Lipids	Antibody	VEGFR1/FSHR	Mouse model	2020	[115]
Kidney	Lipids	Peptide	VEGFR2	Mouse model	2016	[118]
Angiogenesis	Lipid	Peptide	Nucleolin	Mouse model	2017	[110]
	Polymer	Peptide	E-selectin	Mouse model	2016	[119]
	Lipids	Peptide	Neuropilin-1	Mouse model	2015	[120]
Vascular						
Thrombosis	Polymer	Fucoidan	P-selectin	Mouse model	2019	[12]
	Lipids	scAntibody	GPIIb/IIIa	Mouse model	2016	[121]
	Lipids	Peptide	Thrombin	*In vitro* model	2017	[122]
Vessel injury	Polymer	Antibody	VCAM-1	Mouse model	2015	[123]
	Polymer	RGD peptide	αvβ3-integrin	Pig model	2016	[124]
Atherosclerosis	Lipids	Nanobodies	VCAM-1	Mouse model	2019	[112]
	Lipids	Peptide	VCAM-1/vWF/P-selectin/LOX1	Mouse model	2018	[125]
	Polymer	Antibody	JAM-A	Mouse model	2018	[111]
	Lipids	Antibody/sLe^X	VCAM-1/ICAM-1/Selectins	Mouse model	2018	[116]
	Lipids	Antibody	JAM-A	Rabbit Model	2016	[113]
Inflammation						
Liver injury	Polymer	RGD peptide	Myeloid integrins	Mouse model	2018	[77]
Endothelium	Lipids	Peptide	P-selectin	Dog model	2020	[114]
	Lipids	Peptide/Antibody	P-selectin/VCAM-1/vWF-A1/GPIbα	Mouse model	2018	[126]
Abdominal aorta	Lipids	Antibody	P-selectin/VCAM-1	Mouse model	2017	[127]
Liver fibrosis	Lipids	Antibody	VEGFR2	Rat model	2021	[128]
Bowel	Lipids	Peptide	P and E-selectins	Pig model	2015	[129]

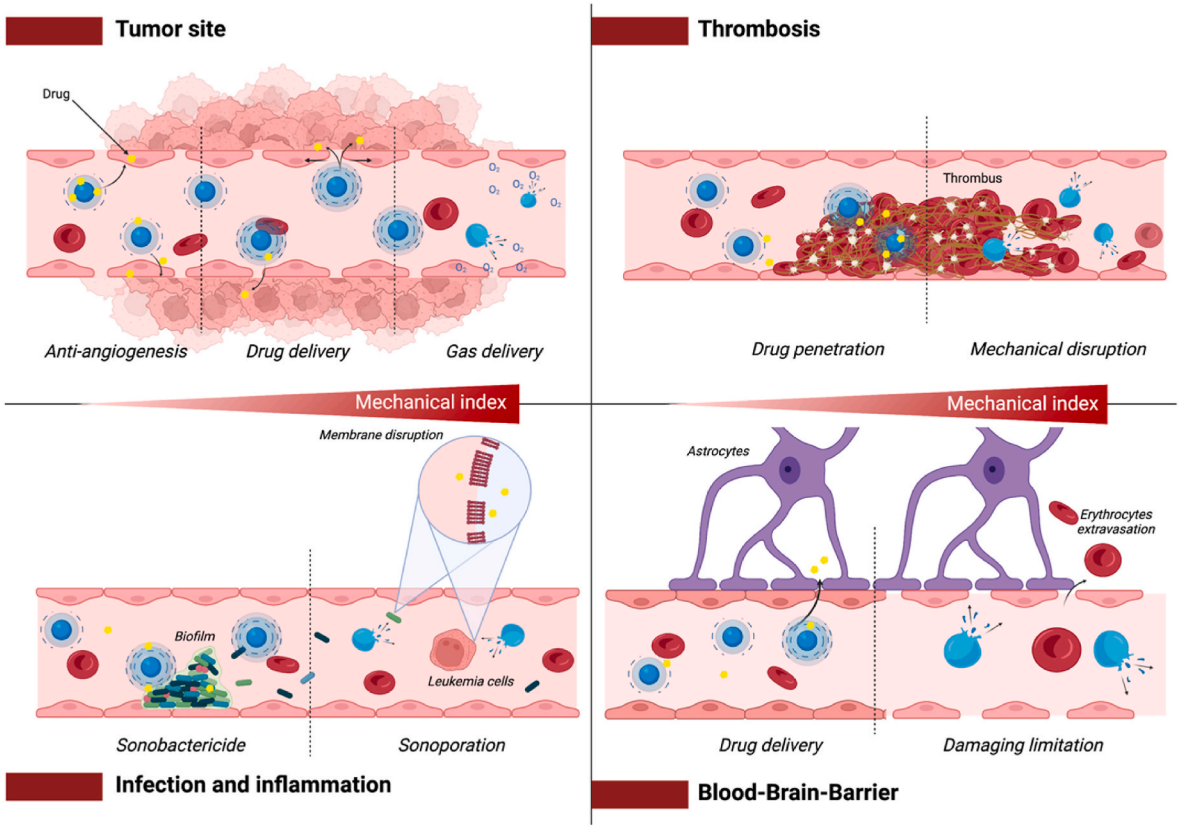

Fig. 3. Therapeutic strategies for tumors, thrombi, infection and Blood-Brain-Barrier. Depending on the mechanical impact of the US signal, MBs therapy can be adapted for different pathologies. Microbubble microstreaming can improve drug delivery to the epithelium and the thrombus. It also destabilizes membrane permeation by fragilizing biofilms and BBB epithelium tight-junctions. The increasing of US mechanical index induces a stronger mechanical impact on the surrounding tissue. Indeed, MBs implosion helps mechanically disrupt thrombi by loosening up the fibrin mesh. This disruption has to be carefully monitored because it promotes cell membrane sonoporation for a therapeutic approach but also vascular permeation causing cerebral hemorrhages. Created with BioRender.com.

it would respond to the oxygen treatment. Unfortunately, most tumors are not accessible for intra-tumoral injection and gas therapy might be delivered via intravenous route. Improvement of radiosensitivity was observed with the intravenous injection of surfactant shelled oxygen MBs on a breast cancer rat model [135]. By increasing tumor oxygenation by 20 mmHg with oxygen MBs, radiosensitivity was almost tripled. This anti-hypoxic treatment leads also to a significant delay in the tumor growth of approximately 30 days compared to radiotherapy only, highlighting great promises for the use of oxygen delivery therapy as a complement of cancer treatment [136]. In order to improve oxygen MBs stability, Peng et al. associated SF_6 to the gas core which showed a 3 times improvement of the circulation half-life *in vivo* [137] (Fig. 4). The study presents lipids O_2SF_6 MBs injected in a nasopharyngeal carcinoma mouse model. Using local US triggered destruction of the MBs, tumor volume significantly dropped from 614 ± 157 mm^3 with regular treatment to 229 ± 31 mm^3. Oxygen therapy is also a promising strategy for wound healing with the embedding of MBs into hydrogels [138].

4.1.2. Nitric oxide

Apart from oxygen therapy, nitric oxide (NO) delivery is a studied strategy because of its function in the regulation of angiogenesis. Thanks to its chemical structure with a very unstable peripherical electron, it is largely used by the cells for signaling and is known for its important role in the promotion of angiogenesis and expending blood vessels [139]. In other words, instead of asphyxiating the tumor, improving its vasculature may overcome the radiotherapy resistance caused by the hypoxic state: it is called tumor vasculature normalization [140]. This hypothesis was studied with the injection of NO micelles combined with radiotherapy [141]. As a result, tumor weight was divided by two compared to the radiotherapy only and survival rate of the mice was also significantly improved. NO is also implicated in the resolution of deep vein thrombosis, by playing a role with the platelets an inflammatory cells aggregation, as well as stimulation the endothelium. Wang et al. injected rats with NO MBs after deep vein thrombosis induction surgery and the resolution of the clot was studied by weighting the clots 8 days later [142]. Interestingly, weight over length ratio of extracted thrombi at day 8 showed a decrease of 40% compared to control group. Compared to anticoagulant therapy this strategy does not involve the risk of collateral bleeding as they measured major indexes of coagulation function. They hypothesized that the antithrombotic effect mainly affected the vessel wall by limiting the leukocyte extravasation (decrease of the expression of VCAM-1 on thrombosis site) and thus maintaining endothelium integrity.

4.1.3. Carbon monoxide

Other gases are potential therapies for cancer such as carbon monoxide (CO) which increases mitochondrial respiration leading to excess production of Reactive Oxygen Species (ROS) and the onset of cell apoptosis [143]. CO also plays a dual role on the nervous central system. Similarly to NO, it is considered as a gasotransmitter in cell signaling and intracellular production of CO can provide neuroprotective effect by upregulating cyclic guanosine phosphate production [144]. Inhalation treatment already proved an infarct volume reduction up to 62.2% in brain ischemia on mice [145]. On the other side, excessive concentration of CO can lead to hypoxia damaging brain cells. Indeed, a strict control of the administered dose creates an unmet medical need for targeted encapsulation of CO as neuroprotective treatment. Looking at another cell signaling pathway, low doses of CO were demonstrated to have an

important protective function in inflammatory diseases [146]. Briefly, macrophages stimulated with a lipopolysaccharide (LPS) inflammatory protocol shown a significant accumulation of anti-inflammatory cytokine IL-10 in contact with low concentration of CO. Same results were observed *in vivo,* allowing interesting perspectives for the role of CO on the regulation of an inflammatory response. This treatment strategy would be all the more interesting as macrophages have the ability to perform phagocytosis on circulating elements of the blood, here MBs. In the recent years, the development of carbon monoxide releasing molecule (CORM) has been studied to control its generation. Pathak et al. adapted this strategy to develop light triggered carbon monoxide generating MBs [147]. By loading CORM onto polybutyl-cyanoacrylate (PBCA) based MBs, they evidenced the enhancement of M2-like anti--inflammatory phenotype upon light triggering CO production on human blood samples. This proof of concept was also studied for the protection over oxidative stress induced in cardiac issue injury. Again, CO triggered delivery allowed a significant reduction of the apoptotic ratio on cardiomyocytes. Altogether, these results indicate the high potential for low dose CO delivery in the resolution of cardiovascular diseases.

4.1.4. Perfluorocarbons

Perfluorocarbons (PFC) do not have direct therapeutic effect; however, they are used as intermediate transporter for oxygen. As mentioned before, O_2 plays an important role in the physiology and consequently in pathologies. PFC in their liquid state like Perfluoro-octyl-bromide (PFOB), or perfluorobutane (PFB) can be employed as O_2, NO and CO carriers [148]. Their very inert property enables the uptake of dioxygen. If we compare the capacity of dissolution of oxygen in water or in a PFC, the molar ratio of dissolved O_2 is 1 mol of O_2 in 200 mol of water compared to 1 mol of O_2 in 0.2 mol of Perfluorodecalin (PFD) [23]. Perfluorocarbons-based oxygen carriers (PFOCs) have nicely been reported in the review from Jäger et al., presenting how PFOCs are an innovative tool from cancer therapy to blood substitute [23]. As presented before, the fluorine atomic structure tends to attract electrons from surrounding atoms giving a stiff structure to the molecules that are not affined to dissolve in aqueous media meaning that PFCs are good candidates as solvent for other gas and especially oxygen, carbon dioxide and nitric oxide [148].

4.2. Ultrasound therapy

US treatments are already widely used without the need of MBs injection. The main advantage of US therapy is the non-invasive characteristic of the method. It is now possible to avoid surgical intervention over kidney stone disease by the use of shock wave lithotripsy [149]. The current use of high peak pressure (up to 100 MPa) and very low rate (2 Hz) safely helps with the resolution of kidney stones [150]. Recent clinical trials of a more efficient burst wave lithotripsy (<12 MPa, <200 Hz) helped to reposition 95% of kidney stones in human [151].

US are also used for ablation therapy without the requirement of surgical intervention. This method called histotripsy uses focused US to destroy tissue, thanks to the induced cavitation, without thermal or ionizing related event [152]. It was first observed as a collateral damaging consequence of lithotripsy, which was finally studied by itself as a new form of non-invasive therapy. Typically used US parameters are performed up to 6 MHz with a high negative pressure up to 15 MPa with low duty cycle to avoid heat generation. Phase I clinical trials were conducted on benign prostatic hyperplasia, liver cancer and calcified aortic stenosis [152]. Limitations of US therapy are still attributed to organs containing gas or acoustically unreachable organs because of bone blockage. If recent clinical trials have not confirmed the evidence of US enhanced sonothrombolysis in limb ischemia yet [153], clinical studies are still ongoing to replace invasive mechanical thrombectomy and overcome collateral damages of high dose thrombolytic therapy. This issue can be resolved by using US as an accelerator of thrombolysis, in supplement of drug delivery. Li et al. meta-analysis highlighted that, out of 5 clinical trials, thrombolytic injection associated with US insonation for acute ischemic stroke showed a significant recanalization rate over thrombolytic injection alone [154]. The studied trials had US parameters from 1.8 MHz to 4 MHz for over 1 h of US monitoring.

For a more local treatment, US emitting catheter can be introduced in the popliteal vein along with plasminogen activator delivery catheter. This method was presented by Kartal et al. and showed 60% of partial reopening in deep vein thrombosis events [155]. Even though the significance was not established compared to local delivery only, they concluded that ultrasound-accelerated-catheter-assisted-thrombolytic therapy had the advantage of preventing from bleeding complications by maintaining a local treatment.

Overall, US exposure can be adapted via different forms, from non-invasive to local US emitting catheter. In opposition to wide range US imaging, focused US can accurately target a zone by focusing high pressure amplitude. Nevertheless, this high accuracy method usually requires the association of MRI imaging to define the area to treat [152, 156]. Lastly, US imaging and treatment of brain related events is still a major challenge because of the skull thickness. Hence, the most accessible part is through the temporal bone enable the visualization and potential treatment with transcranial Doppler approach [157].

4.3. Microbubbles as therapeutic tools

The application of MBs for therapy must be preceded by the study of the interaction between vessel wall and MBs interaction. Indeed, confined behavior of MBs differs from unbounded ones and it seems reasonably clear that the bioeffect of MBs disruption has to be studied to determine therapeutic boundaries. Known limitations consist in the damage of surrounding tissue attributed to vessel distention or wall impairment due to microjetting (Fig. 2). Mathematical models were established by Hosseinkhah et al. to evaluate the wall shear stress and circumferential stress and have been validated with experimental data [158]. *In silico* results assessed that wall shear stress within microvessels could reach 18.3 kPa during MBs expansion and 74 kPa during MB collapse. As constrained MBs behave differently, an *ex vivo* model from perfused rat caecum led to the conclusion that the angle of US insonation on vessels had no impact on the interaction between MBs and the endothelium. It also showed that constrained bubbles in the capillary network had an increased oscillatory lifetime compared to big vessels and that bigger MBs (>4 μm) tend to interact better with the endothelium than very small MBs [159]. Those observed interactions under US insonation consisted in an asymmetrical collapse onto the vessel wall and repeated expansion beyond the vessel limits and the study suggested that the efficacy of ultrasound mediated MBs therapy strongly depends on the MBs concentration and size distribution. On the other hand, *in vitro* vessel phantoms lithotripsy set up with albumin MBs demonstrated that the induced expansion of very large bubble could cause rupture of the vessel wall and therefore pointing out the importance of size distribution regulation [160]. Those general examples are important to understand the mechanical behavior of MBs. Indeed, despite the wide use of MBs for therapy for cancer, inflammation or thrombotic diseases, some therapeutic strategies are actually very similar. As many innovative therapies, the balance has to be found between the different parameters to get the best advantage over risks ratio. The first parameter that can be monitored is the mechanical index (MI) of the US wave. It is a unitless ratio representing the pic of negative pressure (MPa) over the square root of the frequency (MHz) of the signal [161].

$$MI = \frac{P}{\sqrt{f}}$$

This ratio strongly depends on the US device used and the distance to the object, and it can be measured with an hydrophone calibration [162]. Below 0.1, MI will generate only linear oscillation of the MBs; between 0.1 and 1, these oscillations become non-linear allowing the imaging of the MBs. From 1, inertial cavitation leading to disruption of

the MBs can be observed [6]. Eventually, these numbers can be adapted to each application but the scientific community and the FDA agreed on the limit of MI to 1.9 in humans to avoid any damaging bioeffect [163] (except for ophthalmological evaluation where the MI is limited to 0.23 [164]).

4.3.1. Thrombosis

As mentioned before, MBs can be triggered to explode by increasing the amplitude of the US signal (Fig. 3). This bursting associated with thrombi therapy is called sonothrombolysis. Basically, sonothrombolysis consists in the use of ultrasound waves and MBs to mechanically disrupt the clot [41]. It can be influenced by the duration of insonation, the composition and the concentration of MBs or the time between pathological incident and treatment. Positive outcomes are evaluated with the recanalization rate [121] or the study of the related ischemic lesion, like presented by Dixon et al. on an ischemic stroke model [10] (Fig. 4). A very complete review from Nederhoed et al. describes the different therapeutic use of MBs and US on peripheral arterial thrombosis based on 26 preclinical studies and 9 clinical ones [165]. They compared the localization of the thrombosis (middle cerebral artery, abdominal aorta, internal carotid artery …), the age of the clot and the number of subjects for preclinical and clinical studies. Recanalization rate was one of the primary outcomes, meaning the ability of the blood flow to be restored after the treatment. There were two ways of quantifying the reperfusion rate: angiography or transcranial Doppler.

Among the *in vivo* preclinical studies (Table 2) using a thrombolytic drug as a control, here are the interesting conclusions: the US settings used for sonothrombolysis were very heterogeneous varying frequency of the transducer from 1 MHz [166] to 6 MHz [167], the MI from 0.2 [168] to 2 [169] and different pulse length [170]. Preferentially, the strategy was to infuse the MBs over several minutes [168,169,171,172] while continuously insonating the clot with different MI. On the other hand, some studies injected the MBs in bolus but always with long treatment insonation [173–175], which is in contradiction with the fact that MBs are relatively quickly cleared out from the blood. The total exposition of clot to the US remains unclear and very heterogeneous to most of the studies. There is a clear need for *in vivo* study to accurately describe the frequency of the probe, the mechanical index, the duty cycle and the total duration of insonation, in order to better establish comparisons. Moreover, lack of control groups using MBs and thrombolytic agent with US insonation has been highlighted as well as lack of comparison with different shell compositions. According to Nederhoed et al., all the studies included for the *in vivo* sonothrombolysis using contrast enhancer agent and a thrombolytic agent presented a minimum recanalization rate of 56% up to 100% while US alone never allow a reperfusion superior to 63% [165]. The lower recanalization rate was attributed to Tomkins et al. because of the platelet rich composition of the clot that responds less efficiently to thrombolytic therapy [172].

Moving on to clinical studies for sonothrombolysis, most of them were performed on ischemic stroke patient with duration therapy from 1 to 2 h with 2 MHz US insonation but with low or non-indicated MI. The biggest clinical study of sonothrombolysis for ischemic stroke patient was performed at the University Hospital of Vall d'Hebron in Barcelona, including 296 patient with acute stroke [176]. After thrombolytic drug bolus, patients received 3 doses of 2.5 g of air-filled galactose-based MBs along with 2 h of transcranial Doppler monitoring. Conclusion of the study was that MBs administration associated with US insonation helped early recanalization without increasing the risk of intracranial hemorrhage. One limitation however remains, since these results were obtained with an operator dependent technique which is the transcranial doppler imaging. The therapeutic window was not meant to be improved in this study but presents potential leads for reduction of thrombolytic drug dose that still can cause collateral hemorrhages. Short pulse duration (<5 μs) is explored in randomized clinical trial to reduce US exposition [177]. In this study, myocardial infarction patients were randomly treated with high MI and Definity® MBs injection before and after undergoing percutaneous coronary intervention. In combination with regular treatment, MBs treatment help doubling the recanalization rate. One key data was the improvement of the systolic function that remained higher with MBs treatment even after 6 months. Consequently, only 5% of the patients required the implantation of a removable defibrillator while 18% of percutaneous coronary only treated patient required one.

The clinical translation of therapeutic MBs still faces obstacles in order to find the right conditions for an efficient sonothrombolysis and standardize the protocols. Furthermore, the actual clinical studies are based on already approved MBs as contrast enhancers, but have not included payload-carrying or targeted MBs yet. Also, as Porter et al. mentioned, one major drawback to overcome with the use of MBs for therapy is the microvascular obstruction after recanalization of myocardial infarction [178]. Despite many strategies evaluated for its resolution, research has failed finding a solution and recanalization of

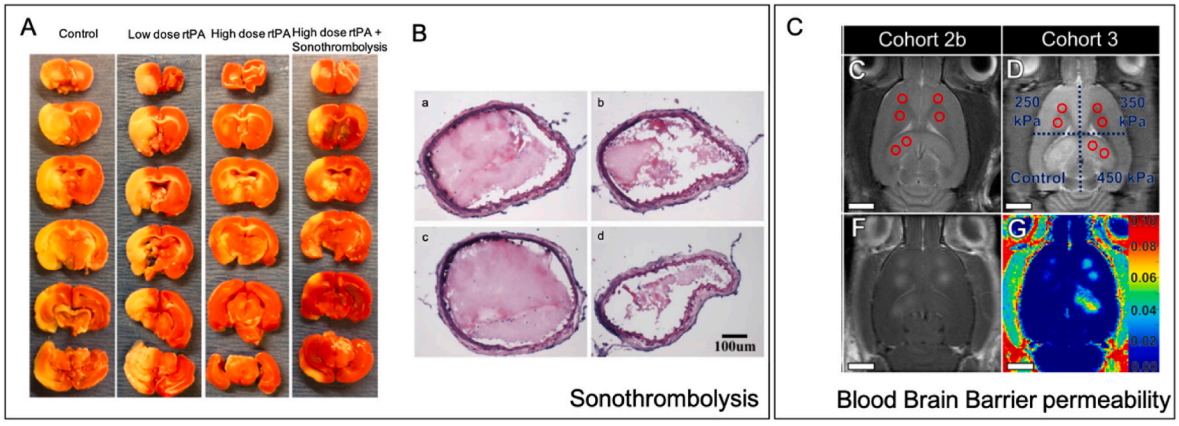

Fig. 4. *MBs and US insonation for sonothrombolysis and Blood Brain Barrier permeability. A) and* ***B)*** *In vivo sonothrombolysis using MBs and US.* ***A)*** *TTC staining of stroke induced cross sectioned brain. Infarct is identified by yellowish areas. Groups are presented as below: control with saline injection; low dose of rtPA (0.09 mg/kg); high dose of rtPA (0.9 mg/kg); low dose of rtPA (0.09 mg/kg) + MBs + US.* ***B)*** *Representative images of hematoxylin and eosin-stained thrombi from mice carotid arteries after different treatments and US imaging. a) Platelet targeted MBs + low dose of rtPA (75 U/g); b) rtPA loaded platelet targeted MBs; c) Platelet targeted MBs + saline; d) Platelet targeted MBs + high dose of rtPA (500U/g).* ***C)*** *MRI images of Targeting Focused US (FUS) on rats. First row red circles represent the MRI guided FUS targets before insonation. Second row corresponds to images after FUS.* ***C–F)*** *Gadolinium contrast enhancement in T1 MRI highlighting BBB permeation on FUS targets.* ***C-G)*** *Dynamic contrast-enhanced-MRI after MBs FUS exposure depending on several US amplitude. TTC = Triphenyltetrazolium Chloride. Adapted with permission from A) [10]; B) [121]; C) [193].* (For interpretation of the references to color in this figure legend, the reader is referred to the Web version of this article.)

Table 2
Synergic therapies of MBs associated with US and drug for thrombosis and cancer. Non exhaustive list of recent pre-clinical studies evaluating the improvement of drug therapy with MBs. (tPA: tissue Plasminogen Activator; TCCS: Transcranial Color Doppler Ultrasound; MI: Mechanical Index; Ab: Antibody).

Application	Targe-ting agent	Drug	Loaded on MBs	Co-injected	US	Outcome	Ref.
Stroke	No	tPA	No	Infusion (NA)	1 MHz, 0.9 MI, 20 min	TCCS + MBs required tPA co-injection for an efficient thrombolysis	[166]
Stroke	No	tPA	No	Infusion (10 mg/kg)	3 MHz, 1.7 MI, 40 min	Resistance of platelet rich clot resolution to any condition	[172]
Stroke	No	Urokinase	No	Infusion (20,000 U/kg)	2 MHz, no MI	Synergy in the recanalization rate using co-injection of drug and MBs	[174]
Coronary thrombosis	Yes (IIb/IIIa)	Pro-Urokinase, Heparin, Aspirin	No	Infusion (50,000 U/kg)	1.5 MHz, MI 1.9, on/off 30 min	Synergy of clot targeting and high MI sequence	[168]
Coronary thrombosis	No	tPA	No	Infusion (1 or 0.5 mg/kg)	1 MHz, 2.0 MI, 30 min	Synergy of high MI with MBs and low drug dose	[169]
Coronary and microvascular thrombosis	No	tPA	No	Infusion (1 or 0.5 mg/kg)	- 1.6 MHz, 1.0 MI, 30 min - 1.6 MHz, 2.0 MI, 30 min	Longer duration pulse over higher MI is more efficient	[170]
Abdominal aorta thrombosis	No	tPA	Yes (rehydration with tPA solution, 200 μg/rabbit)	Control	- 6 MHz, MI 0.4, 2 min - 6 MHz, MI 0.2, 30 min	No difference in the US conditions, efficient thrombolysis but no significant difference between co-injection and tPA-loaded MBs	[167]
Limb arterial thrombosis	No	Urokinase	No	Intra-arterial Infusion (50,000 U/kg)	1.6 MHz, 1.2 MI, 60 min	Synergy of US with MBs and low drug dose for faster resolution	[171]
Limb arterial thrombosis	Yes (RGD)	tPA	Yes (rehydration with tPA solution, 0.06 mg/kg)	Control	12 MHz, 0.5 MI, 30 min	Reduced dose of tPA loaded on MBs with US showed similar recanalization rate compared to free rtPA regular dose with MBs and US	[175]
Breast cancer	No	Cabazitaxel	Yes, loaded during synthesis (10 mg/kg)	Control	1.1 MHz, 0.5 MI, 2 min	US + encapsulated drug onto MBs resulted in the complete remission in all treated animals	[180]
Anti- angiogenic for breast cancer	Yes (CD105 Ab)	Gene therapy (endostatin)	Yes, loaded during synthesis	No	1 MHz, No MI, 30 s	Tumor volume reduction after targeted gene therapy compared to untargeted MBs	[186]
Anti- angiogenic for breast cancer	No	Endostar (endostatin)	Yes (avidin-biotin) (10 mg/kg)	Control	1 MHz 0.5, MI, 30 s	Efficient anti-angiogenesis effect of drug loaded MBs + US compared to group without US insonation.	[187]
Ovarian Cancer	No	Paclitaxel	No	Infusion (10 mg/kg)	1 MHz, 0.4 MI, 3 min	Reversal of drug resistance with the co-injection of MBs associated with US	[182]
Prostate cancer	No	Cabazitaxel	Yes, loaded during synthesis	Control	1 MHz, 0.5 MI,15 min	Efficient reduction of tumor growth with US and either free drug + MBs or drug loaded MBs	[181]
Prostate cancer	No	Oxygen + Doxorubicin	No	Control (7 mg/kg)	2 MHz, 1.4 MI, 30 min	Tumor oxygenation with oxygen MBs assisted with US improved the intratumoral accumulation of anti-cancer drug	[190]
Tumor model	No	Doxorubicin	No	Infusion (6 mg/kg)	1 MHz, 1.0 MI, 10 min	Improved delivery of drug on tumor site with MBs associated with US	[185]
Skin cancer	No	STAT3 decoy	Yes, loaded during synthesis (10 μg)	Control	1.3 MHz, 1.6 MI, 25 min	Tumor growth inhibition after the specific delivery of the encapsulated STAT3 decoy associated with US	[183]

microvasculature still remains an unmet medical need [179].

4.3.2. Cancer

In certain cases, tumor growth is associated with neo-vascularization allowing nutrient transport to the tumor. As presented before with gas therapy for tumors, the hypoxic environment reduces the action potential of radiotherapy. Injection of chemotherapy is still promoting various side effects because of the apoptosis of rapidly dividing cells that include cancer cells but also immune cells or hair follicles. The three mains strategies for US meditated MBs for cancer therapy rely on the oxygenation to overcome the hypoxic state [134], the anti-tumor drug delivery and the anti-angiogenesis strategy [96] (Fig. 3, Table 2).

In terms of drug delivery, biological barriers are a limiting factor, even for nanoparticles (NPs), because of the lack of homogeneity in the tumor vasculature. US assisted delivery with MBs could help drug penetration with the generated microstreaming. This advantage was evaluated by Snipstad et al. in 2017 with polymeric NPs assembled as a MB (NPMBs) [180]. The goal is to take the advantage of MBs behavior under US insonation to disturb the surrounding tissue and deliver the drug loaded NPs. Tumor uptake of drug loaded NPs after US insonation is evaluated with fluorescence confocal microscopy. In the 3rd week following the tumor cells inoculation, animals are treated with Cabazitaxel (mitosis blocker) loaded NPMBs with or without US insonation. The conclusions of this study highlight the influence of US (MI over 0.25) on the uptake efficiency of drug loaded MBs. Attributed to the enhancement of the vasculature permeability, Cabazitaxel loaded NPs were incorporated 2.3 more times in the tumor and complete remission was observed after 50 days. Limits are defined by the heterogenicity of vasculature between every tumor and tissue damage over 1 MI. Overall it suggested that the higher the tumor is vascularized, the more efficient the treatment will be. Also, Enhanced Permeability and Retention (EPR) effect is not sufficient enough for the effective delivery of drug loaded NPs. The subsequent question was, is the drug encapsulation required for cellular uptake? Answering this question could accelerate clinical translation by co-administration of drug and MBs with US insonation. The question was addressed on the same protocol, with either drug loaded NPMBs or free drug co-administered with NPMBs to evaluate the true potential of US induced sonopermeation [181]. Interestingly, no

difference in the survival of the two groups was observed with 50% of survival after 72 days, and free drug uptake was equally effective to encapsulated one. Here again, this indicates the mechanical incidence of US insonated MBs on their environment.

In order to overcome the collateral damages of US insonation, focused US is developed to restrict the size of the insonated area. Using focused low intensity US, drug resistance reversing effect can be studied as the results of enhanced drug incorporation [182]. In this *in vitro* study, focused US and MBs destruction with free Paclitaxel inhibit the proliferation and increase the apoptosis of drug resistant ovarian tumor cells. The inhibition of autophagy developed by those drug resistant cells was defeated by the influence of MBs reaction to focused US. More than overcoming a drug resistance pathway, it gives new direction for *in vivo* treatments. The same strategy was validated *in vivo* with a murine squamous cell carcinoma model [183]. This time, MBs were loaded with a transcription factor for the inhibition of STAT3 (Signal Transducer and Activation of Transcription 3) acting for tumor progression. Gene therapy was proven efficient with a reduction of 51% of the tumor size with encapsulated transcription delivery using focused US. The actual size limit for drug enhanced uptake was evaluated by comparing Evans Blue and FITC dextran as drug model for the respective size of 3.7 nm and 30.6 nm [184]. While neovascular established cut off stands in a range from 380 to 780 nm [184], tumor distribution of free drug is not exactly related [185]. Indeed, US associated decrease of internal pressure of new vessels helps deeper penetration of bigger sized drugs. Even small drugs need environmental stimulation to cross the barriers because of *in vivo* extracellular matrix barrier and circulating protein adsorption that can compromise the uptake.

Antiangiogenic strategy is developed to help depleting tumors from their blood supply. Gene therapy was proven efficient with targeting MBs compared to untargeted MBs with a specific targeting to endoglin (specific marker to newly formed blood vessels higher than VEGFR2) [186]. *In vivo* studies performed on triple negative breast carcinoma xenografts established that low MI focused treatment (0.2) of Sonovue® was sufficient to improve the antiangiogenic effect of the free Apatinib (a tyrosine kinase inhibitor) without observing the drug related systemic effects [187,188]. Regardless, this strategy show some limitations with the emergence of studies promoting the maturation of tumor blood vessels phenotype to reduce their hypoxic state and radiotherapy resistance [140,189]. Recent work from Yi-Ju Ho et al. demonstrated the potential of this tumor vasculature normalization with oxygen MBs [190]. The oxygen release inducing vessels maturation increase the anti-drug treatment penetration by 3–4 folds.

These new cancer strategies are of a worldwide interest. Looking up to clinical trials (up to October 2022), 8 trials are currently recruiting patients in 5 different countries (USA, Canada, Norway, France and Germany). The use of non-targeted commercial MBs in those trials are meant to improve treatment for various cancers type like breast (NCT04431674, NCT03477019, NCT05445050), liver (NCT03199274, NCT02764801), colorectal (NCT03458975, NCT03477019), and pancreas (NCT04146441).

4.3.3. Blood brain barrier

Major controversy on US associated to MBs treatment is the Blood Brain Barrier (BBB) trespassing. Acting as a highly controlled barrier which limits the penetration of most compound, BBB prevents brain from blood contamination for its own neuroprotection. Consequently, systemic injection of treatments for Central Nervous System (CNS) pathologies are challenging as only 2% of molecules below 600 Da can cross [191]. As presented before, MBs expansions generated by US insonation can overcome microvasculature elastic limit and cause microvasculature leakage even in very specific tight junction of the cerebral endothelium. Parallelly, human skull (>6 mm) represents a major obstacle for the use of clinical US transducer because of the large absorption of the emitted waves giving a transmission coefficient only estimated of about 14% [191]. Overall, CNS access is limited both to circulating drugs and US exposure. This limitation is prevented in preclinical studies with the thin thickness of the mouse skull (0.5–1 mm) [192].

On one hand, the improvement of BBB permeability is a major milestone for drug delivery in the brain tissue (Fig. 3). Firstly, boundaries have to be established to obtain a positive advantage over risk ratio for brain treatments. Histology for red blood cells extravasation, Evans Blue permeability test or dynamic contrast enhanced MRI are morphologic evaluation of BBB permeability. McMahon et al. evaluated it through the study of proinflammatory mediators 4 h following US insonation of 3 types of injected MBs [193] (Fig. 4). They exhibited that the MBs size distribution plays a role in the inflammation response. Polydisperse lipids MBs like Definity® or BG8774 (Bracco®) were less likely induce the production of inflammatory mediators compared to monodisperse populations (MSB4, Bracco®). Nevertheless, the elevation of inflammatory response without tissue damage can be an advantage for application linked to the neuroinflammatory system. The study concludes on the relevance of acoustic feedback controls to limit wideband generation and thus diminishing the destructive inertial cavitation [156]. This temporarily opening can be improved with the chemical functionalization into targeting MBs without increasing the required US amplitude [194]. Focused US is currently the best solution for non-invasive and targeting application for CNS treatment with microbubbles widely described in Chen et al. review [195]. Those findings are high potential therapies for degenerative diseases like Alzheimer's [196] or Parkinson's [197]. Once again therapeutic targets are unreachable with BBB impermeability. Parkinson's treatment with MRI guided focused US to the putamen has reached phase I clinical trial in Canada concluding on the safety and feasibility of US assisted drug delivery [197]. A decrease of 12% of Parkinson's disease rating scale motor score evaluation was observed in treated patient who were off medication.

On the other hand, MBs induced leakage of the BBB vasculature may have significant adverse effect (Fig. 3) like hemorrhages [198], sterile inflammation [199] or neurotoxicity [191]. The objective remains to limit inertial cavitation, with previously presented monitoring of the acoustic feedback, in order to keep the permeabilization temporary and localized.

4.3.4. Other pathologies

Other strategies are emerging by taking all the advantages of US mediated MBs treatment. One major complication observed in clinics are nosocomial infections. Particularly life threatening, biofilms cause majors problems in health care system. Bacteria adhering to tissue or surfaces will develop a protective matrix and behavior limiting the action of antibiotics. *In vitro* proof of concept of sonobactericide potential MBs was presented for the infective endocarditis [200]. Briefly, induced *staphylococcus aureus* biofilms on human blood clots were treated under flow conditions. The major factor identified as contributing to the sonobactericide phenomenon (Fig. 3) was the acoustic streaming produced by insonated MBs. In Lattwein et al. study performed in 2018, US alone did not show any improvement in the infected clot resolution compared to regular treatment (antibiotics + thrombolytic). However, the use of commercial bubbles with US insonation at low frequency parameters (120 kHz, 0.44 MPa) achieve almost 100% of infected clot resolution. This strategy can be applied to several sources of infection like chronic bacterial prostatitis, pneumonia or urinary tract infection [96]. Lattwein et al. study was recently updated by comparing five US parameters from 100 kPa to 400 kPa with different duty cycles [201]. This time, the study of sonoporation by measuring the intake of propidium iodide, which is unable to permeate cell membrane and bacteria dispersion, were mostly observed in the high-pressure US rather than high duty cycles ones. This means that the mechanical index has more influence than the continuity of the emitted US on untargeted MBs for biofilms resolution. Also, this study really demonstrated the key role of US and MBs because no significance in the sonobactericide study was

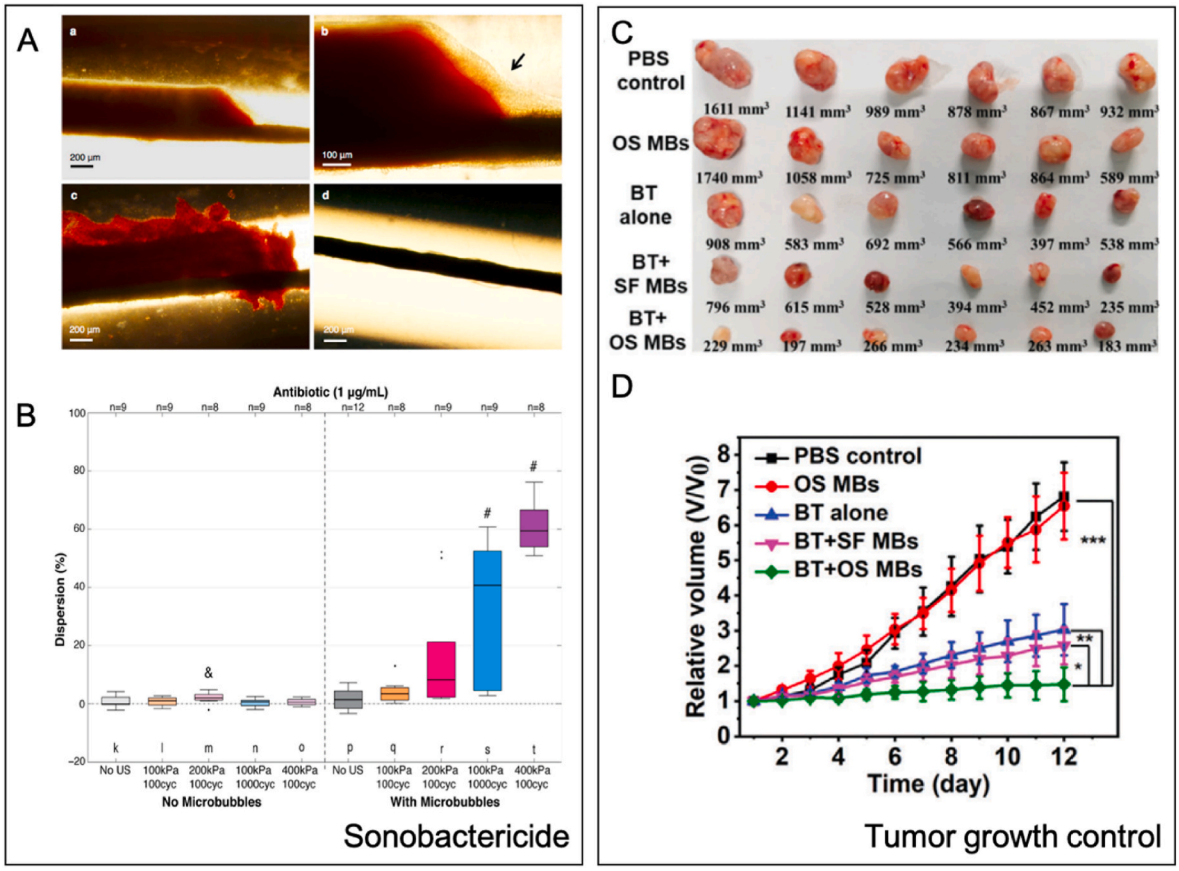

Fig. 5. *MBs and US insonation for sonobactericide and tumor growth control. A) and* ***B)*** *In vitro sonobactericide.* ***A)*** *Bright-field light microscopy images of infected clots following treatments. Groups are presented as follow: a) plasma control; b) control magnification; c) antibiotic + rtPA; d) antibiotic + rtPA + US + MBs.* ***B)*** *Dispersion of bacteria within biofilms with several insonation intensity and duty cycle. Comparing antibiotic treatment with or without MBs (*p < 0.05. or **p < 0.01).* ***C)*** *and* ***D)*** *In vivo tumor growth evaluation with US and MBs mediated radiotherapy treatment. Groups were defined as follow: administration of PBS (PBS control); administration of Oxygen/SF_6 MBs followed by US activation (OS MBs); Brachytherapy (radiotherapy with 125I seeds) alone (BT alone); Brachytherapy with SF6 MBs followed by US activation (BT + SF MBs); Brachytherapy with Oxygen/SF_6 MBs followed by US activation (BT + OS MBs).* ***C)*** *Representative images of ex vivo tumor volumes with different treatments.* ***D)*** *Tumor relative volume growth curve of different groups for 12 days (n=6, *p = 0.001, **p = 0.001, and ***p = 0.0004). cyc = cycles; PBS = Phosphate Buffer Saline. Adapted with permission from A)* [200]*; B)* [201]*; C-D)* [137].

shown with the addition of antibiotics (Fig. 5).

Sonoporation induction can also be a strategy for DNA transfection improvement *in vivo* [54]. Ability of MBs to facilitate intracellular delivery by sonoporation has to be further investigated for an innovative gene therapy strategy. Indeed, as mentioned by Duan et al., there is a lack of information about the membrane repair after MBs + US induced sonoporation [202]. They studied the impact on leukemia cells and found that US insonation in presence of untargeted MBs induced the upregulation of cytoprotective gene (heat shock protein) (Fig. 3). In consequence, if a cytoprotective behavior was observed in the first hours, many of them failed to maintain an ordered proliferative cycle and underwent necrosis or apoptosis. Thus, the addition of targeting MBs should improve the selectivity toward leukemia cells before an eventual emergence of new antitumoral treatment. Additionally, endocytosis enhancement was demonstrated by the alteration of clathrin-mediated endocytosis pathway after US microbubble treatment giving more argument for intracellular drug delivery [203].

It can be recapitulated from these different applications that US triggered MBs disruption therapy is not meant to replace drug therapy. Most probably MBs must be used in complement to improve drug efficacy and/or drug delivery. Overall, the use of MBs for therapeutic application is mainly driven by the aim to reduce drug-dose related side effect and improve the treatment outcome (Table 2). The availability of clinically approved microbubbles helped better understand the effect of US with MBs and co-injection of drugs. The latest works now tend to study the synergy of drug loaded targeting MBs and the use of mechanical disruption with US.

5. New scales and technologies

MBs also suffer from several limitations, including their size which limits extravasation of the vascular compartments, as well as a usually short circulation time (in the magnitude of a few minutes [204]). On the other hand, new approaches based on nanotechnologies offer significant advantages such as surface properties, access to the surrounding tissues and longer circulation time thanks to an array of new materials and expertise in various formulations of both organic and inorganic objects [205].

As such, nanobubbles (NBs) were developed as an alternative to ultrasound-active compounds like MBs to achieve extended circulation time, extravasation to surrounding tissue (especially tumor tissue) and potential molecular targeting capacities [206]. New technological developments have also allowed the emergence of more complex acoustically active objects, while also illustrating some limitations and risks of the current nanoscale ultrasound-active approach. Lastly, US imaging in clinical application shows limitation for a more precise imaging leading to the development of innovative ultrafast imaging.

5.1. Nanobubbles

Among the wide use of MBs for clinical imaging application, the existence of NBs themselves was debated for a long time [207], even after being evidenced as existing in commercially available MBs suspensions [208]. For the most part, their stability was not compatible with standard bubble models and as described above, the ultrasound backscatter significantly decreases with the micro/nanobubble size [206], nullifying NB's participation to ultrasound signal. The main takeaway from the literature before 2010 was therefore that NBs, if existing, were present at traces level and would not contribute in any way to a relevant ultrasound contrast enhancement [209]. However, Oeffinger and Wheatley published their work in 2014 with comprehensive description of ultrasound contrast agents with diameters ranging from 400 to 750 nm and formulated from a previously described model of 1.5 μm microbubbles [209,210]. Hereafter, the field started taking off with the emergence of multiple approaches, notably in the field of cancer imaging and therapy.

Typically, NBs consist of similar components as traditional MBs while having a diameter in the range of 100–500 nm [211]. A gaseous core, mostly filled with PFC gas (or mixtures of them) is encapsulated in a shell which, as for the MBs, is often composed of self-assembling lipids. A broad range of phospholipids, either in single or cocktail formulation, have been used over the years while being coupled to various methods of synthesis [212]. Mostly two approaches exist: either isolation from a bulk heterogeneous microbubble suspension [213] (based on centrifugation [214] or filtration [215]), or *ab initio* synthesis with similar techniques as microbubbles with careful optimization of composition and synthesis parameters, such as sonication, mechanical stirring or thin-layer evaporation [211], as well as recently microfluidics [216]. Other interesting NBs have been formulated with different shell formulations, including surfactants [217] or polymers (e.g., organic polymers such as PLGA nanobubbles from Yang et al. [218] or polysaccharide crosslinking as shown by Bhandari et al. [219]). Others have described various synthetic methods for NBs generation [205, 219–221], and since they mostly resemble techniques for MBs synthesis recapitulated above, we will focus in the following discussion on their applications.

First, the advantage of NBs over MBs is their much smaller size, which allows for extravasation in leaky vasculature (Fig. 6). This has been especially investigated in cancer theranostics, with much attention on the Enhanced Permeation and Retention (EPR) effect, associated to leaky endothelium in certain tumors with fenestrations of a few hundreds of nanometers [211]. As such, NBs have an ideal size for specific imaging of tumors with the generally recognized safe and easy-to-implement ultrasound imaging. Several authors described the use of NBs as means of tumor imaging; among them, Zhang et al. showed in 2019 that a carefully controlled preparation method based on differential centrifugation could yield acoustically active NBs with diameters of 475.2 ± 5.7 nm with significant passive targeting of solid tumors *in vivo* when compared to microbubbles [214], as well as similar ultrasound contrast *in vitro* as MBs across a range of 10^5 to 10^9 bubbles/mL. Similar works demonstrated this by various imaging methods [220,222]; however, precise localization of the acoustically active components inside or outside the vasculature was not evident, and mostly macro-imaging methods or efficacy of a fluorophore or drug delivery were often used as endpoint. Therefore, the results from Pellow et al., were particularly interesting as they demonstrated that acoustically active nanobubbles effectively extravasated, and not only fragments and payloads which could have otherwise been detected: they managed this by careful kinetic assessments including destructive cavitation of extravasated NBs [223]. Furthermore, they described an extravasation enhancement with ultrasound stimulation of their NBs, by showing a contrast enhancement of 1.5x the baseline in tumors and 5x when subjected to ultrasound stimulation. Other groups have coupled passive and active targeting of tumors, with for instance by Kumar et al., 2022, who covalently conjugated anti-PD-L1 nanobodies to NBs for molecular imaging of PD-L1 expression in tumors, with promises related to diagnosis and prognosis of multiple cancer types [216].

Moreover, the use of NBs is not limited to cancer imaging, as therapeutics can be delivered with the combined benefits of NBs. The cavitation properties of MBs and NBs can be utilized to improve delivery of gene therapies [222]. In comparison to MBs, NBs benefit from their smaller size for extravasation and tissue penetration [224] and publications from various groups demonstrated the potential of NBs for tissue gene therapy. For example, since 2020 Kida et al. described the optimization of NBs size to improve genetic material delivery [224] and feasibility of *in vivo* gene transfection in mice with a hand-held ultrasound scanner [225]. Such a controlled release is also relevant for drug delivery as shown by Tan et al., among others, who used nanobubbles loaded with an immune checkpoint inhibitor and a sonosensitizer for antitumoral activity in a xenograft mouse model [226]. Interestingly, growing knowledge on the influence of shell properties and NBs size might allow in the future a better controlled acoustic response of NBs, which might allow multiplexing of NBs in the future for differential imaging or therapy [215].

5.2. Beyond nanobubbles

Over the years, more complex approaches have emerged to benefit

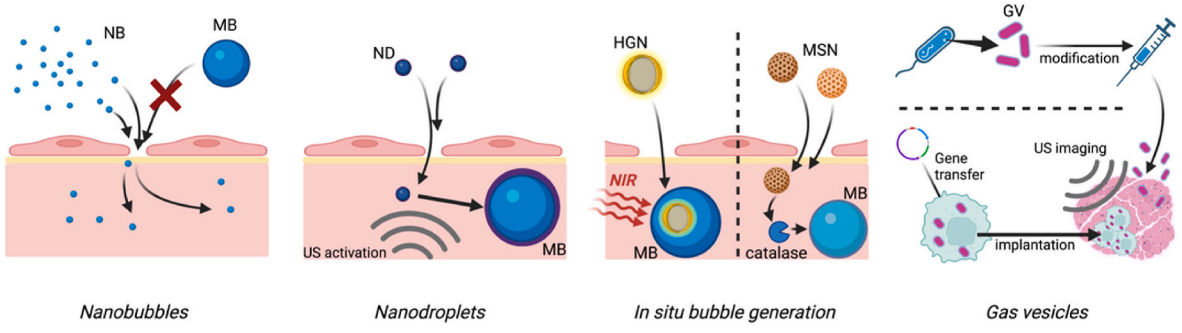

Fig. 6. New scales of US sensitive objects. The rationale behind the different innovations on the nanoscale to MB technologies are represented here. From left to right: NBs are typically smaller than 0.5 μm to allow extravasation, while NDs can be converted from nanosized droplets to MBs to combine NBs and MBs properties. HGNs use plasmonic resonance to locally create vapor MBs, and MSNs can be loaded with enzyme responsible for *in situ* O_2 bubble generation. Finally, gas vesicles can be extracted from bacteria and act as NBs. Otherwise, gas vesicles can be encoded on a genetic cassette, transfected in eukaryotic cells, for the live cell labelling during implantation. *NB = nanobubble, MB = microbubble, ND = nanodroplet, HGN = hollow gold nanoparticle, MSN = mesoporous silica nanoparticle, loaded with the catalase enzyme, GV = gas vesicles.* Created *with* BioRender.com.(For interpretation of the references to color in this figure legend, the reader is referred to the Web version of this article.)

from micro/nanobubbles related acoustic properties while ensuring a better control over the objects, including switchable properties, multimodal imaging or increased stability and robustness [227]. This partly stems from limitations of the NBs.

Indeed, multiple studies showed that in fundamental-mode (or in B-mode) ultrasound imaging, nanobubbles contribute to a negligible extent to the acoustic signal [208,209,228], which is coherent with the backscatter theory in ultrasound imaging [229]. A recent study by Myers et al. in 2020, while limited in its scope, raised doubts about the risk of MB contamination in a NB preparation, where only a small proportion of 2.5 μm MB would be responsible for most of the US acoustic signal when mixed with 700 nm NBs [230]. Even though this work was limited to a single formulation, and focused on fundamental imaging at a classical setting, it pinpoints the extreme care that needs to be taken in formulating such NBs. It is however interesting to note that NBs were repeatedly shown to have strong nonlinear effects which can be detected [206,207,223]. This recapitulates another limitation of NBs: comparison to MBs is rather complex since imaging modalities differ. While some publications directly compare NBs and MBs with standard ultrasound imaging [210,220,231], rigorous comparison based on volume or molar concentrations equivalence is often lacking. Furthermore, imaging modalities differ especially since several publications using the nonlinearity of Nanodroplets (NDs) response to ultrasound for contrast enhancement, in contrast to MBs. On the other hand, an interesting work by Batchelor et al. in 2020 with NBs nested inside liposomes revealed that in their formulations, both NBs of perfluorobutane (PFB) and PFB droplets were actually present, with the PFB droplets being responsible for the cavitation that allowed payload delivery in their liposomes [232]: this pinpointed another rich area of PFC-based acoustically active objects.

Such nanodroplets (NDs) or Phase-Change Contrast Agents (PCCA) have been investigated extensively since 2010 [233,234]. These emulsions of PFC gas in nanoscale droplets can undergo a phase-transition under stimuli to form nano/microbubbles that are acoustically active [235,236]. Interestingly, this shift, which is linked to a vaporization temperature usually close to 37 °C in the pressure conditions of such nanodroplets, can be triggered by both externally applied ultrasounds [221] or photoacoustically by near-infrared illumination [237]. This allows for both the advantages of nanoparticles/nanobubbles of easy extravasation, tissue penetration and targeting abilities, while benefiting from the high backscatter of microbubble *in-situ* formation for clear acoustic imaging (Fig. 6). As shown by Moyer et al. in 2015, these NDs when compared *in vivo* to MBs showed an improved HIFU (High Intensity Focused Ultrasound) effect, which is used for thermal ablation of tumors among others and can be enhanced by ultrasound contrast agents [238]. Moyer's article demonstrated that NDs allowed for more localized, more efficient and overall safer use of HIFU for in-depth tissue thermal ablation. Notably in a rat model, they showed efficacy of NDs from 4 to 10 mm deep in the liver while MBs caused surface and skin burns, due to prefocal heating. Multiple groups have similarly investigated the use of NDs both in imaging and therapy for solid tumors [239] and showed benefits of using NDs to selectively image cancer biomarkers [240].

Recently, super-resolution-based approaches have emerged in photoacoustic imaging with the works from the group of O. Couture starting with the publication of Errico et al., who used MBs to break the diffraction limit in ultrasound imaging [241]; similar work was pursued with both microdroplets [242] for sub-diffraction drug delivery control through ultrasound, and later NDs [243] in a photoacoustic setting to reach unequaled spatial resolution in tissue (less than 10 μm spatial resolution). Such NDs therefore show promises in advancing ultrasound contrast agents further into the tissue and therapeutic potency [227].

Other innovative technologies have emerged: *in-situ* generation of nano/microbubbles without PFC gas, with for instance plasmonic nanobubble generation [244] with Hollow Gold Nanoshells (HGN) [245]. In these objects, HGN or simple gold nanoparticles are able under laser excitation to locally heat the surrounding water and create transient vapor bubbles (Fig. 6). Interestingly, using Nanoshell structure allowed excitation with Near Infrared (NIR) light, therefore enabling this technology to be used *in vivo* thanks to the NIR imaging window [245,246]. As demonstrated by Shin et al. in 2020, a fine tuning of liposomes-loaded HGN based on size, from 10 to 40 nm, or wall thickness and aspect ratio, can be used in a precise delivery of Ca^{2+} and ATP by liposomal rupture, almost in a multiplex manner [247]. Other objects have been investigated to produce similar effects, by directly trapping gas nanobubbles on nanostructures. These include the polymeric nanocups designed by Kwan et al., which can carry air nanobubbles, and use them under cavitation to enhance delivery of an antibody into tumors [248]. Another innovative approach relies on local chemical generation of bubbles: one such research was led by Shi et al. who loaded catalase on 50 nm mesoporous silica nanoparticles to generate locally O2 bubbles that enhanced the HIFU effect in tumors [249] (Fig. 6): under sufficiently low power so that no tumor damage could be observed with a saline injection, a 135 ± 30 mm^3 ablation could be observed with this catalytic nanoreactor. A key benefit of these objects relies in the extensive knowledge of such nanoparticles which allows fine control over synthesis, stability, functionalization, and characterization [250].

Notably, another source of nanoscale contrast agents takes a radically different approach, without requiring artificial synthesis of such compounds: Gas Vesicles (GVs) can be extracted from certain microorganisms, and under proper purification, can act as proper nanobubbles. Such GVs have been described for more than 100 years and can be found in various bacteria and archaea and play roles in buoyancy for these organisms when freely floating in water, but also in regulation of cytoplasm volume and surface-to-volume ratio [251]. They are composed exclusively of proteins self-assembling into cylinders or spindle ranging from 0.1 to 2 μm long vesicles, which are permeable to gas only. However, their use as nanotechnology had not yet been exploited. Pioneering work was led by Shapiro et al. who described the GVs produced in *Anabaena flos-aquae (Ana)* and *Halobacterium NRC-1 (Halo)*, their isolation and characterization as nanoscale nanobubbles both *in vitro* and *in vivo* [252]. Further engineering improved these GVs as contrast agents, with for instance work by Wang et al. which functionalized GVs with PEG and Hyaluronic Acid (HA) to increase their circulation time and escape immune clearance [253]. Shapiro's group also performed the exciting isolation of a minimal gene cluster which can be expressed in mammalian cells as reporter genes, with promising cell lineage tracking capabilities with the desired simplicity of ultrasound imaging [254]. Another proof-of-concept of the efficiency of GVs as NBs can be found in their use for ultrasound-mediated delivery of genetic material by bubble destruction, as described by Gao et al., who managed the gene editing of tumor cells both *in vitro* and *in vivo* with these GVs [255] (Fig. 6). Relying on such bio-sourced nanobubbles allows for a strict monomodal size distribution and control over these objects, which answers to one of the major difficulties of nanobubble synthesis as described above.

Thus, the rich recent research surrounding nanoscale ultrasound contrast agents with the leading nanobubbles illustrate the potential yielded by the junction of microbubble-based ultrasound properties and nanotechnology: targeted, controlled objects with access to extravasation in various tissues for both imaging and therapy while also relying on a broad range of functional technologies brought forth by the vast nanoparticle field [205,250]. The currently understood advantages and limitations of these new approaches are listed in Table 3.

5.3. Ultrafast imaging

On the other hand, advances in the ultrasound imaging method have also benefited from specific MBs use. An especially notable one is the emergence of Ultrafast Ultrasound Imaging. Predicted and developed since the 70s [256–258], it was however first used in practical conditions after the 2000s (following work in 1984 by Shattuck et al. with only four simultaneous lines) [259,260] with the development of new

Table 3
Advantages and limitations of recent contrast agent innovations, based on their imaging, capabilities, circulation properties and tissue penetration.

	Nanobubbles	*Nanodroplets*	In situ *bubble generation: plasmonic effect or enzyme-based*	*Gas vesicles*
Advantages	• Extravasation, tissue penetration • Stability • Nonlinear imaging • EPR effects (tumor passive targeting)	• Extravasation, tissue penetration • Stability • Nonlinear imaging • EPR effects (tumor passive targeting) • MB switching for improved imaging	• Extravasation, tissue penetration • Inorganic (stable, controlled chemistry) • Fine tunability of NP physico-chemical properties • Spatial control, tissue-specific activation	• Extravasation, tissue penetration • Fine size control • Eukaryotic gene reporting • Cell tracking *in vivo* by US imaging
Limits	• Size control can be limited • MB contamination can affect US signal • Modality of imaging is not yet standardized: o Classical mode settings (resonance frequency, intensity) o Nonlinear modes (multiple methods for exploiting nonlinearity, which must be compared)	• Delicate choice of PFC: liquid/gas transition must be fitted to body temperature • Physical activation *in situ* is yet to be mastered (US, light-induced heating) • High pressure/longer pulses are typically required in US activation than usually administered	• No imaging prior activation • Activation control, due to multiple possibilities, is yet to be standardized: o HGN are limited by light penetration and O_2 availability o Enzyme-based NPs require sufficient substrate, ATP and tissue variability can be an issue	• Typically, high concentration is required for similar imaging power as MBs • Differences in imaging with NBs of similar size cannot yet be explained • Nanoengineering capabilities are still recent and requires further refining • *In vivo* cell imaging through gene expression is yet limited to destructive imaging, with possible negative cellular effects

processing units (GPU) that allowed for a software-based parallelization which is especially demanding, in the range of several Gigabytes/s for data transfer to the processing unit, or of 1–2 Gigaflops/s (operations performed by the processing unit) computing power [261]. As explained above, the conventional imaging with an ultrasound probe is based on serialized lines reconstruction by focused beams, and therefore the frame rate is limited by the time to emit, receive, and process the beam on one hand, multiplied by the number of lines necessary for the image [262]; meaning that the building time of an image is directly correlated to the size of the zone being observed with for example at a given depth, an image needing twice more lines will take twice more time to acquire, which either limits the frame rate or the width of the images [261,262]. This can be improved by built-in multiline computation probes, but the serialized design remains the main limitation to the frame rate, typically in the range of 30–100 Hz [261]. On the other hand, in ultrafast imaging the whole process is parallelized, as typically only one (or few) emission is used to simultaneously image the whole region of interest by relying on plane or divergent ultrasound waves [263,264]. All the lines are acquired at once and thus the image frame rate is only limited by the wave time-of-flight, as long as the processing power necessary for data treatment is sufficient. In such ultrafast architectures the image frame rate can reach tens of thousands of Hz [261]. This high frame rate can be

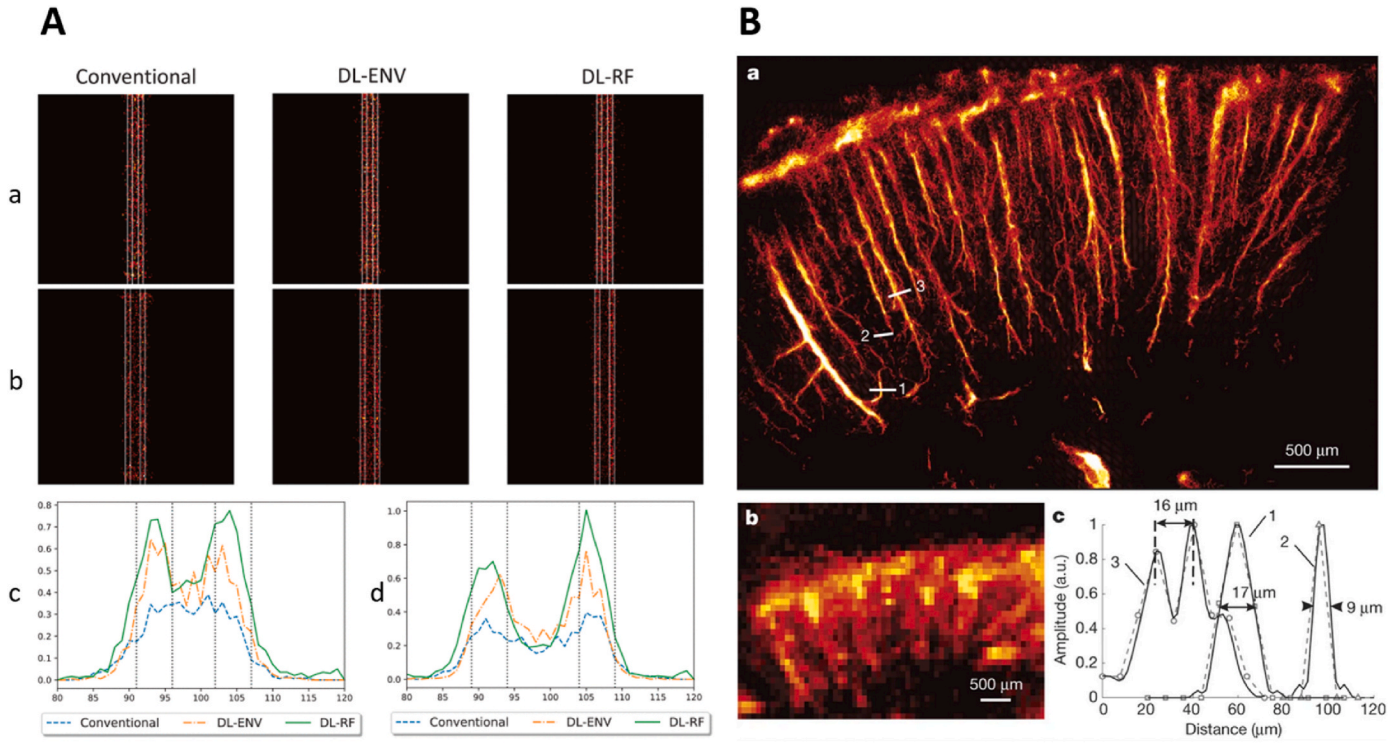

Fig. 7. *Two major applications of Ultrafast Ultrasound imaging: A) Illustration of how different analysis method for MB localization can affect the spatial resolution of ULM. Two deep learning algorithms (DL-ENV and DL-RF) are compared to a conventional localization technique, with (a) and (b), simulated vessels separated by 3.0 µm or 4.9 µm. Transverse reconstruction with the different methods are respectively shown in (c) and (d).* ***B)*** *Comparison of an Ultrasound Localized Microscopy (ULM) images (a) reconstructed through microbubbles localization (pixel size of 10 × 8 µm), with the same area imaged in conventional power Doppler in (b). Based on the (a) image, a linear intensity projection along the displayed line (from 1 to 3) shows a spatial resolution below* 16 µm. *Adapted from A)* [275]; *B)* [241].

put to use for multiple benefits, such as 3D imaging, high temporal resolution or two major innovations enabled by this technique: Shear Wave Elastography, where quantitative viscoelastic measurements of tissue can be acquired in real time without invasive procedures [265] (Fig. 7), or Ultrafast Doppler imaging with simultaneous qualitative and quantitative measurements at high speeds [266]. Notably, functional Ultrasound Imaging (fUSI) was developed, which relies on ultrasound plane waves to attain ultrafast ultrasound Doppler for cerebral blood volume measurement: this approach allows a high spatiotemporal resolution (200 μm, 1 ms) and has already been shown to be beneficial in measuring brain activity [267], and study neurovascular coupling. However, these improvements alone cannot increase the spatial resolution of US imaging beyond the diffraction limit.

Furthermore, when coupled with ultrasound contrast agents such as MBs, ultrafast ultrasound imaging has found an extremely powerful application. Not only can, the benefits of imaging MBs at ultrafast scale, improve the real-time imaging of vasculature or tissue, but it has also been used in a super resolution approach to break the diffraction limit and improve the resolution of ultrasound imaging down to a few microns, in an approach called Ultrasound Localization Microscopy (ULM)) [268,269]. The rationale, inspired by optical super-resolution techniques such as Photo-Activated Localization Microscopy (PALM) and Stochastic Optical Reconstruction Microscopy (STORM), relies in imaging separable punctual sources (here, echoes from a single MB) and deconvoluting the Point Spread Function (PSF) to localize the source beyond the diffraction limit. The repetition of this process over thousands of sources allows the reconstruction of a resolution-enhanced image. In the context of ultrasound imaging, the high frame rate (over thousands of Hz) of ultrafast ultrasound imaging allows this method to be applied in ultrasound imaging of MBs or similar contrast agents [241]. Since the signal of MBs decorrelates much quicker than the surrounding tissue both spatially and temporally, they can be separated from the background and isolated individually [269] with either linear or nonlinear US imaging. This was demonstrated in 2015 by Christensen-Jeffries et al. [270] and by Errico et al. [241]. The latter described *in vivo* ULM and showed that the spatial resolution was improved more than ten times compared to conventional ultrasound imaging, allowing the distinction of 20 μm wide blood vessels, 20 μm apart and up to 8 mm deep in the brain of rats. This is illustrated with comparison of ULM to classic Doppler vasculature imaging in Fig. 7. Moreover, since this approach relies on individual MB spotting, their tracking can be used to measure blood flow velocity inside the imaged vessels, with notable benefits when compared to conventional Doppler. The resolution is significantly enhanced (from hundreds of μm to around 15 μm), and Doppler velocity mapping is limited to the component orthogonal to the imaging direction [241]. In the recent years, several published works have demonstrated the potential of ULM technique, with among others, Hingot et al. (2021), who presented a normalized method to evaluate spatial resolution in ULM [271], Chavignon et al. (2022), who investigated the perfusion differences in ischemic or hemorrhagic strokes in rat models [272], or Andersen et al. (2022), who verified that ULM could correctly assess physiological velocity changes in the vasculature by chemically altering blood velocity in rat kidneys [273]. Most recently, new promising diagnostic applications were described with for instance ULM use in Alzheimer mouse models [274]. This array of publications illustrated the normalization of its use and helped the recognition of this powerful tool for non-invasive quantitative exploration of tissues. Interestingly, among multiple approaches to robustly implement this method, Chen et al. (2022) reported a Deep Learning-based method for MB localization, with apparent imaging benefits when compared to conventional localization [275], while Heiles et al. openly made available methods and metrics for benchmarking ULM algorithms in 2022 [276]. Notably, several groups have focused on bridging the gap to the clinical world, with for instance Yan et al., who translated this method to rhesus monkeys and thus opened the way to clinical trials [277], and Demené et al., who first used ULM in human brain without the need for transcranial aperture and with significant improvement in spatial resolution with at least one order of magnitude enhancement at up to 120 mm depth when compared to a typical clinical contrast CT imaging [278], or Huang et al. who recently published a feasibility study in various human organs [279]. The diagnostic potential was also investigated in tumor bearing mice, then in human patients, by the group of Opacic in 2018 and opened new tumor assessment [280].

As mentioned earlier, this new imaging method can also be coupled to newly developed ultrasound contrast agents in order to further improve resolution and enhance the therapeutic efficacy. Indeed, several groups attempted to break through the diffraction limit with the use of optical super-resolution inspired techniques. For instance, Zhang et al., described Cyanine 7.5-coated NDs for photoacoustic imaging, and similarly to PALM, STORM or ULM, single objects are localized and PSF-deconvoluted; but here, the laser illumination is tuned so that only a small fraction of NDs are converted to MBs which can be imaged by ultrasound, and therefore the tuning of the laser allowed for a fine control of detectable events [243]. Even though tissue penetration can be reduced with NIR light compared to ultrasound imaging (tens of mm versus tens of centimeters [281,282]), the precise activation of these contrast agents and focal precision of NIR laser can prove useful in certain applications.

Thus, ultrafast ultrasound imaging has opened new opportunities in ultrasound imaging by reaching unprecedented imaging frame rates, which have among others been exploited with MBs to reach super-resolution imaging capabilities in ultrasound imaging. It can therefore be expected that innovations in the contrast enhancement agents might be repercussed in combination with ultrafast ultrasound imaging to reach new potential. For instance, further spatial resolution enhancement in super-resolution ultrasound imaging might benefit from the use of NBs or NDs [243,282,]. Functional imaging allowed by targeted MBs or even NBs to extravasate deeper in tissues might open new insights with improved either temporal or spatial resolution through ultrafast or ULM ultrasound imaging, with encouraging results from already existing (though at a less fine spatial resolution) fUSI in terms of clinical applications. Overall, innovations in the contrast agents' field (MBs, NBs, NDs, echogenic NPs, etc …) can converge with advanced imaging methods (Doppler, 3D, ultrafast, ULM, etc …) to improve our exploration of physiology, diagnostics, and therapeutics.

6. Conclusion and perspectives

This work aimed at better understanding the MBs strategies for human treatment and diagnosis. New approaches were described to overcome the unmet medical need for a non-invasive and targeted efficient treatment but also diagnosis tools. Indeed, therapeutic treatments relying on systemic drug injections are still bringing toxicity, collateral damages and uncontrolled pharmacokinetics, such as half-life in circulation or tissue penetration. The use of MBs in clinical application is currently reserved for US imaging thanks to their echogenic properties. Through this review we pointed out the importance of understanding MBs intrinsic characteristics (composition, behavior, stability) to better apprehend their translation to *in vivo* diagnosis and treatment. Secondly, the review focused on the use of commercial MBs for US imaging and the recent prolific development of targeted MBs for molecular imaging that brings a new dimension for early and precise diagnosis. We confronted the applications for cancer, cardiovascular diseases or inflammation to better understand MBs behavior. Depending on their application, MBs can be insonated with US at varying settings to take advantage of different oscillation response. It showed that the frontier between stable cavitation and inertial cavitation *in vivo* is still delicate to establish. According to most pre-clinical studies, it can be concluded that low mechanical index insonation of microbubbles would help mechanically destabilize the surrounding environment. This includes enhancement of drug delivery, biofilms impairment and BBB

opening thanks to microstreaming. In addition, the rise of mechanical index would induce irreversible MBs destruction which can further cause fibrin clot disassembling, cells membrane sonoporation and sometimes vascular leakage with erythrocytes extravasation. Overall, the complete drug-loaded targeting US responsive tools are not yet ready for clinical translation, but the use of clinical MBs co-injected with therapeutic agent and enhanced with US signal showed promising results for the drug doses reduction. In addition, the exact boundaries to avoid damaging features are not established yet except for the FDA fixed 1.9 MI and are highly dependent on MBs intrinsic properties. It has to be understood that MBs mechanical response to US insonation have not been determined completely and a collective effort has to be made to better describe the US transducer parameters (frequency, amplitude, duty cycle) and the set-up characteristics (insonation duration, distance to object, etc.). Due to the broad interest in the MBs potential, there has been multiple advancements and innovations both in designing the right MBs for the right applications, and in adapting the MB rationale to new US contrast agents in order to overcome their limitations. This was described in the last part, including among others the use of nanoscale bubbles and droplets, as well *as in situ* generation of echogenic signals with nanoparticle approaches and new MBs' combined use with recent technologies to breach the physical limits of the US imaging.

In perspective work, it appeared that the emergence of combined technologies could add another dimension to MBs' behavior, including for example photodynamic therapy [283,284], photoacoustic imaging [237,285] or magnetic MBs [286]. Also, the development of US responsive piezoelectric nanomaterial are an interesting new strategy to open the MBs world to cell therapy [287]. As these new therapeutic approaches require the injection of foreign body material, the priority now stands on safety. Clinical trials are widely enrolling patients to established the best parameters for US combination with MBs. These strategies are obviously not meant to replace drug treatments yet but they have the potential to improve their outcome. Since MBs, their applications, and consequent innovations are thriving in multiple fields (oncology, cardiovascular diseases, inflammation), the convergence of expertise and standardization of certain practices are paramount to ensure a quick development and future translation to the clinic.

Authors contribution

Louise FOURNIER: conceptualization, writing and figures development. Thibault DE LA TAILLE: writing, editing and figures development. Cédric CHAUVIERRE: writing, editing, reviewing, supervision and funding acquisition.

Declaration of competing interest

The authors declare that they have no known competing financial interests or personal relationships that could have appeared to influence the work reported in this paper.

Data availability

No data was used for the research described in the article.

Acknowledgment

Authors thank INSERM, Université Paris Cité, Université Sorbonne Paris Nord and the ANR "FightClot" ANR-20-CE18-0005-01 for the financial support.

References

[1] W. Najahi-Missaoui, R.D. Arnold, B.S. Cummings, Safe nanoparticles: are we there yet? Int. J. Mol. Sci. 22 (1) (2021) 1–22, https://doi.org/10.3390/ijms22010385.
[2] R. Gramiak and M. P. Shah, "Echocardiography of the Aortic." .
[3] J. Steinman, M.M. Koletar, B. Stefanovic, J.G. Sled, 3D morphological analysis of the mouse cerebral vasculature: comparison of in vivo and ex vivo methods, PLoS One 12 (10) (2017) 1–17, https://doi.org/10.1371/journal.pone.0186676.
[4] M. Diez-Silva, M. Dao, J. Han, C.T. Lim, S. Suresh, Shape and biomechanics characteristics of human red blood cells in health and disease, MRS Bull. 35 (5) (2010) 382–388, https://doi.org/10.1557/mrs2010.571.
[5] C.I. Ezekiel, A.M. Bapolisi, R.B. Walker, R.W.M. Krause, Ultrasound-triggered release of 5-fluorouracil from soy lecithin echogenic liposomes, Pharmaceutics 13 (6) (2021) 1–14, https://doi.org/10.3390/pharmaceutics13060821.
[6] A. Upadhyay, S.V. Dalvi, Microbubble formulations: synthesis, stability, modeling and biomedical applications, Ultrasound Med. Biol. 45 (2) (2019) 301–343, https://doi.org/10.1016/j.ultrasmedbio.2018.09.022.
[7] T.D. Reusser, K.H. Song, D. Ramirez, R.K.P. Benninger, V. Papadopoulou, M. A. Borden, Phospholipid oxygen microbubbles for image-guided therapy, Nanotheranostics 4 (2) (2020) 83–90, https://doi.org/10.7150/ntno.43808.
[8] D. Liu, et al., Sinapultide-loaded lipid microbubbles and the stabilization effect of sinapultide on the shells of lipid microbubbles, J. Mater. Chem. B 6 (9) (2018) 1335–1341, https://doi.org/10.1039/c7tb02799k.
[9] K.W. Pulsipher, D.A. Hammer, D. Lee, C.M. Sehgal, Engineering theranostic microbubbles using microfluidics for ultrasound imaging and therapy: a review, Ultrasound Med. Biol. 44 (12) (2018) 2441–2460, https://doi.org/10.1016/j.ultrasmedbio.2018.07.026.
[10] A.J. Dixon, J. Li, J.M.R. Rickel, A.L. Klibanov, Z. Zuo, J.A. Hossack, Efficacy of sonothrombolysis using microbubbles produced by a catheter-based microfluidic device in a rat model of ischemic stroke, Ann. Biomed. Eng. (2019), https://doi.org/10.1007/s10439-019-02209-0.
[11] D. Carugo, R.J. Browning, I. Iranmanesh, W. Messaoudi, P. Rademeyer, E. Stride, Scaleable production of microbubbles using an ultrasound-modulated microfluidic device, J. Acoust. Soc. Am. 150 (2) (2021) 1577–1589, https://doi.org/10.1121/10.0005911.
[12] B. Li, et al., Functionalized polymer microbubbles as new molecular ultrasound contrast agent to target P-selectin in thrombus, Biomaterials 194 (2019) (2019) 139–150, https://doi.org/10.1016/j.biomaterials.2018.12.023.
[13] A.H. Liao, H.C. Ho, Y.C. Lin, H.K. Chen, C.H. Wang, Effects of microbubble size on ultrasound-induced transdermal delivery of high-molecular-weight drugs, PLoS One 10 (9) (2015) 1–14, https://doi.org/10.1371/journal.pone.0138500.
[14] E. Stride, et al., Microbubble agents: new directions, Ultrasound Med. Biol. (2020), https://doi.org/10.1016/j.ultrasmedbio.2020.01.027.
[15] U. Farook, E. Stride, M.J. Edirisinghe, Preparation of suspensions of phospholipid-coated microbubbles by coaxial electrohydrodynamic atomization, J. R. Soc. Interface 6 (32) (2009) 271–277, https://doi.org/10.1098/rsif.2008.0225.
[16] S.A. Reisner, et al., Myocardial perfusion imaging by contrast echocardiography with use of intracoronary sonicated albumin in humans, J. Am. Coll. Cardiol. 14 (3) (1989) 660–665, https://doi.org/10.1016/0735-1097(89)90107-1.
[17] S.L. Lin, et al., Left ventricular opacification after peripheral venous injection of a modified albumin solution, Int. J. Card. Imag. 8 (1) (1992) 53–61, https://doi.org/10.1007/BF01137566.
[18] S. Chen, Z. Wang, Y.T. Zhou, P.A. Grayburn, Optimization of the size distribution and myocardial contrast effect of perfluorocarbon-filled albumin microbubbles by lyophilization under continuous negative pressure, J. Am. Soc. Echocardiogr. 13 (8) (2000) 748–753, https://doi.org/10.1067/mje.2000.104644.
[19] A.L. Klibanov, Ultrasound contrast: gas microbubbles in the vasculature, Invest. Radiol. 56 (1) (2021) 50–61, https://doi.org/10.1097/RLI.0000000000000733.
[20] K. Ferrara, R. Pollard, M. Borden, Ultrasound microbubble contrast agents: fundamentals and application to gene and drug delivery, Annu. Rev. Biomed. Eng. 9 (2007) 415–447, https://doi.org/10.1146/annurev.bioeng.8.061505.095852.
[21] P. van Hoogevest, A. Wendel, The use of natural and synthetic phospholipids as pharmaceutical excipients, Eur. J. Lipid Sci. Technol. 116 (9) (2014) 1088–1107, https://doi.org/10.1002/ejlt.201400219.
[22] S. Al-Jawadi, S.S. Thakur, Ultrasound-responsive lipid microbubbles for drug delivery: a review of preparation techniques to optimise formulation size, stability and drug loading, Int. J. Pharm. 585 (2020), 119559, https://doi.org/10.1016/j.ijpharm.2020.119559.
[23] J. Jägers, A. Wrobeln, K.B. Ferenz, Perfluorocarbon-based oxygen carriers: from physics to physiology, Pflugers Arch. Eur. J. Physiol. 473 (2) (2021) 139–150, https://doi.org/10.1007/s00424-020-02482-2.
[24] T.J. Wooster, M. Golding, P. Sanguansri, Impact of oil type on nanoemulsion formation and ostwald ripening stability, Langmuir 24 (22) (2008) 12758–12765, https://doi.org/10.1021/la801685v.
[25] Y. Iida, et al., Bubble population phenomena in sonochemical reactor: II. Estimation of bubble size distribution and its number density by simple coalescence model calculation, Ultrason. Sonochem. 17 (2) (2010) 480–486, https://doi.org/10.1016/j.ultsonch.2009.08.017.
[26] T. Segers, A. Lassus, P. Bussat, E. Gaud, P. Frinking, Improved coalescence stability of monodisperse phospholipid-coated microbubbles formed by flow-focusing at elevated temperatures, Lab Chip 19 (1) (2019) 158–167, https://doi.org/10.1039/c8lc00886h.
[27] S. Sridhar, A. Patel, S.V. Dalvi, Estimation of storage stability of aqueous microbubble suspensions, Colloids Surfaces A Physicochem. Eng. Asp. 489 (Jan. 2016) 182–190, https://doi.org/10.1016/J.COLSURFA.2015.10.044.
[28] R.H. Abou-Saleh, et al., Molecular effects of glycerol on lipid monolayers at the gas-liquid interface: impact on microbubble physical and mechanical properties, Langmuir 35 (31) (2019) 10097–10105, https://doi.org/10.1021/acs.langmuir.8b04130.

[29] A.J. Singer, J.V. Quinn, J.E. Hollander, The cyanoacrylate topical skin adhesives, Am. J. Emerg. Med. 26 (4) (2008) 490–496, https://doi.org/10.1016/j.ajem.2007.05.015.

[30] D. García Cerdá, A.M. Ballester, A. Aliena-Valero, A. Carabén-Redaño, J.M. Lloris, Use of cyanoacrylate adhesives in general surgery, Surg. Today 45 (8) (2015) 939–956, https://doi.org/10.1007/s00595-014-1056-4.

[31] H.S. Cho, Y. Kim, J. Lee, K.S. Yi, C.H. Choi, Use of N-butyl cyanoacrylate in the successful transcatheter arterial embolization of an arteriovenous fistula caused by blunt pelvic fracture: a case report and review of literature, Medicine (Baltim.) 100 (1) (2021), e24215, https://doi.org/10.1097/MD.0000000000024215.

[32] S.R. Sirsi, M.A. Borden, Microbubble compositions, properties and biomedical applications, Bubble Sci. Eng. Technol. 1 (1–2) (2009) 3–17, https://doi.org/10.1179/175889709X446507.

[33] M. Liu, et al., Drug Loading in Poly (Butyl Cyanoacrylate) -based Polymeric Microbubbles, 2020, https://doi.org/10.1021/acs.molpharmaceut.0c00242.

[34] P. Koczera, L. Appold, Y. Shi, M. Liu, A. Dasgupta, PBCA-Based Polymeric Microbubbles for Molecular Imaging and Drug Delivery, 2017, pp. 128–135, https://doi.org/10.1016/j.jconrel.2017.03.006.PBCA-based.

[35] O. Chevallier, et al., Efficacy, safety and outcomes of transcatheter arterial embolization with N-butyl cyanoacrylate glue for non-variceal gastrointestinal bleeding: a systematic review and meta-analysis, Diagn. Interv. Imaging 102 (7–8) (2021) 479–487, https://doi.org/10.1016/j.diii.2021.03.004.

[36] N.J. Butcher, G.M. Mortimer, R.F. Minchin, Drug delivery: unravelling the stealth effect, Nat. Nanotechnol. 11 (4) (2016) 310–311, https://doi.org/10.1038/nnano.2016.6.

[37] S.M. Fix, G.A. Nyankima, M.D. McSweeney, J.K. Tsuruta, S.K. Lai, P.A. Dayton, Accelerated clearance of ultrasound contrast agents containing polyethylene glycol is associated with the generation of anti- polyethylene glycol antibodies, Ultrasound Med. Biol. 176 (1) (2016) 139–148, https://doi.org/10.1016/j.ultrasmedbio.2018.02.006 (Accelerated).

[38] J. Yang, et al., Microbubble functionalization with platelet membrane enables targeting and early detection of sepsis-induced acute kidney injury, Adv. Healthc. Mater. 10 (23) (2021) 1–14, https://doi.org/10.1002/adhm.202101628.

[39] H. Wang, et al., Platelet-membrane-biomimetic nanoparticles for targeted antitumor drug delivery, J. Nanobiotechnol. 17 (1) (2019) 1–16, https://doi.org/10.1186/s12951-019-0494-y.

[40] Z. Fang, J. Fang, C. Gao, R. Gao, P. Lin, W. Yu, Recent trends in platelet membrane-cloaked nanoparticles for application of inflammatory diseases, Drug Deliv. 29 (1) (2022) 2805–2814, https://doi.org/10.1080/10717544.2022.2117434.

[41] A. Zenych, L. Fournier, C. Chauvierre, Nanomedicine progress in thrombolytic therapy, Biomaterials 258 (January, 2020), https://doi.org/10.1016/j.biomaterials.2020.120297.

[42] J.S.M. Yeh, et al., A targeting microbubble for ultrasound molecular imaging, PLoS One 10 (7) (2015) 1–23, https://doi.org/10.1371/journal.pone.0129681.

[43] J.M. Warram, A.G. Sorace, R. Saini, H.R. Umphrey, K.R. Zinn, K. Hoyt, A triple-targeted ultrasound contrast agent provides improved localization to tumor vasculature, J. Ultrasound Med. 30 (7) (2011) 921–931, https://doi.org/10.7863/jum.2011.30.7.921.

[44] B. Wu, et al., Preparation of novel targeting nanobubbles conjugated with small interfering RNA for concurrent molecular imaging and gene therapy in vivo, Faseb. J. (2019), https://doi.org/10.1096/fj.201900716RR fj201900716RR.

[45] K. Yumura, et al., Mutations for decreasing the immunogenicity and maintaining the function of core streptavidin, Protein Sci. 22 (2) (2013) 213–221, https://doi.org/10.1002/pro.2203.

[46] F. Petronzelli, et al., Therapeutic use of avidin is not hampered by antiavidin antibodies in humans, Cancer Biother. Radiopharm. 25 (5) (2010) 563–570, https://doi.org/10.1089/cbr.2010.0797.

[47] S. Fokong, et al., Image-guided, targeted and triggered drug delivery to tumors using polymer-based microbubbles, J. Contr. Release 163 (1) (2012) 75–81, https://doi.org/10.1016/j.jconrel.2012.05.007.

[48] K. Renault, J.W. Fredy, P.Y. Renard, C. Sabot, Covalent modification of biomolecules through maleimide-based labeling strategies, Bioconjugate Chem. 29 (8) (2018) 2497–2513, https://doi.org/10.1021/acs.bioconjchem.8b00252.

[49] M. Lahnsteiner, A. Kastner, J. Mayr, A. Roller, B.K. Keppler, C.R. Kowol, Improving the stability of maleimide–thiol conjugation for drug targeting, Chem. Eur J. 26 (68) (2020) 15867–15870, https://doi.org/10.1002/chem.202003951.

[50] N.J. de Mol, M.J.E. Fischer, Amine coupling through EDC/NHS: a practical approach, Life Sci. (2010) 255, https://doi.org/10.1007/978-1-60761-670-2.

[51] Y. Zhang, J.L. Xu, Z.H. Yuan, W. Qi, Y.Y. Liu, M.C. He, Artificial intelligence techniques to optimize the EDC/NHS-mediated immobilization of cellulase on Eudragit L-100, Int. J. Mol. Sci. 13 (7) (2012) 7952–7962, https://doi.org/10.3390/ijms13077952.

[52] X. Liu, et al., Fast functionalization of ultrasound microbubbles using strain promoted click chemistry, Biomater. Sci. 6 (3) (2018) 623–632, https://doi.org/10.1039/c8bm00004b.

[53] S. Manta, et al., Characterization of positively charged lipid shell microbubbles with tunable resistive pulse sensing (TRPS) method: a technical note, Ultrasound Med. Biol. 42 (2) (2016) 624–630, https://doi.org/10.1016/j.ultrasmedbio.2015.10.010.

[54] C.M. Panje, et al., Ultrasound-mediated gene delivery with cationic versus neutral microbubbles: effect of DNA and microbubble dose on in Vivo transfection efficiency, Theranostics 2 (11) (2012) 1078–1091, https://doi.org/10.7150/thno.4240.

[55] S.R. Sirsi, C. Fung, S. Garg, M.Y. Tianning, P.A. Mountford, M.A. Borden, Lung surfactant microbubbles increase lipophilic drug payload for ultrasound-targeted delivery, Theranostics 3 (6) (2013) 409–419, https://doi.org/10.7150/thno.5616.

[56] E. Stride, The influence of surface adsorption on microbubble dynamics, Philos. Trans. R. Soc. A Math. Phys. Eng. Sci. 366 (1873) (2008) 2103–2115, https://doi.org/10.1098/rsta.2008.0001.

[57] A. Agarwal, W.J. Ng, Y. Liu, Principle and applications of microbubble and nanobubble technology for water treatment, Chemosphere 84 (9) (2011) 1175–1180, https://doi.org/10.1016/j.chemosphere.2011.05.054.

[58] D. Omata, et al., Effects of encapsulated gas on stability of lipid-based microbubbles and ultrasound-triggered drug delivery, 311–312, J. Contr. Release (2019) 65–73, https://doi.org/10.1016/j.jconrel.2019.08.023. August.

[59] R. Battino, The Ostwald coefficient of gas solubility, Fluid Phase Equil. 15 (3) (1984) 231–240, https://doi.org/10.1016/0378-3812(84)87009-0.

[60] A. Kabalnov, D. Klein, T. Pelura, E. Schutt, J. Weers, Dissolution of multicomponent microbubbles in the bloodstream: 1. Theory, Ultrasound Med. Biol. 24 (5) (1998) 739–749, https://doi.org/10.1016/S0301-5629(98)00034-9.

[61] A. Kabalnov, et al., Dissolution of multicomponent microbubbles in the bloodstream: 2. Experiment, Ultrasound Med. Biol. 24 (5) (1998) 751–760, https://doi.org/10.1016/S0301-5629(98)00033-7.

[62] N. De Jong, A. Bouakaz, P. Frinking, Basic acoustic properties of microbubbles, Echocardiography 19 (3) (2002) 229–240, https://doi.org/10.1046/j.1540-8175.2002.00229.x.

[63] D.B. Khismatullin, Resonance frequency of microbubbles: effect of viscosity, J. Acoust. Soc. Am. 116 (3) (2004) 1463–1473, https://doi.org/10.1121/1.1778835.

[64] T. Segers, M. Versluis, Acoustic bubble sorting for ultrasound contrast agent enrichment, Lab Chip 14 (10) (2014) 1705–1714, https://doi.org/10.1039/c3lc51296g.

[65] T. Segers, N. de Jong, M. Versluis, Uniform scattering and attenuation of acoustically sorted ultrasound contrast agents: modeling and experiments, J. Acoust. Soc. Am. 140 (4) (2016) 2506–2517, https://doi.org/10.1121/1.4964270.

[66] D.I. Nikitichev, A. Barburas, K. McPherson, J.M. Mari, S.J. West, A.E. Desjardins, Construction of 3-dimensional printed ultrasound phantoms with wall-less vessels, J. Ultrasound Med. 35 (6) (2016) 1333–1339, https://doi.org/10.7863/ultra.15.06012.

[67] O. Couture, S. Bannouf, G. Montaldo, J.F. Aubry, M. Fink, M. Tanter, Ultrafast imaging of ultrasound contrast agents, Ultrasound Med. Biol. 35 (11) (2009) 1908–1916, https://doi.org/10.1016/j.ultrasmedbio.2009.05.020.

[68] R.H. Abou-Saleh, M. Swain, S.D. Evans, N.H. Thomson, Poly(ethylene glycol) lipid-shelled microbubbles: abundance, stability, and mechanical properties, Langmuir 30 (19) (2014) 5557–5563, https://doi.org/10.1021/la404804u.

[69] X. Chu, et al., Mechanical properties of sub-microbubbles with a nanoparticle-decorated polymer shell, Langmuir 35 (52) (2019) 17090–17095, https://doi.org/10.1021/acs.langmuir.9b02930.

[70] E. Glynos, V. Sboros, V. Koutsos, Polymeric thin shells: measurement of elastic properties at the nanometer scale using atomic force microscopy, Mater. Sci. Eng. B Solid-State Mater. Adv. Technol. 165 (3) (2009) 231–234, https://doi.org/10.1016/j.mseb.2009.06.016.

[71] R.H. Abou-Saleh, S.A. Peyman, K. Critchley, S.D. Evans, N.H. Thomson, Nanomechanics of lipid encapsulated microbubbles with functional coatings, Langmuir 29 (12) (2013) 4096–4103, https://doi.org/10.1021/la304093t.

[72] D.D. Monie, E.P. DeLoughery, Pathogenesis of thrombosis: cellular and pharmacogenetic contributions, Cardiovasc. Diagn. Ther. 7 (Suppl 3) (2017) S291–S298, https://doi.org/10.21037/cdt.2017.09.11.

[73] W. Wiedemair, Z. Tukovic, H. Jasak, D. Poulikakos, V. Kurtcuoglu, The breakup of intravascular microbubbles and its impact on the endothelium, Biomech. Model. Mechanobiol. 16 (2) (2017) 611–624, https://doi.org/10.1007/s10237-016-0840-z.

[74] J.H. Wible, J.K. Wojdyla, G.L. Bales, W.N. McMullen, E.A. Geiser, D.D. Buss, Inhaled gases affect the ultrasound contrast produced by Albunex in anesthetized dogs, J. Am. Soc. Echocardiogr. 9 (4) (1996) 442–451, https://doi.org/10.1016/S0894-7317(96)90115-7.

[75] R.B. Birge, et al., Phosphatidylserine is a global immunosuppressive signal in efferocytosis, infectious disease, and cancer, Cell Death Differ. 23 (6) (2016) 962–978, https://doi.org/10.1038/cdd.2016.11.

[76] R. Watanabe, M. Matsumura, T. Munemasa, M. Fujimaki, M. Suematsu, Mechanism of hepatic parenchyma-specific contrast of microbubble-based contrast agent for ultrasonography: microscopic studies in rat liver, Invest. Radiol. 42 (9) (2007) 643–651, https://doi.org/10.1097/RLI.0b013e31805f2682.

[77] K.T. Warzecha, et al., Targeting and modulation of liver myeloid immune cells by hard-shell microbubbles, Adv. Biosyst. 2 (5) (2018) 1–11, https://doi.org/10.1002/adbi.201800002.

[78] Y.C. Park, et al., Microvessels-on-a-chip to assess targeted ultrasound-assisted drug delivery, ACS Appl. Mater. Interfaces 8 (46) (2016) 31541–31549, https://doi.org/10.1021/acsami.6b09071.

[79] A. Presset, et al., Endothelial cells, first target of drug delivery using microbubble-assisted ultrasound, Ultrasound Med. Biol. 46 (7) (2020) 1565–1583, https://doi.org/10.1016/j.ultrasmedbio.2020.03.013.

[80] N. Malik, et al., Air embolism: diagnosis and management, Future Cardiol. 13 (4) (2017) 365–378, https://doi.org/10.2217/fca-2017-0015.

[81] K. Seitz, D. Strobel, A. Milestone, Approval of CEUS for diagnostic liver imaging in adults and children in the USA, Ultraschall der Med. 37 (3) (2016) 229–232, https://doi.org/10.1055/s-0042-107411.

[82] J.D. Berry, P.S. Sidhu, Microbubble ultrasound contrast agents, in: Clinical Doppler Ultrasound, 2006, pp. 337–355.
[83] J.M. Hyvelin, et al., Use of ultrasound contrast agent microbubbles in preclinical research : recommendations for small animal imaging, Invest. Radiol. 48 (8) (2013) 570–583, https://doi.org/10.1097/RLI.0b013e318289f854.
[84] S. Pochon, et al., BR55: a lipopeptide-based VEGFR2-targeted ultrasound contrast agent for molecular imaging of angiogenesis, Invest. Radiol. 45 (2) (2010) 89–95, https://doi.org/10.1097/RLI.0b013e3181c5927c.
[85] M. Smeenge, et al., First-in-human ultrasound molecular imaging with a VEGFR2-specific ultrasound molecular contrast agent (BR55) in prostate cancer a safety and feasibility pilot study, Invest. Radiol. 52 (7) (2017) 419–427, https://doi.org/10.1097/RLI.0000000000000362.
[86] J.K. Willmann, et al., Ultrasound molecular imaging with BR55 in patients with breast & ovarian lesions: first-in-human results, J. Clin. Oncol. 35 (19) (2017) 2133–2140, https://doi.org/10.1200/JCO.2016.70.8594.
[87] S. Wang, J.A. Hossack, A.L. Klibanov, Targeting of microbubbles: contrast agents for ultrasound molecular imaging, J. Drug Target. 26 (5–6) (2018) 420–434, https://doi.org/10.1080/1061186X.2017.1419362.
[88] O. Schober, F. Kiessling, J. Debus, Debus, J. Debus, Molecular Imaging in Oncology 216 (2020).
[89] A. Rix, A. Curaj, E. Liehn, F. Kiessling, Ultrasound microbubbles for diagnosis and treatment of cardiovascular diseases, Semin. Thromb. Hemost. (2019), https://doi.org/10.1055/s-0039-1688492.
[90] V.S. Lucas, R.S. Burk, S. Creehan, M.J. Grap, Utility of high-frequency ultrasound: moving beyond the surface to detect changes in skin integrity, Plast. Surg. Nurs. 23 (1) (2014) 1–7, https://doi.org/10.1097/PSN.0000000000000031.Utility.
[91] Y. Yong, et al., Diagnostic accuracy and cost-effectiveness of contrast echocardiography on evaluation of cardiac function in technically very difficult patients in the intensive care unit, Am. J. Cardiol. 89 (6) (2002) 711–718, https://doi.org/10.1016/S0002-9149(01)02344-X.
[92] A.J. Sojahrood, et al., Nonlinear dynamics of acoustic bubbles excited by their pressure-dependent subharmonic resonance frequency: influence of the pressure amplitude, frequency, encapsulation and multiple bubble interactions on oversaturation and enhancement of the subharmonic 103 (1) (2021).
[93] H. Haghi, M.C. Kolios, The role of primary and secondary delays in the effective resonance frequency of acoustically interacting microbubbles, Ultrason. Sonochem. 86 (2022), 106033, https://doi.org/10.1016/j.ultsonch.2022.106033. April.
[94] G. Chabouh, B. Dollet, C. Quilliet, G. Coupier, Spherical oscillations of encapsulated microbubbles: effect of shell compressibility and anisotropy, J. Acoust. Soc. Am. 149 (2) (2021) 1240–1257, https://doi.org/10.1121/10.0003500.
[95] P. Martinez, N. Bottenus, M. Borden, Cavitation characterization of size-isolated microbubbles in a vessel phantom using focused ultrasound, Pharmaceutics 14 (9) (2022), https://doi.org/10.3390/pharmaceutics14091925.
[96] K. Kooiman, et al., Ultrasound-responsive cavitation nuclei for therapy and drug delivery, Ultrasound Med. Biol. (2020), https://doi.org/10.1016/j.ultrasmedbio.2020.01.002.
[97] R.G. Holt, R.A. Roy, Measurements of bubble-enhanced heating from focused, MHz-frequency ultrasound in a tissue-mimicking material, Ultrasound Med. Biol. 27 (10) (2001) 1399–1412, https://doi.org/10.1016/S0301-5629(01)00438-0.
[98] S. Wang, et al., Accelerating thrombolysis using a precision and clot-penetrating drug delivery strategy by nanoparticle-shelled microbubbles, Sci. Adv. 6 (31) (2020), https://doi.org/10.1126/sciadv.aaz8204.
[99] H. Yu, S. Chen, A model to calculate microstreaming-shear stress generated by oscillating microbubbles on the cell membrane in sonoporation, Bio Med. Mater. Eng. 24 (1) (2014) 861–868, https://doi.org/10.3233/BME-130878.
[100] Y.H. Chuang, P.W. Cheng, P.C. Li, Combining radiation force with cavitation for enhanced sonothrombolysis, IEEE Trans. Ultrason. Ferroelectrics Freq. Control 60 (1) (2013) 97–104, https://doi.org/10.1109/TUFFC.2013.2541.
[101] P.A. Dayton, K.E. Morgan, A.L. Klibanov, G. Brandenburger, K.R. Nightingale, K. W. Ferrara, A preliminary evaluation of the effects of primary and secondary radiation forces on acoustic contrast agents, IEEE Trans. Ultrason. Ferroelectrics Freq. Control 44 (6) (1997) 1264–1277, https://doi.org/10.1109/58.656630.
[102] A.R. Naji Meidani, M. Hasan, Mathematical and physical modelling of bubble growth due to ultrasound, Appl. Math. Model. 28 (4) (2004) 333–351, https://doi.org/10.1016/j.apm.2003.10.001.
[103] A. Goyal, et al., Inertial cavitation ultrasound with microbubbles improves reperfusion efficacy when combined with tissue plasminogen activator in an in vitro model of microvascular obstruction, Ultrasound Med. Biol. 43 (7) (2017) 1391–1400, https://doi.org/10.1016/j.ultrasmedbio.2017.02.013.
[104] Y. Lin, et al., Effect of acoustic parameters on the cavitation behavior of SonoVue microbubbles induced by pulsed ultrasound, Ultrason. Sonochem. 35 (2017) 176–184, https://doi.org/10.1016/j.ultsonch.2016.09.016.
[105] N. Kudo, K. Okada, K. Yamamoto, Sonoporation by single-shot pulsed ultrasound with microbubbles adjacent to cells, Biophys. J. 96 (12) (2009) 4866–4876, https://doi.org/10.1016/j.bpj.2009.02.072.
[106] M.W. Keller, S.S. Segal, S. Kaul, B. Duling, The behavior of sonicated albumin microbubbles within the microcirculation: a basis for their use during myocardial contrast echocardiography, Circ. Res. 65 (2) (1989) 458–467, https://doi.org/10.1161/01.RES.65.2.458.
[107] S.V. Bachawal, K.C. Jensen, K.E. Wilson, L. Tian, A.M. Lutz, J.K. Willmann, Breast cancer detection by B7-H3 targeted ultrasound molecular imaging, Cancer Res. 95 (6) (2015) 1336–1356, https://doi.org/10.1158/0008-5472.CAN-14-3361.Breast.
[108] R. Bam, et al., Efficacy of affibody-based ultrasound molecular imaging of vascular B7-H3 for breast cancer detection, Clin. Cancer Res. 26 (9) (2020) 2140–2150, https://doi.org/10.1158/1078-0432.CCR-19-1655.Efficacy.
[109] L. Abou-Elkacem, et al., Thy1-targeted microbubbles for ultrasound molecular imaging of pancreatic ductal adenocarcinoma, Clin. Cancer Res. 24 (7) (2018) 1574–1585, https://doi.org/10.1158/1078-0432.CCR-17-2057.
[110] H. Zhang, et al., In vitro characterization and in vivo ultrasound molecular imaging of nucleolin-targeted microbubbles, Biomaterials 118 (2017) 63–73, https://doi.org/10.1016/j.biomaterials.2016.11.026.
[111] A. Curaj, et al., Molecular ultrasound imaging of junctional adhesion molecule A depicts acute alterations in blood flow and early endothelial dysregulation, Arterioscler. Thromb. Vasc. Biol. 38 (1) (2018) 40–48, https://doi.org/10.1161/ATVBAHA.117.309503.
[112] M. Punjabi, et al., Ultrasound molecular imaging of atherosclerosis with nanobodies: translatable microbubble targeting murine and human VCAM (vascular cell adhesion molecule) 1, Arterioscler. Thromb. Vasc. Biol. 39 (12) (2019) 2520–2530, https://doi.org/10.1161/ATVBAHA.119.313088.
[113] Y.J. Zhang, et al., Ultrasound-guided Imaging of Junctional Adhesion Molecule-A-Targeted Microbubbles Identifies Vulnerable Plaque in Rabbits, vol. 94, Elsevier Ltd, 2016.
[114] A. Luong, et al., Development of a translatable ultrasound molecular imaging agent for inflammation, Ultrasound Med. Biol. 46 (3) (2020) 690–702, https://doi.org/10.1016/j.ultrasmedbio.2019.11.009.
[115] A. Ingels, et al., Ultrasound molecular imaging of renal cell carcinoma: VEGFR targeted therapy monitored with VEGFR1 and FSHR targeted microbubbles, Sci. Rep. 10 (1) (2020) 1–8, https://doi.org/10.1038/s41598-020-64433-2.
[116] F. Yan, et al., Ultrasound molecular imaging of atherosclerosis for early diagnosis and therapeutic evaluation through leucocyte-like multiple targeted microbubbles, Theranostics 8 (7) (2018) 1879–1891, https://doi.org/10.7150/thno.22070.
[117] L. Abou-Elkacem, et al., Ultrasound molecular imaging of the breast cancer neovasculature using engineered fibronectin scaffold ligands: a novel class of targeted contrast ultrasound agent, Theranostics 6 (11) (2016) 1740–1752, https://doi.org/10.7150/thno.15169.
[118] J. Zhou, et al., Vegfr2-targeted three-dimensional ultrasound imaging can predict responses to antiangiogenic therapy in preclinical models of colon cancer, Cancer Res. 76 (14) (2016) 4081–4089, https://doi.org/10.1158/0008-5472.CAN-15-3271.
[119] I. Spivak, et al., Low-dose molecular ultrasound imaging with E-selectin-targeted PBCA microbubbles, Mol. Imag. Biol. 18 (2) (2016) 180–190, https://doi.org/10.1007/s11307-015-0894-9.
[120] H. Zhang, et al., Ultrasound molecular imaging of tumor angiogenesis with a neuropilin-1-targeted microbubble, Biomaterials 176 (12) (2015) 139–148, https://doi.org/10.1016/j.biomaterials.2015.03.043.Ultrasound.
[121] X. Wang, et al., Thrombus-targeted theranostic microbubbles: a new technology towards concurrent rapid ultrasound diagnosis and bleeding-free fibrinolytic treatment of thrombosis, Theranostics 6 (5) (2016) 726–738, https://doi.org/10.7150/thno.14514.
[122] J. Lux, et al., Thrombin-activatable microbubbles as potential ultrasound contrast agents for the detection of acute thrombosis, ACS Appl. Mater. Interfaces 9 (43) (2017) 37587–37596, https://doi.org/10.1021/acsami.7b10592.
[123] A. Curaj, et al., Noninvasive molecular ultrasound monitoring of vessel healing after intravascular surgical procedures in a preclinical setup, Arterioscler. Thromb. Vasc. Biol. 35 (6) (2015) 1366–1373, https://doi.org/10.1161/ATVBAHA.114.304857.
[124] A. Rix, et al., Molecular ultrasound imaging of αvβ3-integrin expression in carotid arteries of pigs after vessel injury, Invest. Radiol. 51 (12) (2016) 767–775, https://doi.org/10.1097/RLI.0000000000000282.
[125] F. Moccetti, et al., Ultrasound molecular imaging of atherosclerosis using small-peptide targeting ligands against endothelial markers of inflammation and oxidative stress, Ultrasound Med. Biol. 44 (6) (2018) 1155–1163, https://doi.org/10.1016/j.ultrasmedbio.2018.01.001.
[126] F. Moccetti, et al., Myocardial infarction produces sustained pro-inflammatory endothelial activation in remote arteries, J. Am. Coll. Cardiol. 176 (1) (2018) 139–148, https://doi.org/10.1016/j.jacc.2018.06.044.Myocardial.
[127] S. Wang, S. Unnikrishnan, E.B. Herbst, A.L. Klibanov, F.W. Mauldin, J.A. Hossack, Ultrasound molecular imaging of inflammation in mouse abdominal aorta, Invest. Radiol. 176 (1) (2017) 139–148, https://doi.org/10.1097/RLI.0000000000000373.Ultrasound.
[128] C. Qiu, et al., VEGFR2-targeted ultrasound molecular imaging of angiogenesis to evaluate liver allograft fibrosis, Biomater. Sci. 9 (17) (2021) 5802–5811, https://doi.org/10.1039/d1bm00100k.
[129] H. Wang, et al., US molecular imaging of acute ileitis: anti-inflammatory treatment response monitored with targeted microbubbles in a preclinical model, Radiology 289 (1) (2018) 90–100, https://doi.org/10.1148/radiol.2018172600.
[130] G. Köse, M. Darguzyte, F. Kiessling, Molecular ultrasound imaging, Nanomaterials 10 (10) (2020) 1–28, https://doi.org/10.3390/nano10101935.
[131] X.M. Lingling, et al., Targeted delivery of therapeutic gas by microbubbles, Adv. Ultrasound Diagnosis Ther 5 (3) (2021) 173, https://doi.org/10.37015/audt.2021.200059.
[132] P. Vaupel, M. Höckel, A. Mayer, Detection and characterization of tumor hypoxia using pO2 histography, Antioxidants Redox Signal. 9 (8) (2007) 1221–1235, https://doi.org/10.1089/ars.2007.1628.
[133] H.E. Barker, J.T.E. Paget, A.A. Khan, K.J. Harrington, Barker HE_tumour microenvironment after IRR_cancer reviews 2015.pdf, Nat. Publ. Gr. 15 (7) (2016) 409–425, https://doi.org/10.1038/nrc3958.The.

[134] S.M. Fix, et al., Oxygen microbubbles improve radiotherapy tumor control in a rat fibrosarcoma model – a preliminary study, PLoS One 13 (4) (2018) 1–18, https://doi.org/10.1371/journal.pone.0195667.
[135] J.R. Eisenbrey, et al., Sensitization of hypoxic tumors to radiation therapy using ultrasound-sensitive oxygen microbubbles, Int. J. Radiat. Oncol. Biol. Phys. 101 (1) (2018) 88–96, https://doi.org/10.1016/j.ijrobp.2018.01.042.
[136] C. McEwan, et al., Oxygen carrying microbubbles for enhanced sonodynamic therapy of hypoxic tumours, J. Contr. Release 203 (2015) 51–56, https://doi.org/10.1016/j.jconrel.2015.02.004.
[137] S. Peng, et al., A robust oxygen microbubble radiosensitizer for iodine-125 Brachytherapy, Adv. Sci. 8 (7) (2021) 1–10, https://doi.org/10.1002/advs.202002567.
[138] J. Esmaeili, F.S. Rezaei, F.M. Beram, A. Barati, Integration of microbubbles with biomaterials in tissue engineering for pharmaceutical purposes, Heliyon 6 (6) (2020), e04189, https://doi.org/10.1016/j.heliyon.2020.e04189.
[139] J.P. Cooke, D.W. Losordo, Nitric oxide and angiogenesis, Circulation 105 (18) (2002) 2133–2135, https://doi.org/10.1161/01.CIR.0000014928.45119.73.
[140] R. Zheng, F. Li, F. Li, A. Gong, Targeting tumor vascularization: promising strategies for vascular normalization, J. Cancer Res. Clin. Oncol. 147 (9) (2021) 2489–2505, https://doi.org/10.1007/s00432-021-03701-8.
[141] S.L. Huang, et al., Improving ultrasound reflectivity and stability of echogenic liposomal dispersions for use as targeted ultrasound contrast agents, J. Pharmacol. Sci. 90 (12) (2001) 1917–1926, https://doi.org/10.1002/jps.1142.
[142] C. Wang, et al., Intravenous release of NO from lipidic microbubbles accelerates deep vein thrombosis resolution in a rat model, Thromb. Res. 131 (1) (2013) e31–e38, https://doi.org/10.1016/j.thromres.2012.11.002.
[143] L. Chen, S.F. Zhou, L. Su, J. Song, Gas-mediated cancer bioimaging and therapy, ACS Nano 13 (10) (2019) 10887–10917, https://doi.org/10.1021/acsnano.9b04954.
[144] B. Li, J. Xiong, H.X. Liu, D. Li, G. Chen, Devil or angel: two roles of carbon monoxide in stroke, Med. Gas Res. 12 (4) (2022) 125–130, https://doi.org/10.4103/2045-9912.337993.
[145] E. Zeynalov, S. Doré, Low doses of carbon monoxide protect against experimental focal brain ischemia, Neurotox. Res. 15 (2) (2009) 133–137, https://doi.org/10.1007/s12640-009-9014-4.
[146] A.M.K. Choi, et al., Carbon monoxide has anti-inflammatory effects involving the mitogen-activated protein kinase pathway, Nat. Med. 6 (4) (2000) 422–428.
[147] V. Pathak, et al., Theranostic trigger-responsive carbon monoxide-generating microbubbles, Small 18 (18) (2022), https://doi.org/10.1002/smll.202200924.
[148] P. Cabrales, B.Y.S. Vázquez, A.C. Negrete, M. Intaglietta, Perfluorocarbons as gas transporters for O 2 , NO, CO and volatile anesthetics, Transfus. Altern. Transfus. Med. 9 (4) (2007) 294–303, https://doi.org/10.1111/j.1778-428x.2007.00085.x.
[149] T.T. Chen, P.C. Samson, M.D. Sorensen, M.R. Bailey, Burst wave lithotripsy and acoustic manipulation of stones, Curr. Opin. Urol. 30 (2) (2020) 149–156, https://doi.org/10.1097/MOU.0000000000000727.
[150] Y. Xing, et al., Comparison of broad vs narrow focal width lithotripter fields, J. Endourol. 31 (5) (2017) 502–509, https://doi.org/10.1089/end.2016.0560.
[151] J.C. Dai, et al., Quantitative assessment of effectiveness of ultrasonic propulsion of kidney stones, J. Endourol. 33 (10) (2019) 850–857, https://doi.org/10.1089/end.2019.0340.
[152] Z. Xu, T.L. Hall, E. Vlaisavljevich, F.T. Lee, Histotripsy: the first noninvasive, non-ionizing, non-thermal ablation technique based on ultrasound, Int. J. Hyperther. 38 (1) (2021) 561–575, https://doi.org/10.1080/02656736.2021.1905189.
[153] S.T. Araujo, D.H. Moreno, D.G. Cacione, Percutaneous thrombectomy or ultrasound-accelerated thrombolysis for initial management of acute limb ischaemia, Cochrane Database Syst. Rev. 2022 (1) (2022), https://doi.org/10.1002/14651858.CD013486.pub2.
[154] X. Li, et al., Efficacy and safety of sonothrombolysis in patients with acute ischemic stroke: a systematic review and meta-analysis, J. Neurol. Sci. 416 (2020), 116998, https://doi.org/10.1016/j.jns.2020.116998. May.
[155] H. Kartal, D. Erer, G.L. Oktar, M.H. Zor, K. Akkan, M. Arslan, Ultrasound-accelerated catheter-assisted thrombolytic therapy applicatıons in deep vein thrombosis, Niger. J. Clin. Pract. 22 (3) (2019) 399–405, https://doi.org/10.4103/njcp.njcp_27_18.
[156] N. McDannold, et al., Acoustic feedback enables safe and reliable carboplatin delivery across the blood-brain barrier with a clinical focused ultrasound system and improves survival in a rat glioma model, Theranostics 9 (21) (2019) 6284–6299, https://doi.org/10.7150/thno.35892.
[157] K.B. Bader, G. Bouchoux, C.K. Holland, Sonothrombolysis 880 (2016).
[158] N. Hosseinkhah, H. Chen, T.J. Matula, P.N. Burns, K. Hynynen, Mechanisms of microbubble–vessel interactions and induced stresses: a numerical study, J. Acoust. Soc. Am. 134 (3) (2013) 1875–1885, https://doi.org/10.1121/1.4817843.
[159] C.F. Caskey, S.M. Stieger, S. Qin, P.A. Dayton, K.W. Ferrara, Direct observations of ultrasound microbubble contrast agent interaction with the microvessel wall, J. Acoust. Soc. Am. 122 (2) (2007) 1191–1200, https://doi.org/10.1121/1.2747204.
[160] P. Zhong, Y. Zhou, S. Zhu, Dynamics of bubble oscillation in constrained media and mechanisms of vessel rupture in SWL, Ultrasound Med. Biol. 27 (1) (2001) 119–134, https://doi.org/10.1016/S0301-5629(00)00322-7.
[161] T. Şen, O. Tüfekçioğlu, Y. Koza, Mechanical index, Anadolu Kardiyol. Derg. 15 (4) (2015) 334–336, https://doi.org/10.5152/akd.2015.6061.
[162] V. Wilkens, C. Koch, Improvement of hydrophone measurements on diagnostic ultrasound machines using broadband complex-valued calibration data, J. Phys. Conf. Ser. 1 (2004) 50–55, https://doi.org/10.1088/1742-6596/1/1/012.
[163] Y. Deng, M.L. Palmeri, N.C. Rouze, G.E. Trahey, C.M. Haysteas, K.R. Nightingale, Quantifying image quality improvement using elevated acoustic output in B-mode harmonic imaging, Ultrasound Med. Biol. 43 (10) (2017) 2416–2425, https://doi.org/10.1016/j.ultrasmedbio.2017.06.024 (QUANTIFYING).
[164] M. Modrzejewska, Guidelines for ultrasound examination in ophthalmology. Part iii: color Doppler ultrasonography, J. Ultrason. 19 (77) (2019) 128–136, https://doi.org/10.15557/JoU.2019.0019.
[165] J.H. Nederhoed, et al., Therapeutic use of microbubbles and ultrasound in acute peripheral arterial thrombosis: a systematic review, Ultrasound Med. Biol. 47 (10) (2021) 2821–2838, https://doi.org/10.1016/j.ultrasmedbio.2021.06.001.
[166] X. Ren, et al., Thrombolytic therapy with rt-PA and transcranial color Doppler ultrasound (TCCS) combined with microbubbles for embolic thrombus, Thromb. Res. 136 (5) (2015) 1027–1032, https://doi.org/10.1016/j.thromres.2015.08.027.
[167] S.T. Laing, et al., Thrombolytic efficacy of tissue plasminogen activator-loaded echogenic liposomes in a rabbit thrombus model, Thromb. Res. 130 (4) (Oct. 2012) 629–635, https://doi.org/10.1016/j.thromres.2011.11.010.
[168] F. Xie, J. Lof, T. Matsunaga, R. Zutshi, T.R. Porter, Diagnostic ultrasound combined with glycoprotein IIb/IIIa-targeted microbubbles improves microvascular recovery after acute coronary thrombotic occlusions, Circulation 119 (10) (2009) 1378–1385, https://doi.org/10.1161/CIRCULATIONAHA.108.825067.
[169] J. Wu, F. Xie, J. Lof, S. Sayyed, T.R. Porter, Utilization of modified diagnostic ultrasound and microbubbles to reduce myocardial infarct size, Heart 101 (18) (2015) 1468–1474, https://doi.org/10.1136/heartjnl-2015-307625.
[170] F. Xie, et al., Diagnostic ultrasound induced inertial cavitation to non-invasively restore coronary and microvascular flow in acute myocardial infarction, PLoS One 8 (7) (2013) 1–7, https://doi.org/10.1371/journal.pone.0069780.
[171] H.P. Ebben, et al., Therapeutic application of contrast-enhanced ultrasound and low-dose urokinase for thrombolysis in a porcine model of acute peripheral arterial occlusion, J. Vasc. Surg. 62 (2) (2015) 477–485, https://doi.org/10.1016/j.jvs.2014.02.057.
[172] A.J. Tomkins, et al., Platelet rich clots are resistant to lysis by thrombolytic therapy in a rat model of embolic stroke, Exp. Transl. Stroke Med. 7 (1) (2015) 1–9, https://doi.org/10.1186/s13231-014-0014-y.
[173] S.T. Laing, et al., Ultrasound-enhanced thrombolytic effect of tissue plasminogen activator-loaded echogenic liposomes in an in vivo rabbit aorta thrombus model-brief report, Arterioscler. Thromb. Vasc. Biol. 31 (6) (2011) 1357–1359, https://doi.org/10.1161/ATVBAHA.111.225938.
[174] W.S. Liu, Z.Z. Huang, X.W. Wang, J. Zhou, Effects of microbubbles on transcranial Doppler ultrasound-assisted intracranial urokinase thrombolysis, Thromb. Res. 130 (3) (2012) 547–551, https://doi.org/10.1016/j.thromres.2012.06.020.
[175] X. Hua, et al., In vivo thrombolysis with targeted microbubbles loading tissue plasminogen activator in a rabbit femoral artery thrombus model, J. Thromb. Thrombolysis 38 (1) (2014) 57–64, https://doi.org/10.1007/s11239-014-1071-8.
[176] L. Dinia, et al., Reperfusion after stroke sonothrombolysis with microbubbles may predict intracranial bleeding, Neurology 73 (10) (2009) 775–780, https://doi.org/10.1212/WNL.0b013e3181b6bb45.
[177] W. Mathias, et al., Sonothrombolysis in ST-segment elevation myocardial infarction treated with primary percutaneous coronary intervention, J. Am. Coll. Cardiol. 73 (22) (2019) 2832–2842, https://doi.org/10.1016/j.jacc.2019.03.006.
[178] T. Porter, P. Zeng, F. Xie, Advances in ultrasound therapeutics, Curr. Cardiol. Rep. 23 (10) (2021) 4–11, https://doi.org/10.1007/s11886-021-01563-7.
[179] S.H. Rezkalla, K.C. Dharmashankar, I.B. Abdalrahman, R.A. Kloner, No-reflow phenomenon following percutaneous coronary intervention for acute myocardial infarction: incidence, outcome, and effect of pharmacologic therapy, J. Intervent. Cardiol. 23 (5) (2010) 429–436, https://doi.org/10.1111/j.1540-8183.2010.00561.x.
[180] S. Snipstad, et al., Ultrasound improves the delivery and therapeutic effect of nanoparticle-stabilized microbubbles in breast cancer xenografts, Ultrasound Med. Biol. 43 (11) (2017) 2651–2669, https://doi.org/10.1016/j.ultrasmedbio.2017.06.029.
[181] S. Snipstad, et al., Sonopermeation enhances uptake and therapeutic effect of free and encapsulated Cabazitaxel, Ultrasound Med. Biol. 47 (5) (2021) 1319–1333, https://doi.org/10.1016/j.ultrasmedbio.2020.12.026.
[182] G. Fan, et al., Low-intensity focused ultrasound targeted microbubble destruction enhanced Paclitaxel sensitivity by decreasing autophagy in paclitaxel-resistant ovarian cancer, Front. Oncol. 12 (2022) 1–12, https://doi.org/10.3389/fonc.2022.823956. April.
[183] J.A. Kopechek, et al., Ultrasound targeted microbubble destruction-mediated delivery of a transcription factor decoy inhibits STAT3 signaling and tumor growth, Theranostics 5 (12) (2015) 1378–1387, https://doi.org/10.7150/thno.12822.
[184] Y. Wei, et al., Penetration of different molecule sizes upon ultrasound combined with microbubbles in a superficial tumour model, J. Drug Target. 27 (10) (2019) 1068–1075, https://doi.org/10.1080/1061186X.2019.1588279.
[185] N. Xiao, J. Liu, L. Liao, J. Sun, W. Jin, X. Shu, Ultrasound combined with microbubbles increase the delivery of doxorubicin by reducing the interstitial fluid pressure, Ultrasound Q. 35 (2) (2019) 103–109, https://doi.org/10.1097/RUQ.0000000000000381.
[186] Y. Zhou, et al., Targeted antiangiogenesis gene therapy using targeted cationic microbubbles conjugated with CD105 antibody compared with untargeted cationic and neutral microbubbles, Theranostics 5 (4) (2015) 399–417, https://doi.org/10.7150/thno.10351.
[187] Y. Jing, et al., Ultrasound-targeted microbubble destruction improved the antiangiogenic effect of Endostar in triple-negative breast carcinoma xenografts,

J. Cancer Res. Clin. Oncol. 145 (5) (2019) 1191–1200, https://doi.org/10.1007/s00432-019-02866-7.
[188] D. Hong, J. Yang, J. Guo, Y. Zhang, Z. Chen, Ultrasound-targeted microbubble destruction enhances inhibitory effect of Apatinib on angiogenesis in triple negative breast carcinoma xenografts, Anal. Cell Pathol. 2021 (2021), https://doi.org/10.1155/2021/8837950.
[189] C. Viallard, B. Larrivée, Tumor angiogenesis and vascular normalization: alternative therapeutic targets, Angiogenesis 20 (4) (2017) 409–426, https://doi.org/10.1007/s10456-017-9562-9.
[190] Y.J. Ho, et al., Normalization of tumor vasculature by oxygen microbubbles with ultrasound, Theranostics 9 (24) (2019) 7370–7383, https://doi.org/10.7150/thno.37750.
[191] J. Deprez, G. Lajoinie, Y. Engelen, S.C. De Smedt, I. Lentacker, Opening doors with ultrasound and microbubbles: beating biological barriers to promote drug delivery, Adv. Drug Deliv. Rev. 172 (2021) 9–36, https://doi.org/10.1016/j.addr.2021.02.015.
[192] M.A. O'Reilly, A. Muller, K. Hynynen, Ultrasound insertion loss of rat parietal bone appears to Be proportional to animal mass at submegahertz frequencies, Ultrasound Med. Biol. 37 (11) (2011) 1930–1937, https://doi.org/10.1016/j.ultrasmedbio.2011.08.001.
[193] D. McMahon, A. Lassus, E. Gaud, V. Jeannot, K. Hynynen, Microbubble formulation influences inflammatory response to focused ultrasound exposure in the brain, Sci. Rep. 10 (1) (2020) 1–15, https://doi.org/10.1038/s41598-020-78657-9.
[194] O. Vince, et al., Microbubbles containing lysolipid enhance ultrasound-mediated blood–brain barrier breakdown in vivo, Adv. Healthc. Mater. 10 (3) (2021) 1–11, https://doi.org/10.1002/adhm.202001343.
[195] K.T. Chen, K.C. Wei, H.L. Liu, Focused ultrasound combined with microbubbles in central nervous system applications, Pharmaceutics 13 (7) (2021) 1–22, https://doi.org/10.3390/pharmaceutics13071084.
[196] Y. Shen, et al., Ultrasound with microbubbles improves memory, ameliorates pathology and modulates hippocampal proteomic changes in a triple transgenic mouse model of alzheimer's disease, Theranostics 10 (25) (2020) 11794–11819, https://doi.org/10.7150/thno.44152.
[197] Y. Huang, R.M. Jones, L.M. Oliveira, B. Davidson, A. Bethune, P. Maralani, Putaminal Recombinant Glucocerebrosidase Delivery with Magnetic Resonance – Guided Focused Ultrasound in Parkinson ' s Disease : A Phase I Study (2022) 1–7, https://doi.org/10.1002/mds.29190.
[198] K.F. Timbie, B.P. Mead, R.J. Price, Drug and gene delivery across the blood-brain barrier with focused ultrasound, J. Contr. Release 176 (1) (2015) 139–148, https://doi.org/10.1016/j.jconrel.2015.08.059 (Drug).
[199] Z.I. Kovacsa, et al., Disrupting the blood-brain barrier by focused ultrasound induces sterile inflammation, Proc. Natl. Acad. Sci. U.S.A. 114 (1) (2017) E75–E84, https://doi.org/10.1073/pnas.1614777114.
[200] K.R. Lattwein, et al., An in vitro proof-of-principle study of sonobactericide, Sci. Rep. 8 (1) (Dec. 2018) 1–12, https://doi.org/10.1038/s41598-018-21648-8.
[201] K.R. Lattwein, et al., Dispersing and sonoporating biofilm-associated bacteria with sonobactericide, Pharmaceutics 14 (6) (2022), https://doi.org/10.3390/pharmaceutics14061164.
[202] X. Duan, Q. Zhou, J.M.F. Wan, A.C.H. Yu, Sonoporation generates downstream cellular impact after membrane resealing, Sci. Rep. 11 (1) (2021) 1–12, https://doi.org/10.1038/s41598-021-84341-3.
[203] F. Fekri, R.C. Delos Santos, R. Karshafian, C.N. Antonescu, Ultrasound microbubble treatment enhances clathrin-mediated endocytosis and fluid-phase uptake through distinct mechanisms, PLoS One 11 (6) (2016) 1–22, https://doi.org/10.1371/journal.pone.0156754.
[204] K.E. Landmark, P.W. Johansen, J.A. Johnson, B. Johansen, S. Uran, T. Skotland, Pharmacokinetics of perfluorobutane following intravenous bolus injection and continuous infusion of sonazoid in healthy volunteers and in patients with reduced pulmonary diffusing capacity, Ultrasound Med. Biol. 34 (3) (Mar. 2008) 494–501, https://doi.org/10.1016/j.ultrasmedbio.2007.09.019.
[205] M.J. Mitchell, M.M. Billingsley, R.M. Haley, M.E. Wechsler, N.A. Peppas, R. Langer, Engineering precision nanoparticles for drug delivery, Nat. Rev. Drug Discov. 20 (2) (Feb. 2021) 101–124, https://doi.org/10.1038/s41573-020-0090-8.
[206] A.A. Exner, M.C. Kolios, Bursting microbubbles: how nanobubble contrast agents can enable the future of medical ultrasound molecular imaging and image-guided therapy, Curr. Opin. Colloid Interface Sci. 54 (2021), 101463, https://doi.org/10.1016/j.cocis.2021.101463.
[207] M. Alheshibri, J. Qian, M. Jehannin, V.S.J. Craig, A history of nanobubbles, Langmuir 32 (43) (Nov. 2016) 11086–11100, https://doi.org/10.1021/acs.langmuir.6b02489.
[208] C.T. Chin, P.N. Burns, Predicting the acoustic response of a microbubble population for contrast imaging in medical ultrasound, Ultrasound Med. Biol. 26 (8) (Oct. 2000) 1293–1300, https://doi.org/10.1016/S0301-5629(00)00299-4.
[209] P.C. Sontum, J. Østensen, K. Dyrstad, L. Hoff, Acoustic properties of NC100100 and their relation with the microbubble size distribution, Invest. Radiol. 34 (4) (Apr. 1999) 268.
[210] B.E. Oeffinger, M.A. Wheatley, Development and characterization of a nano-scale contrast agent, Ultrasonics 42 (1) (Apr. 2004) 343–347, https://doi.org/10.1016/j.ultras.2003.11.011.
[211] C. Su, et al., Current advances in ultrasound-combined nanobubbles for cancer-targeted therapy: a review of the current status and future perspectives, RSC Adv. 11 (21) (May 2021) 12915–12928, https://doi.org/10.1039/D0RA08727K.
[212] N. Güvener, et al., Recent advances in ultrasound-based diagnosis and therapy with micro- and nanometer-sized formulations, Methods 130 (Nov. 2017) 4–13, https://doi.org/10.1016/j.ymeth.2017.05.018.
[213] E.C. Abenojar, et al., Effect of bubble concentration on the in vitro and in vivo performance of highly stable lipid shell-stabilized micro- and nanoscale ultrasound contrast agents, Langmuir 35 (31) (2019) 10192–10202, https://doi.org/10.1021/acs.langmuir.9b00462.
[214] J. Zhang, et al., The optimized fabrication of a novel nanobubble for tumor imaging, Front. Pharmacol. 10 (May 2019) 610, https://doi.org/10.3389/fphar.2019.00610.
[215] A. Jafari Sojahrood, et al., Toward precisely controllable acoustic response of shell-stabilized nanobubbles: high yield and narrow dispersity, ACS Nano 15 (3) (2021) 4901–4915, Aug, https://doi.org/10.1021/acsnano.0c09701.
[216] U.S. Kumar, A. Natarajan, T.F. Massoud, R. Paulmurugan, FN3 linked nanobubbles as a targeted contrast agent for US imaging of cancer-associated human PD-L1, J. Contr. Release 346 (Jun. 2022) 317–327, https://doi.org/10.1016/j.jconrel.2022.04.030.
[217] Z. Xing, et al., The fabrication of novel nanobubble ultrasound contrast agent for potential tumor imaging, Nanotechnology 21 (14) (Apr. 2010) 145607, https://doi.org/10.1088/0957-4484/21/14/145607.
[218] H. Yang, et al., Multifunctional PLGA nanobubbles as theranostic agents: combining doxorubicin and P-gp siRNA Co-delivery into human breast cancer cells and ultrasound cellular imaging, J. Biomed. Nanotechnol. 11 (12) (2015) 2124–2136, https://doi.org/10.1166/jbn.2015.2168.
[219] P. Bhandari, X. Wang, J. Irudayaraj, Oxygen nanobubble tracking by light scattering in single cells and tissues, ACS Nano 11 (3) (Mar. 2017) 2682–2688, https://doi.org/10.1021/acsnano.6b07478.
[220] M.A. Wheatley, F. Forsberg, N. Dube, M. Patel, B.E. Oeffinger, Surfactant-stabilized contrast agent on the nanoscale for diagnostic ultrasound imaging, Ultrasound Med. Biol. 32 (1) (Jan. 2006) 83–93, https://doi.org/10.1016/j.ultrasmedbio.2005.08.009.
[221] P.S. Sheeran, et al., Methods of generating submicrometer phase-shift perfluorocarbon droplets for applications in medical ultrasonography, IEEE Trans. Ultrason. Ferroelectrics Freq. Control 64 (1) (2017) 252–263, https://doi.org/10.1109/TUFFC.2016.2619685.
[222] Y. Endo-Takahashi, Y. Negishi, Microbubbles and nanobubbles with ultrasound for systemic gene delivery, Pharmaceutics 12 (10) (2020) 1–14, https://doi.org/10.3390/pharmaceutics12100964.
[223] C. Pellow, E.C. Abenojar, A.A. Exner, G. Zheng, D.E. Goertz, Concurrent visual and acoustic tracking of passive and active delivery of nanobubbles to tumors, Theranostics 10 (25) (2020) 11690–11706, https://doi.org/10.7150/thno.51316.
[224] H. Kida, et al., Nanobubble mediated gene delivery in conjunction with a hand-held ultrasound scanner, Front. Pharmacol. 11 (Apr. 2020) 363, https://doi.org/10.3389/fphar.2020.00363.
[225] H. Kida, L.B. Feril, Y. Irie, H. Endo, K. Itaka, K. Tachibana, Influence of nanobubble size distribution on ultrasound-mediated plasmid DNA and messenger RNA gene delivery, Front. Pharmacol. 13 (2022).
[226] Y. Tan, et al., Nanobubbles containing sPD-1 and Ce6 mediate combination immunotherapy and suppress hepatocellular carcinoma in mice, Int. J. Nanomed. 16 (2021) 3241–3254, https://doi.org/10.2147/IJN.S305857.
[227] A. Yildirim, N. Blum, A. Goodwin, Colloids, nanoparticles, and materials for imaging, delivery, ablation, and theranostics by focused ultrasound (FUS), Theranostics 9 (Apr. 2019) 2572–2594, https://doi.org/10.7150/thno.32424.
[228] J.M. Gorce, M. Arditi, M. Schneider, Influence of bubble size distribution on the echogenicity of ultrasound contrast agents: a study of SonoVue, Invest. Radiol. 35 (11) (2000) 661–671, https://doi.org/10.1097/00004424-200011000-00003.
[229] L. Hoff, Acoustic Characterization of Contrast Agents for Medical Ultrasound Imaging, Springer Netherlands, Dordrecht, 2001.
[230] J.Z. Myers, J.A. Navarro-Becerra, M.A. Borden, Nanobubbles are non-echogenic for fundamental-mode contrast-enhanced ultrasound imaging, *Bioconjug. Chem.*, Apr. (2022), https://doi.org/10.1021/acs.bioconjchem.2c00155.
[231] W. Bin Cai, et al., The optimized fabrication of nanobubbles as ultrasound contrast agents for tumor imaging, Sci. Rep. 5 (1) (Sep. 2015) 13725, https://doi.org/10.1038/srep13725.
[232] D.V.B. Batchelor, R.H. Abou-Saleh, P.L. Coletta, J.R. McLaughlan, S.A. Peyman, S. D. Evans, Nested nanobubbles for ultrasound-triggered drug release, ACS Appl. Mater. Interfaces 12 (26) (Jul. 2020) 29085–29093, https://doi.org/10.1021/acsami.0c07022.
[233] P.S. Sheeran, P.A. Dayton, Phase-change contrast agents for imaging and therapy, Curr. Pharmaceut. Des. 18 (15) (2012) 2152–2165.
[234] N. Rapoport, Phase-shift, stimuli-responsive perfluorocarbon nanodroplets for drug delivery to cancer, WIREs Nanomedicine and Nanobiotechnology 4 (5) (2012) 492–510, https://doi.org/10.1002/wnan.1176.
[235] N. Rapoport, et al., Ultrasound-mediated tumor imaging and nanotherapy using drug loaded, block copolymer stabilized perfluorocarbon nanoemulsions, J. Control. Release Off. J. Control. Release Soc. 153 (1) (Jul. 2011) 4–15, https://doi.org/10.1016/j.jconrel.2011.01.022.
[236] K.-H. Nam, N.Y. Rapoport, Stable Nanoemulsions for Ultrasound-Mediated Drug Delivery and Imaging, Apr-2014 no. US8709451B2.
[237] M. Kuriakose, M.A. Borden, Microbubbles and Nanodrops for photoacoustic tomography, Curr. Opin. Colloid Interface Sci. 55 (2021), 101464, https://doi.org/10.1016/j.cocis.2021.101464.
[238] L.C. Moyer, K.F. Timbie, P.S. Sheeran, R.J. Price, G.W. Miller, P.A. Dayton, High-intensity focused ultrasound ablation enhancement in vivo via phase-shift nanodroplets compared to microbubbles, J. Ther. Ultrasound 3 (2015) 7, https://doi.org/10.1186/s40349-015-0029-4.

[239] D. Qin, et al., A highly efficient one-for-all nanodroplet for ultrasound imaging-guided and cavitation-enhanced photothermal therapy, Int. J. Nanomed. 16 (2021) 3105–3119, https://doi.org/10.2147/IJN.S301734.
[240] A. Ishijima, et al., Selective intracellular delivery of perfluorocarbon nanodroplets for cytotoxicity threshold reduction on ultrasound-induced vaporization, Cancer Rep 2 (4) (2019) e1165, https://doi.org/10.1002/cnr2.1165.
[241] C. Errico, et al., Ultrafast ultrasound localization microscopy for deep super-resolution vascular imaging, Nature 527 (7579) (Nov. 2015) 499–502, https://doi.org/10.1038/nature16066.
[242] V. Hingot, et al., Subwavelength far-field ultrasound drug-delivery, Appl. Phys. Lett. 109 (Nov. 2016) 194102, https://doi.org/10.1063/1.4967009.
[243] G. Zhang, et al., Photoacoustic super-resolution imaging using laser activation of low-boiling-point dye-coated nanodroplets in vitro and in vivo, in: IEEE International Ultrasonics Symposium, IUS, 2019, pp. 944–947, https://doi.org/10.1109/ULTSYM.2019.8926179, 2019-Octob.
[244] S.-Y. Yu, C.-H. Tu, J.-W. Liaw, M.-K. Kuo, Laser-induced plasmonic nanobubbles and microbubbles in gold nanorod colloidal solution, Nanomaterials 12 (7) (Jan. 2022) 1154, https://doi.org/10.3390/nano12071154.
[245] A. Veeren, M.O. Ogunyankin, J.E. Shin, J.A. Zasadzinski, Liposome-tethered gold nanoparticles triggered by pulsed NIR light for rapid liposome contents release and endosome escape, Pharmaceutics 14 (4) (Apr. 2022) 701, https://doi.org/10.3390/pharmaceutics14040701.
[246] M.O. Ogunyankin, J.E. Shin, D.O. Lapotko, V.E. Ferry, J.A. Zasadzinski, Optimizing the NIR fluence threshold for nanobubble generation by controlled synthesis of 10 - 40 nm hollow gold Nanoshells, Adv. Funct. Mater. 28 (10) (Mar. 2018) 1705272, https://doi.org/10.1002/adfm.201705272.
[247] J.E. Shin, M.O. Ogunyankin, J.A. Zasadzinski, Near infrared-triggered liposome cages for rapid, localized small molecule delivery, Sci. Rep. 10 (Feb. 2020) 1706, https://doi.org/10.1038/s41598-020-58764-3.
[248] J.J. Kwan, et al., Ultrasound-propelled nanocups for drug delivery, Small 11 (39) (Oct. 2015) 5305–5314, https://doi.org/10.1002/smll.201501322.
[249] T. Liu, et al., Endogenous catalytic generation of O2 bubbles for in situ ultrasound-guided high intensity focused ultrasound ablation, ACS Nano 11 (9) (Sep. 2017) 9093–9102, https://doi.org/10.1021/acsnano.7b03772.
[250] X. Cui, X. Han, L. Yu, B. Zhang, Y. Chen, Intrinsic chemistry and design principle of ultrasound-responsive nanomedicine, Nano Today 28 (2019), 100773, https://doi.org/10.1016/j.nantod.2019.100773 xxxx.
[251] F. Pfeifer, Distribution, formation and regulation of gas vesicles, Nat. Rev. Microbiol. 10 (10) (Oct. 2012) 705–715, https://doi.org/10.1038/nrmicro2834.
[252] M.G. Shapiro, et al., Biogenic gas nanostructures as ultrasonic molecular reporters, Nat. Nanotechnol. 9 (4) (Apr. 2014) 311–316, https://doi.org/10.1038/nnano.2014.32.
[253] G. Wang, et al., Surface-modified GVs as nanosized contrast agents for molecular ultrasound imaging of tumor, Biomaterials 236 (Apr. 2020) 119803, https://doi.org/10.1016/j.biomaterials.2020.119803.
[254] A. Farhadi, G.H. Ho, D.P. Sawyer, R.W. Bourdeau, M.G. Shapiro, Ultrasound imaging of gene expression in mammalian cells, Science 365 (6460) (Sep. 2019) 1469–1475, https://doi.org/10.1126/science.aax4804.
[255] R. Gao, et al., Biosynthetic nanobubble-mediated CRISPR/Cas9 gene editing of Cdh2 inhibits breast cancer metastasis, Pharmaceutics 14 (7) (Jul. 2022) 1382, https://doi.org/10.3390/pharmaceutics14071382.
[256] B. Delannoy, et al., Acoustical image reconstruction in parallel-processing analog electronic systems, JAPCA 50 (5) (1979) 3153–3159, https://doi.org/10.1063/1.326397.
[257] R. Torguet, C. Bruneel, E. Bridoux, J.M. Rouvaen, B. Nongaillard, Ultrafast echotomographic system using optical processing of ultrasonic signals, Acoust. Hologr. (1977) 79–85, https://doi.org/10.1007/978-1-4757-0653-6_6.
[258] D. Shattuck, M.D. Weinshenker, S.W. Smith, O.T. von Ramm, Explososcan: a parallel processing technique for high speed ultrasound imaging with linear phased arrays, J. Acoust. Soc. Am. 75 (4) (1984) 1273–1282, https://doi.org/10.1121/1.390734.
[259] L. Sandrin, S. Catheline, M. Tanter, X. Hennequin, M. Fink, Time-resolved pulsed elastography with ultrafast ultrasonic imaging, Ultrason. Imag. 21 (4) (1999) 259–272, https://doi.org/10.1177/016173469902100402.
[260] M. Tanter, J. Bercoff, L. Sandrin, M. Fink, Ultrafast compound imaging for 2-D motion vector estimation: application to transient elastography, IEEE Trans. Ultrason. Ferroelectrics Freq. Control 49 (10) (Oct. 2002) 1363–1374, https://doi.org/10.1109/TUFFC.2002.1041078.
[261] J. Bercoff, Ultrafast ultrasound imaging, Ultrasound Imaging - Med. Appl. (Aug. 2011), https://doi.org/10.5772/19729.
[262] A. Ng, J. Swanevelder, Resolution in ultrasound imaging, Cont. Educ. Anaesth. Crit. Care Pain 11 (5) (Oct. 2011) 186–192, https://doi.org/10.1093/BJACEACCP/MKR030.
[263] H. Hasegawa, C.L. de Korte, Ultrafast ultrasound imaging, Ultrafast Ultrasound Imaging (Sep. 2018), https://doi.org/10.3390/BOOKS978-3-03897-128-3.
[264] G. Montaldo, M. Tanter, J. Bercoff, N. Benech, M. Fink, Coherent plane-wave compounding for very high frame rate ultrasonography and transient elastography, IEEE Trans. Ultrason. Ferroelectrics Freq. Control 56 (3) (Mar. 2009) 489–506, https://doi.org/10.1109/TUFFC.2009.1067.
[265] A. Ozturk, J.R. Grajo, M. Dhyani, B.W. Anthony, A.E. Samir, Principles of ultrasound elastography, Abdom. Radiol. 43 (4) (Feb. 2018) 773–785, https://doi.org/10.1007/S00261-018-1475-6, 2018 434.
[266] J. Bercoff, et al., Ultrafast compound Doppler imaging: providing full blood flow characterization, IEEE Trans. Ultrason. Ferroelectrics Freq. Control 58 (1) (Jan. 2011) 134–147, https://doi.org/10.1109/TUFFC.2011.1780.
[267] C. Demene, et al., Functional ultrasound imaging of brain activity in human newborns, Sci. Transl. Med. 9 (411) (Oct. 2017), https://doi.org/10.1126/SCITRANSLMED.AAH6756/SUPPL_FILE/AAH6756_VIDEO_S2.MP4.
[268] O. Couture, M. Tanter, M. Fink, PROCEDE et dispositif D'IMAGERIE ULTRASONORE, Eur. Pat. Off. (Jun. 2012) no. PCT/FR2011/052810.
[269] O. Couture, V. Hingot, B. Heiles, P. Muleki-Seya, M. Tanter, Ultrasound localization microscopy and super-resolution: a state of the art, IEEE Trans. Ultrason. Ferroelectrics Freq. Control 65 (8) (Aug. 2018) 1304–1320, https://doi.org/10.1109/TUFFC.2018.2850811.
[270] K. Christensen-Jeffries, R.J. Browning, M.X. Tang, C. Dunsby, R.J. Eckersley, In vivo acoustic super-resolution and super-resolved velocity mapping using microbubbles, IEEE Trans. Med. Imag. 34 (2) (Feb. 2015) 433–440, https://doi.org/10.1109/TMI.2014.2359650.
[271] V. Hingot, A. Chavignon, B. Heiles, O. Couture, Measuring image resolution in ultrasound localization microscopy, IEEE Trans. Med. Imag. 40 (12) (2021) 3812–3819, Dec, https://doi.org/10.1109/TMI.2021.3097150.
[272] A. Chavignon, V. Hingot, C. Orset, D. Vivien, O. Couture, 3D transcranial ultrasound localization microscopy for discrimination between ischemic and hemorrhagic stroke in early phase, Sci. Rep. 12 (1) (Aug. 2022) 1–11, https://doi.org/10.1038/S41598-022-18025-X, 2022 121.
[273] S.B. Andersen, et al., Super-resolution ultrasound imaging can quantify alterations in microbubble velocities in the renal vasculature of rats, Diagnostics 12 (5) (May 2022), https://doi.org/10.3390/DIAGNOSTICS12051111.
[274] M.R. Lowerison, et al., Super-resolution Ultrasound Imaging of Cerebrovascular Impairment in a Mouse Model of Alzheimer's Disease, bioRxiv, Oct. 2022, p. 2022, https://doi.org/10.1101/2022.10.05.511008, 10.05.511008.
[275] X. Chen, M.R. Lowerison, Z. Dong, A. Han, P. Song, Deep learning-based microbubble localization for ultrasound localization microscopy, IEEE Trans. Ultrason. Ferroelectrics Freq. Control 69 (4) (Apr. 2022) 1312–1325, https://doi.org/10.1109/TUFFC.2022.3152225.
[276] B. Heiles, A. Chavignon, V. Hingot, P. Lopez, E. Teston, O. Couture, Performance benchmarking of microbubble-localization algorithms for ultrasound localization microscopy, Nat. Biomed. Eng. (2022), https://doi.org/10.1038/S41551-021-00824-8.
[277] L. Yan, et al., Study on the application of super-resolution ultrasound for cerebral vessel imaging in rhesus monkeys, Front. Neurol. 12 (Nov. 2021), https://doi.org/10.3389/FNEUR.2021.720320/PDF.
[278] C. Demené, et al., Transcranial ultrafast ultrasound localization microscopy of brain vasculature in patients, Nat. Biomed. Eng. 5 (3) (Mar. 2021) 219–228, https://doi.org/10.1038/S41551-021-00697-X.
[279] C. Huang, et al., Super-resolution ultrasound localization microscopy based on a high frame-rate clinical ultrasound scanner: an in-human feasibility study, Phys. Med. Biol. 66 (8) (Apr. 2021), https://doi.org/10.1088/1361-6560/ABEF45.
[280] T. Opacic, et al., Motion model ultrasound localization microscopy for preclinical and clinical multiparametric tumor characterization, Nat. Commun. 9 (1) (Apr. 2018) 1–13, https://doi.org/10.1038/S41467-018-03973-8, 2018 91.
[281] A. Sun, et al., Evaluation of visible NIR-I and NIR-II light penetration for photoacoustic imaging in rat organs, Opt Express 28 (6) (Mar. 2020) 9002–9013, https://doi.org/10.1364/OE.389714, vol. 28, no. 6, pp. 9002–9013.
[282] H. Yoon, K.A. Hallam, C. Yoon, S.Y. Emelianov, Super-resolution imaging with ultrafast ultrasound imaging of optically triggered perfluorohexane nanodroplets, IEEE Trans. Ultrason. Ferroelectrics Freq. Control 65 (12) (Dec. 2018) 2277–2285, https://doi.org/10.1109/TUFFC.2018.2829740.
[283] Y. Jang, et al., Development of an ultrasound triggered nanomedicine-microbubble complex for chemo-photodynamic-gene therapy, Nanomed. Nanotechnol. Biol. Med. 27 (2020), 102194, https://doi.org/10.1016/j.nano.2020.102194.
[284] H. Li, et al., Instant ultrasound-evoked precise nanobubble explosion and deep photodynamic therapy for tumors guided by molecular imaging, ACS Appl. Mater. Interfaces 13 (18) (2021) 21097–21107, https://doi.org/10.1021/acsami.1c05517.
[285] R. Chen, et al., Photoacoustic molecular imaging-escorted adipose photodynamic–browning synergy for fighting obesity with virus-like complexes, Nat. Nanotechnol. 16 (4) (2021) 455–465, https://doi.org/10.1038/s41565-020-00844-6.
[286] M. de Saint Victor, L.C. Barnsley, D. Carugo, J. Owen, C.C. Coussios, E. Stride, Sonothrombolysis with magnetically targeted microbubbles, Ultrasound Med. Biol. 45 (5) (2019) 1151–1163, https://doi.org/10.1016/j.ultrasmedbio.2018.12.014.
[287] A. Marino, G.G. Genchi, E. Sinibaldi, G. Ciofani, Piezoelectric effects of materials on bio-interfaces, ACS Appl. Mater. Interfaces 9 (21) (2017) 17663–17680, https://doi.org/10.1021/acsami.7b04323.

ANNEX 3

Europäisches Patentamt | European Patent Office | Office européen des brevets

Acknowledgement of receipt

We hereby acknowledge receipt of your request for the processing of an international application according to the Patent Cooperation Treaty as follows:

Submission number	1000505781	
PCT application number	PCT/FR2022/050309	
Date of receipt	21 February 2022	
Receiving Office	Institut National de la Propriété Industrielle	
Your reference	B2200081WO/SSO	
Applicant	INSERM (Institut National de la Santé et de la Recherche Médicale)	
Number of applicants	2	
Country	FR	
Title	METHOD FOR MANUFACTURING BUBBLES HAVING A POLYMERIC SHELL USING SOUND WAVES FOR GENERATING THE BUBBLES	
Documents submitted	eolf-pkda.xml	eolf-requ.xml
	eolf-appb.xml	eolf-decl.xml
	eolf-fees.xml	eolf-vlog.xml
	eolf-othd-000001.pdf (24 p.)	eolf-appb-P000001.pdf (2 p.)
Submitted by	CN=Catherine Touati 8517	
Method of submission	Online	
Date and time receipt generated	21 February 2022, 17:39:47 (CET)	
Digest	EA:D9:D2:BF:67:C5:C6:81:BA:84:40:D8:20:4B:7C:92:ED:A0:6F:EE	

/INPI, section dépôt/

PCT REQUEST

(Original in Electronic Form)

0	**For receiving Office use only**	
0-1	International Application No.	
0-2	International Filing Date	
0-3	Name of receiving Office and "PCT International Application"	

0-4	**Form PCT/RO/101 PCT Request**	
0-4-1	Prepared Using	**PCT Online Filing Version 3.51.000.273e MT/FOP 20141031/0.20.5.24**
0-5	**Petition**	
	The undersigned requests that the present international application be processed according to the Patent Cooperation Treaty	
0-6	**Receiving Office (specified by the applicant)**	**National Institute of Industrial Property (INPI) (France) (RO/FR)**
0-7	**Applicant's or agent's file reference**	**B2200081WO/SSO**
I	**Title of Invention**	**METHOD FOR MANUFACTURING BUBBLES HAVING A POLYMERIC SHELL USING SOUND WAVES FOR GENERATING THE BUBBLES**
II	**Applicant**	
II-1	This person is	**Applicant only**
II-2	Applicant for	**All designated States**
II-4	Name	**INSERM (Institut National de la Santé et de la Recherche Médicale)**
II-5	Address	**101, rue de Tolbiac 75013 PARIS France**
II-6	State of nationality	**FR**
II-7	State of residence	
III-1	**Applicant and/or inventor**	
III-1-1	This person is	**Applicant only**
III-1-2	Applicant for	**All designated States**
III-1-4	Name	**UNIV PARIS XIII PARIS-NORD VILLETANEUSE**
III-1-5	Address	**99, av Jean-Baptiste Clément 93430 VILLETANEUSE France**
III-1-6	State of nationality	**FR**
III-1-7	State of residence	

PCT REQUEST

(Original in Electronic Form)

III-2	**Applicant and/or inventor**	
III-2-1	This person is	Inventor only
III-2-3	Inventor for	All designated States
III-2-4	Name (LAST, First)	FOURNIER, Louise
III-2-5	Address	Inserm U1148 Hôpital Bichat 46 Rue Henri Huchard 75018 PARIS France
III-3	**Applicant and/or inventor**	
III-3-1	This person is	Inventor only
III-3-3	Inventor for	All designated States
III-3-4	Name (LAST, First)	CHAUVIERRE, Cédric
III-3-5	Address	Inserm U1148 Hôpital Bichat 46 Rue Henri Huchard 75018 PARIS France
IV-1	**Agent or common representative; or address for correspondence** The person identified below is hereby/ has been appointed to act on behalf of the applicant(s) before the competent International Authorities as:	Agent
IV-1-1	Name	Plasseraud IP
IV-1-2	Address	66 rue de la Chaussée d'Antin 75440 PARIS CEDEX 09 France
IV-1-3	Telephone No.	00 33 1 40 16 70 00
IV-1-4	Facsimile No.	00 33 1 42 80 01 59
IV-1-5	e-mail	info@plass.com
IV-1-5(a)	E-mail authorization The receiving Office, the International Searching Authority, the International Bureau and the International Preliminary Examining Authority are authorized to use this e-mail address, if the Office or Authority so wishes, to send notifications issued in respect of this international application:	exclusively in electronic form (no paper notifications will be sent)
V	**DESIGNATIONS**	
V-1	**The filing of this request constitutes under Rule 4.9(a), the designation of all Contracting States bound by the PCT on the international filing date, for the grant of every kind of protection available and, where applicable, for the grant of both regional and national patents.**	
VI-1	**Priority Claim**	NONE
VII-1	**International Searching Authority Chosen**	European Patent Office (EPO) (ISA/EP)

PCT REQUEST

(Original in Electronic Form)

VIII	**Declarations**	Number of declarations	
VIII-1	Declaration as to the identity of the inventor	–	
VIII-2	Declaration as to the applicant's entitlement, as at the international filing date, to apply for and be granted a patent	–	
VIII-3	Declaration as to the applicant's entitlement, as at the international filing date, to claim the priority of the earlier application	–	
VIII-4	Declaration of inventorship (only for the purposes of the designation of the United States of America)	–	
VIII-5	Declaration as to non-prejudicial disclosures or exceptions to lack of novelty	1	

PCT REQUEST

(Original in Electronic Form)

VIII-5-1	**Declaration: Non-prejudicial disclosure or exceptions to lack of novelty** Declaration as to non-prejudicial disclosures or exceptions to lack of novelty (Rules 4.17(v) and 51bis.1(a)(v)): Name (LAST, First)	**In relation to this international application** **INSERM (Institut National de la Santé et de la Recherche Médicale) declares that the subject matter claimed in this international application was disclosed as follows:**
VIII-5-1 (i)	Kind of disclosure:	**Publication**
VIII-5-1 (ii)	Date of disclosure:	**02 September 2021 (02.09.2021)**
VIII-5-1 (iii)	Title of disclosure:	**Abstract - Poster - Video "Ultrasound responsive polymer microbubbles for an efficient targeted treatment of thrombotic diseases"**
VIII-5-1 (iv)	Place of disclosure:	**31st conference of the European society for biomaterials**
VIII-5-1 (i)	Kind of disclosure:	**Publication**
VIII-5-1 (ii)	Date of disclosure:	**14 October 2021 (14.10.2021)**
VIII-5-1 (iii)	Title of disclosure:	**Poster "Ultrasound responsive polymer microbubbles for an efficient targeted treatment of thrombotic diseases"**
VIII-5-1 (iv)	Place of disclosure:	**Journées scientifiques de l'ED MTCI**
VIII-5-1 (i)	Kind of disclosure:	**Publication**
VIII-5-1 (ii)	Date of disclosure:	**24 November 2021 (24.11.2021)**
VIII-5-1 (iii)	Title of disclosure:	**Abstract - Video "Ultrasound responsive polymer microbubbles for an efficient targeted treatment of thrombotic diseases"**
VIII-5-1 (iv)	Place of disclosure:	**Conference "Biomarkers of the future"**
VIII-5-1 (i)	Kind of disclosure:	**Publication**
VIII-5-1 (ii)	Date of disclosure:	**06 December 2021 (06.12.2021)**
VIII-5-1 (iii)	Title of disclosure:	**Abstract - Oral Presentation "Ultrasound responsive polymer microbubbles for an efficient targeted treatment of thrombotic diseases"**
VIII-5-1 (iv)	Place of disclosure:	**Conference SFNano**

PCT REQUEST

(Original in Electronic Form)

IX	Check list	Number of sheets	Electronic file(s) attached
IX-1	Request (including declaration sheets)	5	✓
IX-2	Description	17	✓
IX-3	Claims	6	✓
IX-4	Abstract	1	✓
IX-5	Drawings	2	✓
IX-6a	Sequence listing part of the description (also to be used for the purposes of international search)	–	–
IX-7	TOTAL	31	
	Accompanying Items	Paper document(s) attached	Electronic file(s) attached
IX-8	Fee calculation sheet	–	✓
IX-20	**Figure of the drawings which should accompany the abstract**		
IX-21	**Language of filing of the international application**	French	
X-1	**Signature of applicant, agent or common representative**	(PKCS7 Digital Signature)	
X-1-1	Name	Plasseraud IP	
X-1-2	Name of signatory	Catherine Touati 8517	
X-1-3	Capacity (if such capacity is not obvious from reading the request)	(Representative)	

FOR RECEIVING OFFICE USE ONLY

10-1	**Date of actual receipt of the purported international application**	
10-2	**Drawings:**	
10-2-1	Received	
10-2-2	Not received	
10-3	**Corrected date of actual receipt due to later but timely received papers or drawings completing the purported international application**	
10-4	**Date of timely receipt of the required corrections under PCT Article 11(2)**	
10-5	**International Searching Authority**	ISA/EP
10-6	**Transmittal of search copy delayed until search fee is paid**	

FOR INTERNATIONAL BUREAU USE ONLY

11-1	**Date of receipt of the record copy by the International Bureau**	

PCT (ANNEX - FEE CALCULATION SHEET)

(Original in Electronic Form)

(This sheet is not part of and does not count as a sheet of the international application)

0	**For receiving Office use only**	
0-1	International Application No.	
0-2	Date stamp of the receiving Office	

0-4	**Form PCT/RO/101 (Annex)** **PCT Fee Calculation Sheet**				
0-4-1	Prepared Using		PCT Online Filing Version 3.51.000.273e MT/FOP 20141031/0.20.5.24		
0-9	**Applicant's or agent's file reference**		B2200081WO/SSO		
2	**Applicant**		INSERM (INSTITUT NATIONAL DE LA SANTÉ ET DE LA RECHERCHE MÉDICALE)		
12	**Calculation of prescribed fees**		Fee amount/multiplier	Total amounts (EUR)	
12-1	Transmittal fee	**T**	➪	93	
12-2-1	Search fee	**S**	➪	1775	
12-2-2	International search to be carried out by		EP		
12-3	International filing fee (first 30 sheets)	**i1**	1235		
12-4	Remaining sheets		1		
12-5	Additional amount	**(X)**	14		
12-6	Total additional amount	**i2**	14		
12-7	i1 + i2 =	**i**	1249		
12-12	Electronic Filing reduction (Image)	**R**	-186		
12-13	Total International filing fee (i-R)	**I**	➪	1063	
12-14	Fee for priority document Number of priority documents requested		0		
12-15	Fee per document	**(X)**	15		
12-16	Total priority document fee:	**P**	➪		
12-17	Fee for restoration of priority rights Number of requests for restoration of priority rights	**RP**	0		
	Total amount of fees for restoration of priority rights				
12-19	**TOTAL FEES PAYABLE (T+S+I+P+RP)**		➪	2931	
12-21	**Mode of payment**		Authorization to charge deposit or current account		

PCT (ANNEX - FEE CALCULATION SHEET)

(Original in Electronic Form)

(This sheet is not part of and does not count as a sheet of the international application)

12-22	**Deposit or current account instructions** The receiving Office	**National Institute of Industrial Property (INPI) (France) (RO/FR)**
12-22-1	Authorization to charge the total fees indicated above	✓
12-22-2	Authorization to charge any deficiency or credit any overpayment in the total fees indicated above	✓
12-23	Deposit or current account No.	**12070**
12-24	Date	**21 February 2022 (21.02.2022)**
12-25	Name and signature	**/PLASSERAUD IP/,** **/Plasseraud IP/**
12-26	**Reimbursement instructions**	
12-26-1-1	Office processing the reimbursement	**EP**
12-26-1-2	Reimbursement, if any, to be made to the deposit or current account No.	**28040012**
12-26-1-3	Account holder	**/Plasseraud IP/**
12-26-1-4	Date	**21 February 2022 (21.02.2022)**

METHOD FOR MANUFACTURING BUBBLES HAVING A POLYMERIC SHELL USING SOUND WAVES FOR GENERATING THE BUBBLES

The present invention relates to a method for manufacturing bubbles having a polymeric shell and more particularly to a method wherein the bubbles are generated by applying sound waves to an aqueous solution and wherein the polymeric shell is formed by polymerization of a cyanoacrylate monomer.

Micro- and nanobubbles are nowadays used in various biomedical applications. While the most common application of such bubbles is as contrast agents for ultrasound imaging, they have also been used as delivery vehicles (e.g. for drugs, genes or for O_2 delivery) and as thrombolytic agents.
Commercially available bubbles include those sold under the brand names Sonazoid™ and Optison™ (produced by GE Healthcare), Sonovue™ (produced by Bracco) and Definity™ (produced by Lantheus Medical Imaging).
Micro- and nanobubbles generally comprise a gaseous core and a stabilizing shell. Said shell is generally made of surfactants, lipids or proteins. Bubbles having a polymeric shell have also been studied as they can be more stable and can attract less immune response in vivo than bubbles having a proteinic shell.

Bubbles having a polymeric shell made of polycyanoacrylate have been described in Bo Li et al., Functionalized polymer microbubbles as new molecular ultrasound contrast agent to target P-selectin in thrombus, Biomaterials, 2019, Volume 194, Pages 139-150. The bubbles having a polymeric shell made of polycyanoacrylate described therein are obtained by hydrodynamic cavitation. However, the reaction time is of 60 minutes and the bubbles obtained are not homogeneous in shape and generally not spherical.

It would thus be advantageous to be able to produce bubbles having a polymeric shell made of polycyanoacrylate requiring shorter reaction times and being more homogeneous in shape and more spherical.

The present invention discloses a method for manufacturing bubbles having a polymeric shell made of polycyanoacrylate using sound waves to generate the bubbles instead of

hydrodynamic cavitation. Surprisingly, the method of the invention allows to obtain bubbles having a polymeric shell made of polycyanoacrylate with reduced reaction times compared to the method using hydrodynamic cavitation described in Bo Li et al.

It has been found that the application of sound waves for at least 6 minutes in combination with the choice of a specific pH was critical to produce with a high yield stable bubbles having a polymeric shell. This is surprising since it could have been expected that such sonication times would have degraded the structures formed. Indeed, acoustic cavitation is known to generate locally elevated temperature and free radicals that can degrade polymeric molecules.

Moreover, the bubbles obtained with the method of the present invention unexpectedly have an improved sphericity than the bubbles obtained using hydrodynamic cavitation.

SUMMARY OF THE INVENTION

One aspect of the present invention is related to a method for manufacturing bubbles having a polymeric shell comprising the following steps:

a) providing a first volume of an aqueous solution comprising a gas dissolved therein, a surfactant dissolved therein, and having a pH below 6, preferably comprised between 1.5 and 5, more preferably comprised between 2 and 4;
b) in the aqueous solution, generating bubbles comprising the gas by applying sound waves to the aqueous solution;
c) while generating the bubbles, adding a second volume of a cyanoacrylate monomer to the aqueous solution, thereby forming a suspension of the bubbles having a polymeric shell in the aqueous solution, wherein said polymeric shell is formed by polymerization of the cyanoacrylate monomer at the interface between the aqueous solution and the bubbles;
d) recovering the bubbles having a polymeric shell;

characterized in that the sound waves in step b) are applied during a period of at least 6 minutes, preferably between 8 and 30 minutes, more preferably between 15 and 30 minutes after the beginning of the addition of the cyanoacrylate monomer.

Another aspect of the present invention is related to the bubbles obtainable by the method according to the invention.

DESCRIPTION OF THE FIGURES

FIGURE 1 compares the shape and the ability to incorporate a fluorescent probe of:

- Top line: bubbles obtained according to the prior art Bo Li et al., Functionalized polymer microbubbles as new molecular ultrasound contrast agent to target P-selectin in thrombus, Biomaterials, 2019, Volume 194, Pages 139-150;
- Middle line: bubbles comprising Nile red as a fluorescent probe obtained by the method of Example 5;
- Bottom line: bubbles comprising Nile red as a fluorescent probe obtained by the method of Example 4.

In each line, the left image shows the fluorescence of Nile red in the sample, the middle image shows the same view without fluorescence and the right image shows the left image and the middle image merged.

On the left and right images, the lighter parts correspond to fluorescence.

The scale bar on the images corresponds to 10 µm.

It can be seen that the bubbles obtained by the method of Example 5 (middle line), wherein the amplitude of vibration of the tip is set at 369 µm and the sound waves are applied for 10 minutes, did not incorporate fluorescence as efficiently as the bubbles obtained by the method of Example 4 (bottom line), wherein the vibration of the tip is set at 243 µm and the sound waves are applied for 10 minutes. Moreover, the bubbles obtained by the method of the invention (middle and bottom lines) are more spherical and homogeneous in shape than the bubbles obtained according to the prior art (top line).

FIGURE 2 shows a scanning electron microscopy image of the bubbles obtained using the method described in Example 1. The scale bar on the image corresponds to 4 µm.

DETAILED DESCRIPTION OF THE INVENTION

An object of the present invention is a method for manufacturing bubbles having a polymeric shell comprising the following steps:

a) providing a first volume of an aqueous solution comprising a gas dissolved therein, a surfactant dissolved therein, and having a pH below 6, preferably comprised between 1.5 and 5, more preferably comprised between 2 and 4;
b) in the aqueous solution, generating bubbles comprising the gas by applying sound waves to the aqueous solution;
c) while generating the bubbles, adding a second volume of a cyanoacrylate monomer to the aqueous solution, thereby forming a suspension of the bubbles having a polymeric shell in the aqueous solution, wherein said polymeric shell is formed by polymerization of the cyanoacrylate monomer at the interface between the aqueous solution and the bubbles;
d) recovering the bubbles having a polymeric shell;

characterized in that the sound waves in step b) are applied during a period of at least 6 minutes, preferably between 8 and 30 minutes, more preferably between 15 and 30 minutes after the beginning of the addition of the cyanoacrylate monomer.

In step b) of the method of the invention, the bubbles can be generated directly by the sound waves when they lower the pressure of the aqueous solution enough to produce bubbles. In step b), the bubbles can also be generated by the fragmentation or coalescence of other bubbles, said fragmentation or coalescence being itself caused or accelerated by the sound waves. Said other bubbles can themselves be generated directly by the sound waves and/or can originate from e.g. gas bubbling through the aqueous solution, and/or gas trapped at the interface between the aqueous solution and any instrument plunged therein (e.g. a sonotrode), and/or gas trapped at the interface between the aqueous solution and the walls of the reactor.

The bubbles generated by the sound waves in step b) contain the gas dissolved in the aqueous solution together with water vapor at least because of the partition equilibrium between the bubbles and the aqueous solution.

In the method of the invention, the bubbles having a polymeric shell recovered at step d) originate from the bubbles generated by the sound waves in step b). Because of the partition equilibrium between the bubbles and the aqueous solution, the bubbles having a polymeric shell recovered at step d) can be enriched in the gas dissolved in the aqueous solution compared to the bubbles generated by the sound waves in step b).

The gas dissolved in the solution can be one gaseous compound or a mixture of gaseous compounds or a mixture of compounds different from water that would be gaseous in the conditions of temperature and pressure used when the method of the invention is performed.

Preferably, in the method according to the invention, the gas dissolved in the solution has a molar mass of at least 100 g/mol, more preferably of at least 200 g/mol.

Preferably, in the method according to the invention, the gas dissolved in the solution has a density at 20°C and 1013 mbar of at least 7 kg/m^3, more preferably at least 9 kg/m^3.

Preferably, in the method according to the invention, the gas dissolved in the solution is selected from the group consisting of alkanes, fluoroalkanes, and mixtures thereof, more preferably the gas dissolved in the solution is a perfluoroalkane, such as perfluoropropane or perfluorobutane, or a mixture of perfluoroalkanes, even more preferably the gas dissolved in the solution is perfluorobutane.

Surprisingly, the bubbles are obtained in particularly high yields when the gas dissolved in the solution is selected from the group consisting of alkanes, fluoroalkanes, and mixtures thereof, in particular when the gas dissolved in the solution is a perfluoroalkane, such as perfluoropropane or perfluorobutane, or a mixture of perfluoroalkanes, more particularly when the gas dissolved in the solution is perfluorobutane.

Preferably, in the method according to the invention, the amount of the gas dissolved in the aqueous solution is maintained over 0.5 mg/L throughout steps b) and c), more preferably the aqueous solution is saturated with said gas throughout steps b) and c).

A gas can be dissolved in an aqueous solution by bubbling said gas through the aqueous solution.

Preferably, in the method according to the invention, the gas dissolved in the aqueous solution is bubbled through the aqueous solution during steps b) and c), preferably gas dissolved in the aqueous solution is bubbled through the aqueous solution throughout steps b) and c).

The surfactant contributes to the formation of the bubbles and to their stabilization.

Preferably, in the method according to the invention, the surfactant is a nonionic surfactant, for example a polysorbate, a poloxamer, an octylphenol (including ethoxylated derivatives of octylphenols), a nonylphenol (including ethoxylated derivatives of nonylphenols), an ethoxylated fatty alcohol (e.g. a cetomacrogol), a macrogol-glycerol ester (e.g. an ethoxylated hydrogenated castor oil), or a mixture thereof.

Preferably, in the method according to the invention, the surfactant has a hydrophilic-lipophilic balance comprised between 8 and 18, more preferably comprised between 10 and 18, even more preferably comprised between 12 and 18.

Preferably, in the method according to the invention, the amount of surfactant in the first volume of the aqueous solution of step a) is of at least 10 times the critical micelle concentration (CMC) of said surfactant, more preferably of at least 50 times the CMC of said surfactant.

Preferably, in the method of the invention, a source of the sound waves is plunged in the aqueous solution.

Sound waves can be applied in a pulsed mode. As defined herein in a pulsed mode, the sound waves are not applied continuously for more than 10 seconds.

Preferably, in the method according to the invention, the sound waves are not applied in a pulsed mode, more preferably the time interval between two periods of application of the

sound waves is lower than 10 seconds, even more preferably the sound waves are applied continuously in one time.

Preferably, in the method according to the invention, the source of the sound waves vibrates with an amplitude comprised between 50 µm and 500 µm, more preferably between 100 µm and 500 µm, even more preferably between 200 µm and 400 µm, more particularly the amplitude of the sound waves is comprised between 200 µm and 300 µm.

Increasing the amplitude of vibration of the source of the sound waves generally accelerates the formation of the microbubbles having a polymeric shell. It also results in a faster increase of the temperature of the aqueous solution.

In a particular embodiment of the method of the invention, the source of the sound waves vibrates with an amplitude comprised between 200 µm and 400 µm and the period of application of the sound waves after the beginning of the addition of the cyanoacrylate monomer is of between 8 and 30 minutes.

In a particular embodiment of the method of the invention, the source of the sound waves vibrates with an amplitude comprised between 200 µm and 300 µm and the period of application of the sound waves after the beginning of the addition of the cyanoacrylate monomer is of between 15 and 30 minutes.

Surprisingly, with the above conditions of amplitude of vibration for the source of the sound waves and of duration of the application of the sound waves, better incorporation of fluorescent probes is observed, as shown in FIGURE 1.

Preferably, in the method according to the invention, the frequency of the sound waves is comprised between 10 kHz and 100 kHz, more preferably between 15 kHz and 50 kHz.

Preferably, in the method according to the invention, an emitting surface of the source of the sound waves plunged in the aqueous solution is of at least 1 mm^2 per 10 mL of the aqueous solution.

Preferably, in the method according to the invention, the second volume of the hydrophobic cyanoacrylate monomer corresponds to at least 0.01 vol.%, preferably between 0.5 vol.% and 5 vol.%, of the first volume of the aqueous solution.

Preferably, in the method according to the invention, the addition of the second volume of the hydrophobic cyanoacrylate monomer begins less than 5 minutes, more preferably less than 1 minute, even more preferably between 10 seconds and 1 minute after the beginning of step b).

Preferably, in the method according to the invention, the cyanoacrylate monomer is an alkyl cyanoacrylate monomer, more preferably wherein said alkyl group comprises from 2 or 8 carbon atoms, even more preferably wherein said alkyl group is a n-butyl or isobutyl group.

It is believed that the cyanoacrylate monomer has some affinity for the interface between the bubbles and the aqueous solution, allowing the formation of the polymeric shell when the cyanoacrylate monomer polymerizes.

Cyanoacrylate monomer can polymerize through anionic polymerization. In water, higher pH are more favorable to anionic polymerization of cyanoacrylate monomers than lower pH. In the method according to the invention, the pH of the first volume of the aqueous solution is chosen to prevent the anionic polymerization of the cyanoacrylate monomer to be too fast or too slow. The pH of the first volume of the aqueous solution is thus chosen so that the cyanoacrylate monomer polymerizes slow enough for it to have time to migrate to the interface between the bubbles and the aqueous solution and at the same time polymerizes fast enough for the polymeric shell to be formed before the bubbles are destabilized.

In step c), the cyanoacrylate monomer can be added at a controlled speed or all at once. Preferably the time of addition of the cyanoacrylate monomer does not exceed 5 minutes and is such that the sound waves are applied after the end of the addition of the cyanoacrylate monomer for at least 4 minutes.

In some embodiments of the method according to the invention, the first volume of aqueous solution of step a) further comprises a saccharide or a derivative thereof, for example an

oligosaccharide, a polysaccharide, or a derivative thereof, so as to produce bubbles having a polymeric shell wherein the saccharide or derivative thereof is copolymerized with the cyanoacrylate monomer.

Preferably, said saccharide or derivative thereof is present in the first volume of aqueous solution of step a) in an amount of 0.1 to 4% by weight relative to the weight of the first volume of aqueous solution.

It is believed that the saccharides or derivatives thereof copolymerize with the cyanoacrylate via addition of the hydroxyl groups in the saccharides or derivatives thereof to the vinylic group of the cyanoacrylate monomers.

Preferably, in the method according to the invention, the saccharide or derivative thereof is selected from the group consisting of fucoidans, dextrans, mannans, derivatives of fucoidans, derivatives of dextrans (such as carboxymethyl dextran, carboxymethyl dextran FITC, dextran FITC), derivatives of mannans (such as glucomannan and galactomannan), and mixtures thereof.

Including a saccharide in the shell of the bubbles potentially gives them further functionalities. For example, bubbles functionalized with fucoidan have been shown to efficiently target the protein P-selectin, bubbles functionalized with a fluorescent saccharide such as dextran FITC have fluorescent properties useful for optical imaging purposes.

In some embodiments of the method according to the invention, the first volume of aqueous solution of step a) and/or the second volume of the cyanoacrylate monomer added in step c) further comprises a fluorescent probe so as to yield polymer-coated bubbles comprising the fluorescent probe, preferably said fluorescent probe is present in an amount of 0.1 to 40 ppm by weight relative to the weight of the first volume of aqueous solution.

In some embodiments of the method according to the invention, a fluorescent probe is incorporated in the bubbles having a polymeric shell, after steps b) and c) or at any later stage in the method, by adding said fluorescent probe to a suspension of the bubbles having a polymeric shell.

Surprisingly, it has been observed that these embodiments of the method allow to incorporate the fluorescent probe in the bubbles having a polymeric shell in such a way that the fluorescent probe is not released upon subsequent washing of the bubbles.

Preferably, when the fluorescent probe is added to the first volume of aqueous solution of step a) or after steps b) and c), said fluorescent probe is soluble in water, for example said fluorescent probe is rhodamine B.

Preferably, when the fluorescent probe is added to the second volume of the cyanoacrylate monomer added in step c), said fluorescent probe is lipophilic, for example said fluorescent probe is Nile red.

Preferably, in the method according to the invention, steps b) and c) are performed while maintaining the temperature of the aqueous solution below 60°C, more preferably below 35°C.

Applying the sound waves to the aqueous solution generally results in an increase of the temperature of the aqueous solution during step b) and c) of the method of the invention. It is preferred to prevent excessive heating of the aqueous solution. It has thus been observed that when the temperature of the aqueous solution reaches 70°C at the end of step b) lower yields in number of bubbles per mL are obtained. Maintaining the temperature of the aqueous solution below 60°C, more preferably below 35°C can be performed by any means known of the person skilled in the art, e.g. by using an ice bath.

In addition to maintaining the temperature of the aqueous solution below 60°C, more preferably below 35°C, the first volume of aqueous solution just before step b) preferably has a temperature below 10°C.

Surprisingly, in the embodiments of the method of the invention where an oligosaccharide, a polysaccharide, or a derivative thereof, able to target a protein is comprised in the first volume of aqueous solution of step a), it has been observed that the bubbles having a

polymeric shell obtained had improved targeting properties when the temperature of the first volume of aqueous solution just before step b) was below 10°C.

Preferably, in the method according to the invention, the first volume of the aqueous solution is obtained by the following steps:

a1. acidifying a volume a0 of an aqueous solution with a strong inorganic acid, such as HCl, H_2SO_4, or HNO_3, to obtain the first volume of the aqueous solution having a desired pH;

a2. dissolving the gas in the first volume of the aqueous solution to obtain the first volume of the aqueous solution comprising the gas dissolved therein and having the desired pH;

a3. Optionally, cooling the first volume of the aqueous solution comprising the gas dissolved therein and having the desired pH, so as to reach a temperature below 10°C;

a4. While preventing of the aqueous solution from becoming depleted in the hydrophobic gas, preferably by bubbling the gas through the aqueous solution, and, optionally, while maintaining the aqueous solution at a temperature below 10°C, adding the surfactant to obtain the first volume of the aqueous solution comprising the gas dissolved therein, the surfactant dissolved therein, and having the desired pH.

A desired pH is below 6, in particular comprised between 1.5 and 5, more particularly comprised between 2 and 4.

Preferably, in the method according to the invention, step b) starts less than 30 s after the surfactant has been added.

Surprisingly, in the embodiments of the method of the invention where an oligosaccharide, a polysaccharide, or a derivative thereof, is comprised in the first volume of aqueous solution of step a), it has been observed that the bubbles having a polymeric shell obtained showed better incorporation of the oligosaccharide, polysaccharide, or derivative thereof, when step b) starts less than 30 s after the surfactant has been added.

Preferably, in the method according to the invention, the saccharide is comprised in the aqueous solution before step a3, more preferably the saccharide is added to the aqueous solution before step a2, either before or after the acidification of step a1.

Preferably, in the method according to the invention, step d) comprises a step d1) of centrifugating the aqueous solution obtained after steps b) and c) and separating the bubbles having a polymeric shell from the rest of the aqueous solution, for example, said centrifugation is performed at a relative centrifugal force (RCF) comprised between 0.01 and 1, more preferably between 0.05 and 0.2.

Preferably, in the method according to the invention, step d) comprises, after step d1), a step d2) of washing the separated bubbles having a polymeric shell on a sieve, more preferably using a sieve shaker, to obtain a suspension of the polymer-coated bubbles with a size smaller than the sieve opening, preferably the sieve opening is lower than 10 µm, more preferably lower than 5 µm.

Preferably, in the method according to the invention, the washing of step d2) is performed using a washing solution comprising water and less than 0.1%, preferably less than 0.05% by mass of a surfactant. In a preferred embodiment, said surfactant is the same as the surfactant comprised in the first volume of aqueous solution.

Preferably, in the method according to the invention, step d) comprises, after step d1) and, where applicable before step d2), a step d1bis) of resuspending the separated bubbles having a polymeric shell in the washing solution and reseparating the bubbles having a polymeric shell through centrifugation, for example, the centrifugation of step d1bis) is performed at a relative centrifugal force (RCF) comprised between 0.01 and 1, preferably between 0.05 and 0.2.

Preferably, in the method according to the invention, step d1bis) is performed at least two times.

Preferably, in the method according to the invention, step d) comprises, after the last one of steps d1), d1bis), and d2), where applicable, a step d3) of suspending the bubbles having a

polymeric shell in a storage solution, more preferably the storage solution is identical to the washing solution.

Preferably, in the method according to the invention, step d) comprises, after the last one of steps d1), d1bis), d2) and d3), where applicable, a step d4) of storing the suspension of the bubbles having a polymeric shell at a temperature of less than 10°C.

When stored in suspension in the storage solution at a temperature of less than 10°C, the bubbles obtained by the method of the invention are stable at least 6 weeks, as evidenced from size measurements.

Preferably, in the method according to the invention, the obtained bubbles having a polymeric shell have a smallest dimension of less than 10 µm, more preferably less than 7 µm, even more preferably less than 5 µm.

For example, bubbles having a polymeric shell having a smallest dimension of less than 10 µm can be obtained by using a sieve having a sieve opening of less than 10 µm, for example as in step d2).

For biomedical applications, it is generally required that the smallest dimension of the bubbles remains below 10 µm so that they do not block blood flow when they are administered intravenously.

Preferably, in the method according to the invention, the obtained bubbles having a polymeric shell have a volume-weighted mean diameter (Dv(50)) below 4 µm, for example comprised between 1 µm and 4 µm, as measured by laser light scattering using the Mie model assuming that the solvent is water with a refraction index of 1.330 and that the bubbles are spherical polystyrene latex particles with a refraction index of 1.590 and an extinction coefficient (imaginary part of the complex refractive index) of 0.010.

Another object of the present invention are bubbles obtainable by the method of the invention.

Preferably the bubbles obtainable by the method of the invention are spherical.

In some embodiments, the bubbles obtainable by the method of the invention can be used in a method of treatment and/or of diagnosis. For example, they can be used as a contrast agent in a method of diagnosis. In another example, they can be used in sonothrombolysis.

EXAMPLES

Bubble size measurements

The size of the bubbles is measured thanks to a laser diffraction particle size analyzer (Mastersizer 3000, Malvern Instruments).

For analysis, the Mie model is used assuming that the solvent is water with a refraction index of 1.330 and that the bubbles are spherical polystyrene latex particles with a refraction index of 1.590 and an extinction coefficient (imaginary part of the complex refractive index) of 0.010. The analysis yields values for the surface-weighted mean diameter (D[3,2]), the volume weighted mean diameter (D[4,3]), the Dv(10), the Dv(50) and the Dv(90) (the point in the size distribution, up to and including which, 10%, respectively 50%, resp. 90% of the total volume of material in the sample is contained).

Although these values for the optical properties of the bubbles are not accurate, the result of the analysis is still useful for comparison purposes. For example, the measurements can be reproduced over 6 weeks which demonstrate the shelf-stability of the bubbles. Moreover, the value obtained for the median particle size by volume (Dv(50)) is close to the diameter observed by scanning electron microscopy or by optical microscopy (see Figures 1 and 2).

Bubble concentration measurement

The bubble concentration is expressed in number of bubbles per mL and is measured with image analysis. Briefly, a diluted solution of bubbles is injected into a hemocytometer (counting chamber device for cell counting) and pictures are taken with an optical microscope (Zeiss). Bubbles are isolated thanks to ImageJ thresholding and three small squares are averaged for each sample allowing an evaluation of the mean concentration with count extrapolation.

Example 1: Synthesis of bubbles having a poly(isobutyl cyanoacrylate) (PIBCA) shell according to the invention.

50 mL of an aqueous solution are prepared with water and HCl 1M to reach a pH of 2.5. 500 µL of Tween 20 are added to the aqueous solution. A perfluorobutane (PFB) tank is connected to the aqueous solution with a polyethylene catheter (Bioseb Lab Instruments) and PFB is bubbled through the solution. Meanwhile, 700 µL of isobutyl cyanoacrylate (IBCA) are loaded into a 1 mL syringe and placed onto a syringe pump (AL-300, World Precision Instrument, Florida, USA). The aqueous solution is then placed in ice, under the sonotrode (model 101-148-070, Branson Ultrasonic™; diameter of the tip: 3 mm) of a sonicator (Sonifier™ SFX 550, Branson Ultrasonic™) with the tip of the sonotrode centered relative to the aqueous solution and with half of a centimeter of the tip plunged into the aqueous solution. The IBCA is connected to the aqueous solution with a polyethylene catheter (Bioseb Lab Instruments). The amplitude of vibration of the tip is set at 243 µm. The sonicator is turned on in continuous mode, producing sound waves with a frequency of 20 kHz for 20 min, and the IBCA is injected at a controlled speed of 0.45 mL/min about 30 seconds after the sonication begins.

The obtained foam is centrifuged 3 times at 0.1 relative centrifugal force (RCF) in 50 mL Falcon™ tubes for 20 min, and a solution of 0.02% Tween 20 is used to resuspend the floating bubbles. The bubbles are then washed through a 5 µm sieve using a sieve shaker. The obtained suspension is stored at 5 °C in a 0.02% Tween 20 solution.

Example 2: Synthesis of bubbles having a PIBCA shell according to the invention.

The same procedure as example 1 is followed except that the amplitude of vibration of the tip is set at 369 µm and that the sound waves are applied for 10 min.

Example 3: Synthesis of bubbles having a PIBCA shell functionalized with polysaccharides according to the invention.

The same procedure as example 1 is followed except that 500 mg (1%) to 1 g (2%) of the polysaccharide are dissolved in the aqueous solution prior to adjusting its pH to 2.5, that the solution is put into a freezer for 15 min to cool its temperature down to 5°C before adding the Tween 20 and that the Tween 20 is added just before the beginning of the sonication.

Example 4 and 5: Synthesis of bubbles having a PIBCA shell functionalized with Nile red according to the invention.

The same procedures as examples 1 and 2, respectively, are followed except that the IBCA injected contained 30 µg of Nile red, added to the IBCA as a solution in acetone at 1 mg/mL.

Example 6: Effect of the duration and intensity of the acoustic cavitation.

The same procedure as example 1 is followed except for the duration and amplitude of the sonication, which are as described in Table 1. It can be seen that no bubbles are obtained when the duration of the sonication is of 5 minutes whereas for durations of 10 minutes and 20 minutes, stable bubbles are obtained with a high yield.

Table 1

Test No.	Duration (min)	Amplitude (µm)	Bubbles per mL	Dv(10) (µm)	Dv(50) (µm)	Dv(90) (µm)	Observations
4a	5	243	-	-	-	-	no stable bubble
4b	5	306	-	-	-	-	no stable bubble
4c	5	369	-	-	-	-	no stable bubble
4d	5	431	-	-	-	-	no stable bubble
2	**10**	**369**	$3.2 \cdot 10^{10}$	0.35	2.91	6.01	bubbles are stable
1	**20**	**243**	$2.5 \cdot 10^{10}$	0.37	3.27	6.40	bubbles are stable

CLAIMS

1. Method for manufacturing bubbles having a polymeric shell comprising the following steps:
    a) providing a first volume of an aqueous solution comprising a gas dissolved therein, a surfactant dissolved therein, and having a pH below 6, preferably comprised between 1.5 and 5, more preferably comprised between 2 and 4;
    b) in the aqueous solution, generating bubbles comprising the gas by applying sound waves to the aqueous solution;
    c) while generating the bubbles, adding a second volume of a cyanoacrylate monomer to the aqueous solution, thereby forming a suspension of the bubbles having a polymeric shell in the aqueous solution, wherein said polymeric shell is formed by polymerization of the cyanoacrylate monomer at the interface between the aqueous solution and the bubbles;
    d) recovering the bubbles having a polymeric shell;

    characterized in that the sound waves in step b) are applied during a period of at least 6 minutes, preferably between 8 and 30 minutes, more preferably between 15 and 30 minutes after the beginning of the addition of the cyanoacrylate monomer.

2. The method according to claim 1, wherein the gas dissolved in the solution has a molar mass of at least 100 g/mol, preferably of at least 200 g/mol.

3. The method according to claim 1 or 2, wherein the gas dissolved in the solution has a density at 20°C and 1013 mbar of at least 7 kg/m^3, preferably at least 9 kg/m^3.

4. The method according to any one of claims 1 to 3, wherein the gas dissolved in the solution is selected from the group consisting of alkanes, fluoroalkanes, and mixtures thereof, preferably wherein the gas dissolved in the solution is a perfluoroalkane or a mixture of perfluoroalkanes, preferably wherein the gas dissolved in the solution is perfluorobutane.

5. The method according to any one of claims 1 to 4, wherein the amount of the gas dissolved in the aqueous solution is maintained over 0.5 mg/L throughout steps b) and c), preferably wherein the aqueous solution is saturated with said gas throughout steps b) and c).

6. The method according to any one of claims 1 to 5, wherein the gas dissolved in the aqueous solution is bubbled through the aqueous solution during steps b) and c), preferably wherein the gas dissolved in the aqueous solution is bubbled through the aqueous solution throughout steps b) and c).

7. The method according to any one of claims 1 to 6, wherein the surfactant is a nonionic surfactant, for example a polysorbate, a poloxamer, an octylphenol, a nonylphenol, an ethoxylated fatty alcohol, a macrogol-glycerol ester, or a mixture thereof.

8. The method according to any one of claims 1 to 7, wherein the surfactant has a hydrophilic-lipophilic balance comprised between 8 and 18, preferably comprised between 10 and 18, more preferably comprised between 12 and 18.

9. The method according to any one of claims 1 to 8, wherein the amount of surfactant in the first volume of the aqueous solution of step a) is of at least 10 times the critical micelle concentration (CMC) of said surfactant, preferably of at least 50 times the CMC of said surfactant.

10. The method according to any one of claims 1 to 9, wherein a source of the sound waves is plunged in the aqueous solution

11. The method according to any one of claims 1 to 10, wherein the sound waves are not applied in pulsed mode, preferably wherein the time interval between two periods of application of the sound waves is lower than 10 seconds, more preferably the sound waves are applied continuously in one time.

12. The method according to any one of claims 1 to 11, wherein the source of the sound waves vibrates at an amplitude comprised between 50 µm and 500 µm, preferably between 100 µm and 500 µm, more preferably between 200 µm and 400 µm.

13. The method according to any one of claims 1 to 12, wherein the frequency of the sound waves is comprised between 10 kHz and 100 kHz, preferably between 15 kHz and 50 kHz.

14. The method according to any one of claims 10 to 13, wherein an emitting surface of the source of the sound waves plunged in the aqueous solution is of at least 1 mm^2 per 10 mL of the aqueous solution.

15. The method according to any one of claims 1 to 14, wherein the second volume of the cyanoacrylate monomer corresponds to at least 0.01 vol.%, preferably between 0.5 vol.% and 5 vol.%, of the first volume of the aqueous solution.

16. The method according to any one of claims 1 to 15, wherein the cyanoacrylate monomer is an alkyl cyanoacrylate monomer, preferably wherein said alkyl group comprises from 2 or 8 carbon atoms, more preferably wherein said alkyl group is a n-butyl or isobutyl group.

17. The method according to any one of claims 1 to 16, wherein the first volume of aqueous solution of step a) further comprises a saccharide or a derivative thereof, for example an oligosaccharide, a polysaccharide, or a derivative thereof, so as to produce the bubbles having a polymeric shell wherein the saccharide or derivative thereof is copolymerized with the cyanoacrylate monomer, preferably said saccharide or derivative thereof is present in the first volume of aqueous solution of step a) in an amount of 0.1 to 4% by weight relative to the weight of the first volume of aqueous solution.

18. The method according to claim 17, wherein the saccharide or derivative thereof is selected from the group consisting of fucoidans, dextrans, mannans, derivatives of fucoidans, derivatives of dextrans, derivatives of mannans, and mixtures thereof.

19. The method according to any one of claims 1 to 18, wherein the first volume of aqueous solution of step a) and/or the second volume of the cyanoacrylate monomer added in step c) further comprise a fluorescent probe so as to yield polymer-coated

bubbles comprising the fluorescent probe, preferably said fluorescent probe is present in an amount of 0.1 to 40 ppm by weight relative to the weight of the first volume of aqueous solution.

20. The method according to any one of claims 1 to 19, wherein a fluorescent probe is incorporated in the bubbles having a polymeric shell, after steps b) and c) or at any later stage in the method, by adding said fluorescent probe to a suspension of the bubbles having a polymeric shell.

21. The method according to any one of claims 1 to 20, wherein steps b) and c) are performed while maintaining the temperature of the aqueous solution below 60°C, preferably below 35°C.

22. The method according to claim 21, wherein the first volume of aqueous solution just before step b) preferably has a temperature below 10°C.

23. The method according to any one of claims 1 to 22, wherein the first volume of the aqueous solution is obtained by the following steps:

a1. acidifying a volume a0 of an aqueous solution with a strong inorganic acid, such as HCl, H_2SO_4, or HNO_3, to obtain the first volume of the aqueous solution having a pH below 5;

a2. dissolving the gas in the first volume of the aqueous solution to obtain the first volume of the aqueous solution comprising the gas dissolved therein and having a pH below 5;

a3. optionally, cooling the first volume of the aqueous solution comprising the gas dissolved therein and having a pH below 5, so as to reach a temperature below 10°C;

a4. while preventing of the aqueous solution from becoming depleted in the hydrophobic gas, preferably by bubbling the hydrophobic gas through the aqueous solution, and, optionally, while maintaining the aqueous solution at a temperature below 10°C, adding the surfactant to obtain the first volume of the aqueous solution comprising the gas dissolved therein, the surfactant dissolved therein, and having a pH below 5;

24. The method according to claim 23, wherein the saccharide is comprised in the aqueous solution before step a3, preferably wherein the saccharide is added to the aqueous solution before step a2, either before or after the acidification of step a1.

25. The method according to any one of claims 1 to 24, wherein step b) starts less than 30 s after the surfactant has been added.

26. The method according to any one of claims 1 to 25, wherein step d) comprises a step d1) of centrifugating the aqueous solution obtained after steps b) and c) and separating the floating bubbles having a polymeric shell from the rest of the aqueous solution obtained after steps b) and c), preferably said centrifugation is performed at a relative centrifugal force (RCF) comprised between 0.01 and 1, more preferably between 0.05 and 0.2.

27. The method according to claim 26, wherein step d) comprises, after step d1), a step d2) of washing the separated bubbles having a polymeric shell on a sieve to obtain a suspension of the bubbles having a polymeric shell with a size smaller than the sieve opening, preferably the sieve opening is lower than 10 µm, more preferably lower than 5 µm.

28. The method according to claim 27, wherein the washing of step d2) is performed using a washing solution comprising water and less than 0.1%, preferably less than 0.05% by mass of a surfactant.

29. The method according to any one of claims 26 to 28, wherein step d) comprises, after step d1) and, where applicable, before step d2), a step d1bis) of resuspending the separated bubbles having a polymeric shell in the washing solution and reseparating the bubbles having a polymeric shell through centrifugation, preferably the centrifugation of step d1bis) is performed at a relative centrifugal force (RCF) comprised between 0.01 and 1, even more preferably between 0.05 and 0.2.

30. The method according to claim 29, wherein step d1bis) is performed at least two times.

31. The method according to any one of claims 26 to 30, wherein step d) comprises, after the last one of steps d1), d1bis) and d2), where applicable, a step d3) of suspending the bubbles having a polymeric shell in a storage solution, preferably the storage solution is identical to the washing solution.

32. The method according to any one of claims 26 to 31, wherein step d) comprises, after the last one of steps d1), d1bis), d2) and d3), where applicable, a step d4) of storing the suspension of the bubbles having a polymeric shell at a temperature of less than 10°C.

33. The method according to any one of claims 1 to 32, wherein the obtained bubbles having a polymeric shell have a smallest dimension of less than 10 µm, preferably less than 7 µm, even more preferably less than 5µm.

34. The method according to any one of claims 1 to 33, wherein the obtained bubbles having a polymeric shell have a median diameter by volume below 4 µm, preferably comprised between 1 and 4 µm, as measured by laser light scattering using the Mie model assuming that the solvent is water with a refraction index of 1.330 and that the bubbles are spherical polystyrene latex particles with a refraction index of 1.590 and an extinction coefficient of 0.010.

35. Bubbles obtainable by the process according to any one of claims 1 to 34.

36. Bubbles according to claim 35, said bubbles being spherical.

37. Bubbles according to claim 35 or 36 for use in a method of treatment and/or diagnosis.

38. Bubbles according to claim 37 for use as a contrast agent in a method of diagnosis.

39. Bubbles according to claim 37 for use in sonothrombolysis.

ABSTRACT

The invention relates to an improved method for the manufacturing of bubbles having a polycyanoacrylate shell using sound waves for generating the bubbles. It has been found that the application of sound waves for at least 6 minutes in combination with the choice of a specific pH was critical to produce stable bubbles with a high yield. The bubbles produced by the method of the invention have an improved sphericity compared to the bubbles obtained with the methods of the prior art and are obtained in shorter times. With the method of the invention, the bubbles can be functionalized with fluorescent probes or with polysaccharides, which can confer targeting properties to the bubbles. Such bubbles can be used as contrast agents for ultrasound imaging or for sonothrombolysis.

FIGURE 1

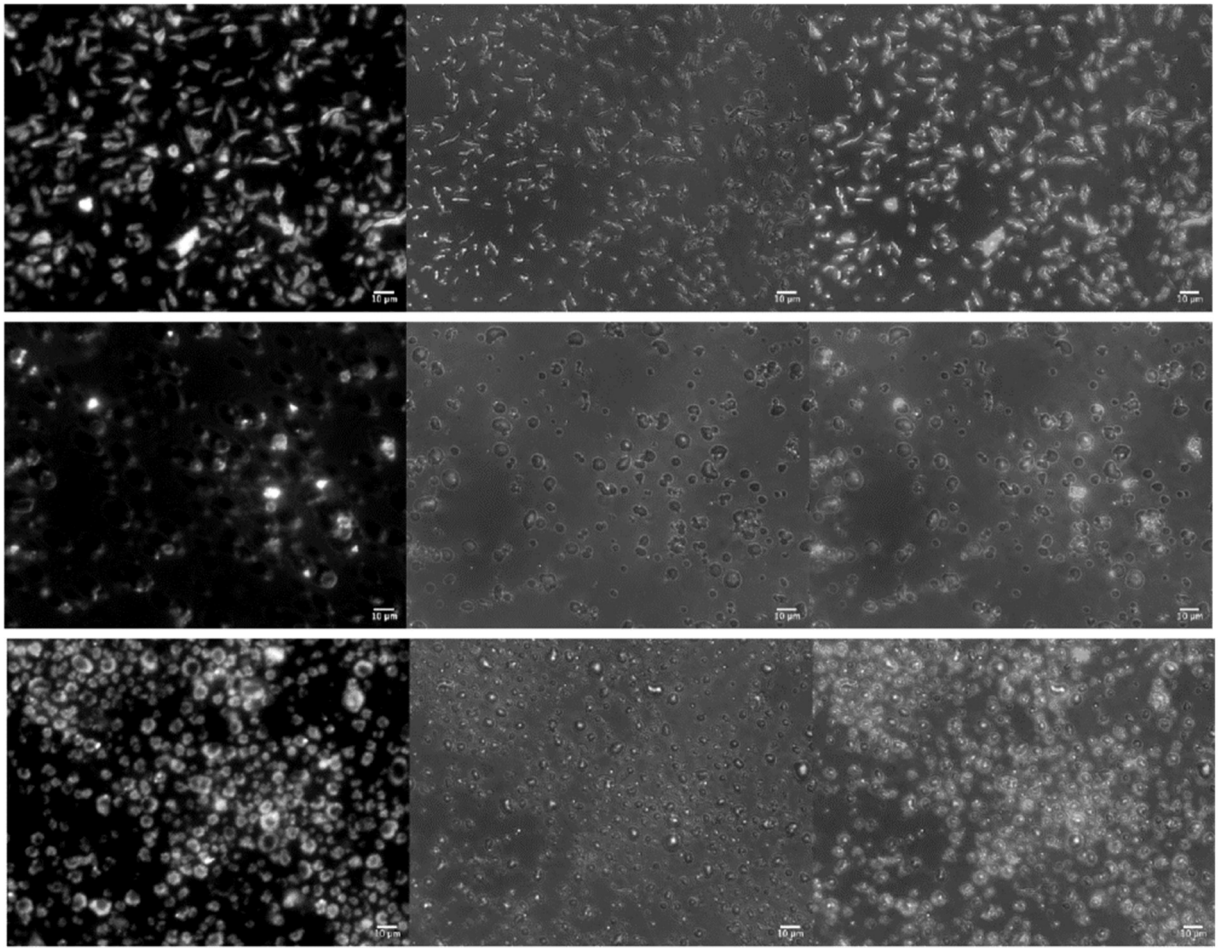

FIGURE 2

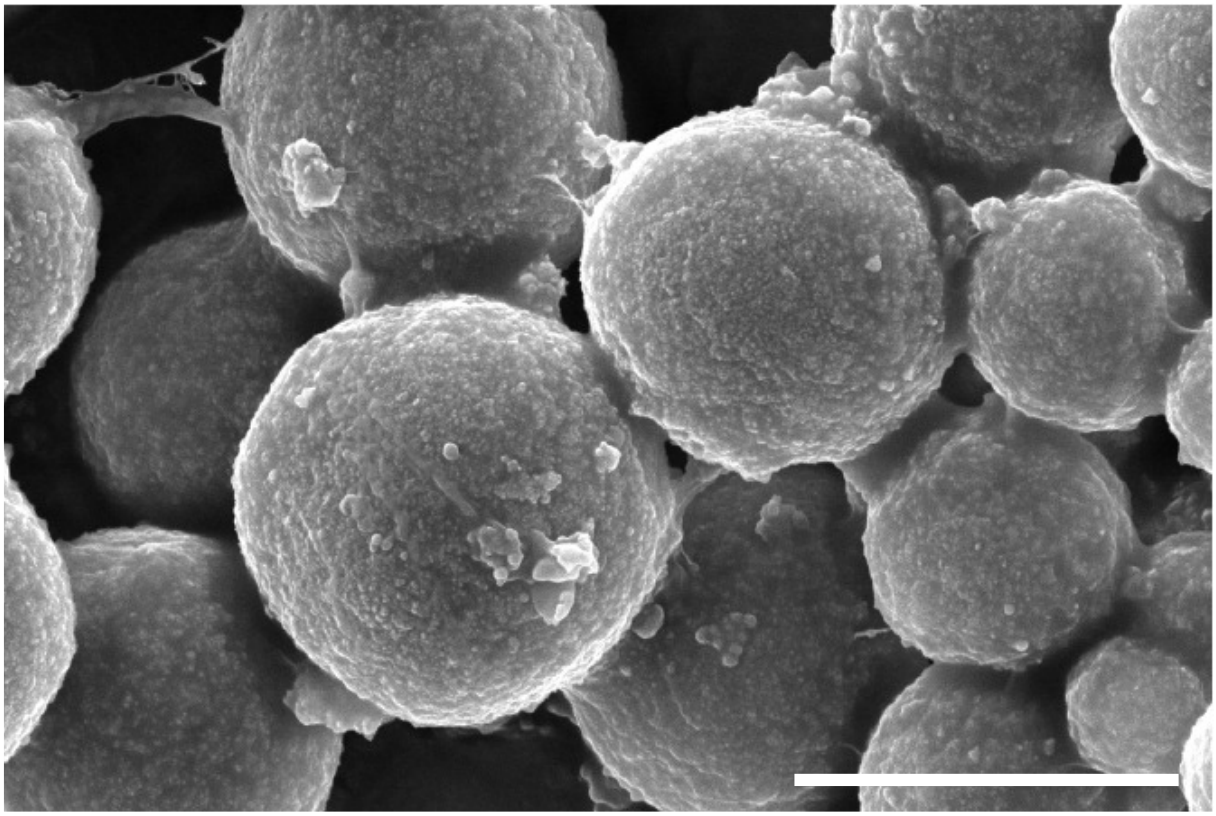

PCT

13-1-1	Applicant Remarks	La demande internationale est en langue anglaise. Nous demandons que l'OMPI soit Office récepteur et nous donnons l'autorisation de débiter notre compte n° 3200 de la taxe de transmission d'un montant de 62€.

13-2-1	Validation messages Request	Yellow Language of the request is not a language accepted by the receiving Office selected; the application will be transmitted to the International Bureau as receiving Office under PCT Rule 19.4
	Validation messages Request	Green? Please note that the entire request (including the title of invention) must be in English
	Validation messages Request	Green? The title of the invention shall be short and precise. Please verify.
13-2-3	Validation messages Names	Green? Applicant 1: Name should preferably be entered in capital letters. Please verify.
	Validation messages Names	Green? Applicant 1:Telephone No. missing
	Validation messages Names	Green? Applicant 1: no e-mail address has been indicated. Please verify.
	Validation messages Names	Green? Applicant 1:State of Residence missing
	Validation messages Names	Green? Applicant 2:State of Residence missing
	Validation messages Names	Green? Agent 1: Name should preferably be entered in capital letters. Please verify.
13-2-4	Validation messages Priority	Green? No priority of an earlier application has been claimed. Please verify
13-2-7	Validation messages Contents	Green? Figure of the drawings which should accompany the abstract not specified. Please verify.
13-2-8	Validation messages Fees	Green? Please verify that modified fee amounts are correct.
13-2-9	Validation messages Payment	Green? Please ensure that you have a valid deposit account with the receiving Office selected.

PCT

13-2-10	**Validation messages Annotate**	**Green? All indications that can be made on the Request form are specifically provided for by the software. Please confirm validity of additional indication.**

ANNEX 4

Biomaterials

rtPA-loaded fucoidan polymer microbubbles for the targeted treatment of stroke

--Manuscript Draft--

Manuscript Number:	
Article Type:	FLA Original Research
Keywords:	Microbubbles; Fucoidan; Fibrinolytic; Ultrasound; Targeted thrombolysis; Stroke
Corresponding Author:	Cedric CHAUVIERRE, Dr INSERM U1148: Laboratoire de Recherche Vasculaire Translationnelle Paris, FRANCE
First Author:	Louise FOURNIER
Order of Authors:	Louise FOURNIER
	Myriam ABIOUI-MOURGUES
	Georges CHABOUH
	Rachida AID
	Thibault de La TAILLE
	Olivier COUTURE
	Cyrille ORSET
	Cedric CHAUVIERRE, Dr
Abstract:	Systemic injection of thrombolytic drugs is the gold standard treatment for non-invasive blood clot resolution. The most serious risks associated with the intravenous injection of tissue plasminogen activator-like proteins are the bleeding complication and the dose related neurotoxicity. Indeed, the drug has to be injected in high concentration since it has a short half-life, due to the presence of its natural blood inhibitor (PAI-1) and fast hepatic clearance (0.9 mg/kg in humans, 10 mg/kg in mouse models). Overall, there is a serious need for a dose reduced targeted treatment to overcome those issues. We present in this article a new acoustic cavitation-based method for polymer MBs synthesis, three times faster than current method. The generated MBs were ultrasound responsive, stable and biocompatible. Their functionalization enabled the efficient and targeted treatment of stroke, without side effects. First, the stabilizing shell of those MBs is composed of Poly-Isobutyl Cyanoacrylate (PIBCA), copolymerized with fucoidan. Widely studied for its targeting properties, fucoidan exhibit a nanomolar affinity for activated endothelium and activated platelets (P-selectins). Second, the thrombolytic agent (rtPA) was loaded onto microbubbles (MBs) with a simple adsorption protocol. Hence, the present study validated the in vivo efficiency of rtPA-loaded Fuco MBs to be over 50% more efficient than regular free rtPA injection for stroke resolution. In addition, the relative injected rtPA grafted onto targeting MBs was 1/10th of the standard effective dose (1 mg/kg in mouse). As a result, no hemorrhagic event, BBB leakage nor unexpected tissue distribution were observed. The echogenic targeting MBs produced in this work now bring promising perspective for the development of US molecular imaging of thrombotic diseases and the US assisted clot resolution: sonothrombolysis.

Powered by Editorial Manager® and ProduXion Manager® from Aries Systems Corporation

Cover Letter
Click here to access/download;Cover Letter;Cover letter Louise FOURNIER - Biomaterials.docx

Paris, january 13, 2023

Dear Editor,

Please find enclosed the manuscript entitled "**rtPA-loaded fucoidan polymer microbubbles for the targeted treatment of stroke**" to be considered for publication in Biomaterials.

Ischemic stroke, myocardial infarction and venous thromboembolism are the main causes of death worldwide. Treatment of acute thrombotic events remains a challenge. Indeed, less than 5% of patients are injected with the standard thrombolytic drug, because of serious side effects associated with the treatment. It is thus important to develop innovative solutions for more efficient and safer thrombolysis with biocompatible thrombus-targeted treatment. In this work, polymer microbubbles were designed with a new green chemistry protocol of acoustic cavitation, firstly described in this article. Microbubbles were functionalized with fucoidan that has a nanomolar affinity for the thrombus biomarker P-selectin and already used in clinical trials for molecular imaging of thrombotic diseases. Alteplase was loaded onto these ultrasound responsive microbubbles and the thrombolytic efficacy of the drug loaded targeting product was successfully validated in a murine model of acute ischemic stroke. This is a proof-of-concept study of the high potential of an efficient targeted treatment of acute thrombotic events, such as ischemic stroke. This work also brings promising perspectives for the application of targeted microbubbles in molecular ultrasound imaging.

We believe that this research article focused on the hot topics of biomaterial approaches with a translational potential for a major health issue would be of interest to the interdisciplinary audience of your highly ranked journal.

All co-authors agree with the contents of the manuscript and there is no financial interest to report. We certify that the submission is an original unpublished work and it has not been submitted to any other journal for review.

Hoping that you will find this work of interest, we are looking forward to hearing from you.

Yours sincerely,

Dr. Cédric Chauvierre
Inserm, U1148, LVTS, Université Paris Cité, CHU X. Bichat, F-75877, Paris, France
E-mail address: cedric.chauvierre@inserm.fr
Tel: (33) 1 4025 8600; Fax: (33) 1 4025 8602

Manuscript

Click here to access/download;Manuscript;Biomaterials - Louise FOURNIER.docx

Click here to view linked References

rtPA-loaded fucoidan polymer microbubbles for the targeted treatment of stroke

Louise FOURNIER[1], Myriam ABIOUI-MOURGUES[2], Georges CHABOUH[3], Rachida AID[1,4], Thibault DE LA TAILLE[1], Olivier COUTURE[3], Cyrille ORSET[2] and Cédric CHAUVIERRE[1*]

[1]Université Paris Cité, Université Sorbonne Paris Nord, UMR-S U1148 INSERM, Laboratory for Vascular Translational Science (LVTS), F-75018 Paris, France

[2]Normandie Université, UNICAEN, INSERM UMR-S U1237, Physiopathology and Imaging of Neurological Disorders (PhIND), GIP Cyceron, Institut Blood and Brain @ Caen-Normandie (BB@C), 14000, Caen, France.

[3]Sorbonne Université, CNRS, INSERM, Laboratoire d'Imagerie Biomédicale, Paris, France

[4]Université Paris Cité, UMS 34, Fédération de Recherche en Imagerie Multi-modalité (FRIM), INSERM, F-75018 Paris, France

[*]Corresponding author: Cédric CHAUVIERRE
Email address: cedric.chauvierre@inserm.fr

Abstract

Systemic injection of thrombolytic drugs is the gold standard treatment for non-invasive blood clot resolution. The most serious risks associated with the intravenous injection of tissue plasminogen activator-like proteins are the bleeding complication and the dose related neurotoxicity. Indeed, the drug has to be injected in high concentration since it has a short half-life, due to the presence of its natural blood inhibitor (PAI-1) and fast hepatic clearance (0.9 mg/kg in humans, 10 mg/kg in mouse models). Overall, there is a serious need for a dose reduced targeted treatment to overcome those issues. We present in this article a new acoustic cavitation-based method for polymer MBs synthesis, three times faster than current method. The generated MBs were ultrasound responsive, stable and biocompatible. Their functionalization enabled the efficient and targeted treatment of stroke, without side effects. First, the stabilizing shell of those MBs is composed of Poly-Isobutyl Cyanoacrylate (PIBCA), copolymerized with fucoidan. Widely studied for its targeting properties, fucoidan exhibit a nanomolar affinity for activated endothelium and activated platelets (P-selectins). Second, the thrombolytic agent (rtPA) was loaded onto microbubbles (MBs) with a simple adsorption protocol. Hence, the present study validated the *in vivo* efficiency of rtPA-loaded Fuco MBs to be over 50% more efficient than regular free rtPA injection for stroke resolution. In addition, the relative injected rtPA grafted onto targeting MBs was 1/10th of the standard effective dose (1 mg/kg in mouse). As a result, no hemorrhagic event, BBB leakage nor unexpected tissue

distribution were observed. The echogenic targeting MBs produced in this work now bring promising perspective for the development of US molecular imaging of thrombotic diseases and the US assisted clot resolution: sonothrombolysis.

Keywords

Microbubbles; Fucoidan; Fibrinolytic; Ultrasound; Targeted thrombolysis; Stroke

Abbreviations

BBB: Blood Brain Barrier; BCA: Bicinchoninic Acid Assay; CMDex: Carboxymethyl Dextran; CVD: Cardiovascular Disease; DMEM: Dulbecco's Modified Eagle Medium; ESEM: Environmental Scanning Electron Microscopy; FIB: Focused Ion Beam; FTIR: Fourier-Transform InfraRed spectroscopy; GA: Gadoteric Acid; HUVEC: Human Umbilical Vein Endothelial Cell; LDH: Lactate DeHydrogenase; MB: Microbubble; MCA: Middle Cerebral Artery; MI: Mechanical Index; MTT: 3-(4,5-dimethyl-2thiazolyl)-2,5-diphenyl-2H-tetrazolium bromide; NET: Neutrophil Extracellular Trap; PAI-1: Plasminogen Activator Inhibitor-1; PFA: ParaFormAldehyde; PFB: PerFluoroButane; PIBCA: Poly-IsoButyl Cyanoacrylate; PRF: Pulse Repetition Frequency; RBC: Red Blood Cell; ROI: Region Of Interest; rtPA: recombinant tissue Plasminogen Activator; SD: Standard Deviation; US: UltraSound; VWF: Von Willebrand Factor; WB: Working Buffer; WHB: Whole Human Blood; WHO: World Health Organization; 3T3: Fibroblasts.

1. Introduction

The global burden of cardiovascular diseases (CVD) places them as the leading cause of mortality around the world. Among those, thrombotic diseases including ischemic heart disease and stroke are the most prevalent and described as the main cause of disability [1]. Every year, 15 million of new cases of stroke are reported according to the World Health Organization (WHO). The prevalence of stroke increases with age with the highest rates typically occurring in people over the age of 75. Stroke is also more common in women, and is more prevalent in certain regions of the world, such as Southeast Asia and sub-Saharan Africa, compared to other region [2]. Overall, the prevalence of stroke is expected to continue to increase in the coming years due to the aging of global population and the increasing of risk factors such as

high blood pressure, diabetes, and obesity. In medical terms, ischemic stroke is defined as the obstruction of vasculature in the brain caused by a thrombus. Those blood clots are highly heterogenous and composed of a variety of cell types [3] including erythrocytes, immune cells and platelets, with the addition of Von Willebrand Factor (VWF) and Neutrophil Extracellular Traps (NETs), tied together by a strong fibrin mesh [4]. Physiologically needed to repair impaired vessel walls, their pathological formation and their circulation in the bloodstream can lead to flow obstruction and distal tissue ischemia if the vessel recanalization is not quickly supported. Patients undergoing stroke event are treated with the gold standard systemic injection of a thrombolytic drug [5] in order to disassemble the fibrin mesh. There are several different types of “clot busters” used depending on their application (myocardial infarction, pulmonary embolism, stroke…) but there are mainly plasminogen activator like (Alteplase: rtPA, Reteplase: rPA, Tenecteplase: TNK) [6]. Indeed, this serine protease is naturally present in the body [7] allowing the cleavage of plasminogen into plasmin, responsible for fibrin degradation in homeostatic regulation. This thrombolytic injection can also be associated to mechanical thrombectomy [8] with the limitation of it being an invasive procedure. In addition, the systemic injection of the thrombolytic drug brings several drawbacks like hemorrhagic transformation [9] and neurotoxicity [10] with a recanalization rate below 50% [11]. To overcome those issues, the strategy to encapsulate rtPA has been explored with different carriers from nanoparticles [6] to microbubbles [12] with the common objective to reduce drug doses and improve the treatment efficiency. Besides drug encapsulation, nanomedicine is also focusing on targeted drug delivery on identified biomarkers. In thrombotic diseases, they are mainly described on activated platelets [13] with P-selectins, GPIIb/IIIa integrins and phosphatidylserines or with circulating molecules like Factor XIII, VWF and fibrin [6]. We focused here on the highly specific interaction between P-selectins expressed on activated platelets or activated endothelium [14] and a sulfated polysaccharide: the fucoidan [15,16]. Their nanomolar affinity [17] makes the fucoidan a very promising targeting agent for thrombotic diseases and already showed its performance *in vivo* [18],[19]. The present strategy relies on polymer microbubbles (MBs) for their carrier ability but also their imaging property and treatment enhancement perspectives. Indeed, microbubbles are widely used as clinical contrast agent (Definity®, Sonovue®…) for US imaging due to their intrinsic echogenic properties [20] and have also been of main interest for the

development of sonothrombolysis [21]. We present in this work, the innovative synthesis of polymer microbubbles via acoustic cavitation, never described in the literature yet and recently patented (PCT/FR2022/050309). Indeed, the use of US for MBs generation was only used for protein shelled MBs [22] or as a side step for lipid shell MBs [23]. This new method improved the yield of polymer MBs synthesis and reduce the synthesis time by 3 compared to standard polymer MBs synthesis with hydrodynamic cavitation.

Functionalized with fucoidan as a targeting agent and rtPA-loaded, these fully competent MBs were studied for the targeted treatment of thrombotic diseases (*Fig. 1*). We characterized those new MBs in terms of stability, biocompatibility, echogenicity, targeting property and thrombolytic activity. Then, in order to validate the efficacy of the treatment, we performed a mouse stroke model and compared gold standard treatment to drug-loaded targeted MBs by measuring the ischemic lesion reduction after 24 hours with MRI imaging. Overall, this paper gives interesting perspectives for the use of drug-loaded targeted polymer MBs for the treatment of thrombotic diseases.

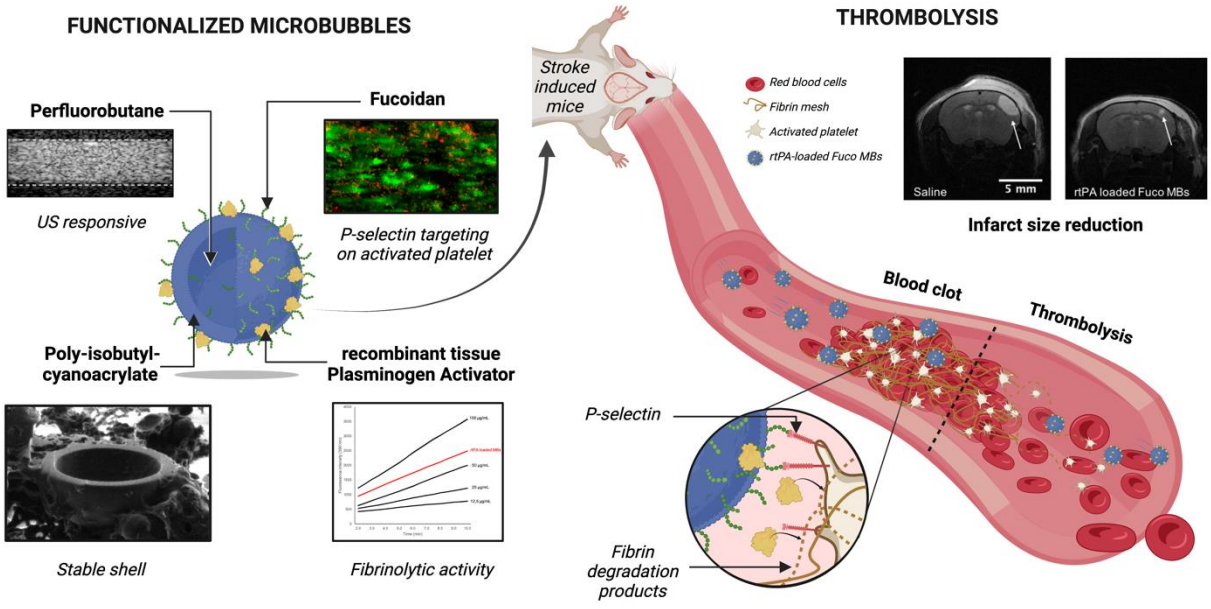

Figure 1: Graphical abstract of functionalized MBs for the treatment of stroke. MBs are composed of a stable poly-isobutyl cyanoacrylate (PIBCA) shell with a perfluorobutane (PFB) gas core enabling US imaging. Their functionalization was validated for P-selectin targeting with fucoidan and for thrombolytic activity with recombinant tissue Plasminogen Activator (rtPA) loading. After in vitro validation, rtPA-loaded targeting MBs were injected in a mouse stroke model to improve thrombolysis recanalization compared to systemic injection of the drug. Fucoidan targeting onto activated platelet P-selectins allowed a specific delivery of rtPA to induce local fibrin degradation. The targeted delivery improved the treatment outcome by reducing the infarcted area after 24h as observed with MRI imaging.

2. Materials and methods

Materials: Isobutyl cyanoacrylate (IBCA) monomers were purchased from Afinitica Technologies (Barcelona, Spain). Carboxymethyl dextran 40 (CMDex) was provided from TdB Labs (Uppsala Sweden). Sulfated polysaccharide fucoidan (Mn = 18 kDa Mw = 104 kDa) was obtained from Algues et Mer (Ouessant, France). Surfactant Tween 20 was purchased from Sigma Aldrich as well as the Rhodamine B fluorochrome. Perfluorobutane (PFB) was obtained from F2 Chemicals (Preston, UK).

Polymer MBs synthesis

Poly-isobutyl cyanoacrylate (PIBCA) microbubbles were obtained from the anionic polymerization of IBCA monomer at the water gas interface. Briefly, 50 mL of an aqueous solution was prepared with HCl 1M to reach a pH of 2.5. This solution was saturated with perfluorobutane for 10 min and put into a freezer for 15 min to cool it down. Meanwhile, 700 µl of IBCA solution was loaded into a 1 mL syringe and placed onto a syringe pump (AL-300, World Precision Instrument, Florida, USA). The aqueous solution was then placed on ice, under the microtip of the Sonifier (SFX 550, BRANSON Ultrasonic Corp, Danbury, USA) so the tip is centered and half of a centimeter plunged into the aqueous solution. The organic solution and the PFB tank were connected into the aqueous solution with polyethylene catheters (Bioseb Lab Instrument, Salon de Provence, France). Just before the insonation, 500 µL of Tween 20 detergent was added drop by drop into the aqueous phase. The Sonifier was turned on for 20 min at 30% of amplitude and the IBCA was injected at a controlled speed of 0.45 mL/min. For the MBs containing polysaccharide, 1 g (2% w/w) was dissolved at the first step of synthesis into the aqueous solution giving fucoidan MBs (Fuco MBs) or carboxymethyl dextran MBs (CMDex MBs) used here as a non-targeting polysaccharide control. Similarly, for the fluorescent MBs, 500 µg of Rhodamine B was added in the first step of the aqueous phase preparation.

The obtained foam was centrifuged 3 times at 0.1 g in 50 mL falcon tubes for 20 min, and a solution of 0.02% Tween 20 was used to resuspend the floating MBs. MBs are then filtered through a 5 µm sieve using a sieve shaker. The obtained suspension was stored at 5 °C in a 0.02% Tween 20 solution. For all experiment requiring fluorescence microscopy visualization, MBs were labelled with Rhodamine B.

MBs concentration, size and zeta potential measurements

MBs concentration is expressed in MBs/mL and measured with image analysis. Briefly, a diluted suspension of MBs was injected into a Malassez cell and imaged with an optical microscope (10x objective, Axio Observer, Zeiss). Counting was performed with ImageJ thresholding of MBs signal allowing an evaluation of the mean concentration with count extrapolation. MBs' size was measured with a Mastersizer 3000 (Malvern Instruments, UK), in water and flow speed of 1500 rpm. For each sample the 10^{th}, 50^{th} and 90^{th} percentile of size in volume (Dv10; Dv50; Dv90) were collected. The measurements were reproduced over the weeks to validate the shelf stability. Zeta potential was measured with electrophoretic light scattering method (Nano ZS, Malvern Instrument, UK). Briefly, MBs were diluted to 1/10 in a KCl 1 mM solution and added to the chamber allowing surface charge measurement, each sample was measured three times and averaged.

FTIR analysis

Fourier-transform infrared spectroscopy (FTIR) spectrums were measured using a Thermo Nicolet AVATAR 370 FTIR spectrometer (Thermo Electron Corporation, Waltham, MA). The lyophilized samples were blended with KBr (1% mass) and compressed to obtain a pellet. Transmission spectra were acquired between 4000 cm^{-1} and 400 cm^{-1}.

Confocal Imaging and Scanning Electron Microscopy

Confocal imaging was performed with Zeiss LSM 780 microscope in phase contrast or filtered for Rhodamine B MBs observation. Environmental Scanning Electron Microscopy (ESEM, Philips XL30, ESEM-FEG, Amsterdam, Netherland) images were performed with the following parameters: HV 10 kV, WD 13.7 mm, pressure $2.50e^{-4}$ Pa and magnification from 2500 to 10000 x. To evaluate the internal structure of the MBs, Focused Ion Beam (FIB) assisted Scanning Electron Microscopy (SEM, Aquilos™ Cryo-FIB, Thermofisher Scientific) was used to cut through the MBs. Samples were deposited onto the SEM grid and dried with paper. The FIB parameters were defined with: HV 30 kV, current 0.10 nA and pressure $1.66e^{-4}$ Pa.

Fucoidan quantification with methylene blue dosage

Fucoidan sulfated groups can be recognized by methylene blue colorimetric assay like previously described [24]. On a grade 1 chromatography paper (Whatman®, GE Healthcare), squares of 1 cm^2 were drawn to delimit the samples. Standard solutions of fucoidan MMW (Algues & Mer, France) were prepared with a serial dilution from 0.5 to 0.3125 mg/mL and the negative control was prepared with a suspension of CMDex MBs. MBs suspension were hydrolyzed with an alkaline solution of NaOH (0.1 M) until no further accumulation at the surface. MBs suspension at a concentration of 1 x 10^{10} MBs/mL and standard samples were successively deposited 5 times 2 µL with an intermediate drying step at 50°C for 10min. Once dry, the paper was treated with a solution of Methanol/Acetone (6:4) for 3 minutes, then treated with the Methylene blue solution of Methanol/Acetone/Water (6:4:15) containing 0.1% (w/w) methylene blue and 50 mM HCl (1M) for 10 min. The paper was then washed with several bath of washing solution (Acetic acid/Methanol/Acetone/Water, 5:6:4:75) until the bath remains translucid. To help with the paper manipulation, it was left to dry under the hood. The drawn squared were then cut and placed in 1.5 mL Eppendorf tubes. 500 µL of 2% SDS methanol solution was incubated with the cut papers at 50°C for 15 min. Then, 200 µL of the tainted solution was then extracted to a 96 well plate and the absorbance was read at 663 nm. Fucoidan final concentration was determined with the linear regression of the standard solution curve.

US phantom model and US burst model

In vitro echogenic MBs properties were studied through a home-made setup. The US phantom employed was a tissue mimicking Doppler flow phantom (ATS Laboratories, CIRS) with a wall-less channel of 8 mm in diameter at 20 mm depth. US imaging were conducted using a medical probe, GE-L3-12-D (General Electrics; 256 elements, 0.2 mm pitch size) connected to a research ultrasound scanner, Vantage 256 (Verasonics, Kirkland, USA) and driven at 5 MHz center frequency. Amplitude modulation sequence used here (checkerboard) was programmed with Matlab (The MathWorks, Inc., Natick, MA). The *in vitro* acquisition consisted of 3 blocks of 200 images each, using a compounded framerate of 150 Hz and five angles (-4°; -2°; 0; 2°; 4°) pulse repetition frequency (PRF) of 3 kHz. Prior to the experiments, the emitted pressures of the probe were measured and calibrated using a 0.2 mm needle hydrophone (Precision Acoustic, UK). Flow rate was modulated using butterfly valves

to stop the flow. The probe was positioned on top of wall-less phantom and various amplitude of signal (from 8 V to 17 V corresponding to Mechanical Index from 0.23 to 0.60) were evaluated to establish the burst threshold of the MBs, with a constant duty cycle of 67%. In that manner, MBs suspension flow was stopped to evaluate the signal before and after US insonation. The signal intensity was measured by image analysis with background noise subtraction.

rtPA incorporation onto MBs

Adsorption method was performed by rising the pH of the MBs suspension to 10 with NaOH 1M. 2 mL of suspension containing 10^{10} MBs at pH 10 was gently mixed with 500 µg of rtPA (Actilyse®, Boehringer) for 2 hours at 5°C. The mix was then placed in a 5 mL syringe with a closing cap and centrifuged for 20 min at 0.1 g. The undernatent was discharged and the mix was rinsed with the storage solution of 0.02 % Tween 20, 3 times. The stability of the incorporated drug was measured with the enzyme activity evaluation over 4 days with a washing step between each day.

Amidolytic activity of incorporated rtPA with PefaFluor® assay

The amidolytic activity of rtPA-loaded MBs was measured by recording the fluorescent signal of the degradation product of PefaFluor in contact with the serine protease. Briefly, 2.5 µL of the rtPA-loaded MBs were put in contact with 97.5 µL of working buffer (0.1 M HEPES, 0.05 % BSA, 0.9 % NaCl) in a 96 well plate. 10 µL of PefaFluor (Interchim, France) solution (1M) was added with a multi pipette and measurement of the fluorescence was performed with monochromatic spectrophotometer (TECAN, Infinite M200 PRO) at λ_{em} = 390, λ_{ex} = 440 during 70 min. A standard range was obtained by serial dilution of rtPA (Actilyse®, Boehringer) from 400 µg/mL to 6.25 µg/mL and negative control was obtained with Tween 0.02% solution. The kinetic of the fluorescent substrate generation is proportional to the concentration of the enzyme. The leading coefficients of the linear part of the standard curves were then used to established the linear regression of the concentration.

Fibrinolytic activity

rtPA ability to lyse fibrin was evaluated *in vitro*, comparing free rtPA to rtPA-loaded MBs on a fibrin gel model. The gel was prepared by mixing a fibrinogen solution

and a thrombin solution. A TRIS buffer (TRIS 0.1 M, NaCl 0.9%, pH 7.6) was prepared to mix the different component of the solutions. In two separated water baths, 5 mL of the fibrinogen solution (5 mg/mL, from Human plasma, Sigma Aldrich) was heated to 37°C while 5 mL of 3% low melting agarose (Thermo Scientific) was heated to 65°C. Once agarose has reached its melting temperature, the solution was cooled down to 37°C and 2.5 U of thrombin (from Human plasma, Sigma Aldrich) was added. The two solutions were mixed and quickly poured into a 9 cm petri dish plate and left for gelation 30 min at 5°C. Holes were defined with a 3 mm punch and 5 µL of samples diluted to 1/15 were dropped where the gel was extracted. The set-up was placed at 37°C overnight and fibrin degradation rings were measured with Fiji software.

In vitro targeting flow experiment on human platelet aggregates

The specific binding of Fuco MBs on P-selectins expressed on activated platelet was evaluated with a microfluidic model [25]. Using the Vena8 Fluoro+ biochip (Cellix Ltd, Ireland). Microchannels were coated overnight with a 200 µg/mL solution of collagen type I at 4°C (equine tendon collagen, Collagen Reagens HORM®, Takeda). Whole human blood (WHB) was collected from healthy volunteers in 75 mM PPACK tubes, and platelets were stained with a DIOC6 solution of 50 µg/mL right before injection into the channel. DIOC6 specifically stains mitochondria membranes in living cells [26], excluding erythrocytes staining. For each channel, the following sequence was performed: channel washing with saline solution (NaCl 0.9 %) for 3 min at arterial flow rate (60 µL/min), WHB with DIOC6 injection at arterial flow rate up to 5 min until platelet aggregates start to appear without obstructing the channel; WHB washing with saline solution (NaCl 0.9 %) for 5 min; Rhodamine B stained Fuco MBs injection at venous flow rate (4 µL/min) for 5 min; Washing of Rhodamine B Fuco MBs with saline solution (NaCl 0.9 %) at venous flow rate (4 µL/min) until no more free MBs were circulating. A microscopy image (Axio Observer, Zeiss) was taken between each step to control the platelet aggregates and the targeting properties of the MBs. A negative control was obtained with the injection of CMDex MBs. Quantification was established by measuring the amount of MBs colocalized on platelet aggregates after the final rinsing and normalized to the size of the aggregates using Fiji thresholding analysis.

Cytotoxicity assays

The evaluation of cytotoxicity was performed with a LDH (Lactate Dehydrogenase) mortality assay and MTT [3-(4,5-dimethyl-2thiazolyl)-2,5-diphenyl-2H-tetrazolium bromide] viability assay. Both HUVECs (Human Umbilical Vein Endothelial Cells, CRL-1730, ATCC) and BALB/3T3 (mouse embryo fibroblast, clone A31, CCL-163, ATCC) were cultured until confluency, at 37°C in a 5% CO_2 incubator, with Dulbecco's Modified Eagle Medium (DMEM) with 10% (v/v) fetal bovine medium, 4mmol of L-glutamine, 1% (v/v) of penicillin and 1% (v/v) of streptomycin. For LDH mortality assay (Cytotoxicity detection kit PLUS, Roche), HUVECs and BALB/3T3 were culture in 96 wells plates. Briefly, after incubation with various concentrations of MBs diluted in cell culture medium (10^8, 10^7, 10^6, 10^5 and 10^4 MBs/mL), supernatants were recovered either after 2, 4 or 6 hours. The recovered culture medias were incubated with LDH reaction mix according to the supplier guidelines for 15 min at room temperature. After addition of the stop solution, the absorbance of the samples was read at 492 and 690 nm (control wavelength). The cell cytotoxicity was then determined by subtracting the control wavelength to the absorbance at 492 nm and normalized to dead cells absorbance: Cell mortality = [(Abs of the sample - Abs of culture medium) / (Abs of 100% of dead cells- Abs of culture medium) x 100].

For the MTT assay, cells were seeded in 24 well plates. This assay was performed with cell culture insert (Falcon®, 1 µm of mesh diameter) to avoid the sedimentation of MBs residues onto the cells, allowing the focus on the degradation product toxicity rather than cell asphyxia in static conditions. Indeed, due to the experimental conditions, 37°C for 6 hours, we expected MBs burst and consequently MBs residues sedimentation rather than intact MBs floating property. Cell culture medium was discharged and replaced by 300 µL of new medium, inserts were placed in each well and 300 µL of MBs diluted in cell culture medium were added inside the inserts for a final MBs concentration of 10^8, 10^7, 10^6, 10^5 and 10^4 MBs/mL. After 6 hours of incubation, cells insert and medium were replaced by 300 µL of MTT solution (0.05% in PBS 1X) and incubated for 3 hours at 37°C in dark environment. The medium was removed by gentle plate reversal on dry paper and the 300 µL of isopropanol was added to each well. After 1 hour at room temperature, absorbance was measured at 490 nm in a TECAN (Infinite M200 PRO) plate reader. The cell viability was measured as: Cell viability = [(Abs of sample - Abs of dead cells control) / (Abs of living cells control - Abs of dead cells control) x 100].

Hemolysis evaluation

Whole human blood from healthy volunteers was centrifuged 5 min at 500 g to isolate Red Blood Cells (RBC) in 25 µM PPACK tube to avoid coagulation. Hematocrit and plasma level were labelled on the tube, plasma phase was aspirated and replaced by 0.9 % saline solution twice. Then 0.9% NaCl was replaced by PBS 1X. The final RBC suspension was diluted to 1/50 in PBS 1X. In a V-bottom 96 well plate, 10 µL of MBs suspension was added at different concentration (from 0.125 x 10^8 to 10^8 MBs/mL). 190 µL of previously prepared RBC suspension was added to the wells and incubated at 37°C for one hour on an orbital shaker. Plates were centrifuged to the same conditions to recover the RBC pellet. Supernatant was then transferred into a clean flat bottomed 96 wells plate and absorbance was measured at 450 nm with a monochromator (TECAN, Infinite M200 PRO). Positive control was obtained with Triton 10X allowing a complete lysis of the RBCs and negative control was performed with PBS 1X. Percentage of hemolysis was obtained with the following formula: Hemolysis = [(Abs of sample - Abs of negative control) / (Abs of positive control - Abs of negative control)].

In vivo stroke model

Animal studies were performed on 6 to 8 weeks old (30 to 40 g) Swiss wild type male (Janvier Labs, Le Genest-Saint-Isle, France). All experiment were adapted according to French (Decree 87/848) and European (2010/63/EU) ethical guidelines. The local committee of Normandy (CENOMEXA) approved the fulfilling of the experiments with the reference number APAFIS#35158. Mice were anesthetized with 5% of isoflurane inhalation and maintained to 2% during the entire procedure. As analgesic, they subcutaneously received buprenorphine (0.1 mg/kg) and ear local anesthesia with lidocaine spay. Mice heads were stabilized in a stereotaxic platform and a catheter was placed in the tail vein for the treatment injection. After a local craniotomy on top of the middle cerebral artery (MCA), the dura mater was excised to expose the MCA bifurcation. Precise pneumatical injection of 1 µL of murine thrombin (1 IU, Stago BNL) was carried out by elongated glass capillaries in the MCA to induce fibrin rich thrombus formation [27]. The treatment procedures were performed intravenously, 30 min after thrombin injection with either, free rtPA (Actilyse®, Boehringer) at 1 mg/kg in infusion (300 µL, 10% bolus + 90% infusion for 40 min, N ≥

16); rtPA-loaded Fuco MBs at 1 mg/kg equivalence in bolus (300µL, 3 x 10^9 MBs, N ≥ 16); or saline in infusion (300µL, 10% bolus + 90% infusion for 40 min, N ≥ 16).

Speckle imaging

Monitoring of the *in vivo* brain perfusion was obtained with Laser Speckle Contrast Imager (MOOR FLPI-2, Moor Instruments), allowing the visualization of blood figurative elements. Speckle images were taken before and after the stroke induction as well as before and after the treatment to control the occlusion. The quantification of the flow mean was generated by comparing stroke Region of Interest (ROI) to the same region on the contralateral hemisphere, before and after treatment. Mice with pre-stroke contrast difference in both hemisphere and mice with complete reperfusion right after treatment were excluded from the study. For the first scenario, it was not possible to define if the clot was ever obtained. For the second scenario, it was not possible to attest if the clot was not formed correctly or completely dissolved by the treatment.

Magnetic Resonance Imaging and BBB permeability

24 hours after treatment, mice brains were imaged with MRI to measure the size of the infarcted areas. Briefly, mice were anesthetized with 5% of isoflurane inhalation and maintained to 2% during the acquisitions. All acquisitions were obtained with a Pharmascan 7 T (Bruker Biospin, France), T2 sequence (echo time 39.9 ms, repetition time 3,500 ms, 2 averages) were used for ischemic lesion visualization and T2 Star sequence (echo time 8.7 ms, repetition time 500 ms, 2 averages) were used for hemorrhagic lesion visualization. Lesion volumes were quantified with image analysis of the hyper signal cut off area on all the brain slices (0.5 mm thickness) with the formula: Ischemic lesion volume = $(\sum ischemic\ areas)\ x\ 0.5$.

For the evaluation of Blood Brain Barrier (BBB) permeability, Gadoteric Acid (GA, Clariscan Gé, GE Healthcare) was injected intravenously in the tail vein (200 µL at 0.75 mmol/kg). After 15 minutes, three dimensional T1 Flash acquisition (echo time 4.4 ms, repetition time 15 ms, 3 averages) was recorded and white hyper signal volume was quantified as BBB leakage of GA compared to acquisition before injection, using Fiji software using the same formula than ischemic lesion volume.

Ex vivo fluorescence biodistribution on complete or sectioned organs

Organs from previously described procedures were harvested 24 hours after treatment. Biodistribution of the Fuco MBs was imaged by near-infrared fluorescence imaging (IVIS® Lumina III, Perkin Elmer, USA). The imaging of complete organs (N=3) was performed on brain, liver, lungs, bladder, spleen, intestines and kidney right after euthanasia without PFA fixation. The quantification of fluorescence intensities (λ_{Ex} = 550 nm, λ_{Em} = 620 nm) in regions of interest (ROIs) were analyzed using Living Image® software. For histology analysis, mice received buprenorphine (0.1 mg/kg) and were deeply anesthetized with 5% of isoflurane inhalation before procedure. After a thoracotomy, a cannula was inserted into the left ventricle, and the right atrium was incised to rinse the circulatory system. Transcardiac perfusion was then performed with 50 mL of heparinized saline (0.5 mL/L) followed by 30 mL of 4% paraformaldehyde (PFA) at a constant speed of 14 mL/min. Organs were post-fixed in 4% PFA overnight at 4°C then plunged in cryoprotective solution (20% sucrose in PBS 1X) overnight before to be stored at -80°C. Organs were subsequently sliced with a cryostat at a 10 µm thickness. Slices were stained with DAPI mounting medium (ABCAM) for nucleus recognition and with rat anti-mouse CD68 primary antibody (Biolegend) followed by a FITC secondary antibody (Biolegend) to highlight tissue macrophages.

Statistical analysis

Quantitative data underwent the statistical analysis of GraphPad PRISM 8 with a 95% confidence level. All presented data are means of at least triplicates expressed with their standard deviation (SD). Normality test were performed using Kolmogorov-Smirnov test and if needed outliers were identified and excluded with ROUT method (1% of aggressivity of the Gaussian distribution). Depending on the design of the experiment and after normality validation, data were evaluated with unpaired t-test (two groups) or ANOVA (more than two groups) in association with multiple comparison in between groups (Tukey's test). P-values were represented as followed, and deemed significant below the 0.05 threshold: * $p < 0.05$; ** $p < 0.01$; *** $p < 0.001$, **** $p < 0.0001$.

3. Results

3.1 Polymer MBs synthesis and characterization

MBs synthesis was inspired by the well-described hydrodynamic cavitation method like recently published by Bo Li. *et al* [19]. In this work, the cavitation energy was replaced by ultrasonic insonation into the polysaccharide solution. This recently patented acoustic cavitation method enabled the production of polymer MBs within 20 minutes (*Fig. 2A*) (PCT/FR2022/050309). The set-up was placed on ice to regulate the synthesis temperature rise and perfluorobutane (PFB) was constantly injected into the polysaccharide solution. The entrapped gas helped for the stability of the anionic copolymerization between cyanoacrylate monomer and polysaccharide chains. Fucoidan (Fuco) was used here as the targeting agent and so carboxymethyl dextran (CMDex) was used as the control polysaccharide for untargeted MBs. Comparing Fuco MBs and CMDex MBs (*Fig. 2B*), it was demonstrated that the amount of MBs produced was independent from the polysaccharide composition with a yield around 2.5 x 10^{10} MBs per batch. The mean size after sieve filtration was measured at 3.13 (± 0.81) µm for Fuco MBs and 3.07 (± 1.49) µm for CMDex MBs, showing no significant difference depending on the shell compositions, in accordance with the close size range of both polysaccharides (*Fig. S1A*). The evaluation of the surface charge was shown negative with a zeta potential close to -45 mV for Fuco MBs and close to -30 mV for CMDex MBs, also in accordance with the negatively charged groups in fucoidan and carboxymethyl dextran (*Fig. S1B*). The size stability was monitored over a month by measuring the size of the MBs. A size augmentation would be attributed to shell destabilization leading to MBs aggregation detected by the apparatus as bigger MBs. In *Fig. 2C,* the shelf stability was measured right after synthesis, after 3 and 4 weeks (independently of their incorporated polysaccharide). MBs were either placed at -5°C or 20°C to establish the best storage conditions for MBs suspension. It has been demonstrated that 5°C was the best storage temperature as the mean MBs was stable at 3.27 (± 0.71) µm for 4 weeks. Room temperature storage showed an increased mean size to 4.09 (± 0.22) µm after 4 weeks, which is still in the range for possible animal injection. The whole size distribution presenting the Dv10, Dv50, Dv90 are plotted on the *Fig. S1C*, highlighting the size stability after 4 weeks. In complement to this size distribution study, we validated that the incorporation of rtPA presented below did not affect the mean size of the MBs *(Fig. S1D*).

The characterization of fucoidan content was obtained with the quantification of sulfated groups as presented in the Supplementary data (*Fig. S2A-B-C*). This colorimetric method based on Methylene Blue staining pointed out the presence of the sulfated polysaccharide in the range of 1x 10^{-14} g/MB using CMDex MBs as negative control. Environmental Scanning Electron Microscopy (ESEM) images presented in *Fig. 2D* validated the rounded shape of MBs as well as the short polydispersity after filtration. To ensure the hollow structure of the MBs observed in confocal imaging (*Fig. S3A*), Focused Ion Beam (FIB) technology was used to cut through individual MBs (*Fig. 2E*). The shell homogeneity was then demonstrated and an estimation of the shell thickness was measured in the range of 500 nm, subsequently emphasized with confocal fluorescence imaging (*Fig. S3B-C-D*).

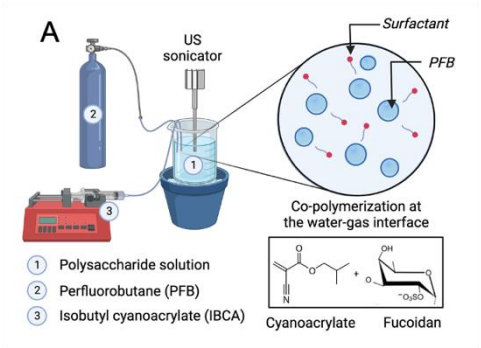

B

	Yield (MBs / Batch)	Mean size (µm)	Zeta potential (mV)	Fuco content (g / MBs)
Fuco MBs	2.46 (± 0.97) x 10^{10}	3.13 (± 0.81)	-44.9 (± 1.9)	1.0 (± 0.1) x 10^{-14}
CMDex MBs	2.64 (± 1.43) x 10^{10}	3.07 (± 1.49)	-30.6 (± 0.8)	-

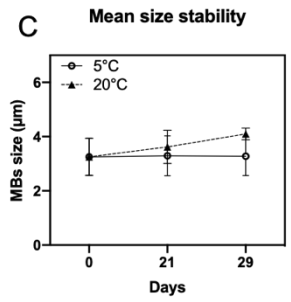

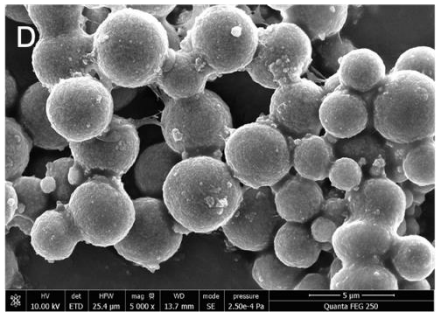

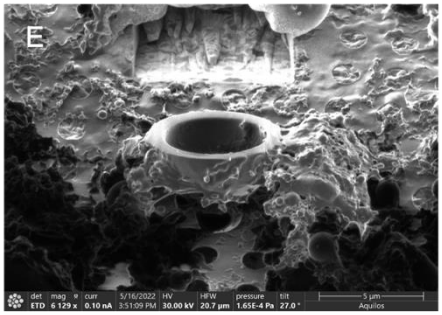

Figure 2: Functionalized polymer MBs characterization. A) Innovative synthesis method. Monomer of isobutyl cyanoacrylate (IBCA) was injected with a needle pusher into the acidic aqueous polysaccharide solution while constant bubbling of perfluorobutane was ongoing. US sonicator was immerged inside the aqueous solution and generates continuous signal for 20 min at 30% of amplitude. The system is placed on ice to avoid temperature rising. Due to high hydrophobicity, IBCA will tend to polymerized at the water-gas interface, copolymerizing with polysaccharides dissolved into the solution and entrapping PFB. B) Summary of principal physicochemical characterization depending on the incorporated polysaccharide. Yield was measured with MBs counting on Malassez cell, mean size was measured with laser diffraction granulometry, zeta potential was obtained with electrophoretic light scattering and fucoidan content was dosed with methylene blue colorimetric assay. C) Mean size of MBs suspension over a month measured with laser diffraction granulometry, comparing 5°C and 20°C for shelf storage. D) Environmental Scanning Electron Microscopy (ESEM) image of MBs pointing out their homogenous rounded shape Scale bar is 5 µm. E) Focus Ion Beam (FIB) cut through a single polymer MBs pointing out the hollow structure and the thick shell around 500 nm thick. Scale bar is 5 µm.

3.2 Echogenicity of MBs

One intrinsic property of MBs is their ability to respond to an ultrasound signal [28,29]. Indeed, microbubbles are now widely used in clinic as US contrast agents for US imaging. Their ability to resonate under US creates bright signal compared to surrounding tissues in cardiac echography for example. The proposed agent can be an answer for the problem of specificity in diagnostic or treatment thanks to its precise targeting. To ensure the echogenic properties of those newly synthetized MBs, a home-made *in vitro* model was established to determine the burst threshold of MBs in function of the intensity of the signal (*Fig. 3A*). Intensities varied from 8 V, 9 V 10 V, 11 V, 12 V, 13 V, 14 V and 17 V corresponding respectively to the following mechanical index 0.230 (± 0.002), 0.270 (± 0.003), 0.310 (± 0.004), 0.350 (± 0.002), 0.390 (± 0.003), 0.430 (± 0.003), 0.470 (± 0.002) and 0.600 (± 0.001). The imaging sequences were measured with a 2 V signal before and after 2 sequences of the burst periods (*Fig. 3B*). The signal was normalized to water and to MBs insonated with 2 V all along. The intensity rise at the beginning of each burst sequence corresponds to a “blinking” phenomenon of MBs before ongoing inertial cavitation. The last part of the graph displays the loss of signal due to some MBs implosion. The difference between the initial intensity signal and the final intensity one in plotted on *Fig. 3C* as the disruptive ratio. This ratio determines the amount of disrupted MBs and clearly states that over 10 V (Mechanical Index = 0.31) more than 50 % of MBs underwent inertial cavitation. This is illustrated with *Fig. 3D*, displaying the US images of the channels before and after 8 V or 17 V US insonation.

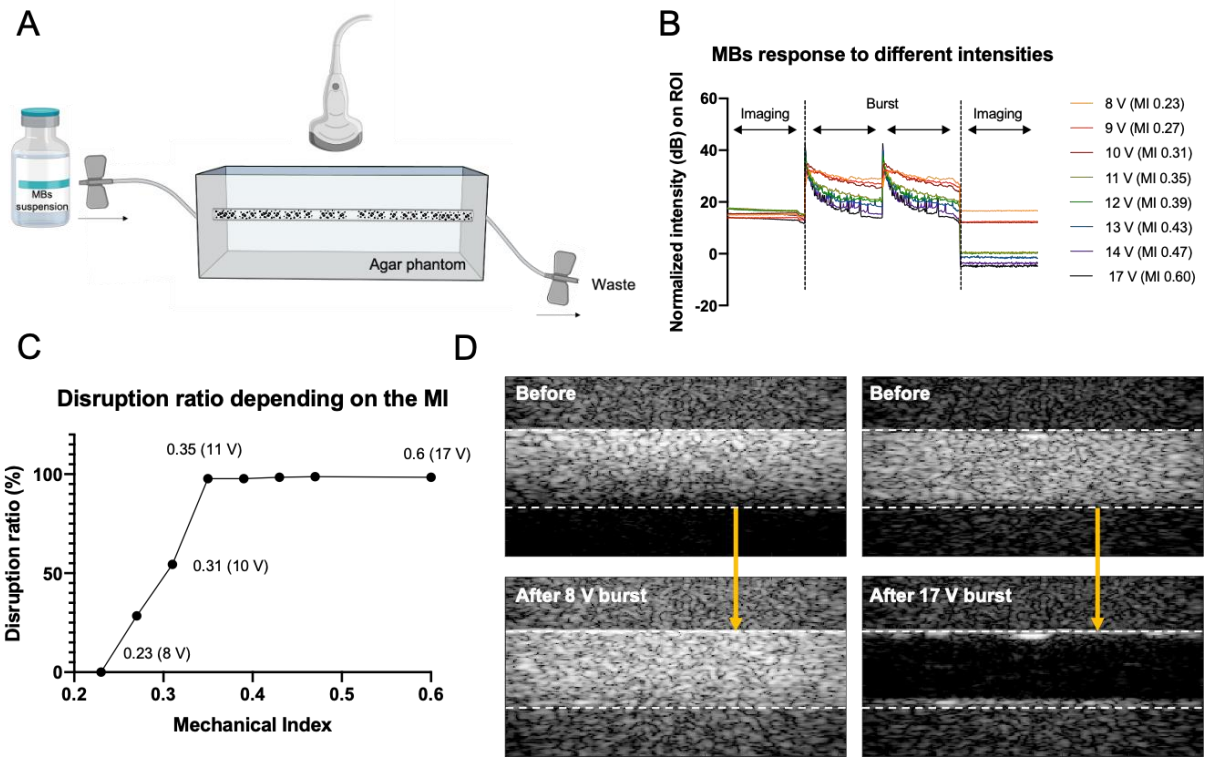

Figure 3: Ecogenicity characterization of MBs. A) Flow phantom setup mimicking blood vessel circulation. The flow can be monitored with a butterfly closure system and the US transducer is placed on top of the phantom. B) Echogenic response of MBs at 5 MHz frequency and different intensities in volt (from 8 to 17). The curve is composed of 4 sequences: 1 imaging at 2 V, 2 burst sequences depending on the different intensities and 1 more imaging sequence at 2 V to compare before and after bursting signal. C) Disruptive ratio calculated from the normalized intensitiy difference before and after burst sequence. Mechanical Index 0.230 (± 0.002), 0.270 (± 0.003), 0.310 (± 0.004), 0.350 (± 0.002), 0.390 (± 0.003), 0.430 (± 0.003), 0.470 (± 0.002) and 0.600 (± 0.001)) correspond to the voltage signal of 8V to 17 V. D) US images from phantom setup before and after 8 V burst and before and after 17 V burst. The channel is highlighted with a dotted line and MBs signal is visible in white contrast.

3.4 Drug loading and targeting of MBs

MBs were functionalized with rtPA (Actilyse®), the recombinant tissue Plasminogen Activator used for human treatment. The incorporation was obtained with an adsorption protocol (*Fig. 4A*) where the pH rising of the MBs suspension allowed the incorporation of the protein within 2 hours. To evaluate the amount of incorporated rtPA, the protein activity was measured, ensuring that its incorporation did not affect its enzymatic activity. Primarily noticed result was the high number of incorporated proteins onto Fuco MBs compared to CMDex MBs (*Fig. 4B*). This specific incorporation is believed to be related to the interaction with activated sulfated groups of fucoidan [30]. Indeed, Fucoidan MBs were able to incorporate 226 (± 32) µg of rtPA for 10^{10} MBs compared to 19 (± 16) µg of rtPA for 10^{10} MBs onto CMDex MBs. Then, rtPA incorporation stability was evaluated over 4 days with centrifugation washing between each day (*Fig. 4C*), pointing out a stable incorporation threshold of 108 (± 5) µg of rtPA for 10^{10} MBs from day 1 to day 4. This stable incorporated score was observed after

the 4th centrifugation washing step on day 1 and stable after the next washing steps. With the aim of producing reproducible results, the stable quantity of incorporated rtPA onto Fuco MBs was set to 100 µg/10^{10} MBs. The fibrinolytic activity of incorporated rtPA was validated with a fibrin agar assay (*Fig. S4A*) by measuring the degradation area of the gel after 2, 5 and 24 hours at 37°C. This semi quantitative method demonstrated that the fibrinolytic activity was maintained when rtPA was encapsulated compared to free rtPA (*Fig. S4B*).

The targeting property of Fuco MBs were evaluated in fluidic condition mimicking *in vivo* blood circulation (*Fig. 4D-F*). Platelet aggregates formation on collagen coating is highly dependent to flow rate (60 µL/min) [31] and was monitored with fluorescent microscopy to avoid channel cloaking. Fuco MBs targeting was measured with Fiji image analysis after rinsing the channel with saline solution and normalized to the platelet aggregate size. Previous work validated the specificity of fucoidan for P-selectins over E and L-selectins [18], here the focus was on expressed P-selectins by activated human platelets. The targeting (*Fig. 4F*) was highly significant (P Value < 0.0001) comparing CMDex MBs (*Fig. 4D)* to Fuco MBs (*Fig. 4E*). Also, the drug-loaded MBs were still enable to target activated platelet with a significant difference to control MBs (P Value < 0.0001). This targeting assay validated that *ex vivo* platelet targeting was highly efficient and that rtPA incorporation did not prohibit MBs targeting despite rtPA interaction with the targeting agent.

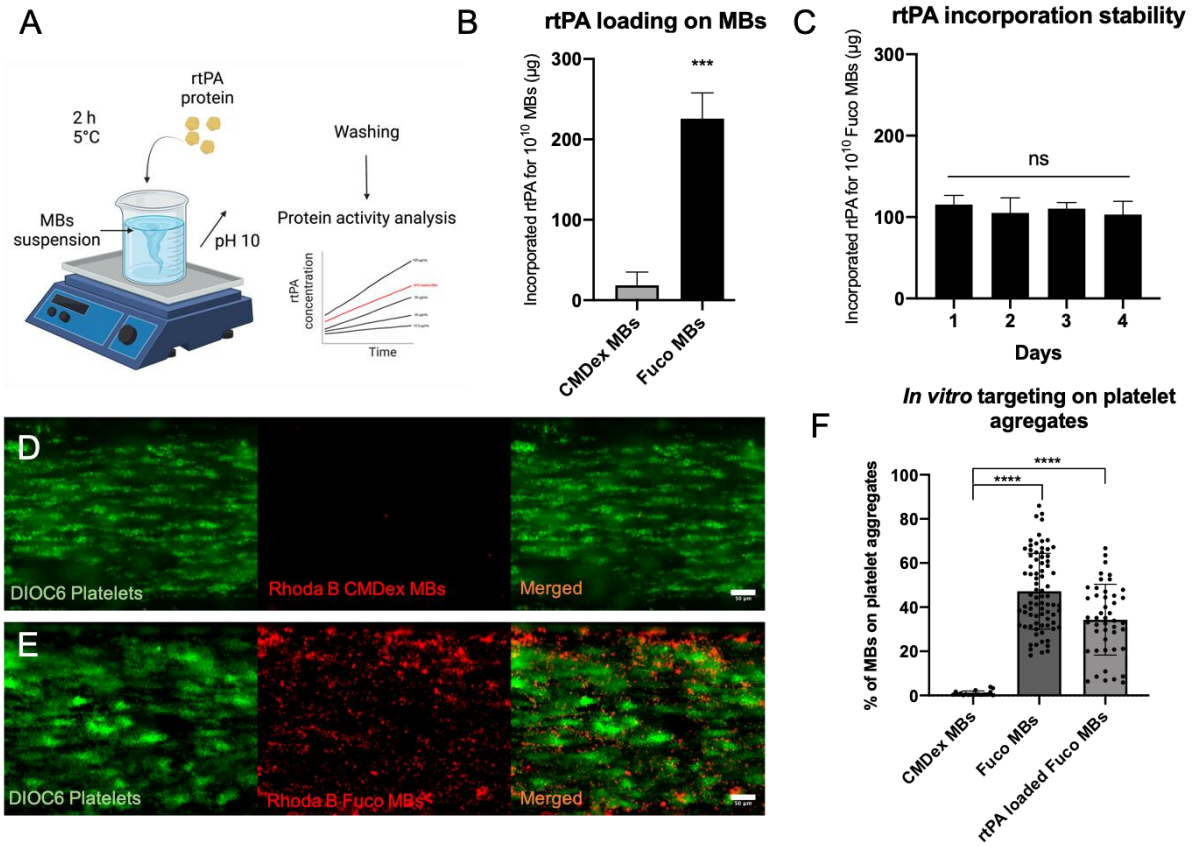

Figure 4: Functionalization of MBs. A-B-C) Drug loading and validation of the rtPA activity after incorporation. A) Drug loading adsorption protocol. Briefly, 500 µg of rtPA in solution was added to a MBs suspension from which the pH has been risen to 10 with NaOH. The mix was left for 2 hours under gentle agitation and then rinsed 3 times by centrifugation and discharge of the undernantent. The protein activity is then monitored on drug-loaded MBs with a kinetic substrate degradation assay (PefaFluor®). B) Protein incorporation determined from protein activity assay of rtPA onto either Fuco MBs or CMDex MBs after 3 centrifugztion wasing step. C) Stability of rtPA incorporation onto Fuco MBs over 4 days with washing centrifugation step in between days. D-E-F) In vitro flow targeting. D-E) Microscopy images of Vena8 Fluoro+ microchannels. Platelets from whole human blood were labelled with DIOC6 and MBs were synthesized with Rhodamine B, the last image is a merge of both DIOC6 and Rhodamine B channels. Images are taken under venous flow indicating that stopped MBs are attached to platelet aggregates. D) is the control group of CMDex MBs and E) is the result of Fuco MBs. Scale bar is 50 µm. F) Quantification of MBs targeting on platelet aggregates normalized to the size of the aggregates. The evaluation of rtPA-loaded Fuco MBs targeting confirmed that the drug loading did not compromise the effective targeting on P-selectins.

3.5 Biocompatibility of MBs

Before *in vivo* injection, cytotoxicity towards red blood cells (RBC), endothelial cells (HUVEC) and fibroblast (3T3) were assessed (*Fig. 5*). Lactate Dehydrogenase (LDH) is a cytoplasmic enzyme, thus its presence in the culture medium is a marker of cell membrane rupture. This mortality assay was performed on two cell types likely to encounters MBs *in vivo*. Mortality tests on endothelial cells were on average of 4.73 (±

2.07) % all conditions reunited (*Fig.5A*) while fibroblasts showed a mortality of 7.9 (± 3.5) % independently of the condition *(Fig. 5B*). Overall, no mortality was measured (above 30% threshold), neither for HUVECs and 3T3 nor 2 hours, 4 hours or 6 hours times points and likewise for increasing MBs concentrations. The second cytocompatibility evaluation was performed on RBC by the measurement of hemoglobin release in the supernatant also marker of cell lysis (*Fig. 5C*). Normalized to Triton 10X lysis, MBs incubation with RBC for one hour did not induce cell lysis even at 10^8 MBs/mL (<4%). Lastly, viability assay was performed for 6 hours with MTT assay. To prevent from cell asphyxia because of MBs debris sedimentation (caused by the assay temperature and time conditions), the MBs suspension was added on top of a 1 µm cell culture insert. The MTT assay evaluates the cell metabolic activity by the reduction of MTT to formazan with mitochondrial reductases. After 6 hours of incubation, none of the conditions showed a diminution in the cell's metabolic activity for HUVECs or 3T3 (*Fig. 5D*) with a mean survival rate above 100% compared to MBs control cells cultured without MBs. The 0.02% tween working buffer (WB) did not influence the cell viability neither. Images of formazan crystals were also taken with optical microscopy comparing the highest concentration (10^8 MBs/mL) to cells that were not in contact with MBs (*Fig. S5*). Those pictures highlighted the healthy phenotypes of cells and the correct metabolization of MTT. Therefore, no cytotoxicity was demonstrated on three different cell types in contact high concentrations of MBs, using three different assays.

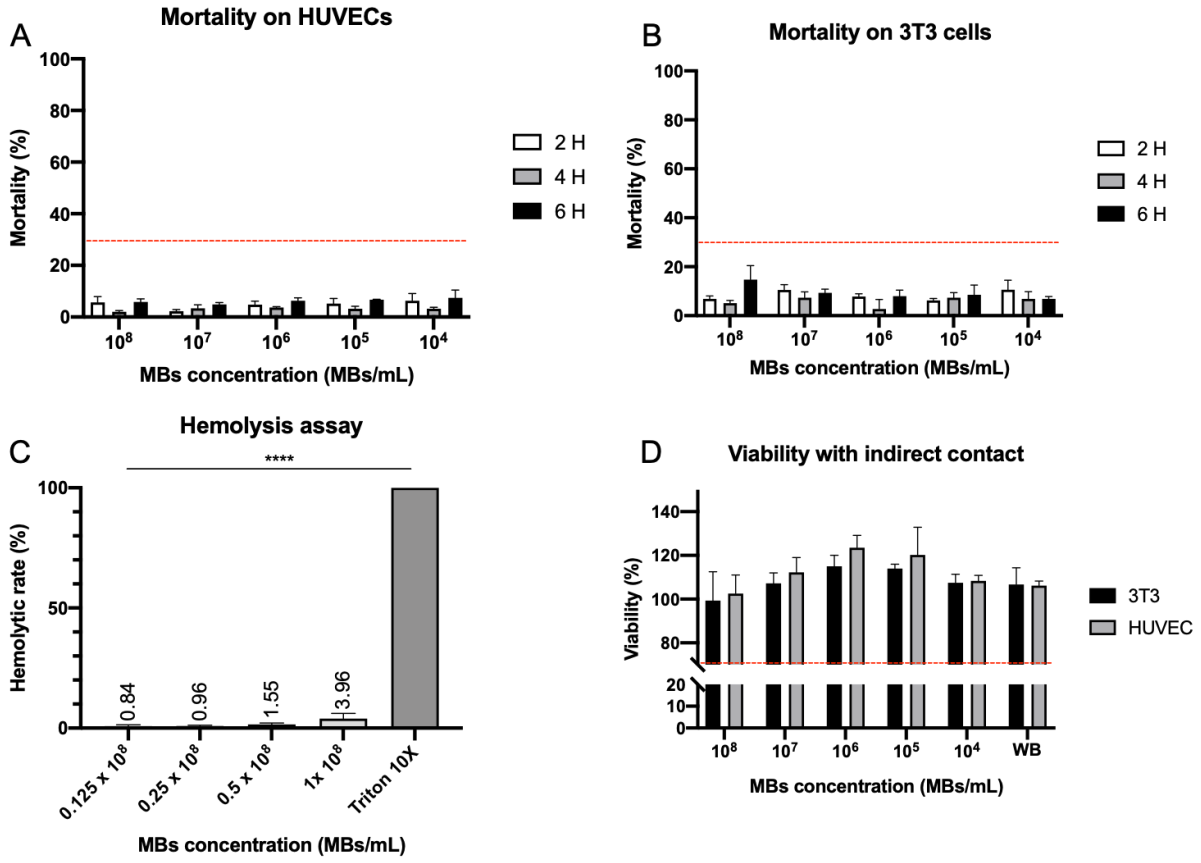

Figure 5: Biocompatibility study of Fuco MBs on different cell types. A-B) LDH quantification assay on endothelial cells (A) and fibroblasts (B) for increasing concentration of MBs and different time points. LDH is a cytoplasmic enzyme only present in the culture medium if cells undergo apoptosis. Here, none of the concentrations or time of contact induced a mortality above the red dotted line of 30% indicating the biocompatibility of Fuco MBs. C) Hemolysis assay of Fuco MBs on human red blood cells. The time of contact here was one hour and showed less that 4% of hemolysis at the highest MBs concentration (10^8 MBs/ml) compared to Triton 10X. D) MTT assay with indirect contact of Fuco MBs on endothelial cells and fibroblasts for 6 hours. The same Fuco MBs concentration was used as the mortality assay and 0.02% tween working buffer (WB) was also put to the test. Again, no condition induced a viability below 70 % (red dotted line). The MBs suspension was added on top of a cell culture insert with 1 µm mesh to avoid the asphyxia of cells due to MBs debris sedimentation after long contact time in culture medium.

3.6 In vivo stroke model

The *in vivo* stroke model was performed as presented in *Fig. 6A.* After a local craniotomy over the MCA, thrombin injection generated fibrin rich clot formation. Speckle imaging was performed before and after each step to validate the reduction of blood flow in the region of the stroke. The clot was left to stabilize for 40 min and treatment were carried out with intravenous tail vein injection. The final checkup was obtained at 24 hours with MRI imaging analysis of the ischemic region. In pre-clinical application, the treatment for an efficient thrombolysis using rtPA injection in mice models is usually performed with 10 mg/kg ratio while we set the threshold here to 1mg/kg of rtPA for both free rtPA and rtPA-loaded MBs [27]. In consequence, there is no significant difference in the ischemic lesion volume between the saline group (N =

16, 10.35 ± 4.84 mm^3) and the free rtPA group (N = 17, 8.08 ± 6.12 mm^3). Nevertheless, the rtPA-loaded Fuco MBs treatment significantly reduced the infarcted area by more than 50 % (N = 16, 3.75 ± 3.67 mm^3) compared to free rtPA treatment (*Fig. 6B*). In addition, we compared the size prevalence in each group (*Fig. 6C*) by defining 4 groups: no lesion, small lesion (<5 mm^3), medium lesions (from 5 to 10 mm^3) and large lesions (>10 mm^3). Large lesions were only observed once in rtPA-loaded Fuco MBs treatment with a majority of small lesion (N = 8). On the contrary, saline group presented a majority of large lesion (N = 9) and free rtPA group presented a similar amount of small and large lesion (N = 6). The MRI images displayed on *Fig. 6D* were taken 24 hours after the treatment, and the white region pointed by an arrow represents the ischemic region on the same coronal plane for the three groups (more images on *Fig. S6A*). Since MBs treatment involves micron size bubbles, we also monitored the Blood Brain Barrier (BBB) permeability (*Fig. 6E-F*). By injecting Gadoteric Acid (GA) intravenously, the leakage of BBB permeability can be observed with T1 MRI acquisition as white spots around the infarcted areas. Nevertheless, this test showed no evidence of BBB impairment comparing saline, free rtPA and rtPA-loaded Fuco MBs groups (*Fig. 6E*). Some spots were identified with saline treatment compared to MRI images taken before GA injection (*Fig. 6F*), but isolated events could also be the consequence of the surgery itself (more images on *Fig. S6B*). Overall, the targeted treatment with rtPA-loaded Fuco MBs was significantly more efficient than gold standard treatment and neither collateral hemorrhage or BBB leakage was observed.

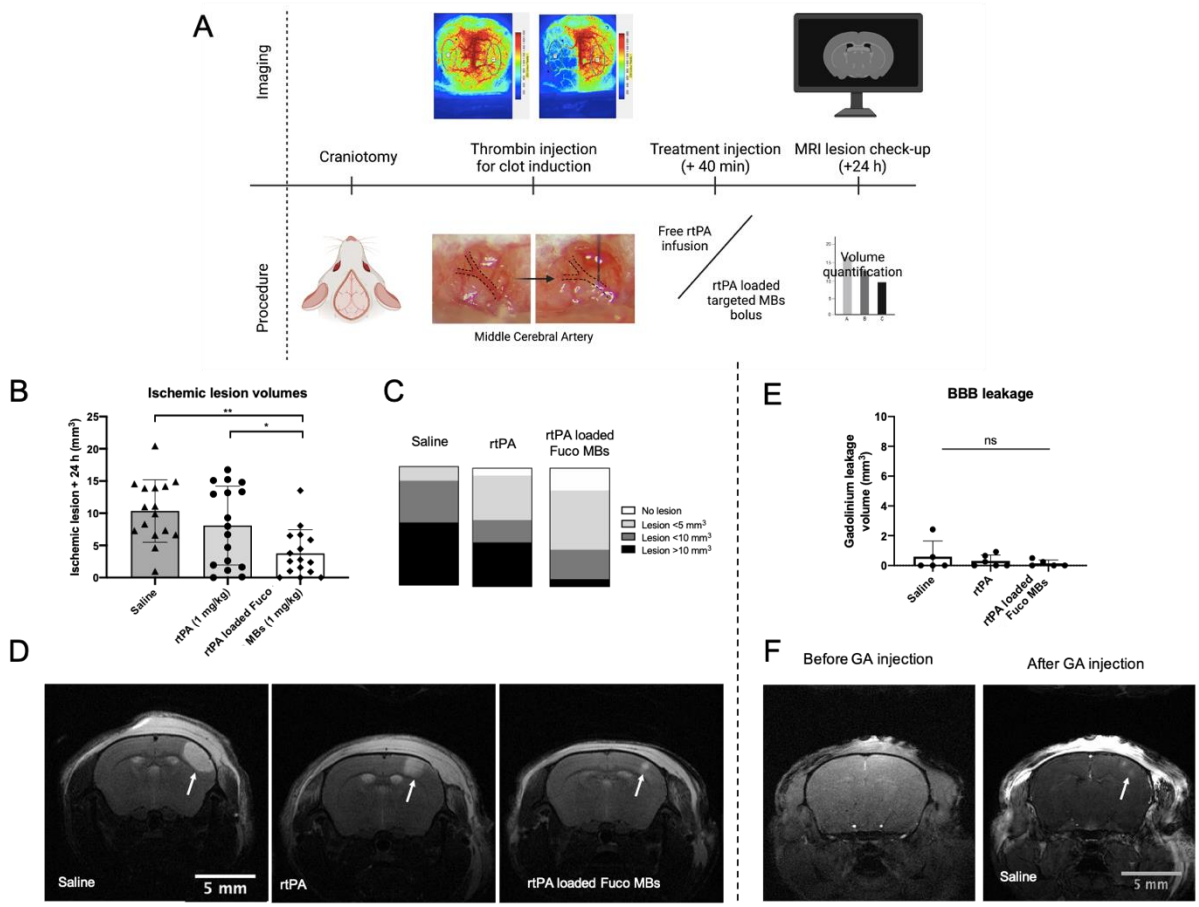

Figure 6: In vivo stroke model study on mice comparing rtPA-loaded Fuco MBs treatment to systemic injection of rtPA. A) Graphical abstract of the experimental setup. Briefly, mice were anesthetized and placed onto a stereotaxic platform. A craniotomy allowed the direct access to the Middle Cerebral Artery (MCA) to inject thrombin. After a few minutes the clot partial occlusion was validated with Speckle imaging looking at the two hemispheres perfusion. After 40 min, either saline infusion, free rtPA infusion or rtPA-loaded Fuco MBs bolus were used as stroke treatment. The MRI images of the mouse brain were taken 24h after the treatement to evaluate the infarcted area volume. B) Lesions volumes quantification from MRI images. Volumes were measured with the Fiji software by compiling areas of all brain slices for saline, free rtPA and rtPA-loaded Fuco MBs treatment. C) Lesion distribution according to their severity from: no lesion, small lesion (<5 mm^3), medium lesion (>5; <10 mm^3) to large lesion (>10 mm^3) depending on the treatment. D) MRI images of the same slice number of the three treatment conditions. The white arrows point out the infarcted area and the scale bar is 5 mm. E-F) Blood Brain Barrier (BBB) permeability evaluation. Gadoteric Acid (GA) was injected intravenously before MRI T1 flash imaging. E) Quantification of GA leakage volume in the brain 24 hours after stroke treatment (ns: not significant). F) MRI T1 flash acquisition of mouse brain before and after GA injection for saline treatment condition. The white arrow is pointing out the contrast generated by BBB leakage of GA, the scale bar is 5 mm.

3.7 Ex vivo fluorescence biodistribution on sectioned or complete organs

The biodistribution of rtPA-loaded Fuco MBs has been studied with organ fluorescence macroscopy (*Fig. 7A-B*). *Ex vivo* organ macroscopy was performed 24 hours after treatment on brain, liver, lungs, bladder, spleen, intestine and kidney compared to saline groups. As MBs were labelled with Rhodamine B, the fluorescence residues of MBs can be observed with an excitation wavelength of 550 nm (*Fig. 7A*). Normalized to the size of the organ, fluorescence count (*Fig. 7B*) gives a qualitative evaluation of MBs biodistribution in the body. As expected, the majority of fluorescence

was observed in the liver, fulfilling its function of blood detoxification. Also, some MBs residues were observed in the lungs most likely related to the gas exchange ongoing after MBs degradation. No fluorescence was observed in the bladder, spleen, intestines or kidney. Interestingly, the specific fluorescence in the stroke area was observed after 24 hours. It enhanced the validation of Fuco MBs targeting capacity *in vivo* but also brings new insights for the P-selectins expression on activated endothelium, after clot resolution and thus interesting perspectives for molecular imaging. In regards to those results, the histology study was performed on liver explanted 2 hours after Fuco MBs injection, to assess their uptake by resident macrophages. In *Fig. 7C*, cell nuclei were colored with DAPI and macrophages were labeled in green with an antibody against CD68 biomarker. Rhodamine B Fuco MBs residues were observed to be colocalized with macrophages biomarker CD68 indicating a potential internalization by the scavenger cells.

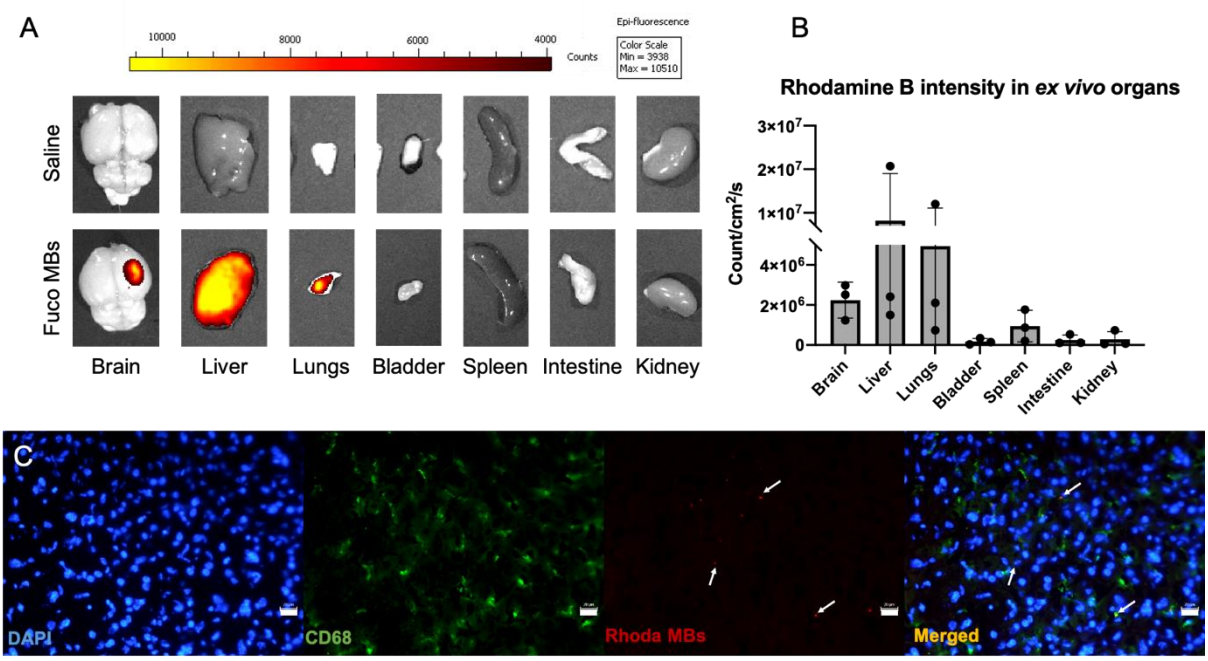

Figure 7: Biodistribution of fluorescent MBs and MBs residues in mice. A-B) Ex vivo fluorescence macroscopy quantification of MBs outcome in brain, liver, lungs, bladder, spleen, intestine and kidney. A) Fluorescence macroscopy images of various organs after stroke treatment (saline: top row, rtPA-loaded Fuco MBs: bottom row). Organs were retrieved 24 hours after treatment and imaged without tissue fixation. The epi fluorescence scale was set between 3938 and 10510 counts. Specific targeting of MBs to the stroke area was still visible after 24 hours and liver and lungs were fulfilling their blood cleaning property as the rest of the fluorescence was observed in those two organs. B) Quantification of the fluorescence in each organ in counts/cm^2/s. The quantification gave similar conclusion to the fluorescence images, with a high fluorescent signal of MBs residues in the liver and the lungs (N=3). C) Histology coloration of liver tissue 2 hours after injection of rhodamine B Fuco MBs in mice. From left to right, DAPI coloration of cell nuclei, CD68 immunostaining of macrophages, Rhodamine B Fuco MBs, Merged image. The white arrows point out the MBs fluorescent residues in red and scale bar is 20 µm. MBs residues were found in liver tissue after 2 hours and some of them seemed to be internalized in liver macrophages.

Discussion

Thrombotic diseases are life threatening conditions. Despite the availability of thrombolytic drugs, there are still a number of unmet medical needs for more effective and safer treatments. We presented in this study the development of drug-loaded targeting polymer MBs for the improvement of stroke treatment. Their stability over time was validated over 4 weeks in suspension (*Fig. S1C*) and their biodistribution aligns with the liver primary function to detoxify the blood. In addition, the shell composition did not affect the shelf stability (*Fig. S1D*) allowing data compilation. Cyanoacrylate are strong adhesives commonly used in surgical procedures for wound closure but are also injected in humans to seal blood vessels [32]. Fucoidans on the other hand are derived from brown algae [16] and were injected in humans with NANO-ATHERO project (NCT03422055) [16,30]. Thereby, this easy to make and scalable acoustic cavitation protocol draws new perspectives for the development of biocompatible acoustic microbubbles. The shell composition was validated by Fourier Transform Infrared (FTIR) as presented on *Fig. S7,* displaying the characteristic pics of ester bound around 1,750 and 2,250 cm^{-1} for cyanoacrylate. However, the polysaccharide incorporation with either fucoidan or carboxymethyl dextran was challenging to identify given the small amount of it. This quantification was better performed with sulfate dosage (*Fig. S2A-B*) and fucoidan targeting properties (*Fig. 4D-E*). In addition, the use of whole human blood rather than P-selectin coating for the evaluation of targeting properties is a much more accurate model for *in vivo* translation. The micron size of MBs helped for imaging characterization with ESEM (*Fig. 2D*), confocal (*Fig. S3A*) and FIB (*Fig. 2E; Fig. S3D*) imaging. In that manner, we were able to estimate the shell thickness by two methods (FIB and confocal fluorescence) to 518 ± 116 nm (*Fig. S3B-C-D*). The wide standard deviation is also the consequence of the FIB sample preparation that affected the MBs integrity limiting the sample number (N=4). After validation of MBs physicochemical properties, rtPA incorporation was obtained with a simple adsorption protocol using no additive chemical and no critical temperature. We validated the rtPA activity through two enzymatic assays, the fibrinolytic activity on agar gel (*Fig. S4A-B*) and the amidolytic activity on fluorescent substrate (*Fig 4 A-B*). Regular protein quantification with copper reduction (BCA assay) was not possible due to the reactivity of MBs without any incorporated drug. The incorporation was also validated by the shift in the surface charge of rtPA-loaded Fuco MBs compared to Fuco MBs (*Fig. S1A*). Lastly, the activity of the incorporated protein

was stable over 4 days (*Fig. 4C*) with no shift in the mean size of the MBs (*Fig. S1E*). Therefore, to ensure the effectiveness and the quality of the treatment, rtPA-loaded MBs were not use after 4 days for *in vivo* injection.

MBs are of main interest because of their acoustic property in US imaging also validated here with a homemade US setup. Establishing echogenic evaluation is not standardized yet and it mainly relies on contrast enhancement validation. Moreover, the system is highly setup dependent (distance, probe, medium) and required probe calibration. The test was computer driven with different voltage but, in order to translate to Mechanical Index, a hydrophone calibration was performed to measure the negative pressure of the signal. Nevertheless, it gives good insights for *in vivo* translation. We wanted to determine the threshold of MBs stability for US imaging but also the disruptive ratio of MBs for later sonothrombolysis experimentation. Indeed, many teams [20;21;22] have been exploring the impact of bursting MBs with US for the mechanical impairment of blood clots. No standards have been determined yet, except for bio-damaging boundaries of high Mechanical Index (MI, 1.9) [37]. A better understanding of MBs response to US signal *in vivo* is a key element to perform safe and monitored sonothrombolysis.

Before *in vivo* injection, we validated the *in vitro* biocompatibility of cyanoacrylate degradation products [38] with hemolytic tests (*Fig. 5C*), viability (*Fig. 5D*) and mortality assays (*Fig. 5A-B*) on endothelial cells and fibroblasts. The safety of MBs was demonstrated for each cell type independently from the MBs concentration (up to 1 x 10^8 MBs/ml) or the duration of the experiment (from 2 hours to 6 hours). The assays durations were selected according to the fact that MBs are not designed to be circulating after a few hours in the bloodstream. Overall, in accordance with the International Standard (ISO 10993-5) the 70% viability and 30% for mortality threshold were not exceeded. Thus, the safety of polymer MBs allowed the translation to the animal stroke model.

Thrombin injection triggers the formation of fibrin rich clot compared to ferric chloride model [39] that induces platelet rich thrombi. In consequence, thrombin-induced clots are more likely to respond to rtPA treatment. In this study rtPA was injected to 1/10^{th} of the treatment usually used in mice [40]. This choice was driven by the ultimate goal to limit rtPA dose related side effects. This constrain did not prevent from an efficient clot resolution thanks to the specific targeting of rtPA-loaded Fuco MBs. Indeed, 1mg/kg injection of rtPA loaded onto targeting MBs, reduced by more

than 50% the size of the ischemic lesion for 16 animals. The drug encapsulation helped protecting the protein and the specific clot targeting lead to the treatment improvement. This result is even more promising as free rtPA treatment at the same concentration was not significantly more efficient than treatment with saline. In consequence, we can hypothesize about the synergic action of rtPA loaded onto Fucoidan MBs for a successful thrombolysis. The specific targeting of fucoidan may also be enhanced with the known affinity of rtPA for fibrin [41] and consequently improve the precise drug delivery. Finally, this efficient targeted drug delivery treatment gets in the range of human recommended dose of 0.9 mg/kg (according to the National Institute of Neurological disorders and Stroke), suggesting that lower dosage of encapsulated rtPA could have beneficial outcomes and reduce dose related side effects in humans too.

No animal was harmed with the injection of rtPA-loaded MBs and we aimed at reducing the number of animals. Hence, control conditions like Fuco MBs, rtPA-loaded CMDex MBs and free rtPA at 10 mg/kg for stroke treatment were not explored. Firstly, Fuco MBs would have been interesting to validate targeting properties *in vivo* compared to rtPA-loaded Fuco MBs. Nevertheless, we demonstrated *in vitro* that the rtPA incorporation did not impair the targeting properties of Fuco MBs (*Fig. 4F*). Secondly, rtPA loaded CMDex MBs treatment evaluation could highlight the importance of targeting for the clot resolution. However, efficient rtPA loading on CMDex MBs was not possible as presented in *Fig. 4B*. Lastly, free rtPA treatment validation of 10 mg/kg efficient thrombolysis on thrombin clot mouse model was largely studied [27], suggesting the real advantage of our dose reduced treatment.

We also studied the outcome and clearance process of MBs after stroke treatment. The circulation time of polymer MBs in the body depends on a number of factors, including size of the MBs, type of polymer, and the density of the gas core [42]. In addition, the circulation time can be influence by the presence of blood proteins that can bind to the surface of MBs and alter their movement through the body. Overall, circulation time is widely dependent of the MBs composition but is usually ranging from minutes to tens of minutes, long enough for conventional diagnosis or therapeutic methods. The biodistribution study was performed at 2 hours after injection in the liver tissue with immunolabelling of resident macrophages to evaluate the early blood detoxification in the liver (*Fig. 7C*). In addition, the biodistribution on *ex vivo* organs revealed the final whereabout of MBs in the body with the expected contrast in liver

and lungs (*Fig. 7A*). The residual fluorescence of rtPA-loaded Fuco MBs was also observed in the stroke region after 24 hours (*Fig. 7A*) validating the specific targeting of fucoidan on P-selectin but also pointed out the long-term expression of the biomarker after the treatment by activated endothelial cells. This suggests an interesting insight for further molecular imaging of thrombotic diseases resolution. Especially since the residual fluorescence is not due to BBB permeability as demonstrated with Gadoteric Acid (GA) injection (*Fig. 6E-F; Fig. S6B*). P-selectin is a known endothelial-related inflammation biomarker [43] and an increase in its concentration within 72 hours could predict the incidence of post stroke infection [44]. Nevertheless, some controversies still remain in the significance of P-selectin expression in stroke versus non stroke patients [45] and molecular imaging could be an alternative way to set the debate. In that manner the study of thrombo-inflammation with Fuco MBs may be investigated over different time points with either fluorescent microscopy or US imaging.

Conclusion

In the present study, we developed ultrasound responsive microbubbles for the targeted treatment of stroke. Acoustic cavitation synthesis was optimized for the production of targeting polymer MBs, firstly described here in the literature. This innovative protocol reduced the production time by three compared to gold standard hydrodynamic cavitation. The physicochemical properties and biocompatibility assessments were intensively evaluated to conclude on their contrast enhancement with US signal, effective targeting of P-selectins, and fibrinolytic potential. The *in vivo* evaluation on mice stroke model demonstrated the efficiency of rtPA-loaded Fuco MBs over clinical systemic injection of the drug. Indeed, we observed a volume reduction of the brain injury by more than 50% with a $1/10^{th}$ lower dose of rtPA than recommended in mice. No BBB permeability or hemorrhagic complication was observed and expected biodistribution was found in detoxification organs including lungs and liver, indicating a high potentiality for a safe and scalable treatment. Our finding now rises new possibilities for the application of drug-loaded targeting MBs. Not only that rtPA gold standard has a short therapeutic window (< 4.5 hours) but can lead to collateral bleeding and neurotoxicity. In consequence, there is a rising interest for the

development of targeted and dose reduced therapies for a safe and efficient clot resolution.

The main perspectives of this work now rely on the US responsive property of MBs. The ischemic memory observed after 24 hours on the stroke region with residual fluorescence on activated endothelium, allowed us to think about the potential of Fuco MBs for molecular imaging [46]. We demonstrated the contrast enhancement capacity of MBs for US signal and targeted imaging with US is an active research field. Indeed, US technology is a non-invasive, safe for pregnant patients and less expensive method compared to other imaging modalities. With the recent advances in stroke US imaging in rats [47], P-selectin targeted MBs present new possibilities for the early diagnosis and clot resolution follow-up of stroke events. Also, chemical thrombolysis alone only achieve good outcomes for 40% of patients [5] and clot migration can cause a variety of serious problems including distal vessels obstruction. The need for non-invasive clot damaging treatment led the scientific community to study microbubble-assisted US clot bursting: the sonothrombolysis. Especially since tissue plasminogen treatment is less efficient on distal occlusions [11], sonothrombolysis could mechanically disrupt the clot [8] in addition to fibrinolysis. Despite the fact that it is an area of active research [48], these therapies are not yet widely available or fully understood. Few boundaries are nevertheless already established, including Mechanical Index threshold of 1.9 and the need of biocompatible MBs. Our technology is then a great candidate for the development of targeted sonothrombolysis for stroke resolution.

Credit author statement

Louise FOURNIER: Conceptualization, Investigation, Experimental work, Data analysis, Writing, Visualization; Myriam ABIOUI-MOURGUES: Investigation (Animal model main investigator), Data validation; Georges CHABOUH: Investigation, Data validation; Rachida AID: Methodology; Thibault DE LA TAILLE: Investigation; Olivier COUTURE: Conceptualization, Methodology; Cyrille ORSET: Conceptualization, Methodology; Cédric CHAUVIERRE: Conceptualization, Review and Editing, Supervision, Project administration, Funding acquisition. All the authors approved the final revised version of the manuscript.

Declaration of competing interest

The author declare that they have no known competing financial interest or personal relationship that could have appeared to influence the work reported in this paper.

Acknowledgments

Authors thank INSERM, Université Paris Cité, Université Sorbonne Paris Nord and the ANR “FightClot” ANR-20-CE18-0005-01, and ANR “FucoChem” ANR-13-LAB1-0005-01 for the financial support. We express our gratitude to Algues & Mer for the supplying of fucoidan. The authors would like to acknowledge Christine CHOQUEUX for the ESEM images performed at Université de Technologie de Compiègne (France). We kindly thank Stephane TACHON from the Nanoimagerie department of Institut Pasteur (France) for the FIB assisted SEM images. We also thank Véronique OLLIVIER and Stéphane LOYAU for their help and expertise on the *in vitro* targeting experiment. The confocal images were also performed with the help of Camille LE GUILCHER and Chloé DUJARDIN, we also thank her and Graciela PAVON-DJAVID for their support in cell culture experiments. The illustrations were designed with BioRender online software (biorender.com).

Supplementary data

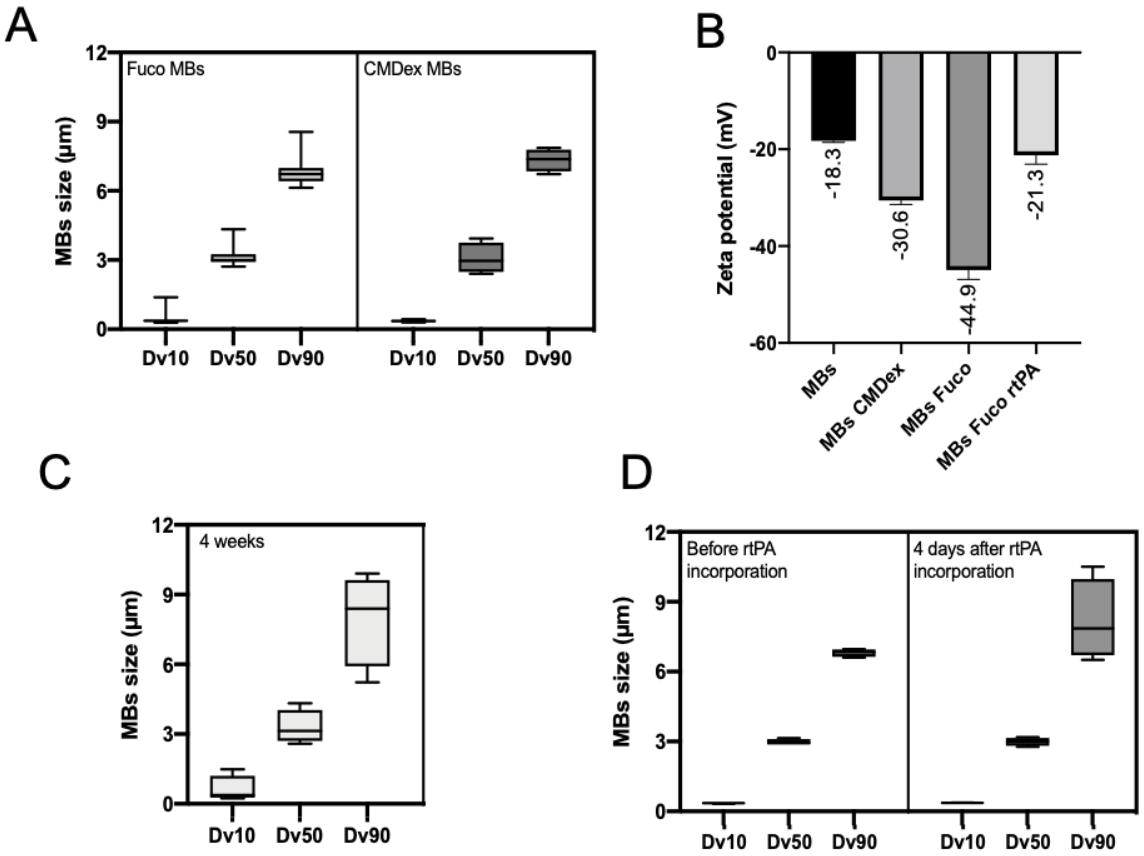

Supplementary Figure 1: MBs size distribution and surface charge. A-C-D) Size measurement of MBs with laser diffraction granulometry. Here, the Dv10; Dv50 and Dv90 are related to the size distribution. For each graph, it corresponds to the size of MBs measured below this percentage. A) MBs size distribution depending on the incorporated polysaccharide, fucoidan or control carboxymethyl dextran. B) Zeta potential measurement with Electrophoretic Light Scattering (ELS). Fuco MBs were demonstrated to be highly negative compared to bare MBs. Carboxymethyl dextran was used as a control polysaccharide not only for its similar size, but for its negative charges close to fucoidan. Also, the incorporation of rtPA onto Fuco MBs decreased the negativity of MBs surface charge. C) MBs size distribution in suspension after 4 weeks at 5°C in 0.02% Tween working buffer. D) MBs size distribution 4 days after rtPA incorporation. The main difference was observed in the big MBs, but still in the range for injection in vivo.

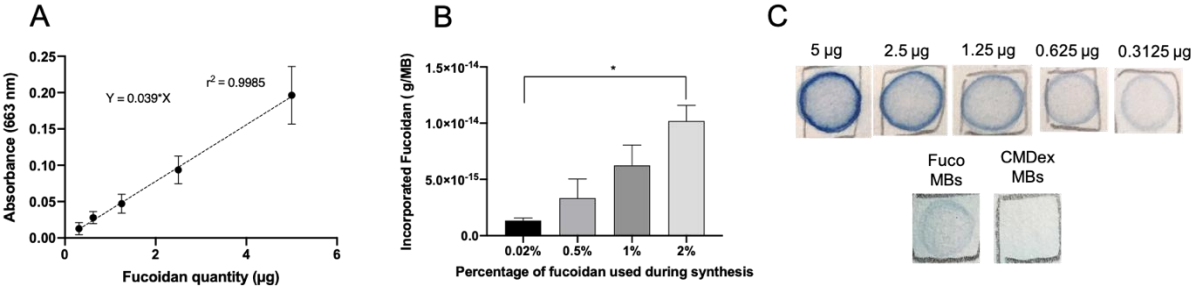

Supplementary Figure 2: Fucoidan quantification with methylen blue colorimetric assay sulfate specific. A) Standard range absorbance of methylene blue in function of fucoidan quantity. B) Linear correlation between the quantity of Fucoidan used for synthesis and the quantity of incorporated Fucoidan. C) Images of methylene blue colorimetric assay. On top, from the most to the least concentrated fucoidan sample. On the bottom, Fucoidan MBs sample compared to Carboxymethyl Dextran MBs.

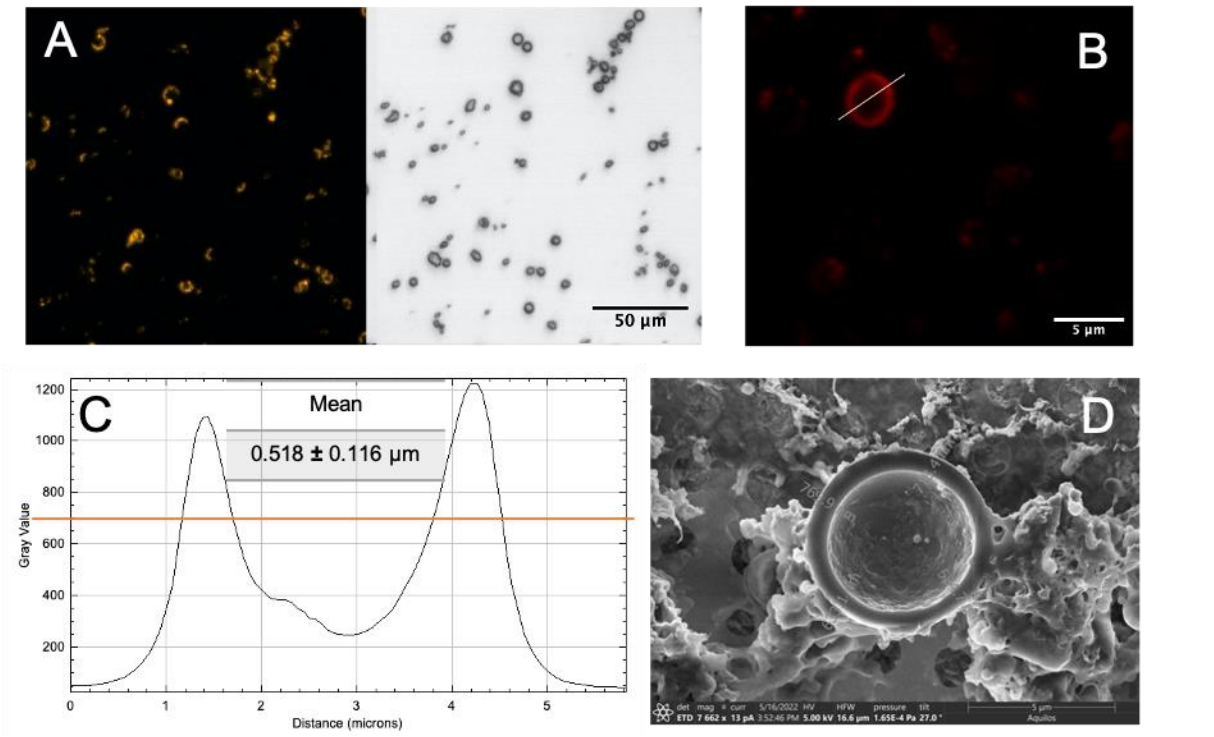

Supplementary Figure 3: MBs shell thickness characterization. A) Confocal images of Rhodamine B MBs. The fluorescent image on the left showed the incorporation of Rhodamine B into MBs shell. The Brightfield image on the right highlighted the hollow structure of the MBs. The scale bar is 50 µm. B-C-D) MBs shell thickness evaluation. B) Confocal fluorescent image of MBs shell and the drawn tangent line. Scale bar is 5 µm. C) Measurement of fluorescent signal with Fiji by plotting the grey value graph of a tangent line to the MBs. The orange line on the graph determines the measured shell thickness reported on the x-axis. It is placed at the mean height of the grey value intensity. D) Scanning Electron Microscopy image of a MBs from the top after being sectioned by a focused ion beam. The shell thickness measured here validated the range of MBs shell thickness. Scale bar is 5 µm.

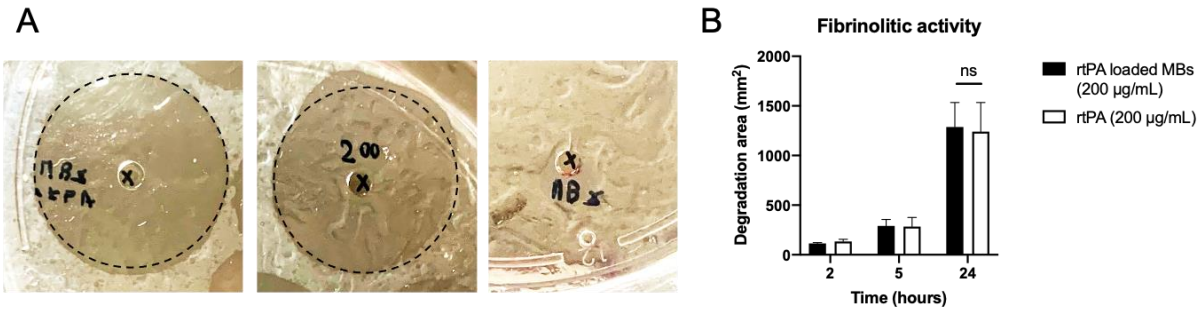

Supplementary Figure 4: Fibrinolytic activity of rtPA-loaded MBs with fibrin gel degradation evaluation. A) Images of fibrin gel degradation circles at same time points. From left to right rtPA-loaded Fuco MBs, free rtPA, Fuco MBs. The well for sample deposition in the center was 5 mm diameter. B) Fibrinolytic activity of rtPA-loaded MBs compared to free rtPA quantification of the degraded area over 24 hours. The degradation kinetic was demonstrated to be similar to free rtPA.

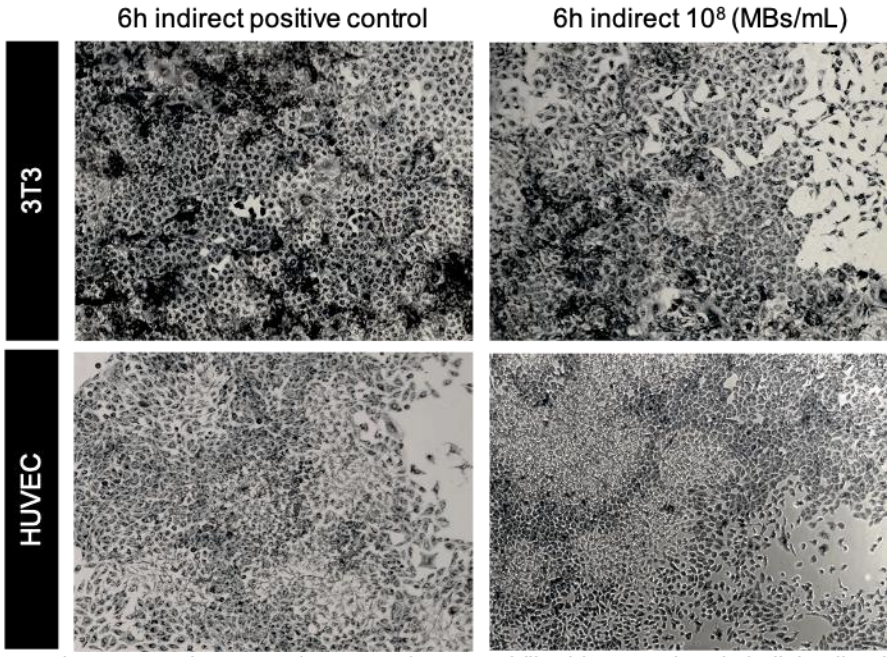

Supplementary Figure 5: Microscopy images of fibroblasts and endothelial cells after MTT assay. The Fuco MBs were incubated for 6 hours with 3T3 and HUVECs. On the left, images of the cells after incubation with Fuco MBs, on the right, images of cells without MBs incubation. The MTT assay consists in the evaluation of the metabolic activity of cells by the reduction of MTT to formazan. Here we can observe the formazan crystals in the cell around the nucleus in the highly concentrated MBs condition and in the control group that validate the harmless behavior of MBs in static conditions.

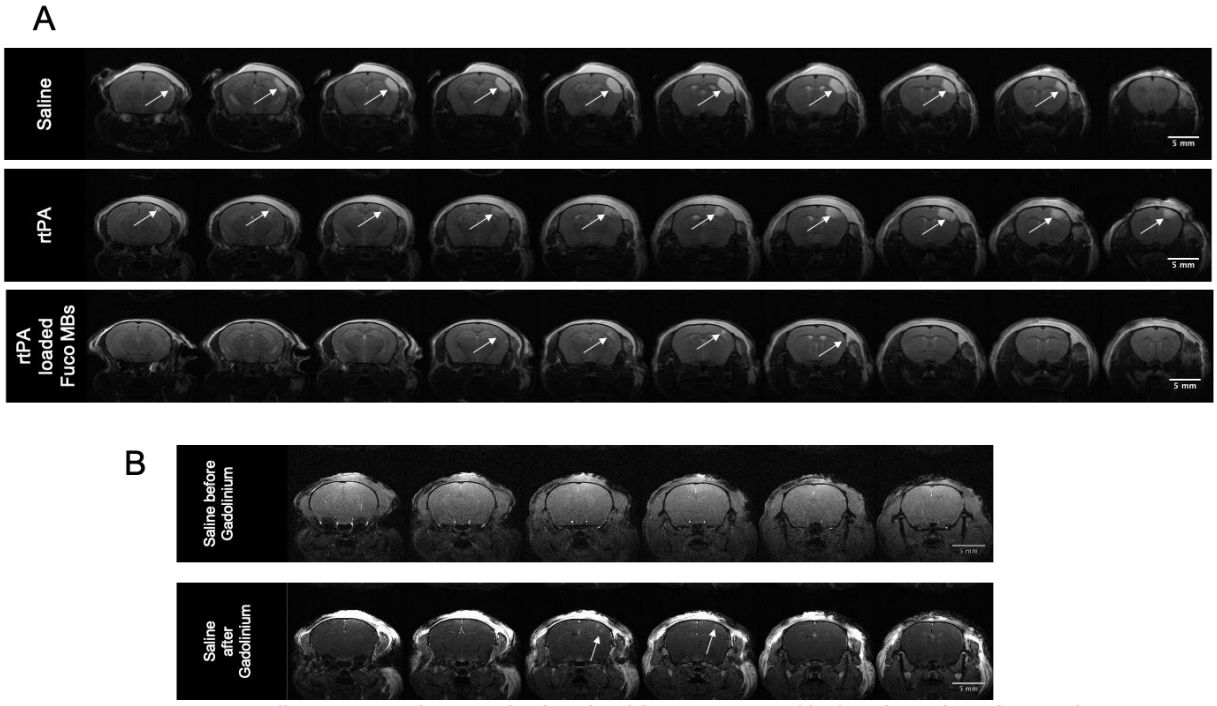

Supplementary Figure 6: Full MRI scan of mouse brain. A) Wider MRI scan of ischemic region after stroke treatment. Slices are ordered from dorsal to frontal and white arrows are pointing at ischemic regions. We observed that the ischemic lesion volume was bigger and present in more plans with saline and free rtPA treatment rather than rtPA-loaded Fuco MBs. Scale bar is 5mm. B) Wider MRI scan of BBB leakage evaluation of stroke mice treated with saline. On top T1 acquisition before injection of Gadoteric Acid (GA), on the bottom after injection ones. White arrows are pointing out what we can observe as a leakage like BBB. Nevertheless, for none of the conditions, a major leakage was observed. Scale bar is 5 mm B.

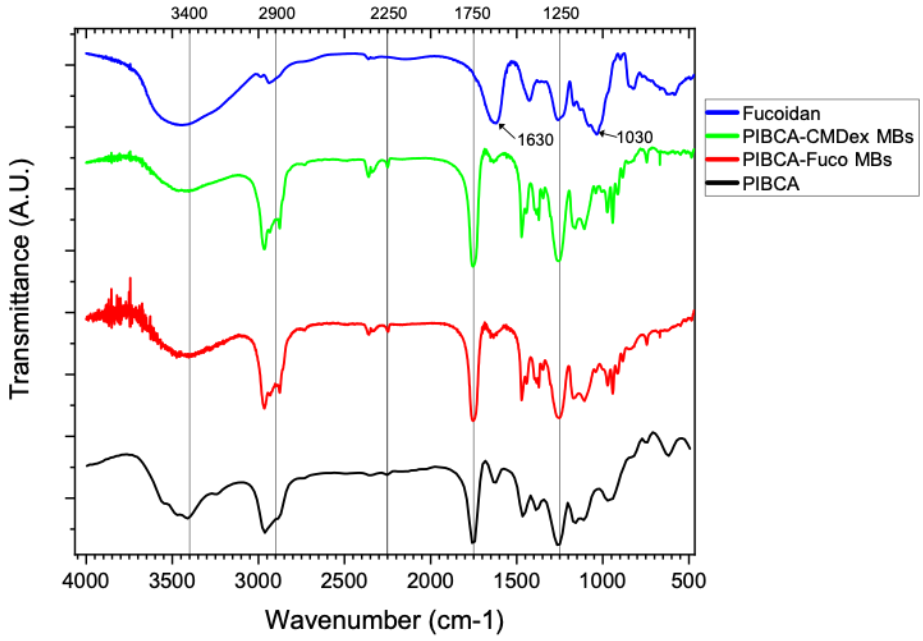

Supplementary Figure 7: FTIR spectra were obtained for different MBs formulations used in this article. The reference formulation is represented with the PIBCA spectrum (black). Fuco MBs are shown in red and CMDex MBs in green. Comparison to fucoidan alone (blue) implies that no fucoidan can be detected by FTIR in MBs formulation, most likely due to its low mass ratio in the MBs. Based on the literature, cyanoacrylate-representative peaks are illustrated (2,900 cm^{-1}, 2,250 cm^{-1}, 1,750 cm^{-1}).

Data availability

The raw/processed data required to reproduce these findings cannot be shared at this time due to legal or ethical reasons.

References

[1] G. A. Roth *et al.*, “GBD-NHLBI-JACC Global Burden of Cardiovascular Diseases Writing Group. Global burden of cardiovascular diseases and risk factors, 1990-2019: update from the GBD 2019 study,” *J Am Coll Cardiol*, vol. 76, no. 25, pp. 2982–3021, 2020.

[2] C. W. Tsao *et al.*, *Heart Disease and Stroke Statistics-2022 Update: A Report from the American Heart Association*, vol. 145, no. 8. 2022.

[3] G. Alkarithi, C. Duval, Y. Shi, F. L. Macrae, and R. A. S. Ariëns, “Thrombus Structural Composition in Cardiovascular Disease,” *Arterioscler. Thromb. Vasc. Biol.*, vol. 41, no. 9, pp. 2370–2383, 2021, doi: 10.1161/ATVBAHA.120.315754.

[4] P. Jolugbo and R. A. S. Ariëns, “Thrombus Composition and Efficacy of Thrombolysis and Thrombectomy in Acute Ischemic Stroke,” *Stroke*, no. March, pp. 1131–1142, 2021, doi: 10.1161/STROKEAHA.120.032810.

[5] S. Prabhakaran, I. Ruff, and R. A. Bernstein, “Acute stroke intervention: A

systematic review," *JAMA - J. Am. Med. Assoc.*, vol. 313, no. 14, pp. 1451–1462, 2015, doi: 10.1001/jama.2015.3058.

[6] A. Zenych, L. Fournier, and C. Chauvierre, "Nanomedicine progress in thrombolytic therapy," *Biomaterials*, vol. 258, no. January, 2020, doi: 10.1016/j.biomaterials.2020.120297.

[7] D. Vivien, "Can the benefits of rtPA treatment for stroke be improved?," *Rev. Neurol. (Paris).*, vol. 173, no. 9, pp. 566–571, 2017, doi: 10.1016/j.neurol.2017.07.003.

[8] A. Chang, E. Beheshtian, E. J. Llinas, O. R. Idowu, and E. B. Marsh, "Intravenous Tissue Plasminogen Activator in Combination With Mechanical Thrombectomy: Clot Migration, Intracranial Bleeding, and the Impact of 'Drip and Ship' on Effectiveness and Outcomes," *Front. Neurol.*, vol. 11, no. December, pp. 1–10, 2020, doi: 10.3389/fneur.2020.585929.

[9] C. Liu *et al.*, "Hemorrhagic Transformation After Tissue Plasminogen Activator Treatment in Acute Ischemic Stroke," *Cell. Mol. Neurobiol.*, vol. 42, no. 3, pp. 621–646, 2022, doi: 10.1007/s10571-020-00985-1.

[10] G. W. J. Harston, B. A. Sutherland, J. Kennedy, and A. M. Buchan, "The contribution of L-arginine to the neurotoxicity of recombinant tissue plasminogen activator following cerebral ischemia: A review of rtPA neurotoxicity," *J. Cereb. Blood Flow Metab.*, vol. 30, no. 11, pp. 1804–1816, 2010, doi: 10.1038/jcbfm.2010.149.

[11] M. Gomis and A. DÃvalos, "Recanalization and Reperfusion Therapies of Acute Ischemic Stroke: What have We Learned, What are the Major Research Questions, and Where are We Headed?," *Front. Neurol.*, vol. 5, no. November, pp. 1–12, 2014, doi: 10.3389/fneur.2014.00226.

[12] A. Rix, A. Curaj, E. Liehn, and F. Kiessling, "Ultrasound Microbubbles for Diagnosis and Treatment of Cardiovascular Diseases," *Semin. Thromb. Hemost.*, 2019, doi: 10.1055/s-0039-1688492.

[13] E. Falk, "Pathogenesis of Atherosclerosis," *J. Am. Coll. Cardiol.*, vol. 47, no. 8 SUPPL., pp. 0–5, 2006, doi: 10.1016/j.jacc.2005.09.068.

[14] L. A. Perkins, C. J. Anderson, and E. M. Novelli, "Targeting P-selectin adhesion molecule in molecular imaging: P-selectin expression as a valuable imaging biomarker of inflammation in cardiovascular disease," *J. Nucl. Med.*, vol. 60, no. 12, pp. 1691–1697, 2019, doi: 10.2967/jnumed.118.225169.

[15] F. Rouzet *et al.*, “Radiolabeled fucoidan as a P-selectin targeting agent for in vivo imaging of platelet-rich thrombus and endothelial activation,” *J. Nucl. Med.*, vol. 52, no. 9, pp. 1433–1440, 2011, doi: 10.2967/jnumed.110.085852.

[16] C. Chauvierre *et al.*, “Pharmaceutical development and safety evaluation of a GMP-grade fucoidan for molecular diagnosis of cardiovascular diseases,” *Mar. Drugs*, vol. 17, no. 12, 2019, doi: 10.3390/md17120699.

[17] L. Bachelet *et al.*, “Affinity of low molecular weight fucoidan for P-selectin triggers its binding to activated human platelets,” *Biochim. Biophys. Acta - Gen. Subj.*, vol. 1790, no. 2, pp. 141–146, 2009, doi: 10.1016/j.bbagen.2008.10.008.

[18] A. Zenych *et al.*, “Biomaterials Fucoidan-functionalized polysaccharide submicroparticles loaded with alteplase for efficient targeted thrombolytic therapy,” *Biomaterials*, vol. 277, no. August, 2021, doi: 10.1016/j.biomaterials.2021.121102.

[19] B. Li *et al.*, “Functionalized polymer microbubbles as new molecular ultrasound contrast agent to target P-selectin in thrombus,” *Biomaterials*, vol. 194, no. 2019, pp. 139–150, 2019, doi: 10.1016/j.biomaterials.2018.12.023.

[20] G. Chabouh, B. Dollet, C. Quilliet, and G. Coupier, “Spherical oscillations of encapsulated microbubbles: Effect of shell compressibility and anisotropy,” *J. Acoust. Soc. Am.*, vol. 149, no. 2, pp. 1240–1257, 2021, doi: 10.1121/10.0003500.

[21] L. Auboire *et al.*, “Microbubbles combined with ultrasound therapy in ischemic stroke: A systematic review of in-vivo preclinical studies,” *PLoS One*, vol. 13, no. 2, pp. 1–19, 2018, doi: 10.1371/journal.pone.0191788.

[22] A. L. Klibanov, “Ultrasound Contrast: Gas Microbubbles in the Vasculature,” *Invest. Radiol.*, vol. 56, no. 1, pp. 50–61, 2021, doi: 10.1097/RLI.0000000000000733.

[23] A. Upadhyay and S. V. Dalvi, “Microbubble Formulations: Synthesis, Stability, Modeling and Biomedical Applications,” *Ultrasound Med. Biol.*, vol. 45, no. 2, pp. 301–343, 2019, doi: 10.1016/j.ultrasmedbio.2018.09.022.

[24] J. M. Lee, Z. U. Shin, G. T. Mavlonov, I. Y. Abdurakhmonov, and T. H. Yi, “Solid-phase colorimetric method for the quantification of fucoidan,” *Appl. Biochem. Biotechnol.*, vol. 168, no. 5, pp. 1019–1024, 2012, doi: 10.1007/s12010-012-9837-y.

[25] B. Li *et al.*, “Development of Polymer Microcapsules Functionalized with

Fucoidan to Target P-Selectin Overexpressed in Cardiovascular Diseases," *Adv. Healthc. Mater.*, vol. 6, no. 4, 2017, doi: 10.1002/adhm.201601200.

[26] A. J. Koning, P. Y. Lum, J. M. Williams, and R. Wright, "DiOC6 staining reveals organelle structure and dynamics in living yeast cells," *Cell Motil. Cytoskeleton*, vol. 25, no. 2, pp. 111–128, 1993, doi: 10.1002/cm.970250202.

[27] C. Orset *et al.*, "Mouse model of in situ thromboembolic stroke and reperfusion," *Stroke*, vol. 38, no. 10, pp. 2771–2778, 2007, doi: 10.1161/STROKEAHA.107.487520.

[28] O. Couture, S. Bannouf, G. Montaldo, J. F. Aubry, M. Fink, and M. Tanter, "Ultrafast Imaging of Ultrasound Contrast Agents," *Ultrasound Med. Biol.*, vol. 35, no. 11, pp. 1908–1916, 2009, doi: 10.1016/j.ultrasmedbio.2009.05.020.

[29] O. Couture, M. Fink, and M. Tanter, "Ultrasound contrast plane wave imaging," *IEEE Trans. Ultrason. Ferroelectr. Freq. Control*, vol. 59, no. 12, pp. 2676–2683, 2012, doi: 10.1109/TUFFC.2012.2508.

[30] K. Renault, J. W. Fredy, P. Y. Renard, and C. Sabot, "Covalent Modification of Biomolecules through Maleimide-Based Labeling Strategies," *Bioconjug. Chem.*, vol. 29, no. 8, pp. 2497–2513, 2018, doi: 10.1021/acs.bioconjchem.8b00252.

[31] L. D. C. Casa and D. N. Ku, "Thrombus Formation at High Shear Rates," *Annu. Rev. Biomed. Eng.*, vol. 19, pp. 415–433, 2017, doi: 10.1146/annurev-bioeng-071516-044539.

[32] O. Chevallier *et al.*, "Efficacy, safety and outcomes of transcatheter arterial embolization with N-butyl cyanoacrylate glue for non-variceal gastrointestinal bleeding: A systematic review and meta-analysis," *Diagn. Interv. Imaging*, vol. 102, no. 7–8, pp. 479–487, 2021, doi: 10.1016/j.diii.2021.03.004.

[33] K. H. Zheng *et al.*, "99Mtc-Fucoidan As Diagnostic Agent For P-Selectin Imaging: First-In-Human Evaluation (Phase I)," *Atherosclerosis*, vol. 287, no. 2019, p. e143, 2019, doi: 10.1016/j.atherosclerosis.2019.06.425.

[34] A. V. Alexandrov *et al.*, "Safety and efficacy of sonothrombolysis for acute ischaemic stroke: a multicentre, double-blind, phase 3, randomised controlled trial," *Lancet Neurol.*, vol. 18, no. 4, pp. 338–347, 2019, doi: 10.1016/S1474-4422(19)30026-2.

[35] X. Li *et al.*, "Efficacy and safety of sonothrombolysis in patients with acute ischemic stroke: A systematic review and meta-analysis," *J. Neurol. Sci.*, vol. 416, no. May, p. 116998, 2020, doi: 10.1016/j.jns.2020.116998.

[36] T. R. Porter and W. Mathias, “Cardiovascular Sonothrombolysis,” *Curr. Cardiol. Rep.*, vol. 21, no. 8, 2019, doi: 10.1007/s11886-019-1167-z.

[37] Y. Deng, M. L. Palmeri, N. C. Rouze, G. E. Trahey, C. M. Haysteas, and K. R. Nightingale, “QUANTIFYING IMAGE QUALITY IMPROVEMENT USING ELEVATED ACOUSTIC OUTPUT IN B-MODE HARMONIC IMAGING,” *Ultrasound Med Biol.*, vol. 43, no. 10, pp. 2416–2425, 2017, doi: 10.1016/j.ultrasmedbio.2017.06.024.QUANTIFYING.

[38] D. García Cerdá, A. M. Ballester, A. Aliena-Valero, A. Carabén-Redaño, and J. M. Lloris, “Use of cyanoacrylate adhesives in general surgery,” *Surg. Today*, vol. 45, no. 8, pp. 939–956, 2015, doi: 10.1007/s00595-014-1056-4.

[39] X. Lin *et al.*, “Establishment of a Modified and Standardized Ferric Chloride-Induced Rat Carotid Artery Thrombosis Model,” *ACS Omega*, vol. 7, no. 10, pp. 8919–8927, 2022, doi: 10.1021/acsomega.1c07316.

[40] C. Orset *et al.*, “Efficacy of Alteplase® in a mouse model of acute ischemic stroke : a Retrospective Pooled Analysis,” *Stroke*, vol. 47, no. 5, pp. 1312–1318, 2016, doi: 10.1161/STROKEAHA.116.012238.Efficacy.

[41] A. Zhu, P. Rajendram, E. Tseng, S. B. Coutts, and A. Y. X. Yu, “Alteplase or tenecteplase for thrombolysis in ischemic stroke: An illustrated review,” *Res. Pract. Thromb. Haemost.*, vol. 6, no. 6, pp. 1–13, 2022, doi: 10.1002/rth2.12795.

[42] E. Stride *et al.*, “Microbubble Agents: New Directions,” *Ultrasound Med. Biol.*, vol. 00, no. 00, 2020, doi: 10.1016/j.ultrasmedbio.2020.01.027.

[43] D. D. Zhang *et al.*, “Inflammatory biomarkers and cerebral small vessel disease: a community-based cohort study,” *Stroke Vasc. Neurol.*, vol. 7, no. 4, pp. 302–309, 2022, doi: 10.1136/svn-2021-001102.

[44] G. Pusch *et al.*, “Early Dynamics of P-selectin and Interleukin 6 Predicts Outcomes in Ischemic Stroke,” *J. Stroke Cerebrovasc. Dis.*, vol. 24, no. 8, pp. 1938–1947, 2015, doi: 10.1016/j.jstrokecerebrovasdis.2015.05.005.

[45] S. Wiseman, F. Marlborough, F. Doubal, D. J. Webb, and J. Wardlaw, “Blood markers of coagulation, fibrinolysis, endothelial dysfunction and inflammation in lacunar stroke versus non-lacunar stroke and non-stroke: Systematic review and meta-analysis,” *Cerebrovasc. Dis.*, vol. 37, no. 1, pp. 64–75, 2014, doi: 10.1159/000356789.

[46] G. Köse, M. Darguzyte, and F. Kiessling, “Molecular ultrasound imaging,” *Nanomaterials*, vol. 10, no. 10, pp. 1–28, 2020, doi: 10.3390/nano10101935.

[47] A. Chavignon, V. Hingot, C. Orset, D. Vivien, and O. Couture, “3D transcranial ultrasound localization microscopy for discrimination between ischemic and hemorrhagic stroke in early phase,” *Sci. Reports 2022 121*, vol. 12, no. 1, pp. 1–11, Aug. 2022, doi: 10.1038/S41598-022-18025-X.

[48] T. Porter, P. Zeng, and F. Xie, “Advances in Ultrasound Therapeutics,” *Curr. Cardiol. Rep.*, vol. 23, no. 10, pp. 4–11, 2021, doi: 10.1007/s11886-021-01563-7.

ANNEX 5

Biomaterials 277 (2021) 121102

Contents lists available at ScienceDirect

Biomaterials

journal homepage: www.elsevier.com/locate/biomaterials

Fucoidan-functionalized polysaccharide submicroparticles loaded with alteplase for efficient targeted thrombolytic therapy

Alina Zenych [a], Charlène Jacqmarcq [b,1], Rachida Aid [a,c,1], Louise Fournier [a], Laura M. Forero Ramirez [a], Frédéric Chaubet [a], Thomas Bonnard [b], Denis Vivien [b,d,1], Didier Letourneur [a,1], Cédric Chauvierre [a,*]

[a] Université de Paris, Université Sorbonne Paris Nord, UMR S1148, INSERM, F-75018, Paris, France
[b] INSERM U1237 Physiopathology and Imaging of Neurological Disorders (PhIND), Institut Blood and Brain @ Caen Normandie (BB@C), GIP Cyceron, 14074, Caen, France
[c] Université de Paris, FRIM, UMS 034, INSERM, F-75018, Paris, France
[d] Department of Clinical Research, Caen Normandie University Hospital (CHU), 14074, Caen, France

ARTICLE INFO

Keywords:
Nanomedicine
Drug delivery
Targeted thrombolysis
Polysaccharides
Fucoidan
P-Selectin

ABSTRACT

Intravenous administration of fibrinolytic drugs is the standard treatment of acute thrombotic diseases. However, current fibrinolytics exhibit limited clinical efficacy because of their short plasma half-lives and might trigger hemorrhagic transformations. Therefore, it is mandatory to develop innovative nanomedicine-based solutions for more efficient and safer thrombolysis with biocompatible and biodegradable thrombus-targeted nanocarrier. Herein, fucoidan-functionalized hydrogel polysaccharide submicroparticles with high biocompatibility are elaborated by the inverse miniemulsion/crosslinking method. They are loaded with the gold standard fibrinolytic – alteplase – to direct site-specific fibrinolysis due to nanomolar interactions between fucoidan and *P*-selectin overexpressed on activated platelets and endothelial cells in the thrombus area. The thrombus targeting properties of these particles are validated in a microfluidic assay containing recombinant *P*-selectin and activated platelets under arterial and venous blood shear rates as well as *in vivo*. The experiments on the murine model of acute thromboembolic ischemic stroke support this product's therapeutic efficacy, revealing a faster recanalization rate in the middle cerebral artery than with free alteplase, which reduces post-ischemic cerebral infarct lesions and blood-brain barrier permeability. Altogether, this proof-of-concept study demonstrates the potential of a biomaterial-based targeted nanomedicine for the precise treatment of acute thrombotic events, such as ischemic stroke.

1. Introduction

Acute thrombotic pathologies such as myocardial infarction, ischemic stroke, and venous thromboembolism remain a major global healthcare challenge contributing to a significant number of deaths and disabilities [1]. Current thrombolytic therapy, the intravenous injection of Plasminogen Activators (PA), is administrated to lyse a clot-induced vascular occlusion and restore the blood flow in the vessel. The recombinant tissue plasminogen activator (rtPA) is the most commonly applied clot-busting drug in clinics and the only one approved to treat acute ischemic stroke [2]. rtPA is a fibrin-specific serine protease that activates the endogenous proenzyme plasminogen and converts it to the active form plasmin, thus, degrading the thrombus fibrin network. However, systemic delivery of rtPA is limited by the rapid drug elimination (half-life 4–6 min), physiological deactivation by its antidotes such as Plasminogen Activator Inhibitors (PAI-1 and PAI-2), and deleterious side-effects such as intracranial hemorrhages [3]. This restricts its use to a narrow therapeutic window (4.5 h of stroke symptom onset when injected alone and 6 h when combined with mechanical thrombectomy), beyond which the deleterious effects of rtPA overcome its benefits. Moreover, the rate of acute recanalization after intravenous administration of rtPA is low: only ~30% of patients experienced full or partial recanalization [4].

Therapeutic strategies that intend to address the challenges of

* Corresponding author.
E-mail address: cedric.chauvierre@inserm.fr (C. Chauvierre).
[1] Equal contribution.

https://doi.org/10.1016/j.biomaterials.2021.121102
Received 9 February 2021; Received in revised form 22 June 2021; Accepted 25 August 2021
Available online 30 August 2021
0142-9612/© 2021 Elsevier Ltd. All rights reserved.

thrombolytic therapy and boost survival rates remain of great clinical interest. Certainly, novel thrombolytic molecules are being researched to increase reperfusion, improve safety, and protect the brain neurovascular unit [5,6]. Apart from that, nanomedical approaches for the targeted delivery of thrombolytic agents have been intensively proposed [7]. Korin et al. reported the microaggregates of poly (lactic-co-glycolic acid) (PLGA) nanoparticles (NPs) dissociated into rtPA-bearing nanocompounds when exposed to abnormally high hemodynamic shear stress, typical for the vascular occlusions, that performed effective thrombolysis in several preclinical models [8]. Colasuonno et al. formulated rtPA-loaded discoidal porous nanoconstructs from a mixture of PLGA and polyethylene glycol (PEG) with high thrombolytic potential presumably attributed to the erythrocyte-mimicking shape of the NPs and their deformability, leading to efficient circulation profiles and accumulation on the clot [9]. While these nanosystems with passive targeting succeeded in a promising thrombolytic efficacy in preclinical studies, more recent and advanced examples are formulated with actively targeted nanocarriers.

Active targeting permits drug accumulation specifically at the thrombus site and has the potential to enhance the enzyme penetration into deeply localized thrombi. Apart from the magnetic nanoparticle targeting under an external magnetic field [10–12] active blood clot targeting is currently achieved by directing the functionalized NPs towards fibrin or activated platelets (mostly integrin GPIIb/IIIa and less adhesion receptor *P*-selectin) with antibodies and/or peptides. Notably, Zhou et al. developed a theranostic system for thrombus molecular imaging and targeted therapy that could bind GPIIb/IIIa owing to a film of cyclic arginine-glycine-aspartic acid (cRGD) peptide grafted onto the chitosan, which covered the surface of rtPA-encapsulated Fe_3O_4-based PLGA NPs [13]. Nevertheless, both antibodies and peptides have their limitations for targeted drug delivery. The immunogenicity, purity, and sufficient circulation time are the main concerns of the application of the antibodies [14], while peptides might suffer from weak binding affinity, immunogenicity, a high costs of peptide synthesis, and metabolic instability with fast renal clearance due to their small sizes [15].

An effective alternative could be the nanoparticle functionalization with fucoidan [16], a naturally-occurring algae-derived sulfated polysaccharide that exhibits a strong and specific tropism for the *P*-selectin overexpression in cardiovascular pathologies [17,18]. Fucoidan emerged as an affordable, high-quality targeting ligand to *P*-selectin that was prior validated by our group on various polysaccharide-based nano- & microsystems for molecular diagnostics and targeted therapy [19–23]. Following the obtention of the label “raw materials for pharmaceutical uses” in 2015 in France, it became a part of the large-scale European Union project NanoAthero as a contrast agent for Single-Photon Emission Computed Tomography (SPECT) imaging in human atherothrombosis, coordinated by our laboratory [24]. The first in the world Phase I clinical trial on intravenous delivery of fucoidan radiolabeled by Technetium-99m reported its safety and favorable biodistribution [25], while Phase IIa for the imaging of deep vein thrombosis and pulmonary embolism is ongoing.

It is critical to ensure an excellent safety profile of the designed nanocarrier for targeted thrombolysis in future clinical translation by selecting biocompatible and fully biodegradable materials with the U.S. Food and Drug Administration (FDA)-approval [26]. Contrary to the attractiveness of synthetic polymers such as PLGA, the NPs made of polysaccharides are explored to a lesser degree for thrombolytic therapy. Yet, they benefit from the general advantages of natural polymers: biocompatibility, low cost, and hydrophilicity. Polysaccharide hydrogels, which are crosslinked three-dimensional polymer networks, absorb large quantities of water and can effectively load macromolecules with high encapsulation efficiency [27], including plasminogen activators. Few publications reported the nanoformulations of thrombolytic agents with chitosan, a cationic chitin-derived polysaccharide that can form polyelectrolyte complexes with negatively charged molecules [28]. For instance, superior thrombolytic potential *in vivo* was demonstrated on self-assembled chitosan NPs crosslinked with sodium tripolyphosphate and loaded with urokinase [29]. Liao et al. formulated the lumbrokinase-bearing NPs from quaternized derivative of chitosan - N, N,N-Trimethyl Chitosan covalently grafted with cRGD peptide to target GPIIb/IIIa receptors that could accelerate thrombolysis [30].

Dextran, an exocellular bacterial water-soluble polysaccharide, is extensively employed in clinics, particularly in its low molecular weight (40 and 70 kDa), for plasma volume expansion, thrombosis prophylaxis, peripheral blood flow enhancement, artificial tears, *etc*. [31] Dextran coating of magnetic NPs is applied to ensure their environmental stability and prolong the blood circulation time [32,33]. However, there is no reported exclusively dextran nanocarrier with hydrogel structure for thrombolytic application to our knowledge. Meeting the requirements of biocompatibility, biodegradability, non-immunogenicity, dextran stands out as an attractive polymer to design an alteplase delivery system.

Herein, we fabricated novel fucoidan-functionalized dextran submicroparticles (SPs) by a green chemistry method using fully biodegradable and biocompatible compounds, all of them approved by the FDA. After physico-chemical and biosafety characterization of these hydrogel-like SPs, rtPA was loaded onto the SPs with a high encapsulation capacity, and its release in saline and *in vitro* amidolytic and fibrinolytic activities were tested. Through the *in vitro* microfluidic experiments under continuous arterial or venous flow, we provided evidence that fucoidan-functionalized SPs (Fuco-SPs) have a high and specific affinity to *P*-selectin and accumulate on activated platelet aggregates. Also, these particles bind to the thrombi *in vivo*. Finally, rtPA-associated Fuco-SPs proved superior *in vivo* thrombolytic efficacy in a mouse stroke thrombin model with a faster vessel recanalization that minimized cerebral tissue damage: the post-ischemic lesion and blood-brain barrier (BBB) permeability.

2. Materials and methods

Materials: Dextran 40 kDa and TRITC-dextran 40 kDa were provided by TdB Consultancy (Uppsala, Sweden). Fucoidan (Mn = 18 kDa/Mw = 104 kDa, 14.1 wt % sulfates by elemental analysis) was a gift from Algues & Mer (Ouessant, France). Sodium trimetaphosphate (STMP), methylene blue hydrate, and Human Serum Albumin (HSA) were purchased from Sigma-Aldrich (Saint-Quentin-Fallavier, France). Polyglycerol polyricinoleate (PGPR) was obtained from Palsgaard France S. A.S. (Lyon, France). Vegetable – sunflower – oil (Lesieur - Huile Coeur de Tournesol, Lesieur S.A.S, Asnières-sur-Seine, France) was purchased from a local supermarket (Monoprix, Paris, France). The SPs were encapsulated with commercially available rtPA (Actilyse®, Boehringer Ingelheim) that was reconstituted at 1 mg/ml, aliquoted, and stored at −80 °C. Chromatography paper was obtained from GE Healthcare (Chicago, Illinois, United States). Fibrillar type I collagen from equine tendon Horm® was purchased from Takeda (Linz, Austria). 96-Well Cell Culture Plates (Costar) were obtained from Corning Incorporated. PPACK (Phe-Pro-Arg-Chloromethylketone) 75 μM tubes were purchased from Cryopep (Montpellier, France). Flow chambers (Vena8 Fluoro+) were provided by Cellix Ltd (Dublin, Ireland).

Submicroparticle synthesis: Polysaccharide submicroparticles (SPs) were obtained via a water-in-oil (w/o) emulsification combined with a crosslinking process [19,20]. Polysaccharide solution (300 mg/ml, 6 M NaCl) was prepared as a mixture of dextran 40 and 5% TRITC-dextran 40 (for fluorescent SPs). To synthesize functionalized SPs with fucoidan (Fuco-SPs), 10% w/w of fucoidan was added. Table S1, Supplementary Data describes the synthesis parameters of SPs.

First, the organic phase of 15 mL of sunflower oil and 6% w/v PGPR in Falcon® 50 mL was prepared and cooled down for 20 min at −20 °C. In the meantime, 1200 mg of the polysaccharide solution was incubated with 120 μL of 10 M NaOH under magnetic stirring for 10 min. 240 μL of STMP solution (30% w/v in water) was added into the aqueous phase under magnetic stirring and mixed for 20 s on ice. Next, emulsification

was achieved by the dropwise injection of 600 μL of the aqueous phase into the organic phase and dispersed with a stand-disperser (Polytron PT 3100, dispersing aggregate PT-DA 07/2 EC-B101, Kinematica, Luzernerstrasse, Switzerland) at 30,000 rpm for 4 min on ice. The obtained w/o emulsion was transferred into 50 °C for the crosslinking reaction of polysaccharides with STMP for 20 min. The crosslinked suspension was washed in 30 mL PBS 10x for 40 min under high magnetic stirring at 750 rpm. The mixture was then centrifuged (BR4i, JOUAN SA, Saint Herblain, France) for 10 min at 3000 g in Falcon tubes. The organic phase was recovered and ultracentrifuged (Optima MAX-XP, Ultracentrifuge, Beckman Coulter, Brea, California, United States) in PBS for 45 min at 15,000 g. The obtained pellet was washed by ultracentrifugation 2 times in 0.04% Sodium Dodecyl Sulfate (SDS) solution and then 3 times in ultrapure water to purify the SPs. The resulting SPs were suspended in water or 0.9% NaCl with 0.02% Tween 20 (Sigma) and stored at 4 °C.

Physico-chemical characterization: The submicroparticle (SP) formulations were studied for particle morphology, size and zeta potential distributions, mass concentration, and elemental composition.

Particle morphology was visualized by Transmission Electron Microscopy (TEM) (Philips FEI Tecnai 12, Amsterdam, Netherlands), negatively stained with 1% (w/v) uranyl acetate for 5 min, and Environmental Scanning Electron Microscopy (ESEM) (Philips XL30 ESEM-FEG, Amsterdam, Netherlands) with the following parameters: HV 5 kV, HFW 25.4 μm, magnification 5 000 x, WD 9.4 mm, mode SE, pressure 3.00e-6 Torr.

Hydrodynamic size and Zeta potential (ζ-potential) were measured by Dynamic Light Scattering (DLS) and Electrophoretic Light Scattering (ELS), respectively (Zetasizer Nano ZS, Malvern Instruments SARL, Orsay, France). Samples were diluted in distilled water or saline for size and in 1 mM KCl for ζ-potential determination. All runs were performed at 25 °C in triplicate.

Mass concentration was determined by freeze-drying. An elemental analyzer-mass spectrophotometer was used for the quantification of the sulfur (presence of fucoidan). To prove the crosslinking with STMP, the total reflection X-ray fluorescence spectroscopy (TXRF) technique was applied to quantify the phosphorus content on the SPs (S2 PICOFOX Bruker, Massachusetts, United States).

Sulfate and fucoidan quantification: The sulfate content of fucoidan was determined by a semi-quantitative solid-phase colorimetric assay [34]. Briefly, 5 μL of Fuco-SPs in suspension at a concentration of 2 mg/ml were dropped on a piece of Whatman Chromatography paper grade 1. This was repeated 5 times on the same point, allowing the paper to dry at 50 °C in between. The paper was first soaked into a methanol/acetone (6:4) solution for 3 min and then into a methanol/acetone/water (6:4:15) solution with 50 mM HCl and 0.1% w/w methylene blue for 10 min. Finally, the paper was extensively washed with acetic acid/methanol/acetone/water (5:6:4:75) until no coloration was detected in the washing solution. The paper was then transferred to the Eppendorf, containing 0.5 mL methanol with 2% w/v SDS, and incubated for 15 min at 50 °C. 0.2 mL of the extracted dye was placed in a 96-well plate, and its concentration was determined by reading absorbance at 663 nm on an Infinite® 200 PRO microplate reader (TECAN Group Ltd, Mannedorf, Switzerland). Standard curves were obtained from fucoidan in solution with known concentrations.

Cell culture and cytotoxicity assay: To evaluate the cytotoxicity of the SPs, Fluorometric Cell Viability Assay (Resazurin) was used on confluent Human Umbilical Vein Endothelial Cells (HUVECs). The cells were cultured in DMEM supplemented with 10% (v/v) fetal bovine serum, 4 mmol of L-glutamine, 100 units/ml of penicillin, and 100 μg/ml of streptomycin and kept in an incubator at 37 °C in a humidified atmosphere of 5% CO_2. Cells were seeded into 96-well plates to adhere, 10,000 cells per well. Following 24 h of incubation to reach ~80% confluency, the medium in the wells was changed to the one containing the SPs at concentrations ranging from 0.1 to 1.5 mg/ml and cultured for another 24 h. The SPs were prior sterilized under the UV light for 15 min. Next, the medium was replaced with 100 μL 10% Resazurin solution, and the plates were covered in foil and incubated for 2 h. Culture media were used as a negative control. The Resazurin's fluorescent signals were monitored using 540 nm excitation and 590 nm emission wavelengths on Infinite® 200 PRO microplate reader (TECAN Group Ltd, Mannedorf, Switzerland). The obtained fluorescence (Fl) values were blank corrected, and the relative cell viability was expressed as $Fl_{SPs}/Fl_{control} \times 100\%$, where $Fl_{control}$ was obtained in the absence of the SPs. The experiment was performed in hexaplicate.

To examine the potential cell cytoskeleton organization mediated by Fuco-SPs, HUVECs cells were cultured in 8-well Lab-Tek II Chamber Slide w/Cover (Lab-Tek®, Thermo Fischer Scientific, Massachusetts, United States) with 10,000 cells per well. The wells' medium was changed 24 h after to the one containing TRITC-Fuco-SPs at 1.5 mg/ml and was incubated for another 24 h. Cells cultured in the medium without the SPs were set as control. Next, cells were fixed with 4% paraformaldehyde for 30 min at room temperature (RT). After rinsing with PBS, cells were labeled and permeabilized with the 200 μl mixture of FITC-Phalloidin (1:200, Sigma-Aldrich, USA)/DAPI (1:100, Thermo Fisher Scientific, Massachusetts, United States)/0.01% v/v Tween 20 in PBS and incubated under low agitation for 1 h at RT. The cells were afterward washed 3 times with PBS. The support of the chamber slides was removed, and the slides were mounted with a few drops of the aqueous mounting medium and kept at 4 °C until visualization with the confocal microscope (Zeiss LSM 780, Iena, Germany).

Hemocompatibility test: Hemolysis assay was adapted from the publication [20] and performed on washed isolated murine erythrocytes. Murine blood was collected in sodium citrate 3.8% (w/v) and centrifuged at 800 g for 5 min to isolate red blood cells. The supernatant was removed, and the pellet of erythrocytes was resuspended at 20% (v/v) in distilled water (positive control, 100% hemolysis), normal saline (negative control, no hemolysis), and the Fuco-SPs at concentrations from 0.1 to 1.5 mg/ml in Eppendorf. The tubes were incubated on a rotator at 37 °C for 1.5 h and then centrifuged at 3000 g for 5 min. The absorbance (A) of the supernatants was measured on Infinite® 200 PRO microplate reader (TECAN Group Ltd, Mannedorf, Switzerland) at 590 nm. Each sample was run in triplicate. The percentage of hemolysis was determined by the formula: Hemolysis degree (%) = 100% x $(A_{sample} - A_{negative\ control})/(A_{positive\ control} - A_{negative\ control})$.

Loading rtPA on the SPs: rtPA was immobilized onto the SPs by adsorption. 100 μl of SPs (5 mg/ml) was mixed with 100 μl of rtPA (1 mg/ml) in ultrapure water and then incubated for 1 h at RT. Free unabsorbed rtPA was removed by 3 cycles of ultracentrifugation (15 min, 15,000 g). The SPs with adsorbed rtPA (rtPA-SPs) were resuspended in water and used for the drug loading efficiency quantification.

Drug encapsulation efficiency: The amount of rtPA loaded on the SPs was measured using the Pierce BCA protein assay kit (Life Technologies SAS, Courtaboeuf, France). Briefly, 200 μl of working reagent was added to 25 μL of each sample in 96 well-plate. The absorbance at 562 nm was read on the Infinite® 200 PRO microplate reader (TECAN Group Ltd, Mannedorf, Switzerland) after 30 min of incubation at 37 °C and cooling to RT for 10 min. The concentration of the drug was extrapolated by a calibration curve prepared with different concentrations of rtPA.

The encapsulation efficacy (EE) was calculated as EE (%) = 100% x B/A, whereas B is the amount of rtPA loaded onto the SPs and A is the total quantity of rtPA put in contact with the SPs.

In vitro rtPA release: The release of rtPA from the Fuco-SPs was assessed by flow cytometry [35]. FITC-rtPA (Abcam, Cambridge, United Kingdom) at 1 mg/ml was placed in contact with TRITC Fuco-SPs at 5 mg/ml for 1 h at RT. The suspensions were added to tubes pre-filled with 400 μL of saline and placed under gentle agitation at 37 °C. At each time point of 0, 15, 30, 45, 60, and 90 min, the tubes were analyzed with a BD FACS Aria™ III flow cytometer (Becton Dickinson, New Jersey, United States). The TRITC-Dextran, excited by a 543 nm laser, was detected at 569 nm, while the FITC-rtPA, excited at 480 nm, was detected on a 530/30 nm PMT. Flow cytometry analyses were performed in triplicates

with Diva software (Becton Dickinson). The protein release curve was obtained by normalizing the values of Mean Fluorescence Intensity (MFI) of the FITC-rtPA still associated with TRITC-Fuco-SPs.

In vitro amidolytic activity of rtPA-loaded SPs: Amidolytic activity of rtPA loaded SPs was assessed with the fluorogenic substrate PefaFluor® tPA (Cryopep, Montpellier, France). 2.5 μL of samples (20 μg/ml) was put in contact with 97.5 μL of 100 mM HEPES buffer (pH 8.0, 154 mM NaCl, 0.1% HAS) in the 96-well plate. After the addition of 10 μL PefaFluor® at 1 mM, a kinetic profile was obtained by measuring the fluorescence level at 440 nm every 2 min for 90 min at 37 °C with Infinite® 200 PRO microplate reader (TECAN Group Ltd, Mannedorf, Switzerland). Free rtPA was used at the same concentration based on the Pierce BCA protein assay. Increase of fluorescence corresponded to the fluorogenic peptide substrate hydrolysis by rtPA. Enzymatic activity was determined from the resulting kinetic profile and compared to the one of free rtPA.

In vitro fibrinolytic activity of rtPA-loaded SPs: To assess the fibrinolytic activity of rtPA-loaded SPs, a fibrin lysis clot experiment was performed. 5 mL of TRIS Buffer with 3% w/v low melting agarose (Carl Roth GmbH þ Co. KG, Karlsruhe, Germany) were heated to 65 °C. 5 mL of fibrinogen (from human plasma, Sigma Aldrich) solution in TRIS buffer (5 mg/ml) was slowly heated to 37 °C. Once the agarose solution reached 65 °C, it was cooled to 37 °C, and 2.5 U of thrombin (from human plasma, Sigma Aldrich) was added. Next, a fibrinogen solution was slowly added into the agarose/thrombin mixture under gentle agitation to avoid the formation of bubbles. The reaction mixture was poured into a 9 cm Petri dish and cooled at 4 °C for 30 min until the fibrin clot became visible. On the solidified agarose gel, round wells were formed using a 3 mm punch as sample reservoirs. 5 μL of each SPs sample (45 μg/ml) was dropped into the wells and incubated overnight at 37 °C in a humid environment. The degree of fibrin lysis was quantified with ImageJ by comparing the size of the fibrinolysis circle of the samples and free rtPA at the equivalent concentration based on the Pierce BCA protein assay.

Flow microchamber experiments: An *in vitro* flow adhesion assay was performed to evaluate the affinity of the Fuco-SPs with their molecular target. Micro-channels of Vena8 Fluoro$^+$ chambers (width: 0.04 cm, height: 0.01 cm, and length: 2.8 cm; Cellix Ltd, Dublin, Ireland) were coated overnight with recombinant human *P*-selectin, L-selectin or E-selectin (R&D systems France, Lille, France) at 100 μg/ml and left overnight at 4 °C. To confirm the concentration-dependent binding of Fuco-SPs to *P*-selectin, some channels were coated with *P*-selectin at a range of concentrations (5, 25, 50, and 100 μg/ml). Channels were then washed with NaCl 0.9% and further incubated with HSA at 10 μg/ml for 2 h.

A suspension of fluorescently labeled Control-SPs or Fuco-SPs (1 mg/ml) in saline was passed through the channels for 5 min at arterial and venous flow conditions (shear stress 67.5 dyne/cm^2 and 6.75 dyne/cm^2) using an ExiGo™ pump (Cellix Ltd, Dublin, Ireland). For the competitive binding experiment, fucoidan solution (10 mg/ml) was injected 5 min prior to the Fuco-SPs at the same rate. Then, all the channels were washed with NaCl 0.9% for 1 min. The binding of the adhered SPs was visualized in real-time under fluorescence microscopy (Axio Observer, Carl Zeiss Microimaging GmbH, Iena, Germany). For the quantitative analysis, the number of fluorescent SP clusters on each channel was measured using the "Analyze particles" tool in the image analysis software ImageJ (NIH, Bethesda, U.S.) with a 4-pixel threshold to eliminate the background noise.

To further investigate the binding efficiency of unloaded and loaded SPs to activated platelets, the microchannels of Vena8 Fluoro$^+$ were coated with fibrillar type I collagen Horm® (50 μg/ml) overnight at 4 °C and rinsed with NaCl 0.9% before use. Human whole blood (EFS, Bichat Hospital, Paris, France), collected in the PPACK tubes and labeled with 5 μM DIOC6 (Life Technologies SAS, Saint-Aubin, France), was perfused at arterial shear stress for 5 min to induce platelet activation and aggregation. Platelet aggregation through contact with collagen was visualized in real-time with phase-contrast microscopy (Axio Observer, Carl Zeiss Microscopy, Oberkochen, Germany). After rinsing with NaCl 0.9%, fluorescent Control-SPs or Fuco-SPs (unloaded or loaded with rtPA) at 1 mg/ml were injected into the channels in saline for 5 min. Their accumulation onto activated aggregates was monitored in real-time. Channels were then washed for 1 min with NaCl 0.9%. Finally, the MFI of the fluorescent SPs bound to the platelets on each channel was analyzed with ImageJ. Intensity settings were kept the same for both types of SPs.

Tissue distribution of Fuco-SPs in vivo: Animal studies were performed on C57BL/6 male mice (EJ, Le Genest, St-Berthevin, France) aged 5–8 weeks (~25 g weight) in respect of the principles of laboratory about animal experimentation and with the approval of the animal care and use committee of the Claude Bernard Institute (APAFIS #8724, Paris, France). Mice were anesthetized under the application of 2% isoflurane (Aerrane, Baxter). 200 μL of Fuco-SPs (5 mg/ml) were injected through the retro-orbital route ($n = 3$). To histologically analyze the particle accumulation, mice were sacrificed 30 min following their administration. The liver, spleen, lungs, and kidneys were excised, washed in saline, and fixed in paraformaldehyde 4%. The tissues were then frozen and cryosectioned at 10 μm thickness. The samples were stained with alcian blue & nuclear fast red staining protocol. Strongly negative structures, including the Fuco-SPs, are stained blue, nuclei are stained pink to red, and cytoplasms appear pale pink. The slides with tissue slices were scanned with the Nanozoomer (Hamamatsu, Hamamatsu City, Japan) and viewed with the NDP.view2 software.

Animals and thromboembolic stroke model in vivo: Animal experiments were carried out on male Swiss wild-type mice (8–9 weeks old; 35–45 g; CURB, Caen, France). All experiments were performed following the French (Decree 87/848) and the European Communities Council (2010/63/EU) guidelines and were approved by the institutional review board (French ministry of Research). All the experiments were validated by the local ethical committee of Normandy (CENOMEXA) registered under the reference number APAFIS#13172. Anesthesia was induced by the application of 5% isoflurane (Aerrane, Baxter) and maintained by 2% isoflurane in a mixture of O_2/N_2O (30%/70%).

Mice were placed in a stereotaxic device, then a small craniotomy was performed, the dura was excised, and the middle cerebral artery (MCA) was exposed. To induce the occlusion of the MCA, the coagulation cascade was triggered by the pneumatical injection of 1 μL murine α-thrombin (1 IU; Stago BNL) with a glass micropipette, as previously described [36]. Successful MCA occlusion was confirmed by the Laser Doppler flowmeter (Oxford Optronix). For the treatment, the animals were intravenously injected through a tail vein catheter (200 μL, 10% bolus, 90% infusion over 40 min) with either saline, Actilyse® rtPA 10 mg/kg, or rtPA-Fuco-SPs (loaded rtPA at 10 mg/kg, SPs at 71 mg/kg) 20 min after thrombus formation ($n \geq 5$). Brain perfusion was monitored by Laser Speckle Contrast Imager (MOOR FLPI-2, Moor Instruments) throughout the treatment. Region of interest (ROI) was selected on the ipsilateral to occlusion and contralateral hemispheres to monitor the relative cerebral blood flow in the affected region Fl_t (%) = 100% x Fl_{ipsi}/Fl_{contra}. The post-stroke reperfusion was expressed as a Growth Rate (GR) of the blood flow increase in the ipsilateral ROI to contralateral one at a time point, and it was quantified as GR (%) = 100% x $(Fl_{t2} - Fl_{t1})/Fl_{t1}$.

Magnetic resonance imaging acquisition and analysis: Mice were anesthetized with 5% isoflurane and maintained with 1.5–2% isoflurane in a mixture of O_2/N_2O (30%/70%) during the acquisitions. Experiments were carried out on a Pharmascan 7 T (Bruker Biospin, Wissembourg, France). Three-dimensional T2-weighted images were acquired using a Multi-Slice Multi-Echo sequence (TE/TR 39.9 ms/3500 ms, 2 averages) 24 h after the stroke. Lesion volumes were quantified on these images using ImageJ software (slice thickness 0.5 mm). Magnetic resonance angiography was performed using a 2D-TOF sequence (TE/TR 4.24 ms/12 ms, 1 average) 24 h after ischemia, and the recanalization status of the MCA was determined blindly from the analysis of the merged MCA angiograms with maximum intensity. The angiographic score is based

on the TICI (Thrombolysis in Cerebral Infarction) grade flow scoring (from Score 0: no perfusion to Score 3: full recanalization). For the *in vivo* detection of the BBB permeability, three-dimensional T1 FLASH sequences (TE/TR 4.37 ms/15.12 ms; 3 averages) were used, 15 min after the intravenous injection of 200 μL gadolinium chelate (DOTAREM) in saline (0.25 mg/ml). BBB leakage was measured 4 days after the stroke induction, and its volume was quantified using ImageJ.

Thrombus targeting by Fuco-SPs in a murine model of venous thrombosis: Animal studies were done following principles of laboratory animal care and with the approval of the animal care and use committee of the Claude Bernard Institute (APAFIS #8724, Paris, France). $FeCl_3$-induced *in vivo* thrombosis model on mesenteric vein was carried out on C57BL/6 male mice (EJ, Le Genest, St-Berthevin, France) aged 5–8 weeks. Mice were anesthetized with an intraperitoneal injection of ketamine (100 mg/kg) and xylazine (10 mg/kg). After midline abdominal incision, the mesentery was exposed, and vessels were visualized by an intravital microscope (Leica MacroFluo, Leica Microsystems SAS, Nanterre Cedex, France) using Orca Flash 4.0 scientific CMOS camera (Hamamatsu Photonics France SARL, Massy, France). For green fluorescent labeling of mitochondria of platelets and leucocytes, DIOC6 (Life Technologies SAS, Saint-Aubin, France) at 25 μM was retro-orbitally injected. The mesentery vein was covered with a 1 mm Whatman chromatography paper that was prior soaked in a 10% w/v iron chloride (Sigma-Aldrich) solution for 1 min, and then washed with saline. The formation of non-occlusive thrombi was monitored in real-time by fluorescence microscopy by an accumulation of fluorescently labeled platelets. TRITC-fluorescent labeled Control-SPs or Fuco-SPs were retro-orbitally injected 10 min after thrombus initiation with the volume of 150 μL (5 mice per group).

For histological evaluation, mice were sacrificed with pentobarbital overdose 5 min after administration of SPs. The affected part of the mesenteric vein was cut, washed in 0.9% NaCl, fixed in paraformaldehyde 4% (w/v), and frozen. The vein samples were cryosectioned at 10 μm thickness. The cell nuclei of a venous vascular wall were labeled with DAPI (Thermo Fisher Scientific, Massachusetts, United States) contained in a mounting medium (Vecto laboratories). The samples were observed by fluorescence microscopy. For the quantitative analysis, normalized MFI of the TRITC signal from SPs was expressed, defined as total TRITC fluorescence intensity divided by the size of the thrombus area on 2 slides from each mouse with the ImageJ (NIH, Bethesda, U.S.).

Statistical analysis: Quantitative data were expressed as mean ± standard error of the mean (SEM) ($n \geq 3$). Statistical tests were carried out with GraphPad Prism 9 (GraphPad Software, Inc, La Jolla, U.S.) with a 95% confidence level. Kolmogorov-Smirnov normality test was utilized to examine if variables are normally distributed. Normally distributed data were analyzed then with unpaired *t*-test or one-way analysis of variance (ANOVA) with post hoc Turkey's test. The Mann-Whitney *U* test was applied otherwise. The p-values of * $p < 0.05$; ** $p < 0.01$; *** $p < 0.001$ were considered statistically significant.

3. Results

3.1. Submicroparticle synthesis and characterization

Novel polysaccharide SPs were elaborated by a simple two-step synthesis process (Fig. 1A). First, a stable w/o miniemulsion of the aqueous phase with hydrophilic polysaccharides and vegetable (sunflower) oil was prepared. Chemical crosslinking of polysaccharides with the crosslinking agent STMP under alkaline conditions (Fig. 1B & Figure S1, Supplementary Data) produced a suspension of uniform SPs. We refer to the hydrogel particles only from dextran as Control-SPs, and

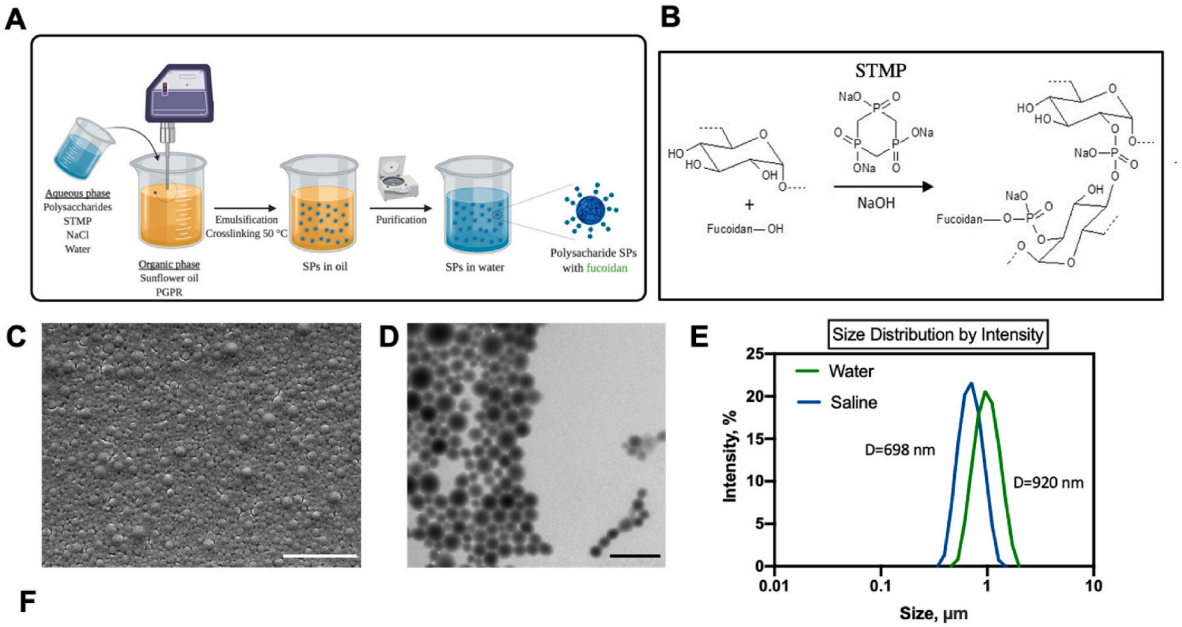

Sample		Size, nm	PDI	Zeta potential, mV	Phosphorus content, mg/l	Fucoidan content (Sulfate), %, w/w	Fucoidan content (Sulfur) %, w/w
Control-SPs	D0	674.87 ± 59.35	0.24 ± 0.05	-24.83 ± 0.09	33.2 ± 0.1	-	-
	D30	662.26 ± 46.04	0.18 ± 0.04	-25.24 ± 0.15			
Fuco-SPs	D0	708.48 ± 40.00	0.21 ± 0.10	-27.07 ± 0.39	30.6 ± 0.1	9.30 ± 1.07	8.60 ± 0.01
	D30	669.35 ± 61.93	0.23 ± 0.07	-27.90 ± 0.20			

Fig. 1. Synthesis and physico-chemical characterization of the SPs. A. Overall schematic of the synthesis process of the SPs – miniemulsion/crosslinking. B. Simplified chemical structures of dextran and fucoidan and crosslinking with STMP in alkaline conditions. SEM (C) (scale bar = 5 μm) and TEM (D) (scale bar = 3 μm) images of the Fuco-SPs. E. Swelling in the water of the Fuco-SPs due to the hydrogel nature of the particles. The size of one sample when resuspended in water (green) and in saline (blue). F. Size, zeta potential, and chemical composition of the SPs; D0 – at the day of synthesis, D30 – one month after the synthesis.

from a mixture of dextran and fucoidan as Fuco-SPs in this manuscript.

To ensure desirable safety of the future drug delivery platform, a thoughtful approach to material selection was effectuated. Low molecular weight dextran 40 kDa of clinical-grade was utilized without any chemical modification. Having a large number of hydroxyl groups, dextran is a suitable compound for subsequent chemical crosslinking with STMP [31], an FDA-approved food additive [37] that is preferred over conventional crosslinker glutaraldehyde known for cytotoxicity [38]. Fucoidan, a marine polysaccharide approved as a pharmaceutical compound [39] that exhibits a nanomolar affinity to *P*-selectin [40], served as a targeting ligand to thrombi. Hence, both natural polysaccharides applied in this study are affordable, biodegradable, biocompatible compounds, non-immunogenic, and approved for clinical applications.

Instead of commonly used organic solvents, sunflower oil was applied as an emulsion continuous phase. The choice of the stabilizing agent plays an important role in reducing the interfacial tension and Laplace pressure when fabricating a stable emulsion and future nanocarrier. In this work, we selected a potent oil-soluble nonionic surfactant for stabilizing w/o emulsions – PGPR, which is also recognized by the FDA as a safe compound and is frequently used as an emulsifier in the food production industry [41]. In addition, to counteract the Ostwald ripening of water droplets, 6 M NaCl was added to the aqueous phase as an osmotic agent to adjust the osmotic gradient and to stabilize the w/o emulsion further. Overall, multiple parameters were optimized to obtain a stable and homogenous miniemulsion and subsequent nano-delivery system. It was found that the size of the templating droplet and the ultimate hydrogel SPs being directly proportional to the polysaccharide molecular weight and inversely proportional to the amount of surfactant and crosslinking agent as well as homogenization speed (data not shown).

ESEM and TEM images revealed a well-defined spherical morphology and uniform size distribution of SPs (Fig. 1C and D). As hydrogel-based particles, they could swell in an aqueous medium while maintaining their network structure (Fig. 1E).

Functionalized Fuco-SPs contained 1.21 ± 0.01 wt% sulfates, which corresponded to a fucoidan content of 8.60 ± 0.01% by elemental analysis of sulfur, and 9.30 ± 1.07% of fucoidan by quantification of the sulfate content by a semi-quantitative colorimetric assay. In such a way, two different techniques estimated ~9% fucoidan composition in the SPs. The physico-chemical properties of these nanoformulations are displayed in Fig. 1F. The SPs exhibited the hydrodynamic size 674.87 ± 59.35 nm (Control-SPs) and 708.48 ± 40.00 nm (Fuco-SPs), determined by DLS. It is important to highlight that a relatively large size of the SPs might limit the accumulation of associated rtPA within the brain parenchyma and reduce the risk of hemorrhagic events. The negative ζ-potential of the SPs −24.83 ± 0.09 mV for Control-SPs and −27.07 ± 0.39 mV for Fuco-SPs ensured colloidal stability as a result of the anionic nature of the fucoidan and the formation of the anionic phosphate functional groups, produced during the crosslinking reaction with STMP. The phosphorus content of the SPs is indicated in Fig. 1F.

The size and zeta potential of both SPs remained relatively stable for at least 30 days at 4 °C (Fig. 1F). Besides, effective storage of the SPs can be ensured by freeze-drying with 5% (w/v) sucrose as a cryoprotectant and subsequent resuspension in an aqueous medium. The overall yield of the synthesis was 11.1 ± 0.6%, resulting in the production 13.4 ± 0.7 mg of SPs per batch.

3.2. Biocompatibility of the SPs

The injectable hydrogel SPs were produced according to the green chemistry principles through the formulation method without using hazardous substances and organic solvents and were expected to be biocompatible.

An initial *in vitro* evaluation of biocompatibility of the developed SPs examined cyto- and hemocompatibility. The cytocompatibility of the SPs was assessed with a resazurin cell viability assay on endothelial cells. Following 24 h exposure, Control-SPs and Fuco-SPs did not affect cellular viability and metabolic activity of HUVECs at concentrations ranging from 0.1 to 1.5 mg/ml, exhibiting an excellent cytocompatible profile (cell survival >90%, up to the highest tested concentrations of SPs) (Fig. 2A). The upper limit for the tested concentration 1.5 mg/ml of the SPs was selected to surpass the tested concentrations for the majority of the nanosystems *in vitro* (typically, maximum 400 μg/ml) [42] and the concentration of the SPs employed for further *in vivo* experiments in this work (71 mg SPs per 1 kg body weight or 1.1 mg SPs per 1 mL of blood). There was no significant difference between the Control-SPs and Fuco-SPs, as both did not provoke cytotoxicity.

Since the SPs in this study were designed for intravenous administration and were expected to have direct contact with blood, the Fuco-SPs were examined for their blood-compatible behavior by a hemolysis test on isolated murine red blood cells *in vitro* (Fig. 2B). Even at the highest concentration of 1.5 mg/ml, the SPs presented a hemolytic index 1.51 ± 0.02%, below 2%, and considered nonhemolytic according to ISO 10993 - 4 standard [43,44].

Morphology of the cells, co-cultured with Fuco-SPs, was visualized with confocal microscopy. No obvious morphological differences were revealed for HUVECs with Fuco-SPs and negative control, as depicted in Fig. 2C. FITC-Phalloidin staining was used to visualize a cytoplasm and DAPI for nuclei.

Collectively, these results suggest that the polysaccharide SPs have favorable biocompatibility for their application *in vivo*.

3.3. Binding of SPs to P-selectin in vitro

Knowing that fucoidan was homogeneously distributed in the structure of the hydrogel Fuco-SPs and constituted ~9% w/w of the composition, we investigated whether its quantity on the surface was sufficient for specific adhesion to its molecular target. While most of the publications assess targeting strategy *in vitro* in static conditions by flow cytometry or confocal microscopy [20,45,46], our group developed a robust and tunable dynamic microfluidic method that mimics arterial or venous blood flow conditions to study the targeting efficacy for recombinant *P*-selectin or/and human activated platelet aggregates expressing *P*-selectin. It was previously validated on fucoidan-coated nano-/microcarriers (Figure S2, Supplementary Data) [21–23].

First, fluorescent Fuco-SPs and Control-SPs were injected in the microchannels coated with recombinant *P*-selectin under arterial or venous shear rates (67.50 dyne/cm^2 vs. 6.75 dyne/cm^2), and their adhesion was visualized and quantified in real-time under fluorescence microscopy. According to obtained results, fluorescent Fuco-SPs depicted a significantly higher adhesion to *P*-selectin coating than Control-SPs both in arterial (374.25 ± 115.33 adhered Fuco-SPs vs. 30.25 ± 13.84 adhered Control-SPs, $^*p < 0.05$) and venous (228.25 ± 36.67 adhered Fuco-SPs vs. 34.50 ± 18.16 adhered Control-SPs, $^{**}p < 0.01$) flow conditions (Fig. 3A, E). There was no significant difference between the fluorescent signal of Fuco-SPs accumulation for arterial and venous flow conditions ($p = 0.27$). Fuco-SPs accumulation after injection onto *P*-selectin coating was in a linear dose-dependent manner as regards to the *P*-selectin concentration, $R^2 = 0.99$ (Fig. 3B). An experiment of competitive interaction illustrates that fucoidan solution pre-injection at 10 mg/ml considerably reduced the attachment of the Fuco-SPs onto the microchannels with *P*-selectin (374.25 ± 115.33 vs. 19.75 ± 10.06, $^*p < 0.05$) (Fig. 3C).

To establish the specificity of the Fuco-SPs binding to *P*-selectin, the targeting assay was extended to other members of the selectin family: E- and L-selectin [47]. The percentage of the Fuco-SPs adhered to the E- and L-selectin was normalized over the mean number of the attached Fuco-SPs to a *P*-selectin coating at the equivalent concentration. Indeed, only 12.73 ± 3.66% of the SPs adhered to E-selectin and 0.26 ± 0.19% to L-selectin coating (Fig. 3D). Thus, our results indicate that Fuco-SPs bind specifically to *P*-selectin but not to E- and L-selectins, and these results

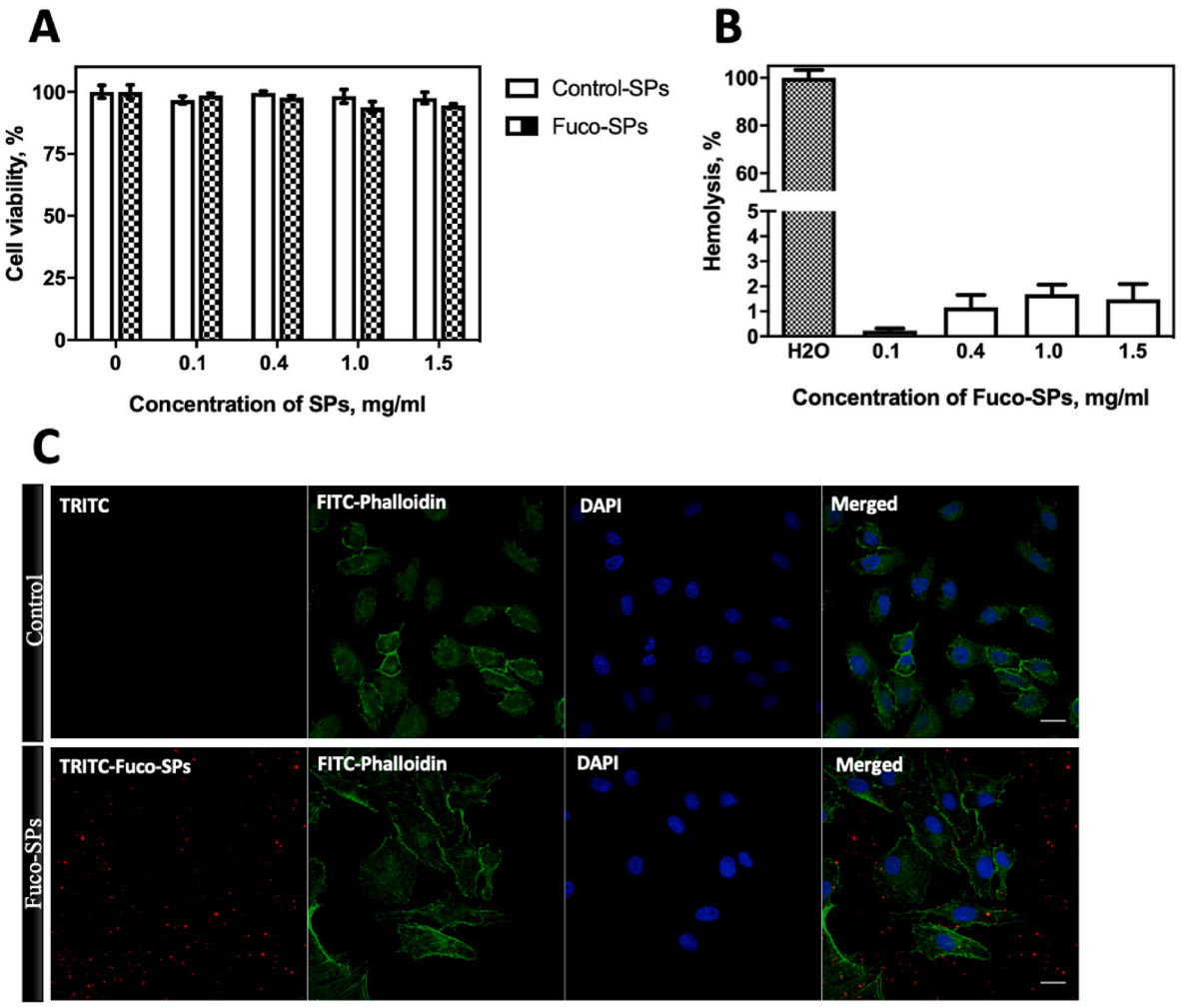

Fig. 2. Biocompatibility of the SPs. Cytocompatibility (A) and hemocompatibility (B). Confocal microscopy of HUVECs cultured without (control) and with Fuco-SPs (C) (scale bar = 30 μm).

are in accordance with a previous work of our group published by Bo Li et al. of fucoidan-functionalized polymer microcapsules [21].

Overall, these findings are encouraging evidence of the sensitivity and selectivity of the Fuco-SPs, confirming fucoidan potential as a natural ligand of *P*-selectin.

3.4. rtPA loading onto the SPs and its release in saline. In vitro thrombolytic activity o rtPA-loaded SPs

Due to rtPA low bioavailability and requirement of high dose administration, coupling this enzyme to the biocompatible nanocarrier could overcome the drawbacks associated with a drug high dosage. Herein, an efficient rtPA encapsulation was achieved through the physical adsorption method due to electrostatic interaction: the protein, which is an amphoteric molecule, was put in contact with negatively charged polysaccharide SPs in the water at pH below rtPA isoelectric point IP = 7.7 [48,49] when rtPA presented a positive charge. The hydrogel nature of the SPs allowed reaching a high encapsulation efficiency of the rtPA of 64.78 ± 2.16% and 81.04 ± 1.86% for Control-SPs and Fuco-SPs, respectively. The confocal microscopy images of FITC-rtPA loaded onto TRITC-labeled Fuco-SPs revealed the uniform distribution of the rtPA within a porous structure of the hydrogel SPs, as evidenced by a green fluorescence from FITC-rtPA colocalized with the red fluorescence from the particles (Figure S3A, Supplementary Data).

The release kinetics of rtPA from fucoidan-functionalized SPs was analyzed *in vitro* by flow cytometry [35] in saline at 37 °C under gentle agitation by quantifying the MFI of the FITC-labeled rtPA associated with TRITC-fluorescent Fuco-SPs. Figure S3B, Supplementary Data indicated a gradual and continuous sustained release of the lytic agent from the SPs during the observation period: 46.41 ± 1.34% of the encapsulated protein was released during the first 15 min, and 76.98 ± 1.74% after 90 min. This release profile is classical for the hydrogels [50].

The thrombolytic activity of the rtPA-loaded SPs *in vitro* was analyzed as a combination of amidolytic and fibrinolytic activities (Fig. 4A, B, C). Amidolytic or enzymatic activity featured the ability of the proteolytic enzyme to hydrolyze the rtPA substrate. Interestingly, the amidolytic activities of rtPA on Control-SPs and Fuco-SPs were comparable to that of free rtPA (Fig. 4A and B). The fibrinolytic experiment *in vitro* of the rtPA-loaded SPs was performed in a fibrin plate assay (Figure S4A, Supplementary Data). The results indicated full retention of fibrinolytic activity (Fig. 4C; Figure S4B, Supplementary Data). rtPA loaded onto the SPs appeared to diffuse into the fibrin-agarose matrix and induce fibrinolysis in contact with fibrin. No significant difference was detected between both types of SPs, enabling us to utilize them in the following experiments.

Overall, the rtPA association with the SPs did not affect the drug amidolytic activity and fibrinolytic potential in our design. This result is in accordance with most studies on nanogels suggesting that drug encapsulation via a passive diffusion into the preformed nanogels does not affect the secondary structure of the adsorbed protein and its biological activity [51].

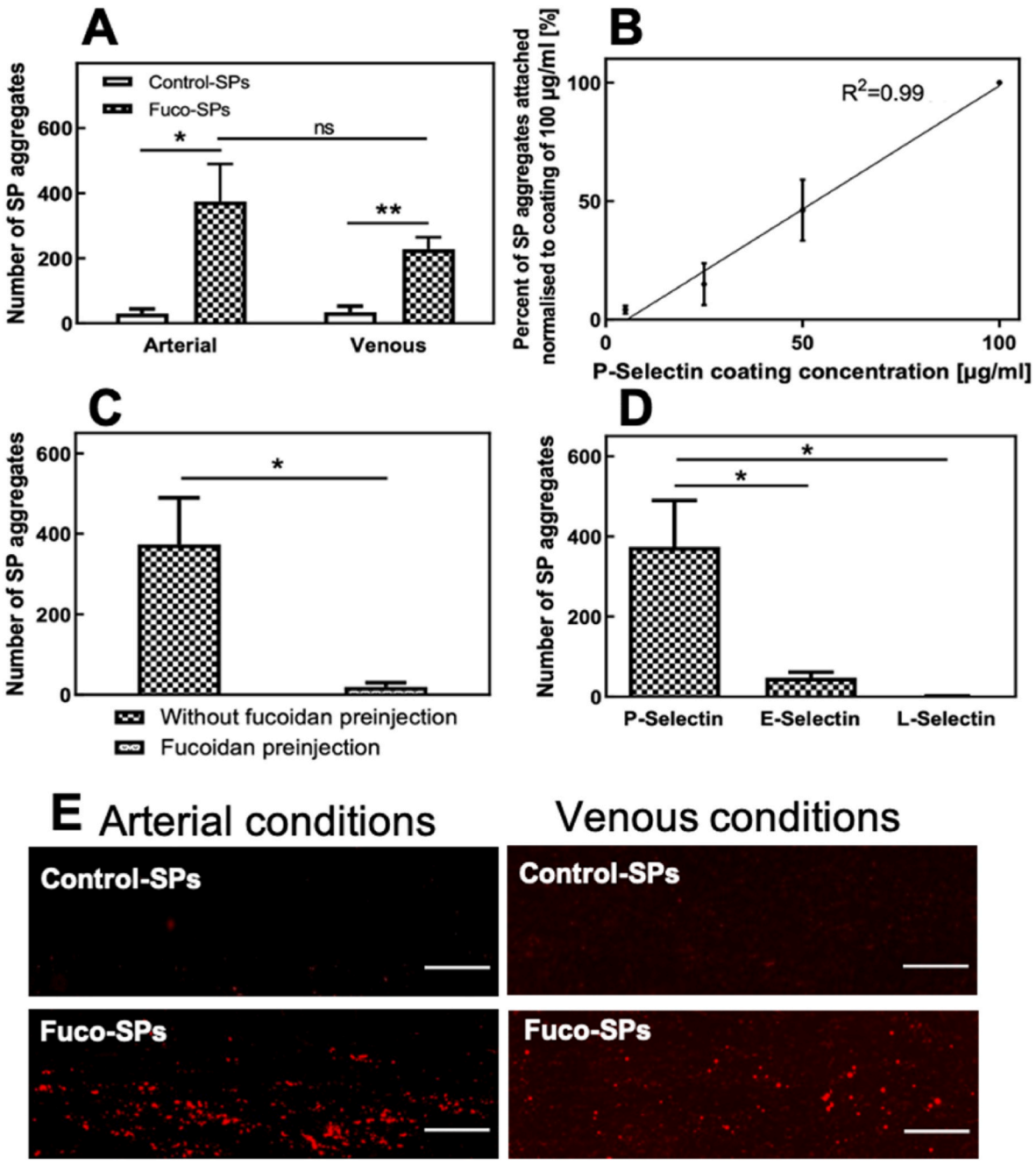

Fig. 3. Evaluation of the SPs interactions with selectins. A. Adhesion of the Control-SPs or Fuco-SPs on the coating of the recombinant *P*-selectin in the microfluidic assay under arterial and venous flow conditions (n = 4). B. Concentration-dependent binding of the Fuco-SPs onto the coating of the *P*-selectin at a range of concentrations. C. Fucoidan pre-injection inhibited Fuco-SPs adhesion onto the *P*-selectin. D. Comparison of the Fuco-SPs binding to other selectins: E-– and L-Selectin. E. Fluorescent microscope view of Control-SPs or Fuco-SPs adhesion over a *P*-selectin coating of 100 µg/ml under arterial and venous shear rates (scale bar = 20 µm).

3.5. Unloaded and rtPA-loaded Fuco-SPs adhere to activated platelet aggregates in vitro under arterial flow

Since aggregation of activated platelets and platelet-mediated coagulation pathways are hallmark events in thrombosis, activated platelets are a suitable cellular target for nanocarrier binding to thrombi [52]. Before the *in vivo* tests, we complemented the targeting evaluation on selectins with the second set of microfluidic experiments to validate Fuco-SPs capability to actively anchor onto the surface of activated platelets, expressing *P*-selectin. Thus, human whole blood was passed into collagen-coated microchannels to induce platelet activation and aggregation. Fuco-SPs or Control-SPs were then perfused at arterial shear stress and the accumulation of the fluorescence from the adhered SPs was detected on the surface of activated platelet aggregates. A quantitative analysis of the MFI revealed that Fuco-SPs adhered significantly more onto activated platelets than Control-SPs (2678.34 ± 237.40 for Fuco-SPs vs. 392.44 ± 137.15 for Control-SPs, ***$p < 0.001$, Fig. 5A–B Left). Notably, adsorption of rtPA did not impair the Fuco-SPs clot-binding ability (1880.80 ± 429.37 for rtPA-Fuco-SPs vs. 77.56 ± 40.25 for rtPA-Control-SPs, **$p < 0.01$, Fig. 5B Right). There was no significant difference between unloaded and rtPA-loaded Fuco-SPs adhering to the activated platelets ($p = 0.11$).

In conclusion, these *in vitro* experiments provided crucial evidence of molecular interaction and high affinity between the *P*-selectin on the activated platelets and fucoidan-functionalized SPs, which was maintained after loading the thrombolytic agent. This finding presumes that

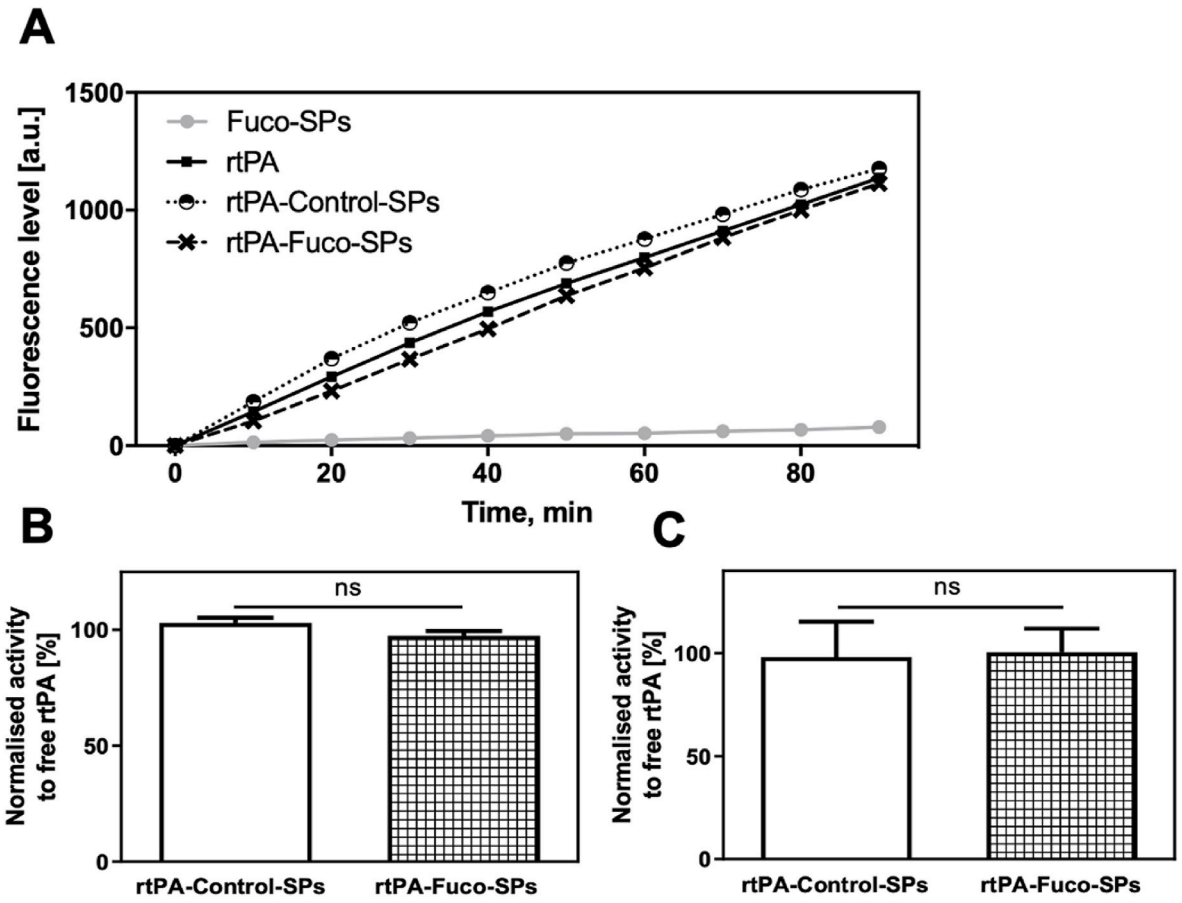

Fig. 4. Thrombolytic efficacy *in vitro* of the rtPA-loaded SPs. A - B. Amidolytic activity measured by the PefaFluor® fluorogenic assay. A. The curves correspond to the mean value of fluorescence release and are correlated with the enzymatic velocity over 90 min. B. Corresponding quantitative analysis normalized to free rtPA at the same concentration at 90 min (n = 3). C. Fibrinolytic activities of the SPs determined by a fibrin-plate agarose assay. The quantitative analysis normalized to free rtPA at the same concentration (n = 3).

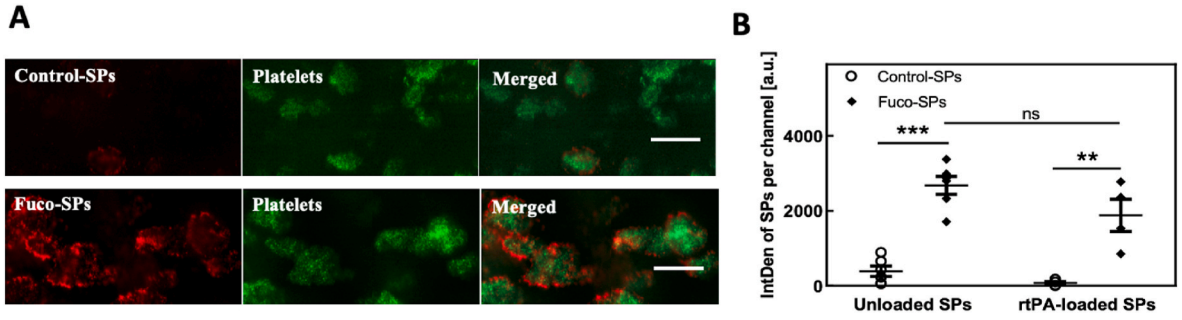

Fig. 5. Adhesion of the SPs over activated platelet aggregates. A. Visualization by fluorescent microscopy of the attached unloaded SPs on the microchannels after the formation of the platelet aggregates (scale bar = 20 μm). B. Corresponding quantification of the integral density of the unloaded (n = 6) and rtPA-loaded (n = 4) Control-SPs and Fuco-SPs in ImageJ.

the administration of the rtPA-Fuco-SPs could enable a specific delivery of the rtPA-immobilized SPs to the platelet-rich thrombus with higher drug accumulation.

3.6. Tissue distribution in vivo of fucoidan-functionalized SPs

After their intravenous injection, the distribution *in vivo* of Fuco-SPs was examined by histological analysis of the excised tissues with alcian blue staining of negatively charged particles in the healthy mouse. The presence of Fuco-SPs in four main organs of excretion (liver, spleen, lungs, and kidneys) was assessed on several sections for each organ. Our results revealed that the polysaccharide Fuco-SPs distributed primarily into the spleen post-administration, indicating the splenic clearance. The particles accumulated in the liver to a lower extent, while their presence in the kidneys and lungs remained minor. These differences are presented in Figure S5, Supplementary Data. Our data are in agreement with other deformable polymer hydrogel-like particles in their submicron and micron size range [53].

3.7. In vivo thrombolytic efficacy

Whereas demonstrating the *in vitro* activity of the rtPA immobilized

on the drug delivery system is important, the *in vivo* therapeutic effect is paramount. A murine thromboembolic stroke model was established by *in situ* injection of 1 IU of thrombin into the MCA by provoking a coagulation cascade and formation of both fibrin- and platelet-rich clots in the lumen of the artery [54,55]. Fig. 6A highlights the *in vivo* experiments design, and Fig. 6B the potential mode of action of the Fuco-SPs in the thrombus. The treatment options – control saline, rtPA 10 mg/kg, or rtPA-Fuco-SPs at 10 mg/kg rtPA – were intravenously injected 20 min after ischemic onset under rtPA clinical mode of administration: 10% bolus followed by 90% infusion. It is important to note that 10 mg/kg is a relevant dose in mice in place of 0.9 mg/kg in humans because of a lower sensitivity of human rtPA in murine plasma [56]. No morbidity or mortality was observed in the mice during therapeutic experiments, suggesting that rtPA-Fuco-SPs do not provoke acute toxicity under the current conditions.

Cerebral blood flow was monitored throughout the treatment via laser Doppler speckle contrast imaging, a high resolution and high-speed technique that instantly visualizes microcirculatory tissue blood perfusion. The reduction of the blood flow in the ipsilateral cerebral hemisphere due to the stroke was restored by 33.97 ± 5.15% after 40 min treatment with rtPA-Fuco-SPs; by contrast, in the rtPA and saline group for which the perfusion was improved only by 15.16 ± 6.49% and 10.33 ± 4.62%, respectively, in this experiment (Fig. 6E). The representative laser Doppler speckle multispectral imaging in the ipsilateral and the contralateral hemispheres at 0 min and 40 min are expressed in Fig. 6D. Accelerated Video S1A, B, C recorded the perfusion in real-time for all conditions. These data were confirmed by the angiographic analysis performed 24 h later and assessed by a blinded observer based on TICI grade flow scoring measured by magnetic resonance angiography (MRA). Indeed, similar to some untreated stroke patients, some blood clots were gradually lysed post-stroke in this murine model: at 24 h after thrombotic occlusion, 40% of mice exhibited a total recanalization (score 3) of the MCA when injected with saline, while treatment of 40% of animals resulted in partial perfusion (score 2), and 20% achieved only minimal flow (score 1) (Fig. 6H; Figure S6A, Supplementary Data). However, after the treatment with rtPA-Fuco-SPs, most of the cases were entirely recanalized (score 3). For the rtPA treated group, no animal achieved a score 1 of minimal perfusion, and 67% of cases showed a partial score 2 level of recanalization.

We then utilized magnetic resonance imaging as a powerful technique to quantify the volume of brain damage at 24 h after stroke onset. Using T2-weighted MRI sequences, we observed that the size of the ischemic brain lesions for the control saline group was 14.80 ± 3.34 mm^3 whereas for the rtPA-loaded fucoidan-targeted SPs it was 4.63 ± 1.59 mm^3 (Fig. 6F and G). rtPA-conjugated Fuco-SPs reduced the ischemic zone almost 2-fold of the free rtPA, despite the fact that these data were non-significant due to the limited number of the animals as to the well-known effect of free rtPA in this murine model [55]. Out of all treated animals with rtPA-Fuco-SPs, 66.6% of the animals displayed small lesion sizes (<3 mm^3), and 33.3% had medium lesion sizes (<11

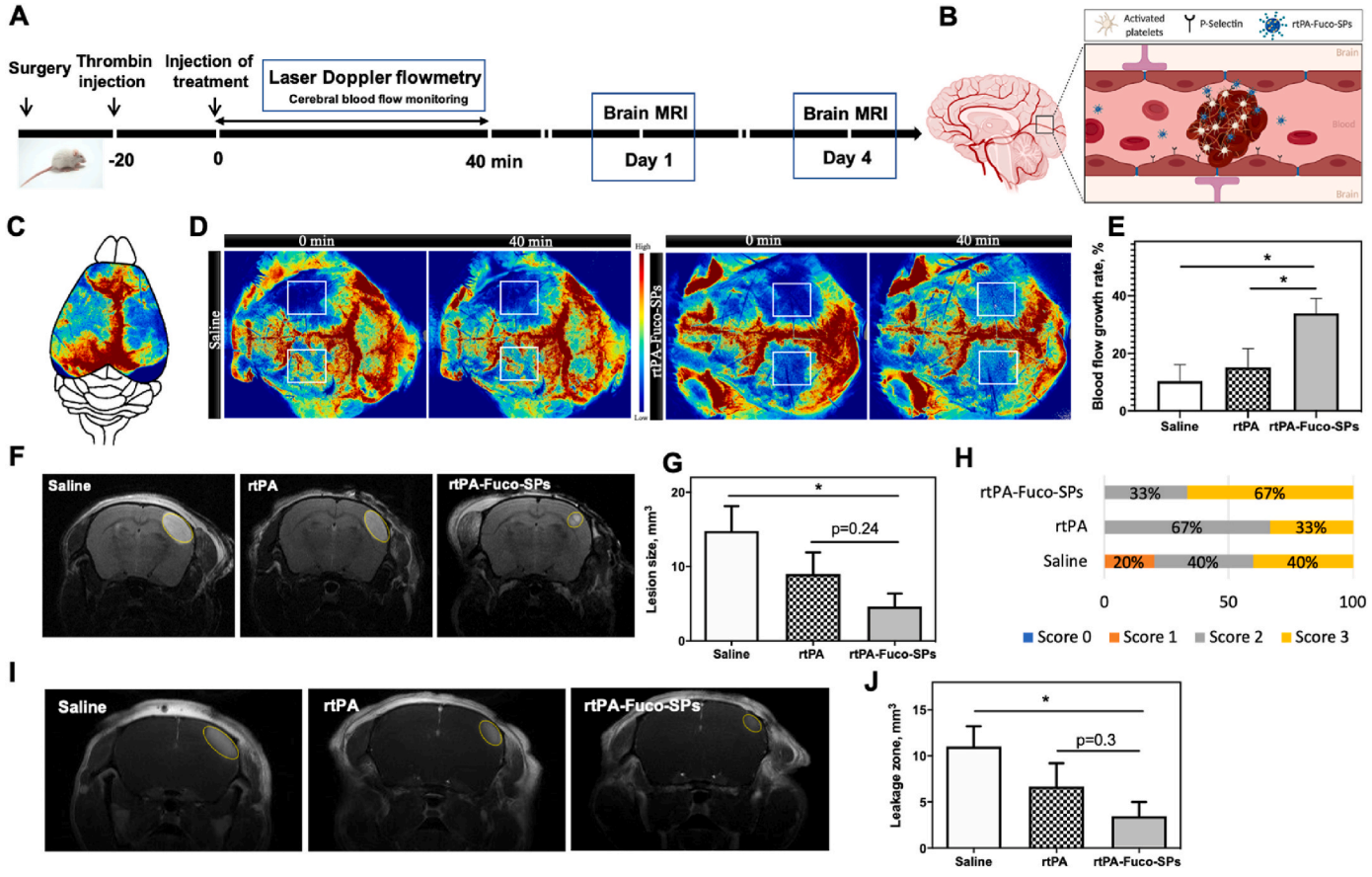

Fig. 6. Thrombolytic efficacy *in vivo* in the murine ischemic stroke model. A. Schematic of the design of the *in vivo* experiment. B. Proposed therapeutic mode of action of the rtPA-loaded Fuco-SPs after the ischemic stroke: the Fuco-SPs accumulate on the surface of the activated platelets due to *P*-selectin affinity of fucoidan and perform local thrombolysis with alteplase. C – E. Cerebral blood flow reperfusion monitored by the laser speckle contrast imaging during the 40-min treatment ($n \geq 5$). Schematic image of the perfusion in the microcirculatory brain tissue (C). The representative multispectral photos in the ROI of ipsilateral (upper) and contralateral (lower) hemispheres at 0 min and 40 min for saline and rtPA-Fuco-SPs groups (D). The growth rate of the cerebral reperfusion in the ipsilateral hemisphere after 40 min treatment injection (E). F. MRI images of the infarct lesion 24 h post-stroke with the corresponding quantification of its volume (G), ($n \geq 5$). H. Angiographic scores of the MCA reperfusion at day 1 after stroke induction by MRI. I. MRI images of the BBB permeability at day 4 post-stroke with the corresponding quantification of its volume (J), ($n \geq 5$).

mm^3). In the rtPA group, only 33.3% of the animals displayed a small infarct zone. In the saline treatment group, we recorded 60% of the animals with severe (<20 mm^3) and critical (>20 mm^3) lesions and no animals with small lesions (Figure S6B, Supplementary Data).

To monitor the BBB integrity disrupted by ischemic stroke [57], extravasation of gadolinium injected intravenously was detected and quantified on T1-weighted MRI images at day 4 after stroke (Fig. 6I and J). Gadolinium extravasation from the blood into the brain parenchyma was unmistakably located at the ischemia-affected region where the BBB was compromised. rtPA-Fuco-SPs treatment group demonstrated a significant BBB preservation over control groups of free rtPA and saline with only a subtle BBB breakdown of 3.45 ± 1.40 mm^3.

In order to confirm the accumulation of Fuco-SPs within the thrombus area *in vivo*, we injected fluorescent-labeled SPs at the therapeutic concentration as in the stroke model into the $FeCl_3$ model of venous thrombosis in mice. Upon histological examination of the thrombus-affected area of the mesenteric vein, Fuco-SPs were clearly identified on the green-fluorescent labeled thrombus (Fig. 7A). By a quantitative analysis of the MFI normalized by the size of the thrombus, it was evidenced a highly increased TRITC signal from fucoidan-functionalized SPs group comparing with Control-SPs (9.48 ± 2.19 for Fuco-SPs vs. 1.48 ± 0.35 for Control-SPs, $^{**}p < 0.01$, Fig. 7B).

Overall, the apparent superiority of rtPA-Fuco-SPs to reduce the brain tissue injury area in comparison with saline and rtPA at the same dose, combined with a favorable safety profile of the SPs, makes them a promising nanomedicine-based approach for the treatment of acute arterial thrombosis.

4. Discussion

The revolutionary treatment with alteplase to dissolve thrombi and restore blood flow is a standard of care in acute thrombotic events, but it is certainly not risk-free. Nanomedicine exploits a profound understanding of the molecular mechanisms involved in thrombus formation and offers outside-the-box strategies to effectively target and dissolve the blood clots in the body with fewer systemic and neurological complications [58].

In this study, rtPA was associated with hydrogel-like polysaccharide SPs, synthesized by a simple miniemulsion/crosslinking process. The soft structure of chemically crosslinked hydrogels resembles those of extracellular matrices and may prevent tissue irritation, providing a convenient and versatile platform for storage and site-specific delivery of a drug to the thrombi [59]. Our approach's novelty is exclusively polysaccharide nature of the particles – from dextran and fucoidan without any prior chemical modification, as well as green chemistry synthesis technique. Intriguingly, several articles claim that dextran [60] and fucoidan [61,62] themselves exert some antithrombotic action that makes them an excellent starting material for the nanocarrier. Hydrophilic polysaccharide surfaces lead to longer circulating NPs since they avert the formation of a protein corona and early macrophage internalization [63]. Moreover, natural polysaccharides are advantageous to synthetic polymers in terms of safety, abundance in nature, and low cost. Overall, we considered the issues imperative for high biosafety and potential future clinical translation of Fuco-SPs by (I) the choice of biocompatible and biodegradable materials, all with FDA-approval; (II) a relatively simple and efficient production by a mild synthesis method without the utilization of the hazardous substances and organic solvents; (III) targeting agent of natural origin – fucoidan – that is being validated in clinical trials for thrombosis.

After fabrication and extensive physico-chemical characterization of the SPs, we confirmed their cyto- and hemocompatibility at concentrations up to 1.5 mg/ml (Figs. 2A and 3B). The main pathway of the polysaccharide Fuco-SPs tissue distribution *in vivo* upon intravenous injection was the spleen (Figure S5, Supplementary Data). Future studies should include the tests of thrombogenicity and immunogenicity *in vivo*.

The Fuco-SPs were associated with a thrombolytic agent by physical adsorption, allowing a high encapsulation efficiency of the rtPA of 81.04 ± 1.86% due to their hydrogel-based structure. Classically, alteplase is loaded onto the NPs using the covalent amide bond formation via EDC/NHS reaction between the primary amines on the rtPA molecule and the nanocarriers containing carboxyl groups. As a mild drug encapsulation method, adsorption is preferred to covalent bioconjugation to load fragile molecules such as proteins to avoid changes in the protein structure and function that might result in its partial denaturation and loss of biological activity [64]. The fibrinolytic diffused through the matrix of the porous SPs (Figure S3A, Supplementary Data), fully preserving its enzymatic and fibrinolytic potential *in vitro* (Fig. 4). Friedrich et al. demonstrated that the adsorptive bound rtPA liberated faster from the particles and spread more readily into the fibrin matrix than covalently bound rtPA [65], which may be beneficial in targeted thrombolysis. Although a rising number of recent articles apply a controlled release of the thrombolytics via endogenous and exogenous stimuli, we chose not to incorporate sophisticated nanodesigns and demonstrated a gradual and continuous rtPA release from the SPs without an external trigger (Figure S3B, Supplementary Data) so as to facilitate future regulatory approvals.

The clot targeting strategy of the SPs was achieved by the introduction of the fucoidan to the polysaccharide solution at 9% w/w. Functionalization with fucoidan permitted the high-affinity binding of Fuco-SPs to its molecular target *P*-selectin in a dynamic microfluidic method that mimics arterial or venous blood flow conditions in a dose-dependent manner (Fig. 3A, B, E). Importantly, this type of interaction is selective, as SPs did not adhere a lot to other selectins: E- and L-selectin *in vitro* (Fig. 3D). When the microchannels were covered with activated platelet aggregates, both unloaded and rtPA-loaded Fuco-SPs were capable of binding these micro-clots (Fig. 5). Once tested in the *in vivo*

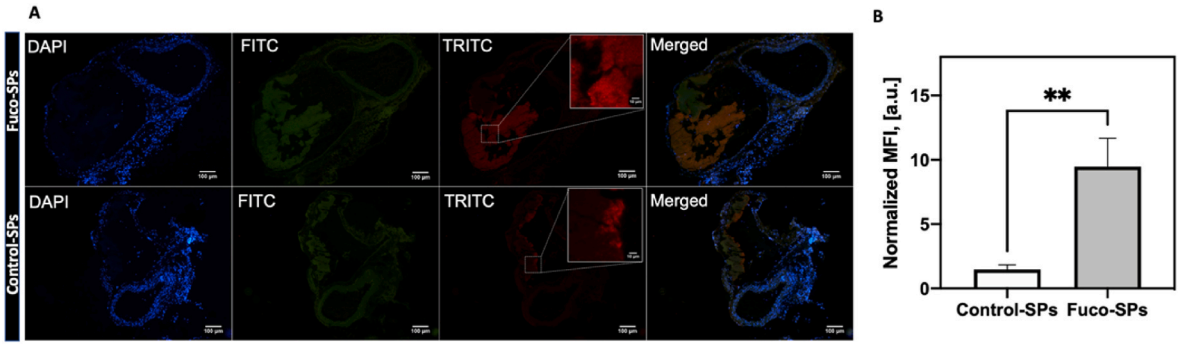

Fig. 7. *In vivo* targeting in the $FeCl_3$ murine model of thrombosis. A. Histological analysis of thrombi in the mesenteric vein by fluorescent microscopy. The venous vascular wall is visualized with DAPI staining; thrombus is stained in green due to DIOC6 labeling of platelets; Fuco-SPs and Control-SPs are fluorescently labeled with TRITC. Inserts are a magnification of dashed Regions of Interest of the TRITC signal. B. Corresponding quantification of MFI from the adhered TRITC-SPs in the thrombi (n = 5).

model of venous thrombosis, Fuco-SPs were identified on the $FeCl_3$-induced thrombi by histological examination, contrary to Control-SPs (Fig. 7). Our data validate an inimitable and efficient thrombus targeting approach of the Fuco-SPs, using a clinical algae-derived compound. Yet, a surge in strategies involving dual or even more surface targeting moieties is being witnessed in academic works. For instance, the combinatory targeting of GPIIb/IIIa receptors and *P*-selectin on activated platelets with two peptide ligands on the lipid nanovesicles enhanced thrombus binding capacities in a synergic manner [66]. Another notable example is the biomimetic functionalization of NPs with platelet membrane coating that enabled thrombus directing via multiple platelet receptors [67]. These combinations of NP modifications represent a promising strategy for developing next-generation blood clot-targeting NP platforms for therapy and/or diagnostics.

The experiments on the murine thrombin-induced thromboembolic stroke model supported the therapeutic effect of the rtPA-Fuco-SPs *in vivo* (Fig. 6). The findings of the submicroparticle-associated rtPA treatment group outperformed those of free rtPA at the same concentration, as we observed a more rapid clot dissolution and MCA reperfusion, which minimized the brain injury and resulted in subsequently smaller infarct area post-stroke by MRI. Several groups previously reported the reduction of the infarct zone in preclinical models by nanomedicinal product. For example, the magnetic iron oxide (Fe_3O_4)-microrods [10] and polyacrylic acid-stabilized magnetic NPs [12] conjugated with rtPA diminished the brain infarct lesion in the $FeCl_3$ murine model of ischemic stroke of MCA. These designs, however, require an external magnet for targeting and to complement chemical lysis with rtPA with mechanical one of the magnetic rotations. Without any clinically approved medical device to impose a high magnetic force on the NPs in deep blood vessels, it would probably be desirable for nanocarrier formulation to avoid external assistance. Mei et al. stated that only the synergistic effect of rtPA-loaded polymer micelles and a reactive oxygen species (ROS)-eliminating antioxidant suppressed an infarct volume and improved neurological deficit after brain ischemia in the mouse model of photo-thrombotic MCA occlusion [68]. In our case, the therapeutic benefit of rtPA-Fuco-SPs could be ascribed to faster MCA reperfusion and, hence, prevention of the major brain injury due to higher rtPA accumulation on the thrombus site as to active targeting and specific *P*-selectin interactions of the Fuco-SPs.

Moreover, the animals in the rtPA-Fuco-SPs group suffered a lower level of BBB disruption by the ischemic stroke that was quantified on T1-weighted MRI images with gadolinium. It is vital to underline that although in this article we utilized fucoidan on the SPs purely for the *P*-selectin targeting purpose, new avenues of research are deciphering its neuroprotective role, particularly after cerebral ischemic events [69]. Altogether, this first proof-of-concept *in vivo* results of Fuco-SPs show an astonishing potential of the nanomedicine-based approach for the targeted treatment of acute thrombosis. We speculate that the submicron size of the particles, along with their active thrombus-targeting moiety, should maintain rtPA-loaded nanocarrier within the intravascular compartment to exert its thrombolytic activity. It should prevent the leakage of rtPA into the brain parenchyma, reducing the risks of NMDA receptors-mediated neurotoxicity and hemorrhages [70]. Further studies could compare a single or a double bolus route of administration of rtPA-Fuco-SPs due to the rtPA preservation by SPs, and, thus, a more comfortable treatment option for patients. Besides, these particles could also vehicle other therapeutic and/or molecular imaging agents in the vascular compartment to target *P*-selectin overexpressed pathologies, such as cardiovascular diseases [71] or some cancers [72,73]. Considering the detrimental role of *P*-selectin in chronic or acute inflammatory pathologies [10], it might be relevant to explore the immunomodulatory and anti-inflammatory effects of fucoidan in the Fuco-SPs, in addition to its binding *P*-selectin, bearing in mind that natural variability of fucoidans (the source, species, molecular weight, composition, and structure of the polysaccharides) influences their biological activity and potential therapeutic application.

Nevertheless, as none of the available *in vivo* rodent experimental models of acute thrombosis accurately recapitulates all the aspects of human disease progression and heterogeneity, it is recommended to validate any translational concept in multiple models to ensure its therapeutic efficacy and safety. Notably, in 2019, Xu et al. proposed a biomimetic strategy of platelet membrane-camouflaged PLGA NPs with rtPA that was studied in several *in vivo* models: pulmonary embolism, $FeCl_3$-induced arterial thrombosis, and ischemic stroke model [67].

Due to technical challenges and strict regulatory requirements, the clinical translation of the nanopharmaceutical products happens slowly. The rtPA-Fuco-SPs representing an actively targeted nanodelivery system reach a balance of safety, simplicity, and functionality concerning the projected clinical application. While they were designed and fabricated in the academic laboratory at the range of ~10 mg per batch, the industrial scale-up of the process with high reproducibility under GMP conditions and intended quality standards is essential to establish in order to obtain the necessary amounts for further screening and, ultimately, clinical use. For instance, high-precision microfluidic and micropatterning methods for the fabrication of monodisperse NPs with uniform physicochemical characteristics and low batch-to-batch variability are becoming prevalent and are compatible with GMP standards [74]. Finally, an adequate sterilization method should be validated to prevent nanoparticle damage and alteration in the product's parameters.

5. Conclusions

In the present study, we designed and fabricated fucoidan-functionalized 100% polysaccharide submicroparticles from biocompatible and FDA approved components as a *P*-selectin targeting drug delivery system for thrombolytic therapy. The physico-chemical properties and a biocompatibility analysis of these SPs were thoroughly evaluated, and alteplase was effectively immobilized onto the SPs with full retention of its enzymatic and fibrinolytic potential *in vitro* and sustained drug-release kinetics. We established *in vitro* by dynamic flow microchamber assays that the fucoidan-functionalized nanosystem specifically adhered to the recombinant *P*-selectin in a dose-dependent manner, but not to E- and L-Selectins, and to human activated platelets. In $FeCl_3$ model of thrombosis, Fuco-SPs accumulated in the thrombus. Finally, our findings revealed in the murine model of ischemic stroke that rtPA conjugation to the Fuco-SPs could enhance the thrombolytic activity of the clinical agent *in vivo*. The blood flow perfusion was restored more rapidly, which resulted in smaller post-ischemic cerebral infarct lesions and higher BBB protection. In summary, an alteplase-associated hydrogel-based nano-delivery system with fucoidan demonstrates a solid argument for improved thrombolytic therapy in terms of safety and efficacy in the preclinical studies.

Credit author statement

Alina ZENYCH: Conceptualization; Investigation; Data curation; Formal analysis; Writing - Original & Revised Draft; Visualization. Charlène JACQMARCQ: Investigation. Rachida AID: Investigation; Validation. Louise FOURNIER: Investigation. Laura M. FORERO RAMIREZ: Methodology. Frédéric CHAUBET: Methodology; Visualization. Thomas BONNARD: Methodology; Investigation; Validation; Writing – review & editing. Denis VIVIEN: Resources; Project administration; Writing – review & editing. Didier LETOURNEUR: Resources; Project administration. Cédric CHAUVIERRE: Conceptualization; Validation; Resources; Writing – review & editing; Supervision; Project administration; Funding acquisition. All the authors approved the final revised version of the manuscript.

Declaration of competing interest

The authors declare that they have no known competing financial

interests or personal relationships that could have appeared to influence the work reported in this paper.

Acknowledgments

The authors would like to acknowledge Marie-Françoise Bricot from the Institut de Chimie des Substances Naturelles of the Université Paris-Saclay for performing a microanalysis of the fucoidan and the Fuco-SPs. We also thank the ImagoSeine core facility of the Institut Jacques Monod, a member of IBiSA and France-Bio-Imaging (ANR-10-INBS-04) infrastructures for the TEM. The authors are grateful for Christine Choqueux, who performed the Environmental SEM at Université de Technologie de Compiègne, Compiègne, France. We kindly thank Pr. Antonino Nicoletti for his advice on designing an *in vitro* release study and Dr. Kevin Guedj for assistance with flow cytometry. We also thank Dr. Yoann Lalatonne for the technical support with the TXRF technique and Dr. Samira Benadda with confocal microscopy. The illustrations were designed with BioRender software (biorender.com). Funding: The authors thank INSERM, Université de Paris, and Université Sorbonne Paris Nord for financial support. This work also received funding from the EU project FP7-NMP-2012-LARGE-6-309820 "NanoAthero" and ANR-13-LAB1-0005-01 "FucoChem". Alina Zenych is grateful for the Ph. D. fellowship from the INSPIRE program of the European Union's Horizon 2020 research and innovation program (Marie Sklodowska-Curie grant # 665850).

Appendix A. Supplementary data

Supplementary data to this article can be found online at https://doi.org/10.1016/j.biomaterials.2021.121102.

References

[1] E.J. Benjamin, P. Muntner, A. Alonso, M.S. Bittencourt, C.W. Callaway, A. P. Carson, A.M. Chamberlain, A.R. Chang, S. Cheng, S.R. Das, F.N. Delling, L. Djousse, M.S.V. Elkind, J.F. Ferguson, M. Fornage, L.C. Jordan, S.S. Khan, B. M. Kissela, K.L. Knutson, T.W. Kwan, D.T. Lackland, T.T. Lewis, J.H. Lichtman, C. T. Longenecker, M.S. Loop, P.L. Lutsey, S.S. Martin, K. Matsushita, A.E. Moran, M. E. Mussolino, M. O'Flaherty, A. Pandey, A.M. Perak, W.D. Rosamond, G.A. Roth, U. K.A. Sampson, G.M. Satou, E.B. Schroeder, S.H. Shah, N.L. Spartano, A. Stokes, D. L. Tirschwell, C.W. Tsao, M.P. Turakhia, L.B. VanWagner, J.T. Wilkins, S.S. Wong, S.S. Virani, Heart disease and stroke statistics—2019 update: a report from the American heart association, Circulation (2019), https://doi.org/10.1161/CIR.0000000000000659.

[2] W.J. Powers, A.A. Rabinstein, T. Ackerson, O.M. Adeoye, N.C. Bambakidis, K. Becker, J. Biller, M. Brown, B.M. Demaerschalk, B. Hoh, E.C. Jauch, C. S. Kidwell, T.M. Leslie-Mazwi, B. Ovbiagele, P.A. Scott, K.N. Sheth, A. M. Southerland, D.V. Summers, D.L. Tirschwell, Guidelines for the early management of patients with acute ischemic stroke: 2019 update to the 2018 guidelines for the early management of acute ischemic stroke: a guideline for healthcare professionals from the American heart association/American stroke, Stroke 50 (2019) e344, https://doi.org/10.1161/STR.0000000000000211. –e418.

[3] J. Mican, M. Toul, D. Bednar, J. Damborsky, Structural biology and protein engineering of thrombolytics, Comput. Struct. Biotechnol. J. 17 (2019) 917–938, https://doi.org/10.1016/j.csbj.2019.06.023.

[4] R. Bhatia, M.D. Hill, N. Shobha, B. Menon, S. Bal, P. Kochar, T. Watson, M. Goyal, A.M. Demchuk, Low rates of acute recanalization with intravenous recombinant tissue plasminogen activator in ischemic stroke: real-world experience and a call for action, Stroke 41 (2010) 2254–2258, https://doi.org/10.1161/STROKEAHA.110.592535.

[5] A.M. Thiebaut, M. Gauberti, C. Ali, S. Martinez De Lizarrondo, D. Vivien, M. Yepes, B.D. Roussel, The role of plasminogen activators in stroke treatment: fibrinolysis and beyond, Lancet Neurol. 17 (2018) 1121–1132, https://doi.org/10.1016/S1474-4422(18)30323-5.

[6] A. Pal Khasa, Y. Pal Khasa, The evolution of recombinant thrombolytics: current status and future directions, Bioengineered 8 (2017) 331–358, https://doi.org/10.1080/21655979.2016.1229718.

[7] S. Liu, X. Feng, R. Jin, G. Li, Tissue plasminogen activator-based nanothrombolysis for ischemic stroke, Expet Opin. Drug Deliv. 15 (2018) 173–184, https://doi.org/10.1080/17425247.2018.1384464.

[8] N. Korin, M. Kanapathipillai, B.D. Matthews, M. Crescente, A. Brill, T. Mammoto, K. Ghosh, S. Jurek, S.A. Bencherif, D. Bhatta, A.U. Coskun, C.L. Feldman, D. D. Wagner, D.E. Ingber, Shear-activated nanotherapeutics for drug targeting to obstructed blood vessels, Science 337 (2012) 738–742, https://doi.org/10.1126/science.1217815, 80.

[9] M. Colasuonno, A.L. Palange, R. Aid, M. Ferreira, H. Mollica, R. Palomba, M. Emdin, M. Del Sette, C. Chauvierre, D. Letourneur, P. Decuzzi, Erythrocyte-Inspired discoidal polymeric nanoconstructs carrying tissue plasminogen activator for the enhanced lysis of blood clots, ACS Nano 12 (2018) 12224–12237, https://doi.org/10.1021/acsnano.8b06021.

[10] J. Hu, S. Huang, L. Zhu, W. Huang, Y. Zhao, K. Jin, Q. Zhuge, Tissue plasminogen activator-porous magnetic microrods for targeted thrombolytic therapy after ischemic stroke, ACS Appl. Mater. Interfaces 10 (2018) 32988–32997, https://doi.org/10.1021/acsami.8b09423.

[11] H.-W. Yang, M.-Y. Hua, K.-J. Lin, S.-P. Wey, R.-Y. Tsai, S.-Y. Wu, Y.-C. Lu, H.-L. Liu, T. Wu, Y.-H. Ma, Bioconjugation of recombinant tissue plasminogen activator to magnetic nanocarriers for targeted thrombolysis, Int. J. Nanomed. 7 (2012) 5159–5173, https://doi.org/10.2147/IJN.S32939.

[12] L. Huang, J. Wang, S. Huang, F. Siaw-Debrah, M. Nyanzu, Q. Zhuge, Polyacrylic acid-coated nanoparticles loaded with recombinant tissue plasminogen activator for the treatment of mice with ischemic stroke, Biochem. Biophys. Res. Commun. 516 (2019) 565–570, https://doi.org/10.1016/j.bbrc.2019.06.079.

[13] J. Zhou, D. Guo, Y. Zhang, W. Wu, H. Ran, Z. Wang, Construction and evaluation of Fe3O4-based PLGA nanoparticles carrying rtPA used in the detection of thrombosis and in targeted thrombolysis, ACS Appl. Mater. Interfaces 6 (2014) 5566–5576, https://doi.org/10.1021/am406008k.

[14] A. Friedman, S. Claypool, R. Liu, The smart targeting of nanoparticles, Curr. Pharmaceut. Des. 19 (2013) 6315–6329, https://doi.org/10.2174/13816128113199990375.

[15] W. jin Jeong, J. Bu, L.J. Kubiatowicz, S.S. Chen, Y.S. Kim, S. Hong, Peptide–nanoparticle conjugates: a next generation of diagnostic and therapeutic platforms? Nano Converg 5 (2018) 1–18, https://doi.org/10.1186/s40580-018-0170-1.

[16] L. Chollet, P. Saboural, C. Chauvierre, J.-N. Villemin, D. Letourneur, F. Chaubet, Fucoidans in Nanomedicine, Mar. Drugs. 14 (2016) 1–24, https://doi.org/10.3390/md14080145.

[17] L. Bachelet, I. Bertholon, D. Lavigne, R. Vassy, M. Jandrot-Perrus, F. Chaubet, D. Letourneur, Affinity of low molecular weight fucoidan for P-selectin triggers its binding to activated human platelets, Biochim. Biophys. Acta Gen. Subj. 1790 (2009) 141–146, https://doi.org/10.1016/j.bbagen.2008.10.008.

[18] P. Saboural, F. Chaubet, F. Rouzet, F. Al-Shoukr, R. Ben Azzouna, N. Bouchemal, L. Picton, L. Louedec, M. Maire, L. Rolland, G. Potier, D. Le Guludec, D. Letourneur, C. Chauvierre, Purification of a low molecular weight fucoidan for SPECT molecular imaging of myocardial infarction, Mar. Drugs 12 (2014) 4851–4867, https://doi.org/10.3390/md12094851.

[19] T. Bonnard, J.-M. Serfaty, C. Journé, B. Ho Tin Noe, D. Arnaud, L. Louedec, M. Derkaoui, D. Letourneur, C. Chauvierre, C. Le Visage, Leukocyte mimetic polysaccharide microparticles tracked in vivo on activated endothelium and in abdominal aortic aneurysm, Acta Biomater. 10 (2014) 3535–3545, https://doi.org/10.1016/j.actbio.2014.04.015.

[20] T. Bonnard, G. Yang, A. Petiet, V. Ollivier, O. Haddad, D. Arnaud, L. Louedec, L. Bachelet-Violette, S.M. Derkaoui, D. Letourneur, C. Chauvierre, C. Le Visage, Abdominal aortic aneurysms targeted by functionalized polysaccharide microparticles: a new tool for SPECT imaging, Theranostics 4 (2014) 592–603, https://doi.org/10.7150/thno.7757.

[21] B. Li, M. Juenet, R. Aid-Launais, M. Maire, V. Ollivier, D. Letourneur, C. Chauvierre, Development of polymer microcapsules functionalized with fucoidan to target P-selectin overexpressed in cardiovascular diseases, Adv. Healthc. Mater. 6 (2017) 1–11, https://doi.org/10.1002/adhm.201601200.

[22] B. Li, R. Aid-Launais, M.-N. Labour, A. Zenych, M. Juenet, C. Choqueux, V. Ollivier, O. Couture, D. Letourneur, C. Chauvierre, Functionalized polymer microbubbles as new molecular ultrasound contrast agent to target P-selectin in thrombus, Biomaterials 194 (2019) 139–150, https://doi.org/10.1016/j.biomaterials.2018.12.023.

[23] M. Juenet, R. Aid-Launais, B. Li, A. Berger, J. Aerts, V. Ollivier, A. Nicoletti, D. Letourneur, C. Chauvierre, Thrombolytic therapy based on fucoidan-functionalized polymer nanoparticles targeting P-selectin, Biomaterials 156 (2018) 204–216, https://doi.org/10.1016/j.biomaterials.2017.11.047.

[24] C. Chauvierre, D. Letourneur, The European project NanoAthero to fight cardiovascular diseases using nanotechnologies, Nanomedicine 10 (2015) 3391–3400, https://doi.org/10.2217/nnm.15.170.

[25] K.H. Zheng, Y. Kaiser, E. Poel, H. Verberne, J. Aerts, F. Rouzet, E. Stroes, D. Letourneur, C. Chauvierre, 99Mtc-Fucoidan as diagnostic agent for P-selectin imaging: first-in-human evaluation (phase I), Atherosclerosis 287 (2019) e143, https://doi.org/10.1016/j.atherosclerosis.2019.06.425.

[26] I. Cicha, C. Chauvierre, I. Texier, C. Cabella, J.M. Metselaar, J. Szebeni, L. Dézsi, C. Alexiou, F. Rouzet, G. Storm, E. Stroes, D. Bruce, N. MacRitchie, P. Maffia, D. Letourneur, From design to the clinic: practical guidelines for translating cardiovascular nanomedicine, Cardiovasc. Res. 114 (2018) 1714–1727, https://doi.org/10.1093/cvr/cvy219.

[27] K. Ganguly, K. Chaturvedi, U.A. More, M.N. Nadagouda, T.M. Aminabhavi, Polysaccharide-based micro/nanohydrogels for delivering macromolecular therapeutics, J. Contr. Release 193 (2014) 162–173, https://doi.org/10.1016/j.jconrel.2014.05.014.

[28] J. Zhang, W. Xia, P. Liu, Q. Cheng, T. Tahirou, W. Gu, B. Li, Chitosan modification and pharmaceutical/biomedical applications, Mar. Drugs 8 (2010) 1962–1987, https://doi.org/10.3390/md8071962.

[29] H.J. Jin, H. Zhang, M.L. Sun, B.G. Zhang, J.W. Zhang, Urokinase-coated chitosan nanoparticles for thrombolytic therapy: preparation and pharmacodynamics in vivo, J. Thromb. Thrombolysis 36 (2013) 458–468, https://doi.org/10.1007/s11239-013-0951-7.

[30] J. Liao, X. Ren, B. Yang, H. Li, Y. Zhang, Z. Yin, Targeted thrombolysis by using c-RGD-modified N,N,N-Trimethyl Chitosan nanoparticles loaded with lumbrokinase, Drug Dev. Ind. Pharm. 45 (2019) 88–95, https://doi.org/10.1080/03639045.2018.1522324.

[31] S.R. Van Tomme, W.E. Hennink, Biodegradable dextran hydrogels for protein delivery applications, Expet Rev. Med. Dev. 4 (2007) 147–164, https://doi.org/10.1586/17434440.4.2.147.

[32] J.R. McCarthy, I.Y. Sazonova, S.S. Erdem, T. Hara, B.D. Thompson, P. Patel, I. Botnaru, C.P. Lin, G.L. Reed, R. Weissleder, F.A. Jaffer, Multifunctional nanoagent for thrombus-targeted fibrinolytic therapy, Nanomedicine 7 (2012) 1017–1028, https://doi.org/10.2217/nnm.11.179.

[33] S. Heid, H. Unterweger, R. Tietze, R.P. Friedrich, B. Weigel, I. Cicha, D. Eberbeck, A.R. Boccaccini, C. Alexiou, S. Lyer, Synthesis and characterization of tissue plasminogen activator-functionalized superparamagnetic iron oxide nanoparticles for targeted fibrin clot dissolution, Int. J. Mol. Sci. 18 (2017), https://doi.org/10.3390/ijms18091837.

[34] J.M. Lee, Z.-U. Shin, G.T. Mavlonov, I.Y. Abdurakhmonov, T.-H. Yi, Solid-phase colorimetric method for the quantification of fucoidan, Appl. Biochem. Biotechnol. 168 (2012) 1019–1024, https://doi.org/10.1007/s12010-012-9837-y.

[35] S. Petersen, A. Fahr, H. Bunjes, Flow cytometry as a new approach to investigate drug transfer between lipid particles, Mol. Pharm. 7 (2010) 350–363, https://doi.org/10.1021/mp900130s.

[36] C. Orset, R. Macrez, A.R. Young, D. Panthou, E. Angles-cano, E. Maubert, V. Agin, D. Vivien, Mouse model of in situ thromboembolic stroke and reperfusion, Stroke 38 (2007) 2771–2778, https://doi.org/10.1161/STROKEAHA.107.487520.

[37] T.E. Furia, CRC Handbook of Food Additives, second ed., CRC Press, 1973.

[38] W.E. Hennink, C.F. van Nostrum, Novel crosslinking methods to design hydrogels, Adv. Drug Deliv. Rev. 54 (2002) 13–36, https://doi.org/10.1016/S0169-409X(01)00240-X.

[39] C. Chauvierre, R. Aid-Launais, J. Aerts, M. Maire, L. Chollet, L. Rolland, R. Bonaf, S. Rossi, S. Bussi, C. Cabella, D. Laszlo, T. Fülöp, J. Szebeni, Y. Chahid, K.H. Zheng, E.S.G. Stroes, D. Le Guludec, F. Rouzet, D. Letourneur, Pharmaceutical development and safety evaluation of a GMP-grade fucoidan for molecular diagnosis of cardiovascular diseases, Mar. Drugs 17 (2019) 1–17, https://doi.org/10.3390/md17120699.

[40] F. Rouzet, L. Bachelet-Violette, J.-M. Alsac, M. Suzuki, A. Meulemans, L. Louedec, A. Petiet, M. Jandrot-Perrus, F. Chaubet, J.-B. Michel, D. Le Guludec, D. Letourneur, Radiolabeled fucoidan as a P-selectin targeting agent for in vivo imaging of platelet-rich thrombus and endothelial activation, J. Nucl. Med. 52 (2011) 1433–1440, https://doi.org/10.2967/jnumed.110.085852.

[41] F. Wolf, K. Koehler, H.P. Schuchmann, Stabilization of water droplets in oil with PGPR for use in oral and dermal applications, J. Food Process. Eng. 36 (2013) 276–283, https://doi.org/10.1111/j.1745-4530.2012.00688.x.

[42] J. Matuszak, J. Baumgartner, J. Zaloga, M. Juenet, A.E. da Silva, D. Franke, G. Almer, I. Texier, D. Faivre, J.M. Metselaar, F.P. Navarro, C. Chauvierre, R. Prassl, L. Dézsi, R. Urbanics, C. Alexiou, H. Mangge, J. Szebeni, D. Letourneur, I. Cicha, Nanoparticles for intravascular applications: physicochemical characterization and cytotoxicity testing, Nanomedicine 11 (2016) 597–616, https://doi.org/10.2217/nnm.15.216.

[43] M. Weber, H. Steinle, S. Golombek, L. Hann, C. Schlensak, H.P. Wendel, M. Avci-Adali, Blood-contacting biomaterials: in vitro evaluation of the hemocompatibility, Front. Bioeng. Biotechnol. 6 (2018) 99, https://doi.org/10.3389/fbioe.2018.00099.

[44] ISO 10993-4:2017, Biol. Eval. Med. Devices — Part 4 Sel. Tests Interact. With Blood, 2017. https://www.iso.org/standard/63448.html.

[45] B. Vaidya, G.P. Agrawal, S.P. Vyas, Platelets directed liposomes for the delivery of streptokinase: development and characterization, Eur. J. Pharmaceut. Sci. 44 (2011) 589–594, https://doi.org/10.1016/j.ejps.2011.10.004.

[46] N. Zhang, C. Li, D. Zhou, C. Ding, Y. Jin, Q. Tian, X. Meng, K. Pu, Y. Zhu, Cyclic RGD functionalized liposomes encapsulating urokinase for thrombolysis, Acta Biomater. (2018), https://doi.org/10.1016/j.actbio.2018.01.038.

[47] K. Ley, The role of selectins in inflammation and disease, Trends Mol. Med. 9 (2003) 263–268, https://doi.org/10.1016/S1471-4914(03)00071-6.

[48] J.-H. Kim, J.-Y. Yoon, Protein adsorption on polymer particles, Encycl. Surf. Colloid Sci. (2002) 4373–4381, https://doi.org/10.1002/jbm.820210202.

[49] I. Politis, L. Wang, J.D. Turner, B.K. Tsang, Changes in tissue-type plasminogen activator-like and plasminogen activator inhibitor activities in granulosa and theca layers during ovarian follicle development in the domestic Hen1, Biol. Reprod. 42 (1990) 747–754, https://doi.org/10.1095/biolreprod42.5.747.

[50] V. Wintgens, C. Lorthioir, P. Dubot, B. Sébille, C. Amiel, Cyclodextrin/dextran based hydrogels prepared by cross-linking with sodium trimetaphosphate, Carbohydr, Polymja 132 (2015) 80–88, https://doi.org/10.1016/j.carbpol.2015.06.038.

[51] L. Arnfast, C.G. Madsen, L. Jorgensen, S. Baldursdottir, Design and processing of nanogels as delivery systems for peptides and proteins, Ther. Deliv. 5 (2014) 691–708, https://doi.org/10.4155/tde.14.38.

[52] Z.M. Ruggeri, Platelets in atherothrombosis, Nat. Med. 8 (2002) 1227–1234, https://doi.org/10.4065/81.1.59.

[53] T.J. Merkel, K. Chen, S.W. Jones, A.A. Pandya, S. Tian, M.E. Napier, W.E. Zamboni, J.M. Desimone, The effect of particle size on the biodistribution of low-modulus hydrogel PRINT particles, J. Contr. Release 162 (2012) 37–44, https://doi.org/10.1016/j.jconrel.2012.06.009.

[54] C. Orset, B. Haelewyn, S.M. Allan, S. Ansar, F. Campos, T.H. Cho, A. Durand, M. El Amki, M. Fatar, I. Garcia-Yébenes, M. Gauberti, S. Grudzenski, I. Lizasoain, E. Lo, R. Macrez, I. Margaill, S. Maysami, S. Meairs, N. Nighoghossian, J. Orbe, J. A. Paramo, J.J. Parienti, N.J. Rothwell, M. Rubio, C. Waeber, A.R. Young, E. Touzé, D. Vivien, Efficacy of alteplase in a mouse model of acute ischemic stroke: a retrospective pooled analysis, Stroke 47 (2016) 1312–1318, https://doi.org/10.1161/STROKEAHA.116.012238.

[55] S.M. De Lizarrondo, C. Gakuba, B.A. Herbig, Y. Repessé, C. Ali, C.V. Denis, P. J. Lenting, E. Touzé, S.L. Diamond, D. Vivien, M. Gauberti, Potent thrombolytic effect of N-acetylcysteine on arterial thrombi, Circulation 136 (2017) 646–660, https://doi.org/10.1161/CIRCULATIONAHA.117.027290.

[56] H.R. Lijnen, B. Van Hoef, V. Beelen, D. Collen, Characterization of the murine plasma fibrinolytic system, Eur. J. Biochem. 224 (1994) 863–871, https://doi.org/10.1111/j.1432-1033.1994.00863.x.

[57] R. Brouns, P.P. De Deyn, The complexity of neurobiological processes in acute ischemic stroke, Clin. Neurol. Neurosurg. 111 (2009) 483–495, https://doi.org/10.1016/j.clineuro.2009.04.001.

[58] A. Zenych, L. Fournier, C. Chauvierre, Nanomedicine progress in thrombolytic therapy, Biomaterials 258 (2020) 120297, https://doi.org/10.1016/j.biomaterials.2020.120297.

[59] K.S. Masters, D.N. Shah, L.A. Leinwand, K.S. Anseth, Crosslinked hyaluronan scaffolds as a biologically active carrier for valvular interstitial cells, Biomaterials 26 (2005) 2517–2525, https://doi.org/10.1016/j.biomaterials.2004.07.018.

[60] C.I. Jones, D.A. Payne, P.D. Hayes, A.R. Naylor, P.R.F. Bell, M.M. Thompson, A. H. Goodall, The antithrombotic effect of dextran-40 in man is due to enhanced fibrinolysis in vivo, J. Vasc. Surg. 48 (2008) 715–722, https://doi.org/10.1016/j.jvs.2008.04.008.

[61] E.M. Balboa, E. Conde, A. Moure, E. Falqué, H. Domínguez, In vitro antioxidant properties of crude extracts and compounds from brown algae, Food Chem. 138 (2013) 1764–1785, https://doi.org/10.1016/j.foodchem.2012.11.026.

[62] Y. Choi, S.K. Min, R. Usoltseva, A. Silchenko, T. Zvyagintseva, S. Ermakova, J. K. Kim, Thrombolytic fucoidans inhibit the tPA-PAI1 complex, indicating activation of plasma tissue-type plasminogen activator is a mechanism of fucoidan-mediated thrombolysis in a mouse thrombosis model, Thromb. Res. 161 (2018) 22–25, https://doi.org/10.1016/j.thromres.2017.11.015.

[63] K. Knop, R. Hoogenboom, D. Fischer, U.S. Schubert, Poly(ethylene glycol) in drug delivery: pros and cons as well as potential alternatives, Angew. Chem. Int. Ed. 49 (2010) 6288–6308, https://doi.org/10.1002/anie.200902672.

[64] M. Di Marco, K.A. Razak, A.A. Aziz, C. Devaux, E. Borghi, L. Levy, C. Sadun, Overview of the main methods used to combine proteins with nanosystems : absorption, bioconjugation, and encapsulation, Int. J. Nanomed. 5 (2010) 37–49.

[65] R.P. Friedrich, J. Zaloga, E. Schreiber, I.Y. Tóth, E. Tombácz, S. Lyer, C. Alexiou, Tissue plasminogen activator binding to superparamagnetic iron oxide nanoparticle-covalent versus adsorptive approach, Nanoscale Res. Lett. 11 (2016) 1–11, https://doi.org/10.1186/s11671-016-1521-7.

[66] C.L. Pawlowski, W. Li, M. Sun, K. Ravichandran, D. Hickman, C. Kos, G. Kaur, A. Sen Gupta, Platelet microparticle-inspired clot-responsive nanomedicine for targeted fibrinolysis, Biomaterials 128 (2017) 94–108, https://doi.org/10.1016/j.biomaterials.2017.03.012.

[67] J. Xu, Y. Zhang, J. Xu, G. Liu, C. Di, X. Zhao, X. Li, Y. Li, N. Pang, C. Yang, Y. Li, B. Li, Z. Lu, M. Wang, K. Dai, R. Yan, S. Li, G. Nie, Engineered nanoplatelets for targeted delivery of plasminogen activators to reverse thrombus in multiple mouse thrombosis models, Adv. Mater. 32 (2019) 1905145, https://doi.org/10.1002/adma.201905145.

[68] T. Mei, A. Kim, L.B. Vong, A. Marushima, S. Puentes, Y. Matsumaru, A. Matsumura, Y. Nagasaki, Encapsulation of tissue plasminogen activator in pH-sensitive self-assembled antioxidant nanoparticles for ischemic stroke treatment-Synergistic effect of thrombolysis and antioxidant, Biomaterials 215 (2019) 1–12, https://doi.org/10.1016/j.biomaterials.2019.05.020.

[69] H. Kim, J.H. Ahn, M. Song, D.W. Kim, T.K. Lee, J.C. Lee, Y.M. Kim, J.D. Kim, J. H. Cho, I.K. Hwang, B.C. Yan, M.H. Won, J.H. Park, Pretreated fucoidan confers neuroprotection against transient global cerebral ischemic injury in the gerbil hippocampal CA1 area via reducing of glial cell activation and oxidative stress, Biomed. Pharmacother. 109 (2019) 1718–1727, https://doi.org/10.1016/j.biopha.2018.11.015.

[70] D. Vivien, M. Gauberti, A. Montagne, G. Defer, E. Touzé, Impact of tissue plasminogen activator on the neurovascular unit: from clinical data to experimental evidence, J. Cerebr. Blood Flow Metabol. 31 (2011) 2119–2134, https://doi.org/10.1038/jcbfm.2011.127.

[71] S. Yokoyama, H. Ikeda, N. Haramaki, H. Yasukawa, T. Murohara, T. Imaizumi, Platelet P-selectin plays an important role in arterial thrombogenesis by forming large stable platelet-leukocyte aggregates, J. Am. Coll. Cardiol. 45 (2005) 1280–1286, https://doi.org/10.1016/j.jacc.2004.12.071.

[72] S.R. Barthel, J.D. Gavino, L. Descheny, C.J. Dimitroff, Targeting selectins and selectin ligands in inflammation and cancer, Expert Opin. Ther. Targets 11 (2007) 1473–1491, https://doi.org/10.1517/14728222.11.11.1473.

[73] Y. Shamay, M. Elkabets, H. Li, J. Shah, S. Brook, F. Wang, K. Adler, E. Baut, M. Scaltriti, P. V Jena, E.E. Gardner, J.T. Poirier, C.M. Rudin, J. Baselga, A. Haimovitz-Friedman, D.A. Heller, P-selectin is a nanotherapeutic delivery target in the tumor microenvironment, Sci. Transl. Med. 8 (2016) 345ra87, https://doi.org/10.1126/scitranslmed.aaf7374.

[74] J.P.A. Ioannidis, B.Y.S. Kim, A. Trounson, How to design preclinical studies in nanomedicine and cell therapy to maximize the prospects of clinical translation, Nat. Biomed. Eng. 2 (2018) 797–809, https://doi.org/10.1038/s41551-018-0314-y.

ANNEX 6

Ultrasound responsive polymer microbubbles for an efficient targeted treatment of thrombotic diseases

L. J. Fournier[1], R. Aid[1, 2], A. W. Aissani[3] , V. Ollivier[1] , M. Maire[1, 4], O. Couture[3] , D. Letourneur[1], C. Chauvierre[1]

[1] INSERM U1148, LVTS, Université de Paris, X Bichat Hospital, PARIS, France; [2] UMS34 FRIM, Université de Paris, PARIS, France; [3] Laboratoire d'Imagerie Biomédicale Sorbonne Université, UMR 7371 - U1146, PARIS, France; [4] INSERM U1148, LVTS, Université Sorbonne Paris Nord, VILLETANEUSE, France

Introduction

Cardiovascular diseases

1st worldwide mortality rate

→ *Thrombotic diseases*

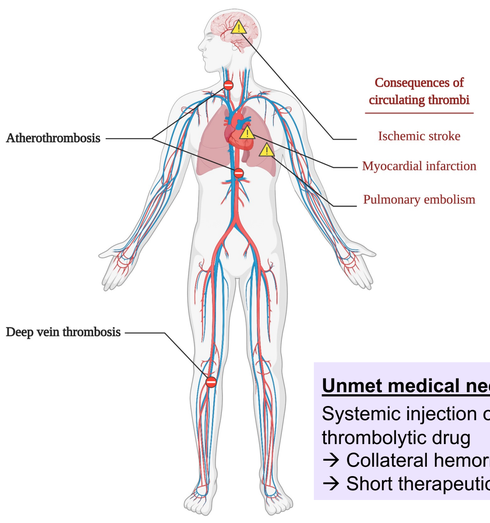

Unmet medical need:
Systemic injection of the thrombolytic drug
→ Collateral hemorrhages
→ Short therapeutic window

[1]

Objectives

Targeted delivery of thrombolytic agent

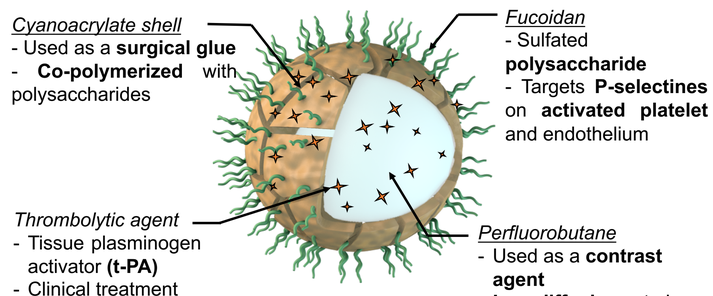

Mechanical disruption of the clot and drug delivery

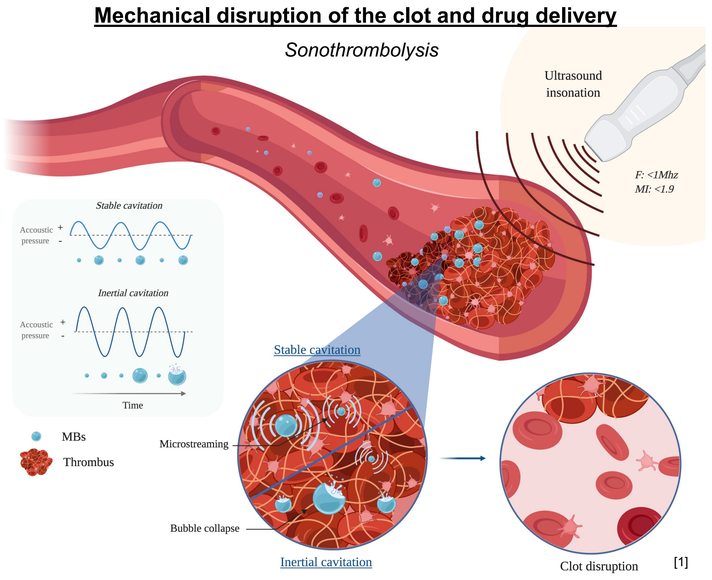

[1]

Conclusion

Our aim is to **deliver safely** a thrombolytic drug to the site of clot formation. Our protocol using **acoustic cavitation** for the synthesis of **polymer targeting MBs** is not described in the literature yet. So far, we have been able to obtain **reproducible and stable MBs** that are not harmful in the blood system. Our results on targeting properties thanks to fucoidan incorporation, showed an **improved targeting** compared to control MBs, in static condition and flow condition. Also the **echogenic property** has been demonstrated in flow experiment to be **comparable to commercial MBs** and the inertial cavitation response to high mechanical index US pulse present great promises for an **effective sonothrombolysis**. Our remaining work is now focused on the the optimization of the **thrombolytic agent incorporation** and the *in vivo* proof of concept of the **sonothrombolysis efficiency in a mice stroke model**.

Acknowledgements

This work is funded by ANR-20-CE18-0005-01 "FightClot" and we acknowledge Université de Paris and the MTCI doctoral school for the PhD grant.

References

[1] A. Zenych, L. Fournier, and C. Chauvierre, "Nanomedicine progress in thrombolytic therapy," *Biomaterials*, vol. 258, no. January, 2020, doi: 10.1016/j.biomaterials.2020.120297.
[2] I. Bertholon, S. Lesieur, D. Labarre, M. Besnard, and C. Vauthier, "Characterization of dextran-poly(isobutylcyanoacrylate) copolymers obtained by redox radical and anionic emulsion polymerization," *Macromolecules*, vol. 39, no. 10, pp. 3559–3567, 2006, doi: 10.1021/ma060338z.
[3] B. Li *et al.*, "Functionalized polymer microbubbles as new molecular ultrasound contrast agent to target P-selectin in thrombus," *Biomaterials*, vol. 194, no. 2019, pp. 139–150, 2019, doi: 10.1016/j.biomaterials.2018.12.023.

Results

1 *Innovative protocol*

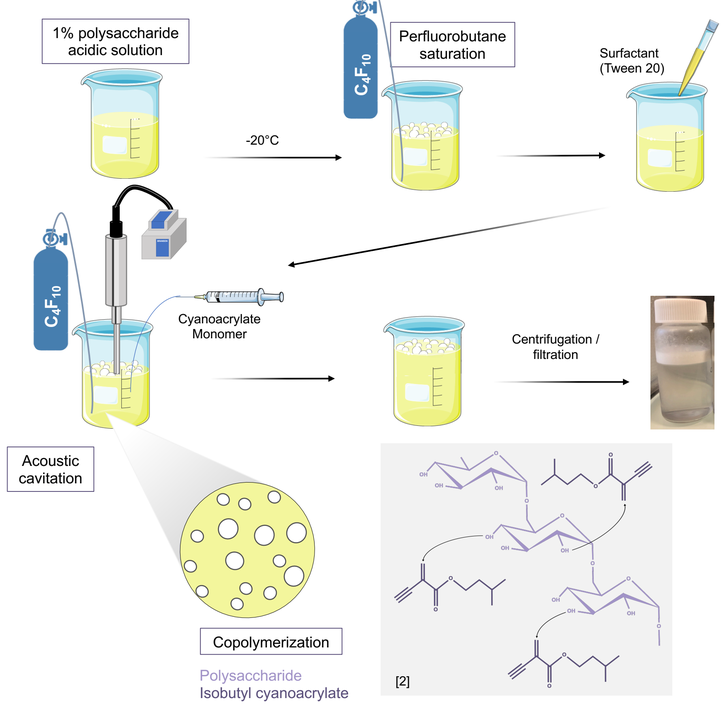

The aim of this new protocol was to develop a **reproducible**, **scalable** and **faster** protocol compared to classic hydrodynamic cavitation. The **aqueous solution** contains the **polysaccharide** (Fucoidan for targeting MBs and carboxymethyl-Dextran for control) and the **cyanoacrylate monomer** is added during the insonation at a controlled speed. Air is replaced by **Perfluorobutane** (C_4F_{10}) saturation into the solution. The insonation of ultrasound (US) induce **acoustic cavitation** so the **hydrophobic** (cyanoacrylate) and the **hydrophilic** (polysaccharide) elements meet at the **water air interface**, generating an **anionic copolymerization** and so **shell** formation entrapping the perfluorobutane.

A

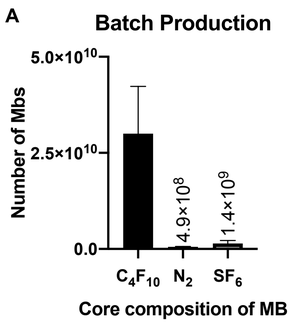

B

	D50 (µm)
Fuco MBs	2.95 ± 0.44
CMDex MBs	2.68 ± 0.61

Perfluorobutane has been chosen for its echogenic contrast property but also because of the **yield of MBs synthesis** (A). After filtration, MBs have a mean size **below 3 µm**.

2 *MBs characterization*

Microscopy images of polymer MBs

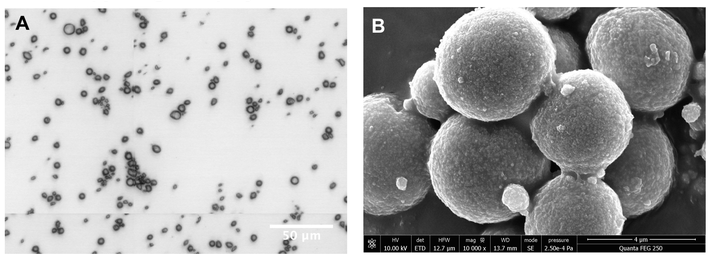

Confocal image of MBs showing the hallow structure filled with gas (A) (scale = 50 µm). Scanning Electron Microscopy image (B) highlighting the 3D rounded shape of the MBs (scale = 4µm).

Shelf stability and blood toxicity

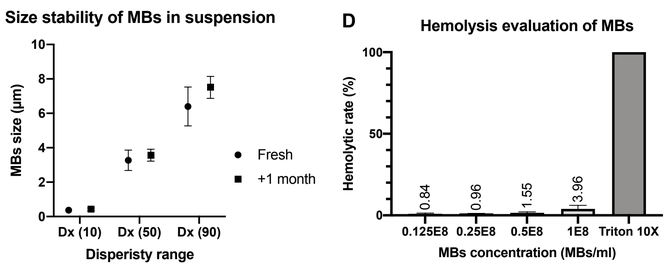

Mastersizer measurement of the size of MBs (C) after a month in a 0.02% tween 20 solution and hemolysis evaluation (D) on a fresh red blood cell solution with increasing concentration of MBs concentration (n=6).

3 *Targeting agent incorporation*

Sulfated polysaccharide quantification with methylene blue dosage

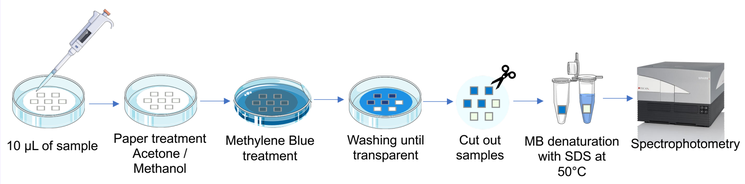

The higher the intensity of methylene blue staining, the higher the sample is sulfated according to the Beer-Lambert equation (A=εlC).

A

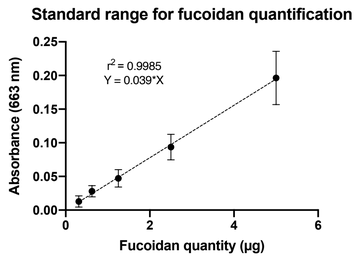

B

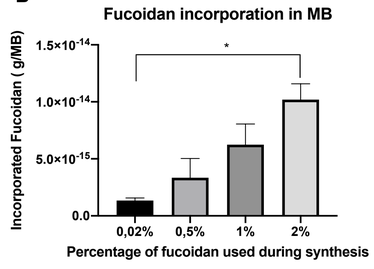

Standard range (A) of the colorimetric dosage allowed the concentration measurement of fucoidan. It has been found a **linear correlation** (B) between the **quantity of fucoidan used** for the synthesis and the **grafted quantity** on MBs.
→ For the following experiment MBs were synthetized using **1% of fucoidan**

4 *Targeting properties*

***Ex vivo* static platelet clot**

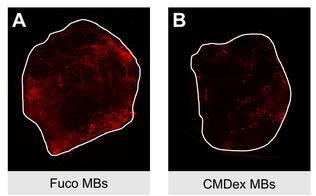

Platelet clots are obtained from platelet rich plasma after 2h of incubation at 37°C.
→ Fluorescence intensity tends to an **increased targeting of Fuco MBs** (A) over CMDex MBs (B) after 1h incubation and 3 washing steps.

***In vitro* flow platelet clot**

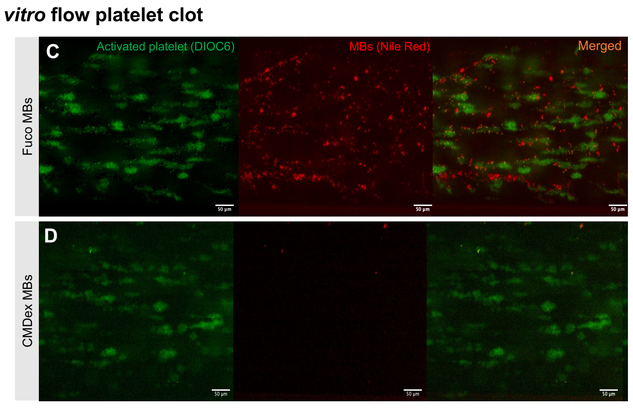

Whole human blood is flown into collagen type I coated channels. After washing, MBs are flown under venous flow rate and **colocalisation** of the platelet aggregates and the fuco MBs is **improved compared to control MBs**.

5 *Echogenic properties*

***In vitro* MBs visualization with US in a flow agar phantom set up**

MBs were flown at a constant rate in an agar phantom and recorded with an **US transducer** (filtered to remove the background).

***In vitro* MBs inertial cavitation with high index US pulse**

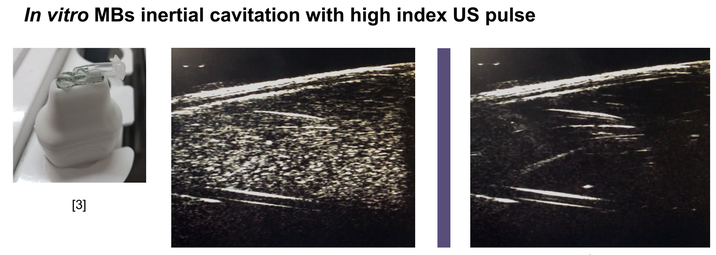

High mechanical index US wave (burst) was sent on the tube containing the MBs, inducing an **inertial cavitation of the MBs**.

Contact email: louise.fournier@inserm.fr

ESB 2021
31st CONFERENCE OF THE EUROPEAN SOCIETY FOR BIOMATERIALS
TOGETHER WITH THE 43rd ANNUAL CONGRESS OF THE IBERIAN SOCIETY OF BIOMECHANICS AND BIOMATERIALS (SIBB)
FUTURING BIOMATERIALS
5 – 9 SEPTEMBER 2021 / PORTO, PORTUGAL
LVTS UMRS 1148 Laboratory for Vascular Translational Science
Université de Paris · Inserm La science pour la santé From science to health · Université Sorbonne Paris Nord
mtci Ecole Doctorale Médicament - Toxicologie Chimie - Imageries

ANNEX 7

Ultrasound responsive polymer microbubbles for an efficient targeted treatment of thrombotic diseases

Louise Fournier, 3rd year PhD student at the Laboratory for Vascular and Translational Science (U1148 LVTS – Hopital Bichat Paris) under the supervision of Dr Cedric Chauvierre.

Cardiovascular diseases are the first worldwide mortality rate, and our team more specifically focuses on thrombotic diseases. Indeed, current treatments to prevent blood clots from obstructing vessels are intravenous injection of plasminogen activator or invasive mechanical removal called thrombectomy [1]. Nevertheless, systemic injection of the drug can cause collateral bleeding. Our strategy focuses on developing innovative carriers for the targeting treatment, and visualization of the blood clot. We synthesize targeting polymer microbubbles (MBs) in a one-pot, scalable, and not described in the literature protocol. Our targeting agent is a sulfated polysaccharide, the fucoidan, already used in clinical trial phase IIa. It was chosen for its affinity for P-selectin, expressed protein on activated platelets and activated endothelial cells. MBs can be visualized with an ultrasound device and the ultrasound insonation can also induce sonothrombolysis [2], a mechanical perturbation of the MBs that can accentuate the clot disruption. In short term, the objective is to incorporate the drug into the MBs, for a complete theragnostic tool.

MBs synthesis is obtained via acoustic cavitation of an aqueous phase containing our targeted agent with a surfactant. The organic phase containing the monomer of isobutyl cyanoacrylate is injected into the aqueous solution at a controlled speed. During the insonation process, perfluorobutane is injected into the aqueous solution to be imprisoned inside the MBs. Size and concentration measurement allowed us to control the shelf stability over the weeks of the MBs. Also, the morphology of the MBs was observed by Scanning Electron Microscopy (SEM). Fucoidan content was determined by a quantitative analysis with methylene blue colorimetric dosage. Targeting tests were performed *ex vivo* in static and fluidic conditions on human platelet clots. Echogenicity evaluation was performed with an ultrasound device. Signals of echogenicity and response to burst for sonothrombolysis are compared to commercial MBs. Ongoing *in vivo* testing aimed to validate the clot targeting with a FeCl model on the mesenterial vein and we also performed the preliminary in vivo validation of effective sonothrombolysis with a stroke mouse model on the middle cerebral artery.

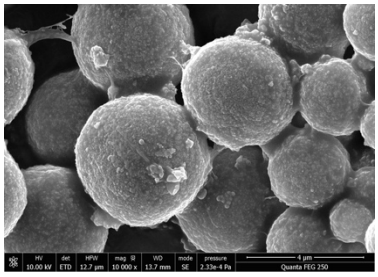

We were able to develop an undescribed synthesis protocol for polymer MBs with acoustic cavitation. Those MBs showed great shelf stability in terms of size distribution and concentration over two months. Convincing results of the targeting experiment in static and fluidic conditions allowed the beginning of *in vivo* testing. Echogenic characterization experiment provided similarities with commercial contrast agent in terms of echogenicity.
We are thrilled to present our innovative carrier for the treatment of thrombotic diseases. Perspectives result in the incorporation of the therapeutic agent [4] to allow its release on the targeted site and enhance mechanical thrombolysis with US insonation.

References

[1] A. Zenych, L. Fournier, and C. Chauvierre, "Nanomedicine progress in thrombolytic therapy," *Biomaterials*, vol. 258, no. January, 2020, doi: 10.1016/j.biomaterials.2020.120297.
[2] K. Kooiman *et al.*, "Ultrasound-Responsive Cavitation Nuclei for Therapy and Drug Delivery," *Ultrasound Med. Biol.*, vol. 00, no. 00, 2020, doi: 10.1016/j.ultrasmedbio.2020.01.002.
[3] B. Li *et al.*, "Functionalized polymer microbubbles as new molecular ultrasound contrast agent to target P-selectin in thrombus," *Biomaterials*, vol. 194, no. 2019, pp. 139–150, 2019, doi: 10.1016/j.biomaterials.2018.12.023.
[4] M. Juenet *et al.*, "Thrombolytic therapy based on fucoidan-functionalized polymer nanoparticles targeting P-selectin," *Biomaterials*, vol. 156, pp. 204–216, 2018, doi: 10.1016/j.biomaterials.2017.11.047.

ANNEX 8

FORMERLY THE BIOMARKER MEETING OF PARIS

BIOMARKERS *of the Future*

FROM BEDSIDE TO PRACTICE

THE JURY OF THE
YOUNG RESERACHERS COMEPTITION
CERTIFIES THAT

LOUISE FOURNIER

HAS BEEN AWARDED THE YOUNG RESEARCHERS COMPETITION'S

RUNNER UP PRIZE

FOR THE PRESENTATION TITLED

ULTRASOUND RESPONSIVE POLYMER MICROBUBBLE FOR AN EFFICIENT TARGETED TREATMENT OF THROMBOTIC DISEASES

PARIS, 24 NOVEMBER 2021

Olink

ANNEX 9

Ultrasound responsive polymer microbubbles for an efficient targeted treatment of thrombotic diseases

L. J. Fournier[1], R. Aid[1,2], A. W. Aissani[3], V. Ollivier[1], D. Vivien[4], O. Couture[3], C. Orset[4], and C. Chauvierre[1]

[1] *INSERM U1148, LVTS, Université de Paris, X Bichat Hospital, Paris, France*

[2] *UMS34 FRIM, Université de Paris, Paris, France*

[3] *Laboratoire d'Imagerie Biomédicale, Sorbonne Université, UMR 7371-U1146, Paris, France*

[4] *INSERM U1237, CYCERON, Université Caen Normandie, Caen, France*

Contact: louise.fournier@inserm.fr

Our team focuses on the first worldwide mortality rate, cardiovascular diseases, and more specifically on thrombotic diseases. The major unmet medical need in the treatment of pathological blood clot, is the systemic injection of the thrombolytic drug (t-PA) causing collateral hemorrhages and showing a short therapeutic window. Our objective is to develop a safe, targeting, visualizable and treating carrier to overcome surgical complications of blood clot related events.

Our technology consists in the innovative synthesis of polymer microbubbles (MBs) via acoustic cavitation. Unseen in the literature, this method allows an improved yield and reduced time of synthesis compared to regular hydrodynamic cavitation. Those polymer MBs are composed of a co-polymer shell of poly-isobutyl cyanoacrylate and a sulfated polysaccharide, fucoidan. Our lab already demonstrated the affinity of fucoidan for activated platelet and activated endothelial cells via P-selectin proteins. MBs are filled with perfluorobutane gas known for its echogenic properties allowing their visualization in optical microscopy but also in ultrasound imaging. In addition, the ultrasound insonation can also induce sonothrombolysis, a mechanical perturbation of the MBs that can accentuate the clot disruption. In short term, the objective is to incorporate the plasminogen activator into the MBs, for a complete theragnostic tool.

So far, we have been able to produce MBs, thanks to an innovative protocol, that are stable over a month in suspension and harmless for red blood cells. Optic and electronic microscopy validated the size distribution, hallow structure and rounded morphology. Targeting properties were evaluated in static and flowing condition on human platelet aggregates demonstrating the true improvement of clot recognition by fucoidan MBs. Also, echogenic and burst properties were demonstrated with a clinical ultrasound device showing great promises for *in vivo* sonothrombolysis. Lastly, ongoing animal experimentations will soon validate the *in vitro* to *in vivo* translation with a stroke model on mice.

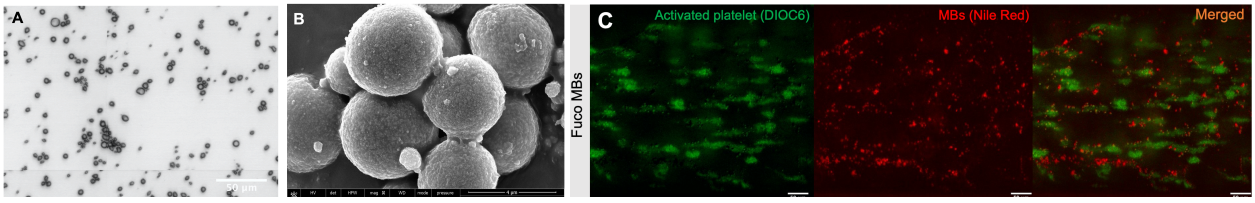

Figure 1 - (A) Confocal microscopy, (B) Scanning electron microscopy, (C) In vitro flow targeting

ANNEX 10

SFNano

FRENCH SOCIETY FOR NANOMEDICINE

The Award for the Best Oral Communication 2021 from SFNano

is granted to

Louise FOURNIER

Dr. Jean-Luc COLL

President of SFNano

ANNEX 11

Ultrasound responsive polymer microbubbles for a targeted treatment of thrombotic diseases

Louise J. Fournier[1*], Rachida Aid[1,2], Cyrille Orset[3], Olivier Couture[4], Denis Vivien[3], Cédric Chauvierre[1]
[1]INSERM U1148, LVTS, Université Paris Cité, Bichat Hospital, Paris, France
[2]UMS34 FRIM, Université de Paris, Paris, France
[3]Inserm U1237, CYCERON, Université Caen Normandie, Caen, France
[4]Laboratoire d'Imagerie Biomédicale, Sorbonne Université, UMR 7371-U1146, Paris, France
[*] louise.fournier@inserm.fr

INTRODUCTION

Our team focuses on the first worldwide mortality rate, cardiovascular diseases, and more specifically on thrombotic diseases. The major unmet medical need in the treatment of pathological blood clot, is the systemic injection of the thrombolytic drug (rtPA) causing collateral hemorrhages and showing a short therapeutic window[1]. Our objective is to develop a safe, targeting, visualizable and treating carrier to overcome surgical complications of blood clot related events. Our technology consists in the innovative synthesis of polymer microbubbles (MBs) via acoustic cavitation. Unseen in the literature, this method allows an improved yield and reduced time of synthesis compared to regular hydrodynamic cavitation. Those MBs are composed of a co-polymer shell of poly-isobutyl cyanoacrylate and a sulfated polysaccharide, fucoidan. Our strategy is based on the affinity of fucoidan for activated platelet and activated endothelial cells via P-selectin proteins[2]. MBs are filled with perfluorobutane gas known for its echogenic properties allowing their visualization in optical microscopy but also in ultrasound (US) imaging. Thereby, we aim to use MBs as a carrier for the treatment of thrombotic diseases. In addition, the ultrasound insonation can also induce sonothrombolysis, a mechanical perturbation of the MBs that can accentuate the clot disruption[2].

EXPERIMENTAL METHODS

MBs synthesis is performed via acoustic cavitation of an aqueous phase containing our targeted agent (fucoidan) with a surfactant. The phase containing the monomer of isobutyl cyanoacrylate is injected into the aqueous solution and the mix is insonated with continuous US. During this process, perfluorobutane is injected into the solution to be imprisoned inside the MBs. The obtained foam is washed and filtered to 5 µm. MBs size characterization was performed with granulometry analysis, and the morphology of the MBs was observed by Scanning Electron Microscopy (SEM). Targeting experimentations are obtained with a microfluidic system[3] that consists in coating microfluidic channels with collagen type I in order to promote platelet aggregation. Whole human blood is then injected at arterial flow speed. When platelet aggregates are formed, the channel is rinsed and the MBs suspension is injected. Microbubbles attachment to the platelet aggregates is observed by fluorescence microscopy. Echogenicity evaluation is performed in static and fluidic conditions with an US scanner to evaluate the response of MBs to different US intensities. Preliminary *in vivo* experiments have been performed on a stroke mice model to observe the effect of US treatment accompanied with the injection of targeted MBs on the recanalization of the occluded artery. Image analysis of the speckle imaging allows recanalization quantification.

RESULTS AND DISCUSSION

The innovative synthesis allowed us to obtained reproducible, stable (> 6 weeks on shelf stability), and non-toxic microbubbles (< 4% of hemolysis at 10^8 MBs /ml). Targeting evaluation (Fig. A) on activated platelet in flow condition was demonstrated to be effective ($p<0,0001$) compared to a group of MBs with a non-targeting polysaccharide (CMDex = carboxymethyl dextran). Preliminary *in vivo* experiments encourage the treatment of US insonation with the injection of targeted MBs in a stroke mouse model (Fig. B).

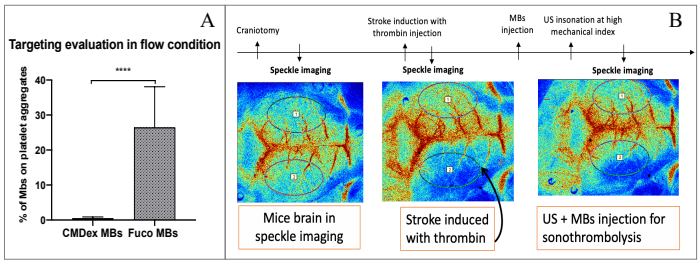

Figures A-B: (A) Targeting efficiency of fucoidan MBs compared to CMDex MBs on platelet aggregate. (B) Stroke model from brain before surgery (left), brain post stroke (center), brain after MBs injection and US treatment (right).

CONCLUSION

We are proud to present our work on an innovative tool for the treatment of thrombotic diseases. We have demonstrated a reproducible synthesis of MBs able to target *ex vivo* activated platelet. Encouraging on going work focuses on the incorporation of the thrombolytic protein (rtPA) with various chemical reactions like adsorption or EDC/NHS. The quantification of this grafting is performed with the evaluation of the amidolytic and fibrinolytic property of the protein, to obtain a full theragnostic tool. *In vivo* validation is also established to validate the live targeting in fluorescence macroscopy and final sonothrombolysis experiment will be performed on the mouse stroke model.

REFERENCES

1. Zenych A. *et al.*, Biomaterials.258, 120297, 2020
2. Li B. *et al.*, Biomaterials. 194:139-150, 2019
3. Kooiman K. *et al.*, Ultrasound Med. Biol. 46, 1296-1325, 2020

ACKNOWLEDGMENTS

This work is supported by the ANR-20-CE18-0005-01 FightClot and ED MTCI doctoral school grant 2019.

ANNEX 12

Ultrasound responsive microbubbles for the targeted treatment of stroke

Louise J. Fournier[1*], Myriam Abioui-Mourgues[3], Cyrille Orset[3], Rachida Aid[1,2], Georges Chabouh[4], Olivier Couture[4], Cédric Chauvierre[1]
[1]Inserm U1148, LVTS, Université de Paris Cité, Bichat Hospital, Paris, France. [2]UMS34 FRIM, Université de Paris, Paris, France. [3]Inserm U1237, CYCERON, Université Caen Normandie, Caen, France. [4]UMR 7371-U1146, Laboratoire d'Imagerie Biomédicale, Sorbonne Université, Paris, France

INTRODUCTION

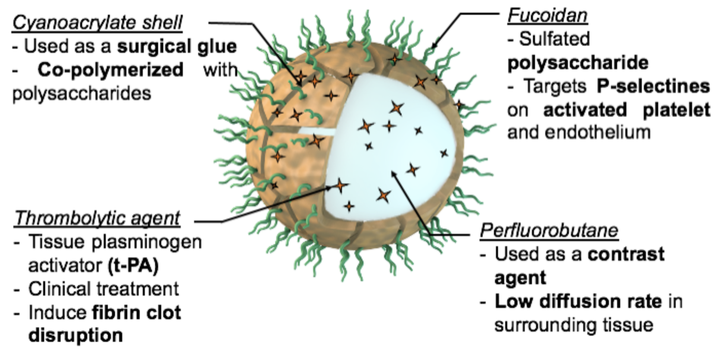

This work aims to overcome the unmet medical need for an **efficient, targeted treatment of stroke**. Indeed, the gold standard for pathological blood clot treatment consists in the **systemic injection** of a thrombolytic agent (tissue Plasminogen Activator). Unspecific delivery implies major **collateral risks like bleeding** and **dose related neurotoxicity**.

We developed **ultrasound responsive microbubbles** with an innovative synthesis method of **acoustic cavitation**. The specific **affinity of fucoidan for P-selectines** on activated platelet brings a major advantage for the **targeted delivery of the thrombolytic agent**. This study presents the latest results with an ***in vivo* stroke model**.

CONCLUSION AND PERSPECTIVES

The **efficient encapsulation of the thrombolytic agent** onto targeted MBs allowed a **specific drug delivery** on the stoke site. The **MBs treatment significantly reduced the infarct size** on a mouse model compared to gold standard free thrombolytic injection. Furthermore, the encapsulated dose corresponded to **1/10 of the mouse treatment indication**. This gives high hopes to **reduce the efficient dose threshold** and thus limit dose related neurotoxicity.

MBs response to ultrasound (US) insonnation for **imaging and self-bursting** now gives perpective for the establishement of **molecular imaging and sonothombolysis**.

Sonothrombolysis

Acknowlegments

This work is funded by ANR-20-CE18-0005-01 "FightClot" and we acknowledge Université de Paris Cité and the MTCI doctoral school for the PhD grant.

METHODS

Acoustic cavitation MBs synthesis

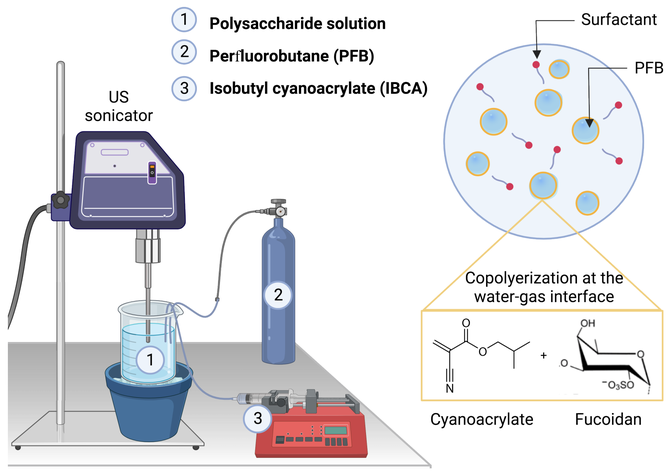

Stroke model

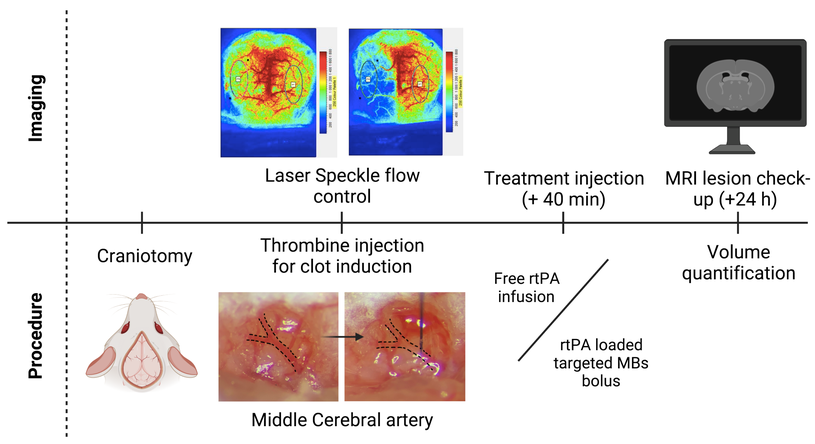

RESULTS

Thrombolytic activity evaluation after incorporation onto MBs

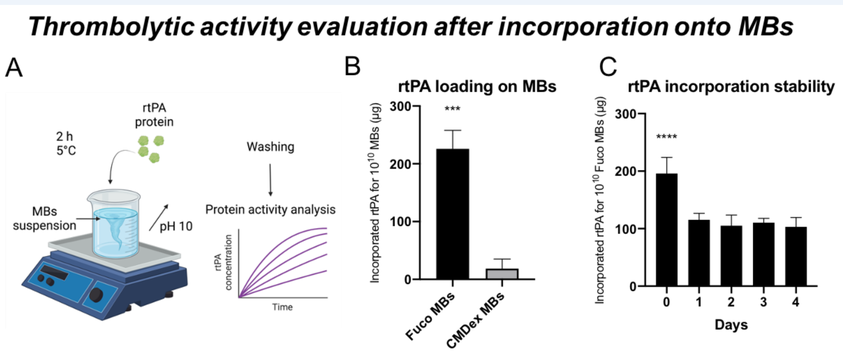

Flow chamber targeting evaluation of targeted MBs

- Thrombolytic drug incorporation: 2 hours **adsorption protocol** (A).
- The drug activity measurement demonstrated the **high incorporation of rtPA onto Fuco MBs** compared to control CMDex MBs due to the sulfated groups (B). Also, the incorporation was **stable over 4 days** (C).
- The targeting property was evaluated with **microfluidic chips,** allowing the formation of **platelet aggregates**. After washing, **targeted MBs (Fuco MBs) showed a high affinity** for the aggregates (D) compared to control MBs (E), **even after drug encapsulation** (F).

- Ischemic lesions were observed 24 hours after treatment either with **saline infusion, rtPa infusion or rtPA loaded targeted MBs.**
- Significant **infact size reduction** was demonstrated for the **rtPA loaded targeted MBs** (A).
- Ischemic lesions present **white contrast on MRI** images (B).

Ischemic lesion measurement after stroke treatment

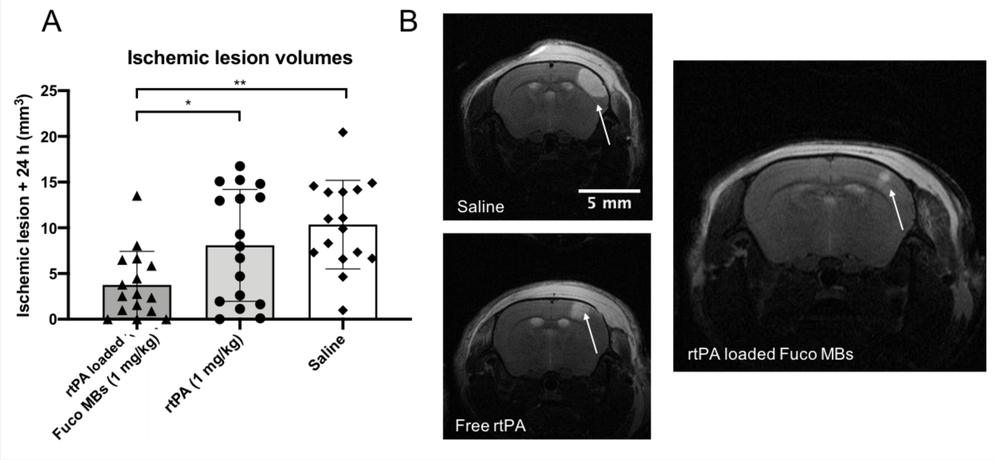

Biodistribution evaluation of fluorescent MBs after stroke treatment

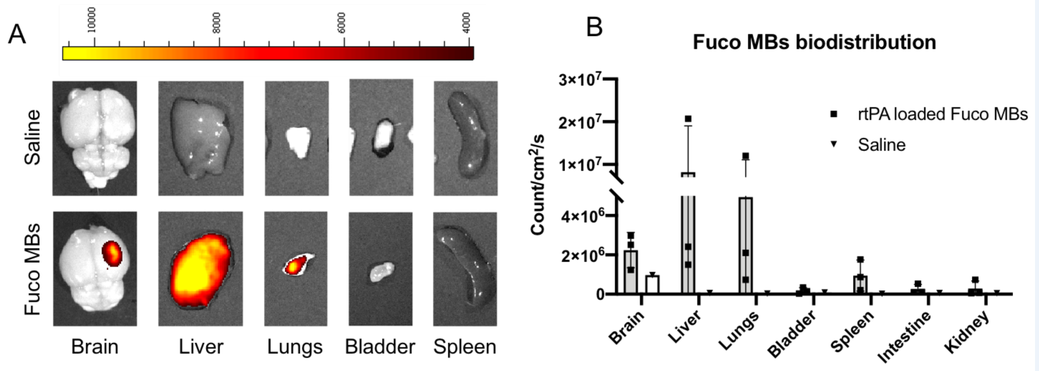

- Fluorecent macroscopy of ***ex vivo* organs** allowed tracking of **fluorescent MBs** after 24 hours.
- Majority of fluorescence was observed in **liver and lungs** (B).
- High affinity for the **stroke region** pointed out the **targeting properties of rtPA loaded Fuco MBs** (A).

*Contact :
louise.fournier@inserm.fr

Created with BioRender Poster Builder

ANNEX 13

Université Paris Cité

Institut des Sciences Cardiovasculaires

Cardiovascular Sciences
GRADUATE SCHOOL

Certificate of Best Poster Presentation

Is presented to

biotechne

Louise Fournier

For their outstanding presentation in the Early Career Research Congress

Awarded on Dec 9, 2022

9-12- 2022

Date

Prof. Jean Sebastian

Signature